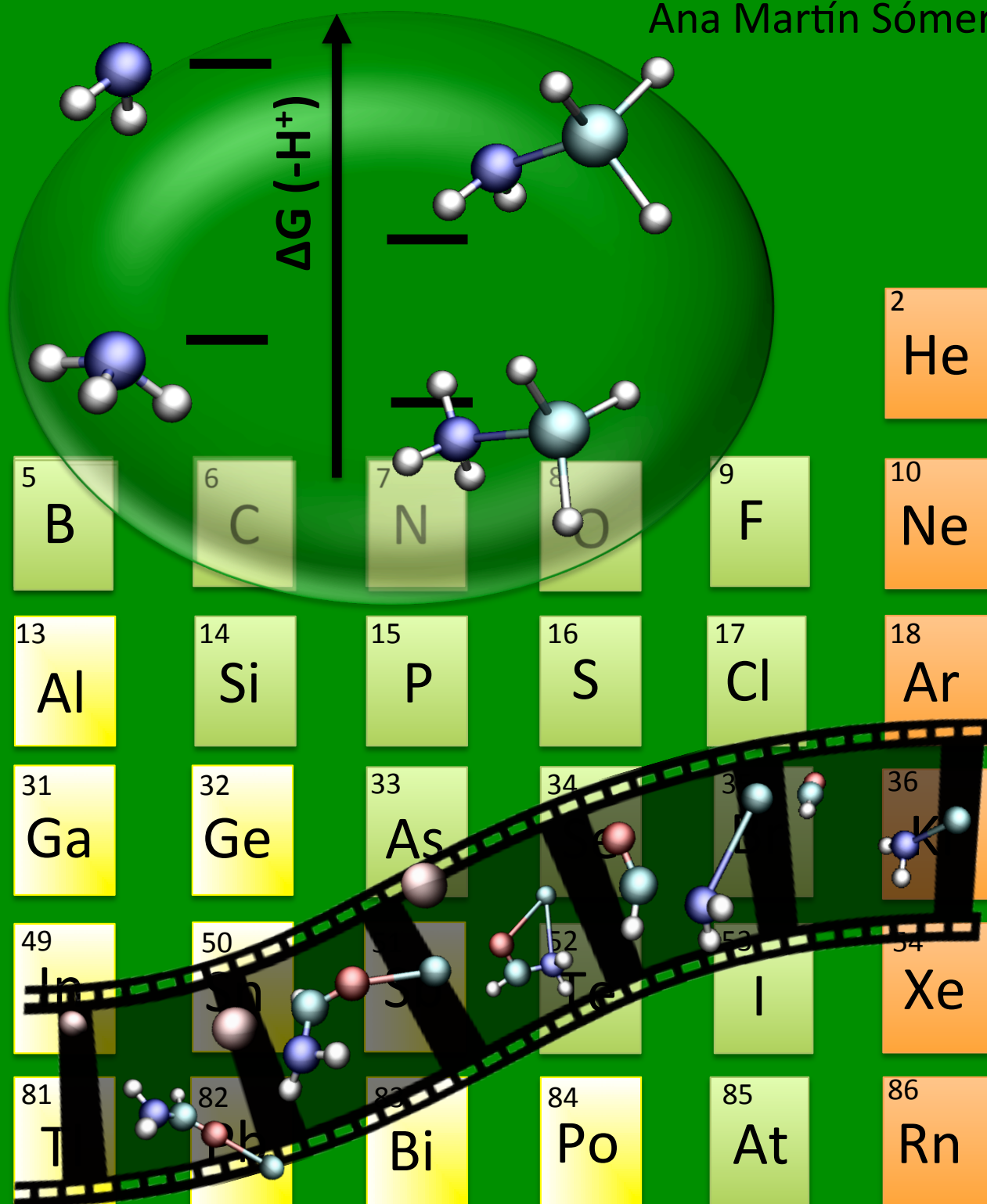


Gas-phase reactivity of Lewis adducts and model biochemical systems.

Quantum chemistry and molecular dynamics perspectives.

Ana Martín Sómer



Gas-phase reactivity of Lewis-adducts and model biochemical systems. Quantum chemistry and molecular dynamics perspectives.

Ana Martín Sómer



Supervisor:
Manuel Yáñez



Supervisor:
Riccardo Spezia

Don't gain the world and lose your soul
wisdom is better than silver and gold.

Agradecimientos

En primer lugar me gustaría agradecer a mi director, Manuel Yáñez, al igual que a Otilia Mó por la oportunidad que me han dado de realizar esta tesis doctoral en su grupo y por la amabilidad y simpatía con la que me han tratado siempre, así como por la ayuda prestada durante estos cuatro años de duro trabajo.

I'm also deeply grateful to Riccardo Spezia, my Italian supervisor in France, for the long hours it has spent teaching me the world of dynamics simulations and his endless patience.

Agradezco calurosamente a los miembros del tribunal, la Dra. Sodupe, Dr. Alcamí, Dr. Spezia, Dra. Barrientos y al Dr. Saulo Vázquez, haber aceptado formar parte del mismo y por tanto armarse de paciencia y consagrar parte de su tiempo y energía a una lectura crítica de éste manuscrito.

También quiero agradecer a todos los compañeros del Departamento de Química, el estar siempre dispuestos a echarme una mano. Y puesto que no todo es trabajo, también he de mencionar los buenos ratos y las experiencias que he vivido junto a ellos. Especialmente con Mai, mi compañera de viajes, habitación, despacho y muchas cosas más y con Lara con la que este último verano se ha hecho mucho más llevadero incluyendo que gracias a su ayuda pude entregar la tesis a tiempo.

Y como no, a mi familia, por que sin su apoyo y ayuda nunca podría haber llegado hasta aquí. Y a todos mis amigos que siempre han estado, están y estarán ahí para ayudarme a desconectar cuando es necesario (y cuando no lo es tanto).

Y último, pero no por ello menos, a Raül y su infinita paciencia, ya que él ha sido el que realmente ha sufrido las consecuencias negativas de esta experiencia.

También tengo que agradecer al Centro de Computación Científica la generosa disponibilidad de tiempo de cálculo, así como a la Universidad Autónoma de Madrid y el Ministerio de Economía y Competitividad por la ayuda FPI para realizar la tesis doctoral, así como por costear los gastos de los viajes y estancias realizados durante la misma.

Résumé

La réactivité à la phase gazeuse, ou *réactivité intrinsèque*, a une grande importance puisque l'absence d'interactions avec un solvant peut donner lieu à une réactivité très différente donc, nous permettant d'avoir une meilleure connaissance des propriétés moléculaires. Avec l'émergence en 1900 de nouvelles techniques expérimentales, plus précisément des techniques pour ioniser plus doucement, la chimie des ions en phase gazeuse s'est développée significativement et a supposé un changement dans l'idée de la réactivité chimique. Cet manuscrit est divisé en deux parties chacune d'elles concernant un aspect différent de la réactivité en phase gazeuse.

La première partie, Part I, étudie l'acidité intrinsèque d'une série de bases de Lewis du group 15 du tableau périodique, l'accent étant mis sur les changements d'acidité ayant lieu après la formation du complexe de Lewis. Divers acides de Lewis appartenant au group 13 ont été tenus en compte. Afin d'expliquer l'origine de l'augmentation d'acidité observée plusieurs méthodes théoriques ont été employées. Pour le calcul de l'acidité intrinsèque on a employé la théorie de la fonctionnelle de la densité (DFT, sigle pour *Density Functional Theory*) et des méthodes qui sont basées sur la fonction d'onde. Pour décrire les variations dans la configuration électronique ayant lieu à la formation du complexe (et qui sont les responsables du changement d'acidité susmentionné) nous avons utilisé des méthodes complémentaires pour l'analyse de la population électronique (AIM, ELF et NBO). Il est important de souligner qu'une partie des résultats présentés dans cet manuscrit ont été déjà corroborés par les résultats expérimentaux.

La deuxième partie, Part II, est centrée sur l'étude de la réactivité unimoléculaire des ions formamide- M^{2+} ($M = Ca, Sr$). Dans ce cas particulier, les ions choisis avaient été déjà étudiés expérimentalement avec la technique de dissociation induite par collision (CID, sigle pour *Collision Induced Dissociation*). Tout au long de cette deuxième partie, nous avons étudié et caractérisé les différents mécanismes de fragmentation des deux ions, en utilisant différentes méthodes théoriques qui sont complémentaires entre eux. Premièrement, on a évalué diverses fonctionnelles afin de trouver la plus appropriée pour maintenir le coût computationnel bas au même temps que d'obtenir des résultats fiables. Ensuite, on a modélisé par moyen de simulations de dynamique la réactivité aux temps courts (< 2.5 femto seconds). En outre, en se servant des données obtenues antérieurement, on a étudié la cinétique de fragmentation avec la théorie statistique RRKM, pour les réactions «lentes» ($t > 2.5$ fs). L'utilisation de cette procédure multi-échelle nous permet de rationaliser l'origine de tous les produits observés expérimentalement ainsi que de donner une explication aux différences entre les deux ions considérés.

Pour finir, dans le quatrième chapitre s'ont énumérés et décrits brièvement les différents méthodes employés au cours de cet travail, tant théorétiques que expérimentaux.

Resumen

La reactividad en fase gas o *reactividad intrínseca*, es de gran importancia ya que la ausencia de interacciones con un solvente puede resultar en una reactividad muy diferente, y permite un mejor concimiento de las propiedades moleculares. Con la aparición en 1900 de nuevas técnicas experimentales, concretamente técnicas de ionización más suaves, la química de iones en fase gas se desarrolló significativamente y supuso un cambio en la idea de la reactividad química. El presente manuscrito está dividido en dos partes cada una de las cuales trata un aspecto distinto de la reactividad en fase gas.

La Parte I estudia la acidez intrínseca de una serie de bases de Lewis del grupo 15 de la tabla periódica, centrándose en los cambios en la acidez que tienen lugar al formarse un complejo de Lewis. Se consideran varios ácidos de Lewis del grupo 13. Con el fin de explicar el origen de este aumento de acidez se utilizan diferentes métodos teóricos. Para calcular la acidez intrínseca empleamos la teoría del funcional de la densidad (DFT) y métodos basados en la función de onda. Para describir los cambios producidos en la configuración electrónica al formarse el complejo (responsables del mencionado aumento de acidez) utilizamos métodos complementarios de análisis de la población electrónica (AIM, NBO y ELF). Es importante destacar que parte de los resultados aquí presentados han sido corroborados mediante técnicas experimentales.

La segunda parte, Part II, se centra en el estudio de la reactividad unimolecular de los iones formamida- M^{2+} ($M = Ca, Sr$). En este caso, los iones habían sido estudiados experimentalmente utilizando la técnica de disociación inducida por colisión, CID. A lo largo de la segunda parte de este manuscrito, estudiamos y caracterizamos los mecanismos de fragmentación de ambos iones, usando distintos métodos teóricos complementarios entre ellos. Primeramente, evaluamos distintos funcionales con el fin de encontrar el más adecuado para realizar cálculos fiables manteniendo el coste computacional lo más bajo posible. Seguidamente, simulamos mediante trayectorias dinámicas la reactividad para tiempos < 2.5 femtosegundos. Por otra parte, utilizando los resultados anteriores estudiamos la cinética de fragmentación usando la teoría estadística RRKM, para las reacciones “lentas” ($t > fs$). El uso de este procedimiento multi-escala nos permite racionalizar el origen de todos los productos observados experimentalmente así como explicar las diferencias entre ambos iones.

Así mismo, en un cuarto capítulo se enumeran y describen brevemente los métodos utilizados a lo largo de este trabajo, tanto teóricos como experimentales.

Abstract

The so-called *intrinsic reactivity* (gas-phase reactivity) is of great importance since the absence of interaction with a solvent can result in very different reactivity patterns; allowing for a better understanding of molecular properties. With the advent in the 1900s of new experimental techniques, notably soft ionization methods such as electrospray ionization, the gas-phase ion chemistry has significantly developed in the last decades of the 1900s with a concomitant change in our view of chemical reactivity. The present manuscript is divided into two different parts each one dealing with different aspects of gas-phase reactivity.

Part I is concerned with the study of the intrinsic acidity of a series of group 15 Lewis bases. The changes on the aforementioned intrinsic acidity as the Lewis bases form adducts with group 13 Lewis acid is the main subject of this part. Thus, the origin for the acidity enhancement observed upon adduct formation is rationalized by means of different theoretical methods. High-level DFT and *ab initio* calculations were performed in order to compute theoretical acidities of the molecules under survey. Complementary to this, population analysis techniques such as AIM, ELF, and NBO were used to analyze the changes on the electronic configurations of those molecules and therefore provide with an explanation to the observed acidities. It is worth to stress the fact that part of the results were as well confirmed by means of experimental measurements.

Part II focuses in unimolecular reactivity of molecular ions, namely, formamide- M^{2+} ($M = \text{Ca}, \text{Sr}$). In this case, experiments studying the Collision Induced Reactivity (CID) of these ions were already performed and through the second part of this manuscript the fragmentation mechanism of both ions are studied and characterized using different, but complementary, theoretical techniques. It is worth to mention that in a very first-step, an assessment of different methods to perform reliable electronic structure calculations while maintaining the lower possible computational cost. On the one hand, a kinetic study of the fragmentation process using the statistical theory, RRKM, to describe the long-time reactivity ($> \text{fs}$). On the other hand, direct dynamics simulations are performed in order to describe the short-time ($< 2.5 \text{ fs}$) non-statistical reactivity. This multi-scale approach allowed us to account for all the products observed in the CID experimental spectra of formamide- M^{2+} ($M = \text{Ca}, \text{Sr}$), as well as the differences between them.

In the fourth chapter a summary of the experimental and theoretical procedures used to perform the work presented in this manuscript is provided.

Contents

Introduction	5
Part I	9
1 Amine-boranes	10
2 Group 13 Lewis acids: BH_3 , AlH_3 and GaH_3	17
3 Group 15 Lewis bases: unsaturate derivatives	31
4 General conclusions	44
5 Lewis acid deformation	45
6 Radicals	49
Part II	51
1 Introduction	51
2 Method assessment	57
3 Direct dynamics simulations	70
4 Coupling RRKM and dynamics	81
5 Conclusions	86
6 Post-Transition State dynamics	88
Methodology	97
1 Theoretical methods	97
1.1 Wave function-based methods.	98
1.2 Atomic basis sets	106
1.3 Density Functional Theory	112
1.4 G4 theory	125
1.5 Population analysis methods	128
1.5.1 NBO: Natural Bond Orbitals	129
1.5.2 AIM: Atoms In Molecules	132
1.5.3 ELF: Electron localization function	137
1.6 RRKM THEORY	142
1.6.1 Introductory remarks	143
1.6.2 Derivation of the RRKM statistical theory	145

1.6.3	Loose TS	151
1.6.4	External rotations	152
1.7	Direct chemical dynamics simulations	155
2	Experimental methods	164
2.1	Collision Induced Dissociation	164
2.2	Cooks kinetic method	166
List of Figures		171
Bibliography		201
Appendix 1		202
Appendix 2		210
Appendix 3		228

Introduction

Gas-phase ion chemistry is a broad field which encompasses various branches of chemistry and physics, from biochemistry to theoretical chemical physics, and which has numerous and diverse applications. The study of gas-phase ion chemistry allows to extract information on the *intrinsic* reactivity and properties of cations or anions in the absence of solvation and counter ion effects. Periodic trends based on, for example, electronic structure or ionic radius can be obtained unambiguously.¹⁻⁵ Reactive intermediates and other chemically exotic species can be generated and studied.⁶ Thus, gas-phase ion chemistry has contributed in remarkable ways towards our understanding of the intrinsic properties and reactivity of a plethora of compounds. The roots of gas phase ion chemistry, perhaps more than those of some disciplines, are found in technique development. Indeed, one of the great strengths of gas-phase ion chemistry is the arsenal of methodologies available for obtaining thermochemical, kinetic and structural information.⁷⁻¹⁰ The last three decades have witnessed an enormous growth in the field of gas-phase ion chemistry,¹¹ motivated in great measure by the the development of soft ionization methods, and notably since the advent of electrospray ionization techniques in 1990.¹²

Another scientific area whose development is intimately linked to technological advances is computational chemistry. From the early 1950s when the first semi-empirical atomic orbital calculations were carried out, the astonishing development of digital computers over the last 45 years or so, together with the development of more powerful algorithms among other reasons, have made of computational methods a powerful tool for determination of molecular structures and properties. The approach is particularly useful where experimental data are difficult to obtain, such as when the system under examination is very weakly bound, highly unstable, or very short lived. Computations are able to reproduce experimental findings very accurately for relatively small molecules. For larger systems or computing time demanding methods, qualitative features usually agree very well with experiment. The real advantage of quantum chemical calculations lies in the very detailed,

INTRODUCTION

sometimes experimentally inaccessible information on molecular properties (energies, dipole moments, polarizabilities, charges, vibrational frequencies, rotational constants, etc.) afforded by the scrutiny of the solutions of the electronic Schrödinger equation. Gas phase ion chemistry is a field showing a particularly rich interplay between experimental and computational chemistry, and few areas of chemistry can probably rival the synergism between theory and experiment.

In summary, with the continuing improvements in instrumentation, ionization sources, and theoretical calculations; and with no obvious end to the types of interesting problems which can be studied, the field of gas-phase ion chemistry remains an active and exciting one.

In this manuscript gas-phase reactivity of Lewis-adducts and model biochemical systems are studied applying a variety of different techniques. It is divided in two parts. The first one, Part I, is concentrated on the study of intrinsic acidities, hence it implies the study of negative ions. In the second part we turn our attention to a different problem concerning reactivity of doubly charged cations in gas-phase. Throughout each part, combination between different theoretical approaches and experimental results will be sought with the aim of providing with a view of the subject as a whole.

As above mentioned, the first part focus on the investigation of the gas-phase acidities of a series of group 15 Lewis bases and the changes induced on their intrinsic acidity by Lewis acid (BeH_2 , BH_3 , AlH_3 , and GaH_3) complexation. This is done by means of high-level G4 *ab initio* calculations and Density Functional Theory (DFT) methods. The association with any of the Lewis acids considered leads to a significant acidity enhancement (see Fig. 1). In terms of the acidity constant, this increase can be as high as 40 orders of magnitude. To study the origin of this acidity enhancement the electron density rearrangements undergone by the Lewis acid and the Lewis base moieties upon adduct formation were analyzed by means of the complementary AIM, ELF, and NBO electronic density distribution analysis approaches. The dependence of the acidity enhancement observed on the nature of the Lewis acid, the active center of the Lewis base and the R substituent of the latter is also analyzed.

This part employs electronic structure methods, *i.e.*, a static approach. Such approach is perfectly suitable for processes thermodynamically controlled where the final products correspond to the most stable ones. However, there are many processes for which this is not the case. When reactions are

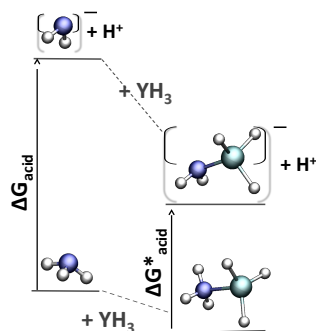


Figure 1: Schematic representation of the gas-phase acidity enhancement upon Lewis adduct formation.

conducted under conditions that do not allow the products to equilibrate one talks about kinetic control. The reactant(s) face(s) a number of competitive reaction paths and the one with the lowest standard free energy of activation will be favored (see Fig. 2). On the other hand, it has also been observed that for many reactions (and the number of cases is growing),¹³ kinetic selectivity does not reduce to a simple choice between paths with different barrier heights, and there are other factors, dynamical factors, coming into play to determine the relative abundance of the final products.

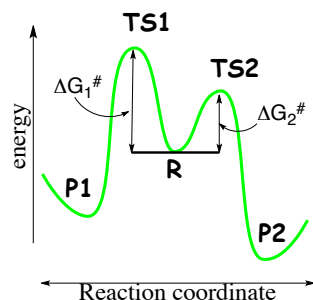


Figure 2: The classical reaction coordinate diagram to explain product selectivity (P1, P2) based on relative heights of the transitions states (TS1, TS2) associated to the competing reaction pathways. Taken from ref.¹³

To describe each of the “controlling factors” mentioned above, there exists some methodologies more suitable than others. Thus, for thermodynamically controlled processes the adequate electronic structure method is enough to discriminate between the different possible products and to describe the fac-

INTRODUCTION

tors favoring one product over the other(s). In this case, mechanisms are irrelevant to the product ratio. For instance, this was the case for the properties studied in the first section of this thesis (Part I). For kinetically controlled reactions statistical theories such as transition state theory¹⁴ (TST) or Rice-Ramsperger-Kassel-Marcus¹⁵ (RRKM) theory are widely used in order to predict and explain the experimental product ratio. One of the main assumptions of these theories is that the energy that the molecule have to react (it is not important how the molecule did acquire it) is completely distributed within the internal modes of the molecule. When this assumption does not hold, for instance if the way of exciting the molecule (where the energy is initially located) is key to determine the reaction course; it is necessary to resort to dynamics simulations.

When this assumption does not hold and the way of exciting the molecule, in that where the energy is initially located, is key to determine the reaction course and the mechanism involved, reactivity can only be understood by means of dynamical simulations.

Throughout Part II such a case is presented, *i.e.*, static methods fail to correctly, or fully, describe the reactivity of the molecules considered. Statistical approaches are able to partially account for that reactivity, but again, there are some loose ends. Dynamical simulations answer the questions that were not resolved with the previous approaches. However, if this method was to be used alone, it would have also been impossible to completely explain the reactivity of the process of interest. Thus, it is the combination of the three approaches that allows to correctly explain the phenomenon under survey.

PART I

Although noncovalent interactions play a significant role in nature,^{16–19} and they are present in most of the known molecular assemblies, there is not a clear-cut definition of them.²⁰ Typically, most of these interactions, such as hydrogen bonds,^{21–28} halogen bonds,^{29–32} beryllium bonds,³³ metal ion–molecule complexes,^{34–46} van der Waals complexes,^{47–51} etc., involve closed-shell species. This would permit a first distinction between noncovalent interactions and typical covalent bonds which usually involve the interaction between open-shell systems. Nevertheless, in most of the aforementioned examples of noncovalent interactions, some charge polarization between the two interacting moieties takes place. This partial charge transfer goes from the lone pair of one of the interacting subunits, which behaves as a Lewis base, toward empty orbitals of the other interacting subunit, acting as a Lewis acid. These charge donations can be very strong in those cases in which the electron acceptor has low-lying empty orbitals and therefore behaves as a strong Lewis acid. This is typically the case of group 13 hydrides, YH_3 , $\text{Y} = \text{B}, \text{Al}, \text{Ga}$, and their derivatives; in which the Y atom has empty low-lying $2p$ orbitals, which easily accept electrons from the lone pair of a Lewis base, leading to a strong interaction usually known as a dative bond. This charge transfer obviously implies a certain redistribution of the electron density of both interacting subunits. The charge redistribution results in changes in the chemical properties of the interacting subunits, changes that affect, in particular, their intrinsic reactivity. A paradigmatic example is the change that phosphines undergo when they interact with BH_3 to form the corresponding phosphine–borane adduct. Both the physical and the chemical properties of the phosphine change.⁵² Whereas the isolated phosphines have low stabilities and are pyrophoric, phosphine–boranes are rather stable solid compounds.⁵² Also, whereas isolated phosphines are weak acids in the gas-phase, phosphine–boranes exhibit an intrinsic acidity, which in terms of the acidity constant, is 17 orders of magnitude greater than that of the isolated phosphine.⁵² Similar acidity enhancements were also reported for complexation involving Lewis bases other than phosphines⁵³ and BF_3 as Lewis acid.⁵⁴

Thus, the aim of this part is to study, through the use of high-level wave function and density functional approaches, the effects that Lewis complexation have on the intrinsic properties of a series of Lewis bases. More specifically we will focus on the changes that the Lewis acid triggers in their intrinsic acidity. The Lewis bases considered are amines, phosphines, arsines and stibines with several substituents. The Lewis acids are BH_3 , AlH_3 , GaH_3 and BeH_2 .

1 Amine-boranes

Perhaps, the most prototypical example of Lewis acid–base reaction is that of amines with boranes.^{55,56} Compounds containing dative bonds between boron and nitrogen have been known since the early 19th century. The first compound of this type, ammonia-trifluoroborane, $\text{H}_3\text{N}-\text{BF}_3$ was prepared in 1809 by Gay-Lussac⁵⁷ and also represented the first coordination compound of any type. A long period of time since its discovery past before the first amine–borane containing only hydride substituents, $\text{Me}_3\text{N}\cdot\text{BH}_3$, was synthesized in 1937.⁵⁸ Since then, the number of reported primary, secondary, and tertiary amine–borane adducts started to grow rapidly.

Historically and to the present day, the most widespread applications of amine–borane adducts are based on their reducing ability, either for uses in organic reactions or in electroless plating process, or as easy to handle borane reagents for hydroborations. On the other hand, recent developed uses of amine–boranes are as precursors to inorganic polymers and as interesting ligands with novel bonding modes.⁵⁹ In addition to this, during the last decade, the use of ammonia–borane as a potential portable hydrogen storage material has attracted a surge of interest as a result of the high hydrogen content (19.6 wt %).⁶⁰ In 2006, sterically hindered amino-boranes were shown to exhibit unexpected reactivity, including the heterolytic cleavage of various bonds, most notably that of dihydrogen.⁶¹

Amine–borane adducts are also used for technical applications as stabilizers in polymer formulations, the bleaching of wood pulp, photographic applications, and as fuel additives.⁶² Based on the polarity of the N–B bond amine–boranes may have applications as liquid crystal lead structures.⁶³ Although not a direct application of amine–borane themselves, the formation of a borane adduct of an existing amine can be used to protect the amine

1. AMINE-BORANES

and often enables alternative chemistry to be performed. For instance, if the masking of an amine’s nucleophilic properties is required, borane can serve as a protecting group. Furthermore, complexation of an amine with a borane may lead to a change in selectivity for further reactions with the amine.⁶⁴ Novel coordination modes for amine–borane adducts are of fundamental interest for the understanding of catalytic dehydrogenation, dehydrocoupling, or cross-coupling reactions, thereby enhancing the potential for improved system design. A fundamental understanding of the intrinsic properties of such adducts allows to improve the design of new systems with the required properties for the desired application. The potential to gain further insight into the bonding in main-group complexes provides further motivation for the investigation of this interesting class of compounds.

Hence, our aim is to study the changes undergone on the intrinsic properties of a series of amines when they complex with BH_3 , more specifically we will focus on the changes in their intrinsic acidity. Herein, we show, using a combined experimental and theoretical study, that typical conventional bases such as aniline become acidic—with acidities as high as phosphoric acid—when they form complexes with borane, whereas the acidity of other nitrogen bases, such as dimethylamine, aziridine, and cyclopropylamine, becomes as high as that of formic, acetic, and propionic acids.

To experimentally determine the gas-phase acidity, deprotonation enthalpy, and deprotonation entropy of the amine–borane complexes under survey, the “extended Cooks kinetic method ” (EKM)^{65–73} was used. More details about the EKM method are given in the methodology section. Concerning the computational approach employed, we need to use a reliable model in order to analyze the electronic changes undergone by the Lewis acid and base when they interact. The first requirement to ensure the reliability of the model is a good agreement between the measured and calculated gas-phase acidities. This will provide an indirect evidence that the structures used in the calculations, for both the neutral and the deprotonated systems, are the same as those being probed experimentally. For this reason we used a high-level *ab initio* approach, that is, the one based on the G4 theory, which has been shown to provide very accurate values for the enthalpies of various reactions.⁷⁴ The G4 methodology may be too intensive when investigating very large systems. Thus, we have also assessed the performance of a “cheaper” model, based on the use of the B3LYP^{75,76} density functional. This approach has been shown to perform very well for the calculation of the intrinsic acidities of phosphine-borane complexes.⁵² Within this model, the geometries are optimized using a 6-31+G(d,p) expansion and the final

1. AMINE-BORANES

energies are obtained in single-point calculations using the aforementioned optimized geometries and a 6-311++G(3df,2p) basis set. All these calculations have been carried out using the Gaussian09 suite of programs.⁷⁷

Since one of the main parts in the bonding between amines and borane is the dative bond formed upon the transfer of electron density from the lone pair of the nitrogen atom of the amine to the empty $2p$ orbital of BH_3 , the NBO approach, as implemented using the NBO-5G suite of programs,⁷⁸ is particularly well suited to describe these interactions. Within the NBO framework it is also possible to calculate the Wiberg bond order.⁷⁹ A complementary description of the bonding in amine-borane complexes can be obtained by means of the atoms in molecules⁸⁰ (AIM) and the electron localization function^{81,82} (ELF) theories. The AIM and ELF calculations were performed with the AimAll⁸³ and the TopMod⁸⁴ packages, respectively.

The calculated and measured gas-phase acidities for the free amines and the corresponding amine-borane complexes, measured as the Gibbs free energy associated with the reaction 1 are summarized in Table 1. In all the cases, it is assumed that the proton is lost from the NH_2 group.



For the sake of completeness, this table also includes the gas-phase acidities of the free amines. Only for some of the amines considered here are the experimental gas-phase acidities known. Unfortunately, the EKM method used in this work is not well suited to measure the acidity of very weak acids, such as the amines. Nevertheless, it is worth noting that for those cases in which the experimental acidity is known, the agreement with our G4-based calculated values is excellent, and therefore, our estimates for the unknown gas-phase acidities should be accurate. This agreement between experimental and calculated values is also excellent for the gas-phase acidities of amine-borane complexes. The agreement is somewhat worse when the B3LYP values are used, values that are, in general, slightly lower than the experimental values. Nevertheless, there is a reasonably good linear correlation between the B3LYP/6-311+G(3df,2p) gas-phase acidities and the G4-based calculated values (Fig. 3), and therefore, in the case where the gas-phase acidities of larger amine-borane complexes needs to be estimated, the theoretical model employed here can be used as a good alternative to G4 theory, which may be prohibitively expensive.

1. AMINE-BORANES

Table 1: Experimental and G4-based calculated gas-phase acidities, ΔG_{acid}^0 [kJ mol⁻¹], for several amines and the corresponding amine-borane complexes; $\Delta\Delta G_{acid}^0$ [kJ mol⁻¹] is the increase in acidity on going from the free amine to the amine-borane complex. All values in kJ mol⁻¹.

Amine	ΔG_{acid}^0		$\Delta\Delta G_{acid}^0$ calc.
	Free amine	Amine-borane complex	
	calc.(exptl. ^a)	calc. ^b (exptl.)	
ammonia	1657.2(1656.8±1.6)	1462.1[1456.7]	195.1
methylamine	1656.1(1651±11.0)	1462.4[1455.2](1461.0±9.2)	193.7
dimethylamine	1621.8(1623±8.8)	1453.7[1444.4](1457.9±9.2)	168.1
allylamine	1616.5	1444.2[1437.4](1443.7±8.8)	172.3
cyclopropylamine	1618.3	1447.3[1442.1](1440.5±9.2)	171.0
benzylamine	1588.9	1438.1[1435.5](1436.7±8.9)	150.8
aziridine	1603.3	1435.5[1432.2](1443.4±8.9)	167.8
propargylamine	1608.8	1431.1[1425.4](1435.1±8.9)	177.7
trifluoroethylamine	1579.4	1400.5[1393.5](1405.0±9.4)	178.9
aniline	1506.7(1502±8.4)	1360.3[1353.6](1365.7±9.4)	146.4

^aValues taken from ref.⁸⁵

^b Values within brackets were obtained at the B3LYP/6-311+G(3df,2p)//B3LYP/6-31+G(d,p) level.

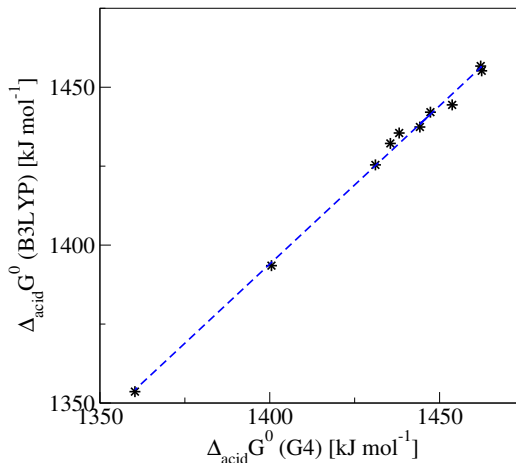


Figure 3: Linear correlation between the B3LYP and G4 calculated acidities for amine-boranes.

Active center for deprotonation. As previously mentioned, to compute the acidity of the amine-borane complexes it is assumed that deprotonation takes place in the amino group of the complex. The anion so produced is in all cases, except for $\text{PhCH}_2\text{NH}_2\cdot\text{BH}_3$ and $\text{CF}_3\text{CH}_2\text{NH}_2\cdot\text{BH}_3$, the most stable one. For both $\text{PhCH}_2\text{NH}_2\cdot\text{BH}_3$ and $\text{CF}_3\text{CH}_2\text{NH}_2\cdot\text{BH}_3$, the most stable anions correspond to structures in which the proton is lost from the borane moiety (see Fig. 4).

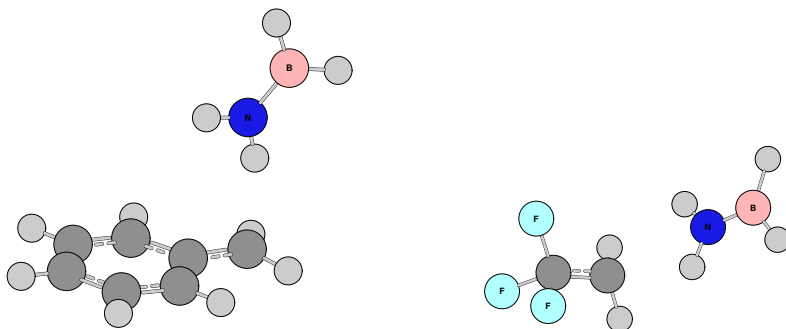


Figure 4: Structure for the most stable anion (B acids) of $\text{PhCH}_2\text{NH}_2\cdot\text{BH}_3$ (left) and $\text{CF}_3\text{CH}_2\text{NH}_2\cdot\text{BH}_3$ (right).

The increased stability of these two structures, which can be viewed as the interaction between a NH_2BH_2 group and either the $\text{C}_6\text{H}_5\text{CH}_2^-$ or the CF_3CH_2^- anions, respectively, just reflects the high stability of both the neutral NH_2BH_2 group and the accompanying anions. Accordingly, these boron-deprotonated structures are predicted to be 22 and 15 kJ mol^{-1} more stable than the corresponding amine-deprotonated species, respectively. Nevertheless, the good agreement between the calculated and experimental values in Table 1 for these two amine-borane complexes seems to indicate that under experimental conditions only the amine-deprotonated species is formed.

To explain this apparent dichotomy we investigated in detail and compared BH_3 and NH_2 deprotonation by using $\text{PhCH}_2\text{NH}_2\cdot\text{BH}_3$ as a suitable example. As illustrated in Fig. 65, the most stable anion (structure **C**) is the result of the dissociation of the borane-deprotonated species **B**, which involves a barrier (transition state, **TS_{BC}**) of 100 kJ mol^{-1} . However, direct deprotonation of the BH_3 group of $\text{PhCH}_2\text{NH}_2\cdot\text{BH}_3$ to yield structure **B** is much less favorable (by 300 kJ mol^{-1}) than the direct deprotonation of the amino group to yield anion **A**; this was found to be the case for all other amine-borane complexes investigated herein. It is also worth noting that the

1. AMINE-BORANES

transfer of a proton from the BH_3 group in anion **A** to the N atom, is accompanied by cleavage of the C-N bond. The consequence is that the transition state associated with this proton transfer, namely **TS_AC**, directly connects anions **A** and **C**, through a barrier of 228 kJ mol^{-1} . Hence, in spite of its increased stability, form **C** can only be reached through a very energetically demanding processes, from either structures **A** or **B**.

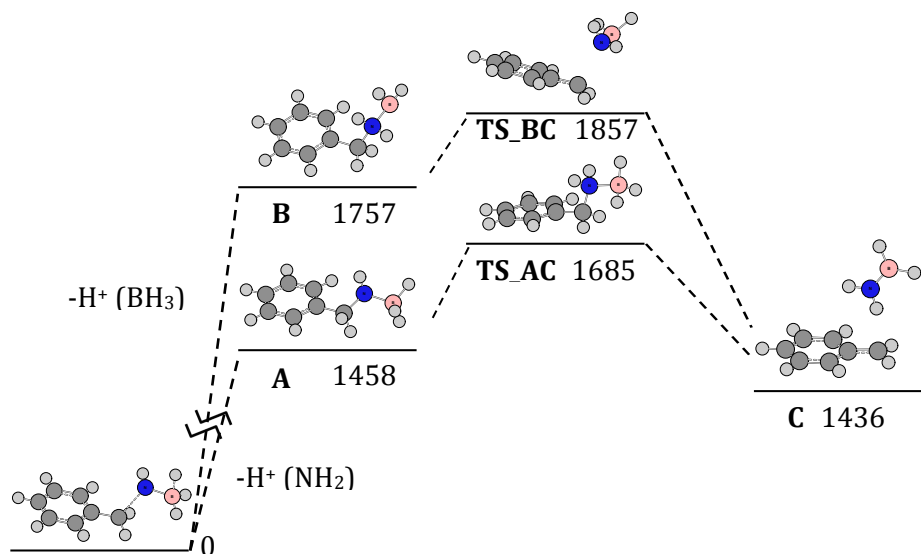


Figure 5: Energy profile of the NH_2 and BH_3 deprotonation processes of benzylamine- BH_3 . All values in kJ mol^{-1} .

In addition, an examination of the molecular electrostatic potential of both benzylamine and $\text{CF}_3\text{CH}_2\text{NH}_2$ shows that for both molecules the positive potential areas (blue) are those close to the amino group (Fig. 6). This means that the association of the molecule with the reference anion takes place at the amino group and never at the BH_3 group; the interaction of the latter with the attacking anion would be highly repulsive because of the hydride character of the BH_3 hydrogen atoms. These data are consistent with the much less favorable deprotonation of the BH_3 group. Hence, under normal experimental conditions, the deprotonation of the amino group will be always favored and, as indicated above, its conversion into the more stable structure **C** would not take place because the transformation would involve a very high activation barrier.

1. AMINE-BORANES

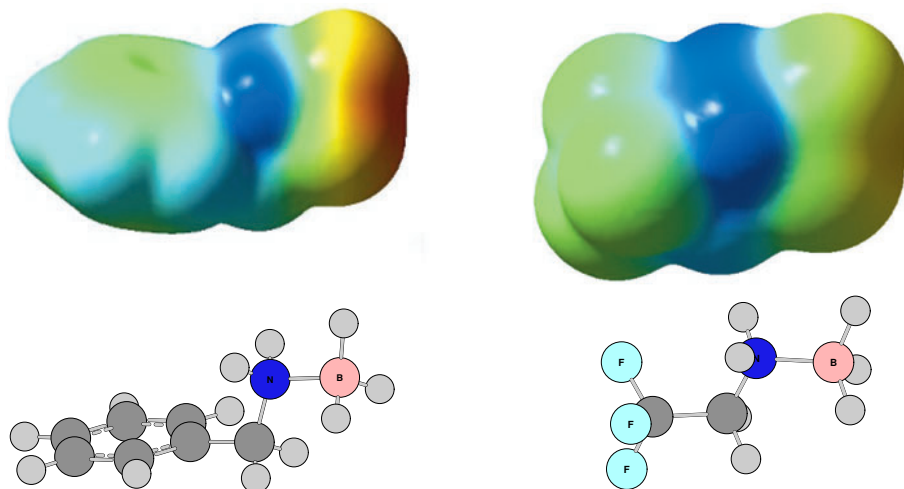


Figure 6: Molecular electrostatic potential of $\text{PhCH}_2\text{NH}_2\cdot\text{BH}_3$ (left) and $\text{CF}_3\text{CH}_2\text{NH}_2\cdot\text{BH}_3$ (right). Blue areas correspond to positive values of the potential, whereas red areas correspond to negative values of the potential.

Acidity enhancement. The first conspicuous fact from the values in Table 1 is the significant increase of the acidity on going from the free amine to the corresponding amine-borane complex. The acidity enhancement is around 180 kJ mol^{-1} and depends on the nature of the group attached to the nitrogen atom. For instance, whereas deprotonation of ammonia and methylamine borane leads to similar values of acidity enhancement ($\Delta\Delta_{\text{acid}}^0 \approx 190 \text{ kJ mol}^{-1}$), deprotonation of dimethylamine borane leads to an acidity enhancement about 25 kJ mol^{-1} lower. Also, smaller increases in acidity are observed for aniline and benzylamine complexes. Nevertheless, it is worth stressing that the increase in acidity that occurs upon coordination of the amines with borane is very large. Aniline borane has practically the same gas-phase acidity as phosphoric acid ($1351 \pm 21 \text{ kJ mol}^{-1}$)⁸⁵ and most of the amine-borane complexes studied herein have gas-phase acidities similar to typical carboxylic acids, such as formic, ethanoic, and propionic acid.⁸⁵ Furthermore, the increase in acidity measured and calculated herein for amine-borane complexes is significantly larger than that measured and calculated for the phosphine-borane analogues.⁵³ For instance, whereas the increase in acidity observed for phenylphosphine and methylphosphine upon BH_3 association is 78 and 123 kJ mol^{-1} , respectively, the increase in acidities for the amine-borane analogues are almost twice these values, 149 and 191 kJ mol^{-1} , respectively. The origin of this acidity enhancement will be explained below in more detail. Before this, we will study whether the same phenomenon

occurs when the Lewis acid is other than BH_3 .

Conclusions. Before starting the following section let us briefly summarize the most important findings of this part. From our combined experimental and theoretical survey we conclude that the complexation of different amines with BH_3 leads to new compounds (amine-borane complexes), which exhibit a much larger gas-phase acidity. The acidity enhancement depends on the R substituent attached to the NH_2 , going from 146 to 195 kJ mol^{-1} . The unexpected consequence is that typical nitrogen bases such as aniline, lead to amine-borane complexes which, in the gas-phase, are nitrogen acids as strong an acid as phosphoric, oxalic, or salicylic acid, and stronger than many carboxylic acids, such as formic, acetic, and propanoic acids. The agreement between experimental and the G4-based calculated values is excellent. Also there is a good agreement between the G4 values and the values computed using the DFT approach.

Conclusiones. Antes de comenzar la siguiente sección resumiremos brevemente las conclusiones más importantes de lo expuesto hasta ahora. Del estudio tanto teórico como experimental llevado a cabo, se puede concluir que la complejación de diferentes aminas con BH_3 conduce a la formación de nuevos compuestos (amino-boranos), que exhiben una acidez intrínseca mucho mayor que las aminas aisladas. Este aumento de acidez depende de la naturaleza del sustituyente, R, unido al grupo NH_2 y varía entre 146 y 195 kJ mol^{-1} . La consecuencia inesperada de esto es que típicas bases de nitrógeno como la anilina se convierten en amino-boranos que son ácidos de nitrógeno en fase gas tan fuertes como al ácido fosfórico, oxálico o salicílico, y mucho más fuertes que un gran numero de ácidos carboxílicos, como el ácido fórmico, acético o propanoico. La concordancia entre los valores obtenidos experimentalmente y los valores calculados utilizando el método G4 es excelente. También existe una buena concordancia entre los valores calculados mediante el método G4 y los calculados utilizando la teoría del funcional de la densidad (DFT).

2 Group 13 Lewis acids: BH_3 , AlH_3 and GaH_3

The aim of this section is to investigate what would be the effect of replacing borane, BH_3 , by alane (AlH_3) or gallane (GaH_3) in the amine adducts pre-

2. GROUP 13 LEWIS ACIDS: BH_3 , AlH_3 AND GaH_3

viously considered and phosphine analogues. Volatile Lewis base adducts of alane, as well as gallane, have an interesting chemistry and play an important role in a wide range of chemical process.^{86–88} Particularly interesting are their applications on areas as material science. Aluminum hydride derivatives (and borane derivatives) can be used as precursors of AlN / BN materials.⁸⁹ Since their adducts have a volatile behavior, alane and gallane are used in chemical vapor deposition (CVD) technology.^{90,91} Different complexes of AlH_3 with nitrogen bases have been proposed as potential hydrogen storage systems⁹² as well as AlH_3PH_3 .⁹³ Gallium hydride derivatives have been used as molecular precursors to thin films of Ga_2O .⁹⁴ Both gallium and gallium suboxide, Ga_2O , are used to make III-V semiconductors. Lewis base adducts of alane and gallane are also known to have important applications in organic synthesis as selective reducing agents^{95,96} and in the preparation of transition metal aluminum and gallium hydrides.^{97–99} Phosphine-alanes can act as catalysts in many chemical processes.¹⁰⁰ There is consequently a lot of interest in how aluminum and gallium molecules interact with other species.

In order to analyze the effect of AlH_3 and GaH_3 on the intrinsic acidity of amines and phosphines we have selected, as suitable model systems, three different R-NH_2 amines and the phosphorus containing analogues, R-PH_2 . The R substituents have been chosen to represent three different situations: an alkyl group (methyl), a saturated non-aromatic ring (*c*- C_3H_5), and an aromatic ring (phenyl). To the aforementioned three amines (phosphines) we have added NH_3 (PH_3) as a good reference system and due to the numerous potential applications these molecules present. Thus we will compute the gas-phase acidities of $\text{RNH}_2\cdot\text{AlH}_3$, $\text{RPH}_2\cdot\text{AlH}_3$, and $\text{RPH}_2\cdot\text{GaH}_3$ Lewis complexes. Then, the values obtained will be compared with those previously reported for the analogues amine-boranes and phosphine-boranes. In this way, we will try to understand the behavior of group 13 trihydrides compounds as Lewis acids.

As shown in the previous section, the B3LYP model is a good alternative to the use of G4 when computing gas phase acids of this kind of Lewis adducts. Thus, we optimized the geometries and computed the thermodynamical data at the B3LYP/6-31+G(d,p) level of theory and the final energies were obtained in single-point calculations at 6-311++G(3df,2p) level. The intrinsic acidities thus calculated for the free amines and the corresponding adducts are listed in Table 2. Table 3 lists the corresponding values for the phosphorus derivatives. In all the cases, it is assumed that the proton is lost from the heteroatom. In order to make easier the comparison between the different adducts, gas-phase acidities for amino-boranes and phosphine-

2. GROUP 13 LEWIS ACIDS: BH₃, ALH₃ AND GAH₃

boranes were also included in Tables 2 and 3, respectively.

Table 2: B3LYP-calculated acidity ($\Delta_{acid}G^0$, kJ mol⁻¹) and acidity enhancement ($\Delta\Delta_{acid}G^0$, kJ mol⁻¹) for R-NH₂ amines and the corresponding R-NH₂·BH₃ amine-boranes and R-NH₂·AlH₃ amine-alanes.

R	$\Delta_{acid}G^0$			$\Delta\Delta_{acid}G^0$	
	Free	Complex		Complex	
	RNH ₂	BH ₃	AlH ₃	BH ₃	AlH ₃
H	1656.3(1656.8±1.6) ^a	1456.7	1398.3	199.6	258.0
CH ₃	1646.5(1651±11.0) ^a	1455.2	1406.3	191.3	240.2
<i>c</i> -C ₃ H ₅	1610.9	1442.1	1386.6	168.8	224.3
C ₆ H ₅	1503.1(1502 ±8.4) ^a	1353.6	1321.7	149.5	181.4

^aExperimental value taken from ref.⁸⁵

Table 3: B3LYP-calculated acidity ($\Delta_{acid}G^0$, kJ mol⁻¹) and acidity enhancement ($\Delta\Delta_{acid}G^0$, kJ mol⁻¹) for R-PH₂ phosphines and the corresponding R-PH₂·AlH₃ phosphine-boranes, R-PH₂·BH₃ phosphine-alanes, and R-PH₂·GaH₃ phosphine-gallanes.

R	$\Delta_{acid}G^0$				$\Delta\Delta_{acid}G^0$		
	Free	Complex			Complex		
	RPH ₂	BH ₃	AlH ₃	GaH ₃	BH ₃	AlH ₃	GaH ₃
H	1504.1(1509.7±2.1) ^a	1384.0	1325.5	1341.7	120.1	179.2	163.0
CH ₃	1533.3(1530.0±2.5) ^b	1410.2 ^c	1359.3	1373.3	123.1 ^c	174.0	160.0
<i>c</i> -C ₃ H ₅	1515.4(1510.0±3.0) ^b	1402.0 ^c	1352.1	1372.8	113.4 ^c	163.3	142.6
C ₆ H ₅	1457.0(1457.3±0.8) ^b	1379.1 ^c	1324.6	1339.5	77.9 ^c	132.4	117.4

^aExperimental value taken from ref.¹⁰¹ ^bExperimental values taken from ref.⁵² ^cCalculated values taken from ref.⁵²

As found for amino-borane complexes, the adducts considered in this section behave as heteroatom (N or P) acids in the gas phase. For example, for the CH₃PH₂·AlH₃ adduct, the C-H deprotonation and the Al-H deprotonation processes are 138 and 201 kJ mol⁻¹, respectively, less favorable than the P-H deprotonation. The corresponding C-H and Ga-H deprotonation of the

2. GROUP 13 LEWIS ACIDS: BH_3 , AlH_3 AND GaH_3

$\text{CH}_3\text{PH}_2\cdot\text{GaH}_3$ adduct are 128 and 153 kJ mol^{-1} less favorable.

For all the molecules considered, and as in the case of the amine-borane complexes, a significant increase of the acidity of the Lewis base is systematically observed when the Lewis adduct is formed, both with alane, AlH_3 , and gallane, GaH_3 (see Tables 2 and 3). Quite unexpected, however, the acidity enhancement predicted for the amine-alanes is significantly larger than that measured for the amine-boranes, around 30%. Accordingly, aniline-alane is predicted to be ca. 30 kJmol^{-1} more acidic than aniline-borane. The consequence is that aniline-borane would become a stronger acid in the gas-phase than phosphoric acid ($1351\pm 21 \text{ kJ mol}^{-1}$)!⁸⁵ Also the acidity enhancement predicted for AlH_3 when forming complexes with phosphines is larger, about 45% and 30%, than that induced by BH_3 or GaH_3 , respectively. This is particularly the case for PhPH_2 where the acidity enhancement triggered by alane is 70% larger than that induced by borane. As for the amine-borane complexes, the acidity enhancement depends on the nature of the R group attached to the heteroatom (N,P). For instance, the acidity enhancement is notably larger for $\text{R} = \text{CH}_3$ or *c*-propyl than for $\text{R} = \text{Ph}$. From Tables 2 and 3 we also concluded that the increase of the gas-phase acidity upon Lewis acid complexation is always larger for amines than for the phosphine analogues. Hence, for the same R, the calculated acidity enhancement follows the trend $\text{RNH}_2\cdot\text{AlH}_3 > \text{RNH}_2\cdot\text{BH}_3 > \text{RPH}_2\cdot\text{AlH}_3 > \text{RPH}_2\cdot\text{GaH}_3 > \text{RPH}_2\cdot\text{BH}_3$, no matter the nature of R. These results raise the following questions: why is the effect of AlH_3 or GaH_3 on the intrinsic acidities larger than that observed upon BH_3 complexation? Why does this effect depend significantly on the nature of the R substituent? Or, why is this effect different for amines than for phosphines? In order to answer these questions it is first necessary to understand why the acidity of the Lewis base is enhanced when it associates with the Lewis acid Y.

Origin of the acidity enhancement. To explain the origin of the acidity enhancement we will use the thermodynamic cycle shown in Fig. 7.

In this thermodynamic cycle, the values of ΔG_1^0 and ΔG_2^0 measure the stabilization undergone by the free amine (or phosphine) and its conjugate base upon Lewis acid, Y, complexation. Accordingly, ΔG_3^0 and ΔG_4^0 are the gas-phase acidities of the free amine (phosphine) and the corresponding Lewis adduct, respectively. Hence, the fact that the acidity of the Lewis adduct is larger than the acidity of the free Lewis base ($\Delta_r G_4^0 > \Delta_r G_3^0$) necessarily

2. GROUP 13 LEWIS ACIDS: BH₃, ALH₃ AND GAH₃

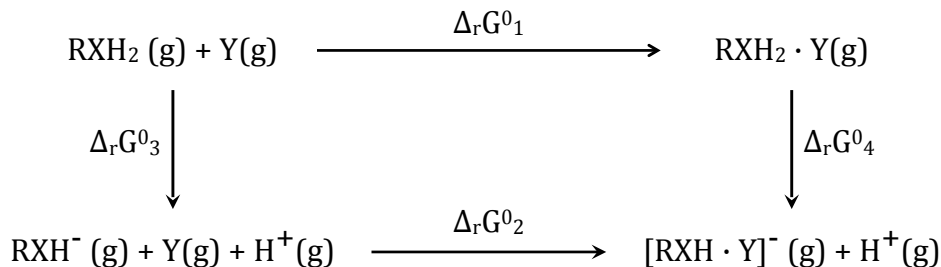


Figure 7: Thermodynamic cycle relating the intrinsic acidities of the isolated Lewis bases, RXH₂, X = N, P, ($\Delta_r G^0_3$) and the corresponding Lewis adducts, RXH₂·Y, Y = BH₃, AlH₃, GaH₃, ($\Delta_r G^0_4$) with the stabilization undergone by the neutral ($\Delta_r G^0_1$) and deprotonated ($\Delta_r G^0_2$) forms of the base upon complexation.

implies that the stabilization of the deprotonated species upon Lewis acid complexation is larger than that undergone by the corresponding neutral free amine (phosphine), $|\Delta_r G^0_2| > |\Delta_r G^0_1|$, see eq. (2). The values for the stabilization upon complexation for the neutral and deprotonated forms of the free amine (phosphine) are listed in Table 4. The corresponding values for the remaining amino-borane molecules computed are shown in Table A1.13 on the Appendix 1.

$$\begin{aligned}
 \Delta_r G^0_1 + \Delta_r G^0_4 &= \Delta_r G^0_3 + \Delta_r G^0_2 \implies \\
 \implies \Delta_r G^0_2 - \Delta_r G^0_1 &= \Delta_r G^0_4 - \Delta_r G^0_3 = \Delta\Delta_{acid}G^0
 \end{aligned} \tag{2}$$

Table 4: Stabilization free energies of neutral ($\Delta_r G^0_1$) and deprotonated ($\Delta_r G^0_2$) amines, R–NH₂, and phosphines, R–PH₂, upon BH₃, AlH₃ and GaH₃ complexation. All values are in kJ mol^{−1}.^a

R	$\Delta_r G^0_1$					$\Delta_r G^0_2$				
	R–NH ₂		R–PH ₂			R–NH ₂		R–PH ₂		
	BH ₃	AlH ₃	BH ₃	AlH ₃	GaH ₃	BH ₃	AlH ₃	BH ₃	AlH ₃	GaH ₃
H	-77.9	-63.4	-49.4	-23.2	0.25	-273.1	-321.4	-169.6	-205.5	-162.8
CH ₃	-96.3	-68.7	-55.7	-43.3	-15.2	-290.1	-308.9	-176.2	-217.6	-175.3
<i>c</i> -C ₃ H ₅	-71.2	-56.8	-56.0	-42.6	-13.6	-251.3	-281.1	-163.2	-203.2	-156.2
C ₆ H ₅	-57.7	-41.1	-50.8	-37.1	-7.2	-209.1	-222.5	-128.8	-170.1	-124.7
average	-75.8	-57.5	-53.0	-36.6	-8.9	-255.9	-283.5	-159.4	-199.1	-154.7

^aValues for complexation with BH₃ taken from ref.,⁵² except for R = H which corresponds to the calculations of this work.

2. GROUP 13 LEWIS ACIDS: BH_3 , AlH_3 AND GaH_3

Indeed, values in Table 4 point out that the stabilization upon Y complexation of the anionic species is significantly higher, one order of magnitude, than the stabilization undergone by the neutral amine (phosphine). This fact can be easily rationalized by taking into account that deprotonated amines (phosphines) are much better electron donors than their neutral counterparts. This is not surprising since the formation of the anion triggers a significant increase of the orbital energies, and in particular the energy of the highest occupied molecular orbital (HOMO), increasing its electron-donor capacity. This change on going from the neutral to the deprotonated species is nicely reflected in the NBO characteristics of the bond formed between the heteroatom, X ($X = \text{N}, \text{P}$), and the Lewis acid atom B, Al, or Ga. In Table 5 and 6 are listed the characteristics of the N–B bond, for some selected amine-borane complexes, in terms of atomic hybrids, Wiberg bond index, and electron density (ρ_b) at the N–B bond critical point (BCP). Similar tables for the rest of the molecules considered in this work can be found in the Appendix 1 (Tables A1.14 to A1.21).

Table 5: Characteristics of the B–N bond in amine-boranes in terms of atomic hybrids.

Amine	neutral	anion
Ammonia	82% N (35% <i>s</i> + 65% <i>p</i>) + 18% B (16% <i>s</i> + 84% <i>p</i>)	75% N (40% <i>s</i> + 60% <i>p</i>) + 25% B (23% <i>s</i> + 77% <i>p</i>)
Methylamine	82% N (34% <i>s</i> + 66% <i>p</i>) + 18% B (16% <i>s</i> + 84% <i>p</i>)	75% N (39% <i>s</i> + 61% <i>p</i>) + 25% B (23% <i>s</i> + 77% <i>p</i>)
Dimethylamine	82% N (32% <i>s</i> + 68% <i>p</i>) + 18% B (16% <i>s</i> + 84% <i>p</i>)	76% N (37% <i>s</i> + 63% <i>p</i>) + 24% B (22% <i>s</i> + 78% <i>p</i>)
Aniline	LP(N) → 2p (B) ^a 1079	77% N (43% <i>s</i> + 57% <i>p</i>) + 23% B (21% <i>s</i> + 79% <i>p</i>)

^aThe value reported corresponds to the second order interaction energy, in kJ mol^{-1} , between the N lone pair (LP(**N**)) and the empty 2*p* orbital of **B** atom.

From the data on Table 5 it can be observed that the donation of the lone pair of the nitrogen atom into the empty 2*p* orbital of the boron atom leads to a strongly polar chemical bond in which the contribution (82%) of the nitrogen-based hybrid orbitals to the bond is dominant. For the deprotonated species, the contribution of the boron-based hybrid orbitals to the

2. GROUP 13 LEWIS ACIDS: BH_3 , ALH_3 AND GAH_3

Table 6: Characteristics of the B–N bond in amine-boranes in terms of Wiberg bond index, and electron density ($\rho_b(\text{B-N})$, a.u.) at the corresponding BCP.

Amine	Wiberg bond index		$\rho_b(N - B)$	
	neutral	anion	neutral	anion
Ammonia	0.618	0.816	0.105	0.147
Methylamine	0.612	0.785	0.112	0.151
Dimethylamine	0.592	0.745	0.114	0.150
Aniline	0.608	0.743	0.109	0.140

bond is significantly higher (from 18% to 24%) than in the neutral species. A concomitant increase of the s character of the hybrid orbitals (from both, N and B) participating in the bond is also observed. Consequently, the bond between the boron atom and the nitrogen atom in the deprotonated amine is stronger than in the neutral complex. This fact is also reflected in both the value of the Wiberg bond index (Table 6) which is about 27% larger in the anion, and the value of the electron density, ρ_b , at the corresponding bond critical point. Same trends are observed for amine-alanes and phosphine-alanes, with the Al contribution to the N(P)–Al bond going from 8% in the neutral amine-alane to 13% in the anion, and from 13% to 24% in the case of phosphine-alanes. Similar values are found for phosphine-gallanes. An increase of the s character of the orbitals participating in the bond is also observed for the deprotonated forms of these complexes (see Tables A1.16, to A1.21 in the Appendix 1).

The ELF plots (Fig. 8) are consistent with the previous analysis. These plots show how the lone pair that is created upon deprotonation of the amino group connects (partially delocalizes) with the disynaptic B–N basin. This effect becomes more apparent in the case of aniline, where the new nitrogen lone pair and the B–N disynaptic basin appear as a unique basin of population 3.64 electrons.

Differences between Lewis acids. Turning now to the differences between distinct Lewis acid, the greater acidity enhancement effect observed for alane and gallane with respect to borane complexes is in principle unexpected taking into account that BH_3 should behave as a better Lewis acid

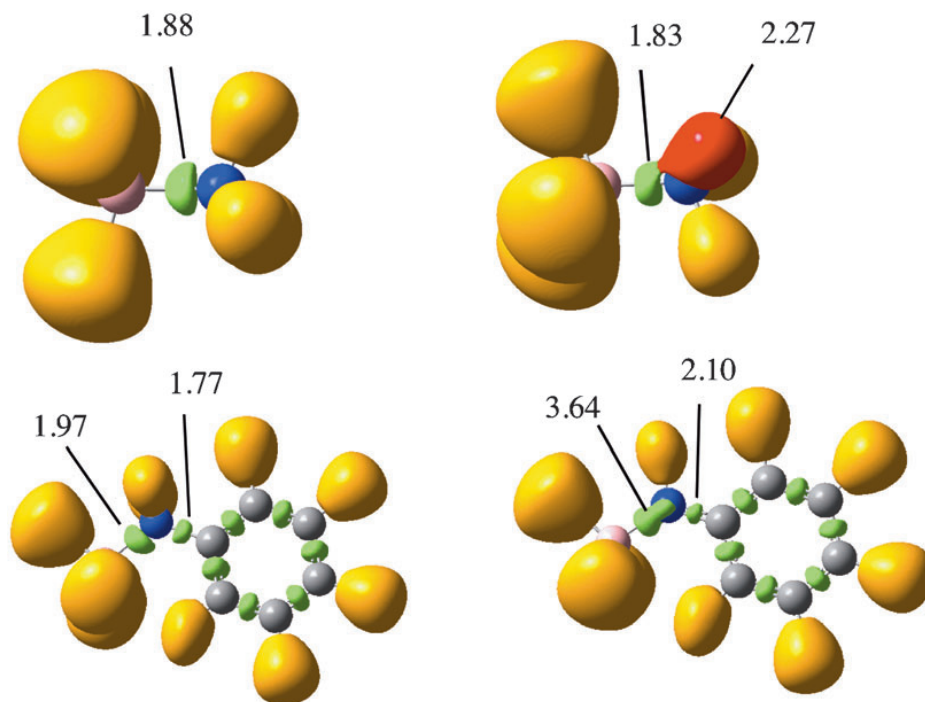


Figure 8: ELF (0.80) for the $\text{NH}_3\cdot\text{BH}_3$ and $\text{C}_6\text{H}_5\text{NH}_2\cdot\text{BH}_3$ complexes and their corresponding nitrogen-deprotonated species. Green lobes denote disynaptic basins involving two heavy atoms. Orange lobes are disynaptic basins in which H is one of the atoms involved. Red lobes correspond to the lone pairs. The populations shown are e^- .

than AlH_3 or GaH_3 . In fact, the dissociation energies of the complexes of AlH_3 with PF_3 , PCl_3 , PMe_3 , and $\text{P}(\text{CN})_3$ were reported to be smaller than for the analogous complexes in which AlH_3 is replaced by BH_3 .¹⁰² Indeed, this is also observed when looking at the stabilization of the neutral amines and phosphines under investigation here ($|\Delta_r G_1^0|(\text{BH}_3) > |\Delta_r G_1^0|(\text{AlH}_3) > |\Delta_r G_1^0|(\text{GaH}_3)$) (see Table 4). Why however, is the stabilization of the anion greater when it donates to AlH_3 than when it does so to BH_3 or GaH_3 ? The explanation is nicely visualized in the corresponding ELF plots (Fig. 9).

Comparing the ELF of $\text{PH}_3\cdot\text{Y}$ ($\text{Y} = \text{BH}_3$, AlH_3 and GaH_3) complexes and their corresponding phosphorus-deprotonated species we observe that, for the neutral complexes the differences are minimal. For the deprotonated species there is a clear delocalization of the lone pair created on the P atom upon its deprotonation and the disynaptic P-Y ($\text{Y} = \text{B}$, Al , Ga) basin. This

2. GROUP 13 LEWIS ACIDS: BH_3 , AlH_3 AND GaH_3

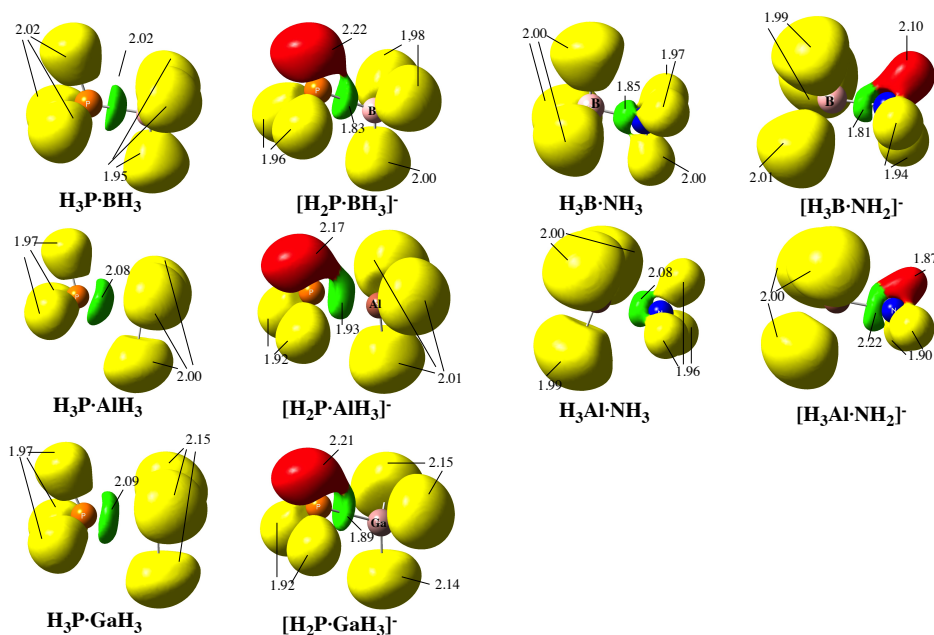


Figure 9: ELF (0.80) for the $\text{XH}_3\cdot\text{Y}$ ($\text{X} = \text{N}, \text{P}$; $\text{Y} = \text{BH}_3, \text{AlH}_3$ and GaH_3) complexes and their corresponding X-deprotonated ($\text{X} = \text{N}, \text{P}$) species. Green lobes denote disynaptic basins involving two heavy atoms. Yellow lobes are disynaptic basins in which H is one of the atoms involved. Red lobes correspond to the lone pairs. The populations shown are e^- .

electron delocalization results in an increase electron flux to the bonding region. It is here where the differences appear. The electron delocalization, likely due to a lower electronegativity of the Al atom, is larger in the case of alane than for borane and gallane which is reflected in an larger electron population of the P–Al dysynaptic basin with respect to the population of the P–B and P–Ga disynaptic basins ($1.93\ e^-$ vs. 1.83 and $1.89\ e^-$). This fact is even more dramatic in the cases of the amines, where the population of the N–B disynaptic basin is 1.81 compared to 2.22 in the N–Al one. This fact would explain the enhanced stability of the $[\text{XH}_3\cdot\text{AlH}_3]^-$ ($\text{X} = \text{N}, \text{P}$) complexes with respect to that of $[\text{XH}_3\cdot\text{YH}_3]^-$ ($\text{X} = \text{N}, \text{P}$; $\text{Y} = \text{B}, \text{Ga}$). Therefore, the larger acidity observed for alane complexes can be attributed to a larger stabilization of the anionic complex compared to the borane and gallane complexes. It is known that the chemistry of gallane is more like borane than alane which is related to the periodic anomaly of the group 13 elements. Notably the increase in electronegativity of gallium over aluminium ($1.8\ \text{Ga}$, $1.5\ \text{Al}$ cf. $2.0\ \text{B}$, Allred Rochow) and the associated lower polarization influence of gallium.⁸⁸ Indeed, the stabilization undergone by

2. GROUP 13 LEWIS ACIDS: BH₃, ALH₃ AND GAH₃

the deprotonated phosphine upon BH₃ and GaH₃ complexation is almost the same. The average of the $\Delta_r G_2^0$ values computed is -159 and -155 kJ mol⁻¹ for borane and gallane complexes, respectively. Also the values for the electron population of the P lone pair and P-B/Ga disynaptic basin in the deprotonated complexes are almost the same (see Fig. 9). The difference in electronegativity has already been pointed out in previous *ab initio* studies as the main factor distinguishing aluminum from its neighboring group 13 elements.¹⁰³

Differences between R substituents. Let us compare the effect of the nature of the R substituent on the acidity enhancement. It can be seen that the acidity enhancement is systematically lower for PhXH₂ (X = N, P) than for the other molecules under study (Tables 1, 2 and 3). The reason is related to the aromatic character of the system. As shown in Table 4, the free aniline (phenylphosphine) is a poorer electron donor than the other amines (phosphines), as reflected in the lower ΔG_1^0 value. The reason is that the conjugation of the lone pair on the nitrogen (phosphorus) atom with the aromatic system. This is consistent with the fact that NBO analysis (see Tables 5 and Ap.15, Ap.17, Ap.19, Ap.21 in the Appendix 1) does not locate a B-N bond (with the default indexes of the NBO 5.0 program) but instead locates a dative bond between the lone pair of the heteroatom (N or P) and the empty *p* orbital on the B, Al or Ga atom. The anion is also significantly stabilized through the conjugation of the X (X = N, P) lone pair created in the deprotonation process with the aromatic system. Complexation of the anion with the Lewis acid, BH₃, AlH₃ or GaH₃, necessarily competes with this delocalization. Since a significant amount of the lone-pair charge is transferred to the Lewis acid molecule upon complexation, less is available for the conjugation with the aromatic ring. This is mirrored in a shortening of the C-X bond, as well as a significant increase of both the electron density at the corresponding BCP and the electron population of the C-X disynaptic basin (see Fig. 10). Still, the deprotonated amine (phosphine) is a better electron donor toward the Lewis acid than the neutral species, through the second lone-pair created. However, the donor capacity of the second lone pair is smaller when R = Ph than in the other examples because the aforementioned conjugation decreases the intrinsic basicity of the XH₂ group.

The origin of the differences between methylamine and dimethylamine is more subtle. As shown in Table A1.13 the stabilization of the neutral form

2. GROUP 13 LEWIS ACIDS: BH_3 , AlH_3 AND GaH_3

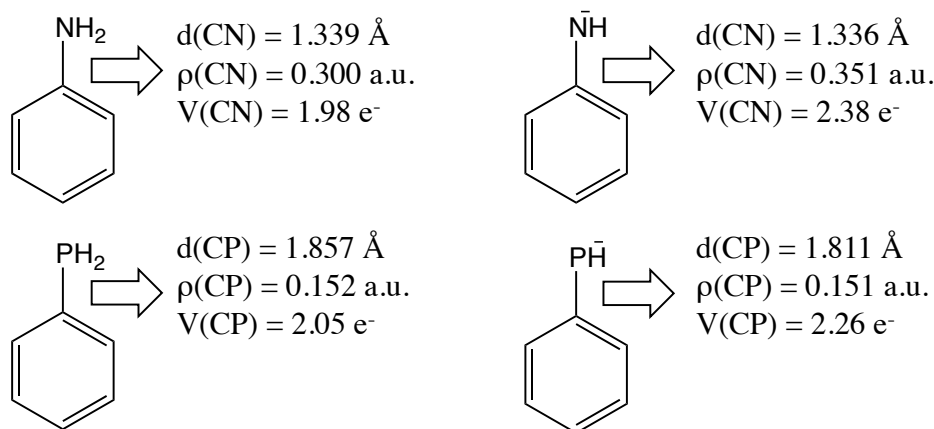


Figure 10: C-X (X= N, P) bond characteristics for Ph-XH_2 and their deprotonated counterparts.

(ΔG_1^0) is larger for dimethylamine than for methylamine as expected from the increase in the number of methyl substituents. However, the values for the stabilization of the anion ΔG_2^0 show the reverse order. This happens because the inductive effect of the methyl group makes dimethylamine a better Lewis base than methylamine. On the other hand, the extra methyl group significantly contributes to the dispersion of the excess of negative charge in the anion, enhancing its stability and attenuating the electron-donor ability of the nitrogen atom. The slightly decrease of the acidity enhancement upon methyl substitution is also observed on going from $\text{NH}_3 \cdot \text{AlH}_3$ to $\text{CH}_3\text{NH} \cdot \text{AlH}_3$ and have been reported for methylamine/ammonia and methanol/water forming complexes with BeH_2 Lewis acid.¹⁰⁴

Lewis base active site. As previously noted, the acidity enhancement effect is smaller when the active site of the base is a phosphorus. Also, the stabilization energies of both the neutral and deprotonated forms are smaller for the phosphorus bases. If we compare the NBO characteristics of the $\text{H}_3\text{N-BH}_3$ with those of the $\text{H}_3\text{P-BH}_3$ bond, we find that the N-B bond has a very large weight of the N atomic orbitals (82%), whereas the weight of the P atomic orbitals in the P-B bond is quite smaller (66%), reflecting the smaller electronegativity of the P atom. The same is observed for the alane complexes (see Tables A1.17 and A1.19). The interaction between the empty p orbital of the boron atom and the lone pair of the nitrogen is stronger than that involving the lone pair of a phosphorus atom. This difference is

2. GROUP 13 LEWIS ACIDS: BH_3 , AlH_3 AND GaH_3

presumably due to the large difference in the size of the orbitals participating in the interaction in the latter case. However, this can not be the reason for the larger stabilization of the neutral and anionic forms of amines than that for phosphines upon complexation with alane. For AlH_3 complexes another factor comes into play, the electrostatic character of the bond. In this case, it is the electrostatic component that makes N–Al interaction stronger than P–Al interaction. Indeed, whereas the natural charges of the N and Al atoms in $\text{H}_3\text{N}\cdot\text{AlH}_3$ are -1.18 and +0.95, respectively, those of the P and Al atoms in the analogous adduct are +0.10 and +0.78, respectively. Fig. 11 shows the natural charges for these two complexes. The coloring code goes from red for the most negative to green for the most positive. Black color correspond to zero (or close) charge. For the sake of comparison the corresponding borane complexes have been also plotted in the figure.

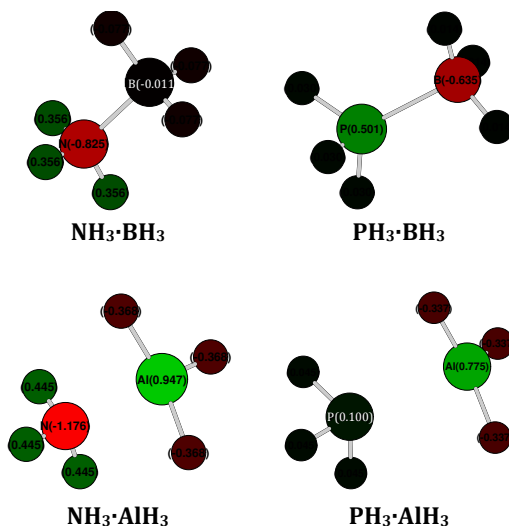


Figure 11: Natural charges for $\text{NH}_3\cdot\text{BH}_3$, $\text{PH}_3\cdot\text{BH}_3$, $\text{NH}_3\cdot\text{AlH}_3$ and $\text{PH}_3\cdot\text{AlH}_3$ Lewis adducts. Red is for the most negative atoms and green for the most positive ones. Black is a charge equal or close to zero.

It is apparent from Fig. 11 that the N–Al bond has the greatest electrostatic character of the four bond considered. These arguments explain why the stabilization energies (ΔG_1^0 and ΔG_2^0) are smaller for RPH_2 than for RNH_2 , but do not explain why the acidity enhancement is also smaller for phosphine derivatives. Second-row atoms disperse the excess of negative charge much better than first-row atoms and thereby its electron-donor ability decreases. However, this effect is more pronounced in the anionic species. Thus, when going from amine to phosphines, the decrease in ΔG_2^0 (stabi-

2. GROUP 13 LEWIS ACIDS: BH₃, ALH₃ AND GAH₃

lization energy for the anion) is larger, in relative terms, than the decrease in ΔG_1^0 (stabilization energy for the neutral). Consequently, the difference between ΔG_1^0 and ΔG_2^0 is smaller in the phosphorus bases. This difference is the acidity enhancement.

In order to stress the significant acidity enhancement observed in the Lewis bases considered upon **Y** complexation let see the effect of the aforementioned acidity enhancement of the acid dissociation constant, k_a . An equilibrium constant is related to the standard Gibbs energy change for the reaction, $\Delta_r G^0$ through eq. 3

$$k_a = \exp\left(-\frac{\Delta_r G^0}{RT}\right) \quad (3)$$

where R is the ideal gas constant and T stands for the absolute temperature (298 K). Because of the exponential relation between k_a and $\Delta_r G^0$ even small changes in the latter produce a large change in k_a . Thus, the acidity enhancements observed in the molecules studied suppose changes in the acidity constant ranging from 21 to 45 orders of magnitude!

Conclusions. The acidity enhancement effect of BH₃ observed in the amino-borane complexes is also found for other Lewis acids of the group 13, AlH₃ and GaH₃ and other Lewis bases, namely phosphines. This acidity increase is huge, going from 78 kJ mol⁻¹ for the PhPH₂·BH₃ adduct to 200 kJ mol⁻¹ for NH₃·AlH₃. In terms of the acidity constant it supposes a change of 21 to 45 orders of magnitude!

The origin of the acidity enhancement is the larger stabilization of the anion than that undergone by the neutral basis upon Lewis acid complexation. The analysis of the electron density rearrangements on both the Lewis base and the Lewis acid shows that the deprotonated base is a much better electron donor than the neutral one. Furthermore, the contribution of the Lewis acid to the dispersion of the excess electron density of the anion is another factor contributing to the increased stability of the anions and therefore, to the increased acidity of the Lewis adducts with respect to the isolated bases.

This acidity enhancement depends on several factors: i) the Lewis acid considered, being larger for AlH₃ than for BH₃ and GaH₃. ii) the nature of the R substituents on the Lewis base, being smaller for R = Ph because of the conjugation of the X lone pair with the aromatic system. iii) the Lewis base active site, being larger for amines than for phosphine derivatives. Hence, the

2. GROUP 13 LEWIS ACIDS: BH_3 , AlH_3 AND GaH_3

calculated acidity enhancement follows this order: $\text{RNH}_2 \cdot \text{AlH}_3 > \text{RNH}_2 \cdot \text{BH}_3 > \text{RPH}_2 \cdot \text{AlH}_3 > \text{RPH}_2 \cdot \text{GaH}_3 > \text{RPH}_2 \cdot \text{BH}_3$, for all R considered. All the molecules considered behave as N or P acids.

Conclusiones. Un aumento de acidez similar al provocado en la amina al formarse el complejo con BH_3 se observa al sustituir el ácido de Lewis BH_3 por otro ácido de Lewis del grupo 13, vease AlH_3 y GaH_3 , así como cuando la base de Lewis es una fosfina en lugar de una amina. Este aumento de acidez es enorme y varía en un rango que va desde 78 kJ mol^{-1} en $\text{PhPH}_2 \cdot \text{BH}_3$ a 200 kJ mol^{-1} para el complejo $\text{NH}_3 \cdot \text{AlH}_3$. ¡En términos de la constante de acidez esto supone un cambio de entre 21 y 45 órdenes de magnitud!

El origen del observado aumento de acidez es la mayor estabilización del anión al formarse el complejo con el ácido de Lewis comparado con la estabilización de la forma neutra de la amina o fosfina al formar el complejo. El análisis de los cambios que tienen lugar en la densidad electrónica tanto en la base como en el ácido de Lewis muestran que la base desprotonada es mucho mejor dador electrónico que la correspondiente forma neutra. A esto hay que añadir la contribución del ácido de Lewis a la dispersión del exceso de densidad electrónica en el anión, lo que supone un factor de estabilización del anión extra y por tanto contribuye también al aumento de la acidez de los aductos en relación con la acidez de las base aisladas.

El aumento de acidez depende de varios factores: i) el ácido de Lewis, siendo mayor cuando se trata de AlH_3 que en el caso de BH_3 o GaH_3 . ii) La naturaleza del sustituyente R en la base de Lewis, siendo más pequeño para $\text{R} = \text{Ph}$ ya que la conjugación del par electrónico del átomo X ($\text{X} = \text{N}, \text{P}$) con el sistema aromático disminuye la capacidad como dador electrónico de la base de Lewis. iii) La naturaleza del sitio activo de la base de Lewis, siendo mayor el aumento de acidez para las aminas que para las fosfinas. Por tanto, el aumento de acidez al formarse un complejo de Lewis sigue el siguiente orden: $\text{RNH}_2 \cdot \text{AlH}_3 > \text{RNH}_2 \cdot \text{BH}_3 > \text{RPH}_2 \cdot \text{AlH}_3 > \text{RPH}_2 \cdot \text{GaH}_3 > \text{RPH}_2 \cdot \text{BH}_3$ para todos los sustituyentes R considerados. Cabe añadir que todas las moléculas estudiadas se comportan como ácidos de N (aminas) o de P (fosfinas).

3 Group 15 Lewis bases: unsaturate derivatives

Up to now we have seen that when typical Lewis bases as amines and phosphines form complexes with group 13 Lewis acids, BH_3 , AlH_3 or GaH_3 , their intrinsic acidity changes dramatically, in most cases thirty orders of magnitude in terms of the equilibrium acidity constant. These acidity enhancements have been shown to be even larger when the Lewis acid is a beryllium derivative,¹⁰⁴ an electron deficient system, that as borane or alane, behaves as a very strong Lewis acid. The hard Be^{2+} cation (31pm) has a very similar charge to size ratio to Al^{3+} (50pm): 0.0645 compared to 0.600. It has typically been compared to aluminium and is even paired with aluminum in recent inorganic chemistry texts.¹⁰⁵ Beryllium was originally discovered by the French chemist Vauquelin in 1797 as a component of the mineral beryl and the gem emerald, and metallic beryllium was later isolated in 1828 independently by Bussy and Wohler.¹⁰⁶ Interest in the use of beryllium began in 1920 when it was demonstrated that a 2% addition of beryllium to copper produced an alloy six times stronger than the original material.¹⁰⁷ Since then, and clearly due to its unique properties that are a great asset in nuclear, aerospace and electronic industries, since beryllium has found extensive use in modern industry. A wide variety of applications have been developed, ranging from aircraft landing gear bushings to undersea telephone cable housings; and from oil field drilling equipment to golf clubs.^{108, 109} Therefore, there is much interest in further develop our understanding of the coordination chemistry of beryllium. However, the chemistry of beryllium compounds has been much less explored than that of the other elements of the first-row of the Periodic System. Some coordination complexes of Be with nitrogen donor ligands have been reported, and few beryllium compounds of second-row elements are known.⁵⁵ This comes from the fact that beryllium compounds are quite toxic which makes experimental studies difficult. Indeed, beryllium is the most toxic non-radioactive element in the Periodic Table.¹¹⁰ Skin poisoning requires surgical removal and, in severe cases, amputation may be required.^{111, 112} Inhalation of beryllium-containing dusts produces chronic pulmonary granulomatosis (berylliosis) or nodules in the lung.^{113–116} The condition develops slowly and it is often fatal. Beryllium is lethal at 1ppm of body weight. Due to the *exceedingly toxic* nature of beryllium compounds, predictive theoretical calculations are specially interesting regarding Be chemistry. Thus, in this section we have considered BH_3 , AlH_3 and BeH_2 as Lewis acids.

3. GROUP 15 LEWIS BASES: UNSATURATE DERIVATIVES

With regard to the Lewis base moiety, there are some evidences that seem to indicate that the acidity enhancement effect also depends on the nature of the Lewis base active site, since in general it has been found that the acidity enhancement is larger in amine adducts than in phosphine adducts, regardless the Lewis acid considered. Hence, in this section, we perform a more thorough study with regard to the Lewis bases. We expand the scope considering as Lewis bases group 15 derivatives, in particular molecules in which the heteroatom is directly bonded to an unsaturated moiety. More specifically to a vinyl or ethynyl group. We have also included the series of the saturated ethyl derivatives as a suitable reference. In Fig. 12 are shown the structures of the Lewis bases to be considered.

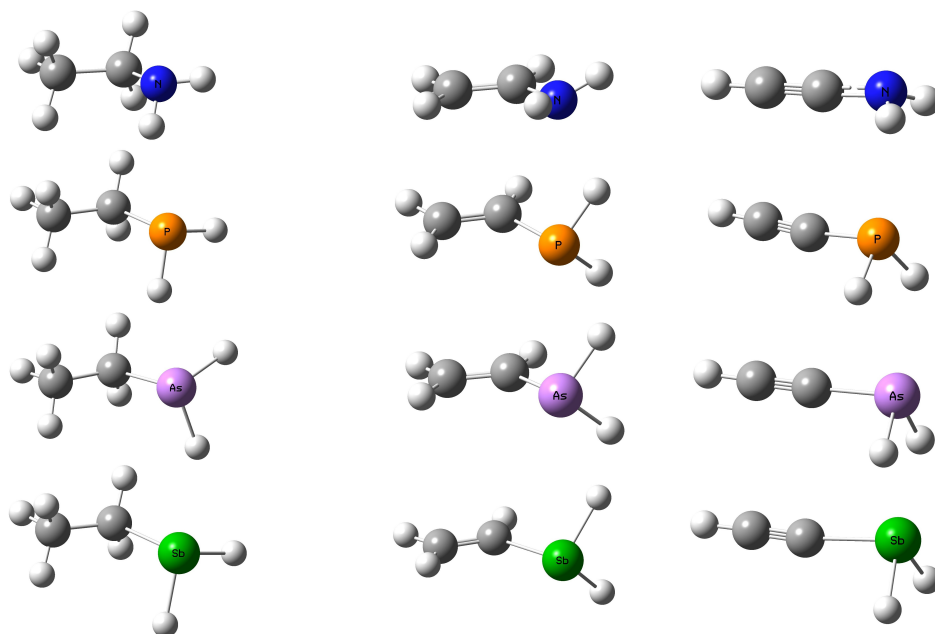


Figure 12: Structures for $\text{H}_3\text{C}-\text{CH}_2\text{XH}_2$, $\text{H}_2\text{C}=\text{CHXH}_2$, and $\text{H}_2\text{C}\equiv\text{CHXH}_2$ ($\text{X} = \text{N}, \text{P}, \text{As}, \text{Sb}$) Lewis bases considered in this section.

The aim of this section is to investigate the acidity trends of the Lewis bases down the group. Then, we will analyze the effect that the association of these compounds, with BH_3 , AlH_3 , or BeH_2 have on their intrinsic acidities. At this point, we will explore if the acidity changes are directly related with the deformation of the base, the acid or both. Finally the possibility that this association may lead to a change in the nature of the group losing the proton will also be analyzed. The methodology used will be the same as

3. GROUP 15 LEWIS BASES: UNSATURATE DERIVATIVES

detailed in previous sections.

Acidity enhancement. The calculated intrinsic acidities, measured as the Gibbs free energy associated with the reaction 1 are presented in Table A1.22. In order to better visualize the trends going down the group these data are plotted in Fig. 13.

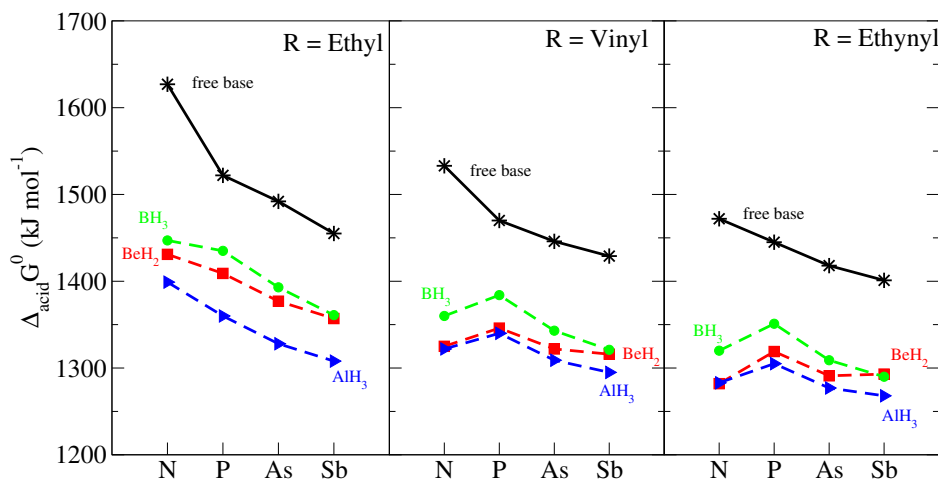


Figure 13: Calculated acidity ($\Delta_{acid}G^0$, kJ mol⁻¹) for R-XH₂ (R = Ethyl, vinyl, ethynyl; X = N, P, As, Sb) bases (solid lines) and the corresponding R-XH₂·BeH₂, R-XH₂·BH₃, and R-XH₂·AlH₃ complexes (dashed lines).

For the free compounds we have considered deprotonation at all possible acidic sites: X, C_α, and C_β. In all cases the systems behave as heteroatom acids since independently of the nature of R or X, the R-XH⁻ anion was found to be always the most stable one. This is in agreement with what has been found before for several amines and phosphines^{52,117} and in the previous sections, as well as for vinylarsine,^{117,118} vinylstibine¹¹⁹ and ethynylarsine.

Again we want to note the very good agreement between our calculated acidities and the experimental values, whenever available (see Table A1.22). Also the estimates of our DFT model are in excellent agreement with the G4 calculated values. It is also apparent that the acidity increases (lower values of $\Delta_{acid}G^0$) down the group for the three families of compounds, although this effect is attenuated on going from the saturated compounds to the vinyl derivatives and further to the ethynyl ones. Indeed, while ethylstibine is predicted to be 172 kJ mol⁻¹ more acidic than ethylamine, for the vinyl and the

3. GROUP 15 LEWIS BASES: UNSATURATE DERIVATIVES

ethynyl analogues this gap is only 104 and 71 kJ mol⁻¹, respectively. As expected, the acidity increases as ethyl < vinyl < ethynyl, reflecting the larger electronegativity of the unsaturated groups with respect to the saturated one.

The complexation of the compounds under investigation whether it is with BeH₂, BH₃ or AlH₃ leads to a significant enhancement of their intrinsic acidities, similar to the ones reported in previous sections for other compounds. The largest calculated acidity enhancement, that can be seen in the figures as the gap between the solid line and the dashed line for each Lewis acid, is found for aluminium complexes, followed by beryllium dihydride complexes and borane complexes. It is worth to note the similarity between BeH₂ and AlH₃ complexes of the unsaturated moieties. As aforementioned, some resemblances between the chemistries of Be and Al have already been observed.⁵⁵

Again, we will use the same thermodynamic cycle shown in Fig. 7 to rationalize these findings (for convenience it is shown here again as Fig. 14). With this purpose the values of the stabilization energies of the neutral and deprotonated Lewis bases upon complexation, $\Delta_r G_1^0$ and $\Delta_r G_2^0$, respectively, have been listed in Table A1.23. In Fig. 15 we show the corresponding graphs.

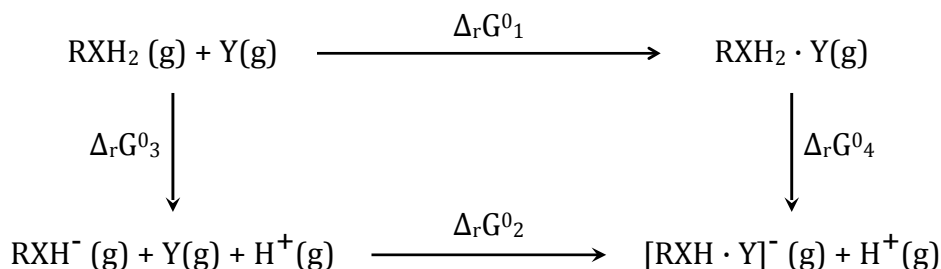


Figure 14: Thermodynamic cycle relating the intrinsic acidities of the isolated Lewis bases and the corresponding Lewis adducts with the stabilization undergone by the neutral and deprotonated forms of the base upon complexation.

The values of $\Delta_r G_1^0$ and $\Delta_r G_2^0$ indicate that for the three kinds of complexes the acidity enhancement is due to a much larger stabilization of the anion than the neutral, when associated with any of the three Lewis acids. Actually, for the three BH₃ and AlH₃ and BeH₂ the strength of the X–Y (X = N, P, As, Sb; Y = B, Al, Be) bond dramatically increases on going from the neutral complex to the deprotonated one. This is well reflected in both,

3. GROUP 15 LEWIS BASES: UNSATURATE DERIVATIVES

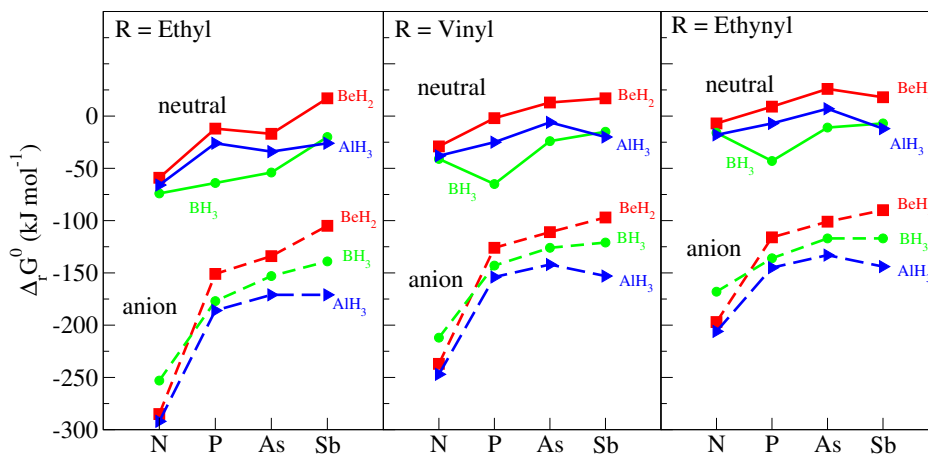


Figure 15: Stabilization free energies of neutral, $\Delta_r G_1^0$, (solid lines) and deprotonated species, $\Delta_r G_2^0$, (dashed lines) when $R\text{-XH}_2$ ($R = \text{Ethyl, vinyl, ethynyl}$; $X = \text{N, P, As, Sb}$) bases interact with BeH_2 , BH_3 , and AlH_3 . The acidity enhancement, $\Delta\Delta_{\text{acid}}G^0$ corresponds to the gap between the solid and dashed line curves for the same Lewis acid. All values are in kJ mol^{-1} .

the values of the electron densities at the N–X BCPs and in the Wiberg bond orders. As shown in Fig. 16, using the complexes with vinylamine as suitable examples, upon deprotonation of the complex, the electron density at the N–B, N–Al and N–Be BCPs increases by 0.039 0.025 and 0.034 a.u., respectively. Consistently, the N–B, N–Al and the N–Be Wiberg bond orders also increase from 0.526 to 0.572 for the BH_3 adduct, from 0.252 to 0.436 in the AlH_3 complex, and from 0.259 to 0.526 for the BeH_2 containing one.

It can be seen in Fig. 13, and values in the first three columns of Table A1.23 which give the magnitude of the acidity enhancement, that systematically, the effect is stronger when the Lewis acid is AlH_3 . However, in general, the stabilization of the neutral base follows the order $\text{B} > \text{Al} > \text{Be}$, whereas the trend change for the anion: $\text{Al} > \text{B} > \text{Be}$ (except for $X = \text{N}$), as can be seen in Fig. 15. Therefore, the larger acidity enhancement observed for alane complexes comes from a larger stabilization of the anion respect to the neutral base compared to those of observed for borane. For BeH_2 , even if in general the stabilization of both the neutral base and the deprotonated form is lower than for borane, the difference between $\Delta_r G_1^0$ (neutral) and $\Delta_r G_2^0$ (anion) is larger than for the latter. Hence, the acidity enhancement for BeH_2 complexes is larger than for BH_3 adducts. Indeed, from the values in Fig. 16, it can be seen that whereas the electron density at the N–Be BCP

3. GROUP 15 LEWIS BASES: UNSATURATE DERIVATIVES

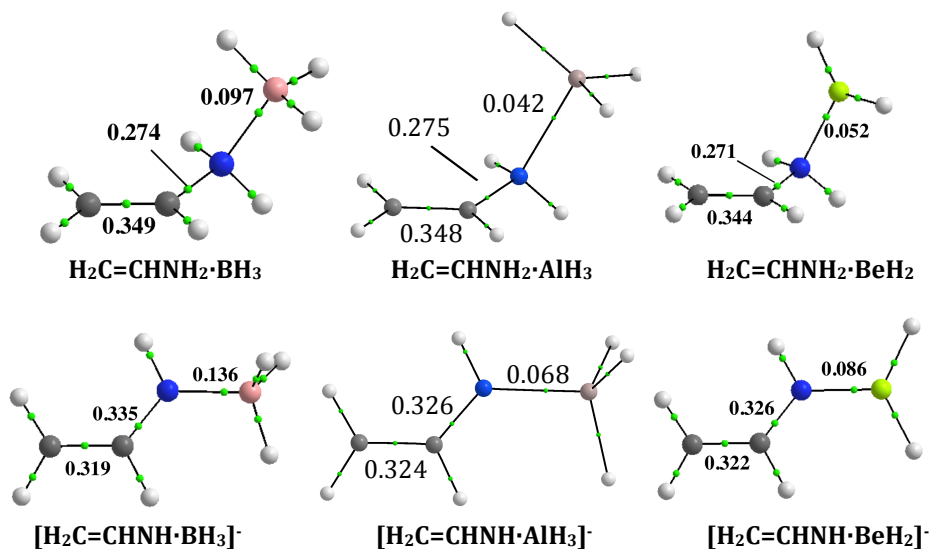


Figure 16: Molecular graphs of the BH_3 , AlH_3 and BeH_2 complexes with vinylamine and their corresponding anionic deprotonated species. Green dots denote BCPs. Electron densities are in a.u.

increases 65% upon deprotonation of the complex, that at the N–B BCP only increases by 40%.

There are other subtle differences between the three series of data. While for the BH_3 complexes the value of $\Delta_r G_1^0$ is always negative, i.e., the neutral compound is always stabilized by association with borane, this is not always the case upon association with BeH_2 or AlH_3 . In principle, as shown in Table A1.23, the formation of BeH_2 complexes for ethylstibine, vinylarsine, vinylstibine, ethynylphosphine, ethynylarsine and ethynylstibine are predicted to be endergonic processes, even though they are exothermic in terms of enthalpies. Since the reaction free-energies are rather small, we decided to verify whether these predictions could be an artifact of the DFT approach used, so for the P and As containing complexes the values of $\Delta_r G_1^0$ were re-evaluated at the G4 level. For the Sb containing compounds, for which the G4 procedure is not available, the *ab initio* reference calculations were carried out at the CCSD(T)/Def2-QZVP level of theory. These high-level *ab initio* values showed that, although the B3LYP method slightly underestimate the stability of the neutral beryllium complexes, the formation of the complexes of BeH_2 with ethynylarsine and ethynylstibine are indeed slightly endergonic (see Table A1.23). This moved us to explore the relative stability

3. GROUP 15 LEWIS BASES: UNSATURATE DERIVATIVES

of complexes in which BeH_2 interacts with the double or triple CC bond rather than with the heteroatom (see Fig. 17).

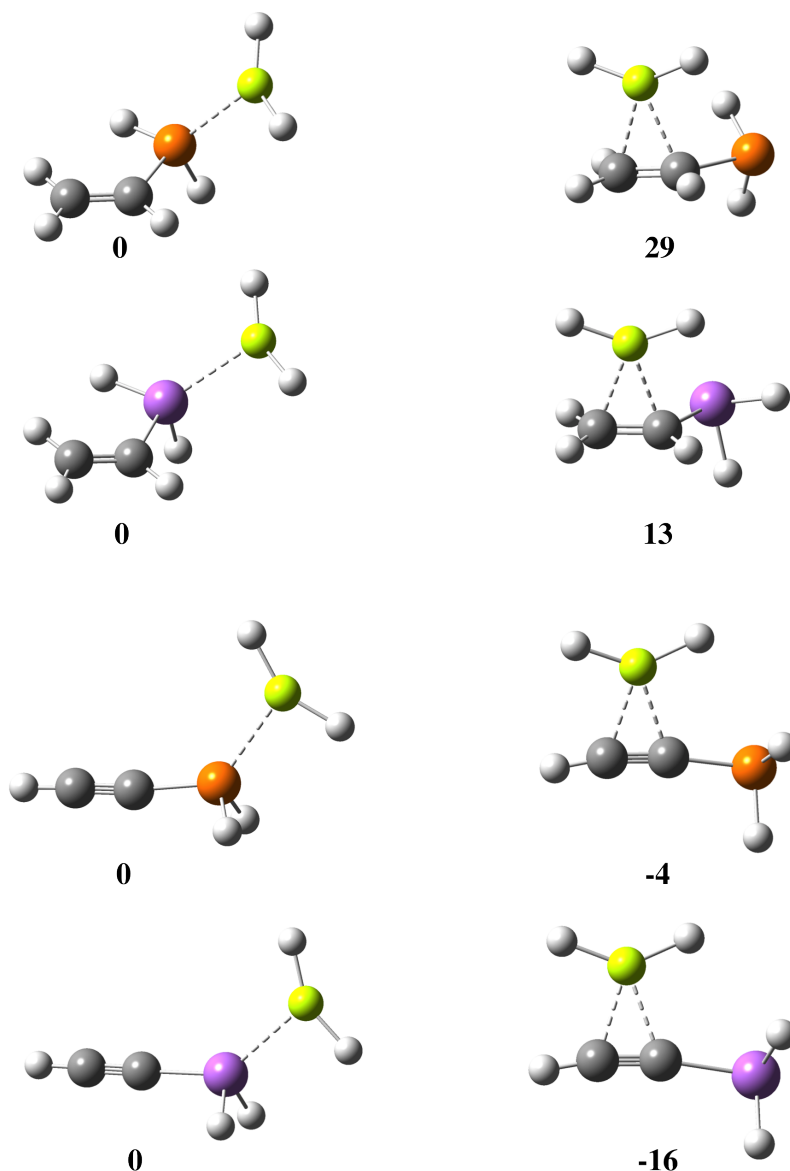


Figure 17: G4 relative stabilities (kJ mol^{-1}) for the more stable conformations of complexes of BeH_2 with vinyl- and ethynyl phosphine and arsine, showing that for ethynyl the π -type complex is the more stable.

This survey, carried out at the G4 level, showed that the global minimum

3. GROUP 15 LEWIS BASES: UNSATURATE DERIVATIVES

for the interaction between both ethynylphosphine or ethynylarsine and BeH_2 corresponds to a π -type complex, which was found to be 4 and 16 kJ mol^{-1} lower in free energy than the complex in which BeH_2 interacts with the P or the As atom, respectively. However, a similar survey for the complexes involving the analogous vinyl derivatives showed that always the complex in which BeH_2 is directly attached to the heteroatom, is more stable than the π -complex (29 kJ mol^{-1} for P and 13 kJ mol^{-1} for As).

It is worth noting that although for BH_3 containing complexes the value of $\Delta_r G_1^0$ for the ethynyl containing systems is smaller in absolute value than for the vinyl containing analogues, in all cases the formation of the complexes is predicted to be exergonic. Same applies for AlH_3 adducts, with the only exception of $\text{HC}\equiv\text{C}-\text{AsH}_2\cdot\text{AlH}_3$, with is predicted to be slightly endergonic (7 kJ mol^{-1}).

Acidity trends. Besides the acidity enhancement discussed above, the complexation also results in a change in the acidity trends. Whereas, as we have indicated before, the acidity of the free compounds increases down the group, the values of $\Delta_{acid}G^0$, for the BH_3 , AlH_3 and the BeH_2 complexes, present a maximum (minimum acidity) for the vinyl and the ethynyl phosphine (dashed lines in Fig. 13).

Why the complexes of vinyl- and ethynyl-phosphine are less acidic than the corresponding amine complexes? Or, put in another way, why is the conjugate base of the amines more stable, in relative terms, than the conjugate base of phosphines? It is due to a significant stabilization of the anion through the conjugation of the N lone pair, created in the deprotonation process, with the π -system of the unsaturated vinyl/ethynyl substituent. This is nicely reflected in the weights of the resonant structures (see Fig. 18) of the neutral and anionic forms of the borane complexes with vinyl and ethynyl amines and phosphines (see Table 7).

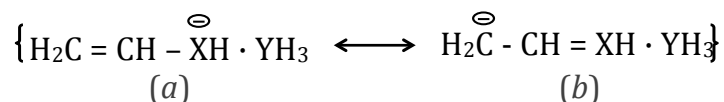


Figure 18: Resonant structures for the anionic forms of the vinyl complexes.

3. GROUP 15 LEWIS BASES: UNSATURATE DERIVATIVES

Table 7: NRT weights for *a*-type resonant structure of the vinyl-XH₂ and ethynyl-XH₂ (X = N, P, As, Sb) neutral and deprotonated BH₃ complexes.

	Vinyl		Ethynyl	
	Neutral	Anion	Neutral	Anion
X = N	92%	60%	91%	60%
X = P	89%	86%	88%	87%
X = As	88%	87%	88%	88%
X = Sb	87%	90%	87%	91%

The results shows that whereas for the neutral complexes the resonant structure (*a*) is clearly predominant, there is not a strong conjugation, this is not the case for the anions. For both, vinyl and ethynyl derivatives, the weight of (*a*) structure for N containing bases decreases significantly, almost to half its value. However, this phenomenon is not observed for the heavier elements of group 15, for which the weight of the resonant structure (*a*) remains almost invariable when the molecule is deprotonated. The greater acidity of As and Sb complexes than the N containing ones just reflects the decrease on the X-H bond strengths going down the group.

The same phenomenon is observed in AlH₃, *i.e.*, it exits in the anions a strong conjugation of the amino group with the π -system of the unsaturated moiety, which is not observed for the phosphines. Several features ratify this. The electron density at the C-N BCP increases dramatically when the anion is formed (0.275 \rightarrow 0.326 a.u. (vinyl) and 0.308 \rightarrow 0.348 a.u. (ethynyl) and consequently the C-N bond length shrinks (0.08 and 0.06 Å for vinyl and ethynyl). The double and triple character of the C-C bonds decreases, increasing the C-C distance (1.331 \rightarrow 1.367 Å and 1.205 \rightarrow 1.236 Å, respectively). It is worth to note that for ethynyl-amine a change in the HCC angle from linear to 159° is also observed, showing the significant change in the hybridization of the C atoms. The behaviour is just the opposite for the P containing systems. The electron density at the C-P BCP decreases (0.161 \rightarrow 0.151 a.u. and 0.161 \rightarrow 0.148) and the C-P bond becomes longer (0.01 and 0.02 Å for vinyl and ethynyl derivatives, respectively). The same kind of behaviour is found for the BeH₂ analogues complexes. Indeed, the similarities between the values of the C-N and C-P BCP electron densities and bond distances are remarkable. All these results indicate that the N containing anions become much more stabilized in relative terms than the P

3. GROUP 15 LEWIS BASES: UNSATURATE DERIVATIVES

containing ones, what should result in a much larger increase in the acidity for the amines than for the phosphines, explaining the appearance of the maxima in Fig. 13. Why the conjugation is favored in amines, is a well known mechanism, related to the efficiency of the overlap between the lone pairs of the heteroatom and the π -system when the heteroatom belongs to the first row.

Active center for deprotonation. In our previous discussion it was implicitly assumed that for the Lewis complexes the proton lost would always come from the XH_2 group. This has been showed to be the case for different Lewis complexes as the ones previously exposed here and some others found in the literature (phosphine-boranes⁵² and complexes with BeH_2 derivatives.¹⁰⁴) Also in the free compounds the proton is lost from the heteroatoms. Thus, in principle, this is a reasonable assumption also in this case. Neither the initial polarity of the bonds, for BeH_2 , BH_3 , and AlH_3 groups would favor the proton lost from any of these groups. For example, the hydrogens at nitrogen are acidic in character because of the increased electronegativity of nitrogen, 3.04,¹²⁰ relative to hydrogen, 2.20.¹²⁰ Inversely, the hydrogens at boron are hydridic in nature because of the reduced electronegativity of boron, 2.04,¹²⁰ which leads to polarization of the bond toward hydrogen. Nevertheless, a thorough exploration of the potential energy surface reveals the existence of a stable anion in which the proton is lost at the Lewis acid site. Furthermore, this anion is in all the cases but for vinylamine derivatives, the most stable anion in terms of free energy (see Table 8). Furthermore, the formation of the anion at Be, B or Al site is accompanied by a significant structural rearrangement. The deprotonated Lewis group (BH_2 , AlH_2 , BeH) bridges between the C_α of the unsaturated moiety and the XH_2 group ($\text{X} = \text{N}, \text{P}, \text{As}, \text{Sb}$), so the anion is $[\text{R}-\text{YH}_2-\text{XH}_2]^-$ (insertion-anion) instead of $[\text{R}-\text{XH}-\text{YH}_3]^-$ (see Fig. 19). Similar structures to that shown in Fig. 19 are found for all the complexes regardless the Lewis acid, Y, the heteroatom, X, or the nature of the R substituent.

In light of the results showed in Table 8, the first thing that comes into mind is that the acidity enhancement reported in Table 22 is much larger for all the unsaturated systems investigated (with the only exception of vinylamine). Hence, in general the complexes of the ethynyl derivatives with BeH_2 are between 75 and 92 kJ mol^{-1} more acidic than expected if the deprotonation would take place at the XH_2 ($\text{X} = \text{N}, \text{P}, \text{As}, \text{Sb}$) group. The increase is slightly weaker, from 57 to 74 and from 42 to 59 kJ mol^{-1} , for

3. GROUP 15 LEWIS BASES: UNSATURATE DERIVATIVES

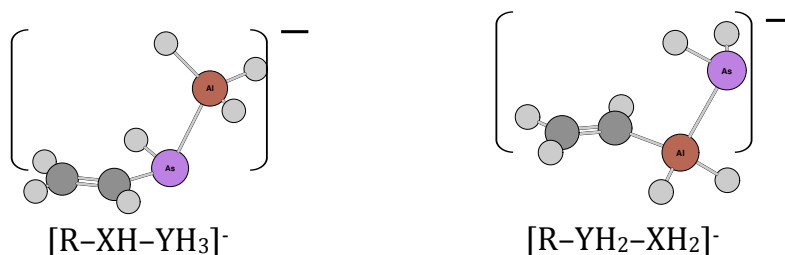


Figure 19: Representative structures for the heteroatom anion, $[R-XH-YH_3]^-$, (left) and the “insertion” anion, $[R-YH_2-XH_2]^-$ (right).

Table 8: Stabilities (kJ mol^{-1}) of the $[R-YH_2-XH_2]^-$ structures (insertion-anion) relative to those of the $[R-XH-YH_3]^-$ ones. R = vinyl-, ethynyl-; X = N, P, As, Sb; Y = Be, B, Al.

Y =	Be		B		Al	
R =	Vinyl	Ethynyl	Vinyl	Ethynyl	Vinyl	Ethynyl
X = N	+3	-75	+21	-42	+14	-57
X = P	-28	-76	-23	-43	-22	-58
X = As	-39	-92	-31	-59	-30	-74
X = Sb	-44	-82	-36	-50	-32	-62

the complexes with AlH_3 and BH_3 respectively. It is also weaker, but still significant, for the complexes involving the vinyl derivatives, with the only exception, already mentioned above, of vinylamine.

However, to form the insertion-anion ($[R-YH_2-XH_2]^-$), it is first necessary to form the *insertion-complex* and then, deprotonate this complex. In Fig. 20 is shown the mechanism using as a suitable example the alane adduct of vinylphosphine. Formation of the *insertion-complex* starts from the π -complex **B**, which in general is less stable than the **A** adduct for vinyl derivatives and slightly more stable for some ethynyl derivatives. From the π -complex **B**, a proton is transferred to the PH_2 group. At the same time two new bonds are formed between Al and each of the C of the vinyl unit, in such a way that a cyclopropane-like ring is formed by Al and the two carbon atoms. This process supposes to cross a very high energy barrier, **TS_{BC}**, of 225 kJ mol^{-1} . Once cyclic structure **C** has been reached, the PH_3 moiety starts to interact with the AlH_2 , shortening the Al-P distance and lengthening the C-P one so that the AlH_2 subunit inserts into the C-P

3. GROUP 15 LEWIS BASES: UNSATURATE DERIVATIVES

bond and the *insertion complex* **D** is formed. Again, to pass from **C** to **D** is necessary to cross a high barrier, **TS_CD**. Therefore, formation of the Be, B or As anion implies a complicate mechanism which involve high activation barriers. Hence, in spite of its increased stability, the Be, B, or As anions will most likely not form.

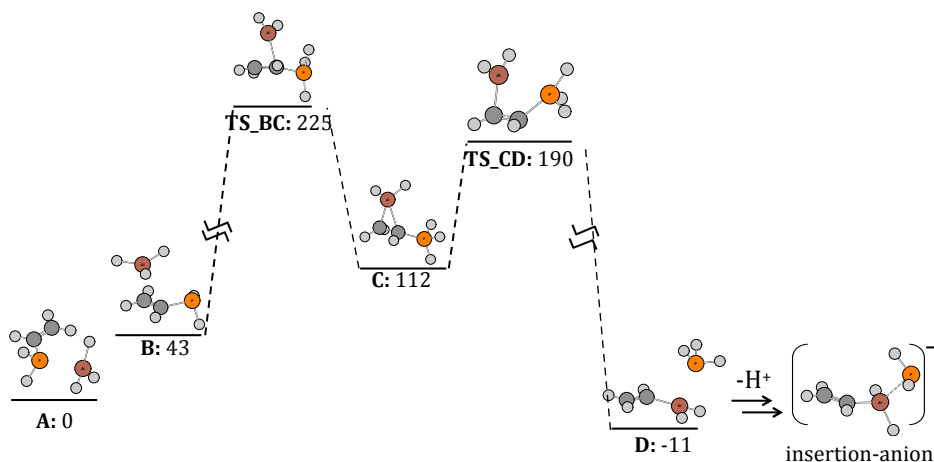


Figure 20: Mechanism to form the insertion-complex **D** starting from the π -complex **B**. Note the high barrier necessary to overcome in this process (225 kJ mol^{-1}). Deprotonation of the *insertion-complex* leads to formation of the most stable anion, $[\text{R-YH}_2\text{-XH}_2]^-$, insertion-anion.

Nevertheless, it is also possible that under the experimental conditions this rearrangement would be promoted (dynamical factors) and the *insertion complex* formed. The formation of this anion has two major implications: i) the acidity enhancement of the bases considered would be even larger. Taking into account the extra stabilization reported in 8, the complexes between ethynylarsine and ethynylstibine with BeH_2 are predicted to be acids as acidic ($\Delta_{\text{acid}}G^0 = 1199$ and 1211 kJ mol^{-1} , respectively) as perchloric acid ($(\Delta_{\text{acid}}G^0 = 1200 \pm 50 \text{ kJ mol}^{-1})$)¹²¹. Similarly, their complexes with borane, are predicted to be ($\Delta_{\text{acid}}G^0 = 1250$ and 1240 kJ mol^{-1} , respectively) more acidic than chloric acid ($(\Delta_{\text{acid}}G^0 = 1284. \pm 16 \text{ kJ mol}^{-1})$)¹²² and sulfuric acid ($(\Delta_{\text{acid}}G^0 = 1265. \pm 23. \text{ kJ mol}^{-1})$).¹²³ ii) The adducts would behave as Be, B, or Al Brønsted acids instead of N, P, As or Sb acids. At this point it would be nice to have the experimental gas-phase acidities, to compare the values and thus discriminate between the two isomers for the deprotonated complexes.

3. GROUP 15 LEWIS BASES: UNSATURATE DERIVATIVES

Conclusions. The intrinsic acidity of the unsaturated vinyl- and ethynyl- amines, phosphines, arsines and stibines is systematically larger than that of the saturated ethyl analogues, reflecting the larger electronegativity of the vinyl and ethynyl groups with respect to the ethyl one. For the free systems a steadily increase of this intrinsic acidity down the group is observed no matter the nature of the organic moiety to which the XH_2 ($\text{X} = \text{N}, \text{P}, \text{As}, \text{Sb}$) acidic site is bound.

Association of the Lewis base with beryllium dihydride, borane or alane leads to a dramatic acidity enhancement due, as aforementioned, to a much larger stabilization of the deprotonated anion than the neutral molecule. This acidity enhancement, that follows the order: $\text{AlH}_3 > \text{BeH}_2 > \text{BH}_3$, is accompanied, for the unsaturated compounds, by a change in the acidity trends which do not steadily increase down the group, as for the free systems, but present a minimum for both the vinyl- and the ethynyl-phosphine. This unexpected result is due to a much larger increase of the acidity of N containing systems, due to the ability of the N to conjugate with the π -system in the anionic deprotonated species.

For the three Lewis acids and for all the unsaturated amines, phosphines, arsines, and stibines, with the only exception of vinylamine, the most stable anion is obtained by deprotonation at the Lewis acid site (Be, B or Al) rather than in the heteroatom (N, P, As or Sb). It implies that the acidity enhancement reported would be even larger, and most importantly, that the adducts would behave as Be, B or Al acids. However, this deprotonation supposes significant structural rearrangements and it is not likely to occur.

Conclusiones. La acidez intrínseca de las vinil- y etinil- aminas, fosfinas, arsinas y estibinas insaturadas es sistemáticamente mayor que la acidez de los análogos saturados, lo que refleja la mayor electronegatividad de los grupos vinilo y etinilo comparado con la del grupo etilo. Para las bases de Lewis aisladas se observa un constante aumento de la acidez al bajar en el grupo, independientemente de la naturaleza de la parte orgánica unida al grupo XH_2 ($\text{X} = \text{N}, \text{P}, \text{As}, \text{Sb}$).

La asociación de las bases de Lewis consideradas con hidruro de berilio, borano o alano supone un aumento drástico de la acidez de la base debido, como ha sido explicado anteriormente, a la mayor estabilización de la forma aniónica que de la forma neutra de la base de Lewis al formarse el aducto.

4. GENERAL CONCLUSIONS

Junto con dicho aumento de acidez, que sigue el orden siguiente: $\text{AlH}_3 > \text{BeH}_2 > \text{BH}_3$, en el caso de los compuestos insaturados se observa un cambio en las tendencias de los valores de acidez al bajar en el grupo. Cuando consideramos los aductos, la acidez no aumenta al bajar en el grupo si no que presenta un mínimo para la vinyl- y etinilfosfina. Este resultado inesperado se debe a que el aumento de acidez en los sistemas que contienen N es mucho mayor ya que la habilidad del par electrónico del N (en las formas aniónicas) para conjugarse con el sistema π del sistema insaturado supone una estabilización extra de dichos aniones.

En el caso de los tres ácidos de Lewis considerados y para todas las aminas, fosfinas, arsinas y estibinas insaturadas estudiadas, excepto la vinilamina, el anión más estable es el que se obtiene al desprotonar el ácido de Lewis (rompiendo el enlace Be-H, B-H o Al-H) en lugar del anión en el que el protón sustraído estaba enlazado al heteroátomo (N, P, As, Sb). Esto implicaría que el citado aumento de acidez es aún mayor, y lo que es más importante, que los aductos serían ácidos de Be, B o Al. Sin embargo, la desprotonación en la parte del ácido de Lewis supone una reorganización estructural considerable que no es probable que ocurra debido a las altas energías de activación que implica el proceso.

4 General conclusions

Through the use of accurate G4 and DFT calculations we have shown that the association of different Lewis acids with group 15 Lewis bases leads to a dramatic increase of their intrinsic acidities. This acidity enhancement is essentially due to a larger stabilization of the deprotonated species when the Lewis base-Lewis acid bond is formed, because the enhanced donor ability of the anion. Consequently, this is a general phenomenon that should be observed for any Lewis base, independently of the nature of its basic site, of its potential acidic site and of the Lewis acid considered. Thus, Lewis adduct formation is a good approach to design stronger Brønsted acids in the gas-phase and even to modulate its gas-phase acidity by appropriately selecting the Lewis acid.

Conclusiones generales. Mediante el uso de cálculos G4 y DFT hemos mostrado que la asociación de distintos ácidos de Lewis con bases de Lewis cuyo centro activo es un átomo del grupo 15 de la Tabla Periódica provoca

un aumento drástico en la acidez intrínseca de las últimas. Este aumento de acidez se debe esencialmente a una mayor estabilización de la especie desprotonada al formarse el enlace entre el ácido y la base de Lewis, debido a la mayor capacidad dadora de la forma aniónica. En consecuencia, este es un fenómeno general que debería observarse para cualquier tipo de base de Lewis, independientemente de la naturaleza del centro activo de esta última, del posible sitio ácido y del ácido de Lewis considerado. Por tanto, puede considerarse la formación de complejos de Lewis como un buen enfoque a la hora de diseñar ácidos de Brønsted más fuertes en la fase gas e incluso una manera de modular la acidez intrínseca de dichas moléculas mediante la elección adecuada del ácido de Lewis.

5 Lewis acid deformation

The adducts of group 13 and group 15 elements effectively comprise two distinct units, a group 13 center and a group 15 center, connected by a dative bond. In this Lewis acid/Lewis base adduct, the group 15 species can be considered to provide both electrons for the bond from a lone pair, acting as a two electron donor. Conversely, the group 13 center is electron deficient, with only 6 valence electrons. To complete the valence shell, it accepts two further electrons from the group 15 center into a vacant *p* orbital. This charge donation is particularly important when it concerns the stability of the anionic complexes since the dispersion of the extra electron density into the Lewis acid moiety contributes to the enhanced stability of the complex with respect to the isolated anionic Lewis bases. An example is shown in Fig. 21. In this figure it can be seen that complex formation supposes a significant reduction of the negative charge bear by the vinyl-XH₂ moiety (about 50% for X = N and 75% when X = P).

Another important common feature observed for all the systems considered is the deformation of the interacting subunits upon complexation. This deformation is usually mirrored in significant changes in their chemical properties. We have already seen the results of adduct formation on the chemical properties of the Lewis bases. Let us focus now on the structural changes undergone by the Lewis acid moiety when it forms complexes and the effects on its intrinsic properties. We will use the adducts of BH₃ and the last set of bases considered, namely, ethyl-, vinyl- and ethynyl-amine, phosphine, arsine and stibine as a suitable example. Formation of the adduct bond leads to a dramatic distortion of the BH₃ which departs significantly from planarity

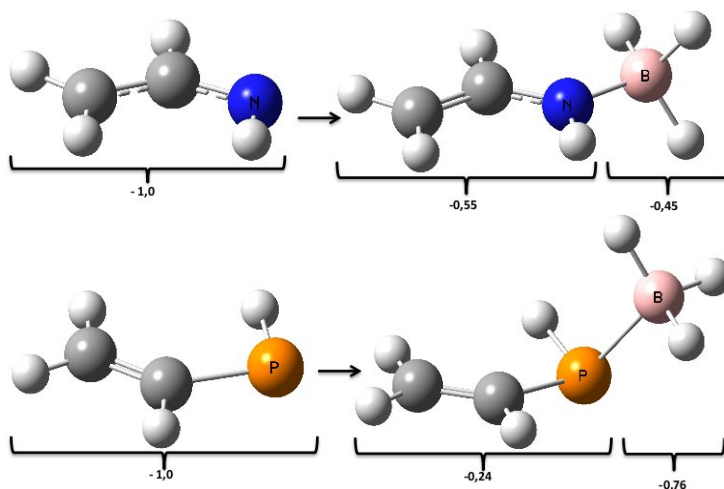


Figure 21: Two examples of the electron distribution within the vinylamine and vinylphosphine molecules upon BH_3 complexation.

to produce an approximately tetrahedral geometry. Concomitantly, there is a change in hybridization at boron from approximately sp^2 to sp^3 . In order to measure the distortion undergone by BH_3 we will use the dihedral angle defined by the four atoms of the molecule. In figure 22 are plotted the values for this angle in the ethyl-, vinyl- and ethynyl- neutral and anionic complexes.

The first conspicuous fact is the notable distortion of BH_3 upon adduct formation, being always larger for the anions than for the neutral complexes (in the free BH_3 equilibrium geometry this angle is zero). The extend of pyramidalization depends however on R substituent or the X heteroatom considered, varying from 19 to 37 degrees. The largest values are always observed for $\text{X} = \text{N}$ in the anion, while this is only true for the neutral saturated derivatives. The distortion becomes less significant when moving down the group 15.

The important question now is how does the distortion affects to the electronic configuration of BH_3 . These electronic changes are clearly mirrored in the Lowest Occupied Molecular Orbital (LUMO) energy of BH_3 , which has been plotted in Fig. 23 for the different complexes under survey. It is important to emphasize that in order to obtain valuable information these energies have been computed for the geometry that BH_3 has *within* the complex, rather than for the relaxed BH_3 geometry.

5. LEWIS ACID DEFORMATION

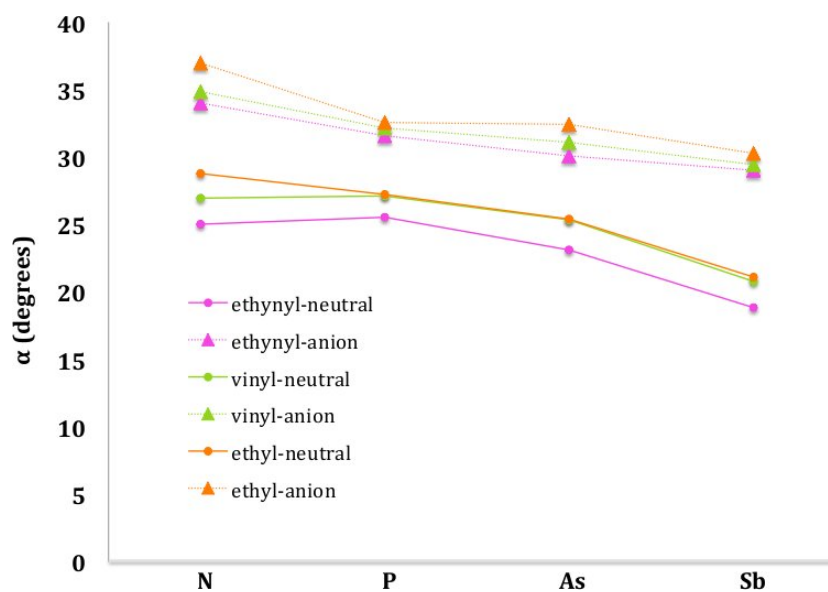


Figure 22: Variation of the BH_3 dihedral angle upon complex formation.

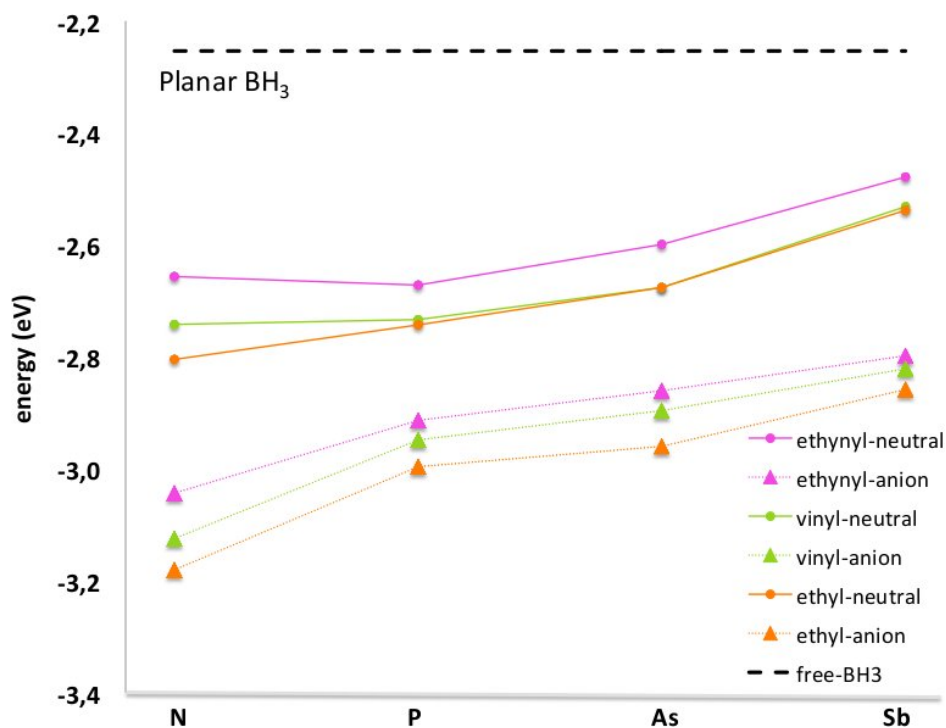


Figure 23: BH_3 LUMO energies within the complex geometry.

5. LEWIS ACID DEFORMATION

Correlation between BH_3 dihedral angle and BH_3 LUMO energy is obvious. Why do the LUMO energies change so dramatically upon complexation and therefore pyramidalization? The bending of BH_3 implies an automatic mixture of the empty $2p$ orbital and the $2s$ orbital. This mix can not occur in the linear system since these two orbitals belong to different irreducible representations. Thus, the pure p orbital is stabilized by pyramidalization through the aforementioned mixing with the $2s$ orbital. The larger the deformation, the larger the mix, and the lower the LUMO energy.

It has been proposed that Lewis acidity should be gauged based upon valence deficiency or the ability of the boron to accept an electron pair.^{124,125} Lewis acidity has also been claimed to be correlated to the LUMO (LUMO) level of the Lewis acid.¹²⁶ According to the frontier orbital model of chemical reactivity, the lower the LUMO energy of the Lewis acid the stronger would be the interaction with the Lewis base. This is clearly seen in Fig. 24 where the LUMO energies of BH_3 computed with the geometry it has within the complex, and the free energies for complexation $\Delta_r G_1^0$ (neutral) and $\Delta_r G_4^0$ (anion) have been plotted.

In the case of the unsaturated bases (Figs. A1.69 and A1.70) the relationship is not so clear since conjugation of the X lone pair with the π -system of the molecule, significant for the anionic species and for neutral amines implies an extra stabilization present on the values of the free energies but, of course, not mirrored on the LUMO energies of the BH_3 .

Therefore, the structural changes undergone by the Lewis acid moiety upon complexation trigger a rearrangement of the electron distribution that implies a decrease on the BH_3 LUMO energy. Consequently, the intrinsic acidity of the Lewis acid is strongly modified upon adduct formation.

The role of Lewis acid deformation on the stability trends of the complexes formed between ammonia and $\text{BeH}_{2-n}\text{X}_n$ ($\text{X} = \text{F}, \text{Cl}, \text{Br}; n \leq 2$) Lewis acids is showed in the paper entitled *The importance of deformation on the strength of beryllium bonds* that is attached in the Appendix 3.

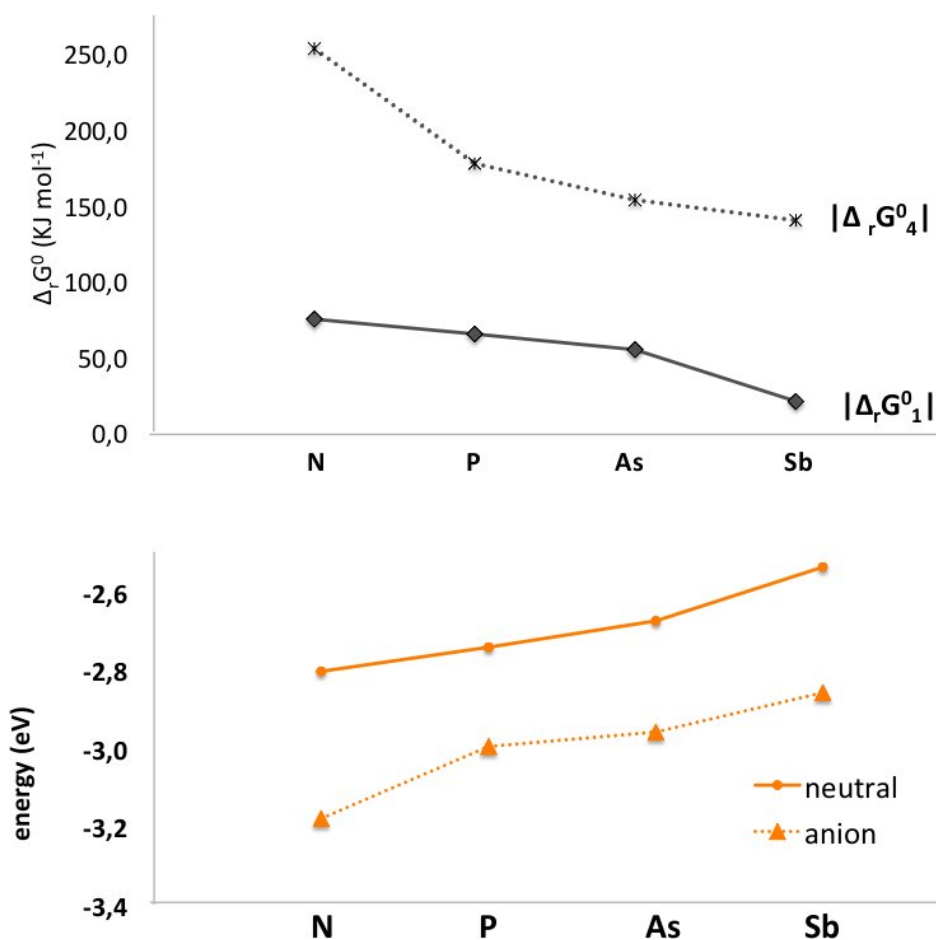


Figure 24: BH_3 LUMO energies within the complex geometry and Gibbs free energies for complex formation. Ethyl derivatives.

6 Radicals

As part of the reactivity of amine-boranes and phosphine-boranes there are the radical reactions. Amine-borane adducts have been shown to react rapidly with radical species, which abstract a hydrogen atom from boron to produce transient amine-boryl radicals (see Fig. 25).

The seminal research in this area was initiated in the mid 1980s by Roberts and co-workers, who performed a large number of electron spin resonance (ESR) based studies on radical species resulting from hydrogen abstraction from N,N,N -trialkyl-boranes^{127, 128} and N,N -dialkylamine-boranes,¹²⁹ and subsequently ammonia-borane.¹³⁰ Various reactivities of these amine-



Figure 25: Hydrogen abstraction from trialkylamine–boranes by *t*-butoxyl radicals.

boryl radicals were demonstrated, all resulting in the quenching of the boryl radical. The reactivity was found to be fundamentally similar to that of carbon centered radicals, with consecutive reactions occurring via (a) self-reaction, (b) abstraction of halide radicals from alkyl halides or $\text{H}\cdot$ radicals from other amine–boranes, and (c) β -scission. The reactivity was strongly dependent on the nature and substitution of the amine, and reaction conditions.

Of particular interest was the reaction in Fig. 26, wherein a *N,N*-dimethylamine–boryl radical reacted with a molecule of its precursor *N,N*-dimethylamine–borane to form *N,N*-dimethylaminyl–borane, a nitrogen centered radical. This reaction was a simple conversion between the kinetic product, where the radical was located at boron, and the thermodynamic product, where the radical was located at nitrogen.¹²⁹



Figure 26: Formation of *N,N*-dimethylaminyl–borane, a nitrogen centered radical.

Furthermore, it has recently been shown that amine–boranes involving secondary amines, $\text{R}_2\text{N}\cdot\text{BH}_3$, may undergo catalytic dehydrocoupling either producing $[\text{R}_2\text{N}\text{--}\text{BH}_2]_2$ cyclic dimers or, if R is a bulky substituent, $\text{R}_2\text{N}=\text{BH}_2$ monomeric species.¹³¹ These results indicate that both the amino and borane centers can behave as active radical center. It is not clear, however, which of the two processes is intrinsically the most favorable; in other words, is the formation of the boryl radical the most favorable process? This is the question we have tried to answer by investigating the stability of boryl radicals obtained from a series of primary and secondary amine– and phosphine–boranes, with respect to the radicals obtained when the H atom is lost from the amino or phosphine group. The results of this research are shown in the paper entitled *Are boryl radicals from amine–boranes and phosphine–boranes the most stable radicals?* which can be consulted in the Appendix 3.

PART II

1 Introduction

Doubly charged molecular ions, formed by association of a neutral base with a doubly charged metal ion, are of great importance in chemical and biochemical processes, both in solution and in the gas phase.¹³² Indeed, they are fundamental in gas-phase ion chemistry and in mass spectrometry in spite of their short life-time.^{133–135} They also play important roles in photochemical processes,^{136,137} as well as in astrochemistry and the chemistry of the atmospheres.^{138–141} It has also been postulated that they may have played some role in the origin of life,^{142–146} since doubly charged metal ions may have induced the precipitation of nucleic acid molecules. Nevertheless, these multiply charged ions were, for a long time oddities in the gas phase due to the difficulties in generating and stabilizing them. The so-called *intrinsic reactivity* is of great importance since the absence of interactions with a solvent can result in very different reactivity patterns; in many cases it allows for a better understanding of chemical bonding.

With the advent of electrospray ionization techniques in 1990,¹² generation of doubly-charged ions in the gas-phase from aqueous solutions became feasible and therefore the interest in gas-phase reactions between di-cations and neutral molecules has grown significantly. Many theoretical studies have been performed to understand the structures and relative stabilities of such ion-molecule complexes, providing detailed information on the nature of their interactions and binding energies.^{147–152} However, information about their unimolecular reactivity is much scarcer and fragmentary. One of the main reasons is that doubly- or multiply-charged species are rare in the gas-phase because many of these species are either thermochemically or kinetically unstable.¹³² This is indeed the case when they are the result of the association of a doubly (or multiply) charged transition metal ion (M^{2+}) with an organic base (B). The system undergoes a spontaneous deprotonation of the base leading to the monocation $[M(B-H)]^+$, the species experimentally ob-

1. INTRODUCTION

served.^{153–156} However, this is not the case with alkaline-earth dications such as Ca^{2+} and Sr^{2+} , since $[\text{CaB}]^{2+}$ and $[\text{SrB}]^{2+}$ are stable and detectable in the gas phase.¹⁵⁷ This opened the possibility of studying for the first time the unimolecular reactivity of complexes formed by these metal dications with different neutral bases such as urea, glycine, thiourea, selenourea, uracil and its thio derivatives.^{158–164} All these studies show that there is a competition between Coulomb explosion and neutral loss fragmentation.

Different techniques can be used for activating ions, which differ by the energy range employed, the instrument and the activation mechanisms.^{8–10} Notable among them is collision induced dissociation (CID), where the ion is made to collide with an inert gas at low collision energies, in such a way that part of the kinetic energy is transferred to the molecular ion as vibrational and rotational internal energy. CID has been extensively used to study ion structure and is one of the most commonly ion activation methods.^{9, 165–171} Nevertheless, there are many details of gas-phase dissociation mechanisms associated with CID that are still unclear. In this realm, theoretical calculations can help to understand the CID processes and in particular provide an atomistic description of the mechanisms and pathways leading to the final fragments.

Recently, Eizaguirre *et al.* studied the interactions and dissociation patterns of $[\text{M}(\text{formamide})]^{2+}$ ($\text{M} = \text{Ca}, \text{Sr}$) complexes.^{172, 173} The study combined collision induced dissociation (CID) experiments and high-level DFT calculations to analyze the topology of the potential energy surface (PES). A mechanism leading to the different fragments observed in the experiment was proposed based on the computed PESs. The experimental CID spectra for formamide- M^{2+} , $\text{M} = \text{Ca}, \text{Sr}$; are shown in Fig. 27 and the corresponding PESs proposed are shown in Fig. 28 ($\text{M} = \text{Ca}$) and 29 ($\text{M} = \text{Sr}$). Although it is possible to extract some conclusions about the reactivity from the topology of the PES, this constitutes only a first rough approach, and there are still open questions. For instance, whereas both molecules display a PES quite similar, the experimental CID spectra for $\text{M} = \text{Ca}$ shows the presence of fragmentation pathways nonexistent when $\text{M} = \text{Sr}$. Some other features of the CID spectra, as the presence of a very intense peak corresponding to the bare metal dication, M^{2+} , cannot be accounted for based solely on the topology of the PES, since this fragmentation corresponds to the most endothermic exit channel. Thus, we decided to further study CID reactivity of formamide- Ca^{2+} and formamide- Sr^{2+} dications by means of theoretical approaches different from the one previously used by Eizaguirre *et al.*

1. INTRODUCTION

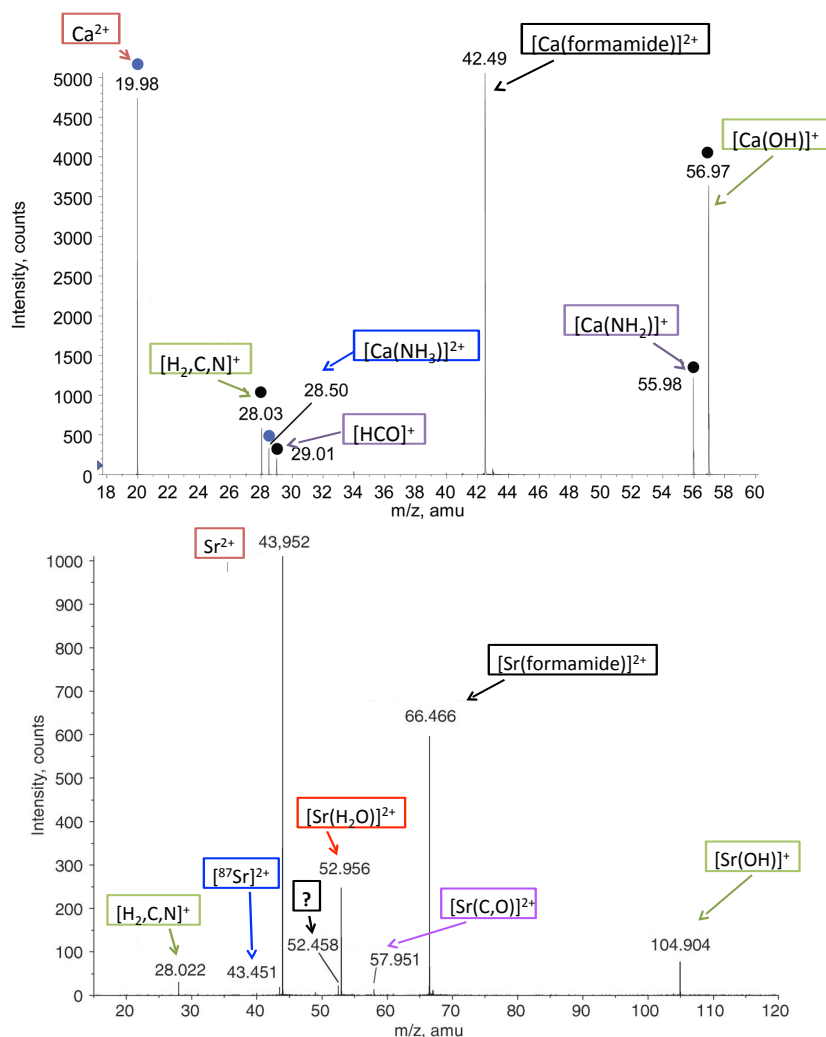


Figure 27: Top: low-energy CID spectrum of the formamide-Ca²⁺ complex recorded with a collision energy of 11eV (laboratory frame). Bottom: low-energy CID spectrum of formamide-⁸⁷Sr²⁺ recorded at a collision energy of 14eV (laboratory frame).

From the theoretical point of view, statistical models such as transition state theory (TST) and Rice-Ramsperger-Kassel-Marcus (RRKM) theory^{174–181} have been (and are) extensively used to describe the kinetics of the unimolecular fragmentation induced by collisions.^{9, 10, 178, 182–186} However, evidence of non-statistical dynamics, also called non-RRKM, in CID has been reported both in experiments^{187, 188} and simulations,^{189–193} as well as the importance of impulsive collision mechanisms to understand CID in protonated

1. INTRODUCTION

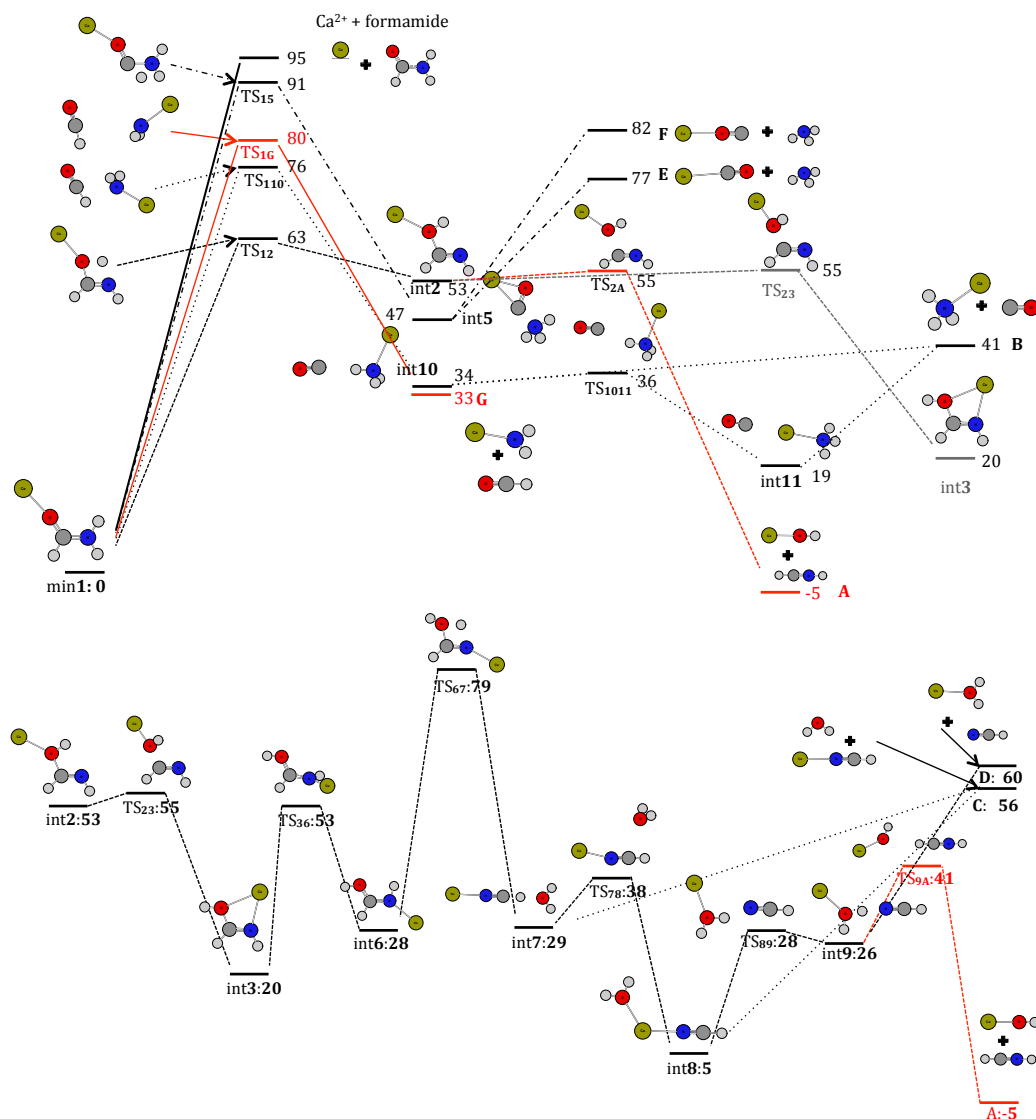


Figure 28: Top: formamide- Ca^{2+} energy profile of the different reaction mechanism with origin in the global minimum **1** and (bottom) local minimum **2**. All values in kcal mol^{-1} .

amino acids and peptides.^{194,195} One nonstatistical mechanism, identified as “shattering”,^{196–198} occurs in surface-induced dissociation (SID),^{199–202} where the projectile ion fragments as it collides with the surface. In CID a similar mechanism, where the bond breaks in one or less vibrational periods after collision, was proposed for a series of examples.^{187–192} This often correspond to an impulsive (*i.e.*, spatially localized) model of the collisional energy transfer

1. INTRODUCTION

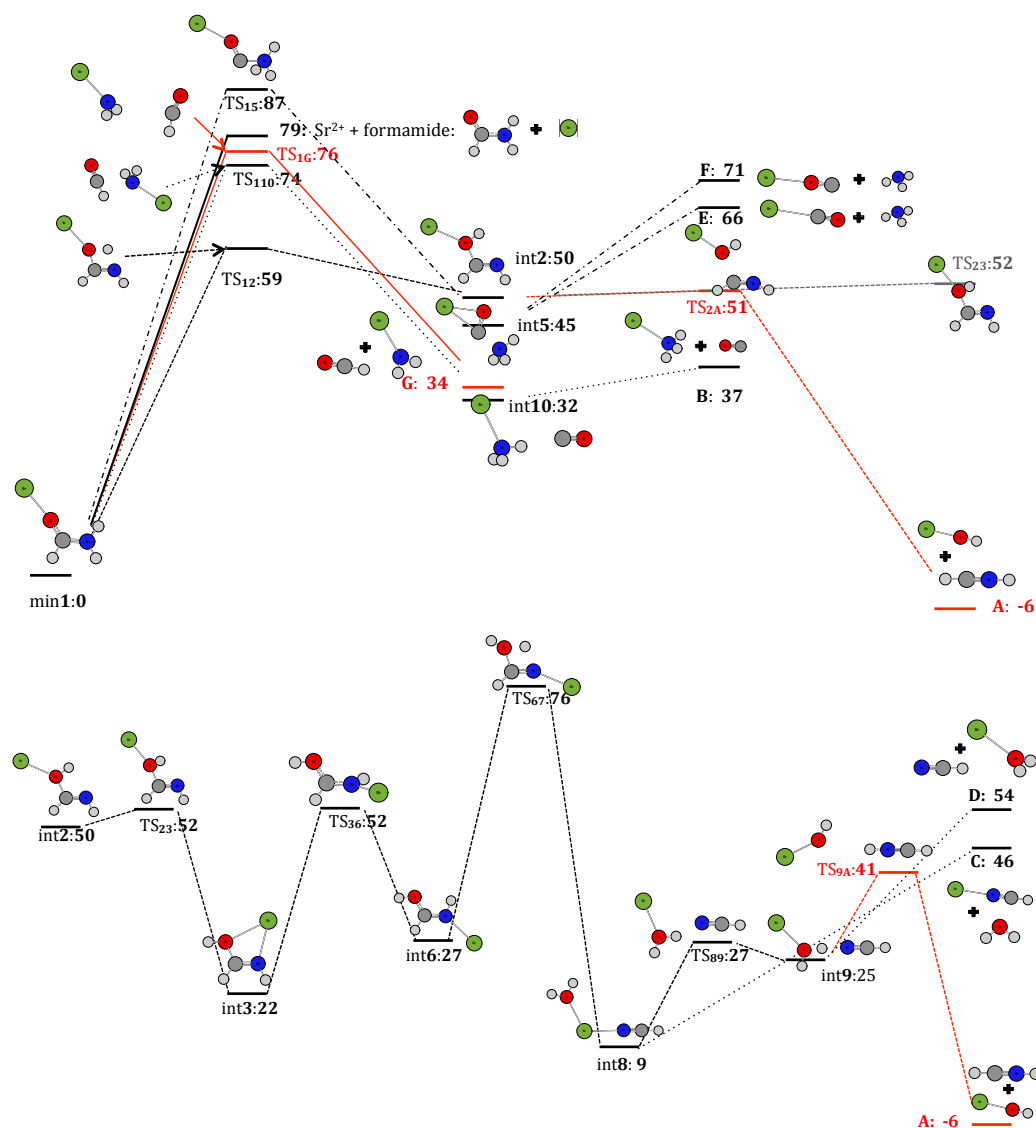


Figure 29: Top: formamide- $^{87}\text{Sr}^{2+}$ energy profile of the different reaction mechanisms with origin in the global minimum **1** and (bottom) local minimum **2** (bottom). All values in kcal mol^{-1} .

mechanism, while RRKM theory uses the assumption that the energy completely delocalizes within the reactant molecule internal degrees of freedom right after the collision.²⁰³

Two limiting fragmentation mechanisms can be described to explain CID reactivity. One in which the collision locally activates one (or few) vibrational

1. INTRODUCTION

mode(s), and the fragmentation occurs within one vibrational period before intramolecular vibrational energy redistribution (IVR) could take place. We will call here and hereafter this mechanism, that implies an impulsive collision energy transfer, direct fragmentation.²⁰⁴ In the second mechanism, the translational energy transferred to the molecule is redistributed among its vibrational and rotational modes. If the energy in a vibrational mode is higher than the energy required for breaking this bond the molecule eventually dissociates. Reactions taking place via the latter mechanism can be accounted for through statistical theories such as RRKM, while in the case of the first mechanism, a pure dynamical picture where the reaction is faster than IVR, the reactivity can only be understood by means of dynamics simulations. Therefore, an important question concerning CID unimolecular reactivity is whether the mechanisms leading to the different fragmentation pathways are statistical or not.

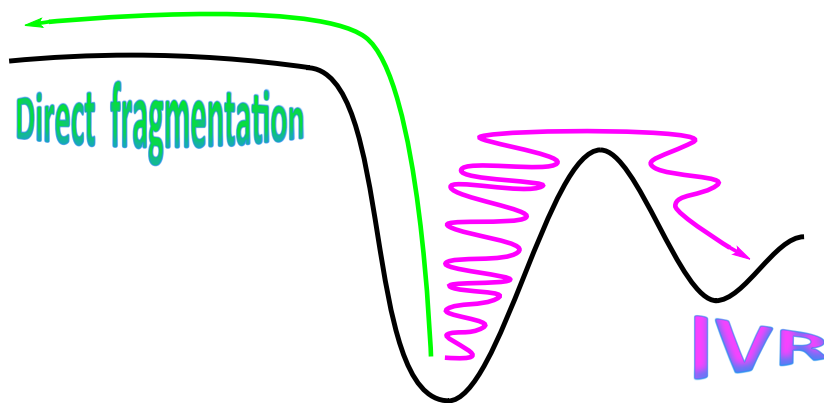


Figure 30: Schematic representation of the limiting fragmentation mechanisms used to explain CID reactivity: direct fragmentation *vs.* RRKM. Dynamical mechanisms happening before IVR can take place or statistical mechanisms after IVR.

Thus, the purpose of this part of the thesis is twofold: on the one hand to investigate and characterize the fragmentation mechanisms on CID experiments and, at the same time, provide an explanation to the differences observed in the CID spectra of $[\text{Ca}(\text{formamide})]^{2+}$ and $[\text{Sr}(\text{formamide})]^{2+}$ dications. With this aim we performed chemical dynamics simulations and compared the results with the predictions obtained using RRKM statistical theory (short-time regime). Furthermore, by coupling the vibrational and rotational energy distributions obtained from chemical dynamics simulations of non-reactive trajectories with RRKM rate constants, $k(E)$, it is possi-

2. METHOD ASSESSMENT

ble to model reactivity in the long-time scale, an important issue that is difficult to directly obtain only from chemical dynamics simulations. Thus, the combination of both methods provides a multi-scale approach allowing to bridge the gap between the different time-scales involved in CID experiments: short-time non-statistical reactivity together with the long-time statistical reactivity.

Concerning the nomenclature, in what follows, *min1* will refer to the global minimum of the PES of formamide-Ca²⁺ and formamide-Sr²⁺ shown in Fig. 28 and 29; *intX*, where *X* is a number according to the nomenclature used in the PES, will name the different intermediates on the PES and TS_X_Y the transition state connecting the *X* and *Y* local minima, *k*_{XY} (*t*_{XY} when considering half-life times) denoting the RRKM rate constants. To denote the exit channels we will use letters *A*, *B*, *C*, and so on.

2 Method assessment

Such calculations require a reliable description of the potential energy surface as well as reliable predictions of molecular properties, and this can be attained through the use of *ab initio* methods. CID experiments are now routinely applied to small and large molecules such as peptides and proteins,^{8,169,205} and combining CID with RRKM in these latter cases requires electronic representations computationally less expensive than *ab initio* methods. A similar situation occurs when coupling RRKM and direct dynamics simulations of the fragmentation.^{188,191,193,194,206} This calls for resorting to less computationally demanding theoretical approaches, such as density functional theory (DFT).²⁰⁷ To be sure about the reliability of the results obtained *via* DFT it is, however, necessary to carry out an assessment in order to choose the most appropriate functional.

Thus, one of the aims of this section is to test a variety of DFT methods, as well as the MP2 wave function method against benchmark CCSD(T) results for the two aforementioned systems, using a small basis set (6-31G(d)). This would allow us to validate the accuracy of non-expensive methods that might be used for computationally expensive treatments such as dynamics simulations or bigger systems like oligopeptides. The geometries and energies will be obtained with 21 different DFT approaches. These methods will also be assessed from the kinetic point of view, a rather unusual approach providing an original way to assess DFT functionals also on kinetics rather

2. METHOD ASSESSMENT

than simply on energetics and/or frequencies.

Preliminary assessment. A wide window of functionals combined with a small basis set were evaluated in a preliminary assessment (“low cost” methods). However, caution must be taken when selecting a DFT method to use for a specific problem or a specific system because often a DFT method that correctly predicts certain properties, such as geometries or binding energies, will prove to be much less accurate for the computation of other properties, such as barrier heights of conformational energy differences. On the other hand, those energies are the energetic properties governing the different reactive pathways. Therefore, the crucial point is whether this “low cost” approach performs well enough when treating di-cationic systems. Hence, in this assessment, we considered energetics corresponding to the principal reaction mechanisms: M^{2+} -O dissociation energy to obtain formamide + M^{2+} , as a representative example of neutral loss, and the barrier height for the fragmentation of the global minimum (min1) into $[M(NH_2)]^+ + [HCO]^+$, as an example of Coulomb explosion. The goal is to find the method that performs better for both processes (metal–ligand bond energy and barrier height). For this assessment we will use CCSD(T) single-point calculations on DFT optimized geometries as reference. We evaluated 21 functionals using the 6-31G(d) basis set plus three functionals (BLYP, G96LYP) and B3LYP) using the 6-31+G(d,p) basis set. In all cases the basis set for Sr is LANL2DZ. For more detailed information about the functionals and basis set employed see the methodology section. The results are shown in Tables 9 and 10 for $M = Ca$ and $M = Sr$, respectively.

2. METHOD ASSESSMENT

Table 9: Ca^{2+} -O dissociation energy (NL) and Coulomb explosion ($[\text{Ca}(\text{NH}_2)]^+ + [\text{HCO}]^+$) energy barrier (CE) computed with different DFT functionals, all with the 6-31G(d) basis set but when explicitly written. The third column shows the energy difference between Ca^{2+} -O dissociation energy and Coulomb explosion energy barrier (gap). The fourth column is the same energy difference without taking into account the ZPVE correction (gap*). The first row corresponds to the benchmark method. All values are in kcal mol⁻¹.

formamide- Ca^{2+}				
	NL	CE	Gap	Gap*
CCSD(T)/cc-pWCVTZ	90.76	77.45	13.31	10.10
BLYP	88.02	81.51	6.51	2.95
BLYP/6-31+G(d,p)	82.74	78.77	3.97	0.38
G96LYP	84.30	82.22	2.09	-1.57
VSXC	86.42	85.34	1.08	-2.60
G96LYP/6-31+G(d,p)	80.19	79.71	0.48	-3.10
PBEPBE ^{a)}	87.50	88.10	-0.60	-4.23
MP2	86.24	87.62	-1.38	-4.46
O3LYP	85.21	88.66	-3.45	-6.70
X3LYP ^{a)}	89.74	93.42	-3.69	-6.94
B3LYP	88.86	92.58	-3.72	-6.94
B3LYP/6-31+G(d,p)	84.58	88.80	-4.22	-7.51
TPSS	87.14	92.32	-5.18	-8.55
M06-2X ^{a)}	89.22	95.53	-6.30	-9.05
M05	87.22	93.90	-6.68	-9.67
M05-2X	90.04	99.18	-9.13	-11.86
M06 ^{a)}	86.21	95.39	-9.17	-12.27
BH&HLYP	90.18	99.68	-9.50	-12.57
B972	85.60	95.23	-9.63	-12.85
B3PW91	86.23	96.05	-9.81	-13.11
M06L ^{a)}	82.73	92.99	-10.26	-13.91
MPW1PW91	87.42	98.17	-10.75	-13.95
PBE1PBE ^{a)}	87.87	98.74	-10.86	-14.17
B3P86	87.27	98.24	-10.97	-14.30
BMK	86.59	99.49	-12.90	-15.95
BH&H	95.56	110.00	-14.44	-17.32

^a ZPVE was not corrected by the scale factor because it was not available.

2. METHOD ASSESSMENT

Table 10: $\text{Sr}^{2+}\text{-O}$ dissociation energy (NL) and Coulomb explosion ($[\text{Sr}(\text{NH}_2)]^+ + [\text{HCO}]^+$) energy barrier (CE) computed with different DFT functionals, all with the 6-31G(d) basis set but when explicitly written. The third column shows the energy difference between $\text{Sr}^{2+}\text{-O}$ dissociation energy and Coulomb explosion energy barrier (gap). The fourth column is the same energy difference without taking into account the ZPVE correction (gap*). The first row corresponds to the benchmark method. All values are in kcal mol^{-1} .

formamide- Sr^{2+}				
	NL	CE	Gap	Gap*
CCSD(T)/6-311+G(3df,2p)	78.97	86.95	-7.98	-11.60
G96LYP/6-31+G(d,p)	73.28	81.57	-8.30	-11.91
BLYP/6-31+G(d,p)	63.82	85.49	-21.67	-25.79
BLYP	63.92	87.52	-23.61	-27.86
VSXC	65.98	91.38	-25.39	-29.18
G96LYP	60.68	87.97	-27.29	-31.31
PBEPBE ^{a)}	64.55	94.35	-29.80	-33.85
B3LYP/6-31+G(d,p)	66.58	98.09	-31.50	-35.26
O3LYP	64.07	97.17	-33.11	-37.29
TPSS	66.32	100.40	-34.07	-38.24
M06L ^{a)}	65.12	99.54	-34.42	-38.66
B3LYP	66.17	101.90	-35.72	-39.68
X3LYP ^{a)}	66.93	103.13	-36.20	-40.15
06-2X ^{a)}	69.08	105.52	-36.44	-38.99
M05	66.02	104.81	-38.80	-42.11
B972	65.56	104.85	-39.29	-43.20
M06 ^{a)}	65.59	105.38	-39.79	-43.14
MP2	63.01	102.86	-39.85	-43.34
B3PW91	65.19	105.31	-40.12	-44.11
BH&HLYP	69.58	110.35	-40.77	-43.69
B3P86	66.21	107.48	-41.27	-45.26
MPW1PW91	66.75	108.35	-41.60	-45.38
PBE1PBE ^{a)}	66.98	109.07	-42.09	-45.96
M05-2X	69.15	112.44	-43.29	-46.48
BMK	65.91	111.91	-46.00	-48.68
BH&H	73.02	119.79	-46.77	-49.75

^{a)} ZPVE was not corrected by the scale factor because it was not available.

2. METHOD ASSESSMENT

From the values in Table 9 we observe that for $M = \text{Ca}$ only five methods give the correct qualitative result showing that as predicted by the reference CCSD(T) calculations the neutral loss is higher in energy than the activation barrier for the Coulomb explosion (positive values). In the case of Sr containing systems (Table 10) all the functionals reproduce CCSD(T) results qualitatively (same sign). The best performing method, as might be expected, depends on the metal: when $M = \text{Ca}$ the best performing model is BLYP/6-31G(d) while when $M = \text{Sr}$ the best one is G96LYP/6-31+G(d,p); it gives almost the same values as the reference. This latter result is in agreement with previous assessments,²⁰⁸ and this level is the one used in geometry optimization for the Sr containing system. Therefore, we have selected these methods for a subsequent assessment evaluating the whole PES, comparing geometries and relative energies, *vide infra*. It should be noted that in general all the functionals investigated perform well for the description of the NL dissociation energy, so the differences in correctly reproducing the gap mainly arise from the significant differences in the estimation of the Coulomb explosion barrier. Indeed, the functionals like BLYP that do not include Hartree-Fock (HF) exchange perform better than the hybrid ones. Actually, it can be observed that the agreement with CCSD(T)-reference value decreases as the amount of Hartree-Fock exchange increases, being worse for BH&HLYP than for B3LYP. In general, the inclusion of HF exchange introduces a partial self-interaction correction, but at the same time it removes the non-dynamic correlation effects described by the GGA functionals.^{209,210} This actually may explain the good performance of methods like BLYP for the particular case of the Coulomb explosion barrier, where static correlation must be important taking into account that, at the barrier, the wavefunction must be the mixture of covalent and ionic components. However, the good performance could be due to cancellation of errors affecting both estimated energies.

Since one of our objectives is to compare the formamide- Ca^{2+} and formamide- Sr^{2+} reactions, it is advisable to use the same theoretical model to reproduce both PESs. Hence, for this purpose we have chosen the G96LYP/6-31G(d) approach, which is among the best performing for both systems. For the sake of completeness, we will also test the heavily used B3LYP functional and the MP2 *ab initio* method using in all cases a 6-31G(d) basis set. In this assessment we have used as reference the potential energy surface obtained by Eizaguirre *et al.* for formamide- Ca^{2+} and formamide- Sr^{2+} .^{172,173}

2. METHOD ASSESSMENT

Geometry assessment. A comparison of the geometries obtained with the aforementioned four methods with those reported previously^{172, 173} shows rather small differences for both metals (Ca and Sr). This is very well reflected by the small errors affecting the rotational constants A , B , and C (see Fig. 31), which are sensitive criteria when comparing different geometries. All the values are given in Tables A2.24–A2.29 in the Appendix 2.

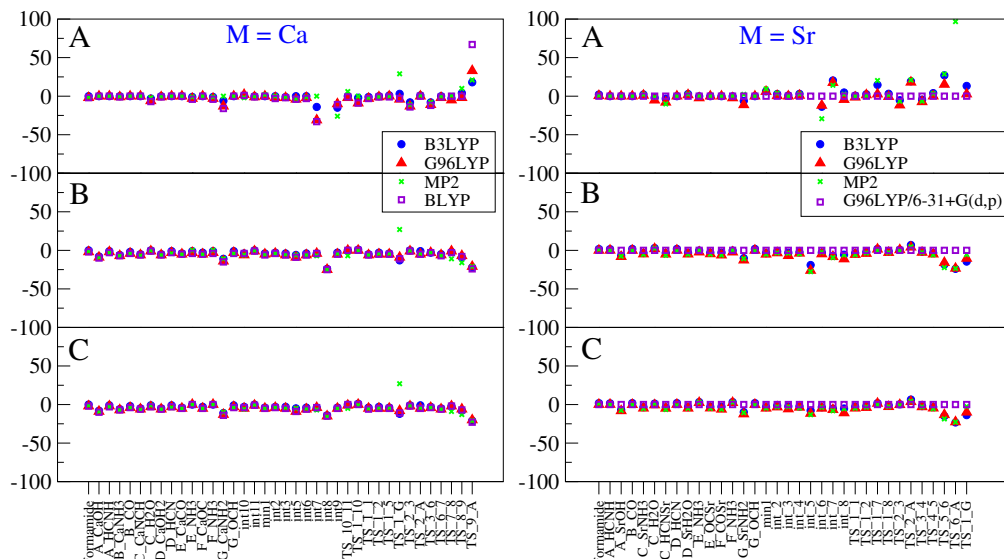


Figure 31: Relative error (%) derivations for rotational constants of (left) formamide- Ca^{2+} computed at B3LYP/6-31G(d) (blue circles), G96LYP/6-31G(d) (red triangles), MP2/6-31G(d) (green crosses), and BLYP/6-31G(d) (purple squares) and (right) formamide- Sr^{2+} computed at B3LYP/6-31G(d) (blue circles), G96LYP/6-31G(d) (red triangles), MP2/6-31G(d) (green crosses), and G96LYP/6-31+G(d,p) (purple squares).

The results show that globally there are no significant differences in the geometries optimized with the low-level approaches, although for some structures the magnitude of the relative error is slightly large. We will briefly comment on the structures with the most significant deviations, namely **int8** and **TS_1_G**. Tables with all relative error values are given in Appendix 2 (Tables A2.24–A2.29).

The structure with highest errors is **int8** for both metals. These errors in three rotational constants arise from differences in the oxygen-metal-nitrogen angle, which is about 180° with the trial methods, and 120° in the reference

2. METHOD ASSESSMENT

structure (see Fig. 32a). As expected, the rotational constant A is the most sensitive to structural changes. The TS_1_G structure is well described with the three DFT functionals while MP2 overestimates the three rotational constants by about 30% for $M = \text{Ca}$ and the rotational constant A (268% relative error) for $M = \text{Sr}$. These discrepancies are mainly due to differences in the relative orientation of the two departing fragments (Fig. 32b). Another structure with remarkably relative errors is TS_9_A, in particular when $M = \text{Sr}$, again due to different relative orientations of the departing fragments.

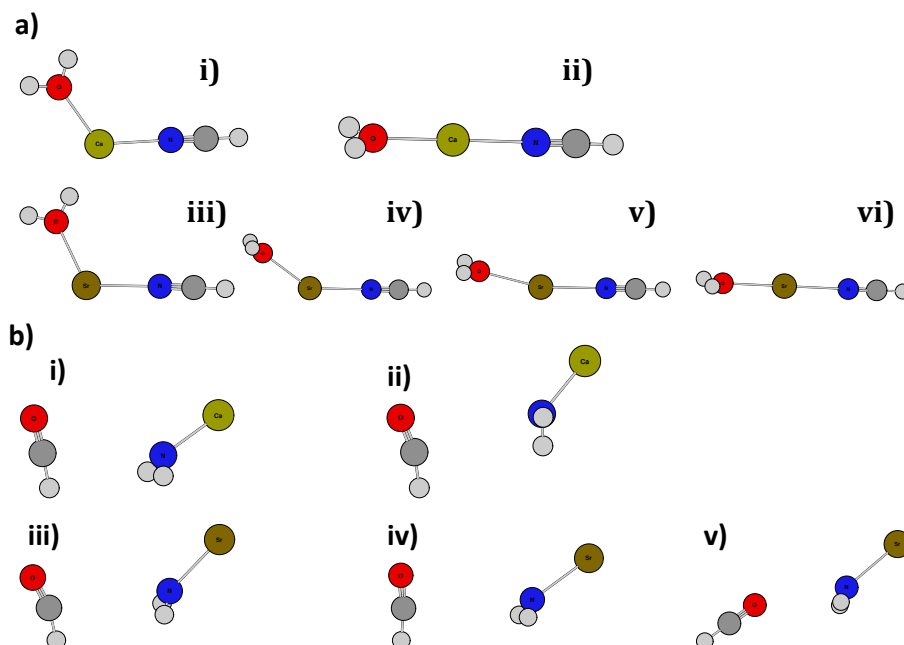


Figure 32: (a) Int8 structure for $M = \text{Ca}$ optimized with (i) B3LYP/cc-pWCVTZ, (ii) BLYP/6-31G(d) and for $M = \text{Sr}$ optimized with (iii) G96LYP/6-31+G(d,p), (iv) B3LYP/6-31G(d), (v) G96LYP/6-31G(d) and (vi) MP2/6-31G(d). (b) TS_1_G structure for $M = \text{Ca}$ optimized with (i) B3LYP/-ccpWCVTZ, (ii) BLYP/6-31G(d) and for $M = \text{Sr}$ optimized with (iii) G96LYP/6-31+G(d,p), (iv) B3LYP/6-31G(d) and (v) MP2/6-31G(d).

In summary, the only structures that show more significant errors with respect to the reference arise from the different orientation of subunits that are weakly bound. The PES, computed at the reference level, together with the structure of the corresponding stationary points are shown in Fig. 28 and 29.

2. METHOD ASSESSMENT

Energy assessment. Let us focus now on the performance of the low level approaches when dealing with energies. Relative energies were evaluated for each method by subtracting from the energy of the corresponding structure (the sum of the energy of the fragments for the exit channels), the energy of the global minimum, min1; including the corresponding ZPVE corrections. The absolute error and relative error values for all the structures are given in Tables A2.30 to A2.33 in Appendix 2. Fig. 33 shows the relative error for $M = \text{Ca}$ (a) and $M = \text{Sr}$ (b). In general the agreement is quite good and the trends are the same for the four methods.

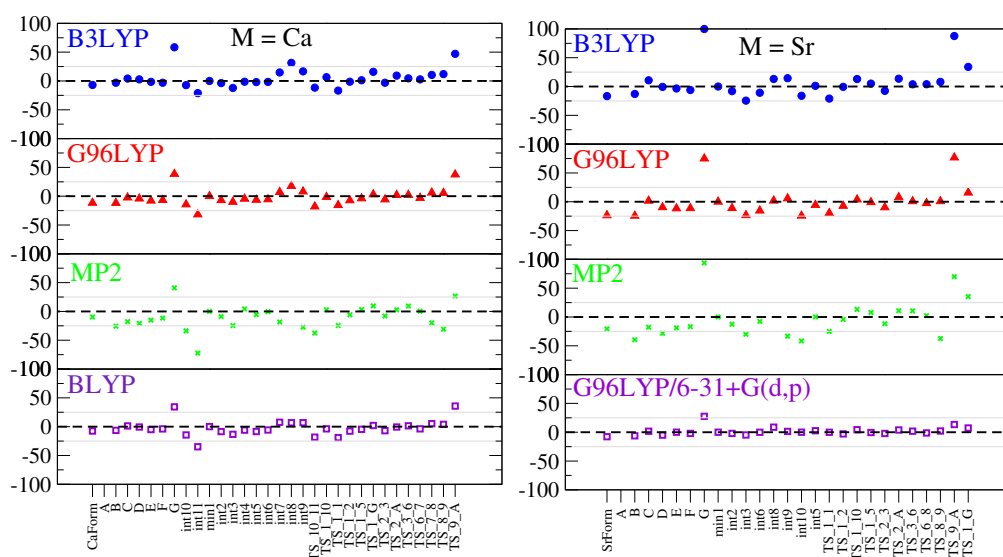


Figure 33: Relative errors in (a) formamide- Ca^{2+} relative energies computed with B3LYP/6-31G(d) (blue circles), G96LYP/6-31G(d) (red triangles), MP2/6-31G(d) (green crosses), and BLYP/6-31G(d) (purple squares) and (b) formamide- Sr^{2+} relative energies with B3LYP/6-31G(d) (blue circles), G96LYP/6-31G(d) (red triangles), MP2/6-31G(d) (green crosses), and G96LYP/6-31+G(d,p) (purple squares).

The root-mean-square error or deviation (RMSD) of the values obtained with the low-level approach from the values computed at high-level is reported in Table 11. The normalized RMSD ($\text{NRMSD} = \text{RMSD}/(b_{\text{max}} - b_{\text{min}})$ where b stands for reference values) is also reported because it is useful to compare how the performance of each method varies when the cationic metal changes from Ca^{2+} to Sr^{2+} .

It can be seen that for $M = \text{Ca}$ all methods perform almost equally well, whereas for $M = \text{Sr}$, G96LYP/6-31+G(d,p) seems to be the best option since

2. METHOD ASSESSMENT

Table 11: Root mean-square-deviation (RMSD) in kcal mol⁻¹ and normalized RMSD (NRMSD).

	Formamide-Ca ²⁺				Formamide-Sr ²⁺			
	B3LYP ^a	G96LYP ^a	MP2 ^a	BLYP ^a	B3LYP ^a	G96LYP ^a	MP2 ^a	G96LYP ^b
RMSD	7.5	6.4	8.6	6.0	14.5	12.5	14.7	3.2
RMSD	8%	6%	9%	6%	16%	13%	16%	3%

^a 6-31G(d). ^b 6-31+G(d,p)

it shows the lowest RMSD. Let us recall that G96LYP/6-31+G(d,p) is the method used in the geometry optimization of the benchmark values for M = Sr. These results are in agreement with those obtained in the first assessment discussed above. The next best performance is obtained using G96LYP/6-31G(d) for both systems. In general, there is a better agreement between low-level and high-level when the cation is Ca²⁺.

It is worth noting that whereas the first assessment of formamide-Ca²⁺ (see Table 9) shows a better performance for MP2/6-31G(d) than for B3LYP/6-31G(d), this is not the case when comparing the whole PES, where B3LYP has a slightly better performance than MP2.

Kinetic assessment. A further step in our assessment needs to include the kinetic behavior. To this end, we computed the RRKM rate constants, $k(E)$, corresponding to the different reactions shown in Fig. 34. This figure shows the kinetic schemes associated with the PES for formamide-M²⁺ (M = Ca, Sr) unimolecular reactions (see Fig. 28 and 29). For the exit channels there is no backward reaction because in CID experiments there is no equilibrium between fragments and parent ions. To compute the values for $k(E)$ we employed the same four methods used before for the geometry and energy assessments. The evaluation of the rate constant will imply an indirect assessment of three properties: energy barriers, geometries, and harmonic frequencies, needed to compute the RRKM rate constants.

From now on we will use half-life times, $t_{1/2}$, instead of rate constants, k . This quantity is proportional to the reaction rate constant $t_{1/2} = -(\ln 0.5)/k(E)$ and gives us an idea of how fast a reaction occurs. In order to compare the performance of the different methods, the curves for $t_{1/2}$ vs. E were shifted

2. METHOD ASSESSMENT

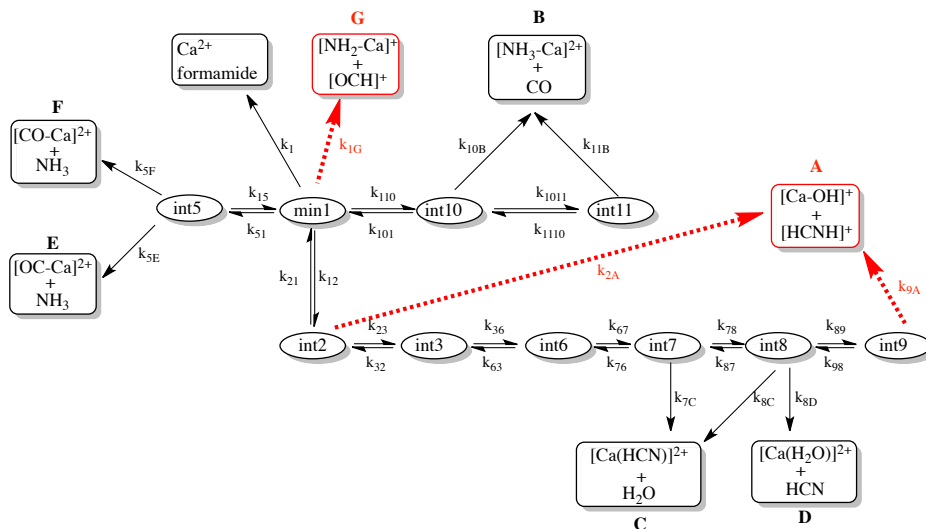


Figure 34: Mechanistic model for the kinetic study employed in this work. The corresponding one for $M = \text{Sr}$ is not shown since is practically the same. Solid black lines denote neutral loss reactions while the red dashed lines correspond to Coulomb explosions.

in the x -axis by a quantity equal to the activation barrier energy, E_{act} . Thus E stands for the internal energy available to react, *i.e.*, internal energy over the activation barrier. A graphical example is shown in Fig. 35. The average of the relative errors is plotted in Fig. 36.

It should be noted that $t_{1/2}$ is a very sensitive quantity, especially at small E , just over the energy barrier, so not surprisingly the relative errors are large in this region. As the energy increases the errors decrease and the curves tend to converge to a given value. In general, trends are similar for both metals. The MP2 method is clearly the most unfavorable with very high relative errors. B3LYP and G96LYP perform much better than MP2, but still the relative errors are significant. At small energies G96LYP is better than B3LYP but as the energy increases the order changes, with B3LYP becoming slightly more preferable. The best performance is observed for BLYP when $M = \text{Ca}$, and G96LYP/6-31+G(d,p) for $M = \text{Sr}$.

As an additional way to assess the performance of the trial methods from the kinetic viewpoint we evaluated the kinetic of the system obtained using the reference methods and with G96LYP/6-31G(d). With this aim, we compared between them the rate constants for the different reactions that the

2. METHOD ASSESSMENT

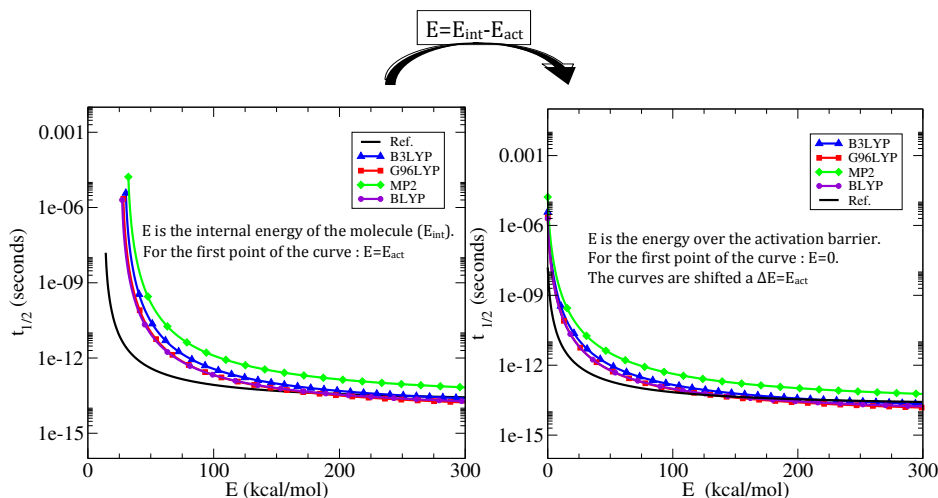


Figure 35: Graphical example showing the x -axis shift performed in the $t_{1/2}(E)$ curves in order to compare the different methods tested.

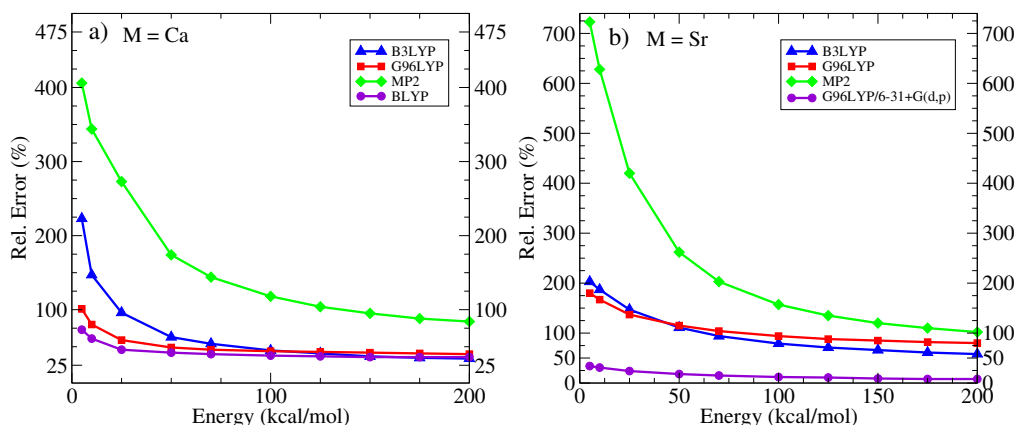


Figure 36: Relative errors in (a) formamide- Ca^{2+} relative energies computed with B3LYP/6-31G(d) (blue triangles), G96LYP/6-31G(d) (red squares), MP2/6-31G(d) (green diamonds), and BLYP/6-31G(d) (purple circles) and (b) formamide- Sr^{2+} relative energies with B3LYP/6-31G(d) (blue triangles), G96LYP/6-31G(d) (red squares), MP2/6-31G(d) (green diamonds), and G96LYP/6-31+G(d,p) (purple circles).

system may undergo. Due to the complex kinetics of formamide- M^{2+} species, characterized by a large number of intermediates, as a first approach, we will consider only the reactivity of the global minimum, min1 (see Fig. 37). There are five reactions that can take place starting from min1: formamide

2. METHOD ASSESSMENT

neutral loss (k_{01} , t_{01}), **G** Coulomb explosion yielding $[M(NH_2)]^+ + [HCO]^+$ (k_{1G} , t_{1G}), and three isomerization reactions to the intermediates **2**, **5**, and **10** (k_{12} , k_{15} , and k_{110}) with their corresponding backward reactions (k_{21} , k_{51} , and k_{101}). In Fig. 38, are plotted these half-life times as a function of the energy for $M = Ca$ (up) and $M = Sr$ (bottom). In contrast with the previous figures of half-life times (Fig. 36), and in order to compare the times predicted for the different reactions, in Fig. 38 the x -axis corresponds to the total internal energy of the molecule. The trial method, G96LYP/6-31G(d) chosen to compare with, was selected since it is the best performing method when considering both systems at a same time.

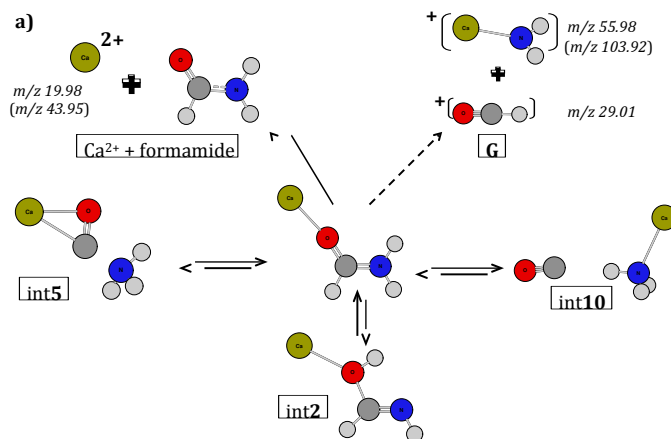


Figure 37: Reactions that can take place starting from min1 structure.

At this point, since we have the values for the rate constant, we could perform a kinetic analysis and compare the kinetic of the two systems. However, we will see that much more information about the differences between both molecular ions, formamide- Ca^{2+} and formamide- Sr^{2+} , can be extracted when combining these results with those obtained using direct dynamics simulations. Thus, in this section we will restrict the comparison to the differences between high and low level approaches.

In Fig. 38 we observe that there are no significant differences between the kinetic picture obtained with the reference and with the trial method. The main discrepancy is in the formamide neutral loss channel (t_{01}) whose rate constant is overestimated, with the consequence that this reaction is faster in relation to the others (that remain unchanged) and the energy range for which this reaction is the fastest becomes also larger. Also we noted that, in

2. METHOD ASSESSMENT

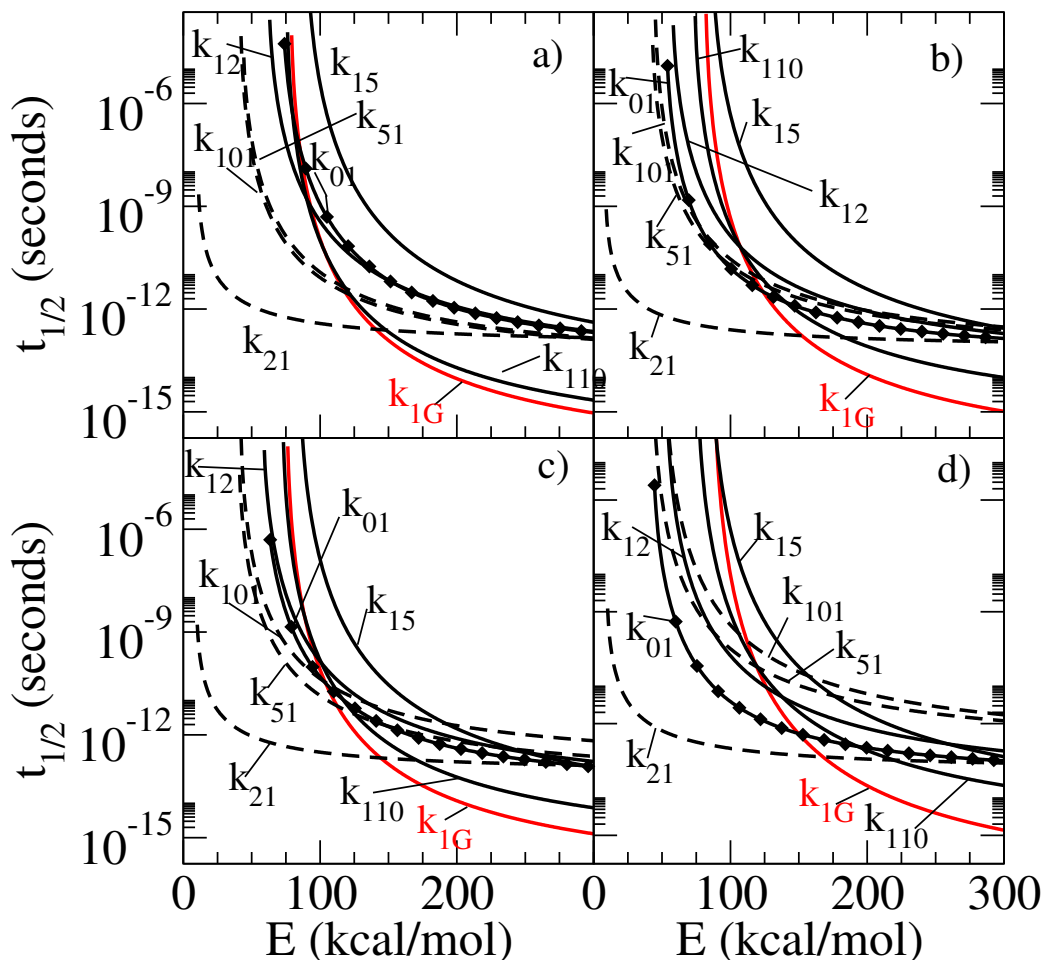


Figure 38: Half-life reaction time ($t_{1/2}$) as a function of internal energy for the corresponding RRKM rate constants describing the reaction pathways starting from min1. The top panels are for the formamide- Ca^{2+} system at (a) B3LYP/cc-pWCVTZ and (b) G96LYP/6-31G(d). The bottom panels show formamide- Sr^{2+} using (c) G96LYP/6-311+G(3df,2p) and (d) G96LYP/6-31+G(d). Solid lines correspond to forward reactions while dashed lines stand for the backward reactions.

the case of formamide- Sr^{2+} , t_{51} is underestimated with respect to the high-level value, so the min1 \rightarrow int5 reaction becomes faster than the backward reaction (around $E = 190 \text{ kcal mol}^{-1}$) in contrast with the picture when the reference level is considered. Still, min1 \rightarrow int5 is the slowest reaction at the reference level and it remains as the slowest with the low level. Thus this difference does not imply a remarkable change in the qualitative kinetic picture. In conclusion, even though relative errors are large when comparing

3. DIRECT DYNAMICS SIMULATIONS

the rate constants individually, the whole kinetic picture is qualitatively well described at the G96LYP/6-31G(d) level.

Conclusions. Among all the approaches considered, G96LYP/6-31G(d) was found to be the best compromise to reproduce PES and kinetics obtained from higher level calculations, for both systems, formamide- Ca^{2+} (B3LYP/cc-pWCVTZ) and formamide- Sr^{2+} (G96LYP/6-311+G(d,p)). Thus, this level of theory will be used to compare the reactivity of both systems. In addition, when considering separately the two systems, BLYP/6-31G(d) was found to be the best performing level when the metal is Ca and G96LYP/6-31+G(d,p) when the metal is Sr. Hence, these approaches will be also used in the dynamics simulations.

3 Direct dynamics simulations

As mentioned in the introduction, one of the approaches we used to characterize the fragmentation mechanisms taking place on CID experiments, as well as to understand the differences observed between formamide- Ca^{2+} and formamide- Sr^{+2} experimental spectra, is dynamics simulations. In this section, a description is given of the results obtained from these simulations and the main conclusions that can be drawn are exposed.

Set-up. In the direct dynamics simulations performed in this work, the molecule's nuclei positions, q_i and momenta p_i , evolve on the Born-Oppenheimer potential energy surface obtained by solving the time independent Schrödinger equation at each configuration. More details are given in the Methodology section. To compute the potential and gradient needed at each step of the simulation, and based on the previous assessment work, we used the G96LYP^{76,211} and BLYP^{76,212} functionals, both with the 6-31G(d) basis set for $M = \text{Ca}$ and the G96LYP functional with 6-31G(d) basis set for one set of trajectories with $M = \text{Sr}$ and 6-31+G(d,p) for another set of trajectories with $M = \text{Sr}$.

In our approach we just modelled a single collision, which is a good approximation when the gas pressure is very low. For the initial conditions we used the minimum energy structure (min1) of formamide- M^{2+} ($M = \text{Ca}, \text{Sr}$) (see Fig. 39). Since the electrospray ionization source used in the CID

3. DIRECT DYNAMICS SIMULATIONS

experiments is not thermalized we choose an initial temperature of 300 K for the ions as it is usually done in similar studies.^{213–216} Energies for the normal modes of vibration were selected from a 300 K Boltzmann distribution. The resulting normal mode energies were partitioned between kinetic and potential energy by choosing a random phase for each normal mode. Rotational energy and angular momentum for the molecule were selected by assuming separability of vibrational and rotational motion. Thus initial rotational conditions are obtained by assuming a thermal partitioning of $RT/2$ about each internal rotational axis. Afterwards, vibrational and rotational energies are transformed into Cartesian coordinates and momenta following algorithms implemented in the VENUS package.^{217,218} Random orientations in Euler angles between the (rigid body) Ar and the projectile (ion) are sampled in order to account for the random directions of the Ar – formamide- M^{2+} collisions. Then the ion – projectile relative energy is set and possible impact parameters are considered. The impact parameter, b , is sampled between zero and $b_{max} = 3.0$ Å. Finally the collision is done at a given energy defined in the center-of-mass of the system composed by the ion and the projectile, E_{com} . We considered three center-of-mass collision energies: 180, 230 and 280 kcal mol⁻¹, which match the experimental energy range of the available experiments.^{172,173} An schematic example of how the initial conditions for the collision simulation are set-up is shown in Fig. 39.

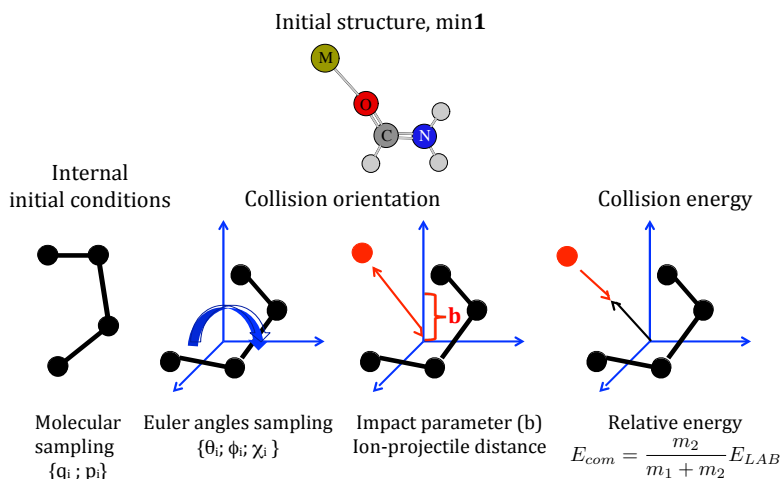


Figure 39: Top: Global energy minimum (min1) of $[M(\text{formamide})]^{2+}$ ($M = \text{Ca}, \text{Sr}$). This structure is used to select the initial conditions for the dynamics simulations. Bottom: Schematic representation of how the CID molecular dynamics is generally set-up

3. DIRECT DYNAMICS SIMULATIONS

The trajectories were calculated using the VENUS^{217,218} package coupled to Gaussian09.⁷⁷ The classical equations of motion were integrated using the velocity Verlet algorithm²¹⁹ with a time step of 0.2 fs that gives energy conservation for both reactive and nonreactive trajectories. The initial ion–Ar distance is 8.0 Å and the trajectories are stopped at a 100 Å ion–Ar distance. This corresponds to a total integration time of about 2.5 ps *per* trajectory. A trajectory was also stopped if a reactive channel was identified. In that case a criterion distance of 7.0 Å was used to guarantee no interactions between fragments. 300 trajectories for each case were computed to correctly describe the process under study.

Dynamical reaction products. The main processes after the collision with Ar are: (i) conversion of collisional energy into internal energy of scattered ions; (ii) sequential activation of a bond and reactivity observed in the simulation time length (2.5 ps); (iii) direct reaction after the collision (for example, an atom is knocked out). Fig. 40 summarizes the products obtained during the 2.5 ps simulations. The product ratios are also given in Table 12.

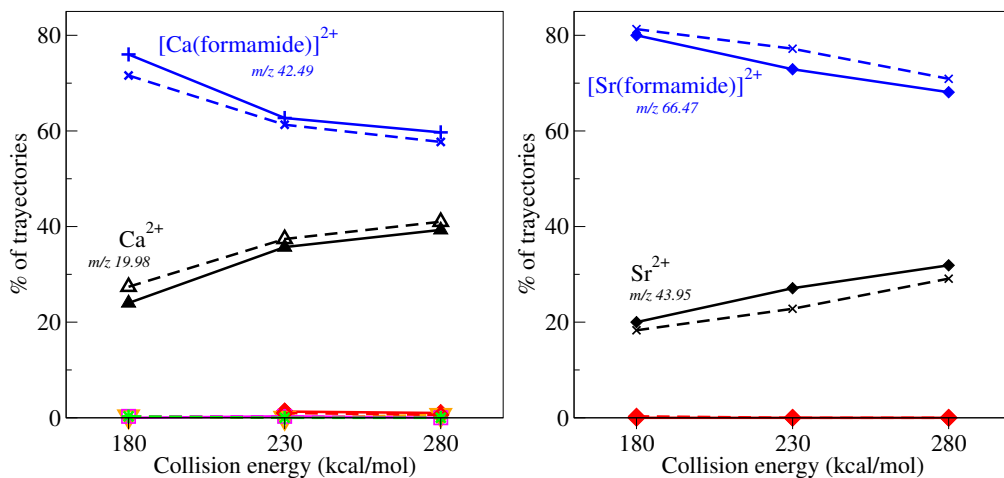


Figure 40: Percentages of trajectories for each channel as a function of the collision energy. Non-reactive trajectories (blue); product M^{2+} + formamide (black). For details on products observed in less than 2% see Table 12. The simulations were performed at two levels of theory: for $M = \text{Ca}$ (left) G96LYP/6-31G(d) (solid lines) and BLYP/6-31G(d) (dashed lines). For $M = \text{Sr}$ (right) G96LYP/6-31G(d) (solid lines) and G96LYP/6-31+G(d,p) (dashed lines).

3. DIRECT DYNAMICS SIMULATIONS

Table 12: Products ratio obtained from chemical dynamics simulations starting in the global minimum, **min1**.^a

Formamide-Ca ²⁺						
Collision energy	G96LYP/6-31G(d)			BLYP/6-31G(d)		
	180	230	280	180	230	280
Non reactive	76.0%	62.7%	59.7%	71.6%	61.3%	57.7%
Ca ²⁺ + formamide	24.0%	35.7%	39.3%	27.4%	37.4%	41.0%
[Ca(NH ₂)] ⁺ + [HCO] ⁺	—	1.3%	1.0%	—	1.0%	0.6%
[Ca(NH ₃)] ²⁺ + CO	—	0.3%	—	0.3%	0.3%	—
int10	—	—	—	0.3%	—	—

Formamide-Sr ²⁺						
Collision energy	G96LYP/6-31G(d)			G96LYP/6-31+G(d,p)		
	180	230	280	180	230	280
Non reactive	80.0%	72.9%	68.1%	81.3%	77.2%	70.9%
Sr ²⁺ + formamide	20.0%	27.1%	31.9%	18.3%	22.8%	29.1%
[Sr(NH ₂)] ⁺ + [HCO] ⁺	—	—	0.3%	—	—	—

^a The products observed correspond to excited **min1** (non-reactive), M²⁺ + formamide, **int10**, product **G**: [M(NH₂)]⁺ + [HCO]⁺ and product **B**: [M(NH₃)]²⁺ + CO showed in the PES of Fig. 28 (54) and Fig. 29 (55) for M = Ca and M = Sr, respectively.

The results do not significantly differ from one method to another. The first conspicuous fact is that the reactivity is not very high (< 40% of the trajectories react), and it is larger for calcium than for strontium. In the time length of our simulations (2.5 ps maximum) both kinds of reactive channels, neutral losses and Coulomb explosions, are observed. The former correspond to the loss of formamide and CO yielding as accompanying ions M²⁺ and [Ca(NH₃)]²⁺, respectively, and the latter to the fragmentation into [M(NH₂)]⁺ + [HCO]⁺. Note that the loss of CO is only observed for M = Ca.

These results are in good agreement with CID experimental spectra. The products obtained in the experiments^{172,173} have been summarized in figure Fig. 41. The experimental spectra are shown in Fig. 27 on page 53. Most of the trajectories did not react, which agrees with the fact that the peak for

3. DIRECT DYNAMICS SIMULATIONS

the parent ion is the most intense one. Among the reactive ones, the vast majority undergo formamide neutral loss, the second most intense peak in the experiment. Similarly, neither the loss of CO nor the ions corresponding to the **G** Coulomb explosion are observed in the formamide-Sr²⁺ reactions, in agreement with our simulations. Indeed, no trajectories end in products **B** when M = Sr and only 0.3% of the trajectories follow the **G** Coulomb explosion pathway. It is worth noting however that some other products which appear in the experimental spectra did not show up in our chemical dynamics simulations, likely because the simulation time (2.5 ps) was too short. Note that some products are observed with very low percentage (0.3 – 1.3 %) that, given the relative low number of DFT-based trajectories, correspond to a few trajectories (1–4). Of course the uncertainty associated is relatively high, such that the appearance of these products should be considered here just as the possibility of obtaining them and not quantitatively. Furthermore, it should also be noticed that under the experimental conditions the ions might undergo multiple collisions while with direct dynamics trajectories we only model reactivity due to a single collision.

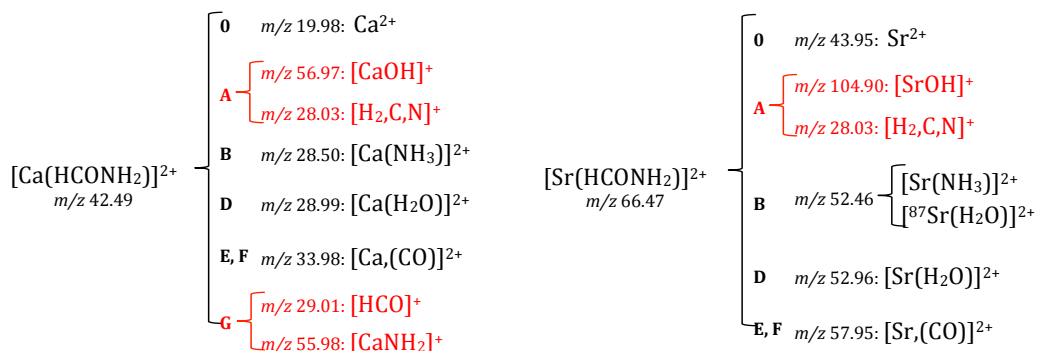


Figure 41: Masses observed in the experimental CID spectrum of formamide-M²⁺ together with their molecular formulas. M = Ca (left), M = Sr (right). In black are neutral losses and in red Coulomb explosions. Data taken from ref.¹⁷² and¹⁷³ respectively.

Effects of the collision energy on the reactivity. The agreement between our simulations and the experiments is also good as far as the effects of the collision energy on the reactivity are concerned. Indeed, our theoretical results show that for all collision energies formamide neutral loss (O–M bond dissociation) clearly prevails over the other fragmentation pathways (which

3. DIRECT DYNAMICS SIMULATIONS

are observed for less than 1.5% of the trajectories), increasing almost linearly with the collision energy (see Fig. 40). This is consistent with an impulsive collision mechanism occurring for this reactive channel (*vide infra*). For the **G** Coulomb explosion channel, giving rise to $[\text{HCO}]^+$ and $[\text{M}(\text{NH}_2)]^+$ peaks, the maximum number of trajectories following this path is observed for 230 kcal mol⁻¹ collision energy while it does not appear for the lowest collision energy used in the simulations (180 kcal mol⁻¹). Contrary, the **B** exit channel is not observed at the highest energy while it appears at low (BLYP) and middle energies (BLYP and G96LYP). Int**10** that appears for 180 kcal mol⁻¹ collision energy (BLYP), is an intermediate structure between min**1** and product **B** that will eventually evolve to product **B** (Fig. 28). The different effects of the collision energy on each reactive channel are better understood when considering the mechanisms for each pathway.

Reaction mechanisms. An important feature of the chemical dynamics simulations is that they provide an atomic-level description of the fragmentation mechanisms. There are three main ways in which the collision between the Ar and the molecular ion takes place providing subsequent reactivity (Fig. 42): (i) Ar hits the metal more or less perpendicularly to the M–O–C bond, (ii) Ar strikes formamide molecule on the C=O bond and perpendicularly to the molecular plane or, (iii) the collision takes place on the NH₂ group side and its rotation is thus activated.

The vast majority of trajectories result in formamide neutral loss, regardless of the collision site. When Ar hits calcium perpendicular with respect to the M–O–C bond (i), the collision drives the metal away from formamide. This mechanism is similar to the “golf like” mechanism found by Spezia et al.²¹³ for CID of $[\text{Ca}(\text{urea})]^{2+}$. When the collision is perpendicular to the C=O bond (ii), M^{2+} also detaches from formamide, breaking the M–O bond. Also, the M–O easily breaks for the collisions at the NH₂ group, when enough energy is transferred to the ion. Still, there is a difference due to the metal in the complex. In the case of Ca, more than one third of the reactive trajectories directly strip off the metal, whereas for Sr, which is more than twice heavier than Ca, the number of these trajectories is much smaller. Therefore, such neutral loss of formamide in the formamide– M^{2+} systems studied here can be classified as a “impulsive collision” mechanisms, as the M–O bond breaks just after the Ar collision on the same M–O bond. Hence, the probability of breaking the M–O bond increases with the collision energy.

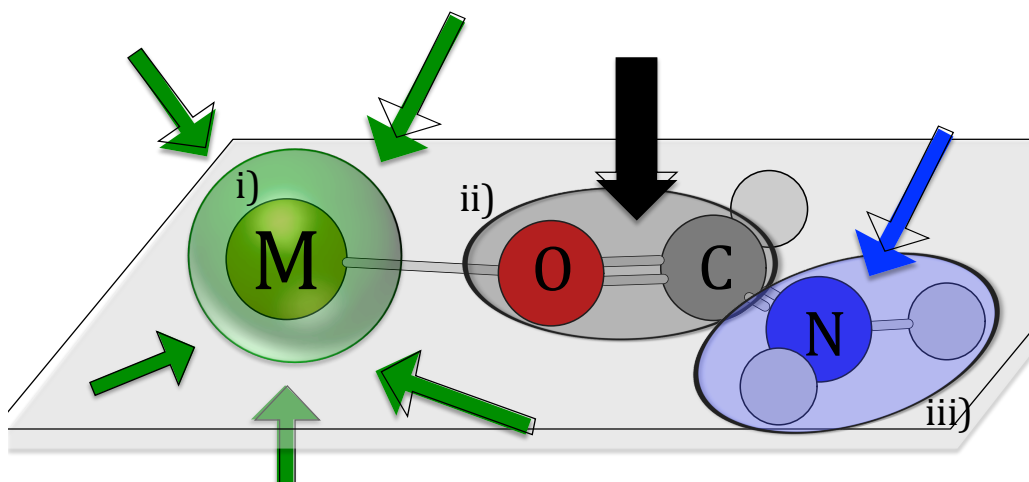


Figure 42: Different possibilities for the collision between Ar and the molecular ion providing subsequent dissociation, observed in our chemical dynamics simulations.

When the collision takes place at the NH_2 group (iii) also products **G** (Coulomb explosion), **B** (neutral loss), as well as the formation of int10 are observed. The mechanism to arrive to **G** and **B** is very similar, with only very subtle differences between the two. In Fig. 43 the evolution of the natural charge with time for the two final fragments is plotted, as well as some representative distances, for one trajectory yielding **G** and another yielding **B**.

In both processes the first 50 fs correspond to the approaching of Ar towards the molecular dication. After the collision in process **G** the first significant change is a decrease of the COCa angle, which brings the metal closer to the amino group, such that after 100 fs the Ca-N bond is practically formed and at that time both the Ca-O and the C-N bonds start cleaving in an almost synchronous way. This leads to $[\text{CaNH}_2]^+$ and $[\text{HCO}]^+$ fragments, which repel each other as shown by the steep increase of both Ca-O and C-N distances. Coherently, the net charges of the two fragments start to change also significantly at ca. 100 fs. Conversely, for process **B** the first effect of the collision is the almost synchronous cleavage of Ca-O and C-N bonds, so that after 100 fs Ca-O and Ca-N distances become very similar indicating that the metal is bridging between the HCO and the NH_2 groups. The separation of both subunits is not taking place until later. This allows the HCO group to reorient itself in order to favor a proton transfer towards the

3. DIRECT DYNAMICS SIMULATIONS

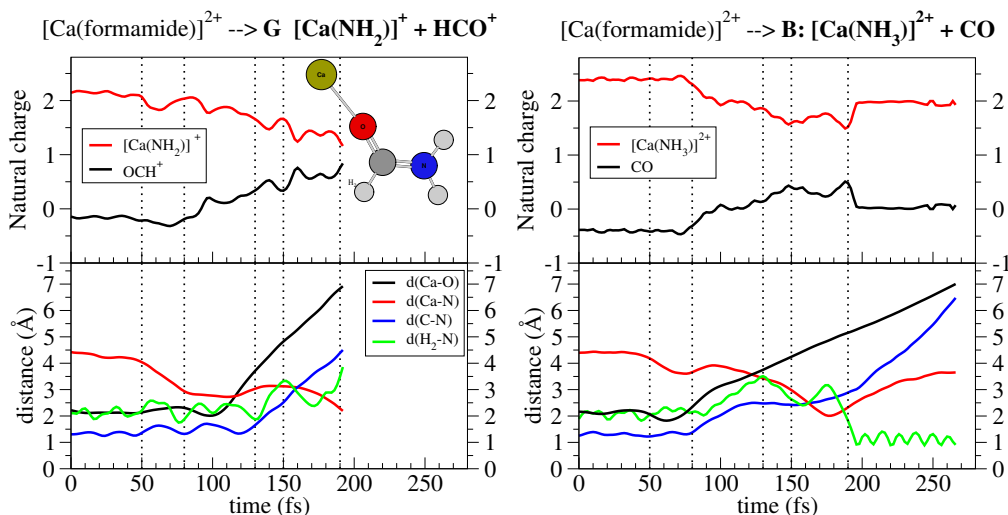


Figure 43: Evolution with time of natural charge (top panel) and distances (bottom panel) for a trajectory yielding **G**: $[\text{Ca}(\text{NH}_2)]^+ + \text{HCO}^+$ Coulomb explosion (left) and **B**: $[\text{Ca}(\text{NH}_3)]^{2+} + \text{CO}$ neutral loss (right).

CaNH_2 moiety at around 200 fs, reflected by the sudden decrease of the N–H distance (light-green line). Thus, for low collision energies, there are more probabilities of obtaining **B** since the relative movement of the two subunits will be slow, facilitating the aforementioned proton transfer, whereas at high collision energies the Coulomb explosion should be greatly favored.

Fig. 44 shows the simulation times (in fs) for chemical reactivity for the reactive trajectories. It is apparent that formamide neutral loss reaction covers a long time-span, from few femtoseconds up to ≈ 1.7 picoseconds, whereas the other reactions observed (**G** Coulomb explosion and CO neutral loss, **B**) always take place in less than 1 ps. Looking into the details of each trajectory, we observe that the fast (< 1 ps) formamide neutral loss reactions occur thanks to an impulsive collision energy transfer mechanism, in which the energy is deposited into the $\text{M}^{2+} + \text{formamide}$ relative motion leading to direct dissociation before one M–O vibrational period, thus following the direct fragmentation mechanism described in the introduction. For the remaining reactions, namely, “slow” formamide neutral loss, **G** Coulomb explosion and CO neutral loss, **B**, there are some molecular rearrangements and/or energy distribution within the internal modes of the molecule. However, does a complete IVR occur? To answer this question we plotted in Fig. 45 the reaction times as a function of the internal energy for each trajectory yield-

3. DIRECT DYNAMICS SIMULATIONS

ing Ca^{2+} (left) and **G** Coulomb explosion (right), together with the half-life times ($t_{1/2}$) predicted with RRKM rate constants as a function of the internal energy of the molecule. The corresponding graphs for formamide neutral loss at the BLYP/6-31G(d) level, as well as for Sr^{2+} at G96LYP/6-31G(d) and G96LYP/6-31+G(d,p) are shown in Figs. A2.71 and A2.72 on Appendix 2, respectively.

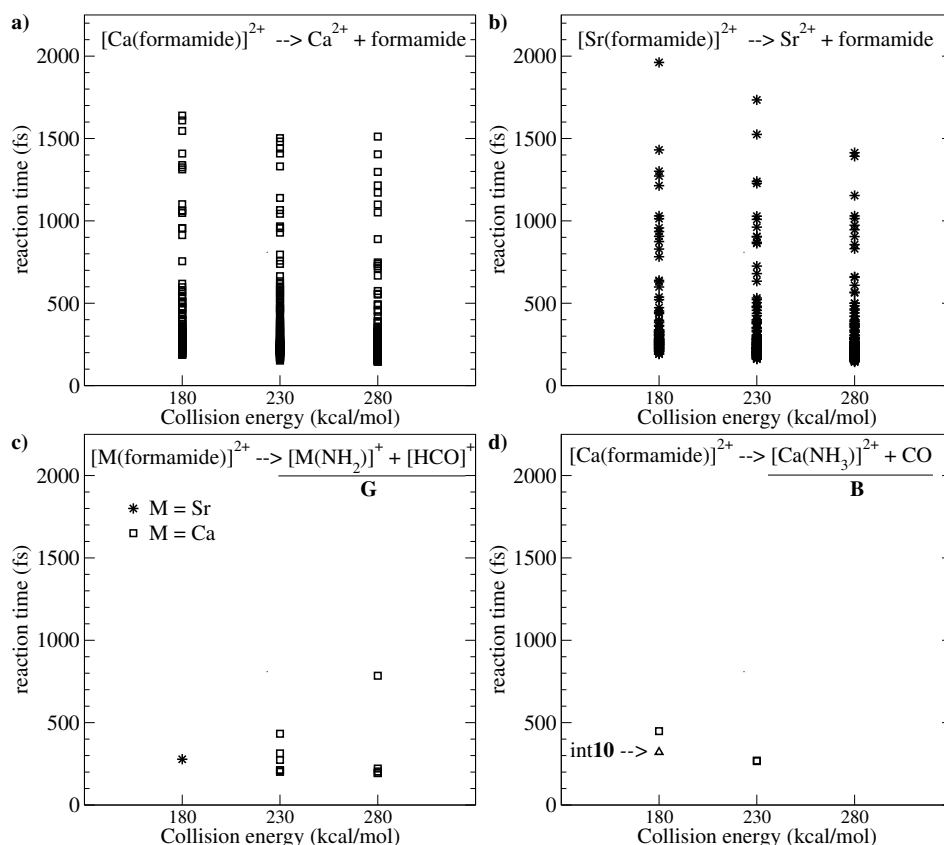


Figure 44: Simulation times (fs) for the reactive trajectories at the different collision energies: 180, 230 and 280 kJ mol^{-1} . Each point represents one trajectory. Squares are for $\text{M} = \text{Ca}$ and stars for $\text{M} = \text{Sr}$.

There are only two points on the figure on the right (k_{1G}) that match with the predicted RRKM reaction times. However, in general, both sets of times differ significantly indicating that the trajectories which do not follow a direct fragmentation mechanism neither react through a full IVR mechanism, which is assumed in the RRKM theory. This suggests that the actual mechanism is in between these two limiting cases, *i.e.*, the energy is distributed within

3. DIRECT DYNAMICS SIMULATIONS

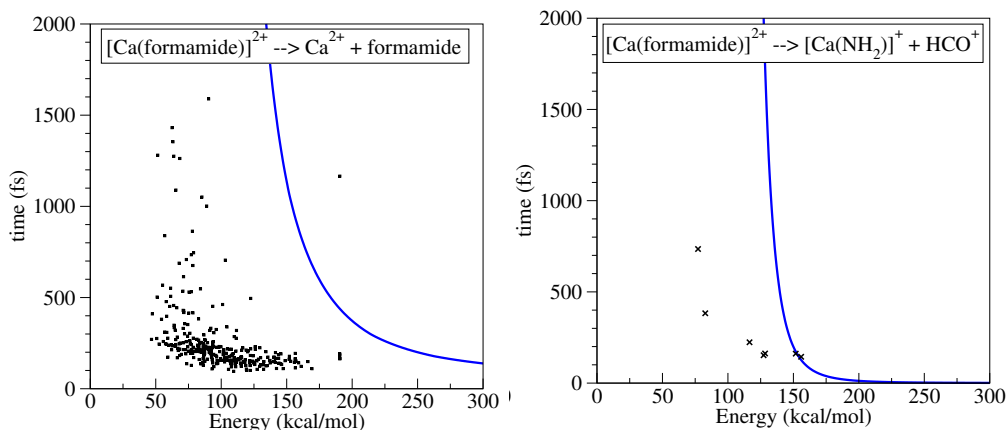


Figure 45: Reaction time *vs.* energy transfer obtained from chemical dynamics simulations (squares) and half-life times ($t_{1/2}$) predicted by RRKM (solid lines). Both were obtained using G96LYP/6-31G(d) level of theory. Results are shown for trajectories yielding formamide neutral loss (left) and **G** Coulomb explosion (right). M = Ca.

the internal degrees of freedom of the molecule, but the reaction takes place before a *complete* IVR could be achieved. Thus we called this mechanism “energy transfer”, ET, as already proposed by Spezia et al.²²⁰ These reactions are slower than if they react following a direct fragmentation mechanism, but still faster than predicted by RRKM theory (complete IVR mechanism).

Non-reactive trajectories. Another piece of information that can be extracted from our chemical dynamics simulations is the amount of energy that has been transferred during the collision to the molecular ion, shown in Fig. A2.73 and A2.74 in Appendix 2. Much more important, however, is to know how this energy is distributed after collision among the vibrational and rotational degrees of freedom of the starting ion, **min1**, population that has not reacted in the 2.5 ps simulated by chemical dynamics. Fig. 46 shows the vibrational (**a** panels) and rotational (**b** panels) energy distributions for both Ca and Sr containing molecular ions, computed at the G96LYP/6-31G(d) level of theory. Similar results (Fig. A2.77, Appendix 2) are found with the other levels of theory.

We should note that the vibrational activation for the molecules that did not react is very important, reaching values up to 120 kcal mol⁻¹. One striking feature is that the energy found in the rotational degrees of free-

3. DIRECT DYNAMICS SIMULATIONS

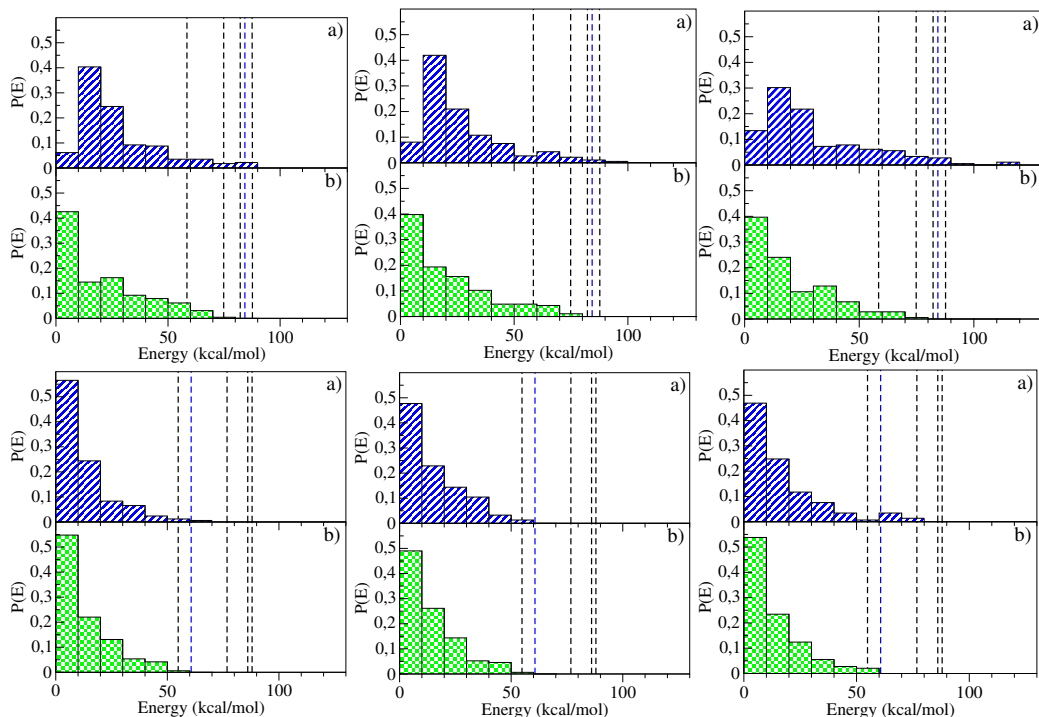


Figure 46: Vibrational (a panels) and rotational (b panels) energy distribution for the non-reactive trajectories at the three collision energies: 180, 230 and 280 kcal mol⁻¹ from left to right. The three upper graphs correspond to M = Ca while the three bottom ones are for M = Sr. Dashed vertical lines mark the energy for the different TS that can be reached from min1 structure. All the values are computed at the G96LYP/6-31G(d) level of theory.

dom is also very high with values up to 80 kcal mol⁻¹. Hence, despite the fact that rotational activation is rarely considered in RRKM models applied to CID reactivity,^{221–224} and in agreement with previous simulations of collisional activation of peptides,²⁰⁶ planar Al clusters,²²⁵ and molecular ions such as [Ca(urea)]²⁺ colliding with Ar,¹⁹³ and protonated urea colliding with Ar²²⁰ and N₂,²¹⁶ both vibrational and rotational excitations play a role in the process, being slightly larger for [Ca(formamide)]²⁺ ions than for the Sr analogue. Due to the different masses, for Ca most of the ions have vibrational energies in the 10-20 kcal mol⁻¹ interval while for Sr they are mainly in the 0-10 kcal mol⁻¹ interval. In both cases the population decreases sharply as the energy increases. The same patterns are found for the rotational excitation of both ions having most of the ions a rotational energy within the 0-10 kcal mol⁻¹ range.

More importantly, for Ca there is a fraction of the non-reactive molecules with enough vibrational energy to cross the barriers between min1 and the five accessible TSs (showed as dashed vertical lines in Fig. 46). Since the vibrational excitation is lower for Sr, only the lowest lying TSs can be reached. This suggests that **G** products are not observed in the CID experimental spectrum of [Sr(formamide)]²⁺ (in contrast to what is found for [Ca(formamide)]²⁺ ions) due to the lack of energy to reach the corresponding TSs.

4 Coupling RRKM and dynamics

In the kinetic assessment section we computed the rate constants, $k(E)$, as a function of the internal energy. Since we did not know the internal energy of the molecule, internal energies up to 300 kcal mol⁻¹ were considered. This upper limit was chosen on the basis that for the low collision energy regime of the CID experiments the energy transferred in the collision process is rarely a high percentage of the collision energy. Indeed, this assumption is in agreement with the results obtained from the direct dynamics simulations (Fig. A2.73). As previously exposed, an interesting result that can be extracted from the dynamics simulations is the internal energy distribution for the non-reactive molecules (Fig. 46). Thus, assuming that with enough time there will be extensive IVR, we can now couple the aforementioned chemical dynamics simulations with RRKM theory to build up a multi-scale approach that assesses longer time-scales.

The first step for combining the results from dynamics simulations and RRKM statistical theory was to evaluate the possible correlation between vibrational and rotational excitation. The scattering plot of vibrational *vs.* rotational internal energy depicted in Fig. A2.75 in Appendix 2 show that the vibrational excitation is independent from the rotational excitation, thus simplifying the coupling.

The upper part of Fig. 47 shows again the kinetic scheme for the reactions that can take place starting from min1. The bottom part shows the corresponding RRKM rate constants, k , instead of the half-life times ($t_{1/2}$) shown in Fig. 38. As aforementioned, knowing the internal vibrational energy distribution, it is possible to perform a kinetic analysis by means of the RRKM rate constants. In order to do so, we selected an upper value for the

4. COUPLING RRKM AND DYNAMICS

internal energy (vertical blue line in Fig. 47-b and -c) of formamide- Ca^{2+} (84 kJ mol^{-1}) and formamide- Sr^{2+} (65 kJ mol^{-1}) ions.

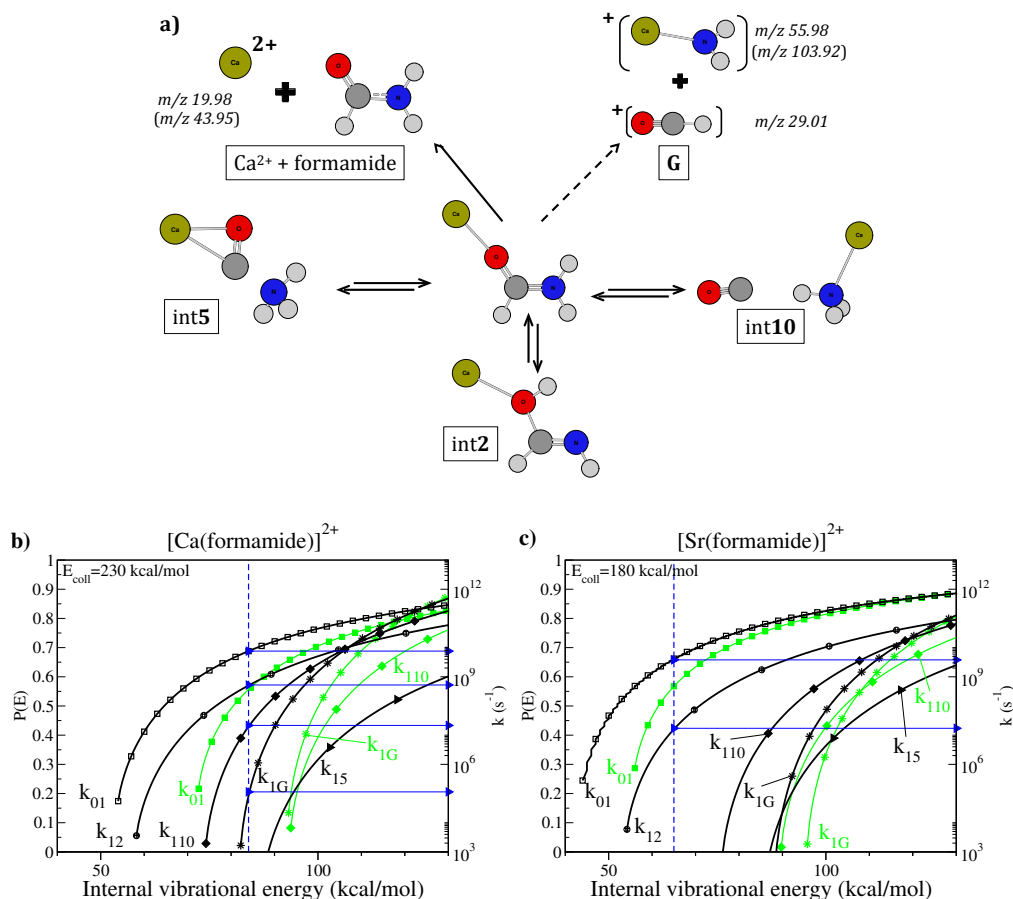


Figure 47: a) Kinetic scheme for the reactions that can take place starting from min1 for both $[\text{Ca(formamide)}]^{2+}$ and $[\text{Sr(formamide)}]^{2+}$. m/z ratios within parentheses are for $M = \text{Sr}$. In the bottom, RRKM rate constants corresponding to the aforementioned kinetic scheme (black lines). Rate constants taking into account rotational energy (27 and 18 kcal mol^{-1} for Ca and Sr, respectively) are also shown (green curves) when relevant (see text). Vertical dashed blue lines mark the selected upper value for the ions internal energy.

It can be easily seen that for these internal energies (vertical blue lines) all reactive channels but the latest (k_{15}) starting from min1 are open in the case of $[\text{Ca(formamide)}]^{2+}$ whereas only the first two channels are open (k_{01} and k_{12}) when $M = \text{Sr}$. Thus, the difference between the two systems is mainly due to the difference in the internal vibrational energy distributions

4. COUPLING RRKM AND DYNAMICS

after collisional activation, given that the kinetic schemes for both metals are quite similar. Fig. 47 also shows that in the case of $[\text{Ca}(\text{formamide})]^{2+}$ for an internal energy of 84 kcal mol^{-1} , the fastest reaction (in the order of hundreds of ps) is the one leading to formamide neutral loss yielding Ca^{2+} followed by the ones leading to **int2** (in the tens of nanoseconds time scale) and to **int10** (in the nanoseconds time scale). Finally, the **G** Coulomb explosion takes place in the microsecond time scale, four orders of magnitude slower than the formamide neutral loss. Note that even the fastest reaction obtained by RRKM analysis (*i.e.* hundreds of ps) does not happen in the time-span covered by the direct dynamics simulations ($< 2.5 \text{ ps}$) and consistently, a reactivity following a complete IVR mechanism is not observed during the simulations.

Rotational effects. Finally, it is worth noting that rotational excitation may play also an important role in the dynamics of these systems, especially when the moments of inertia of the TS are significantly different from those of the reactant. This is the case of the **min1** to formamide neutral loss, **G** products, and **int10** reactions. In the framework of RRKM theory, external rotation can be considered when computing the rate constant if the external rotational degrees of freedom are added to the modes treated as active.²²⁶ There are different ways of doing so which are explained in more detail in the Methodology section. In Appendix 2, a detailed discussion is showed of the role of external rotation energy in the rate constants depending on the way of including the external rotation to compute $k(E, J)$. Note the different notation when referring to the rate constants including rotation $k(E, J)$ compared to the rate constant with $J = 0$, $k(E)$.

In Fig. 47-b and -c it is showed the effect of rotational energy on the rate constants k_{01} , k_{1G} , and k_{110} (green curves). To compute these $k(E, J)$ the molecule was treated as an *almost symmetric top* ($I_x \approx I_y$). J and K quantum numbers were treated adiabatically (no energy exchange between vibrational and rotational modes is allowed). The total rotational energy ($E_T(\text{rot}) = 27 \text{ kcal mol}^{-1}$ (Ca) and $E_T(\text{rot}) = 18 \text{ kcal mol}^{-1}$ (Sr)) was equally distributed among the three axes ($E_{x,y,z}(\text{rot}) = 1/3 E_T(\text{rot})$). It is apparent that for both metal ions all the rate constants decrease and the curves appear shifted to higher energies, this shifting being different depending on the process. As a consequence, for $M = \text{Ca}$, the Coulomb explosion, k_{1G} , and the isomerization to yield **int10**, k_{110} , channels are closed whereas k_{01} and k_{12} channels become competitive, *i.e.* both rate constant have a similar value.

4. COUPLING RRKM AND DYNAMICS

For $M = \text{Sr}$ the effects are less dramatic, because although k_{01} is also shifted to higher energies, it does not cross k_{12} , *i.e.* it remains faster than k_{12} , and the other reactions do not take place at the energy considered.

Extending the kinetic analysis. This multi-time-scale approach can also be applied to investigate the evolution of the intermediates that can be reached from **min1**. This will be illustrated, as a suitable example for **int2** and **int10** (see Fig. 48 and 49).

Int2. The upper part of Fig. 48 shows the kinetic scheme of the possible reactions with **int2** as initial structure. In the bottom part are represented the RRKM rate constants for the matching reactions for $M = \text{Ca}$ (left) and $M = \text{Sr}$ (right).

From **int2** there are three possible options: going back to the origin, **min1**; fragmentation of **int2** via Coulomb explosion into products **A**, and an isomerization to **int3** that would eventually loose ammonia to provide product **D** (see Fig. 28, p.54). For the sake of consistency, the curves were shifted to the left by a quantity corresponding to the relative energy of each intermediate with respect to **min1**. The first conspicuous observation is that for both Ca and Sr the backward reaction to **min1** (k_{21}) is faster than the forward one (k_{12}). However, reactions towards **int3** (k_{23}) and products **A** (k_{2A}) are even faster. There are, however, some subtle differences between the two metals as far as the reaction to **A** products is concerned. Whereas for $M = \text{Ca}$ this reaction is much faster than the one going back to **min1** and that yielding **int3**, for $M = \text{Sr}$ it is slower than k_{23} and competes with k_{21} . Thus, for $M = \text{Ca}$, **int2** would rapidly evolve to products **A** and a very small fraction would isomerize to **int3**, whereas for $M = \text{Sr}$ most of the flux will follow the path leading to **int3**. In both cases this intermediate will eventually evolve to product **D**: $[\text{M}(\text{H}_2\text{O})]^{2+}$ ($M = \text{Ca}, \text{Sr}$).

Int10. In the case of the $[\text{Ca}(\text{formamide})]^{2+}$ ion, a small fraction of the non-reactive ions has energy enough to follow the path leading to **int10**. Hence a similar analysis can be performed for the intermediate **int10** (Fig. 49) that eventually yields product **B**: $[\text{Ca}(\text{NH}_3)]^{2+}$. **Int10** \rightarrow **min1** backward reaction is slower than the forward, so once **int10** is formed it will not interconvert back to products. From **int10** there are two possible pathways: either fragment into **B** products or isomerize to **int11**, which can also evolve

4. COUPLING RRKM AND DYNAMICS

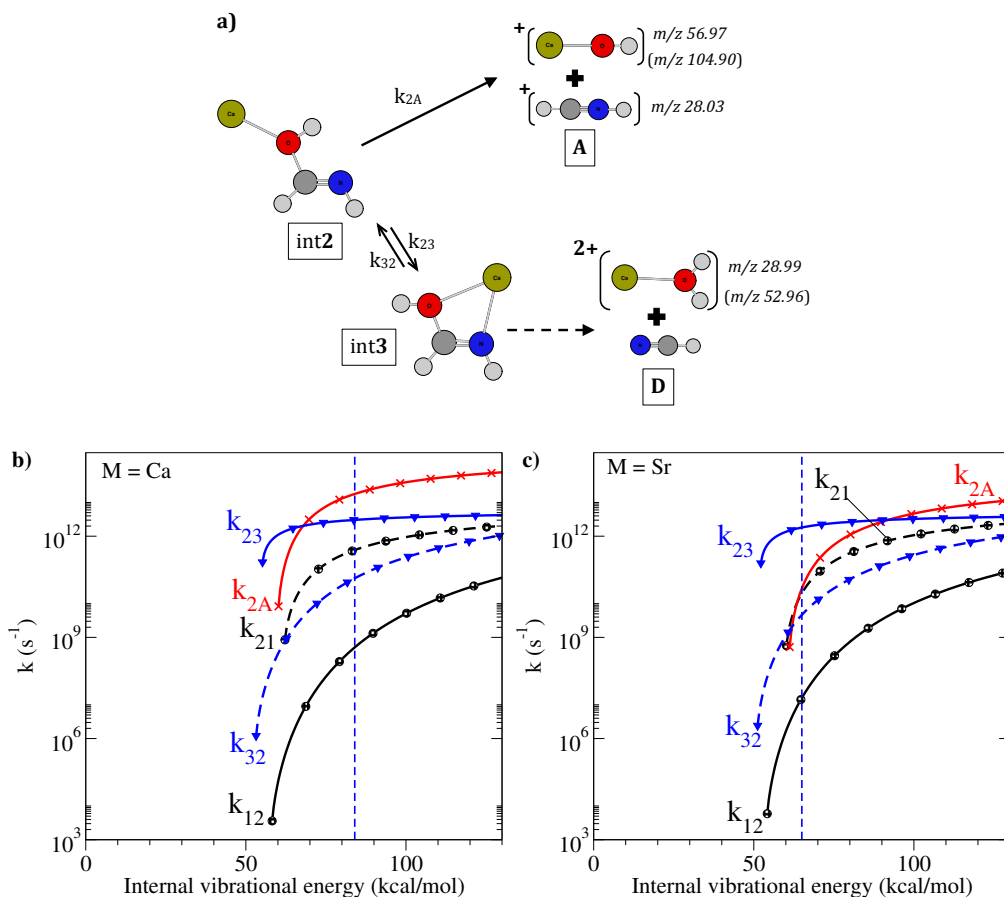


Figure 48: Upper part: kinetic scheme for the reactions that can take place starting from **int2**. Bottom part: corresponding rate constants as a function of the internal energy for (b) M = Ca and (c) M = Sr. Dashed lines correspond to backward reactions.

to **B**. Between these two options the fastest is the first one. Therefore, most of the flux will follow this path.

Summarizing, M^{2+} ions are obtained from both fast direct fragmentation mechanism and slow IVR statistical mechanisms. Following statistical mechanisms, the two systems will also form **A** Coulomb explosion products: $[MOH]^+ + [HCNH]^+$ and **D** neutral loss product: $[M(H_2O)]^{2+}$. However, formation of **D** will be dominant with respect to the formation of **A** for M = Sr, whilst the opposite is true for the M = Ca, in agreement with the experimental evidence. For M = Ca, in which the vibrational excitation of the ions is higher, two more reaction channels are open, **B**: $[Ca(NH_3)]^{2+}$ and

5. CONCLUSIONS

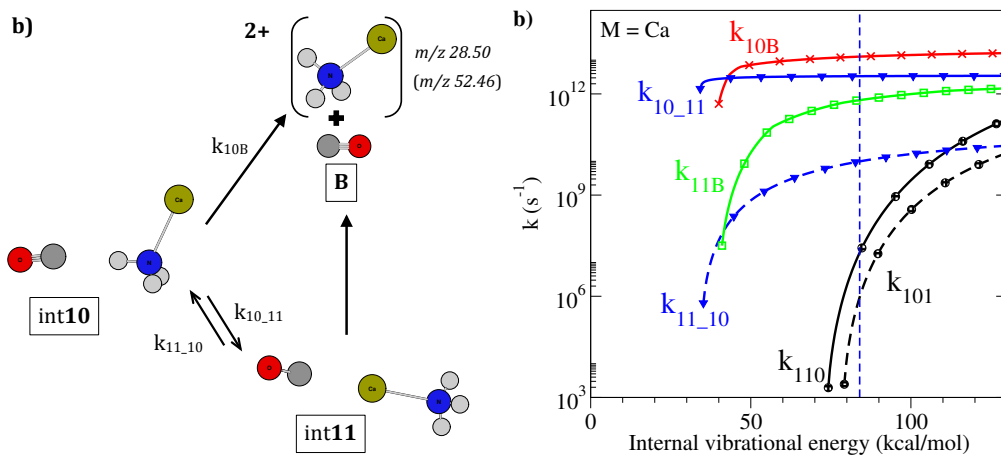


Figure 49: (a) Kinetic scheme for possible reactions starting from **int10**, (b) corresponding RRKM rate constants. Dashed lines correspond to backward reactions.

G: $[Ca(NH_2)]^+ + [HCO]^+$, which are however not accessible when $M = Sr$, again in agreement with the experimental observations. Therefore, the unassigned peak at m/z 52.46 in the $[formamide-Sr]^{2+}$ mass spectrum should correspond to $[^{87}Sr(H_2O)]^{2+}$ rather than to $[Sr(NH_3)]^{2+}$.

5 Conclusions

The fragmentation of $[formamide-M]^{2+}$ complexes follows both statistical and dynamically driven mechanisms. Indeed, almost half of the trajectories reacts in a short time scale following a dynamical mechanism. The time to form the different products varies in a wide range, from few femtoseconds to nanoseconds. In the short-time scale (< 2.5 ps) we observed mainly dynamically driven reactions (impulsive collision mechanisms for energy transfer leading in the case of CID to a direct fragmentation mechanism), as formamide neutral loss. Coupling the internal vibrational energy distributions obtained from chemical dynamics simulations with RRKM rate constants we could explore phenomena occurring at longer time-scales. Thus, we could also account for “slow” reactions occurring via IVR mechanisms and leading to a wider range of products.

The use of direct dynamical simulations allowed us to explain the presence of the M^{2+} peak, otherwise impossible to explain based on PES analyses only

5. CONCLUSIONS

(*i.e.* corresponding to the most endothermic exit channel). Furthermore, the dissimilarities between the two molecular ions such as the larger reactivity of the $[\text{Ca}(\text{formamide})]^{2+}$ system or the absence of **G** Coulomb explosion in $[\text{Sr}(\text{formamide})]^{2+}$ fragmentations, that cannot be explained neither from the PES topology nor using RRKM theory, can only be accounted for when using chemical dynamics. Therefore, by combining the three approaches: CID dynamics simulations, static (PES) and statistical (RRKM) analysis, we could explore a wide range of reaction time-scales and ultimately account for all the products observed in the CID experimental spectra of $[\text{Ca}(\text{formamide})]^{2+}$ and $[\text{Sr}(\text{formamide})]^{2+}$ doubly-charged cations, as well as explain the differences observed between these ions.

Conclusiones. La fragmentación de los iones moleculares formamida- M^{2+} ($\text{M} = \text{Ca}, \text{Sr}$) ocurre tanto mediante mecanismos dinámicos como estadísticos. De hecho, aproximadamente la mitad de las trayectorias reacciona en una escala de tiempo corta siguiendo mecanismos dinámicos. Los tiempos observados para la formación de los distintos fragmentos/productos varía en una amplia escala de tiempo que abarca desde unos pocos femtosegundos hasta los nanosegundos. La mayoría de las reacciones observadas para la escala de tiempos pequeños (< 2.5 ps) siguen mecanismos dinámicos, mecanismos de colisión impulsiva para la transferencia de energía que conducen en el caso de la disociación inducida por colisión (CID) a mecanismos de fragmentación directa, como es el caso de la pérdida neutra de formamida. Acomplando las distribuciones de energía vibracional y rotacional obtenidas a partir de las simulaciones de dinámica con las constantes de reacción calculadas usando la teoría estadística RRKM hemos sido capaces de explorar fenómenos que tienen lugar en tiempos más largos. Esto nos permitió describir las reacciones “lentas” que ocurren después de una completa y uniforme redistribución de la energía interna adquirida por la molécula en el choque en todos los modos internos de la molécula (IVR), así como explicar la aparición de un mayor número de fragmentos/productos.

El uso de simulaciones de dinámica proporcionó una explicación a la presencia de la señal del espectro correspondiente al dicatión metálico, M^{2+} , imposible de explicar basándose en el análisis topológico de la superficie de energía potencial, PES, (puesto que este producto es el canal de salida más endotérmico). Además, mediante las simulaciones de dinámica, al contrario que con otras técnicas usadas previamente como el análisis de la PES o la teoría RRKM, fuimos capaces de proponer una explicación a las diferencias

observadas en los espectros de los dos iones moleculares como por ejemplo la mayor reactividad del sistema $[\text{Ca}(\text{formamida})]^{2+}$ o la ausencia del producto de explosión culombiana **G** en el espectro de $[\text{Sr}(\text{formamida})]^{2+}$. Por tanto, combinando las tres metodologías: simulaciones de dinámica del proceso de CID, y los análisis estáticos (PES) y estadísticos (RRKM); hemos podido explorar un amplio rango de tiempos de reacción y finalmente dar cuenta de todos los productos observados en el espectro de CID experimental de los cationes doblemente cargados $[\text{Ca}(\text{formamida})]^{2+}$ y $[\text{Sr}(\text{formamida})]^{2+}$, así como proporcionar una explicación a las diferencias observadas entre ambos espectros, lo cual hubiera sido imposible mediante el uso aislado de cualquiera de las técnicas mencionadas a lo largo de este manuscrito.

6 Post-Transition State dynamics

As we have previously seen, the static and statistical approaches are not enough for completely understanding the fragmentation processes after collisional activation and dynamic effects play a role in such reactions. Thus, with the aim of deepen the understanding on the mechanism of these reactions we decided to run trajectories starting from the different TS structures that can be reached from min**1**. We will restrict this study to the Ca containing ion, $[\text{Ca}(\text{formamide})]^{2+}$. Coming back to the previous results from dynamics trajectories, we saw that after the simulated time (≈ 2.5 ps) the non-reactive molecules (excited min**1**) have enough internal energy to reach the different TSs accessible from min**1** (see Fig. 50).

As it was previously done, we assume that after enough time, the internal energy that the ion acquired during the collision will be fully and uniformly redistributed within the internal degrees of freedom of the molecule, reaching a microcanonical ensemble. Thus it is possible to start trajectories from the TS and study the evolution from this point of the PES towards different reaction channels. This can be taken as a kind of shortcut in the dynamics simulations, *i.e.* instead of simulating nanoseconds to arrive to all the products we skip the time needed for IVR and structural rearrangements leading to the TS structure. Thus, we started trajectories from the four G96LYP/6-31G(d) TS optimized structures shown in Fig. 50. This figure also shows the products that can be reached from those TSs following an IRC (solid lines) or a multi-step mechanism (dashed lines) according to the PES proposed in ref.¹⁷³

6. POST-TRANSITION STATE DYNAMICS

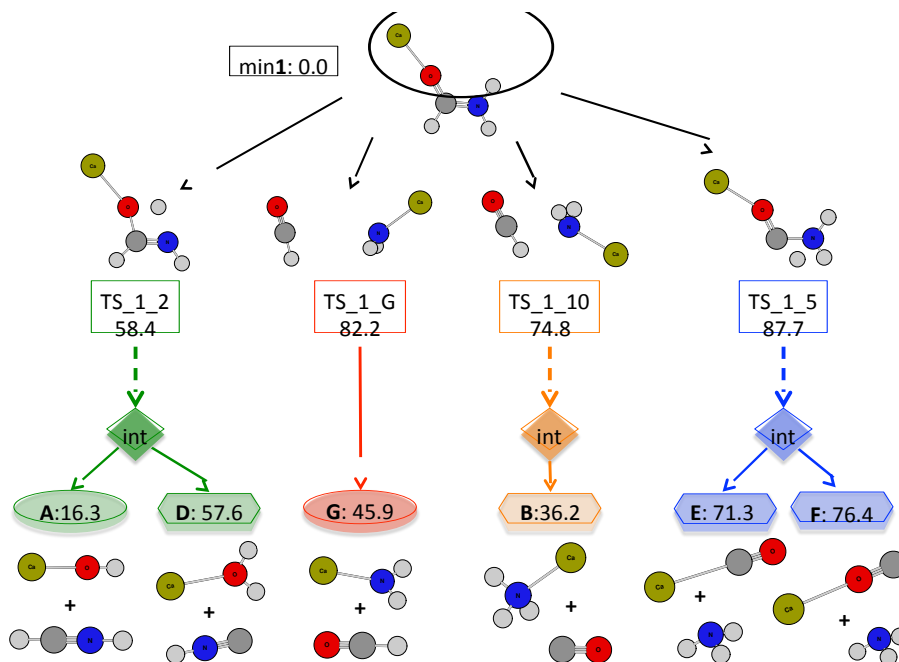


Figure 50: Different TSs that can be reached from the global minimum, min1 (this is the structure found at the end of the non-reactive trajectories), and the final product structures. The numbers below the structures are the activation barriers and product energies relative to min1 in kcal mol⁻¹.

We run a set of trajectories for which the energy was distributed within the internal degrees of freedom and another set for which the energy was used to activate the external rotation (see Fig. 51). Additionally, a set for which the initial structure has no activation energy was computed. For this set, the initial TS structure has $E_{vib} = E_{TS} + \text{ZPVE}$ (minimum energy possible) and $E_{rot} = 300 \text{ K} (= 0.4 \text{ kcal mol}^{-1})$. Within the first option (vibrational excitation) we used two different activation energies: (i) 35 kcal mol⁻¹ and (ii) 120 kcal mol⁻¹ relative to min1 (so the energy will vary depending on the TS considered). For the second option (rotational excitation) we considered two activation energies: (i) 35 kcal mol⁻¹ and (ii) 64 kcal mol⁻¹. These excitation energies were chosen according to the rotational and vibrational energy distributions obtained from CID trajectories (Fig. 46 on p.80). To select the initial conditions of each trajectory a quassiclasical microcanonical sampling was used when exciting the internal modes. For the rotational activation $1/2RT$ was added to each of the three rotational axis. More details are given in the Methodology section. Again we used Venus^{217,218} code to

6. POST-TRANSITION STATE DYNAMICS

propagate the trajectories and selecting the initial conditions coupled with Gaussian09⁷⁷ to compute the potential, gradients and Hessians at each point of the trajectory. As aforementioned we computed trajectories starting from four different TS structures. However, we will just show here the results for two suitable examples: TS_1.2 and TS_1.10, which show interesting features of the PES (*vide infra*).

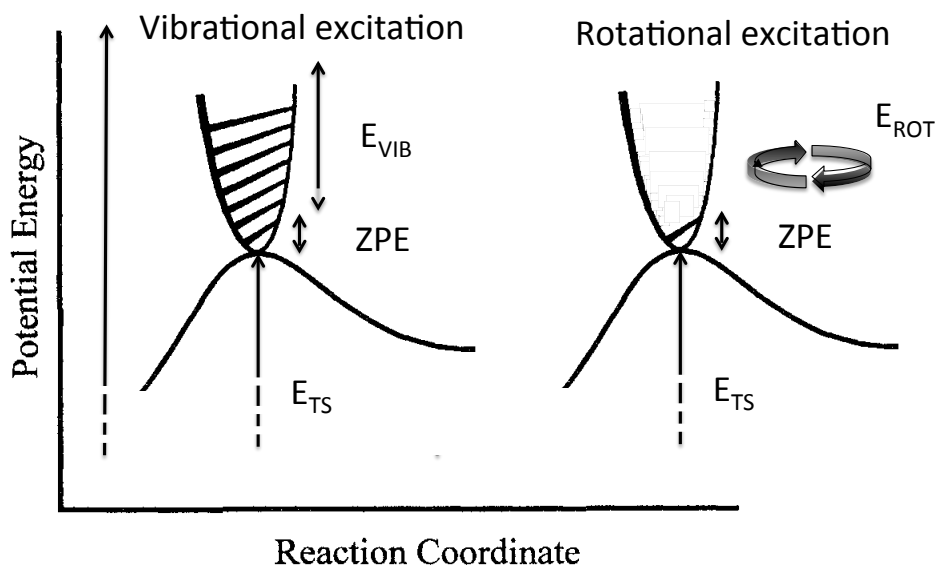


Figure 51: Different possibilities of initially placing the excitation energy on the transition state structure. Left, the energy is distributed within the internal degrees of freedom. Right, the energy activates the external rotation.

TS_1.2. The first striking conclusion reached after carefully analyzing all the trajectories run from TS_1.2 is that the PES surface will more closely resemble to the one showed in the bottom part of Fig. 52 than to the PES previously proposed by Eizaguirre *et al.*¹⁷³ (top part of Fig. 52).

The most interesting feature of the PES obtained by the dynamics simulations is the bifurcation observed when the system reaches TS_2.A structure. This means that from a single TS two different products can be reached! This has enormous implications concerning control over selectivity, *i.e.*, product ratio. As mentioned in the introduction usually it is assumed that under thermodynamic control conditions the selectivity is completely determined

6. POST-TRANSITION STATE DYNAMICS

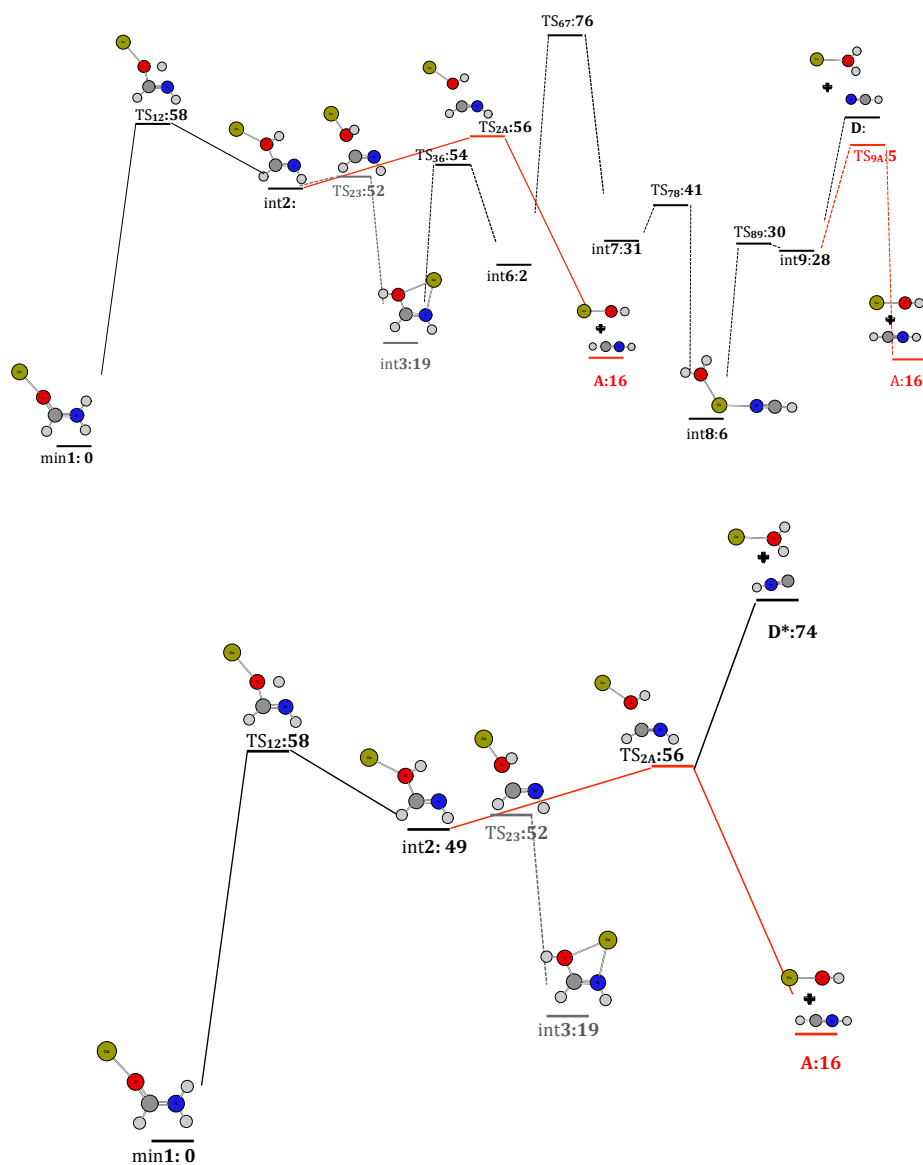


Figure 52: Potential energy surface proposed by Eizaguirre *et al.*,¹⁷³ top and PES obtained from trajectories started at TS12, bottom. All the energies are in kcal mol^{-1} .

by the free energies of the possible products, whereas in the case of kinetically controlled reactions the selectivity reduces to a matter of differences in the activation free energy to reach the different products. However, in recent years it has become apparent that for many reactions, kinetic selec-

6. POST-TRANSITION STATE DYNAMICS

tivity does not reduce to a simple choice between paths with different barrier heights.¹³ Such a case is the one showed here for the unimolecular reactivity of $[\text{Ca}(\text{formamide})]^{2+}$ ion.

Bifurcation points. The mechanistic understanding of bifurcating PES is still in its beginning¹³ and there are numerous unanswered questions around the subject. One among them is what causes product selectivity on bifurcating PES. In order to shed some light on the controlling factors when selecting one path after a bifurcation point we used the post-TS dynamics simulations previously described. The first set of trajectories considered was with no activation energy in the internal modes nor in the external rotation. We run 50 trajectories starting from TS_1_2 structure. We obtained the product distribution shown in Fig. 53-a) ($E_{\text{ROT}} = 0.4$). To analyze the role of rotation on the selectivity on the bifurcating PES we run two additional sets of 50 trajectories, one with 35 kcal mol⁻¹ in the external rotation and another one with 75 kcal mol⁻¹.

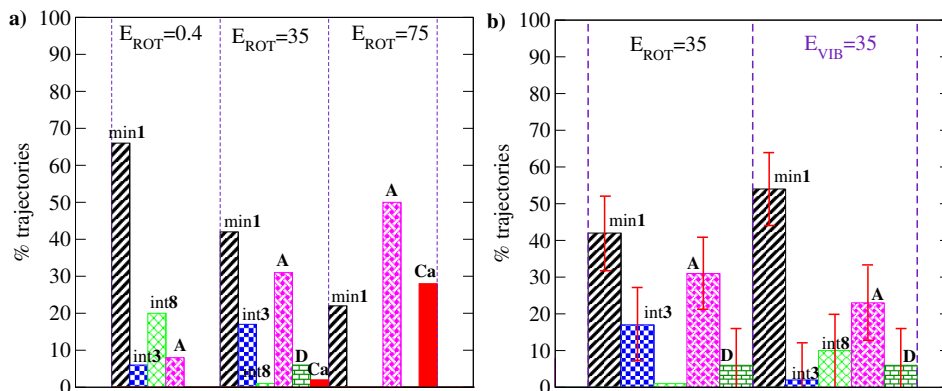


Figure 53: Product distribution for trajectories starting from TS_1_2 structure (a) adding energy to external rotation. (b) Comparison of the results obtained when 35 kcal mol⁻¹ are initially added to the external rotation (left) or to the internal modes (right).

We observe that as the rotational energy given to the initial structure increases the product distribution changes. The number of trajectories going back to min1 decreases, while those ending up in **A** Coulomb explosion product ($[\text{Ca}(\text{OH})]^+ + [\text{HCNH}]^+$) increase. For $E_{\text{ROT}} = 35$ kcal mol⁻¹ few trajectories follow the path ending in **D*** neutral loss product ($[\text{Ca}(\text{H}_2\text{O})]^{2+}$

6. POST-TRANSITION STATE DYNAMICS

+ HNC). Note that the neutral fragment, HNC, is different from the one initially proposed in ref.:¹⁷³ CNH.

To be sure that the differences on the product distribution were due to the initial rotational energy, *i.e.* not simply to the fact that the molecule has more energy to react, we compared these results to those obtained when the energy is initially placed on the internal degrees of freedom. The results for the comparison using 35 kcal mol⁻¹ are shown in Fig. 53-b). The error bars were also plotted since the number of trajectories is low (50 for each energy) the associated uncertainties are quite large. Hence, taking into account this errors, Fig. 53-b) shows that there are no significant differences between both sets of trajectories. Thus, in this case the rotational energy is not the decision-making factor when selecting one path over the other, but rather the total amount of energy available. A higher energy favors the thermodynamic product: **A** Coulomb explosion. It should also be noticed, that the initial structure for trajectories is TS_1_2, but the bifurcation point is in the TS_2_A region. So it would be interesting to perform the same analysis starting from the latest structure.

TS_1_G. Let us turn now to a different transition state, TS_1_G. This is a Coulomb explosion TS that directly links min1 to **G** products in the initial proposed PES.¹⁷³ Again, after analyzing the output from dynamics simulations we found a bifurcation point of the PES for trajectories starting from TS_1_G. As in the previous case, the two possible reactions after the bifurcation are a Coulomb explosion **G** and a neutral loss (CO neutral loss, **B** product), being the latest the less endergonic product (relative to min1). The PES as obtained from trajectories is shown in Fig. 54 .

First we analyzed the effect of increasing the rotational energy on the initial structure (see Fig. 55-a)) and then we compared the results with those from trajectories for which the same amount of energy is initially located on the internal degrees of freedom (Fig. 55-b)).

For this structure, dramatic changes on the product distribution are observed when the rotational energy is increased. When trajectories are started with no excitation energy ($E_{ROT} = 0.4$ kcal mol⁻¹) we observe four different products. However, when some rotational energy is given to the initial structure, the product distribution completely changes and product **G** is selectively obtained on 100% of the trajectories (Fig. 55-a)). However, when

6. POST-TRANSITION STATE DYNAMICS

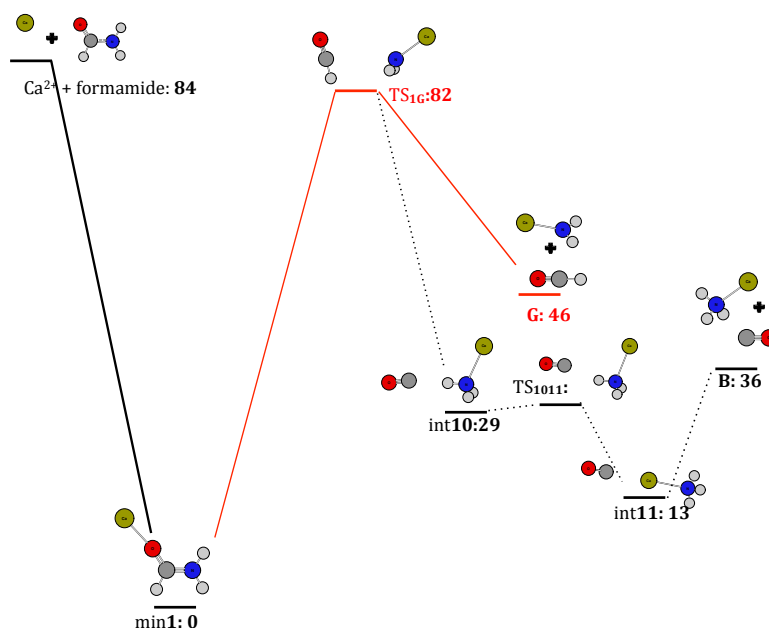


Figure 54: Potential energy surface obtained from trajectories started at the TS_1_G. The dashed pathway leading to **B** does not appear in the initially proposed PES.¹⁷³ All the energies are in kcal mol⁻¹.

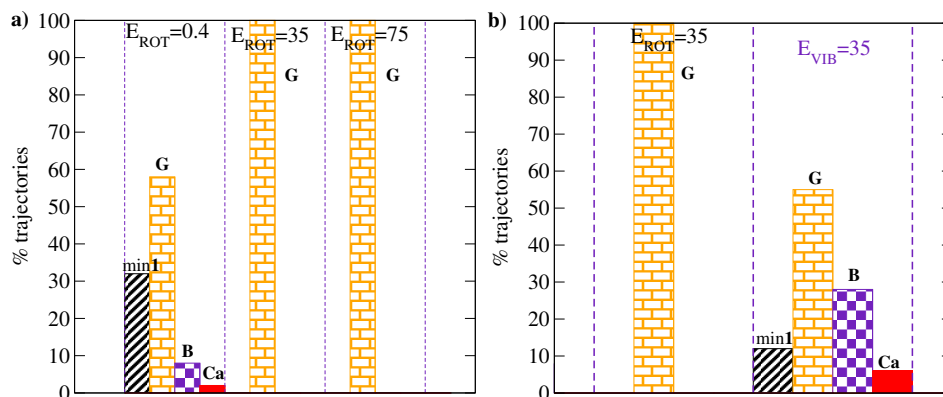


Figure 55: Product distribution for trajectories starting from TS_1_G structure (a) adding energy to external rotation. (b) Comparison of the results obtained when 35 kcal mol⁻¹ are initially added to the external rotation (left) or to the internal modes (right).

the initial excitation is on the internal degrees of freedom, the selectivity is lost and other products apart from **G** are obtained (Fig. 55-b)). Hence,

6. POST-TRANSITION STATE DYNAMICS

there is a clear difference on the product ratio depending upon where the energy is initially located. In this case, rotational energy clearly favors one path over the other, illustrating the importance that rotational energy might have on product selectivity. It is also interesting to note that it is the non-thermodynamic product the one preferably formed.

Another important question related with bifurcating PES is how to predict the bifurcation points in a reliable way. Here we want to emphasize the fact that when performing an IRC from TS_1_G structure, product **G** is systematically obtained. In order to arrive to int**10** and eventually to product **B** it is necessary to start an IRC from a different transition state structure (TS_1_10). Only by means of direct dynamics simulations we were able to start sampling the features of this “difficult” region of the potential energy surface.

Preliminary conclusions. Direct dynamic trajectories revealed the presence of bifurcations on the PES otherwise completely unnoticed. These calculations also show that the IRC or MEP is not necessarily followed by the trajectories. Furthermore, in all the cases in which a bifurcation was found the two options were a Coulomb explosion, **G**: $[\text{Ca}(\text{NH}_2)]^+ + [\text{HCO}]^+$, for instance, or a neutral loss reaction, **B**: $[\text{Ca}(\text{NH}_3)]^{2+} + \text{CO}$, being the difference where the H^+ is located on the product fragments.

For TS_1_2 increasing the energy favors the most stable product (**A** Coulomb explosion) whereas there is not a clear role of rotational energy on product selectivity. On the contrary, for TS_1_G, rotational energy totally favors formation of **G** Coulomb explosion product, that is also the less stable of the two products. Therefore, rotational energy can play an important role in tuning the selectivity between the different pathways.

Conclusiones preliminares. Las simulaciones dinámicas revelaron la presencia de bifurcaciones en la superficie de energía potencial previamente pasadas por alto. Los cálculos también muestran que las trayectorias no siguen necesariamente la coordenada interna de reacción (IRC) o el camino de mínima energía (MEP). Además, en todos los casos en los que se encontró una bifurcación las dos posibles opciones a la hora de fragmentarse la molécula son siempre o una explosión Coulombiana o una pérdida neutra, cuyos productos se diferencian en cuál de los dos fragmentos se encuentra el H^+ .

6. POST-TRANSITION STATE DYNAMICS

El aumento de energía en el caso del TS_1_2 favorece la formación del producto más estable (**A**, explosión Coulombiana) mientras que no existe un papel de la energía de rotación en la selectividad. Para el TS_1_G, al contrario, el aumento de la energía de rotación supone la formación del producto **G** exclusivamente, que además es el producto menos estable entre los dos productos posibles. Por tanto, la energía rotacional puede jugar un papel importante a la hora de modular la reactividad entre distintos caminos de reacción.

METHODOLOGY

1 Theoretical methods

Quantum Chemistry aims to interpret and predict the electronic structure and reactivity of chemical systems, using the principles of Quantum Mechanics. With this goal, since Schrödinger solved the hydrogen atom equation in 1926, several approaches with increasing levels of complexity have been developed. At the same time, more and more efficient computational programs have been developed, using at each moment the state of the art informatics technology to deal more accurately with systems of ever increasing complexity and size.²²⁷

To overcome the impossibility of exactly solving the Schrödinger equation for many electron systems, in 1930 Hartree and Fock proposed the Self-Consistent-Field (SCF) method, the origin of the current *ab initio* calculations. However, the SCF calculations were not to become truly operative until the introduction of the Linear Combination of Atomic Orbitals (LCAO) approximation. The introduction of a basis set transformed the numerical problems of solving integro-differential equations into the well-known resolution of linear algebra equations.

SCF is only a first approach to most chemical systems, because it is generally insufficient for correctly describing systems with unpaired electrons or breaking bonds. Another of its drawbacks is that it considers electrons to be independent particles that move in an average field, thus the electrons movements are not correlated within this approach. In order to address this problem different methods where the electron correlation is included have been developed. These methods start with an orbital set usually obtained by a self-consistent method. Since they include the electron correlation *a posteriori*, they are often referred to as *post* Hartree-Fock methods. They belong to three main categories: Configuration Interaction methods (CI), Coupled Cluster (CC) methods and Many body Perturbation Theory methods (PT).

In 1964, Hohenberg and Kohn showed that the ground state energy depends only on the electron density and thus they established the basis of the Density Functional Theory (DFT). A year later, the Kohn-Sham equations enabled the application of this method to molecular and solid state systems. In recent years, DFT applications have grown spectacularly because the good results that can be obtained at low cost. Its main drawbacks are due to the fact that it is a single configuration methodology and there is not a systematic way to improve its performance.

1.1 Wave function-based methods.

The existence of matter waves suggests the existence of a wave equation describing them. Such a wave equation was first proposed by the Austrian physicist Erwin Schrödinger in 1926.²²⁸ According to this approach, for any system it exists a function Ψ , the wavefunction, that contains all the information about the system. A particular solution for this equation is (4). It is known as the *time-independent Schrödinger* equation and it represents *stationary states* of the system

$$\hat{H}\Psi = E\Psi \tag{4}$$

where \hat{H} is called the *hamiltonian operator*, $\hat{H} = -\frac{\hbar^2}{2m}\nabla^2 + \hat{V}$. Due to the presence of the ∇^2 operator, eq. (4) can be solved only if it can be separated on its different variables. In the \hat{V} operator there are terms involving the coordinates of more than one particle at the same time and consequently the Schrödinger equation cannot be solved in an analytical way. It is necessary to resort to different approximations in order to obtain approximate solutions.

Born-Oppenheimer approximation. Born and Oppenheimer made the first of these approximations in 1927.²²⁹ It is based on the large disparity in mass between nuclei and electrons (on the order of 2000 to 1 or more). Since the nuclei are much more massive than the electrons, they tend to move considerably more slowly than do the electrons. The assumption is made that the electrons readjust themselves very rapidly to any configurational change of the nuclei. In the Born-Oppenheimer approximation we assume that both movements are uncoupled. Thus, first the nuclei positions are fixed and the electrons movements around them are considered. In this way, an energy value for the electrons in the fixed nuclei configuration is obtained. This energy together with the internuclear repulsion makes up the potential energy

1. THEORETICAL METHODS

to which the nuclei are subject. With this potential and the kinetic energy for the nuclei the nuclear part of the equation can be solved and therefore the total energy and wavefunction for the system can be calculated.

The orbital approximation. As abovementioned, for an N-electron system the Schrödinger equation cannot be solved exactly and we need to consider approximate wavefunctions. One of the simplest models used to describe many-electron systems is known as the *orbital approximation*.²³⁰ In this approximation the hamiltonian is assumed to be of the *spin-free* form, and the many-electron wavefunction is assumed to have the general form of a determinantal product of orbitals:

$$\Psi(1, 2, \dots, N) = \frac{1}{\sqrt{N!}} \begin{vmatrix} \phi_1(1) & \overline{\phi}_1(1) & \dots & \overline{\phi}_N(1) \\ \phi_1(2) & \overline{\phi}_1(2) & \dots & \overline{\phi}_N(2) \\ \dots & \dots & \dots & \dots \\ \phi_1(N) & \overline{\phi}_1(N) & \dots & \overline{\phi}_N(N) \end{vmatrix} \quad (5)$$

A wavefunction of this form is called a *Slater determinant*.²³¹ The quantity $\phi_i(\mu)$ is called a *spin orbital* (product of the spatial part and the spin function, see eq. (6)) and μ is used to designate each electron. A spin orbital is a one-electron distribution function involving the full coordinates (three spatial and one spin) of an electron.

$$\chi_1(1) = \phi_1(1)\alpha(1) \quad \text{or} \quad \chi_1(1) = \phi_1(1)\beta(1) = \overline{\chi}_1(1) \quad (6)$$

The Slater determinant is the simplest form for an antisymmetric wavefunction. Since a determinant will change sign when any two of its rows are interchanged, such a wavefunction will incorporate the antisymmetry required whenever two fermions have their full coordinates interchanged. It also fulfills the restriction known as the Pauli exclusion principle: two electrons cannot have the same full set of quantum numbers,²³² because if there are two identical columns (or rows) the determinant is equal to zero.

Linear expansion of the wavefunction. If we consider a complete basis set $\{\chi_i(x)\}$, any one-electron function $\Phi(x)$ can be exactly expanded using this basis set

$$\Phi(x) = \sum_i a_i \chi_i(x) \quad (7)$$

1. THEORETICAL METHODS

where a_i are the coefficients for the linear combination. Let us suppose now a function of two electrons, in principle with a fixed second variable, x_2 . This function can be expanded as:

$$\Phi(x_1, x_2) = \sum_i a_i(x_2) \chi_i(x_1) \quad (8)$$

Since the expansion coefficients are also functions of a single variable, they can be expressed as:

$$a_i(x_2) = \sum_j b_{ij} \chi_j(x_2) \quad (9)$$

and

$$\Phi(x_1, x_2) = \sum_i \sum_j b_{ij} \chi_j(x_2) \chi_i(x_1) \quad (10)$$

To satisfy the antisymmetry principle, $b_{ij} = -b_{ji}$; $b_{ii} = 0$, and then

$$\begin{aligned} \Phi(x_1, x_2) &= \sum_i \sum_{j>i} b_{ij} [\chi_i(x_1) \chi_j(x_2) - \chi_i(x_2) \chi_j(x_1)] \\ &= \sum_{j>i} b_{ij} \frac{1}{\sqrt{2}} \begin{vmatrix} \chi_i(x_1) & \chi_j(x_1) \\ \chi_i(x_2) & \chi_j(x_2) \end{vmatrix} \end{aligned} \quad (11)$$

Thus, an N-electron wavefunction can exactly be expanded in a linear combination of all the determinants obtained from N one-electron functions.²³³ As far the one-electron basis-set is complete, the expansion is exact. The problem now is to choose this basis set, because the wavefunction and the energy depend on it.

The Hartree-Fock Self-Consistent-Field Method. Within the Hartree-Fock method framework the variational theorem is used to determine the electronic energy of a molecular system using as trial function a Slater determinant composed of orthonormal molecular spin-orbitals.

Hartree introduced the first procedure for this kind of calculations in 1928²³⁴ and is called the *Hartree SCF method*. He arrived at the SCF procedure by intuitive physical arguments. The proof that Hartree's procedure gives the best possible variation function was given by Slater²³⁵ and by Fock²³⁶ in 1930, giving rise to the actual name of the method: Hartree-Fock approximation. Within this approximation, the expansion of the wavefunction Φ in a linear combination of determinants (see eq. (11)) is truncated to a single term Φ_0 , whose elements are molecular orbitals.

1. THEORETICAL METHODS

Variational theorem. The importance of this theorem lies on the fact that it gives a systematic way to improve the energy of a system obtained by means of a trial function. It says that the energy associated to a normalized wavefunction Ψ , W , is an upper limit to the ground state energy of the system E .

$$W = \langle \Psi | \hat{H} | \Psi \rangle \geq E \quad (12)$$

So now we have a systematic way of improving the trial wavefunction used as a solution of the Schrödinger equation. It is worth to note that the wavefunction that gives the best energy estimate does not necessarily do the same for other properties of the system.²³⁰

Energy minimization. The general problem is to seek those spin orbitals which make the total energy $\langle \Psi | \hat{H} | \Psi \rangle$ a minimum. There are no restrictions on the spin orbitals other than that they lead to a well-behaved wavefunction. However there are other imposed restrictions. The determinant is to be of closed-shell form, with each spin orbital expressed as a product of a spatial orbital ϕ and a spin function (α or β). An additional restriction, introduced to facilitate numerical computations, is that the spatial orbitals are chosen to be orthonormal,

$$\langle \phi_i | \phi_j \rangle = \delta_{ij} \quad (13)$$

The total energy of a system having a wavefunction of the form 5 and consisting on N doubly occupied spatial orbitals is given by:

$$E = 2 \sum_{i=1}^N \epsilon_i^{(0)} + \sum_{i,j}^N (2J_{ij} - K_{ij}) \quad (14)$$

We now wish to find the best possible orbitals (subject to the restrictions mentioned) to use in a wavefunction of single-determinantal form; “best possible” meaning leading to the lowest energy. For this the lagrangian multipliers technique will be used.

The treatment is greatly simplified in a notational sense if coulomb and exchange operators are defined as follows:

$$J_i(\mu)\phi_j(\mu) = \langle \phi_i(\nu) | \frac{1}{r_{\mu\nu}} | \phi_i(\nu) \rangle \phi_j(\mu) \quad (15)$$

$$K_i(\mu)\phi_j(\mu) = \langle \phi_i(\nu) | \frac{1}{r_{\mu\nu}} | \phi_j(\nu) \rangle \phi_i(\mu) \quad (16)$$

1. THEORETICAL METHODS

With the above definitions of the coulomb and exchange operators, the coulomb and exchange integrals (both representing electron repulsions) occurring in the expression given by eq. (14) can be written:

$$J_{ij} = \langle \phi_i(\nu) | J_i(\nu) | \phi_i(\nu) \rangle = \langle \phi_j(\mu) | J_i(\mu) | \phi_j(\mu) \rangle \quad (17)$$

$$K_{ij} = \langle \phi_i(\nu) | K_i(\nu) | \phi_i(\nu) \rangle = \langle \phi_j(\mu) | K_i(\mu) | \phi_j(\mu) \rangle \quad (18)$$

It is seen that the coulomb operator is just the operator for the potential energy which would arise from an electron distribution $|\phi_i|^2$. Such operators represent the effective potentials for an electron moving in the repulsive field of other electrons. The exchange operator, on the other hand, has no classical analogue, since it arises from the non-classical antisymmetry principle.

After some mathematical treatment that we will not discuss here the *Hartree-Fock equations* are obtained:

$$\left[\hat{h}_i^{core}(1) + \sum_j^{n/2} (2\hat{J}_j(1)) \right] \phi_i(1) = \sum_j^{n/2} \epsilon_{ij} \phi_j(1) \quad (19)$$

where (1) emphasizes that the orbital or operator depend on the coordinates of one single electron.

The Hartree-Fock equations can be written in a matrix form

$$\hat{F}\Psi = E\Psi \quad (20)$$

where \hat{F} is the Hartree-Fock operator defined by

$$\hat{F} = h_\nu + \sum_j^N (2J_j - K_j) \quad (21)$$

It should be emphasized that the sole function of the Hartree-Fock operator is to generate the orbitals to be used in the wavefunction given by eq. (5). Once these orbitals are obtained, they are used in eq. (14) to calculate the energy of the system.

Also, it is worth to mention that \mathbf{E} in eq. (20) is not a diagonal matrix. However, a unitary transformation of these orbitals will leave the total wavefunction invariant. Such transformation can be found which diagonalizes the matrix \mathbf{E} and transform eq.(20) in a pseudo-eigenvalue equation

$$\hat{F}\Psi_i = \epsilon_i \Psi_i \quad (22)$$

1. THEORETICAL METHODS

the $\{\epsilon_i\}$ are called the *Hartree-Fock eigenvalues* and are the energies associated in a specific way with the Hartree-Fock orbitals.

Since the operators $J_i(\nu)$ and $K_i(\nu)$ appearing in the Hartree-Fock operator depend on the orbitals generated by this operator, it is not possible to solve the Hartree-Fock equations in the same manner as a true eigenvalue equations are solved, hence the reference to these as *pseudo-eigenvalue* equations. One of the oldest procedures used to solve these equations is the *self-consistent field* (SCF) method. The basic procedure is to choose some beginning set of orbitals $\{\phi_i^{(0)}\}$, which are used to construct an initial approximation of the coulombic and exchange operators found in \hat{F} . A first approximation to the optimized orbitals is then obtained by solving

$$\hat{F}^{(0)}\Phi_i^{(1)} = \epsilon_i^{(1)}\Phi_i^{(1)} \quad (23)$$

The new orbitals $\{\phi_i^{(1)}\}$ are now used to redefine the Hartree-Fock operator, and a second, further improved, set of orbitals is obtained by solution of

$$\hat{F}^{(1)}\Phi_i^{(2)} = \epsilon_i^{(2)}\Phi_i^{(2)} \quad (24)$$

At some point the functions obtained in an iteration become virtually the same as those of the subsequent iteration (to within some specified tolerance limit) and therefore the *self-consistent field* has been reached. This final set of SCF orbitals, which constitutes the optimized orbitals, is used to calculate the energy via eq. (14).

The physical significance of the eigenvalues of the Hartree-Fock operator \hat{F} is made clear by a theorem first proved by the Dutch physicist T. C. Koopmans.²³⁷ He showed that the optimized orbitals used to construct the single-determinantal wavefunction of an atom X and its two ions X^+ and X^- are the same. Thus, the energies of the ions are related to that of the neutral atoms by the simple relationships

$$\begin{aligned} E(X^+) &= E(X) - \epsilon_k & k &= 1, 2, \dots, N \\ E(X^-) &= E(X) + \epsilon_m & m &= N + 1, N + 2, \dots \end{aligned} \quad (25)$$

where k refers to an orbital used to describe the ground state of the neutral atom and m refers to what is called a *virtual* orbital. The expressions in eq. (25) thus imply that the energies of the occupied orbitals should be approximations to the negatives of various ionization energies of the neutral atom. Thus, if ϕ_k is the highest (in terms of energy) occupied orbital of the

1. THEORETICAL METHODS

ground state $-\epsilon_k$ is an approximation of the first ionization energy of the atom. Similarly, the energies of the virtual orbitals are approximations of the electron affinities of the atom.

Solutions to the HF equations generally involve numerical integration techniques, and the orbitals themselves are not expressible in the usual analytical form but rather in terms of tabulated numerical values over a grid of spatial positions. A great deal of computation is required to perform a Hartree-Fock SCF calculation for a many-electron atom. Hartree did several SCF calculations in the 1930s, when electronic computers did not exist. Fortunately, Hartree's father, a retired engineer, enjoyed numerical computation as a hobby and helped his son.²³⁸ In 1951, Roothaan²³⁹ and Hall²⁴⁰ proved, independently, that this problem can be solved if the molecular orbitals are expressed as a linear combination of basis set functions.

$$\Psi_i = \sum_s c_{is} \phi_s \quad (26)$$

or in a matrix way

$$\Psi = C\phi \quad (27)$$

where \mathbf{C} is the matrix for the coefficients of the expansion and $\{\phi\}$ the set of basis functions. The representation of the molecular orbitals as in eq. (26) is a purely chemical point of view: as a molecule is composed by atoms, a molecular orbital can be composed by a set of atomic orbitals. That is the reason why this approximation is known as *Linear Combination of Atomic Orbitals* (LCOA).

The transcription of the Hartree-Fock equations when an atomic orbital basis set has been defined to expand the spatial part of each spin orbital gives rise to the Roothaan-Hall equations. Before applying this approximation, the decision of adopting or not the spin restriction has to be taken. For systems with an even number of electrons in their ground state, closed-shell systems, the spin restriction is the most appropriate form, and the method is known as *Restricted Hartree-Fock* (RHF). For open-shell systems, both solutions can be chosen. If we maintain the restriction, the method is known as *Open-Shell Restricted Hartree-Fock* (OSRHF), and otherwise, *Unrestricted Hartree-Fock* (UHF).

The equations for a closed-shell systems are known as the Roothaan-Hall equations.

$$FC = SCE \quad (28)$$

1. THEORETICAL METHODS

in the compact matrix form. \mathbf{F} is the matrix representation of the Fock operator in the atomic orbital basis, \mathbf{c} the vector of coefficients of the expansion for the corresponding orbital ϕ_i , \mathbf{C} the matrix of columns $\{c_a\}$ and \mathbf{E} the diagonal matrix of the energies $\{\epsilon_i\}$. On the other hand, if spin restriction is not taken into account, the UHF method leads to two series of equations analogous to eq. (28), the Pople-Nesbet equations:

$$\begin{aligned} F^\alpha C^\alpha &= S C^\alpha E^\alpha \\ F^\beta C^\beta &= S C^\beta E^\beta \end{aligned} \tag{29}$$

These two sets of equations are not independent since the two Fock matrices depend on the total density matrix, \mathbf{P} , and they must be solved simultaneously.

Hartree-Fock method limitations. Energies calculated by the Hartree-Fock method are typically in error by about 0.5% for light atoms. On an absolute basis this is not much, but for the chemist is too large. For example, the total energy of the carbon atom is about -1000 eV, and 0.5% of this is 5 eV. Chemical single-bond energies run about 5 eV. Calculating a bond energy by taking the difference between Hartree-Fock molecular and atomic energies, which are in error by several electronvolts for light atoms, is an unreliable procedure. Consequently, a way to improve HF wavefunctions and energies have been developed.

A Hartree-Fock SCF wavefunction takes into account the interactions between electrons only in an average way, but the instantaneous interactions between electrons must be considered as well. Since, the electrons repel each other, they tend to keep out of each other's way. Thus, the motions of electrons are correlated with each other, and we speak of *electron correlation*. Different methods have been developed in order to include the instantaneous electron correlation into the wavefunction.

Actually, a HF wavefunction does have some instantaneous electron correlation because it satisfies the antisymmetry requirement. Therefore, for a HF function there is a little probability of finding electrons of the same spin in the same region of space, so it has some correlation of the motions of electrons with the same spin. This region in which the probability of finding another electron with the same spin is small is usually referred to as *Fermi hole*. We can also speak of a *Coulomb hole* surrounding each electron in an atom. This is a region in which the probability of finding another electron is

small.

A quantity called the *electron correlation energy* has been defined and it is a measure of the ability (or inability) of the HF wavefunction to provide an accurate description of the electronic structure of an atom (or molecule). After Löwdin, the electron correlation energy is defined as follows: the correlation energy of a certain state with respect to a specified Hamiltonian is the difference between the exact eigenvalue of the Hamiltonian and its expectation value in the Hartree-Fock approximation for the state under consideration.²⁴¹ The correlation energy defined in this way depends on the hamiltonian and may be expressed mathematically as

$$E_{corr} = \langle \hat{H} \rangle(\text{exact}) - \langle \hat{H} \rangle(\text{HF}) \quad (30)$$

There are several methods that introduce the electronic correlation. The conventional ones start with the Hartree-Fock wavefunction and consequently they are often referred to as *post* Hartree-Fock methods. Within these methods the most well known are: Configuration Interaction (CI) methods, Coupled Cluster (CC) methods and the perturbational method of Møller-Plesset (MP).²⁴²

There are other no conventional methods that include the electronic correlation in an alternative way. These are the methods based on the *Density Functional Theory* (DFT) that will be discussed later.

1.2 Atomic basis sets

The LCAO formulation, which is used almost universally in quantum chemistry methods, requires the definition of a set of functions to expand the spatial part of spin orbitals according to eq. (26). Thus, most molecular quantum-mechanical methods, whether SCF, CI, perturbation theory, coupled cluster or density functional, begin the calculation with the choice of a set of basis functions. This set is normally known as the *atomic basis set*. In fact, any mathematical function can be exactly represented as a linear combination of basis functions, if the set is complete, which unfortunately involves an infinite number of functions. In practice, then, we have to do with an approximate representation of our orbitals since we necessarily use a finite basis. The use of an adequate basis set is an essential requirement for success of the calculation. The two most commonly used orbitals are described in this section.

1. THEORETICAL METHODS

Slater-type orbitals (STO). At the dawn of quantum chemistry, Slater proposed using functions that, although simpler than hydrogen like orbitals, preserved the same exponential dependence on the electron-nucleus distance, r . These functions, known as Slater-type orbitals (STO)²⁴³ have the general form:

$$\phi_{\zeta,n,l,m}(r, \theta, \varphi) = N r^{n-1} e^{-\zeta r} Y_{l,m}(\theta, \varphi) \quad (31)$$

where N , is a normalization constant and $Y_{l,m}$ the spherical harmonics.

Although the exponential dependence on r guarantees a good description of the function maximum on the nucleus ($r \rightarrow 0$) and a rapid convergence with the number of functions, the calculation of tri-and tetra centric integrals is not analytical, so the use of STO has been restricted almost exclusively to the treatment of atoms and diatomic molecules.

Gaussian-type orbitals (GTO). To speed up molecular integral evaluation, Boys proposed in 1950²⁴⁴ the use of Gaussian-type functions instead of STOs for the atomic orbitals in an LCAO wavefunction. A Cartesian Gaussian centered on atom b is defined as

$$g_{ijk} = N x_b^i y_b^j z_b^k e^{-\alpha r_b^2} \quad (32)$$

where i , j and k are nonnegative integers, α is a positive orbital exponent, x_b , y_b and z_b are Cartesian coordinates with the origin at the nucleus b , and r_b is the distance to the nucleus b . The sum $i + j + k$ determines the type of orbital (for example, $l_x + l_y + l_z = 0$ is an s-type orbital, whereas $l_x + l_y + l_z = 1$ is a p-type orbital). In general the GTOs have the basic deficiency that they do a very poor job of representing the electron probability both near the nucleus and far away from it. However, this deficiency may be overcome by using a large number of GTOs. For example, a linear combination of several GTOs will essentially replace a single STO.²⁴⁵

A number of unconventional basis sets have been used by various investigators over the course of time, but none has enjoyed the overall utility of STOs. Some basis sets may appear to surpass STOs when employed for certain types of simple calculations, but these quickly lose their advantages when used in more complicated wavefunctions.²³⁰

Types of basis sets.

Minimal basis set. Let us discuss some of the terminology used to describe STO basis sets. A minimal basis set consists of one STO for each inner-shell and valence shell atomic orbital of each atom. For example, for C_2H_2 a minimal basis set consists of 1s, 2s, $2p_x$, $2p_y$ and $2p_z$ atomic orbitals on each carbon and a 1s STO on each hydrogen. There are five STOs on each C atom and one on each H, for a total of 12 basis functions. This set contains two s-type STOs and one set of p-type STOs on each carbon and one s-type STO on each hydrogen. Such a set is denoted by (2s1p) for the carbon functions and (1s) for the hydrogen functions, a notation, which is further abbreviated to (2s1p/1s).

An example of this kind of basis set is the STO-NG basis set generated by Pople and co-workers as an effective way of conjugating the advantages of STO at short and long distances and the advantage of using Gaussian functions. Thus, all the integrals are analytical. The idea is very simple and consists of using least squares to fit an expansion of N Gaussian functions to a particular STO:

$$\phi_{STO-NG} = \sum_l^N a_l \chi_l \quad (33)$$

where χ_l is a Gaussian function and the coefficients of the expansion, a_l , are obtained as mentioned above by least squares fitting to a particular STO. Although the expansion can include as many terms as are desired it is easily verified that the description of the corresponding STO for $N > 3$ improves very little in comparison with the increase in computational cost. So, the most widely used expansion is STO-3G. This means that, when the basis set of functions is used $\{\phi_i\}$, what is in fact being used for each function is an expansion such as the one given in eq. (33) in which the coefficients are predetermined. Therefore, these types of expansions are usually called *contracted Gaussian functions* and the functions χ_l , that are used in the contraction are called *primitive Gaussian functions*. A STO-3G, for instance, is a contracted Gaussian made up of three primitives.

The advantage of the minimal basis sets is that, due to the fact that they are composed by few functions, they are very fast to evaluate, so they are quite useful to have a qualitative idea of the problem. However, they are not very flexible and, therefore, if a correlated method is used, the amount of electronic correlation that we recuperate is lower than when using a bigger

1. THEORETICAL METHODS

basis set. Consequently, they are not appropriate to obtain very accurate quantitative results.

N-zeta and Split-Valence basis sets. When a bond is formed between two different atoms, the charge is not distributed equitatively thus leading to the bond polarization and a different distribution of the atom's charge within the molecule. For example, the atom that has a larger partial positive charge would have a more contracted electronic cloud while for the other one, the electronic cloud would be more disperse. Another common feature of the charge distribution in a bond is the anisotropy. For instance, in a multiple bond, the π orbitals are more diffused than in the isolated atoms in order to enhance the overlapping between them and reinforce the bond. In molecular calculations using contracted GTOs, the orbital exponents and contraction coefficients of the basis functions are kept fixed at the predetermined values for the basis sets used. Therefore, there is no way for the basis functions to adjust their sizes to differing molecular environments.

One way of improving basis set flexibility is to double the number of orbitals, what is normally known as *Double-Zeta* basis set (DZ). For H this base set contains two s orbitals ($1s$ and $1s'$), one of which is more contracted than the other. For Li to Ne atoms, there will be four s functions ($1s$, $1s'$, $2s$, $2s'$) and two sets of p functions ($2p$ and $2p'$). The extra flexibility provided by DZ basis set enables the electronic cloud to expand and contract, and take into account dynamic correlation and in particular radial correlation or in-out (if an electron approaches to the nucleus the others would move away from the nucleus) and also makes it possible for the effects of anisotropy to be correctly described. Indeed, the electronic cloud expansion or contraction is obtained through the greater or lesser participation of the most diffuse function of each pair. We can improve even more the flexibility by adding another extra set of basis functions: *Triple-Zeta*, and another one (QZ) and so on.

It is clear that this improvement of the basis set involves doubling the number of functions and therefore significantly increasing the computational effort. The aforementioned flexibility is only required in the valence orbitals of the atom, since the characteristics of the internal atoms remain almost unchanged when going from the isolated atom to the atom in the molecule. This led to Pople's group to propose an alternative that was equally flexible but more economical than the double Z basis set. Namely the *split-valence*

1. THEORETICAL METHODS

basis method, which may be described as a valence double Z method.

The general representation of this approach has the form “x-*yz*G” where *x*, *y* and *z* are integers defined as follows: *x* is the number of Gaussian functions whose sum is used to represent each inner-shell basis AO, and *yz* implies that each valence AO ϕ is to be represented by a sum of two AOs (ϕ' and ϕ''), with ϕ' represented by a sum of *y* Gaussians and ϕ'' by a sum of *z* Gaussians. The number of “splits” is indicated by the presence of two integers, *y* and *z*. If more splits than two are desired, one must indicate so by using more integers; for example, 31 implies two splits, and 311 implies three splits.

Polarization functions. There are some aspects of the bonding between atoms that can only be described if functions are added with larger angular momentum than the ones in the atom ground state. For example, a hydrogen atom in a molecular environment that polarizes it in a preferential direction cannot be described with any of the basis set mentioned above. The reason is that all the functions that are centered on the hydrogen are *s* orbitals that have spherical symmetry. This polarization could be described if *p* orbitals were added to hydrogen basis set because the mixing with the *s* orbitals breaks their spherical symmetry (see Fig. 56).

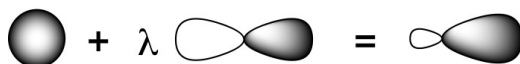


Figure 56: Schematic representation of the mixing between *s* and *p* orbitals

These type of functions that have high angular momentum are usually called *polarization functions*. For the atoms of the first row the polarization functions are *d* orbitals. For transition metals, the polarization functions are *f* orbitals and, in general, orbitals that have a higher angular momentum than the occupied ones in the atom. The polarization functions are generally added to the chosen *sp* basis set. So, DZP or TZP basis sets would be DZ or TZ basis to which polarization functions have been added. The polarization functions (*d*) can be added in the heavy atoms and not on hydrogen atoms (6-31G(*d*) or 6-31G*) or in both kind of atoms (6-31G(*d,p*) or 6-31G**).

Diffuse functions. To properly describing some systems, very small exponents (very diffuse functions) must be included in the basis set, in such

1. THEORETICAL METHODS

a way that the maximum of the function, and therefore the maximum of the density probability associated to it, is attained at relatively high values of the electron-nucleus distance. This is for instance, the case of the anions, which have an electron that is very weakly linked by the Coulomb field of the nuclei and which is therefore at a much larger distance from them than the other electrons in the system. The situation is similar in weakly bonded systems such as hydrogen-bonded complexes where the distance between the proton donor and the proton acceptor is much larger than in conventional chemical bonds and, for a proper description, the electron density in regions separated from the nuclei has to be accounted for. In general diffuse functions are included as an *s* function and a set of *p* functions for each atom of the system. When Pople basis sets are used, the inclusion of diffuse functions is indicated with a symbol +. Therefore, a 6-31+G(d) basis set is a 6-31G(d) set in which diffuse functions have been added to the heavy atoms. In a 6-31++G(d) basis set diffuse functions have also been added to the hydrogen atoms.

Effective core potentials. In the study of systems including heavy elements, the size of the atomic basis set increases quickly. However, the orbitals of the most internal shells of these atoms are hardly modified by their participation in the molecular environment since their energies are much lower than those of the orbitals participating in the bonds. This observation has prompted several authors to define an *Effective Core Potential* (ECP) to represent the effect of the core electrons on the valence ones, preserving the symmetry properties of the atom. Given that the relativistic effects in heavy elements can be considerable, several effective potentials have been developed to include these effects (*relativistic* ECP).

Core potentials can be obtained by least squares fit to accurate *ab initio* calculations. The atomic basis sets to describe the explicit electrons are also given. The size of the core is an important parameter that depends on the type of application, since the polarization of the electrons of the shells close to the valence region can be important. *Large core* ECP include all the electrons except the valence ones and *small core* ECP include in general one shell less.

1.3 Density Functional Theory

Density Functional Theory (DFT) represents an alternative to the conventional *ab initio* methods of introducing the effects of electron correlation into the solution to the electronic Schrödinger equation. In 1964, Hohenberg and Kohn showed that the ground state energy depends only on the electron density and thus, they established the basis of the Density Functional Theory (DFT). Its basic premise being that all the intricate motions and pair correlations in a many-electron system are somehow contained in the *total electron density* alone. The only problem is that the precise mathematical formula relating energy to electron density is not known, so it is necessary to resort to approximate expressions.²⁴⁶

Density functions. Let us consider a system of N electrons described by a wavefunction $\Psi(x_1, x_2, \dots, x_N)$. The product

$$\Psi(x_1, x_2, \dots, x_N) \Psi^*(x_1, x_2, \dots, x_N) dx_1 dx_2 \dots dx_N \quad (34)$$

gives us the probability of finding electron 1 between x_1 and $x_1 + dx_1$, electron 2 between x_2 and $x_2 + dx_2$, ..., and electron N between x_N and $x_N + dx_N$. The probability of finding electron 1 between x_1 and $x_1 + dx_1$, independently of where the others are found is given by:

$$dx_1 \int \Psi(\mathbf{x}_1, \mathbf{x}_2, \dots, \mathbf{x}_N) \Psi^*(\mathbf{x}_1, \mathbf{x}_2, \dots, \mathbf{x}_N) d\mathbf{x}_2 \dots d\mathbf{x}_N \quad (35)$$

and taking into account that the electrons are indistinguishable:

$$\rho(\mathbf{x}_1) d\mathbf{x}_1 = N d\mathbf{x}_1 \int \Psi(\mathbf{x}_1, \mathbf{x}_2, \dots, \mathbf{x}_N) \Psi^*(\mathbf{x}_1, \mathbf{x}_2, \dots, \mathbf{x}_N) d\mathbf{x}_2 \dots d\mathbf{x}_N \quad (36)$$

give us the probability of finding an electron between x_1 and $x_1 + dx_1$, independently of where the others are found. $\rho(x)$ is so called *density function*. The electron density $\rho(\mathbf{r})$, which can also be obtained experimentally through the X-ray technique, is obtained integrating with respect to the spin coordinate.

$$\begin{aligned} \rho(\mathbf{r}_1) &= \int \rho(\mathbf{x}_1) ds_1 \\ &= N \int \Psi(\mathbf{x}_1, \mathbf{x}_2, \dots, \mathbf{x}_N) \Psi^*(\mathbf{x}_1, \mathbf{x}_2, \dots, \mathbf{x}_N) ds_1 d\mathbf{x}_2 \dots d\mathbf{x}_N \end{aligned} \quad (37)$$

When Ψ is normalized:

$$\int \rho(\mathbf{r}) d\mathbf{r} = N \quad (38)$$

1. THEORETICAL METHODS

On the other hand, the integral:

$$d\mathbf{x}_1 d\mathbf{x}_2 \int \Psi(\mathbf{x}_1, \mathbf{x}_2, \dots, \mathbf{x}_N) \Psi^*(\mathbf{x}_1, \mathbf{x}_2, \dots, \mathbf{x}_N) d\mathbf{x}_3 \dots d\mathbf{x}_N \quad (39)$$

give us the probability of finding electron 1 between x_1 and $x_1 + dx_1$ and electron 2 between x_2 and $x_2 + dx_2$, independently of where the others are found. The *second order density*, $\gamma_2(x_1, x_2)$, is defined as:

$$\gamma_2(\mathbf{x}_1, \mathbf{x}_2) = N(N-1) \int \Psi(\mathbf{x}_1, \mathbf{x}_2, \dots, \mathbf{x}_N) \Psi^*(\mathbf{x}_1, \mathbf{x}_2, \dots, \mathbf{x}_N) d\mathbf{x}_3 \dots d\mathbf{x}_N \quad (40)$$

where $N(N-1)$ are all the possible electrons pairs that can be formed, and given that the electrons are indistinguishable, $\gamma_2(x_1, x_2) dx_1 dx_2$ consequently gives us the probability of finding any electron between x_1 and $x_1 + dx_1$ and another between x_2 and $x_2 + dx_2$. Integrating with respect to the spin variables, we obtain the *two-electron density* or *pair function*:

$$\gamma_2(\mathbf{r}_1, \mathbf{r}_2) = \int \gamma_2(\mathbf{x}_1, \mathbf{x}_2) ds_1 ds_2 \quad (41)$$

which gives us the probability of finding any two electrons, one between \mathbf{r}_1 and $\mathbf{r}_1 + d\mathbf{r}_1$ and the other between \mathbf{r}_2 and $\mathbf{r}_2 + d\mathbf{r}_2$, under any spin combination ($\alpha\alpha, \alpha\beta, \beta\alpha, \beta\beta$).

Exchange-correlation hole. Two-electron density $\gamma_2(\mathbf{r}_1, \mathbf{r}_2)$, gives us the probability density of simultaneously finding two electrons, one in \mathbf{r}_1 and the other in \mathbf{r}_2 . In other words, the two-electron density contains information about the correlated motion of two electrons. The same information about the electron correlation is contained in the exchange-correlation density, the conditional probability density, and the exchange-correlation holes described below.

The exchange correlation density, $\Gamma_{XC}(\mathbf{r}_1, \mathbf{r}_2)$, is defined as follows:

$$\gamma_2(\mathbf{r}_1, \mathbf{r}_2) = \rho(\mathbf{r}_1)\rho(\mathbf{r}_2) + \Gamma_{XC}(\mathbf{r}_1, \mathbf{r}_2) \quad (42)$$

Considering electrons as uncorrelated independent particles, the term $\rho(\mathbf{r}_1)\rho(\mathbf{r}_2)$ is the probability density of finding an electron in \mathbf{r}_1 and another in \mathbf{r}_2 . Consequently, the exchange-correlation density, $\Gamma_{XC}(\mathbf{r}_1, \mathbf{r}_2)$, represents the difference between the probability density of finding two electrons, one in \mathbf{r}_1 and the other in \mathbf{r}_2 , correlated or uncorrelated.

1. THEORETICAL METHODS

If we divide eq. (42) by $\rho(\mathbf{r}_1)$ we obtain the conditional probability density, $P(\mathbf{r}_1, \mathbf{r}_2)$:

$$\frac{\gamma_2(\mathbf{r}_1, \mathbf{r}_2)}{\rho(\mathbf{r}_1)} = P(\mathbf{r}_1, \mathbf{r}_2) \quad (43)$$

$P(\mathbf{r}_1, \mathbf{r}_2)$ gives us the probability of finding an electron in \mathbf{r}_2 when there is already another one in \mathbf{r}_1 . It can be more clearly seen if we rearrange eq. (43) in the following way:

$$\gamma_2(\mathbf{r}_1, \mathbf{r}_2) = \rho(\mathbf{r}_1)P(\mathbf{r}_1, \mathbf{r}_2) \quad (44)$$

If we divide eq. (42) by $\rho(\mathbf{r}_1)$ we obtain:

$$P(\mathbf{r}_1, \mathbf{r}_2) = \rho(\mathbf{r}_2) + \rho_{XC}(\mathbf{r}_1, \mathbf{r}_2) \quad (45)$$

where $\rho_{XC}(\mathbf{r}_1, \mathbf{r}_2)$ is given by:

$$\rho_{XC}(\mathbf{r}_1, \mathbf{r}_2) = \frac{\Gamma_{XC}(\mathbf{r}_1, \mathbf{r}_2)}{\rho(\mathbf{r}_1)} \quad (46)$$

$\rho_{XC}(\mathbf{r}_1, \mathbf{r}_2)$ is called the *exchange-correlation* or *Fermi-Coulomb hole*. According to eq. (45), the exchange correlation hole is the correction term which must be added to the unconditional probability in order to obtain the conditional probability. It is the region around the electron in which the presence of other electrons is excluded to a greater or lesser degree. Substituting eq. (45) eq. into (44) we have:

$$\gamma_2(\mathbf{r}_1, \mathbf{r}_2) = \rho(\mathbf{r}_1)\rho(\mathbf{r}_2) + \rho(\mathbf{r}_1)\rho_{XC}(\mathbf{r}_1, \mathbf{r}_2) \quad (47)$$

Because the total electron density is the sum of densities α and β , it is possible to separate the different contributions into $\rho_{XC}(\mathbf{r}_1, \mathbf{r}_2)$. Thus:

$$\gamma_2^{\alpha\alpha}(\mathbf{r}_1, \mathbf{r}_2) = \rho^\alpha(\mathbf{r}_1)\rho^\alpha(\mathbf{r}_2) + \Gamma_{XC}^{\alpha\alpha}(\mathbf{r}_1, \mathbf{r}_2) \quad (48)$$

$$\begin{aligned} \frac{\gamma_2^{\alpha\alpha}(\mathbf{r}_1, \mathbf{r}_2)}{\rho^\alpha(\mathbf{r}_1)} = P^{\alpha\alpha}(\mathbf{r}_1, \mathbf{r}_2) &= \rho^\alpha(\mathbf{r}_2) + \frac{\Gamma_{XC}^{\alpha\alpha}(\mathbf{r}_1, \mathbf{r}_2)}{\rho^\alpha(\mathbf{r}_1)} \\ &= \rho^\alpha(\mathbf{r}_2) + \gamma_{XC}^{\alpha\alpha}(\mathbf{r}_1, \mathbf{r}_2) \end{aligned} \quad (49)$$

where $\gamma_{XC}^{\alpha\alpha}(\mathbf{r}_1, \mathbf{r}_2)$ is the *Fermi hole* and represents for a specific reference electron with α spin located in \mathbf{r}_1 , the region of the space from which the presence of another electron of the same spin is excluded to a greater or lesser

1. THEORETICAL METHODS

extent. The probability of finding an electron in \mathbf{r}_2 when there is another of the same spin in \mathbf{r}_1 is reduced, especially for small $|\mathbf{r}_1 - \mathbf{r}_2|$. In addition:

$$\frac{\gamma_2^{\alpha\beta}(\mathbf{r}_1, \mathbf{r}_2)}{\rho^\alpha(\mathbf{r}_1)} = P^{\alpha\beta}(\mathbf{r}_1, \mathbf{r}_2) = \rho^\beta(\mathbf{r}_2) + \frac{\Gamma_{XC}^{\alpha\beta}(\mathbf{r}_1, \mathbf{r}_2)}{\rho^\alpha(\mathbf{r}_1)} = \rho^\beta(\mathbf{r}_2) + \gamma_{XC}^{\alpha\beta}(\mathbf{r}_1, \mathbf{r}_2) \quad (50)$$

(51)

where $\rho_{XC}^{\alpha\beta}(\mathbf{r}_1, \mathbf{r}_2)$ is called the *Coulomb hole* and would give us the region where the presence of a β electron is excluded or favored in the case in which we have a reference electron with α spin located at \mathbf{r}_1 .

It can be demonstrated that

$$\int \rho_{XC}(\mathbf{r}_1, \mathbf{r}_2) d\mathbf{r}_2 = -1 \quad (52)$$

which constitutes the so-called sum rule. Thus an electron located in \mathbf{r} creates around itself a hole, a charge deficit, with the displaced charge being exactly equal to that of a positive electron. This hole follows the motion of the electron.

Expected value expression. The expected value of the electron energy can be expressed for a system of n electrons and N nuclei for a given nuclear configuration as a function of the first-order density matrix and of the two-electron density. The operator which must be taken into consideration is the electronic Hamiltonian, \hat{H}_{el} , by which:

$$E_{el} = \langle \Psi | \hat{H}_{el} | \Psi \rangle = \int_{r'_1=r_1} \left(-\frac{1}{2} \nabla^2(1) + \hat{v}(1) \right) \rho_1(\mathbf{r}_1, \mathbf{r}'_1) d\mathbf{r}_1 + \frac{1}{2} \int \int \frac{\gamma_2(\mathbf{r}_1, \mathbf{r}_2)}{|\mathbf{r}_1 - \mathbf{r}_2|} d\mathbf{r}_1 d\mathbf{r}_2 \quad (53)$$

substituting eq. (47) in the previous equation we are left with:

$$E_{el} = \int_{r'_1=r_1} \left(-\frac{1}{2} \nabla^2(1) \right) \rho_1(\mathbf{r}_1, \mathbf{r}'_1) d\mathbf{r}_1 + \int \hat{v}(1) \rho_1(\mathbf{r}_1) d\mathbf{r}_1 + \frac{1}{2} \iint \frac{\rho(\mathbf{r}_1) \rho(\mathbf{r}_2)}{|\mathbf{r}_1 - \mathbf{r}_2|} d\mathbf{r}_1 d\mathbf{r}_2 + \frac{1}{2} \iint \frac{\rho(\mathbf{r}_1) \rho_{XC}(\mathbf{r}_1, \mathbf{r}_2)}{|\mathbf{r}_1 - \mathbf{r}_2|} d\mathbf{r}_1 d\mathbf{r}_2 \quad (54)$$

The different terms appearing in eq. (54) are, respectively, the kinetic energy of the electrons, the electron-nuclear potential energy, the Coulomb

1. THEORETICAL METHODS

electron repulsion and the electronic exchange-correlation energy. For this last term it is possible to write:

$$W_{XC}[\rho] = \frac{1}{2} \int \rho(\mathbf{r}_1) d\mathbf{r}_1 \int \frac{\rho_{XC}(\mathbf{r}_1, \mathbf{r}_2)}{|\mathbf{r}_1 - \mathbf{r}_2|} d\mathbf{r}_2 = \int \rho(\mathbf{r}_1) \mu_{XC}^{hole}(\mathbf{r}_1) d\mathbf{r}_1 \quad (55)$$

W_{XC} represents the interaction of $\rho(\mathbf{r}_1)$ with its exchange-correlation hole $\rho_{XC}(\mathbf{r}_1, \mathbf{r}_2)$. The electron interacts with an effective charge distribution corresponding to a positive electron, as follows from the sum rule.

Eq. (54) shows that it is possible to express the energy from the first- and second-order density functions and matrices and the energy is consequently said to be a functional of the density. Understanding by functional a mathematical expression associating a number to a function, *i.e.*, a functional is a function whose argument is also a function.

The Hohenberg-Kohn theorems.

The first theorem. Eq. (54) shows that it is possible to express the electron energy of a system as a functional of first- and second-order density functions and matrices. The first Hohenberg-Kohn theorem,²⁴⁷ which is considered to have given rise to the rigorous DFT, goes further to demonstrate that:

Any observable of a stationary non-degenerate ground state can be calculated, exactly in theory, from the electron density of the ground state. In other words, any observable can be written as a functional of the electron density of the ground state.

For the cases where this theorem is valid we have that:

$$E[\rho] = T[\rho] + V_{Ne}[\rho] + V_{ee}[\rho] (+V_{NN}) \quad (56)$$

$T[\rho]$ and $V_{ee}[\rho]$ are universal functionals, given that they do not depend on the external potential. They are usually encompassed within the Hohenberg-Kohn functional $F_{HK}[\rho]$, with which:

$$E_\mu[\rho] = \int \rho(\mathbf{r}) \mu(\mathbf{r}) d\mathbf{r} + F_{HK}[\rho] \quad (57)$$

where $E_\mu[\rho]$ indicates that, for a specific external potential $v(\mathbf{r})$, the energy is a functional of density.

1. THEORETICAL METHODS

The second theorem. The second Hohenberg-Kohn theorem provides the variational principle for $E[\rho]$. It can be expressed as follows:

The electron density of a non-degenerate ground state can be calculated, exactly in theory, determining the density that minimizes the energy of the ground state.

Or what is the same, for a trial density, $\tilde{\rho}(\mathbf{r})$, that is v-representable and N-representable it is fulfilled that:

$$E_0 \leq E_\mu[\tilde{\rho}(\mathbf{r})] \quad (58)$$

With this equation we obtain a variational principle for the energy in the framework of the DFT. This principle assures that any trial density results in an energy greater or equal to the exact energy of the ground state. Therefore, to obtain the exact density of the ground state, we will have to find the density that minimizes the energy:

$$\left[\frac{\delta E_\mu[\rho]}{\delta \rho} \right] = 0 \quad (59)$$

Fundamental equation. The minimization of the energy functional with respect to the electron density, $\delta E_\mu[\rho] = 0$, must be carried out assuring the conservation of the N-representability during the optimization process. This is done by introducing the restriction $\int \rho(\mathbf{r}) d\mathbf{r} - N = 0$ by means of Lagrange undetermined multipliers method. For that the following function is constructed:

$$E_\mu[\rho] - \nu \left[\int \rho(\mathbf{r}) d\mathbf{r} - N \right] \quad (60)$$

where ν is the undetermined Lagrange multiplier and has the meaning of a chemical potential. Next it is minimized:

$$\delta \left[E_\mu[\rho] - \nu \left(\int \rho(\mathbf{r}) d\mathbf{r} - N \right) \right] = 0 \quad (61)$$

and proceeding from the definition of a functional differential we are left with:

$$\int \frac{\delta E_\mu[\rho]}{\delta \rho(\mathbf{r})} \delta \rho(\mathbf{r}) d\mathbf{r} - \nu \int \delta \rho(\mathbf{r}) d\mathbf{r} = 0 \quad (62)$$

1. THEORETICAL METHODS

and rearranging:

$$\int \left\{ \frac{\delta E_\mu[\rho]}{\delta \rho(\mathbf{r})} - \nu \right\} \delta \rho(\mathbf{r}) d\mathbf{r} = 0 \quad (63)$$

which provides the condition of constrained minimization and allows the minimum value of ν to be obtained:

$$\nu = \frac{\delta E_\mu[\rho]}{\delta \rho(\mathbf{r})} = \mu_n(\mathbf{r}) + \frac{\delta F_{HK}[\rho]}{\delta \rho(\mathbf{r})} \quad (64)$$

Eq. (64) is known as *fundamental equation of density functional theory*.

The Kohn and Sham method. Eq. (64) gives us a formula to minimize the energy and thereby determine the density of the ground state. The problem that arises is that the exact expression relating F_{HK} with the density is unknown. In particular, the exact form of $T[\rho]$ is not known precisely enough. On the other hand, the kinetic energy is easily calculated if Ψ is known. Proceeding from the expression of $T[\Psi]$ for a single determinant function, Kohn and Sham in 1965 proposed an ingenious method to calculate the energy from ρ .²⁴⁸

In 1975 Gilbert²⁴⁹ proved that for any electron density normalized to n electrons there is a finite set of one-electron functions $\{\varphi_i\}$ that:

$$\rho(\mathbf{r}) = \sum_i \varphi_i^*(\mathbf{r}) \varphi_i(\mathbf{r}) \quad (65)$$

known as the Gilbert decomposition of the electronic density. Kohn and Sham considered these one-electron functions as orbitals, establishing analogies between DFT and the wavefunction based methods. They used as a reference system a system of n electrons that do not interact among themselves and that move under an effective potential created by the other electrons, as in the Hartree-Fock model. Thus, they introduced this finite set of orbitals $\{\varphi_i\}$ where each orbital describes one of the n interacting electrons. Within this assumption, an analogue to the HF functional for the kinetic energy can be proposed:

$$T_s[\rho] = \sum_i \langle \varphi_i | -\frac{1}{2} \nabla^2 | \varphi_i \rangle \quad (66)$$

where $T_s[\rho]$ does not represent the exact kinetic energy but an approximation, due to the fact that the functions φ_i are not the orbitals that make up

1. THEORETICAL METHODS

the wavefunction. To avoid confusions, from now on we will call the set $\{\varphi_i\}$ Kohn-Sham (KS) orbitals.

Now the total energy of the system can be expressed as:

$$E[\rho] = T_s[\rho] + \frac{1}{2} \int \frac{\rho(\mathbf{r}_1)\rho(\mathbf{r}_2)}{\mathbf{r}_{12}} d\mathbf{r}_1 d\mathbf{r}_2 + \int \rho(\mathbf{r}) V_{eN} d\mathbf{r} + E_{XC}[\rho] \quad (67)$$

Thus the effective potential within the electrons are moving in the Kohn-Sham model is given by:

$$\mu_{eff}(\mathbf{r}) = \frac{1}{2} \int \frac{\rho(\mathbf{r}_2)}{\mathbf{r}_{12}} d\mathbf{r}_2 + V_{eN} + \frac{\delta E_{XC}[\rho]}{\delta \rho(\mathbf{r})} \quad (68)$$

where the last terms represents the exchange-correlation potential

$$\mu_{XC} = \frac{\delta E_{XC}[\rho]}{\delta \rho(\mathbf{r})} \quad (69)$$

Now we are able to construct the Hamiltonian:

$$\hat{H}_s = \sum_i \left[-\frac{1}{2} \nabla_i^2 + \mu_{eff} \right] \quad (70)$$

As in the Hartree-Fock approximation, we can construct a Slater determinant with the set of M KS orbitals $\{\varphi_i\}$. Therefore, to apply the Hamiltonian \hat{H}_s to such a wavefunction and minimize the energy is the same as solving the M uncoupled equations:

$$\left[-\frac{1}{2} \nabla_i^2 + \mu_{eff}(\mathbf{r}) \right] \varphi_i^{KS} = \epsilon_i \varphi_i^{KS} \quad (71)$$

that is known as the *Kohn-Sham equations*. As in the Hartree-Fock model, the effective potential μ_{eff} depends on the electronic density eq. (68), so an initial set of KS orbitals $\{\varphi_i^{(0)}\}$ is needed, that would be improved iteratively. The only unknown quantity from these equations is the exchange-correlation potential, μ_{XC} . If the exact form was known, we would get the exact value for the energy of the ground state of the system via the Kohn-Sham equations, because this treatment does not include any approximations. The only approximation made in the DFT method is the expression of μ_{XC} . Thus it is expected that the electron density $\rho(\mathbf{r})$ will approach the exact density as $\mu_{XC}(\mathbf{r})$ approaches the exact exchange-correlation energy. In this way, DFT has the potential capacity to incorporate all the correlation energy, unlike HF. These are the summarized steps of the algorithm to solve eq. (71):

1. THEORETICAL METHODS

- Step 1:** Definition of a first set of trial orbitals $\{\varphi_i^{(0)}\}$.
- Step 2:** Propose a functional for the exchange-correlation energy and calculate the exchange-correlation potential as in eq. (69).
- Step 3:** Construct the effective potential as given by eq. (68).
- Step 4:** Solve the Kohn-Sham equations, eq. (71), in order to obtain an improved set of KS orbitals: $\{\varphi_i^{(1)}\}$.
- Step 5:** With the new set of improved KS orbitals, a new density $\rho^{(1)}$ is constructed (eq. (65)). If the calculation has converged (with some pre-established criteria as in the HF method), the approximate value for the ground state energy is obtained by means of eq. (67). If the calculation has not converged, we return to the 3rd step.

Approximations to the exchange-correlation potential. A basic aspect of DFT is to use a good exchange-correlation potential. Good approximations to the exchange-correlation energy are required to put this theory into practice. The simplest but at the same time tremendously useful approximation is the local density approximation (LDA). At the following level the so-called non-local or generalized gradient approximations (GGA) are found. These two types of approximations together with the meta-GGA and hybrid functionals are discussed below.

Local Density Approximation (LDA). Hohenberg and Kohn showed that if ρ varies extremely slowly with position, then $E_{XC}[\rho]$ is accurately given by

$$E_{XC}^{LDA}[\rho] = \int \rho(\mathbf{r}) \epsilon_{XC}(\rho) d\mathbf{r} \quad (72)$$

where the integral is over all space, $d\mathbf{r}$ stands for $dx dy dz$ and $\epsilon_{XC}(\rho)$ is the exchange plus correlation energy per electron in a homogeneous electron gas with electron density ρ . This electron density is called *jellium*. It is a hypothetical electrically neutral, infinite-volume system consisting of an infinite number of interacting electrons moving in a space throughout which positive charge is continuously and uniformly distributed. The number of electrons per unit volume in the jellium has a nonzero constant value ρ . The electrons in the jellium constitute an homogeneous electron gas. Taking the

1. THEORETICAL METHODS

functional derivative of E_{XC}^{LDA} , we find:

$$\mu_{XC}^{LDA} = \frac{\delta E_{XC}^{LDA}}{\delta \rho} = \epsilon_{XC}(\rho(\mathbf{r})) + \rho(\mathbf{r}) \frac{\delta \epsilon_{XC}(\rho)}{\delta \rho} \quad (73)$$

Kohn and Sham suggested the use of eq. (72) and (73) as approximations to E_{XC} and μ_{XC} . This procedure is called the *local density approximation* (LDA). It can be shown that ϵ_{XC} can be written as the sum of exchange and correlation parts:

$$\epsilon_{XC}(\rho) = \epsilon_X(\rho) + \epsilon_c(\rho) \quad (74)$$

where the expression for the correlation energy as a function of the electronic density was found by Slater²⁵⁰ to be

$$\epsilon_x(\rho) = -\frac{3}{4} \left(\frac{3}{\pi} \right)^{\frac{1}{3}} (\rho(\mathbf{r}))^{\frac{1}{3}} \quad (75)$$

Thus the exchange functional is known as the Slater exchange and is abbreviated with an S. The correlation part ϵ_C has been calculated and the results have been expressed as a very complicated function ϵ_C^{VWN} of ρ by Vosko, Wilk and Nusair²⁵¹ (VWN). Thus

$$\epsilon_C(\rho) = \epsilon_C^{VWN}(\rho) \quad (76)$$

where ϵ_C^{VWN} is a known function. Taking this into account, an E_{XC}^{LDA} would be the SVWN, that indicates that the exchange part is given by the Slater functional while the correlation part is describe by the Vosko, Wilk and Nusair functional.

The Local-Spin-Density Approach (LSDA). For open-shell molecules and molecular geometries near dissociation, the local-spin-density approximation, LSDA, gives better results than the LDA. Whereas in the LDA, electrons with opposite spins paired with each other have the same spatial KS orbitals, the LSDA allows such electrons to have different spatial KS orbitals $\varphi_{i\alpha}^{KS}$ and $\varphi_{i\beta}^{KS}$. The LSDA is thus the analogous to the UHF method. As in the UHF method, allowing differing KS orbitals for electrons with different spins can produce a wavefunction for the reference system that is not an eigenfunction of \hat{S}^2 , but this spin contamination is less of a problem in KS DFT than in the UHF method.

1. THEORETICAL METHODS

Despite the fact that ρ in a molecule is not a slowly varying function of position, the LSDA works surprisingly well for calculating molecular equilibrium geometries, vibrational frequencies, and dipole moments, even for transition-metal compounds, where Hartree-Fock calculations often give poor results. However, calculated LSDA molecular atomization energies are very inaccurate. Accurate dissociation energies require functional that go beyond LSDA.²³⁸

Gradient-Corrected (GGA) Functionals. The LDA and LSDA are based on the uniform-electron-gas model, which is appropriate for a system where ρ varies slowly with position. The integrand in eq. (72) for E_{XC}^{LDA} is a function of only ρ , and the integrand in E_{XC}^{LSDA} is a function of only ρ^α and ρ^β . Functionals that go beyond LSDA aim to correct the LSDA for the variation of electron density with position. A common way to do this is by including the gradients of ρ^α and ρ^β in the integrand. Thus

$$E_{XC}^{GGA}[\rho^\alpha, \rho^\beta] = \int f(\rho^\alpha(\mathbf{r}), \rho^\beta(\mathbf{r}), \nabla\rho^\alpha(\mathbf{r}), \nabla\rho^\beta(\mathbf{r})) d\mathbf{r} \quad (77)$$

where f is some function of the spin densities and their gradients. The letters GGA stand for *generalized-gradient approximation*. The term gradient-corrected functional is also used. E_{XC}^{GGA} is usually split into exchange and correlation parts, which are modelled separately:

$$E_{XC}^{GGA} = E_X^{GGA} + E_C^{GGA} \quad (78)$$

Approximate gradient-corrected exchange and correlation energy functionals are developed using theoretical considerations such as the known behavior of the true (but unknown) functionals E_X and E_C in various limiting situations as a guide, with often some empiricism thrown in, by choosing the values of parameters in the functionals to give good performance for known values of various molecular properties.

Some commonly used GGA exchange functionals, E_X^{GGA} , are Perdew and Wang's 1986 functional²⁵² (PW86 or PWx86) (which contains non empirical parameters), Becke's 1988 functional²¹² (B or B88), Perdew and Wang's 1991 exchange functional²⁵³ (PWx91 or PW91) and Gill's 1996²¹¹ functional (G96). The explicit form of the B88 exchange functional is

$$E_X^{B88} = E_X^{LSDA} - b \sum_{\sigma=\alpha,\beta} \int \frac{(\rho^\sigma)^{\frac{4}{3}} \chi_\sigma^2}{1 + 6b\chi_\sigma \ln[\chi_\sigma + (\chi_\sigma^2 + 1)^{\frac{1}{2}}]} d\mathbf{r} \quad (79)$$

1. THEORETICAL METHODS

where $\chi_\sigma \equiv |\nabla \rho^\sigma|/(\rho^\sigma)^{\frac{4}{3}}$, b is an empirical parameter whose value, 0.0042 atomic units, was determined by fitting known Hartree-Fock exchange energies of several atoms, and

$$E_X^{LSDA} = -\frac{3}{4} \left(\frac{6}{\pi} \right)^{\frac{1}{3}} \int [(\rho^\alpha)^{\frac{4}{3}} + (\rho^\beta)^{\frac{4}{3}}] d\mathbf{r} \quad (80)$$

Commonly used GGA correlation functionals, E_C^{GGA} , include the Lee-Yang-Parr⁷⁶ (LYP) functional, Perdew's 1986 correlation functional²⁵⁴ (P86 or P86), and the Perdew-Wang 1991²⁵³ parameter-free correlation functional (PW91 or PW91). Also, the Perdew-Burke-Ernzerhof²⁵⁵ (PBE) exchange and correlation functional that has no empirical parameters.

Any exchange functional can be combined with any correlation functional. For example, the notation BLYP/6-31G* denotes a density functional calculation done with the Becke 1988 exchange functional and the Lee-Yang-Parr correlation functional, with the KS orbitals expanded in a 6-31G* basis set.

Hybrid GGA Functionals. Hybrid exchange-correlation functionals are widely used. These functionals mix together the formula in eq. (81) for E_X with GGA E_X and E_C formulas.

$$E_X \equiv -\frac{1}{4} \sum_{i=1}^n \sum_{j=1}^n \langle \theta_i^{KS}(1) \theta_j^{KS}(2) \left| \frac{1}{r_{12}} \right| \theta_j^{KS}(1) \theta_i^{KS}(2) \rangle \quad (81)$$

In eq. (81), E_X is defined by the same formula used for the exchange energy in Hartree-Fock theory, except that the Hartree-Fock orbitals are replaced by the Kohn-Sham orbitals. Since, in practice, KS orbitals are found to rather closely resemble the HF orbitals, the DFT exchange energy so computed is close to the Hartree-Fock exchange energy.

One example of hybrid functional is the popular B3LYP^{75,76} hybrid GGA functional (where the 3 indicates a three-parameter functional). It is defined by

$$E_{XC}^{B3LYP} = (1 - a_0 - a_x) E_X^{LSDA} + a_0 E_X^{exact} + a_x E_X^{B88} + (1 - a_c) E_C^{VWN} + a_c E_C^{LYP} \quad (82)$$

where E_X^{exact} (often denoted E_X^{HF} , since it uses Hartree-Fock definition of E_X) is given by eq. (81), and where the parameter values $a_0 = 0.20$, $a_x = 0.72$,

1. THEORETICAL METHODS

and $a_c = 0.81$ were chosen to give good fits to experimental molecular atomization energies.

Other well known hybrid GGA functionals are: PBE0 (also called PBE1PBE, which adds 25% of HF exchange to the PBE functional), B3P86,^{75, 254} B3PW91,^{75, 253} B97-2,²⁵⁶ BH&H ($0.5E_X^{HF} + 0.5E_X^{LSDA} + E_C^{LYP}$), BH&HLYP ($0.5E_X^{HF} + 0.5E_X^{LSDA} + 0.5\Delta E_X^{Becke88} + E_C^{LYP}$), mPW1PW91,^{253, 257} O3LYP,^{76, 258, 259} and X3LYP.^{76, 260}

Meta-GGA Functionals. The GGA density functionals of the form shown in eq. (77) depend on the ground state electron probability density ρ and its first derivatives. One way to improve on GGA functionals is to go to functionals that also depend on the second derivatives of ρ and/or a quantity called the kinetic-energy density. Such functionals are called *meta-GGA* functionals and have the form:

$$E_{XC}^{MGGA}[\rho^\alpha, \rho^\beta] = \int f(\rho^\alpha, \rho^\beta, \nabla\rho^\alpha, \nabla\rho^\beta, \nabla^2\rho^\alpha, \nabla^2\rho^\beta, \tau_\alpha, \tau_\beta) d\mathbf{r} \quad (83)$$

where the Kohn-Sham kinetic-energy density for the spin α electrons is defined by

$$\tau_\alpha \equiv \frac{1}{2} \sum_i |\nabla\theta_{i\alpha}^{KS}|^2 \quad (84)$$

The M06L,²⁶¹ TPSS,²⁶² and VSXC²⁶³ functionals belong to this category.

Hybrid meta-GGA Functionals. This kind of functionals depend on HF exchange, the electron density and its gradient, and the kinetic energy density. Some examples are M05,²⁶⁴ M05-2X,²⁶⁵ M06,²⁶⁶ M06-2X,²⁶⁶ and BMK.²⁶⁷

The GGA, meta-GGA, hybrid-GGA and hybrid-meta-GGA functionals give not only good equilibrium geometries, vibrational frequencies and dipole moments, but also generally accurate molecular atomization energies.

Evaluation of Functionals. There is not correct answer to the question “which is the best DFT functional?” Since one finds that functionals that give good results for organic compounds may give inferior results for inorganic compounds, and functionals that give good results for energy changes

1. THEORETICAL METHODS

in reactions may give inferior results for activation energies of reactions. Thus the best functional to use depends on the kind of compounds being studied and on which properties are being calculated.

Advantages and disadvantages of DFT. The main advantage of DFT is that allows for correlations effects to be included in a calculation that takes roughly the same time as a Hartree-Fock calculation, which does not include correlation. However, despite its success DFT is not a panacea and it has some drawbacks and failings, some of them are that:

- Due to the fact that the Hohenberg-Kohn-Sham theory is basically a ground-state theory it fails in general when dealing with electronic excited states.
- Because approximate functionals are used, KS DFT is not variational and can yield an energy below the true ground-state energy.
- The true E_{XC} contains a self-interaction correction that exactly cancels the self-interaction energy in $\frac{1}{2} \iint \rho(\mathbf{r}_1)\rho(\mathbf{r}_2)\mathbf{r}_{12}^{-1}d\mathbf{r}_1d\mathbf{r}_2$, but most currently used functionals are not completely free of self-interaction.
- Many of the currently used E_{XC} functionals fail for van der Waals molecules and systems weakly bonded.

1.4 G4 theory

A number of approaches, based on quantum chemical methods, have been developed over the past decade and a half to make accurate predictions of thermochemical data. The Gaussian- n (G n) theories ($n = 1, 2, 3$),^{268–271} employ a set of calculations with different levels of accuracy and basis sets with the goal of approaching the exact energy. Within this approach, a high level correlation calculation [e.g., QCISD(T) and CCSD(T)] with a moderate sized basis set is combined with energies from lower level calculations (e.g. MP4 and MP2) with larger basis sets to approximate the energies of more expensive calculations. In addition, several molecule-independent empirical parameters [higher level correction (HLC) terms] are included to estimate remaining deficiencies, assuming that they are systematic. Therefore, the Gaussian-4 theory⁷⁴ (G4 theory) is a composite technique aimed at getting accurate energies without requiring extensive computer resources. This approach depends on a cancellation of errors as well as well-defined parameters

1. THEORETICAL METHODS

to achieve this.

In the G4 theory, a sequence of well-defined *ab initio* molecular orbital calculations is performed to arrive at a total energy for a given molecular species. This method allows the calculation of energies of molecular species containing first-row (Li-F), second row (Na-Cl), and third-row main group elements. The steps in the G4 theory are as follows.

1. The equilibrium structure is obtained at the B3LYP/6-31G(2df,p) level. Spin-restricted theory is used for singlet states and spin-unrestricted theory for others.
2. The B3LYP/6-31G(2df,p) equilibrium structure is used to calculate harmonic frequencies, which are then scaled by a factor of 0.9854²⁷² to take into account of known deficiencies at this level. These frequencies give the zero-point energy, $E(ZPE)$, used to obtain E_0 .
3. The Hartree-Fock energy limit, $E(HF/limit)$, is calculated. The Hartree-Fock basis set limit is determined using a linear two-point extrapolation scheme^{273,274} and Dunning's aug-cc-pVnZ basis sets,²⁷⁵⁻²⁷⁷

$$E_{HF/aug-cc-pVnZ} = E_{HF/limit} + B \exp(-\alpha n). \quad (85)$$

where n is the number of contractions in the valence shell of the basis set and α is an adjustable parameter. The authors found that calculating the HF limit using $n=4$, and $n+1=5$ (aug-cc-pVQZ and aug-cc-pV5Z basis sets), and $\alpha = 1.63$ gave nearly converged values for a set of large molecules from the G3/05 test set. In order to reduce the computational time required, the authors also modified the standard aug-cc-pVQZ and aug-cc-pV5Z basis sets by reducing the number of diffuse functions on heavy atoms and by reducing the hydrogen basis set as described in the paper.⁷⁴ These modifications save significant computer time, without reducing the accuracy.

4. A series of single point correlation energy calculations is then carried out. The first is based on the complete fourth-order Møller-Plesset perturbation theory with the 6-31G(d) basis set, MP4/6-31G(d). This is modified by corrections from additional calculations.

(a) a correction for diffuse functions,

$$\Delta E(+) = E[MP4/6-31+G(d)] - E[MP4/6-31G(d)], \quad (86)$$

1. THEORETICAL METHODS

- (b) a correction for higher polarization functions,

$$\Delta E(2df, p) = E[\text{MP4}/6\text{-}31\text{G}(2df, p)] - E[\text{MP4}/6\text{-}31\text{G}(d)], \quad (87)$$

- (c) a correction for correlation effects beyond a fourth-order perturbation theory using a coupled cluster theory,

$$\Delta E(\text{CC}) = E[\text{CCSD(T)}/6\text{-}31\text{G}(d)] - E[\text{MP4}/6\text{-}31\text{G}(d)], \quad (88)$$

- (d) a correction for larger basis set effects and for the nonadditivity caused by the assumption of separate basis set extensions for diffuse functions and higher polarization functions,

$$\begin{aligned} \Delta E(\text{G3LargeXP}) &= E[\text{MP2}(\text{full})/\text{G3LargeXP}] \\ &- E[\text{MP2}/6\text{-}31\text{G}(2df, p)] \\ &- E[\text{MP2}/6\text{-}31+\text{G}(d)] \\ &+ E[\text{MP2}/6\text{-}31\text{G}(d)]. \end{aligned} \quad (89)$$

The MP4 and CCSD(T) calculations are done in the frozen core approximation, while the MP2 calculation with the large basis set is done with all electrons correlated.

5. The MP4/6-31G(d) energy and the four correlation corrections from step 4 are combined in an additive manner along with a correction for the HF limit (step 3) and a spin-orbit correction, $\Delta E(\text{SO})$

$$\begin{aligned} \Delta E(\text{combined}) &= E[\text{MP4}/6\text{-}31\text{G}(d)] + \Delta E(+) \\ &+ \Delta E(2df, p) + \Delta E(\text{CC}) \\ &+ \Delta E(\text{G3LargeXP}) + \Delta E(\text{HF}) \\ &+ \Delta E(\text{SO}). \end{aligned} \quad (90)$$

The $\Delta E(\text{HF})$ is calculated as the difference between $E(\text{HF}/\text{G3LargeXP})$ calculated in step 4 and $E(\text{HF}/\text{limit})$ calculated in step 3 [*i.e.*, $\Delta E(\text{HF}) = E(\text{HF}/\text{limit}) - E(\text{HF}/\text{G3LargeXP})$].

6. A high level correction (HLC) is added to take into account the remaining deficiencies in the energy calculations,

$$E_e(\text{G4}) = E(\text{combined}) + E(\text{HLC}). \quad (91)$$

where the HLC form is

$$E(\text{HLC}) = \begin{cases} -An_\beta & \text{closed shell molecules} \\ -A'n_\beta - B(n_\alpha - n_\beta) & \text{open shell systems} \\ -Cn_\beta - D(n_\alpha - n_\beta) & \text{for atoms (including atomic ions)} \end{cases} \quad (92)$$

1. THEORETICAL METHODS

The n_β and n_α are the number of β and α valence electrons, respectively, with $n_\alpha \geq n_\beta$. The A , A' , B , and C values are chosen to give the smallest average absolute deviation from experiment for the G3/05 test set. The values obtained are, $A = 6.947$ mhartree, $B = 2.441$ mhartree, $C = 7.116$ mhartree, $D = 1.414$ mhartree, and $A' = 7.128$ mhartree.

7. Finally, the total energy at 0 K is obtained by adding the zero-point energy, obtained from the frequencies of step 2, to the total energy,

$$E_0(\text{G4}) = E_e(\text{G4}) + E(\text{ZPE}). \quad (93)$$

The energy E_0 is referred to as the “G4-energy”. If the different additivity approximations work well, the final total energy obtained with such procedure is effectively at the CCSD(T,full)/G3LargeXP + HF limit level.

The G3/05 test set²⁷⁸ was used to assess the performance of the G4-theory.⁷⁴ This test set contains thermochemical data chosen based on a listed accuracy of ± 1 kcal mol⁻¹ or better. The G3/05,²⁷⁸ contains 270 enthalpies of formation, 105 ionization energies, 63 electron affinities, 10 proton affinities, and 6 hydrogen-bonded complexes. The overall absolute deviation for the 454 energies in the G3/05 test set is 0.83 kcal mol⁻¹.

1.5 Population analysis methods

The previous sections were devoted to the several methods used for finding a wavefunction, more or less precise, by means of different approximations to the Schrödinger equation. Solving this equation, the energy and geometry of the system are obtained, but there is much more information contained in the wavefunction. In particular, appropriate auxiliary tools allowing electron pair localization^{279,280} have been long pursued in quantum chemistry to explain the nature of the chemical bond^{281–283} and with the aim of establishing a link between the rigorous but abstract wavefunction and the classical chemical concepts based on the Lewis theory^{284,285} and the valence shell electron pair repulsion (VSEPR) model of molecular geometry.^{286,287} In this section we will briefly describe three of these methods used during this work, namely, the natural bond orbital (NBO) method, the Quantum Theory of Atoms in Molecules (QTAIM), and the electron localization function (ELF).

1.5.1 NBO: Natural Bond Orbitals

On a wide range of quantum-chemistry studies it is very important to determine the electronic configuration and the net charge of each atom, namely the electronic distribution within the molecule, since these properties are of great utility to understand the chemical processes.

Over all the several approaches proposed to analyze the atomic population, the one developed by Mulliken²⁸⁸ has been the most widely used to characterize the charge distribution hitherto. However, it has been showed repeatedly that the Mulliken method fails when it concerns to the calculation of the atomic charges and orbitals population. Some of the drawbacks are that sometimes it yields to results with no physical meaning, it is highly dependent on the basis set and the low reliability of the charge distributions obtained when dealing with compounds with high ionic character. These limitations have encourage the search for new methods to analyze the electronic population.

A quite popular one is based on Natural Orbitals (NO). These orbitals are the eigenvectors of the first-order reduced density matrix, eq. (94), whereas the population (occupancy) numbers are the eigenvalues.

$$\gamma_i(\mathbf{r}_1, \mathbf{r}'_1) = N_{elec} \int \Psi^*(\mathbf{r}'_1, \dots, \mathbf{r}_{N_{elec}}) \int \Psi^*(\mathbf{r}_1, \dots, \mathbf{r}_{N_{elec}}) \dots d\mathbf{r}_{N_{elec}} \quad (94)$$

Weinhold and co-workers,²⁸⁹ used this Natural Orbital definition to distribute the electrons between atomic and molecular orbitals and thus obtain the natural charges and the molecular bonds. Let us suppose that the basis functions are arranged in such a way that the functions corresponding to the A atom are found first that the ones of the B atom and so forth:

$$\chi_1^A, \chi_2^A, \chi_3^A, \dots, \chi_1^B, \chi_2^B, \chi_3^B, \dots, \chi_1^C, \chi_2^C, \chi_3^C, \dots \quad (95)$$

so now, the density matrix, \mathbf{D} , can be written as basis set functions blocks belonging to an specific center:

$$D = \begin{pmatrix} D^{AA} & D^{AB} & D^{AC} & \vdots \\ D^{AB} & D^{BB} & D^{BC} & \vdots \\ D^{AC} & D^{BC} & D^{CC} & \vdots \\ \dots & \dots & \dots & \ddots \end{pmatrix} \quad (96)$$

1. THEORETICAL METHODS

The A *natural atomic orbitals* (NAOs) are obtained by diagonalizing the \mathbf{D}^{AA} block, the B NAOs are obtained by diagonalizing the \mathbf{D}^{BB} and so on. In general, the NAOs are not orthogonal and therefore, their populations does not sum up to the total number of electrons. Hence, it is necessary to make them orthogonal.

The NAOs are automatically ordered in importance by occupancy. Consistently with chemical intuition, only the core and valence shell NAOs are found to have significant occupancies, compared to the extra-valence Rydberg-type NAOs that complete the span of the basis. The effective dimensionality of the NAO space is therefore reduced to that of the formal *natural minimal basis*, NMB, spanning core and valence-shell NAOs only, whereas the residual *natural Rydberg basis*, NRB, of extra-valence NAOs plays practically no significant role in NBO analysis. This condensation of occupancy into the much smaller set of NMB orbitals (allowing the large residual NRB set from the original basis to be effectively ignored) is one of most dramatic and characteristic simplifying features of “natural” analysis.⁷ The way to obtain the NAOs is as follows:

1. Each atomic block of the density matrix is diagonalized to obtain a set of non-orthogonal NAOs, *pre*-NAOs.
2. An occupancy-weighted orthogonalization is carry out over the highly occupied *pre*-NAOs of one atom with respect to the other atoms’ highly occupied *pre*-NAOs.
3. The negligible occupied *pre*-NAOs (such Rydberg-type NAOs) of each center are orthogonalized with the highly occupied *pre*-NAOs of the same center through a Gram-Schmidt orthogonalization algorithm.
4. The negligible occupied *pre*-NAOs of a specific center are orthogonalized with the negligible occupied *pre*-NAOs of the other centers by means of a occupancy-weighted orthonormalization.

After performing all the steps of the algorithm a set of orthogonal NAOs is obtained. The diagonal matrix elements of the density matrix on this basis are the orbitals occupancies. If we sum up the population of all the orbitals belonging to the A atom we obtain the charge of the A atom. One advantage of this population analysis compared to the Mulliken analysis, is the fact that the NAOs are defined starting from the density matrix so their occupancies will always be between 0 and 2. Another advantage is that as the basis set is extended they converge to well defined values.

1. THEORETICAL METHODS

Once the density matrix has been converted into the NAOs basis, the bond between atoms arises from the extra-diagonal blocks of the matrix. To determine these *Natural Bond Orbitals* the following steps are followed:

1. The NAOs belonging to an atomic block of the density matrix which an occupancy number very close to 2 (> 1.999) are classified as core orbitals and deleted from the density matrix.
2. The NAOs belonging to an atomic block of the density matrix which has high occupancy (> 2) are identified as lone pair orbitals and they are deleted from the density matrix too.
3. Each atomic pair is considered (AB, AC, BC, ...) and these sub-blocks, two by two, are diagonalized (the core and lone pair have been deleted from these sub-blocks). The NBOs are the eigenvalues with high occupancy (normally over 1.90).

If the sum of the occupancy of core, lone pair and NBOs orbitals is lower than the total number of electrons, it is considered that the number of NBOs is not enough and in the next step the occupancy threshold to select the NBOs is lowered. Alternatively, it is possible to search for three center bonds.

Natural Resonance Theory. The *natural resonance theory*, NRT,^{290,291} provides an analysis of molecular electron density (correlated or uncorrelated) in terms of resonance structures and weights.

The NRT algorithm is based on representing the one-electron reduced density operator, $\hat{\Gamma}$, as an optimized “resonance hybrid” of density operators, $\{\hat{\Gamma}_\alpha\}$

$$\hat{\Gamma} \simeq \sum_{\alpha} \omega_{\alpha} \hat{\Gamma}_{\alpha} \quad (97)$$

where each $\hat{\Gamma}_{\alpha}$ is the reduced density operator corresponding to an idealized resonance structure wavefunction, Ψ_{α} (determinant of doubly occupied NBOs for the chosen Lewis structure). The NRT resonance weights, $\{\omega_{\alpha}\}$, are constrained to satisfy

$$\omega_{\alpha} \geq 0, \quad \sum_{\alpha} \omega_{\alpha} = 1 \quad (98)$$

in order to preserve the normalization, hermiticity and positivity of the true $\hat{\Gamma}$. NRT analysis can be performed on any wavefunction or density functional

method that leads to a one-electron density matrix. Also bond orders and valences can be evaluated from the final optimized resonance weights, $\{\omega_\alpha\}$.

1.5.2 AIM: Atoms In Molecules

This method is based on the topological analysis of the charge density function⁸⁰ that allows to define the concepts of atom, bond, molecular structure and structural stability.

The charge density is given by:

$$\rho(\mathbf{r}) = \int |\psi|^2 d\tau \quad (99)$$

where the square of the wavefunction is integrated over the coordinates of all the electrons except for one. The electronic density is obtained for a fixed nuclear configuration so it is a one-electron function that depends on the nuclear coordinates parametrically.

Topological properties of the charge density. Each topological feature of the electronic density, $\rho(\mathbf{r})$, whether it is a maximum, a minimum or a saddle point, has associated with it a point in space called *critical point* (CP), where the first derivatives of $\rho(\mathbf{r})$ vanish:

$$\nabla\rho(\mathbf{r}) = 0 \quad (100)$$

diagonalization of the Hessian matrix of the charge density gives the three main curvatures for the electronic density, that would be positive in a minimum or negative for a maximum. The *rank*, ω , of a critical point is equal to the number of non-zero curvatures of ρ at the CP. The *signature*, σ , is the algebraic sum of the signs of the curvatures. The CP are labelled giving the duo of values (ω, σ) .

With relatively few exceptions, the CPs of charge distribution for molecules at or in the neighbourhood of energetically stable geometrical configurations of the nuclei are all of rank three ($\omega = 3$). It is in terms of such CPs that the elements of molecular structure are defined. A CP with $\omega < 3$ is said to be degenerated. Such a CP is unstable in the sense that a small change in the charge density, as caused by displacement of the nuclei, makes it to either vanish or to bifurcate into a number of stable ($\omega = 3$) CPs. There are just

1. THEORETICAL METHODS

four possible signature values for critical points of rank three.

- (3,-3) All curvatures are negative and ρ is a local maximum at \mathbf{r}_c . These points are associated with nuclear positions.
- (3,-1) Two curvatures are negative and ρ is a maximum at \mathbf{r}_c in the plane defined by their corresponding axes. ρ is a minimum at \mathbf{r}_c along the third axis which is perpendicular to this plane. These critical points are found between every pair of nuclei which are considered to be linked by a chemical bond and therefore are called *bond critical points* (BCPs).
- (3,+1) Two curvatures are positive and ρ is a minimum at \mathbf{r}_c , in the plane defined by their corresponding axes. ρ is a maximum at \mathbf{r}_c along the third axis which is perpendicular to this plane. These critical points are related with the structural concept of ring and thus are called *ring critical points* (RCPs).
- (3,+3) All curvatures are positive and ρ is a local minimum at \mathbf{r}_c . These critical points are called *cage critical points* (CCPs).

The link between the topological features of the electronic density and the different elements of the molecular structure is based on the gradient vector field of the charge density theory.

Gradient vector field of the charge density. The gradient vector field of the charge density is represented through a display of the trajectories traced out by the vector $\nabla\rho$. A trajectory of $\nabla\rho$, starting at some arbitrary point, is obtained by calculating $\nabla\rho(\mathbf{r}_0)$, moving a distance $\Delta\mathbf{r}$ away from this point in the direction indicated by the vector $\nabla\rho(\mathbf{r}_0)$ and repeating this procedure until the path so generated terminates. Some general properties are that i) the vector $\nabla\rho(\mathbf{r})$ is tangent to its trajectory at each point \mathbf{r} and that ii) every trajectory must originate or terminate at a point where $\nabla\rho(\mathbf{r})$ vanishes, *i.e.*, at a critical point in ρ .

Elements of molecular structure. A (3,-3) critical point, as occurring at each of the nuclear positions, serves as the terminus of all the paths starting from, and contained in some neighbourhood of the CP. Thus, the nuclei act as attractors of the gradient vector field of $\rho(\mathbf{r};\mathbf{X})$. The result of this identification is that the space of a molecular charge distribution, real space,

1. THEORETICAL METHODS

is partitioned into disjoint regions, the basins, each of which contains one point attractor or nucleus. An atom, free or bound, is defined as the union of an attractor and its associated basin.

Alternatively, an atom can be defined in terms of its boundary. For an atom in a molecule the atomic basin is separated from neighbouring atoms by interatomic surfaces. The existence of an interatomic surface S_{AB} denotes the presence of a (3,-1) CP between the neighbouring nuclei A and B . Thus, the presence of these surfaces provides the boundaries between the basins of neighbouring atoms. The trajectories which terminate at a (3,-1) CP define a surface, the interatomic surface S_{AB} . Therefore, the atomic surface S_A of atom A is defined as the boundary of its basin. Generally, this boundary comprises the union of a number of interatomic surfaces separating two neighbouring basins and some portions that may be infinitely distant from the attractor.

At the (3,-1) bond critical points a series of pairs of gradient paths are originated that terminate at the neighbouring attractors. Each such pair of trajectories is defined by the eigenvector associated with the unique positive eigenvalue of a (3,-1) CP. These two unique gradient paths define a line through the charge distribution linking the neighbouring nuclei along which $\rho(\mathbf{r})$ is a maximum with respect to any neighbouring line. Such a line is found between every pair of nuclei whose atomic basins share a common interatomic surface. This line of maximum charge density linking the nuclei is called a *bond path* and the (3,-1) critical point referred to as a *bond critical point* as previously mentioned.

For a given configuration X of the nuclei, a *molecular graph* is defined as the union of the closures of the bond paths or atomic interaction lines. Pictorially, the molecular graph is the network of bond paths linking pairs of neighbouring nuclear attractors. The network of bond paths thus obtained is found to coincide with the network generated by linking together those pairs of atoms, which are assumed to be bonded to one another on the basis of chemical considerations.

The remaining critical points of rank three occur as consequence of particular geometrical rearrangements of bond paths and they define the remaining elements of molecular structure: rings and cages. If the bond paths are linked so as to form a ring of bonded atoms then, a (3,+1) CP is found in the interior of the ring. The eigenvectors associated with the two positive eigenvalues of the Hessian matrix of ρ at this CP generate an infinite set of gradient paths

1. THEORETICAL METHODS

which originate at the CP and define a surface called the ring surface.

If the bond paths are so arranged as to enclose the interior of a molecule with ring surfaces, then a (3,+3) or cage CP is found in the interior of the resulting cage. The charge density is a local minimum at a CCP. Trajectories only originated at such a CP and terminate at nuclei, and at bond and ring CPs.

The number and type of CPs which can coexist in a system with a finite number of nuclei is governed by the Poincaré-Hopf relationship:

$$n-b+r-c=1 \quad (101)$$

where n is the number of nuclei, b is the number of bond paths (or atomic interaction lines), r is the number of rings, and c is the number of cages. The collection of numbers (n , b , r , and c) is called the characteristic set of the molecule.

Bonds and structure. The value of the charge density at the BCP can be used to define a bond order. Multiple bonds do not appear as such in the topology of the charge density. Instead, one finds that the extent of charge accumulation between the nuclei increases with the assumed number of electron pair bonds. This increase is faithfully monitored by the value of ρ at the BCP, ρ_b . Thus, the values of ρ_b obtained for ethane, benzene, ethylene and acetylene can be related through a mathematical equation to the bond orders of 1.0, 1.6, 2.0 and 3.0 respectively. Also, the value of ρ_b is found to increase as a bond length decreases.

The bond path has not necessarily to match up with the internuclear axis, being the former larger. This happens when the bond path is curved, a typical situation when there are strained bonds as in cyclic small hydrocarbons. The differences between the both path angle, α_b , the limiting value of the angle subtended at a nucleus by two bond paths, and the geometrical so called bond angle, α_e , is important to quantifying the previously mentioned concept of strain in these kind of molecules.

Properties of the Laplacian of the charge density. The Laplacian of the charge density, $\nabla^2\rho$, is defined as the trace of the Hessian matrix. It determines where the field is locally concentrated ($\nabla^2\rho(\mathbf{r}) < 0$) and depleted

1. THEORETICAL METHODS

($\nabla^2\rho(\mathbf{r}) > 0$). Thus, it follows that the value of $\rho(\mathbf{r})$ is greater than the average of its values over an infinitesimal sphere centered on \mathbf{r} when the sum of the three curvatures of ρ is negative, that is, when $\nabla^2\rho(\mathbf{r}) < 0$, and $\rho(\mathbf{r})$ is lower than this average when $\nabla^2\rho(\mathbf{r}) > 0$.

The electronic density is a maximum within the interatomic surface associated to the BCP, where it reaches its maximum value. At the same time, the electronic density has a minimum in this point through the bond path. Thus, the generation of an interatomic surface and of an interatomic interaction along the molecular bond is the result of two concomitant effects: the perpendicular contraction of the electronic density that triggers the concentration of electronic charge along the bond path, and the parallel expansion of the electronic density that leads to the depletion of the electronic charge within the surface and its concentration in the basins of the neighbouring atoms. The sign of $\nabla^2\rho(\mathbf{r})$ will determine which of these two effects dominates.

In the case of covalent bonds in which the electronic density is concentrated at the internuclear region as a result of the distribution of the electrons between the two nuclei, the BCP will have associated a negative value for the Laplacian. On the other hand, when there are interactions between closed-shell systems as ionic bonds, hydrogen bonds, van der Waals complexes, etc, the electronic density on the proximities of the interatomic surface is depleted and it is concentrated in the basins of the neighbouring atoms. Therefore, the BCP has a positive Laplacian value associated.

Using the expression of the virial theorem as a function of the Laplacian, eq. (102), it is also possible to determine which kind of interaction is taken place between an atom pair.

$$\frac{\hbar^2}{4m}\nabla^2\rho(\mathbf{r}) = 2G(\mathbf{r}) + V(\mathbf{r}) \quad (102)$$

where $G(\mathbf{r})$ represents a kinetic energy having always positive values. $V(\mathbf{r})$ stands for the potential energy density, and is always negative. The Laplacian sign indicates which of these two contributions dominates over the other. In the regions where the Laplacian has a negative value, the stabilization is reached through lowering the potential energy as a result of charge concentration inbetween the two nuclei. If, in turn, the Laplacian is positive, the kinetic contribution predominates over the potential one and the charge accumulation on this point destabilizes the system. Consequently, for the covalent interactions the bond regions stabilize the system and the Laplacian

1. THEORETICAL METHODS

is negative whereas for the electrostatic-type interactions the Laplacian has positive values in the region between the nuclei.

Thus, the Laplacian sign is a criterion that can be used to determine the ionic/covalent character of the interactions in most of the systems. Nevertheless, there are some exceptions for which this criterion fails. This is for example the case for molecules with weak covalent bonds such as F_2 , $HOOH$, In these cases, it is necessary to resort to the energy density in order to classify the interactions.

Energy density. The energy density, $H(\mathbf{r})$, is defined as :

$$H(\mathbf{r}) = G(\mathbf{r}) + V(\mathbf{r}) \quad (103)$$

where $G(\mathbf{r})$ and $V(\mathbf{r})$ are the same kinetic and potential densities as described in eq. (102). Using this equation we can relate the Laplacian and the energy density as follows:

$$H(\mathbf{r}) = \frac{1}{4}\nabla^2\rho(\mathbf{r}) - G(\mathbf{r}) \quad (104)$$

Now, the sign of the energy density can be used instead of the sign of the Laplacian to determine the ionic/covalent character of an interaction. The advantage of this criterion²⁹² is that it makes disappear the 2:1 factor existing in eq. (102) and which give rise to troubles in the cases where $2G(\mathbf{r}) > |V(\mathbf{r})| > G(\mathbf{r})$. In the case of eq. (104), the sign of $H(\mathbf{r})$ exactly determines which of both contributions, $G(\mathbf{r})$ or $V(\mathbf{r})$ dominates.

1.5.3 ELF: Electron localization function

The concepts of electron localization and delocalization are highly relevant in chemistry. Electron localization is essential for descriptive chemistry because in this field one needs to know where local groups of electrons such as core or valence electrons, electron pairs, bonding pairs, unpaired electrons, or π -electron subsystems are placed. The electron localization function (ELF) is a function introduced by Becke and Edgecombe as a mean to measure the electron localization in molecular systems.⁸¹ They showed that the leading term in the Taylor expansion of the spherically averaged conditional pair probability is given by

$$P_{cond}^{\sigma\sigma}(\mathbf{r}, s) = \frac{1}{3} \left[\tau_\sigma - \frac{1}{4} \frac{(\nabla\rho_\sigma)^2}{\rho_\sigma} \right] s^2 + \dots, \quad (105)$$

1. THEORETICAL METHODS

where the argument (\mathbf{r}, s) denote spherical average on a shell of radius s about the reference point \mathbf{r} , and τ_σ is the positive-definite kinetic energy density defined by eq. (106)

$$\tau_\sigma = \sum_i^\sigma |\nabla \Psi|^2 \quad (106)$$

and where the contents of the squared brackets in eq. (105) are evaluated at the reference point. Eq. (105) succinctly conveys electron localization information. The smaller the probability of finding a second like-spin electron near the reference point, the more highly localized is the reference electron. Hence, the electron localization is related to the smallness of the expression

$$D_\sigma = \tau_\sigma - \frac{1}{4} \frac{(\nabla \rho_\sigma)^2}{\rho_\sigma} \quad (107)$$

The drawback of eq. (107) as a measure of electron localization is that high localizability is implied by small values of D_σ . Also, D_σ is not bounded from above. Therefore, Becke and Edgecombe proposed an alternative “electron localization function” (ELF) with more desirable features:

$$ELF = (1 + \chi_\sigma^2)^{-1} \quad (108)$$

where

$$\chi_\sigma = D_\sigma / D_\sigma^0 \quad (109)$$

and

$$D_\sigma^0 = \frac{3}{5} (6\pi^2)^{2/3} \rho_\sigma^{5/3} \quad (110)$$

where D_σ^0 corresponds to a uniform electron gas with spin-density equal to the local value of $\rho_\sigma(\mathbf{r})$. The ratio χ_σ is thus a dimensionless localization index calibrated with respect to the uniform-density electron gas as reference. The transformation of eq. (108) is designed to restrict the ELF’s possible values to the range $0 \leq \text{ELF} \leq 1$ with the upper limit ELF corresponding to perfect localization and the value $\text{ELF} = 0.5$ corresponding to electron-gas-like pair probability. Two years later Silvi and Savin⁸² showed that ELF measures the excess of kinetic energy density due to the Pauli repulsion in comparison with an uniform electron gas. In the region of space where the Pauli repulsion is strong (single electron or opposite spin-pair behavior) ELF is close to 1, whereas where the probability of finding the same-spin electrons

1. THEORETICAL METHODS

close together is high, ELF tends to 0. This orbital-independent (*i.e.*, with respect to unitary transformations) localization function nicely reveals the location of atomic shells, and core, binding, and lone electron pairs in atomic and molecular systems.

As in QTAIM analysis, it is possible to partition the molecular space into subsystems (basins) of attractors which allow the calculation of several properties by integration over these basins. The gradient vector field of ELF, $\nabla\eta$, enables one to divide the Euclidian space in basins of attractors where electron pairs are located. These basins are either core basins surrounding a nucleus or valence basins that do not include a nucleus (except for protonated valence basins that include a proton). The number of connections of a given valence basin with core basins is called the synaptic order. A disynaptic valence basin corresponds to a two-center bond, whereas a monosynaptic one characterizes a lone pair. Multicenter bonds, such as three-center two-electron (3c-2e) bonds, are accounted for by polysynaptic basins.²⁹³

Basin related properties are calculated by integrating a certain property over the volume of the basins. Let N be the number of electrons and $\rho(\mathbf{r}) = \sum_{j=1}^N |\phi_j(\mathbf{r})|^2$. For a basin labeled Ω_A , one can define its average population and pair populations by integrating the electron density and the pair densities as

$$\begin{aligned}\overline{N}(\Omega_A) &= \int_{\Omega_A} \rho(\mathbf{r}) \, d\mathbf{r} \\ \overline{N}^{\alpha\alpha}(\Omega_A) &= \iint_{\Omega_A} \Gamma^{\alpha\alpha}(\mathbf{r}_1, \mathbf{r}_2) \, d\mathbf{r}_1 \, d\mathbf{r}_2 \\ \overline{N}^{\beta\beta}(\Omega_A) &= \iint_{\Omega_A} \Gamma^{\beta\beta}(\mathbf{r}_1, \mathbf{r}_2) \, d\mathbf{r}_1 \, d\mathbf{r}_2 \\ \overline{N}^{\alpha\beta}(\Omega_A) &= \iint_{\Omega_A} \Gamma^{\alpha\beta}(\mathbf{r}_1, \mathbf{r}_2) \, d\mathbf{r}_1 \, d\mathbf{r}_2\end{aligned}\tag{111}$$

where the subscript A on Ω indicates that the integration has to be carried out only through the space corresponding to the atomic basin of atom A and $\Gamma^{\alpha\alpha}(\mathbf{r}_1, \mathbf{r}_2)$, $\Gamma^{\beta\beta}(\mathbf{r}_1, \mathbf{r}_2)$ and $\Gamma^{\alpha\beta}(\mathbf{r}_1, \mathbf{r}_2)$ are the same-spin and opposite-spin components of the pair density.²⁹⁴ Summation of all the atomic populations in a molecule yields the total number of electrons, N .

Multivariate analysis of electron densities. The multivariate analysis is a basic statistical method enabling one to reveal the correlation between

1. THEORETICAL METHODS

different groups of data. It relies upon the construction of the covariance matrix elements defined by

$$\langle \text{cov}(A, B) \rangle = \langle AB \rangle - \langle A \rangle \langle B \rangle \quad (112)$$

where $\langle A \rangle$, $\langle B \rangle$, and $\langle AB \rangle$ are the averages of the data values and of their product. The diagonal elements of the covariance matrix are the variances

$$\sigma^2(A) = \langle A^2 \rangle - \langle A \rangle^2 \quad (113)$$

which measure the dispersion of the data among the group. The square root of the variance is the standard deviation. Finally, the correlation coefficients are the ratios of the covariance matrix elements by the corresponding standard deviation, that is, $[\text{cov}(A, B)]/[\sigma(A)\sigma(B)]$. Positive and negative values of the correlation coefficients indicate that the A and B data are respectively correlated or anticorrelated, whereas a value close to 0 corresponds to independent behaviors. Applied to electrons distributed among a collection of adjacent regions spanning the geometrical space occupied by a molecule, the multivariate analysis provides a convenient tool to study electron delocalization. Consider such a partition in M basins for an N electron system. The number of electrons within each region is a quantum mechanical observable to which corresponds the population operator introduced by Diner and Claveries.²⁹⁵

$$\hat{N}(\Omega_A) = \sum_i^N \hat{y}(\mathbf{r}_i) \quad \text{with} \quad \hat{y}(\mathbf{r}_i) = \begin{cases} \hat{y}(\mathbf{r}_i) = 1 & \mathbf{r}_i \in \Omega_A \\ \hat{y}(\mathbf{r}_i) = 0 & \mathbf{r}_i \notin \Omega_A \end{cases} \quad (114)$$

In an N -electron system the population operators obey the closure relation²⁹⁶

$$\sum_A \hat{N}(\Omega_A) = N \quad (115)$$

The eigenvalues of the population of the population operators, the electron numbers $N(\Omega_A)$, are integers in the range $0, \dots, N$. As they also obey the closure relationship, the electron count in a region is not independent of those in the other regions and, therefore, these eigenvalues must be determined simultaneously. The closure relationship of the basin population operators enables one to carry out the multivariate statistical analysis of the basin populations through the definition of the covariance operator.²⁹⁶ The expectation values of this operator

$$\langle \text{cov}(\Omega_A, \Omega_B) \rangle = \int_{\Omega_A} \int_{\Omega_B} \Gamma(\mathbf{r}_1, \mathbf{r}_2) d\mathbf{r}_1 d\mathbf{r}_2 - \overline{N}(\Omega_A) \overline{N}(\Omega_B) \quad (116)$$

1. THEORETICAL METHODS

where $\Gamma(\mathbf{r}_1, \mathbf{r}_2)$ denotes the spinless pair density,²⁹⁴ provide pieces of information about electron delocalization. In particular, the diagonal elements, the variances

$$\sigma^2(\Omega_A) = \int_{\Omega_A} \int_{\Omega_A} \Gamma(\mathbf{r}_1, \mathbf{r}_2) d\mathbf{r}_1 d\mathbf{r}_2 - [\overline{N}(\Omega_A)]^2 + \overline{N}(\Omega_A) \quad (117)$$

are a measure of the quantum mechanical uncertainty of the basin's population, namely, the degree of fluctuation of the electron pair (*i.e.*, the square of the standard deviation), which can be interpreted as the dispersion of the electronic structures. According the partition scheme, the multivariate analysis enables one to build a phenomenological classical model of the charge distribution of a molecule in terms of the superposition of mesomeric structures.

The variance, $\sigma^2(\Omega_A)$, can also be spread in terms of contribution from other basins, the covariance, $\text{cov}(\Omega_A, \Omega_B)$, which has a clear relationship with the so-called delocalization index (DI), $\delta(\Omega_A, \Omega_B)$, defined by Fradera in the AIM framework:

$$\begin{aligned} \text{cov}(\Omega_A, \Omega_B) &= \langle N(\Omega_A) \cdot N(\Omega_B) \rangle - \langle N(\Omega_A) \rangle \langle N(\Omega_B) \rangle \\ &= \int_{\Omega_A} \int_{\Omega_B} (\Gamma(\mathbf{r}_1, \mathbf{r}_2) - \rho(\mathbf{r}_1)\rho(\mathbf{r}_2)) d\mathbf{r}_1 d\mathbf{r}_2 \\ &= \int_{\Omega_A} \int_{\Omega_B} \Gamma_{XC}(\mathbf{r}_1, \mathbf{r}_2) d\mathbf{r}_1 d\mathbf{r}_2 = -\frac{\delta(\Omega_A, \Omega_B)}{2} \end{aligned} \quad (118)$$

The DI, $\delta(\Omega_A, \Omega_B)$, accounts for the electrons delocalized or shared between basins Ω_A and Ω_B .²⁸⁵ As the total variance in a certain basin can be written in terms of covariance, we have

$$\sigma^2(\Omega_A) = - \sum_{B \neq A} \text{cov}(\Omega_A, \Omega_B) = \sum_{B \neq A} \frac{\delta(\Omega_A, \Omega_B)}{2} \quad (119)$$

From the quantity above one can do the usual contribution analysis (CA), given normally as a percentage:

$$CA(\Omega_A|\Omega_B) = \frac{\text{cov}(\Omega_A, \Omega_B)}{\sum_{A \neq B} \text{cov}(\Omega_A, \Omega_B)} \times 100 = -\frac{\text{cov}(\Omega_A, \Omega_B)}{\sigma^2(\Omega_B)} \times 100 \quad (120)$$

The CA gives us the main contribution arising from other basins to the variance, that is, the delocalized electrons of basin Ω_B on basin Ω_A , providing a measure of electron pair sharing between two regions of the molecular space.

1.6 RRKM THEORY

The Rice-Ramsperger-Kassel-Marcus (RRKM) theory is a statistical theory of chemical reactivity that allows to compute unimolecular reaction rates by using characteristics of the potential energy surface.²⁹⁷ It was developed by Rice and Ramsperger in 1927²⁹⁸ and Kassel in 1928²⁹⁹ (RRK theory). In 1952 and taking into account the transition state theory (TST) developed by Eyring in 1935, Marcus generalized this theory to the so called RRKM theory.¹⁵

What is a unimolecular reaction? A unimolecular reaction is defined as any system that evolves in time as a result of some prior stimulus or excitation step. Thus, both dissociation and isomerization are examples of unimolecular processes. Phenomenologically, the kinetics of a unimolecular reaction, $A \rightarrow \text{products}$, is written as

$$-\frac{dN_A}{dt} = kN_A \quad (121)$$

which, when integrated, gives rise to the time dependence of the concentration of $A(t)$:

$$N_A(t) = N_A(t=0)e^{-kt} \quad (122)$$

where k is the unimolecular rate constant with units of reciprocal time, and $N_A(t=0)$ is the number of molecules of species A at time $t=0$. The rate constant k depends on the internal energy of A , or in the case of an equilibrium ensemble of A , its temperature. For a given state of excitation, the exponential decay is a result of the assumption that the rate is a function only of the concentration of A .

Important questions in the study of unimolecular reactions are:

- a) what is the initial state produced in the excitation step,
- b) how fast does the system evolve toward products,
- c) what are the reaction products, and
- d) what are the product energy states?

It was recognized that a dissociation rate depends on the internal energy of the molecule.³⁰⁰ Thus, all detailed statistical theories of unimolecular reactions begin with the calculation of $k(E)$, the rate constant as a function of

1. THEORETICAL METHODS

the internal energy, E .

The connection between $k(T)$, often called the canonical rate constant, and $k(E)$, the microcanonical rate constant, involves averaging $k(E)$ over the energy distribution

$$k(T) = \int_{E_0}^{\infty} P(E, T) k(E) dE \quad (123)$$

where E_0 is the activation energy and $P(E, T)$ is the distribution of internal energies at a given temperature, T . In many applications the quantity of interest is $k(T)$, however we will work with $k(E)$ since we assume a microcanonical ensemble, *i.e.*, $E^{TOT} = \text{const.}$ It is also worth to stress that the theory can be tested adequately only by comparing the measured and calculated $k(E)$. Once this has been accomplished, the rate constant of any system with a known distribution of internal states can be calculated.

1.6.1 Introductory remarks

Before going more into details of the RRKM theory, few introductory remarks about some concepts used for its derivation will be introduced.

Phase space. Statistics involves the counting of states, and the state of a classical particle is completely specified by the measurement of its position \mathbf{q} and momentum \mathbf{p} . It is often convenient in statistics to imagine a $2N$ -dimensional space composed of the N position and N momentum coordinates. Such space is conventionally called “phase space”. The counting tasks can then be visualized in a geometrical framework where each point in phase space corresponds to a particular position and momentum. That is, each point in phase space represents a unique state of the particle. In Fig. 57 is shown an example of a phase space plot for a simple pendulum.

At point **A** the pendulum is in the maximum positive distance from the bob’s neutral point but its velocity is zero. This is shown as point **A** on the phase space diagram. At **B** the distance of the bob from its neutral position is zero, but its velocity is at a maximum (in a negative sense). The other points of the phase space plot show the relation between the velocity and position for other pendulum positions. The state of a system of particles corresponds to a certain distribution of points in phase space.

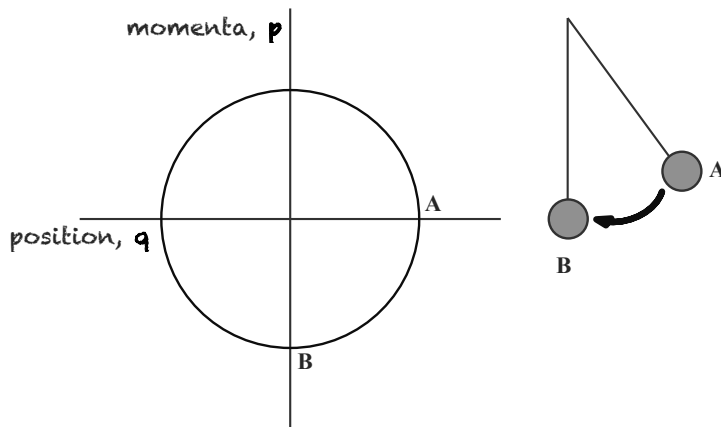


Figure 57: Illustration of phase space for a pendulum.

Sum of states. The counting of the number of states available to a particle amounts to determining the available volume in phase space. Let us consider a molecule consisting of N atoms with a Hamiltonian $H(\mathbf{p}, \mathbf{q})$. The momenta, \mathbf{p} and the position \mathbf{q} , vectors will consist of $m = 3N - 6$ terms, considering that there is no rotational-vibrational coupling. The classical phase space volume of such a system with a maximum energy E is defined by the integral

$$\text{Phase Space Volume} = \int_{H=0}^{H=E} \dots \int dp_1 \dots dp_m dq_1 \dots dq_m \quad (124)$$

This volume integral in $2m$ -dimensional space, has units of $[\text{Joules} \cdot \text{sec}]^m$. In one dimension, the units of phase space are Joule·sec. This is often referred to as a unit of action. According to the uncertainty principle, momentum and position are conjugate quantities which cannot be simultaneously and precisely known, that is $\Delta p \Delta q \geq \hbar/2$. Hence, the smallest allowable unit in phase space must be on the order of h , so that the quantum phase space is divided up into units of h . We can convert the phase space volume into a sum of states simply by dividing by h^m , one unit of h each dimension. The sum of states, $N(E)$, is then

$$N(E) = \frac{1}{h^m} \int_{H=0}^{H=E} \dots \int dp_1 \dots dp_m dq_1 \dots dq_m \quad (125)$$

It represents the total number of states for a system corresponding to an energy less than or equal to a specified value, E . Even though the phase space has been divided into quanta of action, this is still considered the classical sum of states because the classical phase space volume is first calculated

1. THEORETICAL METHODS

and converted into quantum states only at the end.

Density of states. A quantity related to the sum of states is the density of states, $\rho(E)$, which is defined as the number of states per unit energy. The number of states in the range E and $E + dE$ is denoted by $W(E)$. It is obtained by integrating $d\mathbf{p}d\mathbf{q}$ between $H = E$ and $H = E + dE$, and dividing the resulting volume by h^m :

$$W(E) = \frac{1}{h^m} \int_{H=E}^{H=E+dE} \int d\mathbf{p}_1 \dots d\mathbf{p}_m d\mathbf{q}_1 \dots d\mathbf{q}_m \quad (126)$$

Eq. (126) can be expressed as a product of a surface integral evaluated at $H = E$ and the energy interval dE . Since $\rho(E) = W(E)/dE$, the density of states is the surface integral

$$\rho(E) = \frac{1}{h^m} \int_{H=E} \dots \int d\mathbf{p}_1 \dots d\mathbf{p}_m d\mathbf{q}_1 \dots d\mathbf{q}_m \quad (127)$$

The density of states can also be obtained from $N(E)$ by taking the derivative with respect to the energy E , $\rho(E) = dN(E)/dE$.

1.6.2 Derivation of the RRKM statistical theory

There are several ways to derive the RRKM equation. The one adopted here is based on **classical transition state theory** and was first proposed by Wigner.^{301,302} It is worth pointing out that what we call RRKM has also been termed quasi-equilibrium theory (QET).³⁰³ The basic assumptions of statistical theories is that the rate constant $k(E, J)$ depends only on the total energy E and the total angular momentum J . It is assumed that the rate constant does not depend upon where the energy is initially located and that a microcanonical ensemble is maintained as the molecule dissociates. This is equivalent to assuming that IVR (intramolecular vibrational energy redistribution) is rapid compared to the lifetime with respect to dissociation. That is, vibrations are assumed to be strongly coupled by higher order terms (anharmonicities, Fermi resonances, etc) in the expansion of the potential energy function.

The derivation presented here is a simple derivation of the microcanonical rate constant $k(E)$ in which rotations are ignored and in which the location of the transition state is assumed to be fixed at a saddle point and is thus

1. THEORETICAL METHODS

independent of the energy in the system: tight transition state.

As aforementioned the state of a system of particles corresponds to a certain distribution of points in the phase space. The assumption is made that the total phase space is populated statistically which means that the population density over the whole surface of the phase space is uniform, in other words, the molecule populates the phase space uniformly throughout its dissociation.

In a microcanonical system (constant energy) the phase space is limited to a surface in which the Hamiltonian $H = E$, see Fig. 58. Consequently, the dimensionality of this hypersurface is reduced to $2m - 1$. If the energy, E , is greater than the dissociation energy, E_0 , the molecule has a chance to dissociate and thus to reach a part of the hypersurface which is associated with the critical surface.

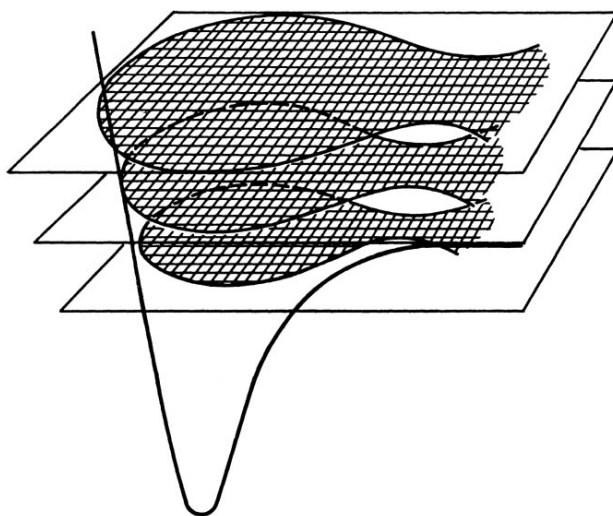


Figure 58: Reaction coordinate with a saddle point. Above it is a diagram of the phase space which varies with the reaction coordinate and with the total energy. Figure taken from ref.¹⁷⁸

The critical surface is defined as the surface which divides reactants and products. It has a dimension of $2m - 2$. The critical surface is so located that a trajectory, once having passed through it, will proceed on to reaction products without returning back. For reactions with substantial saddle points, the critical surface is located at the saddle point. For systems with

1. THEORETICAL METHODS

small or no saddle points, that is, very small or no reverse activation energy, the location of the critical surface depends upon the total energy, as it would be discussed later.

The rate of reaction is then related to the total flux of reactants which passes through this critical surface.¹⁷⁸ At the critical surface, the molecule is in the process of dissociating along a one-dimensional reaction coordinate, which is the minimum energy reaction path. It is generally assumed that at the saddle point, the reaction path is perpendicular to all other coordinates, that is, the system is separable. Hence, from now on the spatial and the conjugate momentum \mathbf{q}^\ddagger and \mathbf{p}^\ddagger (without subscripts) are assigned to these two special coordinates.

Since it was assumed that the phase space is statistically populated, *i.e.*, the population density over the whole surface of the phase space is uniform, the ratio of molecules near the critical surface over the total number of molecules can be expressed as the ratio of the phase space at the dividing surface over the total phase space.

$$\frac{dN(q^\ddagger, p^\ddagger)}{N} = \frac{dq^\ddagger dp^\ddagger \int \dots \int_{H=E-\epsilon_t-E_0} \int dq_1^\ddagger \dots dq_{n-1}^\ddagger dp_1^\ddagger \dots dp_{n-1}^\ddagger}{\int_{H=E} \int dq_1 \dots dq_n dp_1 \dots dp_n} \quad (128)$$

where E_0 is the activation energy and ϵ_t is the translational energy associated with the momentum \mathbf{p}^\ddagger in the reaction coordinate. Both, the activation energy, E_0 , and the translational energy, ϵ_t , must be subtracted from the total energy at the saddle point because these energies are not available for the $n - 1$ momenta, \mathbf{p}_i^\ddagger , and $n - 1$ coordinates, \mathbf{q}_i^\ddagger .

Eq. (128) gives the ratio of molecules whose special coordinates have values that range from \mathbf{q}^\ddagger to $\mathbf{q}^\ddagger + d\mathbf{q}^\ddagger$ and from \mathbf{p}^\ddagger to $\mathbf{p}^\ddagger + d\mathbf{p}^\ddagger$ over the total phase space, at any instant time. The rate of reaction is obtained from the time derivative of the molecules near the critical surface, that represents the flux of molecules passing through the critical region.

$$Flux = \frac{dN(q^\ddagger, dp^\ddagger)}{dt} \quad (129)$$

Because it was assumed that the reaction coordinate is perpendicular to, and separable from, all other coordinates the time derivative involves only the $d\mathbf{q}^\ddagger d\mathbf{p}^\ddagger$ term:

$$\frac{dN(q^\ddagger p^\ddagger)}{dt} = \frac{N \frac{dq^\ddagger dp^\ddagger}{dt} \int_{H=E-\epsilon_t-E_0} \int dq_1^\ddagger \dots dq_{n-1}^\ddagger dp_1^\ddagger \dots dp_{n-1}^\ddagger}{\int_{H=E} \int dq_1 \dots dq_n dp_1 \dots dp_n} \quad (130)$$

1. THEORETICAL METHODS

noting that

$$\frac{dq^\ddagger}{dt} = \frac{p^\ddagger}{\mu^\ddagger} \Rightarrow \frac{dq^\ddagger dp^\ddagger}{dt} = \frac{p^\ddagger dp^\ddagger}{\mu^\ddagger} \quad (131)$$

where μ^\ddagger is the reduced mass of the two separating fragments, Eq. (130) becomes

$$\frac{d\mathbb{N}(q^\ddagger, p^\ddagger)}{dt} = \frac{\mathbb{N} \frac{p^\ddagger dp^\ddagger}{\mu^\ddagger} \int_{H=E-\epsilon_t-E_0} \int dq_1^\ddagger \dots dq_{n-1}^\ddagger dp_1^\ddagger \dots dp_{n-1}^\ddagger}{\int_{H=E} \int dq_1 \dots dq_n dp_1 \dots dp_n} \quad (132)$$

Since the energy in the reaction coordinate is

$$\epsilon_t = \frac{p^{\ddagger 2}}{2\mu^\ddagger} \Rightarrow d\epsilon_t = \frac{p^\ddagger dp^\ddagger}{\mu^\ddagger} \quad (133)$$

and Eq. (132) can be written as:

$$\frac{d\mathbb{N}(q^\ddagger, p^\ddagger)}{dt} = \frac{\mathbb{N} d\epsilon_t \int_{H=E-\epsilon_t-E_0} \int dq_1^\ddagger \dots dq_{n-1}^\ddagger dp_1^\ddagger \dots dp_{n-1}^\ddagger}{\int_{H=E} \int dq_1 \dots dq_n dp_1 \dots dp_n} \quad (134)$$

Eq. (134) expresses the reaction rate (molecules per unit time) in terms of \mathbb{N} , the number of molecules, multiplied by the rate constant $k(E, \epsilon_t)$.

$$\frac{d\mathbb{N}(q^\ddagger, dp^\ddagger)}{dt} = \mathbb{N} k(E, \epsilon_t) \quad (135)$$

$k(E, \epsilon_t)$ is expressed in terms of a ratio of phase space areas

$$k(E, \epsilon_t) = \frac{d\epsilon_t \int_{H=E-\epsilon_t-E_0} \int dq_1^\ddagger \dots dq_{n-1}^\ddagger dp_1^\ddagger \dots dp_{n-1}^\ddagger}{\int_{H=E} \int dq_1 \dots dq_n dp_1 \dots dp_n} \quad (136)$$

These phase space areas can be converted into densities of states. In fact, the denominator of Eq. (136) is just the density of states multiplied by the factor h^n . The numerator is an integral over one less dimension, so that it is a density multiplied by h^{n-1} . Thus, we can rewrite the rate constant as:

$$k(E, \epsilon_t) = \frac{\rho(E - E_0 - \epsilon_t) h^{n-1}}{\rho(E) h^n} \Rightarrow k(E, \epsilon_t) = \frac{\rho(E - E_0 - \epsilon_t)}{h \rho(E)} \quad (137)$$

Eq. (137) expresses the rate constant in terms of the total energy, E , and the translational energy of the departing fragments at the transition state, ϵ_t . As shown in Fig. 59 there are many different ways for the reaction to pass through the transition state region. They differ in how the available energy,

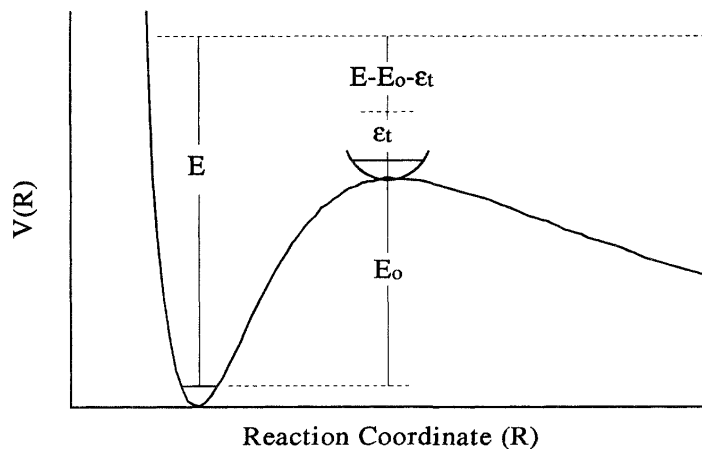


Figure 59: The reaction coordinate and the partitioning of the energy in the transition state ($E - E_0$) between the translational energy, ϵ_t , and the vibrational energy of the modes normal to the reaction coordinate. Figure taken from ref.¹⁷⁸

$E - E_0$, is partitioned between the internal energy of the transition state and the translational energy of the fragments. Eq. (137) is a state-to-state reaction rate constant. In order to obtain the total dissociation rate we must integrate over all the different translational energies in the transition state.

$$k(E) = \frac{\int_0^{E-E_0} \rho^\ddagger(E - E_0 - \epsilon_t) d\epsilon_t}{h\rho(E)} = \frac{N^\ddagger(E - E_0)}{h\rho(E)} \quad (138)$$

where $N^\ddagger(E - E_0)$ is the sum of states at the transition state from 0 to $E - E_0$. Because in the calculation of densities and sums of states, the reactant and transition state symmetries are ignored we must multiply the rate constant in Eq. (138) by the reaction symmetry, σ ,

$$k(E) = \frac{\sigma N^\ddagger(E - E_0)}{h\rho(E)} \quad (139)$$

Eq. (139) is known as the RRKM equation.

Assumptions in the RRKM theory. The RRKM equation has been derived in terms of a classical mechanical flux in phase space. The conversion of this equation into a quantum mechanical theory is done converting the phase space volume and surfaces into sum and density of states by dividing

1. THEORETICAL METHODS

these quantities by h^{n-1} . However the zero point energy (ZPE) must be taken into account somehow. With this purpose all energies are referred at the zero point energy. Hence, E_0 is defined as the dissociation energy at 0 K (see figure 60).

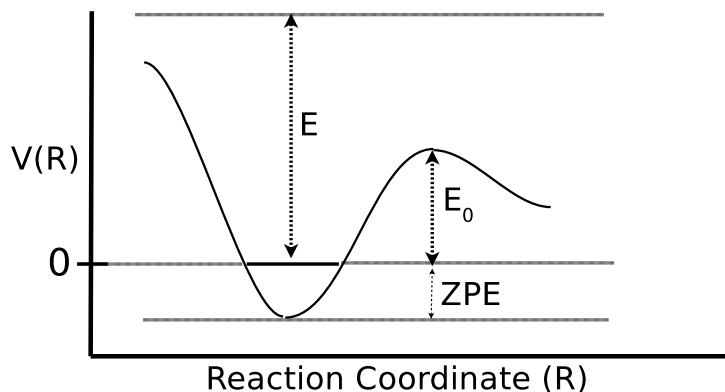


Figure 60: Zero energy reference to compute $k(E)$.

The fundamental assumption of the statistical theory is that the molecule populates the phase space uniformly throughout its dissociation. A micro-canonical ensemble is maintained. This is only true when the intramolecular vibrational energy redistribution (IVR) is very fast compared to the rate of reaction. That is known as intrinsic RRKM behavior.

$$\mathbb{N}(t) = \mathbb{N}(0)e^{-k(E)t} \Rightarrow \text{Intrinsic RRKM behavior} \quad (140)$$

The second assumption is that all the molecules within the region of phase space bounded by \mathbf{q}^\ddagger and $\mathbf{q}^\ddagger + d\mathbf{q}^\ddagger$ and \mathbf{p}^\ddagger and $\mathbf{p}^\ddagger + d\mathbf{p}^\ddagger$ lead to products. That is, all the molecules that cross the critical surface lead to products. There is no recrossing. These recrossing would reduce the rate so that RRKM theory would overestimate the rate constant. The TS is located in the region where the recrossing are minimized.

The third assumption is that the coordinates, $d\mathbf{q}^\ddagger$ and $d\mathbf{p}^\ddagger$, are perpendicular to all other coordinates and therefore, separable from the other coordinates. This assumption becomes less valid when the energy increases and the coupling between the reaction coordinate and the rest of the modes becomes more important.

1.6.3 Loose TS

For channels with no reverse activation energy (loose-TS) the TS is more difficult to define because there is no saddle point along the reaction path. In these cases, the TS is located on the basis of the minimum sum of states and, as aforementioned, its location varies with the internal energy.

To compute the RRKM rate constants for the loose-TS we adopted the microcanonical variational transition state theory (μ VTST) in its vibrator formulation.^{304,305} First we perform a scan along the reaction coordinate. Then, at each point of the scan we do an optimization, freezing this internal coordinate and the energy is computed. The Hessian matrices describing the modes orthogonal to the reaction path are evaluated according to the standard procedure of Hu and Hase,³⁰⁵ and the sum of states are calculated for the corresponding optimized structure. We repeat this procedure for each internal energy considered and the structure corresponding to the minimum sum of states is assigned as the TS. An example of a loose-TS is the formamide neutral loss reaction: $[\text{M}(\text{formamide})]^{2+} \rightarrow \text{M}^{2+} + \text{formamide}$. In this example, the reaction coordinate corresponds to the Ca–O distance and thus we used this as the scanned coordinate. In Fig. 61 it can be seen how the location of the TS (minimum sum of states) with respect to the reaction coordinate changes with the internal energy of the reactant molecule, getting closer to the reactants as the molecule’s internal energy increases.

1. THEORETICAL METHODS

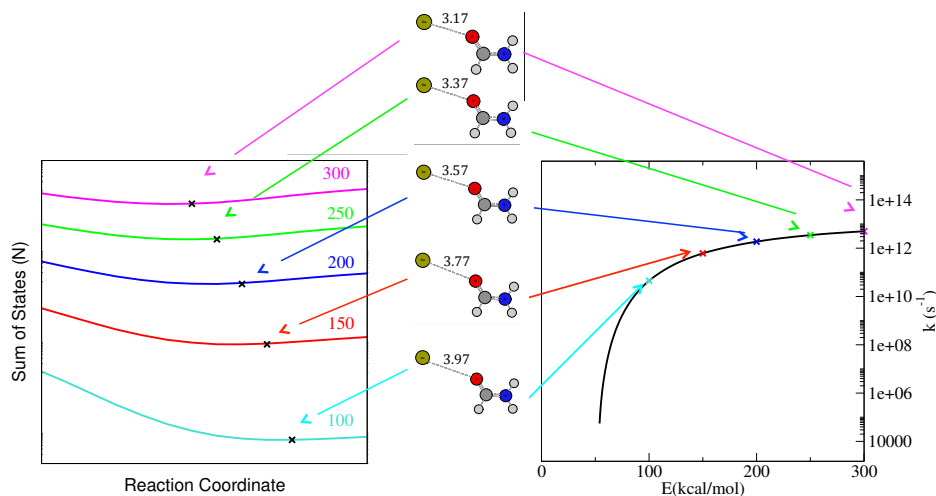


Figure 61: On the left side the sum of states *vs.* the reaction coordinate for formamide-Ca²⁺ at different internal energies (all in kcal mol⁻¹). The crosses mark the minimum of the sum of states for each energy. On the right side the microcanonical rate constant k is represented *vs.* the internal energy. The crosses mark the $k(E)$ values corresponding to the minimum sum of states for specific internal energies. In the middle the formamide-Ca²⁺ geometries are represented for each of the points with the values (in Å) for Ca-O distance.

1.6.4 External rotations

RRKM theory treats modes either as active, which exchange energy freely, or adiabatically, which remain in the same quantum number during the unimolecular decomposition. Normally, the modes treated as active are all the normal modes. If the external rotational degrees of freedom are to be taken into account there are different ways of doing so in the framework of RRKM theory.²²⁶ In this study we have considered an *almost symmetric top*, where $I_x \approx I_y$, for which rotational energy is given by the following approximation:³⁰⁶

$$E_{rot}(J, K) = \left(\frac{1}{I_x} + \frac{1}{I_y} \right) \frac{[J(J+1) - K^2] \hbar^2}{4} + \frac{K^2 \hbar^2}{2I_z} \quad (141)$$

that can be written as

$$E_{rot}(J, K) = BJ(J+1) + (A - B)K^2 \quad (142)$$

1. THEORETICAL METHODS

where $A = \hbar^2/2I_z$, $B = \left(\frac{1}{I_x} + \frac{1}{I_y}\right) \frac{\hbar^2}{4}$, and J and K are the rotational quantum numbers that vary as: $J = 0, 1, 2, \dots$ and $K = 0, \pm 1, \pm 2, \dots, \pm J$. The symmetry axis is the z -axis and the other two moments of inertia are $I_x \approx I_y$. A symmetric top can be visualized as a rotating cylinder. For a given J , the cylinder can rotate in a total of $2J + 1$ orientations, each with a different K which determines its projection along the symmetry axis. Fig. 62 shows the case of a prolate top rotating with $K \approx J$ and $K = 0$.

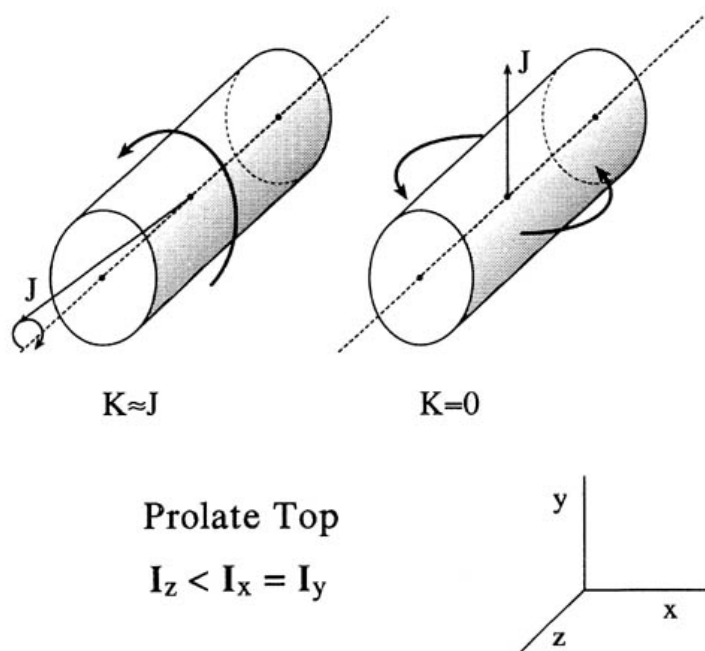


Figure 62: Prolate symmetric top molecule represented as a cylinder. The rotational motion due to J and K are indicated. Figure taken from ref.¹⁷⁸

The quantum number J is a constant of motion and therefore is always adiabatic, *i.e.*, there is no exchange of energy. On the other hand, the quantum number K can be treated as an active rotor—it allows energy exchange between vibrational and rotational modes— or as an adiabatic rotor.

If we assume that K is conserved, and thus treated as adiabatic, the RRKM unimolecular rate constant for energy E and specific values of J and K is¹⁷⁸

1. THEORETICAL METHODS

$$k(E, J, K) = \frac{\sigma}{h} \frac{N^\ddagger \left[E - E_0 - E_{rot}^\ddagger(J, K) \right]}{\rho \left[E - E_{rot}(J, K) \right]} \quad (143)$$

where E_{rot}^\ddagger is the rotational energy for the transition state and E_{rot} is the same for the minimum energy structure (both obtained by eq. (141)). Within this assumption (J and K being adiabatic) we consider three particular cases for partitioning the rotational energy within the molecular axes. In case **1**, all the rotational energy is placed on the x, y -plane, and corresponds to $K = 0$, and

$$J = \frac{\left(-1 + \sqrt{1 + 4 \frac{E_{rot}}{\bar{B}}} \right)}{2}; \quad \bar{B} = \left(\frac{1}{I_x} + \frac{1}{I_y} \right) \frac{\hbar^2}{4} \quad (144)$$

where E_{rot} is the rotational energy of the ion after collision. In case **2** the rotational energy is equally distributed among the three axes, so $E_{x,y} = 2/3 E_{rot}$ and $E_z = 1/3 E_{rot}$. Finally, in case **3** all the rotational energy is placed along the z -axis such that

$$K = \sqrt{\frac{1}{3} \frac{E_{rot}}{A - \bar{B}}} \quad (145)$$

The $k(E, J)$ microcanonical rate constant with K active can be determined by two different approaches. One way of treating the K -dependent term as an active degree of freedom is to calculate the density of states for the reactant and the sum of states for the TS by summing over contributions from all possible values of K to give²²⁶

$$k(E, J) = \frac{\sigma}{h} \frac{\sum_{K=-J}^{K=J} N^\ddagger \left[E - E_0 - E_{rot}^\ddagger(J, K) \right]}{\sum_{K=-J}^{K=J} \rho \left[E - E_{rot}(J, K) \right]} \quad (146)$$

In the second approach, the unimolecular rate constant, $k(E, J)$, for a total energy E and angular momentum J is written as²²⁶

$$k(E, J) = \sigma h \frac{N^\ddagger \left[E - E_{rot}^\ddagger(J) - E_0 \right]}{\rho \left[E - E_{rot} \right]} \quad (147)$$

1. THEORETICAL METHODS

where N^\ddagger and ρ are written as convolutions between the densities and the sum of states for the internal degrees of freedom and the active external rotation, respectively,

$$N^\ddagger(E^\ddagger) = \int_0^{E^\ddagger} N_{vib}^\ddagger(E) \rho_{rot}(E^\ddagger - E) dE \quad (148)$$

$$\rho(E_\nu) = \int_0^{E_0} \rho_{vib}(E) \rho_{rot}(E_\nu - E) dE \quad (149)$$

E^\ddagger is the active energy of the TS and E_ν is the active energy of the energized reactant; the total energy is $E = E_\nu + E_{rot}(J) = E^\ddagger + E_{rot}^\ddagger(J) + E_0$ with $E_{rot}(J)$ and $E_{rot}^\ddagger(J)$ being the adiabatic rotational energies of the reactant and the TS respectively.

For all the calculations, the sum and density of states were computed using a semiclassical state counting.^{307–309} We used the quantum RRKM model which assumes that ZPE flows freely within the molecule.^{310,311} All calculations were performed using the RRKM code given by Zhu and Hase.³¹²

1.7 Direct chemical dynamics simulations

Since the early 1960s classical trajectory simulations have been used to study the atomistic dynamics of chemical reactions, energy transfer, and molecular motion.^{313,314} The components of a classical trajectory simulation are³¹⁵ (1) developing or choosing a potential energy surface for the chemical problem under investigation; (2) selecting initial conditions for the ensemble of trajectories to be calculated; (3) numerical integration of the classical equations of motion, that is, either Newton’s or Hamilton’s,³¹⁶ to determine the atomic-level motion for each trajectory; and (4) transformation of the trajectory’s final atomic coordinates and momenta to properties that may be compared with experiment and/or theoretical models. Included in this last component are bond lengths and angles to identify product structures; product vibrational, rotational, and translational energies; quantum numbers for vibrational and rotational degrees of freedom; the amount of energy in individual molecular degrees of freedom; and scattering angles.

During the classical simulation, the motion of the atoms in the chemical system is determined by solving the classical equations of motion, which can

1. THEORETICAL METHODS

be either Newtonian

$$-\frac{\partial V}{\partial q_i} = m_i \frac{d^2 q_i}{dt^2} \quad (150)$$

or Hamiltonian

$$\frac{\partial H_n}{\partial p_i} = \frac{dq_i}{dt}, \quad \frac{\partial H_n}{\partial q_i} = -\frac{dp_i}{dt}, \quad (151)$$

where $H = T(\mathbf{p}) + V(\mathbf{q})$ is the molecular system's total energy, and the index i encompasses all the atoms' coordinates and momenta. We know the kinetic energy expression $T(\mathbf{p})$ –essentially, it's $T = p^2/2m$ for one atom. What we need to know for this calculation is the system's potential energy function (or surface), $V(\mathbf{q})$, as well as the gradient of the potential (and in some cases also the Hessian).

Until the 1990s the standard way to perform a classical trajectory chemical dynamics simulation was to represent the potential energy surface, $V(\mathbf{q})$, by an analytic potential energy function. For example, we can model $V(\mathbf{q})$ for a cluster of rare gas atoms by a sum of Lennard-Jones potentials. The molecular mechanics (MM) model,³¹⁷ consisting of functions to represent atomic stretching, bending, wagging, and torsional motions, was developed to describe $V(\mathbf{q})$ for organic and biological molecules with thermal energies. However, this function generally does not correctly describe a PES for some processes as bond-breaking, for which highly excited molecules undergo bond rupture reactions to form new molecules. Another approach, for a small molecular system consisting of a few atoms, is to calculate a high density of points in the coordinate space and fit them with arbitrary functions to give a smooth and accurate PES. However, developing such a function is a formidable and lengthy task that becomes computationally impractical as the number of atoms of the system becomes large. A different technique to obtain $V(\mathbf{q})$ for large reactive systems is to derive an analytic potential energy function for the degrees of freedom thought to be most critical for the reaction dynamics using electronic structure calculations. Then, empirical analytic potential energy terms are used for the remaining degrees of freedom.³¹⁸ All these approaches for representing $V(\mathbf{q})$ have limitations and contain ambiguities and difficulties.

Trajectories on the Fly. With increased computer speed and more powerful computer algorithms, it has become possible to perform *direct dynamics*

1. THEORETICAL METHODS

simulations,³¹⁹ also known as “on-the-fly” calculations. In a direct dynamics simulation, the classical equations of motion are numerically integrated without the need for an analytic potential energy function.³²⁰ Instead, the trajectories are integrated on the fly, with the potential energy $V(\mathbf{q})$ and derivative $\partial V/\partial q_i$ obtained directly from an electronic structure theory by solving at each numerical integration step the time-independent Schrödinger equation

$$H_e(\mathbf{r}; \mathbf{q})\Psi(\mathbf{r}; \mathbf{q}) = E_e(\mathbf{q})\Psi(\mathbf{r}; \mathbf{q}) \quad (152)$$

where \mathbf{r} and \mathbf{q} are the electron and nuclear coordinates, and H_e , Ψ , and E_e are the electrons’ Hamiltonian operator, wavefunction, and energy at the specific nuclear configuration given by the set of coordinates \mathbf{q} . The potential energy $V(\mathbf{q})$ is the sum of the electronic energy $E_e(\mathbf{q})$ and the nuclear-nuclear repulsion $V_{NN}(\mathbf{q})$. Eq. (152) can be solved either by means of a wavefunction based method or by means of density functional theory. Since the time-independent Schrödinger equation, eq. (152), is solved at each step of the trajectory integration, providing the potential energy $V(\mathbf{q})$ and gradient $\partial V/\partial q_i$, these kind of direct dynamics simulations are called Born-Oppenheimer (BO) direct dynamics.^{321,322}

Time-step. Over any arbitrary time interval, the relationship between two positions is given by

$$\mathbf{q}(t_2) = \mathbf{q}(t_1) + \int_{t_1}^{t_2} \frac{\mathbf{p}(t)}{m} dt \quad (153)$$

Similarly, the relationship between two momentum vectors is given by

$$\mathbf{p}(t_2) = \mathbf{p}(t_1) + m \int_{t_1}^{t_2} \mathbf{a}(t) dt \quad (154)$$

for the sake of simplicity we have remove the subindex i for atoms coordinate and momenta. It is almost never possible to write down analytical expressions for the position and momentum components of the phase space trajectory as a function of time. However, using Euler’s approximation eqs. (153) and (154) can be rewritten as

$$\mathbf{q}(t + \Delta t) = \mathbf{q}(t) + \frac{\mathbf{p}(t)}{m} \Delta t \quad (155)$$

and

$$\mathbf{p}(t + \Delta t) = \mathbf{p}(t) + m\mathbf{a}(t)\Delta t \quad (156)$$

1. THEORETICAL METHODS

this approximation being exact in the limit of $\Delta t \rightarrow 0$. Thus, given a set of initial positions and momenta (initial conditions), and a means for computing the forces acting on each particle at any instant (and thereby deriving the acceleration), we have a formalism for simulating a trajectory. The way of choosing the initial conditions will be explained in more details later on. The mean for computing the forces, as aforementioned is the electronic structure theory used to solve the time-independent Schrödinger equation.

While the use of eqs. (155) and (156) seems entirely straightforward, the finite time step introduces very real practical concerns. Fig. 63 illustrates the variation of a single momentum coordinate of some arbitrary phase space trajectory, which is described by a smooth curve. When the acceleration is computed for a point on the true curve, it will be a vector tangent to the curve. If the curve is not a straight line, any mass-weighted step along the tangent (eq. (156)) will necessarily result in a point off the true curve. There is no guarantee that computing the acceleration at this new point will lead to a step that ends in the vicinity of the true curve. Indeed, with each additional step, it is quite possible that we will move further and further away from the true trajectory. The problem is compounded for position coordinates, since the velocity vector being used is already only an estimate derived from eq. (156), *i.e.*, there is no guarantee that it will even be tangent to the true curve when a point on the true curve is taken.

In the limit of an infinitesimally small time step, we will recover eqs. (153) and (154). But, since each time step requires a computation of all of the molecular forces (at least), which is computationally intensive, we do not want to take too small a time step, or we will not be able to propagate the trajectory for any chemically interesting length of time. What then is the optimal length for a time step that balances numerical stability with chemical utility? The general answer is that it should be at least one and preferably two orders of magnitude smaller than the fastest periodic motion within the system. In a typical molecular system, the fastest motion is bond vibration which, for a heavy-atom-hydrogen bond has a period of about 10^{-14} s. Thus, for a system containing such bonds, an integration time step Δt should not much exceed 0.1 fs. This rather short time step means that simulations are rarely run for more than some 100 fs of simulation time.

Integration algorithms. Using Euler’s approximation and taking integration steps in the direction of the tangent is a particularly simple integration

1. THEORETICAL METHODS

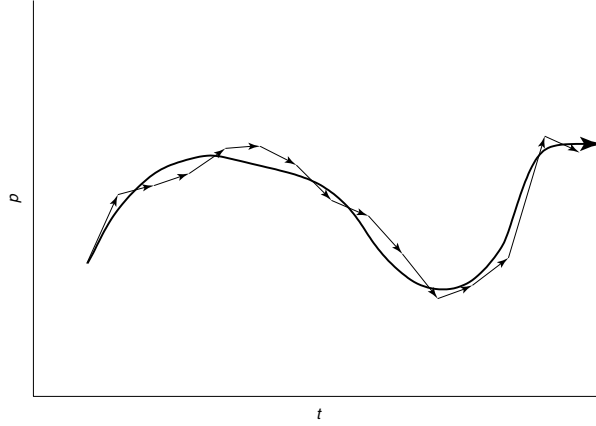


Figure 63: An actual phase-space trajectory (bold curve) and an approximate trajectory generated by repeated application of eq. (156) (series of arrows representing individual time steps). In the illustration, the approximate trajectory hews relatively closely to the actual one, but this will not be the case if too large a time step is used. Taken from ref.³²³

approach, and as such is not particularly stable. Considerably more sophisticated integration schemes have been developed for propagating trajectories. If we restrict ourselves to consideration of the position coordinate, most of these schemes derive from approximate Taylor expansions in \mathbf{r} , *i.e.*, making use of

$$\mathbf{q}(t + \Delta t) = \mathbf{q}(t) + \mathbf{v}(t)\Delta t + \frac{1}{2!}\mathbf{a}(t)(\Delta t)^2 + \frac{1}{3!}\left.\frac{d^3\mathbf{q}(\tau)}{dt^3}\right|_{\tau=t}(\Delta t)^3 + \dots \quad (157)$$

where the abbreviations \mathbf{v} and \mathbf{a} for the first and second time derivatives, respectively, of the position vector \mathbf{q} were used.

One such method, first used by Verlet in 1967,³²⁴ considers the sum of the Taylor expansions corresponding to forward and reverse time steps Δt . In that sum, all odd-order derivatives disappear since the odd powers of Δt have opposite sign in the two Taylor expansions. Rearranging terms and truncating at second order (which is equivalent to truncating at third-order, since the third-order term has a coefficient of zero) yields

$$\mathbf{q}(t + \Delta t) = 2\mathbf{q}(t) - \mathbf{q}(t - \Delta t) + \mathbf{a}(t)(\Delta t)^2 \quad (158)$$

Thus, for any particle, each subsequent position is determined by the current position, the previous position, and the particle's acceleration (determined from the forces on the particle). For the very first step (for which

1. THEORETICAL METHODS

no position $\mathbf{q}(t - \Delta t)$ is available) one might use eqs. (155) and (156).

The Verlet scheme propagates the position vector with no reference to the particle velocities. However, often knowledge of the momentum coordinates is also essential. To propagate the position and velocity vectors in a coupled fashion, a modification of Verlet's approach called the leapfrog algorithm has been proposed. An even better implementation of the same basic algorithm is the so-called velocity Verlet²¹⁹ algorithm, where positions, velocities, and accelerations at time $t + \Delta t$ are obtained from the same quantities at time t in the following way:

$$\begin{aligned} \mathbf{q}(t + \Delta t) &= \mathbf{q}(t) + \mathbf{v}(t)\Delta t + (1/2)\mathbf{a}(t)\Delta t^2 \\ \mathbf{v}(t + \Delta t/2) &= \mathbf{v}(t) + (1/2)\mathbf{a}(t)\Delta t \\ \mathbf{a}(t + \Delta t) &= -(1/m)\nabla V(\mathbf{q}(t + \Delta t)) \\ \mathbf{v}(t + \Delta t) &= \mathbf{v}(t\Delta + t/2) + (1/2)\mathbf{a}(t + \Delta t)\Delta t \end{aligned} \quad (159)$$

Initial conditions. The selection of initial conditions will be briefly summarized considering the collision induced dissociation process studied in Part II of this PhD thesis, namely, Ar + formamide-M²⁺ ion. The properties to be sampled in this case are the rotational and vibrational energies of the formamide-M²⁺ ion and the relative properties of Ar + formamide-M²⁺. The formamide-M²⁺ molecule may be considered as a symmetric top and its rotational energy may be sampled from a thermal distribution at temperature T_r ³²⁵ or be defined as a specific rotational state with quantum numbers J and K . For most polyatomic molecules and for room temperature, the rotational energy distribution is classical and the total angular momentum J and its component on the symmetric top axis J_z are selected by sampling this distribution. Since no specific rotational state is selected in the experiments, we used the classical distribution at a temperature T to sample the rotational energy.

The vibrational energy of the polyatomic formamide-M²⁺ may be that for a given vibrational state specified by quantum numbers n or chosen for a vibrational temperature T_v . For the latter, the quantum number n_i for each vibrational mode is randomly sampled from the probability distribution

$$P(n_i) \propto \exp \left[-(n_i + \frac{1}{2})h\nu_i / k_B T_v \right] \quad (160)$$

The energy for each individual normal mode is then $E_i = (n_i + 1/2)h\nu_i$. The coordinate Q_i and momenta P_i are chosen by sampling a random phase

1. THEORETICAL METHODS

for the mode. The \mathbf{Q} and \mathbf{P} vectors are then transformed to Cartesian coordinates and momenta using the normal mode eigenvector.

The relative Ar + formamide-M²⁺ properties include (1) the impact parameter, b , which may be chosen randomly between 0 and b_{max} ; (2) random rotation of formamide-M²⁺ about its Euler angles; and (3) the Ar + formamide-M²⁺ relative collision energy.

Sampling at a Transition State. Once the transition state is identified and the energy transfer obtained, it is possible to use dynamics in order to study how a system evolves from the transition state towards different reaction channels.

Thus, in some cases it is meaningful to initialize trajectories at a TS with either initial conditions for a constant T in accord with TST or at constant energy for a unimolecular reaction in accord with RRKM. This TS sampling allows proper ZPE conditions at the TS and quasiclassical sampling to the TS energy levels. Quasiclassical refers to the selection of the initial conditions in order to represent quantum mechanical vibrational and rotational energy levels. Canonical, constant temperature, sampling at a TS is identical to canonical sampling for a polyatomic molecule, as described above for CID reaction sampling, except that there are only $3N - 7$ vibrational degrees of freedom (nonlinear polyatomic) instead of $3N - 6$. The new degree of freedom at the TS is reaction coordinate translation, which is treated classically and whose probability distribution is

$$P(E_t^\ddagger) = \frac{\exp(-E_t^\ddagger/k_B T)}{k_B T}, \quad (161)$$

which may be sampled by its cumulative distribution function

$$E_t^\ddagger = -kT \ln(1 - R), \quad (162)$$

where R is a freshly chosen random number in the range of 0–1. E_t^\ddagger is related to the reaction coordinate momentum via $E_t^\ddagger = (P_t^\ddagger)^2/2$ and the normal mode eigenvector of the TS is used to transform to Cartesian momentum.

For statistical unimolecular decomposition at constant energy, there is a microcanonical ensemble of states for the dissociating molecules and every vibrational/rotational state at the TS with energy $E_{v,r}^\ddagger$ in the range 0 to $E - E_0$ has equal probability of being populated.^{326,327} Here E is the energy

1. THEORETICAL METHODS

of the unimolecular reactant above its ZPE level and E_0 is the difference between the TS and reactant ZPE levels; that is, the quantum threshold. The total TS energy $E^\ddagger = E - E_0$ is the sum $E^\ddagger = E_{v,r}^\ddagger + E_t^\ddagger$. With the TS vibrational/rotational state chosen randomly to give $E_{v,r}^\ddagger$, the remaining energy is added to reaction coordinate translation.

When sampling the ZPE level at a TS, either quasiclassical sampling, with random normal mode phases or Wigner sampling may be used to transform the ZPE level to normal mode coordinates and momenta. These two sampling algorithms were found to give similar dynamics for trajectories initialized at a TS ZPE level.³²⁸

CID direct dynamics simulations. For complex problems with many atoms the potential energy surface may be represented as a combination of two components; that is, atoms treated directly by a QM method and the remainder by analytic MM functions. Such a simulation is referred to as QM + MM or QM/MM.³²²

In the direct dynamics simulations performed to modeling the CID process between Ar and formamide- M^{2+} ($M = \text{Ca}, \text{Sr}$) there is no need to treat explicitly by quantum mechanics the Ar atom, since no bonds will form or break between Ar and the ion. Hence, in order to reduce computation time, the interaction Ar-formamide- M^{2+} is described by an analytical potential, MM. Thus, the potential energy used in the simulations is

$$V = V_{ion} + V_{Ar-ion} \quad (163)$$

where V_{ion} and V_{Ar-ion} are the ion intramolecular and the Ar-formamide- M^{2+} interaction potentials, respectively. A QM description is used to treat the intramolecular ion potential (V_{ion}), while the ion-projectile intermolecular interaction (V_{Ar-ion}) is treated via the analytical potential developed by Meroueh and Hase to simulate CID of protonated peptides.²¹⁵ This potential is a sum of two-body terms between Ar and each of the atoms of the molecular ion:

$$V_{Ar-ion} = \sum_i a_i \exp(-b_i r) + \frac{c_i}{r^9} \quad (164)$$

where r is the Ar-ion-atom distance and the a , b and c coefficients are obtained by fitting the analytic potential to the *ab initio* interaction potential. The values for parameters a , b and c for the Ar-formamide and Ar- Ca^{2+}

1. THEORETICAL METHODS

interactions were taken from ref.²¹⁵ and ref.³²⁹ Parameters for the Ar-Sr²⁺ interaction were found by fitting eq. (164) to the Ar-Sr²⁺ potential energy curve obtained at the QCISD(T)(full) level, together with a 6-31++G(d,p) basis set expansion for Ar atom and a Stuttgart basis set with pseudo potential for Sr²⁺ cation.³²⁹ BSSE was taken into account using the counterpoise method.³³⁰ The *ab initio* and fitted curves, as well as a , b and c parameters are shown in Fig. 64. Note that the curve is fitted with a purely repulsive energy function in order to better describe the repulsive wall that is the most important feature in CID for the energies considered here.²¹⁵

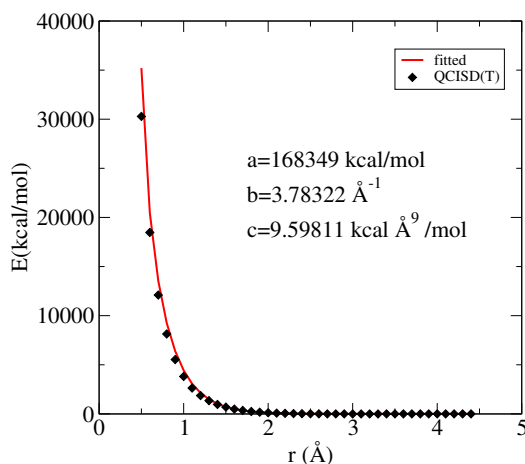


Figure 64: QCISD(T)/6-31++G(d,p) *ab initio* (diamonds) and fitted (solid line) potential energy curves for the Ar-Sr²⁺ interaction.

A general and broadly applicable approach for performing a classical trajectory chemical dynamics simulation is to obtain the potential energy function, and its gradient and Hessian, directly from an electronic structure theory.³²¹ The latter is a component of a quantum chemistry software package such as Gaussian09.⁷⁷ Hence, the software needed for such a chemical dynamics simulation requires to interface the technology of a chemical dynamics simulation with that of quantum chemistry. We used VENUS^{217,218} package for the propagation of the trajectories and Gaussian09⁷⁷ for the QM evaluation of energies, gradients and Hessians, to enable QM/MM direct dynamics.

Concluding remarks. It is important to recognize the difference between this chemical dynamics simulation for which *an ensemble of trajectories* are

2. EXPERIMENTAL METHODS

calculated and a molecular dynamics (MD) simulation.³³¹ For both the atomistic dynamics are obtained by numerically integrating the classical equations of motion. However, for a traditional MD simulation *a single trajectory* is calculated whose motion is assumed to be ergodic. If this trajectory is coupled to a thermal bath,³³¹ the properties of a constant temperature T canonical ensemble are determined by following the trajectory *vs.* time.

With direct dynamics simulations, we can probe reaction mechanisms at the atomic level and use the results to interpret the experiments. The simulations also allow a deeper understanding of reaction mechanisms than that provided by the widely used reaction path, transition state theory, and Rice-Ramsperger-Kassel-Marcus (RRKM) theory models.³¹⁸ By means of direct dynamics simulations it is also possible to discover new reaction pathways and chemical dynamics.

2 Experimental methods

2.1 Collision Induced Dissociation

The first observations of the products of the collision-induced decomposition (CID) of ions were made in the early days of the development of mass spectrometry and for many years, they were regarded as little more than a nuisance.³³² Over the past 40 years, the CID of ions has been transformed from a nuisance, through being a curiosity to being a major technique used in determining traces of specific components in complex mixtures without the use of chromatography. Modern applications of CID, also referred to as collision activated dissociation (CAD) are detection, identification, and structural analysis of organic molecules, to complex mixture analysis, and to biopolymer sequencing.^{333–337} CID has proven extremely useful for the identification and characterization of ions and for complex mixture analysis.³³⁸

Tandem mass spectrometry (MS/MS) refers to the coupling of two mass spectrometers in time and space with the objective of obtaining further information about the sample in question. Tandem mass spectrometry is based upon the activation of an isolated precursor ion and the analysis of its fragmentation products. In the last decades, a wide range of strategies and tools have been developed in order to improve the activation of ions and therefore the structural elucidation of molecules.^{9,339} The most common ion activation method used in present day instruments remains being CID.^{170,171,340} In a

2. EXPERIMENTAL METHODS

CID experiment, the previously selected and accelerated ions are admitted into the collision cell where they collide with neutral gas targets (typically helium, nitrogen or argon).

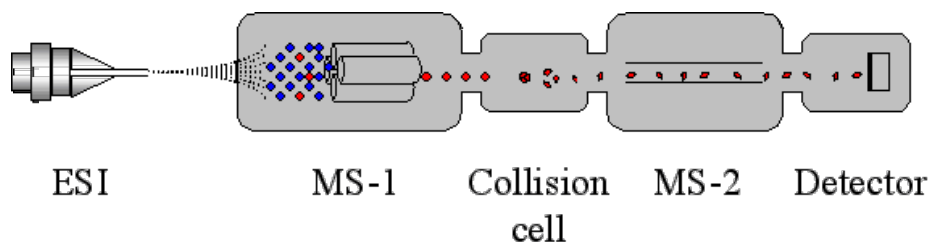
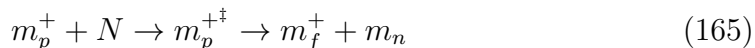


Figure 65: Schematic representation of CID set-up.

When an ion with a high translational energy undergoes an inelastic collision with a neutral, part of the translational energy is converted into internal energy of the ion, leading to subsequent fragmentation.³⁴¹ The overall CID process is assumed to occur by a two-step mechanism, where the excitation of the precursors and their fragmentations are separated in time:



where m_p^+ , N , $m_p^{+\dagger}$, m_f^+ , and m_n represent the masses for the precursor ion, neutral target, excited precursor ion, and charged and neutral fragments, respectively. In the first step a fraction of the ion kinetic energy is transferred into the internal modes of the selected ion. The second part of this mechanism is a unimolecular dissociation of an excited ion, what explains the use of statistical theories such as TST or RRKM to rationalize CID spectra. Fragmentation of the precursor ion can occur if the collision energy is sufficiently high that the ion is excited beyond its dissociation threshold.

The transfer of kinetic energy to internal energy can be represented by the laws of physics involving a mobile species (ion) and a static target (gas). To simplify the description of such a process, it is more useful to work in the center-of-mass, com, framework instead of the laboratory reference frame. In the latter, a binary collision is described by the two separate particles involved with their individual position and velocity vectors. The velocities of the ion and neutral gas are stated as velocities relative to each other. The com kinetic energy of the colliding particles, not the laboratory kinetic energy of the ion, is the important parameter determining the nature of the

2. EXPERIMENTAL METHODS

activation step of the collision process. The total available energy for the transfer of kinetic energy to internal energy is the relative energy (E_{com}) and depends on the collision partners' masses. Eq. (166) relates the center of mass and laboratory collision energies:

$$E_{com} = \frac{N}{m_p + N} E_{lab}; \quad E_{lab} = q \cdot V \quad (166)$$

where E_{lab} is the ion's kinetic energy and q and V are the charge and acceleration voltage of the ion, respectively. The CID process is highly dependent on the relative masses of the two species. Conservation of energy means that if the relative translational energies of the colliding particles change by a certain amount this energy must appear as internal energy. E_{com} represents the maximum amount of energy that can be converted into internal energy of the precursor ion. This energy, as seen in the equation above, increases with the target's mass, allowing more of the ion's kinetic energy to be converted into internal energy. Furthermore, E_{com} decreases as a function of $1/m_p$, so larger precursor ions have less internal energy available for fragmentation through the collision process.³⁴²

All CID processes occurring routinely can be separated into one of two categories based primarily on the translational energy of the precursor ion. For ions of moderate mass (several hundred daltons), *low-energy collisions* occur in the 1–100 eV range of collision energy; and *high-energy collisions* are in the kiloelectronvolt range. Intermediate collision energies (100–1000 eV) do not occur in commonly used tandem mass spectrometers. In the work present in this PhD thesis (Part II) we will be dealing with low-energy collisions.

2.2 Cooks kinetic method

The “kinetic method”, initiated 30 years ago by Cooks and co-workers^{343–348} is one of the most widely used mass spectrometry technique for the determination of thermochemical quantities in the gas-phase.⁷³ It provides a relatively easy way to determine a variety of thermochemical values. Enthalpy determinations are relatively straightforward.

In the “standard kinetic method”,³⁴⁷ the entropy term is assumed to be zero. The “extended kinetic method”³⁴⁷ developed by Fenselau,^{65,349} Wedemiotis^{66,350,351} and their co-workers employs different instrumental conditions to vary the effective temperature parameter as a thermodynamic tem-

2. EXPERIMENTAL METHODS

perature to extract apparent entropy differences between pairs of cluster ions. Armentrout proposed an improved statistical treatment of extended kinetic method data to obtain enthalpy differences and the apparent entropies with realistic uncertainties.⁶⁷

To determine the deprotonation thermochemistry of a molecule AH, $AH \rightarrow A^- + H^+$, the kinetic method considers the competitive dissociations of a series of proton bound heterodimers $[AHB_i]^-$, where B_i is a set of reference acids with known gas-phase acidity values:

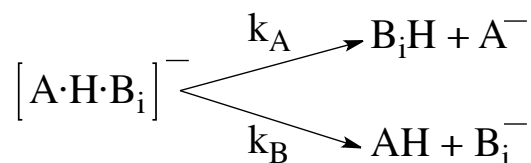


Figure 66: Collision induced dissociations of $[A\cdot H\cdot B_i]^-$.

$[AHB_i]^-$ adduct ions can be produced by means of chemical ionization or an electrospray ion source and their dissociations (spontaneous or induced by collision) are analyzed after selection of the adduct ion by the first mass analyzer.

The method generally supposes that the peak intensities $[A]^-$ and $[B_i]^-$ reflect the corresponding rate constants as shown in eq. (167). Implicit in this expression and the followings is the assumption that there is no reverse activation barrier to either dissociation process.

$$\frac{[A]^-}{[B_i]^-} = \frac{k_A}{k_{B_i}} \quad (167)$$

According to the absolute rate theory, the canonical rate constant k associated with a population of species in thermal equilibrium at a given temperature T is given by eq. (168)

$$k = \left(\frac{k_B T}{h} \right) \exp \left(\frac{-\Delta G}{RT} \right) \quad (168)$$

where k_B is the Boltzmann constant, h the Planck constant, R the gas constant and ΔG is the activation energy of the considered reaction. Then, according to eq. (168), the natural logarithm of the peaks ratio may be

2. EXPERIMENTAL METHODS

expressed by eq. (169)

$$\ln \left(\frac{k_A}{k_{B_i}} \right) = \frac{\Delta G}{RT} \quad (169)$$

where ΔG is the free energy of the equilibrium reaction, $A^- + HB_i \leftrightarrow AH + B_i^-$. The free energy of reaction is then related to enthalpy by the standard thermodynamic expression

$$\Delta G = \Delta(\Delta H) - T\Delta S = \Delta H(AH) - \Delta H(B_iH) - T\Delta S \quad (170)$$

where ΔS is the entropy change for the equilibrium reaction. At this point, it should be emphasized that, since the system cannot be considered at thermal equilibrium, the temperature T is an “effective temperature”, T_{eff} . The effective temperature parameter is an empirical parameter, which is closely related to the internal energy of ions actually dissociating in the mass spectrometer.^{352,353} However it is not directly related to the mean internal energy of the whole ion population, nor is it necessarily an approximation of the “real” temperature.

What Fenselau and Wesdemiotis realized is that by acquiring $\ln(k_A/K_{B_i})$ data at several values of T_{eff} , they could independently determine $\Delta(\Delta H)$ and ΔS . T_{eff} can be varied in several ways: by using collision induced dissociation (CID) and varying the kinetic energy or by changing the collision gas (thereby, changing the laboratory to center of mass energy conversion).

To determine entropic effects, the procedure of Fenselau and Wesdemiotis first combines eq. (169) and eq. (170) to give eq. (171).

$$\ln \left(\frac{k_A}{k_{B_i}} \right) = \left[\frac{\Delta H(AH)}{RT_{eff}} - \frac{\Delta S}{R} \right] - \frac{\Delta H(B_iH)}{RT_{eff}} \quad (171)$$

By plotting $\ln(k_A)/k_{B_i}$ vs. the known deprotonation enthalpies, $\Delta H(B_iH)$, one can extract a slope (m_1) of $-1/RT_{eff}$ and an intercept (y_{01}) given by eq. (172).

$$\frac{DG^{app}(AH)}{RT_{eff}} = \frac{\Delta H(AH)}{RT_{eff}} - \frac{\Delta S}{R} \quad (172)$$

where Wesdemiotis introduces the “apparent” free energy of deprotonation (eq. (173))

$$DG^{app}(AH) = \Delta H(AH) - T_{eff}\Delta S \quad (173)$$

2. EXPERIMENTAL METHODS

The term “apparent” refers to the fact that the ΔS term contains the difference in entropies of dissociation for AH and B_iH , rather than being just the entropy of dissociation of AH. It is useful to note that $DG^{app}(AH)$ is the x intercept of the $\ln(k_A/k_{B_i})$ vs. $\Delta H(B_iH)$ plot.

In a next step, the desired quantities $\Delta H(AH)$ and ΔS are determined by plotting $DG^{app}(AH)/RT_{eff}$ (the intercept y_{01}) vs. $1/RT_{eff}$, (the negative of the slope m_1). Eq. (172) shows that the slope of this second plot (m_2) equals $\Delta H(AH)$ and the intercept (y_{02}) equals $-\Delta S/R$.

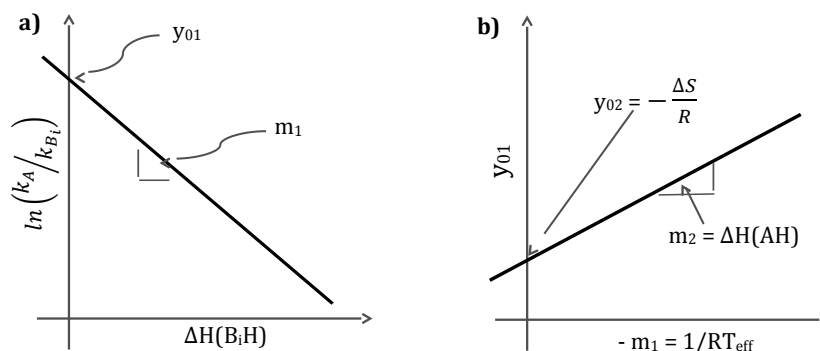


Figure 67: EKM plots for a) $\ln(k_A/k_{B_i})$ vs. $\Delta H(B_iH)$ and b) the intercept y_{01} vs. the slope m_1 both obtained from plot a).

In 2000, Armentrout⁶⁷ pointed out a conceptual error in the previously explained statistical analysis performed to determine $\Delta H(AH)$ and ΔS and proposed “statistically significant ways of handling the same data to acquire the same information”. The problem with the plot in the right side of Fig. 67 is that in the linear regression analysis of this figure, the slope and the intercept used to describe the best fit of the available data are strongly correlated. Therefore, small changes in the slope of the data result in large changes in the y intercept, mirrored in very large uncertainties in the y intercept.

To rigorously remove the correlation between the slope and intercept of a linear regression analysis, one merely needs to plot y vs. $x'_i = x_i - x_{avg}$ where x_{avg} is the average deprotonation enthalpy of the reference acids, B_iH . The slope of such a plot is identical to that obtained from plotting $\ln(k_A/K_{B_i})$ vs. $\Delta H(B_iH)$, but now the y intercept (y'_{01}) is an interpolated point (and hence much more accurate and precise), rather than being extrapolated. It can be verified that the covariance between y'_{01} and m is zero, *i.e.*, the y intercept

2. EXPERIMENTAL METHODS

and slope of this plot are uncorrelated.

For kinetic method data, the slope of this plot (m_1) is again $-1/RT_{eff}$ and the y intercept is given by the expression (174)

$$y'_{01} = \frac{[DG^{app}(AH) - \Delta H_{avg}]}{RT_{eff}} = \frac{\Delta H(AH) - \Delta H_{avg}}{RT_{eff}} - \frac{\Delta S}{R} \quad (174)$$

Now a plot of the intercept (y'_{01}) *vs.* the negative slope ($-m_1 = 1/RT_{eff}$) will give a slope (m'_2) of $\Delta H(AH) - \Delta H_{avg}$ and a y intercept (y_{02}) of $-\Delta S/R$.

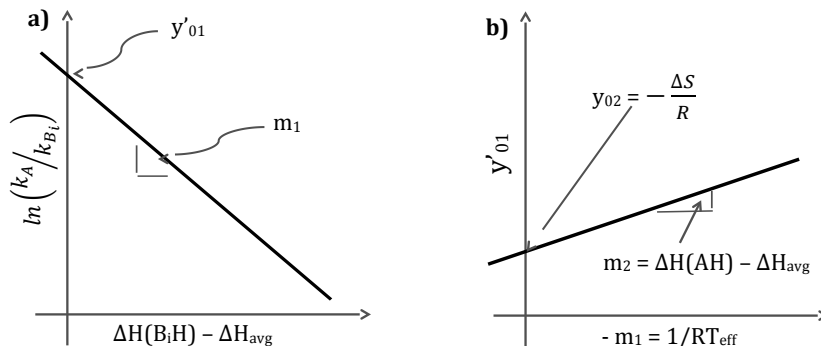


Figure 68: EKM plots for a) $\ln(k_A/k_{B_i})$ *vs.* $\Delta H(B_iH) - \Delta H_{avg}$ and b) the intercept y'_{01} *vs.* the slope m_1 both obtained from plot a).

In spite of much controversy about using the kinetic method to evaluate entropy differences, now it seems widely accepted that the kinetic method can be used to determine enthalpy and entropy differences.⁷²

For the experimental acidity values presented here, eighteen compounds with known gas-phase acidities ranging from 1343.5 to 1463.1 kJ mol⁻¹ were chosen as the reference acids, B_iH . The ionization technique used to produce the $[AHB_i]^-$ adduct ions was electrospray ionization. The dissociation of the adduct ions after selection by the first mass analyzer was induced by collision with Ar at a nominal pressure of 0.2 mTorr to maintain single collision conditions. The CID experiments were performed using 6 to 13 different center-of-mass collision energies varying from 0.75 to 3.0 eV.

List of Figures

1	Schematic representation of the gas-phase acidity enhancement upon Lewis adduct formation.	7
2	The classical reaction coordinate diagram to explain product selectivity (P1, P2) based on relative heights of the transitions states (TS1, TS2) associated to the competing reaction pathways. Taken from ref. ¹³	7
3	Linear correlation between the B3LYP and G4 calculated acidities for amine-boranes.	13
4	Structure for the most stable anion (B acids) of PhCH ₂ NH ₂ ·BH ₃ (left) and CF ₃ CH ₂ NH ₂ ·BH ₃ (right).	14
5	Energy profile of the NH ₂ and BH ₃ deprotonation processes of benzylamine·BH ₃ . All values in kJ mol ⁻¹	15
6	Molecular electrostatic potential of PhCH ₂ NH ₂ ·BH ₃ (left) and CF ₃ CH ₂ NH ₂ ·BH ₃ (right). Blue areas correspond to positive values of the potential, whereas red areas correspond to negative values of the potential.	16
7	Thermodynamic cycle relating the intrinsic acidities of the isolated Lewis bases, RXH ₂ , X = N, P, ($\Delta_r G_3^0$) and the corresponding Lewis adducts, RXH ₂ ·Y, Y = BH ₃ , AlH ₃ , GaH ₃ , ($\Delta_r G_4^0$) with the stabilization undergone by the neutral ($\Delta_r G_1^0$) and deprotonated ($\Delta_r G_2^0$) forms of the base upon complexation.	21
8	ELF (0.80) for the NH ₃ ·BH ₃ and C ₆ H ₅ NH ₂ ·BH ₃ complexes and their corresponding nitrogen-deprotonated species. Green lobes denote disynaptic basins involving two heavy atoms. Orange lobes are disynaptic basins in which H is one of the atoms involved. Red lobes correspond to the lone pairs. The populations shown are e ⁻	24

LIST OF FIGURES

9	ELF (0.80) for the $\text{XH}_3\cdot\text{Y}$ ($\text{X} = \text{N}, \text{P}$; $\text{Y} = \text{BH}_3, \text{AlH}_3$ and GaH_3) complexes and their corresponding X-deprotonated ($\text{X} = \text{N}, \text{P} =$ species. Green lobes denote disynaptic basins involving two heavy atoms. Yellow lobes are disynaptic basins in which H is one of the atoms involved. Red lobes correspond to the lone pairs. The populations shown are e^-	25
10	C–X ($\text{X} = \text{N}, \text{P}$) bond characteristics for Ph-XH_2 and their deprotonated counterparts.	27
11	Natural charges for $\text{NH}_3\cdot\text{BH}_3$, $\text{PH}_3\cdot\text{BH}_3$, $\text{NH}_3\cdot\text{AlH}_3$ and $\text{PH}_3\cdot\text{AlH}_3$ Lewis adducts. Red is for the most negative atoms and green for the most positive ones. Black is a charge equal or close to zero.	28
12	Structures for $\text{H}_3\text{C-CH}_2\text{XH}_2$, $\text{H}_2\text{C=CHXH}_2$, and $\text{H}_2\text{C}\equiv\text{CHXH}_2$ ($\text{X} = \text{N}, \text{P}, \text{As}, \text{Sb}$) Lewis bases considered in this section. . .	32
13	Calculated acidity ($\Delta_{\text{acid}}G^0$, kJ mol^{-1}) for R-XH_2 ($\text{R} = \text{Ethyl}$, vinyl, ethynyl; $\text{X} = \text{N}, \text{P}, \text{As}, \text{Sb}$) bases (solid lines) and the corresponding $\text{R-XH}_2\cdot\text{BeH}_2$, $\text{R-XH}_2\cdot\text{BH}_3$, and $\text{R-XH}_2\cdot\text{AlH}_3$ complexes (dashed lines).	33
14	Thermodynamic cycle relating the intrinsic acidities of the isolated Lewis bases and the corresponding Lewis adducts with the stabilization undergone by the neutral and deprotonated forms of the base upon complexation.	34
15	Stabilization free energies of neutral, $\Delta_r G_1^0$, (solid lines) and deprotonated species, $\Delta_r G_2^0$, (dashed lines) when R-XH_2 ($\text{R} = \text{Ethyl}$, vinyl, ethynyl; $\text{X} = \text{N}, \text{P}, \text{As}, \text{Sb}$) bases interact with BeH_2 , BH_3 , and AlH_3 . The acidity enhancement, $\Delta\Delta_{\text{acid}}G^0$ corresponds to the gap between the solid and dashed line curves for the same Lewis acid. All values are in kJ mol^{-1} . . .	35
16	Molecular graphs of the BH_3 , AlH_3 and BeH_2 complexes with vinylamine and their corresponding anionic deprotonated species. Green dots denote BCPs. Electron densities are in a.u.	36
17	G4 relative stabilities (kJ mol^{-1}) for the more stable conformations of complexes of BeH_2 with vinyl- and ethynyl phosphine and arsine, showing that for ethynyl the π -type complex is the more stable.	37
18	Resonant structures for the anionic forms of the vinyl complexes.	38
19	Representative structures for the heteroatom anion, $[\text{R-XH-YH}_3]^-$, (left) and the “insertion” anion, $[\text{R-YH}_2\text{-XH}_2]^-$ (right).	41

LIST OF FIGURES

20	Mechanism to form the insertion-complex D starting from the π -complex B . Note the high barrier necessary to overcome in this process (225 kJ mol ⁻¹). Deprotonation of the <i>insertion-complex</i> leads to formation of the most stable anion, [R-YH ₂ -XH ₂] ⁻ , insertion-anion.	42
21	Two examples of the electron distribution within the vinylamine and vinylphosphine molecules upon BH ₃ complexation.	46
22	Variation of the BH ₃ dihedral angle upon complex formation.	47
23	BH ₃ LUMO energies within the complex geometry.	47
24	BH ₃ LUMO energies within the complex geometry and Gibbs free energies for complex formation. Ethyl derivatives.	49
25	Hydrogen abstraction from trialkylamine-boranes by <i>t</i> -butoxylradicals.	50
26	Formation of <i>N,N</i> -dimethylaminyl-borane, a nitrogen centered radical.	50
27	Top: low-energy CID spectrum of the formamide-Ca ²⁺ complex recorded with a collision energy of 11eV (laboratory frame). Bottom: low-energy CID spectrum of formamide- ⁸⁷ Sr ²⁺ recorded at a collision energy of 14eV (laboratory frame).	53
28	Top: formamide-Ca ²⁺ energy profile of the different reaction mechanism with origin in the global minimum 1 and (bottom) local minimum 2 . All values in kcal mol ⁻¹	54
29	Top: formamide- ⁸⁷ Sr ²⁺ energy profile of the different reaction mechanisms with origin in the global minimum 1 and (bottom) local minimum 2 (bottom). All vales in kcal mol ⁻¹	55
30	Schematic representation of the limiting fragmentation mechanisms used to explain CID reactivity: direct fragmentation <i>vs.</i> RRKM. Dynamical mechanisms happening before IVR can take place or statistical mechanisms after IVR.	56
31	Relative error (%) derivations for rotational constants of (left) formamide-Ca ²⁺ computed at B3LYP/6-31G(d) (blue circles), G96LYP/6-31G(d) (red triangles), MP2/6-31G(d) (green crosses), and BLYP/6-31G(d) (purple squares) and (right) formamide-Sr ²⁺ computed at B3LYP/6-31G(d) (blue circles), G96LYP/6-31G(d) (red triangles), MP2/6-31G(d) (green crosses), and G96LYP/6-31+G(d,p) (purple squares).	62

LIST OF FIGURES

32	(a) Int8 structure for M = Ca optimized with (i) B3LYP/cc-pWCVTZ, (ii) BLYP/6-31G(d) and for M = Sr optimized with (iii) G96LYP/6-31+G(d,p), (iv) B3LYP/6-31G(d), (v) G96LYP/6-31G(d) and (vi) MP2/6-31G(d). (b) TS_1_G structure for M = Ca optimized with (i) B3LYP/-ccpWCVTZ, (ii) BLYP/6-31G(d) and for M = Sr optimized with (iii) G96LYP/6-31+G(d,p), (iv) B3LYP/6-31G(d) and (v) MP2/6-31G(d).	63
33	Relative errors in (a) formamide-Ca ²⁺ relative energies computed with B3LYP/6-31G(d) (blue circles), G96LYP/6-31G(d) (red triangles), MP2/6-31G(d) (green crosses), and BLYP/6-31G(d) (purple squares) and (b) formamide-Sr ²⁺ relative energies with B3LYP/6-31G(d) (blue circles), G96LYP/6-31G(d) (red triangles), MP2/6-31G(d) (green crosses), and G96LYP/6-31+G(d,p) (purple squares).	64
34	Mechanistic model for the kinetic study employed in this work. The corresponding one for M = Sr is not shown since is practically the same. Solid black lines denote neutral loss reactions while the red dashed lines correspond to Coulomb explosions.	66
35	Graphical example showing the x -axis shift performed in the $t_{1/2}(E)$ curves in order to compare the different methods tested.	67
36	Relative errors in (a) formamide-Ca ²⁺ relative energies computed with B3LYP/6-31G(d) (blue triangles), G96LYP/6-31G(d) (red squares), MP2/6-31G(d) (green diamonds), and BLYP/6-31G(d) (purple circles) and (b) formamide-Sr ²⁺ relative energies with B3LYP/6-31G(d) (blue triangles), G96LYP/6-31G(d) (red squares), MP2/6-31G(d) (green diamonds), and G96LYP/6-31+G(d,p) (purple circles).	67
37	Reactions that can take place starting from min1 structure.	68
38	Half-life reaction time ($t_{1/2}$) as a function of internal energy for the corresponding RRKM rate constants describing the reaction pathways starting from min1. The top panels are for the formamide-Ca ²⁺ system at (a) B3LYP/cc-pWCVTZ and (b) G96LYP/6-31G(d). The bottom panels show formamide-Sr ²⁺ using (c) G96LYP/6-311+G(3df,2p) and (d) G96LYP/6-31+G(d). Solid lines correspond to forward reactions while dashed lines stand for the backward reactions.	69
39	Top: Global energy minimum (min1) of [M(formamide)] ²⁺ (M = Ca, Sr). This structure is used to select the initial conditions for the dynamics simulations. Bottom: Schematic representation of how the CID molecular dynamics is generally set-up	71

LIST OF FIGURES

40	Percentages of trajectories for each channel as a function of the collision energy. Non-reactive trajectories (blue); product M^{2+} + formamide (black). For details on products observed in less than 2% see Table 12. The simulations were performed at two levels of theory: for $M = \text{Ca}$ (left) G96LYP/6-31G(d) (solid lines) and BLYP/6-31G(d) (dashed lines). For $M = \text{Sr}$ (right) G96LYP/6-31G(d) (solid lines) and G96LYP/6-31+G(d,p) (dashed lines).	72
41	Masses observed in the experimental CID spectrum of formamide- M^{2+} together with their molecular formulas. $M = \text{Ca}$ (left), $M = \text{Sr}$ (right). In black are neutral losses and in red Coulomb explosions. Data taken from ref. ¹⁷² and ¹⁷³ respectively.	74
42	Different possibilities for the collision between Ar and the molecular ion providing subsequent dissociation, observed in our chemical dynamics simulations.	76
43	Evolution with time of natural charge (top panel) and distances (bottom panel) for a trajectory yielding G : $[\text{Ca}(\text{NH}_2)]^+ + \text{HCO}^+$ Coulomb explosion (left) and B : $[\text{Ca}(\text{NH}_3)]^{2+} + \text{CO}$ neutral loss (right).	77
44	Simulation times (fs) for the reactive trajectories at the different collision energies: 180, 230 and 280 kJ mol^{-1} . Each point represents one trajectory. Squares are for $M = \text{Ca}$ and stars for $M = \text{Sr}$	78
45	Reaction time <i>vs.</i> energy transfer obtained from chemical dynamics simulations (squares) and half-life times ($t_{1/2}$) predicted by RRKM (solid lines). Both were obtained using G96LYP/6-31G(d) level of theory. Results are shown for trajectories yielding formamide neutral loss (left) and G Coulomb explosion (right). $M = \text{Ca}$	79
46	Vibrational (a panels) and rotational (b panels) energy distribution for the non-reactive trajectories at the three collision energies: 180, 230 and 280 kcal mol^{-1} from left to right. The three upper graphs correspond to $M = \text{Ca}$ while the three bottom ones are for $M = \text{Sr}$. Dashed vertical lines mark the energy for the different TS that can be reached from min1 structure. All the values are computed at the G96LYP/6-31G(d) level of theory.	80

LIST OF FIGURES

47	a) Kinetic scheme for the reactions that can take place starting from min 1 for both $[\text{Ca}(\text{formamide})]^{2+}$ and $[\text{Sr}(\text{formamide})]^{2+}$. m/z ratios within parentheses are for $M = \text{Sr}$. In the bottom, RRKM rate constants corresponding to the aforementioned kinetic scheme (black lines). Rate constants taking into account rotational energy (27 and 18 kcal mol ⁻¹ for Ca and Sr, respectively) are also shown (green curves) when relevant (see text). Vertical dashed blue lines mark the selected upper value for the ions internal energy.	82
48	Upper part: kinetic scheme for the reactions that can take place starting from int 2 . Bottom part: corresponding rate constants as a function of the internal energy for (b) $M = \text{Ca}$ and (c) $M = \text{Sr}$. Dashed lines correspond to backward reactions.	85
49	(a) Kinetic scheme for possible reactions starting from int 10 , (b) corresponding RRKM rate constants. Dashed lines correspond to backward reactions.	86
50	Different TSs that can be reached from the global minimum, min 1 (this is the structure found at the end of the non-reactive trajectories), and the final product structures. The numbers below the structures are the activation barriers and product energies relative to min 1 in kcal mol ⁻¹	89
51	Different possibilities of initially placing the excitation energy on the transition state structure. Left, the energy is distributed within the internal degrees of freedom. Right, the energy activates the external rotation.	90
52	Potential energy surface proposed by Eizaguirre <i>et al.</i> , ¹⁷³ top and PES obtained from trajectories started at TS_1_2, bottom. All the energies are in kcal mol ⁻¹	91
53	Product distribution for trajectories starting from TS_1_2 structure (a) adding energy to external rotation. (b) Comparison of the results obtained when 35 kcal mol ⁻¹ are initially added to the external rotation (left) or to the internal modes (right).	92
54	Potential energy surface obtained from trajectories started at the TS_1_G. The dashed pathway leading to B does not appear in the initially proposed PES. ¹⁷³ All the energies are in kcal mol ⁻¹	94
55	Product distribution for trajectories starting from TS_1_G structure (a) adding energy to external rotation. (b) Comparison of the results obtained when 35 kcal mol ⁻¹ are initially added to the external rotation (left) or to the internal modes (right).	94

LIST OF FIGURES

56	Schematic representation of the mixing between s and p orbitals	110
57	Illustration of phase space for a pendulum.	144
58	Reaction coordinate with a saddle point. Above it is a diagram of the phase space which varies with the reaction coordinate and with the total energy. Figure taken from ref. ¹⁷⁸	146
59	The reaction coordinate and the partitioning of the energy in the transition state ($E - E_0$) between the translational energy, ϵ_t , and the vibrational energy of the modes normal to the reaction coordinate. Figure taken from ref. ¹⁷⁸	149
60	Zero energy reference to compute $k(E)$	150
61	On the left side the sum of states <i>vs.</i> the reaction coordinate for formamide- Ca^{2+} at different internal energies (all in kcal mol^{-1}). The crosses mark the minimum of the sum of states for each energy. On the right side the microcanonical rate constant k is represented <i>vs.</i> the internal energy. The crosses mark the $k(E)$ values corresponding to the minimum sum of states for specific internal energies. In the middle the formamide- Ca^{2+} geometries are represented for each of the points with the values (in Å) for Ca-O distance.	152
62	Prolate symmetric top molecule represented as a cylinder. The rotational motion due to J and K are indicated. Figure taken from ref. ¹⁷⁸	153
63	An actual phase-space trajectory (bold curve) and an approximate trajectory generated by repeated application of eq. (156) (series of arrows representing individual time steps). In the illustration, the approximate trajectory hews relatively closely to the actual one, but this will not be the case if too large a time step is used. Taken from ref. ³²³	159
64	QCISD(T)/6-31++G(d,p) <i>ab initio</i> (diamonds) and fitted (solid line) potential energy curves for the Ar- Sr^{2+} interaction.	163
65	Schematic representation of CID set-up.	165
66	Collision induced dissociations of $[\text{A}\cdot\text{H}\cdot\text{B}_i]^-$	167
67	EKM plots for a) $\ln(k_A/k_{B_i})$ <i>vs.</i> $\Delta H(B_iH)$ and b) the intercept y_{01} <i>vs.</i> the slope m_1 both obtained from plot a).	169
68	EKM plots for a) $\ln(k_A/k_{B_i})$ <i>vs.</i> $\Delta H(B_iH) - \Delta H_{avg}$ and b) the intercept y'_{01} <i>vs.</i> the slope m_1 both obtained from plot a).	170
69	BH_3 LUMO energies within the complex geometry and Gibbs free energies for complex formation. Vinyl derivatives.	209
70	BH_3 LUMO energies within the complex geometry and Gibbs free energies for complex formation. Ethynyl derivatives.	209

LIST OF FIGURES

71	Reaction time <i>vs.</i> energy transfer for trajectories yielding formamide neutral loss, obtained from chemical dynamics simulations (squares) and half-life times ($t_{1/2}$) predicted by RRKM (solid lines). Both were obtained using BLYP/6-31G(d) level of theory.	221
72	Reaction time <i>vs.</i> energy transfer obtained from chemical dynamics simulations (squares) and half-life times ($t_{1/2}$) predicted by RRKM (solid lines). Both are for trajectories yielding formamide neutral loss using G96LYP/6-31G(d) in the left and G96LYP/6-31+G(d,p) in the right.	221
73	Probability of transferring a given % of the collision energy to the $[M(\text{formamide})]^{2+}$ ion for the non-reactive trajectories (white) and the reactive ones (blue), at the three collision energies considered (180, 230, and 280 kcal mol ⁻¹ from left to right). G96LYP/6-31G(d) is used for the two molecular ions. .	222
74	Probability of transferring a given % of the collision energy to the $[M(\text{formamide})]^{2+}$ ion for the non-reactive trajectories (white) and the reactive ones (blue), at the three collision energies considered (180, 230, and 280 kcal mol ⁻¹ from left to right). The trajectories were calculated using BLYP/6-31G(d) for M = Ca and G96LYP/6-31+G(d,p) for M = Sr.	222
75	Scattering plot of vibrational versus rotational energy distributions obtained from nonreactive $[M(\text{formamide})]^{2+}$ trajectories for the three collision energies considered. The level of theory used for both metals is: G96LYP/6-31G(d).	223
76	Scattering plot of vibrational versus rotational energy distributions obtained from nonreactive $[M(\text{formamide})]^{2+}$ trajectories for the three collision energies considered. The trajectories were calculated using BLYP/6-31G(d) for M = Ca and G96LYP/6-31+G(d,p) for M = Sr.	223
77	Vibrational (a panels) and rotational (b panels) energy distribution for the non-reactive trajectories at the three collision energies: 180, 230 and 280 kcal mol ⁻¹ from left to right. The top panels correspond to M = Ca while the bottom ones are for M = Sr. The dashed vertical lines mark the energy for the different TS that can be reached from min1 structure. The values for M = Ca are compute using the BLYP/6-31G(d) approach while the values for M = Sr are computed at the G96LYP/6-31+G(d,p) level of theory.	224

LIST OF FIGURES

- 78 RRKM rate constants for $M = \text{Ca}$ taking into account rotational energy in different ways (see text). The $k(E, J)$ showed are computed at the B3LYP/cc-pWCVTZ level of theory. . . . 226
- 79 RRKM rate constants for $M = \text{Sr}$ taking into account rotational energy in different ways (see text). The $k(E, J)$ showed are computed at the G96LYP/6-311+G(3df,2p) level of theory. 227

Bibliography

- [1] P. B. Armentrout, L. F. Halle, and J. L. Beauchamp. *J. Am. Chem. Soc.*, 103(21):6501–6502, 1981.
- [2] P. B. Armentrout and B. L. Kickel. *Organometallic Ion Chemistry*. Kluwer Academic Publisher, Dordrecht, 1996.
- [3] C. W. Bauschlicher Jr., S. R. Langhoff, and H. Partridge. *Organometallic Ion Chemistry*. Kluwer Academic Publisher, Dordrecht, 1996.
- [4] P. B. Armentrout and R. Georgiadis. *Polyhedron*, 7(16–17):1573 – 1581, 1988.
- [5] R. Tonkyn and J. C. Weisshaar. *J. Phys. Chem.*, 90(11):2305–2308, 1986.
- [6] K. Eller and H. Schwarz. *Chem. Rev.*, 91(6):1121–1177, 1991.
- [7] J. M. Farrar and W. H. Saunders Jr., editors. *Techniques for the Study of Ion-Molecule Reactions*. John Wiley & Sons, New York, 1988.
- [8] J. Laskin and J. H. Futrell. *Mass Spectrom. Rev.*, 22(3):158–181, 2003.
- [9] L. Sleno and D. A. Volmer. *J. Mass Spectrom.*, 39(10):1091–1112, 2004.
- [10] P. M. Mayer and C. Poon. *Mass Spectrom. Rev.*, 28(4):608–639, 2009.
- [11] M. T. Bowers, editor. *Gas Phase Ion Chemistry*, volume 1,2,3. Academic Press, New York, 1984.
- [12] J. B. Fenn. *Angew. Chem. Int. Ed.*, 42(33):3871–3894, 2003.
- [13] J. Rehbein and B. K. Carpenter. *Phys. Chem. Chem. Phys.*, 13:20906–20922, 2011.
- [14] K. J. Laidler and M. C. King. *J. Phys. Chem.*, 87(15):2657–2664, 1983.

BIBLIOGRAPHY

- [15] R. A. Marcus and O. K. Rice. *J. Phys. Colloid Chem.*, 55:894, 1951.
- [16] P. Hobza, R. Zahradnik, and K. Muller-Dethlefs. *Czech. Chem. Commun.*, 71(4):443–531, 2006.
- [17] P. Hobza and K. Müller-Dethlefs. *Non-covalent Interactions: Theory and Experiment*. RSC, London, 2009.
- [18] G. R. Whittell, M. D. Hager, U. S. Schubert, and I. Manners. *Nat. Mater.*, 10:176–188, 2011.
- [19] J. V. Yakhmi. *J. Mater. Educ.*, 33:149–160, 2011.
- [20] E. Espinosa, I. Alkorta, J. Elguero, and E. Molins. *J. Chem. Phys.*, 117(12):5529–5542, 2002.
- [21] G. C. Pimentel and A. L. McClelland. *The Hydrogen Bond*. Freeman, W. H. and Co., San Francisco, CA, 1960.
- [22] P. A. Kollman and L. C. Allen. *Chem. Rev.*, 88:899–926, 1988.
- [23] A. E. Reed, L. A. Curtiss, and F. Weinhold. *Chem. Rev.*, 72:283, 1972.
- [24] L. A. Curtiss and M. Blander. *Chem. Rev.*, 88:827–841, 1988.
- [25] I. Alkorta, I. Rozas, and J. Elguero. *Chem. Soc. Rev.*, 27:163–170, 1998.
- [26] M. Meot-Ner. *Chem. Rev.*, 105:213–284, 2005.
- [27] S. J. Grabowski, editor. *Hydrogen Bonding. New Insights*. Springer, Heidelberg, Germany, 2006.
- [28] S. J. Grabowski. *Chem. Rev.*, 111:2597–2625, 2011.
- [29] S. A. Cooke, G. Cotti, C. M. Evans, J. H. Holloway, Z. Kisiel, A. C. Legon, and J. M. A. Thumwood. *Chem. —Eur. J.*, 7:2295–2305, 2001.
- [30] A. Karpfen. *Theor. Chem. Acc.*, 110:1–9, 2003.
- [31] W. T. Pennington, T. W. Hanks, and H. D. Arman. *Halogen Bonding: Fundamentals and Applications*, volume 126. Springer-Verlag, Berlin, Germany, 2008.
- [32] I. Alkorta, F. Blanco, and J. Elguero. *Struct. Chem.*, 20:63–71, 2009.

BIBLIOGRAPHY

- [33] M. Yáñez, P. Sanz, O. Mó, I. Alkorta, and J. Elguero. *J. Chem. Theory Comput.*, 5:2763–2771, 2009.
- [34] A. T. Blades, P. Jayaweera, M. G. Ikononou, and P. Keberle. *Int. J. Mass Spectrom. Ion Processes*, 102:251–267, 1990.
- [35] M. Alcamí, O. Mó, M. Yáñez, F. Anvia, and R. W. Taft. *J. Phys. Chem.*, 94:4796–4804, 1990.
- [36] B. A. Cerda and C. Wesdemiotis. *J. Am. Chem. Soc.*, 118:11884–11892, 1996.
- [37] J. V. Burda, J. Sponer, and P. Hobza. *J. Phys. Chem.*, 100:7250–7255, 1996.
- [38] E. Leon, B. Amekraz, J. Tortajada, J.-P. Morizur, A. I. González, O. Mó, and M. Yáñez. *J. Phys. Chem. A*, 101:2489–2495, 1997.
- [39] J. V. Burda, J. Sponer, J. Leszczynski, and P. Hobza. *J. Phys. Chem. B*, 101:9670–9677, 1997.
- [40] A. Luna, B. Amekraz, J. Tortajada, J.-P. Morizur, M. Alcamí, O. Mó, and M. Yáñez. *J. Am. Chem. Soc.*, 120:5411–5426, 1998.
- [41] M. Peschke, A. T. Blades, and P. Kebarle. *J. Am. Chem. Soc.*, 10440–10449:122, 2000.
- [42] O. Mó, M. Yáñez, J.-F. Gal, P.-C. Maria, and M. Decouzon. *Chem. —Eur. J.*, 9:4330–4338, 2003.
- [43] I. Corral, O. Mó, and M. Yáñez. *J. Phys. Chem. A*, 107:1370–1376, 2003.
- [44] I. Corral, O. Mó, M. Yáñez, J.-Y. Salpin, J. Tortajada, and L. Radom. *J. Phys. Chem. A*, 108:10080–10088, 2006.
- [45] I. Corral, O. Mó, and M. Yáñez. *Int. J. Quantum Chem.*, 106:659–663, 2006.
- [46] I. Corral, C. Trujillo, J.-Y. Salpin, and M. Yáñez. *Challenges and Advances in Computational Chemistry and Physics. Vol. 12 Kinetics and Dynamics: From Nano- to Bio-Scale*, volume 12. Springer, London, 2010.
- [47] B. L. Blaney and G. E. Ewing. *Annu. Rev. Phys. Chem.*, 27:553–584, 1976.

BIBLIOGRAPHY

- [48] H. M. Hutson. *Annu. Rev. Phys. Chem.*, 41:123–154, 1990.
- [49] B. Jeziorski, R. Moszynski, and K. Szalewicz. *Chem. Rev.*, 94:1887–1930, 1994.
- [50] G. Chalasinski and M. M. Szczesniak. *Chem. Rev.*, 94:1723–1765, 1994.
- [51] K. Muller-Dethlefs and P. Hobza. *Chem. Rev.*, 100:143–167, 2000.
- [52] M. Hurtado, M. Yáñez, R. Herrero, A. Guerrero, J. Z. Dávalos, J.-L. M. Abboud, B. Khater, and J.-C. Guillemin. *Chem. —Eur. J.*, 15(18):4622–4629, 2009.
- [53] H. H. Ren, D. B. Workman, and R. R. Squires. *J. Am. Chem. Soc.*, 120:10511–10522, 1998.
- [54] J. H. Ren, C. J. Cramer, and R. R. Squires. *J. Am. Chem. Soc.*, 121:2633–2634, 1999.
- [55] A. F. Cotton, G. Wilkinson, C. A. Murillo, and M. Bochmann. *Advanced Inorganic Chemistry*. John Wiley & Sons, New York, sixth edition edition, 1999.
- [56] N. N. Greenwood and A. Earnshaw. *Chemistry of the elements*. Pergamon Press, 1984.
- [57] J. L. Gay-Lussac. *Mem. Phys. Chim. Soc. d’Arcueil*, 2:211, 1809.
- [58] A. B. Burg and H. I. Schlesinger. *J. Am. Chem. Soc.*, 59(5):780–787, 1937.
- [59] A. Staubitz, A. P. M. Robertson, M. E. Sloan, and I. Manners. *Chem. Rev.*, 110(7):4023–4078, 2010.
- [60] A. Staubitz, A. P. M. Robertson, and I. Manners. *Chem. Rev.*, 110(7):4079–4124, 2010.
- [61] G. C. Welch, R. R. S. Juan, J. D. Masuda, and D. W. Stephan. *Science*.
- [62] C. F. Lane. *Aldrichim. Acta*, page 51, 1973.
- [63] P. Kaszynski, S. Pakhomov, M. E. Gurskii, S. Y. Erdyakov, Z. A. Starikova, K. A. Lyssenko, M. Y. Antipin, V. G. Young, and Y. N. Bubnov. *J. Org. Chem.*, 74:1709, 2009.
- [64] B. Carboni and L. Monnier. *Tetrahedron*, 55:1197, 1999.

BIBLIOGRAPHY

- [65] X. Cheng, Z. Wu, and C. Fenselau. *J. Am. Chem. Soc.*, 115(11):4844–4848, 1993.
- [66] B. A. Cerda and C. Wesdemiotis. *J. Am. Chem. Soc.*, 118(47):11884–11892, 1996.
- [67] P. B. Armentrout. *J. Am. Soc. Mass Spectrom.*, 11(5):371 – 379, 2000.
- [68] X. Zheng and R. G. Cooks. *J. Phys. Chem. A*, 106(42):9939–9946, 2002.
- [69] K. M. Ervin. *J. Am. Soc. Mass Spectrom.*, 13(5):435 – 452, 2002.
- [70] L. Drahos and K. Vékey. *J. Mass Spectrom.*, 38(10):1025–1042, 2003.
- [71] K. M. Ervin and P. B. Armentrout. *J. Mass Spectrom.*, 39(9):1004–1015, 2004.
- [72] L. Drahos, C. Peltz, and K. Vékey. *J. Mass Spectrom.*, 39(9):1016–1024, 2004.
- [73] G. Bouchoux. *Mass Spectrom. Rev.*, 26(6):775–835, 2007.
- [74] L. A. Curtiss, P. C. Redfern, and K. Raghavachari. *J. Chem. Phys.*, 126(8):084108, 2007.
- [75] A. D. Becke. *J. Chem. Phys.*, 98:1372–1377, 1993.
- [76] C. Lee, W. Yang, and R. G. Parr. *Phys. Rev. B*, 37:785–789, Jan 1988.
- [77] M. J. Frisch, G. W. Trucks, H. B. Schlegel, G. E. Scuseria, M. A. Robb, J. R. Cheeseman, G. Scalmani, V. Barone, B. Mennucci, G. A. Petersson, H. Nakatsuji, M. Caricato, X. Li, H. P. Hratchian, A. F. Izmaylov, J. Bloino, G. Zheng, J. L. Sonnenberg, M. Hada, M. Ehara, K. Toyota, R. Fukuda, J. Hasegawa, M. Ishida, T. Nakajima, Y. Honda, O. Kitao, H. Nakai, T. Vreven, J. A. Montgomery, Jr., J. E. Peralta, F. Ogliaro, M. Bearpark, J. J. Heyd, E. Brothers, K. N. Kudin, V. N. Staroverov, T. Keith, R. Kobayashi, J. Normand, K. Raghavachari, A. Rendell, J. C. Burant, S. S. Iyengar, J. Tomasi, M. Cossi, N. Rega, J. M. Millam, M. Klene, J. E. Knox, J. B. Cross, V. Bakken, C. Adamo, J. Jaramillo, R. Gomperts, R. E. Stratmann, O. Yazyev, A. J. Austin, R. Cammi, C. Pomelli, J. W. Ochterski, R. L. Martin, K. Morokuma, V. G. Zakrzewski, G. A. Voth, P. Salvador, J. J. Dannenberg, S. Dapprich, A. D. Daniels, O. Farkas, J. B. Foresman, J. V. Ortiz, J. Cioslowski, and D. J. Fox. Gaussian 09 Revision C.01. Gaussian Inc. Wallingford CT 2010.

BIBLIOGRAPHY

- [78] E. D. Glendening, J. Badenhoop, K. A. E. Reed, J. E. Carpenter, J. A. Bohmann, J. A. Morales, and F. Weinhold. Nbo 5g program, 2001. Theoretical Chemistry Institute, University of Wisconsin, Madison.
- [79] K. B. Wiberg. *Tetrahedron*, 24(3):1083 – 1096, 1968.
- [80] R. F. W. Bader. *Atoms in Molecules. A Quantum Theory*. Clarendon Press, Oxford, 1990.
- [81] A. D. Becke and K. E. Edgecombe. *J. Chem. Phys.*, 92(9):5397–5403, 1990.
- [82] B. Silvi and A. Savin. *Nat.*, 371(6499):683–686, 1994.
- [83] T. A. Keith. Aimall (version 11.12.19), 2011. TK Gristmill Software, Overland Park KS, USA.
- [84] S. Noury, X. Krokidis, F. Fuster, and B. Silvi. Topmod package, 1997. Universite Pierre et Marie Curie.
- [85] P.J. Linstrom and W. G. Mallard, editors. *NIST Chemistry Webbook. Standard Reference Database Number 69*. National Institute of Standards and Technology, Gaithersburg MD, 20899, release june 2005 edition, 2012.
- [86] C. Jones, G. A. Koutsantonis, and C. L. Raston.
- [87] C. L. Raston. *J. Organomet. Chem.*, 475(1–2):15 – 24, 1994.
- [88] M. G. Gardiner and C. L. Raston. *Coordin. Chem. Rev.*, 166(0):1 – 34, 1997.
- [89] D. Dou, D. R. Ketchum, E. J. M. Hamilton, P. A. Florian, K. E. Vermillion, P. J. Grandinetti, and S. G. Shore. *Chem. Mater.*, 8(12):2839–2842, 1996.
- [90] P. C. Andrews, M. G. Gardiner, C. L. Raston, and V.-A. Tolhurst. *Inorg. Chim. Acta*, 259(1–2):249 – 255, 1997.
- [91] F. M. Elms, M. G. Gardiner, G. A. Koutsantonis, C. L. Raston, J. L. Atwood, and K. D. Robinson. *J. Organomet. Chem.*, 449(1–2):45 – 52, 1993.
- [92] N. Vinh-Son, S. Swinnen, M. H. Matus, M. T. Nguyen, and D. A. Dixon. *Phys. Chem. Chem. Phys.*, 11:6339–6344, 2009.

BIBLIOGRAPHY

- [93] D. J. Grant and D. A. Dixon. *J. Phys. Chem. A*, 109(44):10138–10147, 2005.
- [94] D. Pugh, P. Marchand, I. P. Parkin, and C. J. Carmalt. *Inorg. Chem.*, 51(11):6385–6395, 2012.
- [95] E. M. Marlett and W. S. Park. *J. Org. Chem.*, 55(9):2968–2969, 1990.
- [96] C. L. Raston, A. F. H. Siu, C. J. Tranter, and D. J. Young. *Tetrahedron Lett.*, 35(32):5915 – 5918, 1994.
- [97] G. A. Koutsantonis, F. C. Iee, and C. L. Raston. *J. Chem. Soc., Chem. Commun.*, pages 1975–1976, 1994.
- [98] R. A. Fischer, J. Behm, T. Priermeier, and W. Scherer. *Angew. Chem.Int. Ed.*, 32(5):746–748, 1993.
- [99] K. Khan, C. L. Raston, J. E. McGrady, B. W. Skelton, and A. H. White. *Organometallics*, 16(15):3252–3254, 1997.
- [100] Ghenwa Bouhadir, Abderrahmane Amgoune, and Didier Bourissou. Chapter 1 - phosphine-boranes and related ambiphilic compounds: Synthesis, structure, and coordination to transition metals. volume 58 of *Advances in Organometallic Chemistry*, pages 1 – 107. Academic Press, 2010.
- [101] K. M. Ervin and W. C. Lineberger. *J. Chem. Phys.*, 122(19):194303, 2005.
- [102] C. Loschen, K. Voigt, J. Frunzke, A. Diefenbach, M. Diedenhofen, and G. Frenking. *Z. Anorg. Allg. Chem.*, 628(6):1294–1304, 2002.
- [103] M. Czerw, A. S. Goldman, and K. Krogh-Jespersen. Addition of ammonia to AlH_3 and BH_3 . why does only aluminum form 2:1 adducts? *Inorg. Chem.*, 39(2):363–369, 2000.
- [104] M. Yáñez, O. Mó, I. Alkorta, and J. Elguero. *Chem. —Eur. J.*, 19(35):11637–11643, 2013.
- [105] T. M. McCleskey and B. L. Scott. *J. Occup. Environ. Hyg.*, 6(12):751–757, 2009. PMID: 19894176.
- [106] Beryllium. In J. P. Hammel and G. G. Hawley, editors, *The Encyclopedia of Chemistry*. Renihold, New York, 1973.

BIBLIOGRAPHY

- [107] T. P. Taylor, M. Ding, D. S. Ehler, T. M. Foreman, J. P. Kaszuba, and N. N. Sauer. *J. Environ. Sci. Heal. A*, 38(2):439–469, 2003.
- [108] P. G. Greenfield. *Engineering Applications of Beryllium*. Mills and Boon Ltd., London, 1971.
- [109] M. D. Rossman, O. P. Preuss, and M. B. Powers, editors. *Beryllium, Biomedical and Environmental Aspects*. Williams and Wilkins, Baltimore, MD, 1991.
- [110] D. McFarlan, editor. *The Guinness Book of Records 1992*. Guinness Publishing, London, 1991.
- [111] L. Parmeggiani, editor. *Encyclopaedia of Occupational Health and Safety*, volume I. International Labour Office, 1983.
- [112] P. Cooper, editor. *Poisoning by Drugs and Chemicals, Plants and Animals*. Alchemist Publications, 3rd edition, 1974.
- [113] D. N. Skilleter. *Chem. Br.*, 26:26, 1990.
- [114] H. Schmidbaur. *Gmelin Handbook of Inorganic Chemistry*. Springer, Berlin, 8th edition, 1987. Preface.
- [115] O. Kumberger and H. Schmidbaur. *CHIUZ*, 27:310, 1993.
- [116] G. L. Finch, T. L. March, and C. H. Hobbs. *Toxicol. Pathol.*, 26:484, 1998.
- [117] O. Mó, M. Yáñez, M. Decouzon, J.-F. Gal, P.-C. Maria, and J.-C. Guillemin. *J. Am. Chem. Soc.*, 121(19):4653–4663, 1999.
- [118] J.-C. Guillemin, M. Decouzon, P.-C. Maria, J.-F. Gal, O. Mó, and M. Yáñez. *J. Phys. Chem. A*, 101(49):9525–9530, 1997.
- [119] J.-C. Guillemin, H. Riague, J.-F. Gal, P.-C. Maria, O. Mó, and M. Yáñez. *Chem. —Eur. J.*, 11(7):2145–2153, 2005.
- [120] D. R. Lide. *CRC Handbook of Chemistry and Physics*. CRC Press, Boca Raton, FL, 69th edition, 2008.
- [121] Y. Markus. *J. Chem. Soc. Farad. Trans. I*, 83:339–343, 1987.
- [122] M. M. Meyer and S. R. Kass. *J. Phys. Chem. A*, 114:4086–4092, 2010.

BIBLIOGRAPHY

- [123] X. B. Wang, J. B. Nicholas, and L. S. Wang. *J. Phys. Chem. A*, 104:504–508, 2000.
- [124] J. A. Plumley and J. D. Evanseck. *J. Phys. Chem. A*, 113:5985, 2009.
- [125] T. Brinck, J. S. Murray, and P. Politzer. *Inorg. Chem.*, 32:2622, 1993.
- [126] F. Bessac and G. Frenking. *Inorg. Chem.*, 42:7990, 2003.
- [127] J. A. Baban, V. P. J. Marti, and B. P. Roberts. *J. Chem. Soc., Perkin Trans. 2*, page 1723, 1985.
- [128] J. A. Baban and B. P. Roberts. *J. Chem. Soc., Chem. Commun.*, page 1224, 1983.
- [129] I. G. Green and B. P. Roberts. *J. Chem. Soc., Perkin Trans. 2*, page 1597, 1986.
- [130] J. A. Baban, V. P. J. Marti, and B. P. Roberts. *J. Chem. Res.*, page 90, 1985.
- [131] C. A. Jaska, K. Temple, A. J. Lough, and I. Manners. *J. Am. Chem. Soc.*, 125:9424–9434, 2003.
- [132] D. Schöder and H. Schwarz. *J. Phys. Chem. A*, 103(37):7385–7394, 1999. and references therein.
- [133] D. N. Heller, J. Yergey, and R. J. Cotter. *Anal. Chem.*, 55(8):1310–1313, 1983.
- [134] J. M. Miller, K. Balasanmugam, J. Nye, G. B. Deacon, and N. C. Thomas. *Inorg. Chem.*, 26(4):560–562, 1987.
- [135] A. R. Katritzky, P. A. Shipkova, R. D. Burton, S. M. Allin, C. H. Watson, and J.R. Eyler. *J. Mass Spectrom.*, 30(11):1581–1587, 1995.
- [136] L. M. Roth and B. S. Freiser. *Mass Spectrom. Rev.*, 10(4):303–328, 1991.
- [137] S. D. Price. *J. Chem. Soc., Faraday Trans.*, 93:2451–2460, 1997.
- [138] E. L. Breig, M. R. Torr, D. G. Torr, W. B. Hanson, J. H. Hoffman, J. C. G. Walker, and A. O. Nier. *J. Geophys. Res.*, 82(7):1008–1012, 1977.

BIBLIOGRAPHY

- [139] G. A. Victor and E. R. Constantinides. *Geophys. Res. Lett.*, 6(6):519–522, 1979.
- [140] C. Simon, K. Lilensten, O. Dutuit, R. Thissen, O. Witasse, C. Alcaraz, and H. Solde-Lose. *Ann. Geophys.*, 23:781–797, 2005.
- [141] R. Thissen, O. Witasse, O. Dutuit, C. S. Wedlund, G. Gronoff, and J. Lilensten. *Phys. Chem. Chem. Phys.*, 13:18264–18287, 2011.
- [142] R. R. Julian and J. L. Beauchamp. *Int. J. Mass Spectrom.*, 227(1):147 – 159, 2003. In honour of Robert C. Dunbar.
- [143] G. O. Arrhenius. *Helv. Chim. Acta*, 86:1569–1586, 2003.
- [144] R. Lathe. *Icarus*, 168:18–22, 2003.
- [145] M. Franchi, J. P. Ferris, and E. Gallori. *Origins Life Evol. Biospheres*, 33:1–16, 2003.
- [146] *Biol. Bull.*
- [147] E. Magnusson. *J. Phys. Chem.*, 98(48):12558–12569, 1994.
- [148] S. Petrie. *J. Phys. Chem. A*, 106(30):7034–7041, 2002.
- [149] G. N. Merrill, S. P. Webb, and D. B. Bivin. *J. Phys. Chem. A*, 107(3):386–396, 2003.
- [150] R. Spezia, G. Tournois, T. Cartailier, J. Tortajada, and Y. Jeanvoine. *J. Phys. Chem. A*, 110(31):9727–9735, 2006. PMID: 16884205.
- [151] M. Belcastro, T. Marino, N. Russo, and M. Toscano. *J. Mass Spectrom.*, 40(3):300–306, 2005.
- [152] I. S. Saminathan, J. Zhao, K. W. M. Siu, and A. C. Hopkinson. *Phys. Chem. Chem. Phys.*, 13:18307–18314, 2011.
- [153] S. Guillaumont, J. Tortajada, J.-Y. Salpin, and M Lamsabhi. *Int. J. Mass Spectrom.*, 243(3):279 – 293, 2005.
- [154] N. G. Tsierkezos, D. Schroder, and H. Schwarz. *Int. J. Spectrom.*, 235(1):33 – 42, 2004.
- [155] M. Lamsabhi, M. Alcamí, O. Mó, M. Yáñez, J. Tortajada, and J.-Y. Salpin. *ChemPhysChem*, 8(1):181–187, 2007.

BIBLIOGRAPHY

- [156] W. Buchmann, R. Spezia, G. Tournois, T. Cartailier, and J. Tortajada. *J. Mass Spectrom.*, 42(4):517–526, 2007.
- [157] A. Eizaguirre, O. Mó, M. Yáñez, J. Tortajada, and J.-Y. Salpin. *J. Phys. Chem. B*, 117(7):2088–2095, 2013. and references therein.
- [158] I. Corral, O. Mó, M. Yáñez, J.-Y. Salpin, J. Tortajada, and L. Radom. *J. Phys. Chem. A*, 108(46):10080–10088, 2004.
- [159] I. Corral, O. Mó, M. Yáñez, J.-Y. Salpin, J. Tortajada, D. Moran, and L. Radom. *Chem. —Eur. J.*, 12(26):6787–6796, 2006.
- [160] C. Trujillo, O. Mó, M. Yáñez, J.-Y. Salpin, and J. Tortajada. *ChemPhysChem*, 8(9):1330–1337, 2007.
- [161] C. Trujillo, O. Mo, M. Yáñez, J. Tortajada, and J.-Y. Salpin. *J. Phys. Chem. B*, 112(17):5479–5486, 2008.
- [162] C. Trujillo, M. Lamsabhi, O. Mo, M. Yáñez, and J.-Y. Salpin. *Org. Biomol. Chem.*, 6:3695–3702, 2008.
- [163] A. Cimas, J. A. Gámez, O. Mó, M. Yáñez, and J.-Y. Salpin. *Chem. Phys. Lett.*, 456(4–6):156 – 161, 2008.
- [164] I. Corral, C. Trujillo, J.-Y. Salpin, and M. Yáñez. *Kinetics and dynamics: from nano- to bio-scale*, volume 12 of *Challenges and Advances in Computational Chemistry and Physics*. Springer, 2010. Piotr Paneth and Agnieszka Dybala-Defratyka, ed.
- [165] A. M. Palumbo, S. A. Smith, C. L. Kalcic, M. Dantus, P. M. Stemmer, and G. E. Reid. *Mass Spectrom. Rev.*, 30(4):600–625, 2011.
- [166] H. J. An and C. B. Lebrilla. *Mass Spectrom. Rev.*, 30(4):560–578, 2011.
- [167] J. H. Banoub, A. E. Aneed, A. M. Cohen, and N. Joly. *Mass Spectrom. Rev.*, 29(4):606–650, 2010.
- [168] N. C. Polfer and J. Oomens. *Mass Spectrom. Rev.*, 28(3):468–494, 2009.
- [169] A. G. Harrison. *Mass Spectrom. Rev.*, 28(4):640–654, 2009.
- [170] A. K. Shukla and J. H. Futrell. *J. Mass Spectrom.*, 35(9):1069–1090, 2000.
- [171] S. A. McLuckey. *J. Am. Soc. Mass Spectrom.*, 3(6):599 – 614, 1992.

BIBLIOGRAPHY

- [172] A. Eizaguirre, O. Mo, M. Yáñez, and J.-Y. Salpin. *Phys. Chem. Chem. Phys.*, 13:18409–18417, 2011.
- [173] A. Eizaguirre, O. Mo, M. Yáñez, J.-Y. Salpin, and J. Tortajada. *Org. Biomol. Chem.*, 10:7552–7561, 2012.
- [174] E. Wigner. *Trans. Faraday Soc.*, 34:29–41, 1938.
- [175] D. L. Bunker. *Theory of Elementary Gas Reaction Rates*. Pergamon, Oxford, 1966.
- [176] R. J. Robinson and K. A. Holbrook. *Unimolecular reactions*. Wiley, New York, 1972.
- [177] Forst. *Theory of Unimolecular REactions*. Academic, New York, 1973.
- [178] T. Baer and W. L. Hase. *Unimolecular Reaction Dynamics. Theory and experiments*. Oxford University Press, New York, 1986.
- [179] D. G. Truhlar, B. C. Garrett, and S. J. Klippenstein. *J. Phys. Chem.*, 100(31):12771–12800, 1996.
- [180] Forst. *Unimolecular REactions*. Cambridge University Press, Cambridge, 2003.
- [181] N. E. Henriksen and F. Y. Hansen. *Theories of Molecular Reaction Dynamics: The Microscopic Foundation of Chemical Kinetics*. Oxford University Press, New York, 2008.
- [182] T. Baer and P. M. Mayer. *J. Am. Soc. Mass Spectrom.*, 8(2):103 – 115, 1997.
- [183] M. Zimnicka, T. W. Chung, C. L. Moss, and F. Tureček. *J. Phys. Chem. A*, 117(6):1265–1275, 2013. PMID: 22765351.
- [184] F. Ichou, D. Lesage, X. Machuron-Mandard, C. Junot, R. B. Cole, and J.-C. Tabet. *J. Mass Spectrom.*, 48(2):179–186, 2013.
- [185] F. Ichou, A. Schwarzenberg, D. Lesage, S. Alves, C. Junot, X. Machuron-Mandard, and J.-C. Tabet. *J. Mass Spectrom.*, 49(6):498–508, 2014.
- [186] Á. Kuki, L. Nagy, K. Szabó, B. Antal, M. Zsuga, and S. Kéki. *J. Am. Soc. Mass Spectrom.*, 25(3):439–443, 2014.

BIBLIOGRAPHY

- [187] P. T. Fenn, Y.-J. Chen, S. Stimson, and C. Y. Ng. *J. Phys. Chem. A*, 101(36):6513–6522, 1997.
- [188] Y.-J. Chen, P. T. Fenn, Kai-Chung Lau, C. Y. Ng, Chi-Kin Law, and Wai-Kee Li. *J. Phys. Chem. A*, 106(42):9729–9736, 2002.
- [189] J. Liu, K. Song, L. W. Hase, and S. L. Anderson. *J. Chem. Phys.*, 119(6):3040–3050, 2003.
- [190] E. Martínez-Núñez, S. A. Vázquez, and J. M. C. Marqués. *J. Chem. Phys.*, 121(6):2571–2577, 2004.
- [191] E. Martínez-Núñez, A. Fernández-Ramos, S. A. Vázquez, J. M. C. Marqués, M. Xue, and W. L. Hase. *J. Chem. Phys.*, 123(15):154311, 2005.
- [192] E. Martínez-Núñez, S. A. Vázquez, F. J. Aoiz, and J. F. Castillo. *J. Phys. Chem. A*, 110(4):1225–1231, 2006. PMID: 16435783.
- [193] R. Spezia, A. Cimas, M.-P. Gageot, J.-Y. Salpin, K. Song, and W. L. Hase. *Phys. Chem. Chem. Phys.*, 14:11724–11736, 2012.
- [194] S. O. Meroueh, Y. Wang, and W. L. Hase. *J. Phys. Chem. A*, 106(42):9983–9992, 2002.
- [195] U. Lourderaj and W. L. Hase. *J. Phys. Chem. A*, 113(11):2236–2253, 2009. PMID: 19243125.
- [196] E. Hendell, U. Even, T. Raz, and R. D. Levine. *Phys. Rev. Lett.*, 75:2670–2673, Oct 1995.
- [197] T. Raz and R. D. Levine. *J. Chem. Phys.*, 105(18):8097–8102, 1996.
- [198] D. G. Schultz and L. Hanley. *J. Chem. Phys.*, 109(24):10976–10983, 1998.
- [199] J. A. Burroughs, S. B. Wainhaus, and L. Hanley. *J. Chem. Phys.*, 103(15):6706–6715, 1995.
- [200] O. Meroueh and W. L. Hase. *Phys. Chem. Chem. Phys.*, 3:2306–2314, 2001.
- [201] K. Song, O. Meroueh, and W. L. Hase. *J. Chem. Phys.*, 118(6):2893–2902, 2003.

BIBLIOGRAPHY

- [202] Y. Wang, W. L. Hase, and K. Song. *J. Am. Soc. Mass Spectrom.*, 14(12):1402 – 1412, 2003.
- [203] S. Nordholm, H. W. Schranz, B. C. Freasier, and N. D. Hamer. *Chem. Phys.*, 129(3):351 – 361, 1989.
- [204] In some works this is also called “shattering” while the same term is used in the SID with a different implication, since in SID this does not imply a non-statistical mechanism.
- [205] B. Paizs and S. Suhai. *Mass Spectrom. Rev.*, 24(4):508–548, 2005.
- [206] O. Meroueh and W. L. Hase. *Int. J. Mass Spectrom.*, 201(1–3):233 – 244, 2000.
- [207] W. Kohn. *Rev. Mod. Phys.*, 71:1253–1266, Oct 1999.
- [208] A. Eizaguirre, M. Yáñez, J. Tortajada, and J.-Y. Salpin. *Chem. Phys. Lett.*, 464(4–6):240 – 244, 2008.
- [209] N. E. Schultz, Y. Zhao, and D. G. Truhlar. Density functionals for inorganometallic and organometallic chemistry. *J. Phys. Chem. A*, 109(49):11127–11143, 2005.
- [210] J. N. Harvey. *Annu. Rep. Prog. Chem., Sect. C: Phys. Chem.*, 102:203–226, 2006.
- [211] P. M. W. Gill. *Mol. Phys.*, 89(2):433–445, 1996.
- [212] A. D. Becke. *Phys. Rev. A*, 38:3098–3100, Sep 1988.
- [213] R. Spezia, A. Cimas, M.-P. Gaigeot, J.-Y. Salpin, K. Song, and W. L. Hase. *Phys. Chem. Chem. Phys.*, 14:11724–11736, 2012.
- [214] S. O. Meroueh, Y. Wang, and W. L. Hase. *J. Phys. Chem. A*, 106(42):9983–9992, 2002.
- [215] O. Meroueh and W. L. Hase. *J. Phys. Chem. A*, 103(20):3981–3990, 1999.
- [216] Y. Jeanvoine, M.-P. Gaigeot, W. L. Hase, K. Song, and R. Spezia. *Int. J. Mass Spectrom.*, 308(2–3):289 – 298, 2011. Eyer Special Issue.
- [217] X. Hu, W. L. Hase, and T. Pirraglia. *J. Comput. Chem.*, 12(8):1014–1024, 1991.

BIBLIOGRAPHY

- [218] W. L. Hase, R. J. Duchovic, X. Hu, A. Komornicki, K. F. Lim, D.-H. Lu, G. H. Peslherbe, K. N. Swamy, S. R. V. Linde, A. Varandas, H. Wang, and R. J. Wolf. *QCPE*, 16:671, 1996.
- [219] W. C. Swope, H. C. Andersen, P. H. Berens, and K. R. Wilson. *J. Chem. Phys.*, 76(1):637–649, 1982.
- [220] R. Spezia, J.-Y. Salpin, M.-P. Gageot, W. L. Hase, and K. Song. *J. Phys. Chem. A*, 113(50):13853–13862, 2009. PMID: 19886650.
- [221] M. T. Rodgers and P. B. Armentrout. *J. Chem. Phys.*, 109(5):1787–1800, 1998.
- [222] V. F. DeTuri and K. M. Ervin. *J. Phys. Chem. A*, 103(35):6911–6920, 1999.
- [223] P. B. Armentrout, K. M. Ervin, and M. T. Rodgers. *J. Phys. Chem. A*, 112(41):10071–10085, 2008. PMID: 18808103.
- [224] M. T. Rodgers, K. M. Ervin, and P. B. Armentrout. *J. Chem. Phys.*, 106(11):4499–4508, 1997.
- [225] P. Sainte Claire, G. H. Peslherbe, and W. L. Hase. *J. Phys. Chem.*, 99(20):8147–8161, 1995.
- [226] L. Zhu and W. L. Hase. *Chem. Phys. Lett.*, 175(1–2):117 – 124, 1990.
- [227] J. Andres, J. Bertran, editor. *Theoretical and Computational Chemistry: foundations, methods and techniques*. Publicacions de la Universitat Jaume I, Spain, Castelló de la Plana, 1st edition, 2007.
- [228] E. Schrödinger. *Ann. Physik.*, 79(361), 1926.
- [229] M. Born and J. R. Oppenheimer. *Ann. Physik.*, 84(457), 1927.
- [230] F. L. Pilar. *Elementary Quantum Chemistry*. Dover Publications, Mineola, New York, 1st, revised edition, 1989.
- [231] J. C. Slater. *Phys. Rev.*, 34(1293), 1929.
- [232] C. Cohen-Tannoudji and D. F. L. Bernard. *Quantum Mechanics*, volume 1. Herrmann, Paris, France, 3rd edition, 1977. p.898.
- [233] A. Szabo and N. S. Ostlund. *Modern Quantum Chemistry*. Dover Publications, Mineola, New York, 1996.

BIBLIOGRAPHY

- [234] D. R. Hartree. *Proc. Cambridge Phil. Soc.*, 24(89), 1928.
- [235] J. C. Slater. *Phys. Rev.*, 35(210), 1930.
- [236] V. Z. Fock. *Physik.*, 61(126), 1930.
- [237] T. C. Koopmans. *Physica*, 1(104), 1934.
- [238] I. N. Levine. *Quantum Chemistry*. Pearson Prentice Hall, New York, 6th edition, 2009.
- [239] C. C. J. Roothaan. *Rev. Mod. Phys.*, 23(69), 1951.
- [240] G. G. Hall. *Proc. Roy. Soc.*, A205(541), 1951.
- [241] P. O. Löwdin. *Advan. Chem. Phys.*, 2(207), 1959.
- [242] V.; Moreno M. Bertran, J.; Branchadell and M. Sodupe. *Química Cuántica*. Síntesis S.A., Madrid, 2000.
- [243] J. C. Slater. *Phys. Rev.*, 36(57), 1930.
- [244] S. F. Boys. *Proc. Royal Soc. London*, 258(402), 1950.
- [245] S. Huzinaga. *J. Chem. Phys.*, 42(1293), 1965.
- [246] W. Kocj and M.C. Holthausen. *A chemist's Guide to Density Functional Theory*. Wiley-VCH, Weinheim, 2nd edition, 2001.
- [247] P. Hohenberg and W. Kohn. *Phys. Rev.*, 136(B896), 1964.
- [248] W. Kohn and L. J. Sham. *Phys. Rev.*, 1133(A140), 1965.
- [249] T. L. Gilbert. *Phys. Rev. B*, 12(2111), 1975.
- [250] J. C. Slater. *Phys. Rev.*, 81(385), 1951.
- [251] Wilk L. Vosco, S. J. and M. Nusair. *Can. J. Phys.*, 58(1200), 1980.
- [252] J. P. Perdew and W. Yue. *Phys. Rev. B*, 33:8800–8802, Jun 1986.
- [253] J. P. Perdew. Akademie Verlag, Berlin, 1991.
- [254] J. P. Perdew. *Phys. Rev. B*, 33:8822–8824, Jun 1986.
- [255] J. P. Perdew, K. Burke, and M. Ernzerhof. *Phys. Rev. Lett.*, 77:3865, 1996. Erratum: *Phys. Rev. Lett.*, **1997**, 78, 1396.

BIBLIOGRAPHY

- [256] P. J. Wilson, T. J. Bradley, and D. J. Tozer. *J. Chem. Phys.*, 115(20):9233–9242, 2001.
- [257] C. Adamo and V. Barone. *J. Chem. Phys.*, 108(2):664–675, 1998.
- [258] N. C. Handy and A. J. Cohen. *Mol. Phys.*, 99(5):403–412, 2001.
- [259] W.-M. Hoes, A. J. Cohen, and N. C. Handy. *Chem. Phys. Lett.*, 341(3–4):319 – 328, 2001.
- [260] X. Xu and W. A. Goddard. *Proc.Natl. Acad. Sci.*
- [261] Y. Zhao and D. G. Truhlar. *J. Chem. Phys.*, 125(19):–, 2006.
- [262] J. Tao, J. P. Perdew, V. N. Staroverov, and G. E. Scuseria. *Phys. Rev. Lett.*, 91:146401, Sep 2003.
- [263] T. Van Voorhis and G. E. Scuseria. *J. Chem. Phys.*, 109(2):400–410, 1998.
- [264] Y. Zhao, N. E. Schultz, and D. G. Truhlar. *J. Chem. Phys.*, 123(16), 2005.
- [265] Y. Zhao, N. E. Schultz, and D. G. Truhlar. *J. Chem. Theory Comput.*, 2(2):364–382, 2006.
- [266] Y. Zhao and D. G. Truhlar. *Theor. Chem. Acc.*, 120(1-3):215–241, 2008.
- [267] A. D. Boese and J. L. Martin. *J. Chem. Phys.*, 121(8):3405–3416, 2004.
- [268] J. A. Pople, M. Head-Gordon, D. J. Fox, K. Raghavachari, and L. A. Curtiss. *J. Chem. Phys.*, 90(10):5622–5629, 1989.
- [269] L. A. Curtiss, C. Jones, G. W. Trucks, K. Raghavachari, and J. A. Pople. *J. Chem. Phys.*, 93(4):2537–2545, 1990.
- [270] L. A. Curtiss, K. Raghavachari, G. W. Trucks, and J. A. Pople. *J. Chem. Phys.*, 94(11):7221–7230, 1991.
- [271] L. A. Curtiss, K. Raghavachari, P. C. Redfern, V. Rassolov, and J. A. Pople. *J. Chem. Phys.*, 109(18):7764–7776, 1998.
- [272] L. A. Curtiss, P. C. Redfern, K. Raghavachari, and J. A. Pople. *J. Chem. Phys.*, 114(1):108–117, 2001.

BIBLIOGRAPHY

- [273] Asger Halkier, Trygve Helgaker, Poul Jørgensen, Wim Klopper, and Jeppe Olsen. *Chem. Phys. Lett.*, 302(5–6):437 – 446, 1999.
- [274] D. Feller. *J. Chem. Phys.*, 98(9):7059–7071, 1993.
- [275] T. H. Dunning. *J. Chem. Phys.*, 90(2):1007–1023, 1989.
- [276] D. E. Woon and T. H. Dunning. *J. Chem. Phys.*, 98(2):1358–1371, 1993.
- [277] A. K. Wilson, D. E. Woon, K. A. Peterson, and T. H. Dunning. *J. Chem. Phys.*, 110(16):7667–7676, 1999.
- [278] L. A. Curtiss, P. C. Redfern, and K. Raghavachari. *J. Chem. Phys.*, 123(12):124107, 2005.
- [279] R. Daudel and R. F. W. Bader. *Can. J. Chem.*, 52:1310, 1974.
- [280] R. F. W. Bader. *J. Am. Chem. Soc.*, 97:7391, 1975.
- [281] R. Daudel, H. Brion, and S. Odier. *J. Chem. Phys.*, 23:2080, 1955.
- [282] R. Ponec. *J. Math. Chem.*, 21:323, 1997.
- [283] R. Ponec and A. J. Duben. *J. Comput. Chem.*, 20:760, 1999.
- [284] G. N. Lewis. *J. Am. Chem. Soc.*, 38:762, 1916.
- [285] M. A. Fradera, X. Austen and R. F. W. Bader. *J. Phys. Chem. A*, 103(2):304–314, 1999.
- [286] R. J. Gillespie and I. Hargittai. *Angew. Chem., Int. Ed. Engl.*, 35:495, 1996.
- [287] R. J. Gillespie and P. L. A. Popelier. *Chemical Bonding and Molecular Geometries: From Lewis to Electron Densities*. Oxford University Press, New York, 2001.
- [288] R. S. Mulliken. *J. Chem. Phys.*, 23:1833, 1955.
- [289] Curtiss L. A. Reed, A. E. and F. Weinhold. *Chem. Rev.*, 88:899, 1988.
- [290] E. D. Glendening and F. Weinhold. *J. Comp. Chem.*, 19:593–609, 610–627, 1998.
- [291] E. D. Glendening, J. K. Badenhoop, and F. Weinhold. *J. Comp. Chem.*, 19:628–646, 1998.

BIBLIOGRAPHY

- [292] R. F. W. Bader. *J. Chem. Phys.*, 73:2871, 1980.
- [293] B. Silvi. *THEOCHEM*, 614(1–3):3 – 10, 2002.
- [294] R. McWeeney. *Methods of Molecular Quantum Mechanics*. Academic, New York, 2nd edition, 1976.
- [295] S. Diner and P. Claverie. *Localization and Delocalization in Quantum Chemistry*. Reidel, Dordrecht, The Netherlands, 1976. Vol. II.
- [296] B. Silvi. *Phys. Chem. Chem. Phys.*, 6:256–260, 2004.
- [297] IUPAC. Compendium of Chemical Terminology, 1997. Compiled by A. D. McNaught and A. Wilkinson.
- [298] O. K. Rice and H. C. Ramsperger. *J. Am. Chem. Soc.*, 49(7):1617–1629, 1927.
- [299] L. S. Kassel. *J. Phys. Chem.*, 32(2):225–242, 1927.
- [300] C. N. Hinshelwood. *Proc. R. Soc. A*, 113(763):230–233, 1926.
- [301] E. Wigner. *J. Chem. Phys.*, 5(9):720–725, 1937.
- [302] J. O. Hirschfelder and E. Wigner. *J. Chem. Phys.*, 7(8):616–628, 1939.
- [303] H. M. Rosenstock, M. B. Wallenstein, A. L. Wahrhaftig, and H. Eyring. *Proc. Natl. Acad. Sci.*, 38(8):667–678, 1952.
- [304] B. C. Garrett and D. G. Truhlar. *J. Chem. Phys.*, 70(4):1593–1598, 1979.
- [305] X. Hu and W. L. Hase. *J. Chem. Phys.*, 95(11):8073–8082, 1991.
- [306] C. H. Townes and Schadow A. L. *Microwave Spectrometry*. McGraw-Hill, New York, 1955.
- [307] D. C. Tardy, B. S. Rabinovitch, and G. Z. Whitten. *J. Chem. Phys.*, 48(3):1427–1429, 1968.
- [308] G. Z. Whitten and B. S. Rabinovitch. *J. Chem. Phys.*, 41(6):1883–1883, 1964.
- [309] G. Z. Whitten and B. S. Rabinovitch. *J. Chem. Phys.*, 38(10):2466–2473, 1963.

BIBLIOGRAPHY

- [310] G. Vayner, S. V. Addepalli, K. Song, and W. L. Hase. *J. Chem. Phys.*, 125(1):–, 2006.
- [311] U. Lourderaj, K. Park, and W. L. Hase. *Int. Rev. Phys. Chem.*, 27(3):361–403, 2008.
- [312] L. Zhu and W. L. Hase. *QCPE*, 14:664.
- [313] D. L. Bunker. *J. Chem. Phys.*, 37(2):393–403, 1962.
- [314] N. C. Blais and D. L. Bunker. *J. Chem. Phys.*, 37(11):2713–2720, 1962.
- [315] D. L. Bunker. Classical trajectory methods. In B Alder, S. Fernbach, and M. Rotenberg, editors, *Atomic and Molecular Scattering*, volume 10 of *Methods in Computational Physics: Advances in Research and Applications*, pages 287 – 325. Elsevier, 1971.
- [316] H. Goldstein. *Classical Mechanics*. Addison-Wesley, Menlo Park, CA, 1950.
- [317] U. Burkert and N. L. Allinger. *Molecular Mechanics*. Am. Chemical Soc., 1982.
- [318] J. I. Steinfeld, J. S. Francisco, and W. L. Hase. *Chemical Kinetics and Dynamics*. Prentice-Hall, 2nd edition, 1999.
- [319] A. Gonzalez-Lafont, T. N. Truong, and D. G. Truhlar. *J. Phys. Chem.*, 95(12):4618–4627, 1991.
- [320] K. Bolton, W. L. Hase, and G. H. Peslherbe. *Modern Methods for Multidimensional Dynamics Computations in Chemistry*. World Scientific, 1998.
- [321] K. Bolton, W. L. Hase, and G. H. Peslherbe. Direct dynamics simulations of reactive systems. In D. L. Thomson, editor, *Multidimensional Molecular Dynamics Methods.*, pages 143–189. World Scientific, London, 1998.
- [322] L. Sun and W. L. Hase. *Rev. Comput. Chem.*, 19:79–146, 2003.
- [323] C. J. Cramer. *Essentials of Computational Chemistry. Theories and Models*. John Wiley & Sons, Ltd., 2nd edition, 2004.
- [324] L. Verlet. *Phys. Rev.*, 159:98–103, Jul 1967.

BIBLIOGRAPHY

- [325] D. L. Bunker and E. A. Goring-Simpson. *Faraday Discuss. Chem. Soc.*, 55:93–99, 1973.
- [326] L. Sun and W. L. Hase. *J. Chem. Phys.*, 121(18):8831–8845, 2004.
- [327] C. Doubleday, G. H. Bolton, K. and Peslherbe, and W. L. Hase. *J. Am. Chem. Soc.*, 118(41):9922–9931, 1996.
- [328] L. Sun and W. L. Hase. *J. Chem. Phys.*, 133(4):044313, 2010.
- [329] M. Kaupp, P. V. R. Schleyer, H. Stoll, and H. Preuss. *J. Chem. Phys.*, 94(2):1360–1366, 1991.
- [330] S.F. Boys and F. Bernardi. *Mol. Phys.*, 19(4):553–566, 1970.
- [331] M. P. Allen and D. J. Tildesley. *Computer simulation of liquids*. Clarendon, Oxford, UK, 1987.
- [332] R. G. Cooks. *J. Mass Spectrom.*, 30(9):1215–1221, 1995.
- [333] J. H. Beynon, R. G. Cooks, J. W. Amy, W. E. Baitinger, and T. Y. Ridley. *Anal. Chem.*, 45(12):1023A–1031A, 1973.
- [334] J. H. Futrell and T. O. Tiernan. Tandem mass spectrometric studies of ino-molecule reactions. In J. L. Franklin, editor, *Ion-Molecule Reactions*, volume 2, pages 485–549. Plenum Press, New York, 1972.
- [335] K.R. Jennings. *Int. J. Mass Spectrom. Ion Phys.*, 1(3):227 – 235, 1968.
- [336] F. W. McLafferty, P. F. Bente, Richard. Kornfeld, Shih-Chuan. Tsai, and Ian. Howe. *J. Am. Chem. Soc.*, 95(7):2120–2129, 1973.
- [337] Timothy Wachs, Paul F. Bente III, and F.W. McLafferty. *Int. J. Mass Spectrom. Ion Phys.*, 9(3):333 – 341, 1972.
- [338] J. M. Wells and S. A. McLuckey. volume 402. 2005.
- [339] M. Mentinova and S. A. McLuckey. *J. Am. Soc. Mass Spectrom.*, 22(5):912–921, 2011.
- [340] K. R. Jennings. *Int. J. Mass Spectrom.*, 200(1–3):479 – 493, 2000. Volume 200: The state of the field as we move into a new millenium.
- [341] K. Levsen. *Fundamental Aspects of Organic Mass Spectrometry*. Verlag Chemie, Weinheim, 1978. 138 (collision process), 92 (energy dependence of CID products).

BIBLIOGRAPHY

- [342] K. L. Busch, G. L. Glish, and S. A. McLuckey. Techniques and applications of tandem mass spectrometry. In *Mass Spectrometry/Mass Spectrometry*. VCH, New York, 1988. 64 (Ecom), 84 (pressure effects).
- [343] R. G. Cooks and T. L. Kruger. *J. Am. Chem. Soc.*, 99(4):1279–1281, 1977.
- [344] S. A. McLuckey, D. Cameron, and R. G. Cooks. *J. Am. Chem. Soc.*, 103(6):1313–1317, 1981.
- [345] R. G. Cooks, J. S. Patrick, T. Kotiaho, and S. A. McLuckey. *Mass Spectrom. Rev.*, 13(4):287–339, 1994.
- [346] R. G. Cooks and P. S. H. Wong. *Acc. Chem. Res.*, 31(7):379–386, 1998.
- [347] R. G. Cooks, J. T. Koskinen, and P. D. Thomas. *J. Mass Spectrom.*, 34(2):85–92, 1999.
- [348] X. Zheng, R. G. Cooks, R. Augusti, and W. A. Tao. The kinetic method: Thermochemical determinations and chiral analysis. In M. L. Gross, R. M. Caprioli, and P. B. Armentrout, editors, *Encyclopedia of mass spectrometry, Vol. 1*, pages 350–362. Elsevier, Amsterdam, 2003.
- [349] Z. Wu, C. Fenselau, and R. G. Cooks. *Rapid Commun. Mass Spectrom.*, 8(9):777–780, 1994.
- [350] B. A. Cerda, S. Hoyau, G. Ohanessian, and C. Wesdemiotis. *J. Am. Chem. Soc.*, 120(10):2437–2448, 1998.
- [351] B. A. Cerda and C. Wesdemiotis. *Int. J. Mass Spectrom.*, 185–187:107 – 116, 1999.
- [352] L. Drahos and K. Vékey. *J. Mass Spectrom.*, 34(2):79–84, 1999.
- [353] K. M. Ervin. *Int. J. Mass Spectrom.*, 195–196(0):271 – 284, 2000.

Appendix 1

Additional tables and figures for Part I.

Appendix 1

Table 13: Stabilization free energy of neutral ($\Delta_r G_1^0$) and deprotonated ($\Delta_r G_2^0$) amines upon BH_3 association. G4-based values. All the values in kJ mol^{-1} .

Amine	$\Delta_r G_1^0$	$\Delta_r G_2^0$
ammonia	-77.9	-273.1
methylamine	-96.3	-290.1
dimethylamine	-107.8	-276.0
allylamine	-95.0	-209.1
cyclopropylamine	-71.2	-251.3
benzylamine	-112.4	-263.2
aziridine	-97.7	-265.5
propargylamine	-90.2	-267.9
trifluoroethylamine	-78.5	-257.3
aniline	-57.7	-209.1

Table 14: Characteristics of the B–N bond in amine-boranes in terms of atomic hybrids.

Amine	neutral	anion
Ammonia	82% N (35% <i>s</i> + 65% <i>p</i>) + 18% B (16% <i>s</i> + 84% <i>p</i>)	75% N (40% <i>s</i> + 60% <i>p</i>) + 25% B (23% <i>s</i> + 77% <i>p</i>)
Methylamine	82% N (34% <i>s</i> + 66% <i>p</i>) + 18% B (16% <i>s</i> + 84% <i>p</i>)	75% N (39% <i>s</i> + 61% <i>p</i>) + 25% B (23% <i>s</i> + 77% <i>p</i>)
Dimethylamine	82% N (32% <i>s</i> + 68% <i>p</i>) + 18% B (16% <i>s</i> + 84% <i>p</i>)	76% N (37% <i>s</i> + 63% <i>p</i>) + 24% B (22% <i>s</i> + 78% <i>p</i>)
Allylamine	82% N (33% <i>s</i> + 67% <i>p</i>) + 18% B (16% <i>s</i> + 84% <i>p</i>)	76% N (38% <i>s</i> + 62% <i>p</i>) + 24% B (22% <i>s</i> + 78% <i>p</i>)
Cyclopropylamine	82% N (33% <i>s</i> + 67% <i>p</i>) + 18% B (16% <i>s</i> + 84% <i>p</i>)	76% N (40% <i>s</i> + 60% <i>p</i>) + 24% B (22% <i>s</i> + 78% <i>p</i>)
Benzylamine	LP(N) → 2p (B) ^a 1079	76% N (39% <i>s</i> + 61% <i>p</i>) + 24% B (22% <i>s</i> + 78% <i>p</i>)
Aziridine	82% N (40% <i>s</i> + 60% <i>p</i>) + 18% B (17% <i>s</i> + 83% <i>p</i>)	76% N (39% <i>s</i> + 61% <i>p</i>) + 24% B (22% <i>s</i> + 78% <i>p</i>)
Trifluoroethylamine	82% N (33% <i>s</i> + 67% <i>p</i>) + 18% B (16% <i>s</i> + 84% <i>p</i>)	76% N (38% <i>s</i> + 62% <i>p</i>) + 24% B (22% <i>s</i> + 78% <i>p</i>)
Aniline	LP(N) → 2p (B) ^a 1079	77% N (43% <i>s</i> + 57% <i>p</i>) + 23% B (21% <i>s</i> + 79% <i>p</i>)

^aThe value reported corresponds to the second order interaction energy, in kJ mol^{-1} , between the N lone pair (LP(**N**)) and the empty 2*p* orbital of **B** atom.

Appendix 1

Table 15: Characteristics of the B–N bond in amine-boranes in terms of Wiberg bond index, and electron density ($\rho_b(\text{B–N})$, a.u.) at the corresponding BCP.

Amine	Wiberg bond index		$\rho_b(N - B)$	
	neutral	anion	neutral	anion
Ammonia	0.618	0.816	0.105	0.147
Methylamine	0.612	0.785	0.112	0.151
Dimethylamine	0.592	0.745	0.114	0.150
Allylamine	0.610	0.769	0.112	0.148
Cyclopropylamine	0.598	0.779	0.102	0.147
Benzylamine	0.613	0.762	0.113	0.147
Aziridine	0.613	0.760	0.116	0.147
Trifluoroethylamine	0.593	0.761	0.108	0.146
Aniline	0.608	0.743	0.109	0.140

Table 16: Characteristics of the N–Al bond in amine-alanes in terms of atomic hybrids.

R	neutral	anion
H	92% N(22% <i>s</i> + 78% <i>p</i>) + 8% Al(14% <i>s</i> + 84% <i>p</i>)	87% N(42% <i>s</i> + 58% <i>p</i>) + 13% Al(25% <i>s</i> + 74% <i>p</i>)
CH ₃	92% N(30% <i>s</i> + 70% <i>p</i>) + 8% Al(15% <i>s</i> + 84% <i>p</i>)	88% N(39% <i>s</i> + 61% <i>p</i>) + 12% Al(25% <i>s</i> + 74% <i>p</i>)
<i>c</i> -C ₃ H ₅	92% N(29% <i>s</i> + 71% <i>p</i>) + 8% Al(15% <i>s</i> + 84% <i>p</i>)	88% N(38% <i>s</i> + 62% <i>p</i>) + 12% Al(24% <i>s</i> + 74% <i>p</i>)
C ₆ H ₅	LP(N)→3p(Al) ^a 247.2	LP(N)→ 3p (Al) ^a 499.3

^aThe value reported corresponds to the second order interaction energy, in kJ mol^{−1}, between the N lone pair (LP(N)) and the empty 3*p* orbital of Al atom.

Table 17: Characteristics of the N–Al bond in amine-alanes in terms of Wiberg bond index, and electron density ($\rho_b(\text{N–Al})$, a.u.) at the corresponding BCP.

R	Wiberg bond index		$\rho_b(\text{N} - \text{Al})$	
	neutral	anion	neutral	anion
H	0.290	0.510	0.044	0.072
CH ₃	0.279	0.484	0.047	0.073
<i>c</i> -C ₃ H ₅	0.276	0.465	0.046	0.071
C ₆ H ₅	0.255	0.433	0.043	0.067

Table 18: Characteristics of the P–Al bond in phosphine-alanes in terms of atomic hybrids.

R	neutral	anion
H	87% P (39% <i>s</i> + 61% <i>p</i>) + 13% Al (12% <i>s</i> + 87% <i>p</i>)	76% P (23% <i>s</i> + 77% <i>p</i>) + 24% Al (22% <i>s</i> + 77% <i>p</i>)
CH ₃	85% P (37% <i>s</i> + 62% <i>p</i>) + 15% Al (12% <i>s</i> + 86% <i>p</i>)	76% P (23% <i>s</i> + 77% <i>p</i>) + 24% Al (22% <i>s</i> + 78% <i>p</i>)
<i>c</i> -C ₃ H ₅	85% P (36% <i>s</i> + 64% <i>p</i>) + 15% Al (13% <i>s</i> + 87% <i>p</i>)	76% P (22% <i>s</i> + 78% <i>p</i>) + 24% Al (22% <i>s</i> + 78% <i>p</i>)
C ₆ H ₅	LP(P) → 3p (Al) ^a 426	77% P (17% <i>s</i> + 83% <i>p</i>) + 23% Al (22% <i>s</i> + 78% <i>p</i>)

^aThe value reported corresponds to the second order interaction energy, in kJ mol^{−1}, between the P lone pair (LP(**P**)) and the empty 3*p* orbital of **Al** atom.

Table 19: Characteristics of the P–Al bond in phosphine-alanes in terms of Wiberg bond index and electron density ($\rho_b(\text{P–Al})$, a.u.) at the corresponding BCP.

R	Wiberg bond index		$\rho_b(P - Al)$	
	neutral	anion	neutral	anion
H	0.457	0.739	0.032	0.049
CH ₃	0.489	0.728	0.036	0.052
<i>c</i> -C ₃ H ₅	0.493	0.726	0.037	0.051
C ₆ H ₅	0.488	0.675	0.036	0.048

Table 20: Characteristics of the P–Ga bond in phosphine-gallanes in terms of atomic hybrids.

R	neutral	anion
H	86% P (39% <i>s</i> + 61% <i>p</i>) + 14% Ga (10% <i>s</i> + 89% <i>p</i>)	74% P (22% <i>s</i> + 78% <i>p</i>) + 26% Ga (22% <i>s</i> + 78% <i>p</i>)
CH ₃	84% P (37% <i>s</i> + 63% <i>p</i>) + 16% Ga (12% <i>s</i> + 88% <i>p</i>)	73% P (22% <i>s</i> + 78% <i>p</i>) + 27% Ga (22% <i>s</i> + 78% <i>p</i>)
<i>c</i> -C ₃ H ₅	83% P (36% <i>s</i> + 64% <i>p</i>) + 17% Ga (13% <i>s</i> + 87% <i>p</i>)	72% P (22% <i>s</i> + 78% <i>p</i>) + 28% Ga (23% <i>s</i> + 77% <i>p</i>)
C ₆ H ₅	LP(P) → 4p (Ga) ^a 510.5	74% P (17% <i>s</i> + 83% <i>p</i>) + 26% Ga (22% <i>s</i> + 78% <i>p</i>)

^aThe value reported corresponds to the second order interaction energy, in kJ mol^{−1}, between the P lone pair (LP(**P**)) and the empty 3*p* orbital of **Ga** atom.

Appendix 1

Table 21: Characteristics of the P–Ga bond in phosphine-gallanes in terms of Wiberg bond index and electron density ($\rho_b(\text{P-Ga})$, a.u.) at the corresponding BCP.

R	Wiberg bond index		$\rho_b(P - Ga)$	
	neutral	anion	neutral	anion
H	0.491	0.787	0.048	0.068
CH ₃	0.541	0.784	0.055	0.072
<i>c</i> -C ₃ H ₅	0.562	0.799	0.056	0.071
C ₆ H ₅	0.552	0.721	0.056	0.068

Table 22: Calculated acidity ($\Delta_{acid}G^0$, kJ mol^{−1}) for R-XH₂ (R = Ethyl, vinyl, ethynyl; X = N, P, As, Sb) bases ($\Delta_r G_3^0$) and the corresponding R-XH₂·Y (Y = BeH₂, BH₃, AlH₃) complexes ($\Delta_r G_4^0$).

$\Delta_{acid}G^0$				
	$\Delta_r G_3^0$	$\Delta_r G_4^0$		
	free base	BeH ₂	BH ₃	AlH ₃
R = Ethyl				
X = N	1627 (1638.9 ± 2.9) ^a	1431	1447	1399
X = P	1522 (1531. ± 12.) ^b	1409	1435	1360
X = As	1492 (1501. ± 8.8) ^c	1377	1393	1328
X = Sb	1455	1357	1361	1308
R = Vinyl				
X = N	1533	1325	1360	1322
X = P	1470 [1474] ^d (1477. ± 9.6) ^a	1346 [1343] ^d	1384	1340
X = As	1446 [1446] ^d (1448. ± 8.8) ^c	1322 [1320] ^d	1343	1309
X = Sb	1429	1316	1321	1295
R = Ethynyl				
X = N	1472	1282	1320	1283
X = P	1445 [1451] ^d (1459. ± 9.6) ^a	1319 [1315] ^d	1351	1305
X = As	1418 [1419] ^d (1434. ± 8.8) ^c	1291 [1292] ^d	1309	1277
X = Sb	1401 [1397] ^e	1293	1290	1268

Appendix 1

Table 23: Acidity enhancement, $\Delta\Delta_{acid}G^0$, and stabilization free energies of neutral, $\Delta_rG_1^0$, and deprotonated species, $\Delta_rG_2^0$, when R-XH₂ (R = Ethyl, vinyl, ethynyl; X = N, P, As, Sb) bases interact with BeH₂, BH₃, and AlH₃. All values are in kJ mol⁻¹.

Y =	$(\Delta\Delta_{acid}G^0)^a$			$\Delta_rG_1^0$			$\Delta_rG_2^0$		
	BeH ₂	BH ₃	AlH ₃	BeH ₂	BH ₃	AlH ₃	BeH ₂	BH ₃	AlH ₃
R = Ethyl									
X = N	226	179	226	-59	-74	-66	-285	-253	-292
X = P	139	113	160	-12	-64	-26	-151	-177	-186
X = As	117	99	137	-17	-54	-34	-134	-153	-171
X = Sb	121	119	145	+17	-20	-26	-105	-139	-171
R = Vinyl									
X = N	208	171	209	-29	-41	-38	-237	-212	-247
X = P	124	78	129	-2[-11] ^b	-65	-25	-126	-143	-154
X = As	124	102	136	+13[-2] ^b	-24	-6	-111	-126	-142
X = Sb	114	106	132	+17	-15	-20	-97	-121	-153
R = Ethynyl									
X = N	190	152	188	-7	-16	-18	-197	-168	-206
X = P	125	93	138	+9[+1] ^b	-43	-7	-116	-136	-145
X = As	127	106	140	+26[+9] ^b	-11	+7	-101	-117	-133
X = Sb	108	110	132	+18[+17] ^c	-7	-12	-90	-117	-144

^a These values measure the acidity enhancement upon BeH₂, BH₃ and AlH₃ complexation and are given by the difference $\Delta_rG_3^0 - \Delta_rG_4^0$.

^b Values calculated at the G4 level of theory.

^c Value calculated at the CCSD(T)/Def-QZVP level of theory.

Appendix 1

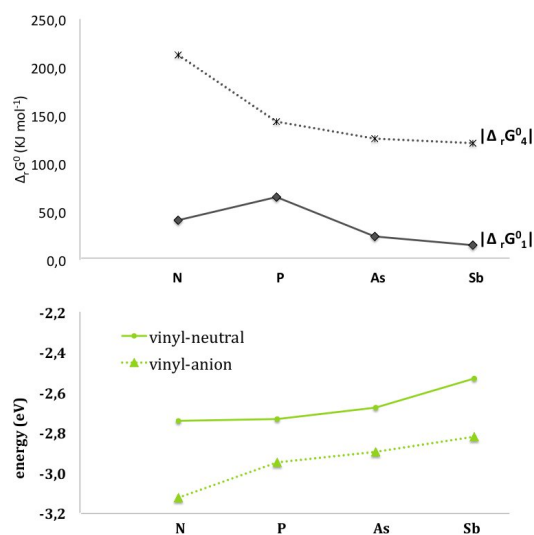


Figure 69: BH₃ LUMO energies within the complex geometry and Gibbs free energies for complex formation. Vinyl derivatives.

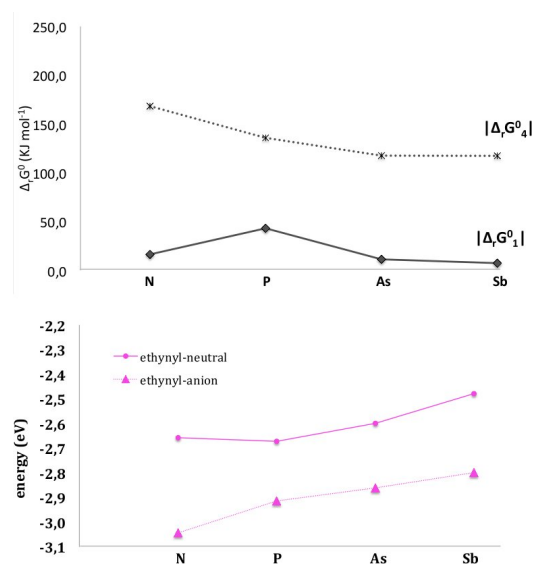


Figure 70: BH₃ LUMO energies within the complex geometry and Gibbs free energies for complex formation. Ethynyl derivatives.

Appendix 2

Additional tables and figures for Part II.

Appendix 2

Table 24: Relative errors (%) in A rotational constants. M = Ca.

Structure	B3LYP ^a	G96LYP ^a	MP2 ^a	BLYP ^a
Formamide	-0.9	-2.4	-1.9	-2.8
A_CaOH ⁺	0.0	0.0	0.0	0.0
A_HCNH ⁺	0.0	0.0	0.0	0.0
B_CaNH ₃ ²⁺	-0.2	-1.4	0.1	-1.8
B_CO	0.0	0.0	0.0	0.0
C_CaHCN ²⁺	0.0	0.0	0.0	0.0
C_H ₂ O	-3.4	-6.7	-2.7	-7.6
D_CaH ₂ O ²⁺	-0.1	-1.4	-0.1	-1.7
D_HCN	0.0	0.0	0.0	0.0
E_CaCO ²⁺	0.0	0.0	0.0	0.0
E_NH ₃	-1.9	-4.0	-1.0	-4.4
F_CaOC ²⁺	0.0	0.0	0.0	0.0
F_NH ₃	-1.9	-4.0	-1.0	-4.4
G_CaNH ²⁺	-6.3	-13.6	-0.1	-16.3
G_OCH ⁺	0.0	0.0	0.0	0.0
int_10	1.3	2.8	-2.7	1.5
int_11	0.0	-1.3	0.2	-1.9
int_1	0.4	0.1	2.2	0.1
int_2	-0.5	-2.7	-0.2	-3.1
int_3	-1.3	-2.6	-1.7	-3.0
int_5	-0.3	-4.7	-3.6	-4.9
int_6	-0.6	-2.9	-1.5	-3.4
int_7	-14.0	-31.5	0.7	-33.2
int_8	2683.2	2673.1	2689.3	2642.1
int_9	-15.0	-10.6	-26.4	-11.8
TS_10_11	0.0	-2.7	6.1	-1.1
TS_1_10	-2.7	-9.6	-0.6	-9.5
TS_1_1	-1.6	-3.5	-2.3	-4.0
TS_1_2	0.0	-1.1	-1.6	-1.2
TS_1_5	1.8	-0.8	0.4	-1.3
TS_1_G	3.4	-5.0	29.4	-3.1
TS_2_3	-8.9	-13.7	-11.0	-14.4
TS_2_A	1.4	-0.8	1.4	-1.0
TS_3_6	-8.8	-11.6	-9.0	-12.4
TS_6_7	0.0	-2.7	-0.5	-2.0
TS_7_8	-3.1	-5.7	1.9	0.1
TS_8_9	4.5	-2.4	10.8	0.7
TS_9_A	18.5	33.7	21.7	67.0

^a 6-31G(d) basis set.

Appendix 2

Table 25: Relative errors (%) in B rotational constants. M = Ca.

Structure	B3LYP ^a	G96LYP ^a	MP2 ^a	BLYP ^a
formamide	-0.91	-2.72	-1.25	-2.83
A_CaOH ⁺	-8.95	-9.7	-9.88	-10.08
A_HCNH ⁺	-1.47	-2.99	-3.26	-3.12
B_CaNH ₃ ²⁺	-6.19	-7.54	-7.28	-7.63
B_CO	-2.22	-4.18	-4.45	-4.34
C_CaHCN ²⁺	-5.25	-6.61	-7.61	-6.38
C_H ₂ O	-0.32	-1.25	-0.74	-1.21
D_CaH ₂ O ²⁺	-5.21	-6.51	-6.68	-6.26
D_HCN	-1.8	-3.58	-4.62	-3.7
E_CaCO ²⁺	-4.37	-5.75	-5.69	-5.2
E_NH ₃	-1.77	-3.87	-0.92	-4.32
F_CaOC ²⁺	-3.28	-5.56	-5.99	-5.02
F_NH ₃	-1.77	-3.87	-0.92	-4.32
G_CaNH ²⁺	-11.38	-14.1	-11.04	-15.25
G_OCH ⁺	-1.99	-3.82	-4.53	-4.02
int_10	-4.24	-6.33	-6.37	-4.71
int_11	0.0	-1.43	-0.88	-1.16
int_1	-4.6	-5.97	-5.68	-6.03
int_2	-3.14	-4.74	-4.12	-4.89
int_3	-4.51	-6.59	-5.27	-6.07
int_5	-6.26	-9.67	-6.06	-9.62
int_6	-4.92	-6.09	-6.11	-6.14
int_7	-4.19	-4.48	-7.88	-4.39
int_8	-24.3	-25.32	-25.7	-25.13
int_9	-3.77	-5.5	-4.45	-5.09
TS_10_11	0.0	-0.9	-7.16	0.02
TS_1_10	1.19	0.62	-1.04	-0.04
TS_1_1	-5.36	-6.73	-6.67	-6.67
TS_1_2	-3.99	-5.59	-4.86	-5.64
TS_1_5	-4.29	-5.75	-4.98	-5.58
TS_1_G	-13	-9.22	27.35	-11.89
TS_2_3	-0.58	-1.11	-0.94	-1.07
TS_2_A	-1.34	-5.15	-4.9	-5.68
TS_3_6	-3.02	-3.82	-3.82	-3.72
TS_6_7	-5.48	-6.86	-7.13	-7.08
TS_7_8	-2.0	-1.59	-11.71	-3.3
TS_8_9	-9.9	-7.35	-16.47	-8.75
TS_9_A	-22.14	-21.12	-21.72	-24.21

^a 6-31G(d) basis set.

Appendix 2

Table 26: Relative errors (%) in C rotational constants. M = Ca.

Structure	B3LYP ^a	G96LYP ^a	MP2 ^a	BLYP ^a
formamide	-0,91	-2,66	-1,24	-2,76
A_CaOH ⁺	-8,95	-9,7	-9,88	-10,08
A_HCNH ⁺	-1,47	-2,99	-3,26	-3,12
B_CaNH ₃ ²⁺	-6,19	-7,54	-7,28	-7,63
B_CO	-2,22	-4,18	-4,45	-4,34
C_CaHCN ²⁺	-5,25	-6,61	-7,61	-6,38
C_H ₂ O	-1,42	-3,2	-1,44	-3,55
D_CaH ₂ O ²⁺	-5,12	-6,42	-6,57	-6,18
D_HCN	-1,8	-3,58	-4,62	-3,7
E_CaCO ²⁺	-4,37	-5,75	-5,69	-5,2
E_NH ₃	0	-0,83	-0,29	-0,71
F_CaOC ²⁺	-3,28	-5,56	-5,99	-5,02
F_NH ₃	0	-0,83	-0,29	-0,71
G_CaNH ²⁺	-11,03	-13,57	-10,8	-14,65
G_OCH ⁺	-1,99	-3,82	-4,53	-4,02
int_10	-3,86	-5,72	-6,13	-4,28
int_11	0	-1,44	-0,88	-1,16
int_1	-4,43	-5,77	-5,43	-5,83
int_2	-3,06	-4,68	-4,01	-4,84
int_3	-3,71	-5,61	-4,4	-5,31
int_5	-5,83	-9,34	-5,9	-9,3
int_6	-4,8	-6,01	-5,99	-6,07
int_7	-4,15	-4,37	-7,86	-4,27
int_8	-14,83	-15,98	-16,4	-15,77
int_9	-4,31	-5,73	-5,64	-5,4
TS_10_11	0	-1,12	-5,74	-0,12
TS_1_10	1,22	0,67	-1,04	0,03
TS_1_1	-4,47	-5,99	-5,66	-6,04
TS_1_2	-3,85	-5,43	-4,75	-5,49
TS_1_5	-4,15	-5,63	-4,86	-5,47
TS_1_G	-12,05	-8,6	27,6	-11,04
TS_2_3	-1,3	-2,32	-1,86	-2,37
TS_2_A	-1,32	-5,09	-4,78	-5,6
TS_3_6	-3,46	-4,36	-4,25	-4,34
TS_6_7	-5,2	-6,61	-6,8	-6,78
TS_7_8	-2,19	-2,32	-9,71	-2,74
TS_8_9	-8,35	-6,77	-13,86	-7,69
TS_9_A	-21,77	-20,68	-21,34	-23,64

^a 6-31G(d) basis set.

Appendix 2

Table 27: Relative errors (%) in A rotational constants. M = Sr.

Structure	B3LYP/6-31G(d)	G96LYP/6-31G(d)	MP2/6-31G(d)
formamide	2.12	0.57	1.03
A_HCNH ⁺	0.0	0.0	0.0
A_SrOH ⁺	0.0	0.0	0.0
B_CO	0.0	0.0	0.0
B_SrNH ₃ ²⁺	2.18	1.03	2.28
C_H ₂ O	-2.07	-5.21	-1.36
C_HCNSr ²⁺	-3.2	-7.89	-10.07
D_HCN	0.0	0.0	0.0
D_SrH ₂ O ²⁺	2.81	1.68	2.7
E_NH ₃	-0.25	-2.31	0.6
E_OC-Sr ²⁺	0.0	0.0	0.0
F_CO-Sr ²⁺	0.0	0.0	0.0
F_NH ₃	-0.25	-2.31	0.6
G_SrNH ₂ ⁺	-6.12	-11.18	2.38
G_OCH ⁺	0.0	0.0	0.0
int1	6.24	5.93	9.43
int2	2.82	0.54	3.78
int3	0.86	0.02	0.1
int4	2.92	0.97	2.79
int5	159.18	1184.09	4998.26
int6	-13.75	-11.99	-29.26
int7	20.38	17.63	14.11
int8	4.73	-4.43	2.57
TS_1.1	0.72	-1.38	-0.05
TS_1.2	2.55	1.62	0.7
TS_1.7	14.61	2.68	20.29
TS_1.8	3.12	-0.58	1.67
TS_2.3	-5.33	-11.56	-6.43
TS_2_A	19.29	18.02	20.94
TS_3.4	-4.49	-7.31	-6.33
TS_4.5	3.92	0.13	3.41
TS_5.6	26.97	15.26	28.7
TS_6_A	169.39	178.99	96.73
TS_1_G	13.24	2.73	268.41

Appendix 2

Table 28: Relative errors (%) in B rotational constants. M = Sr.

Structure	B3LYP/6-31G(d)	G96LYP/6-31G(d)	MP2/6-31G(d)
formamide	1.74	-0.11	1.4
A_HCNH ⁺	1.57	0.02	-0.26
A_SrOH ⁺	-6.94	-8.19	-7.6
B_CO	1.9	-0.12	-0.42
B_SrNH ₃ ²⁺	-3.46	-4.8	-5.26
C_H ₂ O	3.04	2.0	2.6
C_HCNsr ²⁺	-3.56	-4.99	-6.42
D_HCN	1.87	0.03	-1.05
D_SrH ₂ O ²⁺	-3.37	-4.95	-5.08
E_NH ₃	-0.25	-2.31	0.6
E_OC-Sr ²⁺	-2.99	-4.58	-5.02
F_CO-Sr ²⁺	-2.95	-6.21	-6.12
F_NH ₃	-0.25	-2.31	0.6
G_SrNH ₂ ⁺	-10.07	-12.73	-10.82
G_OCH ⁺	1.85	-0.04	-0.78
int1	-3.57	-5.12	-5.06
int2	-1.63	-3.35	-3.25
int3	-3.06	-6.93	-3.68
int4	-2.53	-3.75	-4.56
int5	-18.99	-26.08	-27.67
int6	-3.03	-4.66	-2.35
int7	-7.1	-8.23	-9.41
int8	-5.68	-11.24	-5.9
TS_1.1	-3.67	-5.42	-5.73
TS_1.2	-2.28	-4.08	-3.47
TS_1.7	1.87	1.43	-0.28
TS_1.8	-1.15	-2.85	-2.74
TS_2.3	0.69	0.64	-0.76
TS_2_A	6.87	4.07	4.7
TS_3.4	-1.8	-2.75	-2.67
TS_4.5	-3.57	-4.95	-5.78
TS_5.6	-18.49	-16.01	-22.39
TS_6_A	-24.01	-23.38	-23.45
TS_1_G	-14.59	-10.47	-5.5

Appendix 2

Table 29: Relative errors (%) in C rotational constants. M = Sr.

Structure	B3LYP/6-31G(d)	G96LYP/6-31G(d)	MP2/6-31G(d)
formamide	1.8	0.0	1.46
A_HCNH ⁺	1.57	0.02	-0.26
A_SrOH ⁺	-6.94	-8.19	-7.6
B_CO	1.9	-0.12	-0.42
B_SrNH ₃ ²⁺	-3.46	-4.8	-5.26
C_H ₂ O	1.23	-0.59	1.2
C_HCNSr ²⁺	-3.56	-4.99	-6.42
D_HCN	1.87	0.03	-1.05
D_SrH ₂ O ²⁺	-3.3	-4.87	-4.99
E_NH ₃	3.15	2.4	2.84
E_OC-Sr ²⁺	-2.99	-4.58	-5.02
F_CO-Sr ²⁺	-2.95	-6.21	-6.12
F_NH ₃	3.15	2.4	2.84
G_SrNH ₂ ⁺	-9.75	-12.32	-10.61
G_OCH ⁺	1.85	-0.04	-0.78
int1	-3.34	-4.87	-4.74
int2	-1.54	-3.27	-3.11
int3	-2.41	-5.81	-3.05
int4	-2.44	-3.67	-4.43
int5	-7.77	-11.55	-13.2
int6	-3.47	-4.95	-3.7
int7	-5.5	-6.71	-8.01
int8	-5.16	-10.94	-5.48
TS_1.1	-2.96	-4.77	-4.82
TS_1.2	-2.17	-3.94	-3.37
TS_1.7	1.79	1.44	-0.38
TS_1.8	-1.09	-2.82	-2.7
TS_2.3	0.27	-0.26	-1.25
TS_2_A	6.43	3.68	4.35
TS_3.4	-2.04	-3.04	-3.01
TS_4.5	-3.32	-4.74	-5.48
TS_5.6	-14.96	-13.28	-18.65
TS_6_A	-23.25	-22.61	-22.81
TS_1.G	-13.76	-9.96	-2.51

Appendix 2

Table 30: Absolute errors (kcal mol⁻¹) for relative energies computed with the four trial methods. M = Ca.

Structure	B3LYP ^a	G96LYP ^a	MP2 ^a	BLYP ^a
Form/Ca ²⁺	6.59	11.15	9.23	7.22
A	25.29	21.07	17.28	20.89
B	1.28	4.97	10.51	2.64
C	2.35	1.54	9.93	0.73
D	1.64	2.71	12.32	0.38
E	1.16	6.22	11.60	3.91
F	2.51	5.65	9.43	3.22
G	19.41	12.64	13.67	11.43
int10	2.51	4.97	11.50	4.93
int11	4.03	6.15	13.79	6.67
min1	0.00	0.00	0.00	0.00
int2	2.00	3.75	4.72	4.50
int3	2.49	2.06	5.05	2.75
int4	0.72	2.53	2.41	3.33
int5	0.94	3.04	2.59	3.99
int6	0.45	1.59	0.16	1.63
int7	4.33	1.93	5.30	2.25
int8	1.65	0.81	10.63	0.36
int9	4.41	2.02	7.20	1.84
TS_10_11	4.20	6.56	13.48	6.58
TS_1_10	4.95	1.23	2.28	2.90
TS_1_1	4.85	4.55	7.04	5.51
TS_1_2	0.86	4.72	3.61	4.93
TS_1_5	1.10	3.72	3.08	4.23
TS_1_G	12.67	2.31	7.72	1.61
TS_2_3	1.71	3.22	4.33	3.86
TS_2_A	5.06	0.89	1.56	0.34
TS_3_6	2.41	1.06	5.02	0.76
TS_6_7	2.14	2.59	0.40	2.97
TS_7_8	4.00	2.23	7.61	1.99
TS_8_9	3.34	1.45	8.66	1.13
TS_9_A	19.23	15.20	11.01	14.65

^a 6-31G(d) basis set.

Appendix 2

Table 31: Relative errors (%) for relative energies computed with the four trial methods. M = Ca.

Structure	B3LYP ^a	G96LYP ^a	MP2 ^a	BLYP ^a
Form/Ca ²⁺	-6.9	-11.7	-9.7	-7.6
A	-528.6	-440.5	-361.2	-436.6
B	-3.1	-12.1	-25.5	-6.4
C	4.2	-2.7	-17.6	1.3
D	2.7	-4.5	-20.4	-0.6
E	-1.5	-8.0	-15.0	-5.0
F	-3.1	-6.9	-11.5	-3.9
G	58.4	38.0	41.1	34.4
int10	-7.3	-14.5	-33.6	-14.4
int11	-21.1	-32.2	-72.1	-34.8
min1	0.0	0.0	0.0	0.0
int2	-3.8	-7.1	-8.9	-8.5
int3	-12.1	-10.0	-24.6	-13.3
int4	-1.3	-4.5	4.3	-6.0
int5	-2.0	-6.5	-5.5	-8.5
int6	-1.6	-5.6	-0.6	-5.8
int7	14.7	6.5	-18.0	7.6
int8	31.3	15.3	-201.9	6.9
int9	16.6	7.6	-27.1	6.9
TS_10_11	-11.6	-18.2	-37.3	-18.2
TS_1_10	6.5	-1.6	3.0	-3.8
TS_1_1	-16.7	-15.7	-24.3	-19.0
TS_1_2	-1.4	-7.5	-5.7	-7.8
TS_1_5	1.2	-4.1	3.4	-4.6
TS_1_G	15.9	2.9	9.7	2.0
TS_2_3	-3.1	-5.9	-7.9	-7.0
TS_2_A	9.2	1.6	2.8	-0.6
TS_3_6	4.5	2.0	9.5	1.4
TS_6_7	2.7	-3.3	0.5	-3.8
TS_7_8	10.4	5.8	-19.8	5.2
TS_8_9	11.8	5.1	-30.7	4.0
TS_9_A	47.0	37.2	26.9	35.8

^a 6-31G(d) basis set.

Table 32: Absolute errors (kcal mol⁻¹) for relative energies computed with the four trial methods. M = Sr.

Structure	B3LYP ^a	G96LYP ^a	MP2 ^a	G96LYP ^b
Form/Sr ²⁺	13.25	18.74	16.41	6.14
A	45.16	40.10	37.33	7.14
B	4.80	9.05	14.61	2.29
C	4.93	0.76	8.09	0.78
D	0.33	5.21	15.29	2.74
E	2.23	7.67	12.44	0.02
F	4.32	8.00	11.97	1.44
G	33.58	25.21	31.59	9.29
min1	0.00	0.00	0.00	0.00
int2	3.96	5.50	6.26	1.03
int3	5.45	5.20	6.66	1.07
int6	2.97	4.25	2.11	0.01
int8	1.23	0.18	11.04	0.81
int9	3.58	1.42	8.27	0.33
int10	5.11	7.74	13.22	0.00
int5	0.56	2.57	0.09	1.16
TS_1_1	6.23	5.86	7.45	0.03
TS_1_2	0.32	4.23	2.46	1.74
TS_1_10	9.64	2.83	9.81	3.20
TS_1_5	4.38	0.81	6.75	0.41
TS_2_3	3.89	5.12	6.06	1.09
TS_2_A	6.99	3.97	5.59	2.01
TS_3_6	2.00	0.37	5.54	0.92
TS_6_8	3.02	1.94	1.73	0.96
TS_8_9	2.15	0.21	9.95	0.56
TS_9_A	35.87	31.39	28.58	5.49
TS_1_G	25.91	11.99	26.88	5.59

^a 6-31G(d) basis set.

^b 6-31+G(d,p) basis set.

Table 33: Relative errors (%) for relative energies computed with the four trial methods. M = Sr.

Structure	B3LYP ^a	G96LYP ^a	MP2 ^a	G96LYP ^b
Form/Sr ²⁺	-16.7	-23.6	-20.7	-7.7
A	-755.1	-670.4	-624.2	-119.4
B	-12.9	-24.4	-39.4	-6.2
C	10.8	1.7	-17.7	1.7
D	-0.6	-9.6	-28.3	-5.1
E	-3.4	-11.6	-18.8	0.0
F	-6.1	-11.2	-16.8	-2.0
G	99.9	75.0	94.0	27.6
min1	0.0	0.0	0.0	0.0
int2	-8.0	-11.1	-12.6	-2.1
int3	-24.5	-23.4	-29.9	-4.8
int6	-10.8	-15.4	-7.7	0.0
int8	13.2	1.9	-118.3	8.7
int9	14.4	5.7	-33.2	1.3
int10	-16.0	-24.3	-41.5	0.0
int5	1.2	-5.7	0.2	2.6
TS_1_1	-21.0	-19.8	-25.1	-0.1
TS_1_2	-0.5	-7.2	-4.2	-2.9
TS_1_10	13.0	3.8	13.3	4.3
TS_1_5	5.0	-0.9	7.8	-0.5
TS_2_3	-7.5	-9.9	-11.7	-2.1
TS_2_A	13.6	7.7	10.9	3.9
TS_3_6	3.8	0.7	10.6	1.8
TS_6_8	4.0	-2.5	2.3	-1.3
TS_8_9	8.1	0.8	-37.5	2.1
TS_9_A	87.7	76.7	69.9	13.4
TS_1_G	34.1	15.8	35.4	7.3

^a 6-31G(d) basis set.

^b 6-31+G(d,p) basis set.

Appendix 2

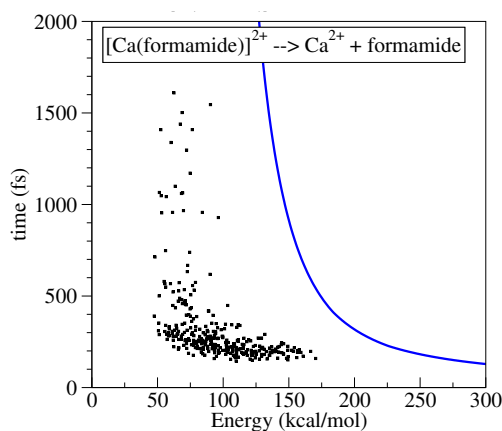


Figure 71: Reaction time *vs.* energy transfer for trajectories yielding formamide neutral loss, obtained from chemical dynamics simulations (squares) and half-life times ($t_{1/2}$) predicted by RRKM (solid lines). Both were obtained using BLYP/6-31G(d) level of theory.

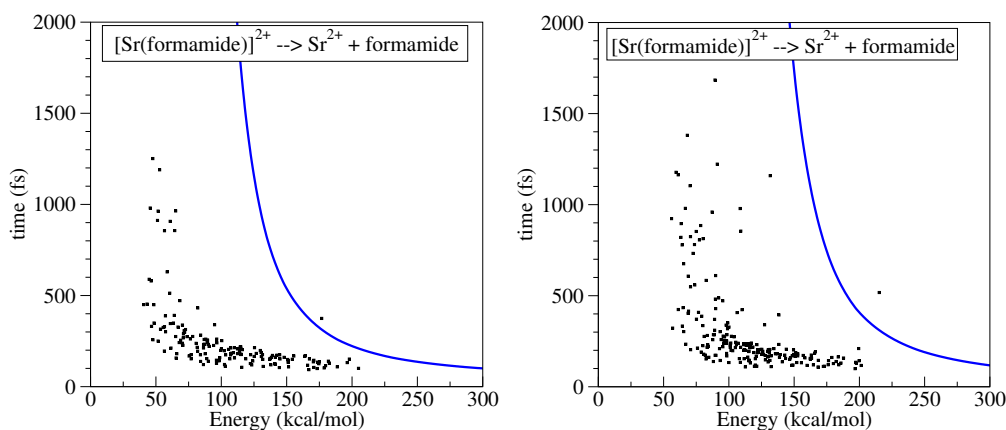


Figure 72: Reaction time *vs.* energy transfer obtained from chemical dynamics simulations (squares) and half-life times ($t_{1/2}$) predicted by RRKM (solid lines). Both are for trajectories yielding formamide neutral loss using G96LYP/6-31G(d) in the left and G96LYP/6-31+G(d,p) in the right.

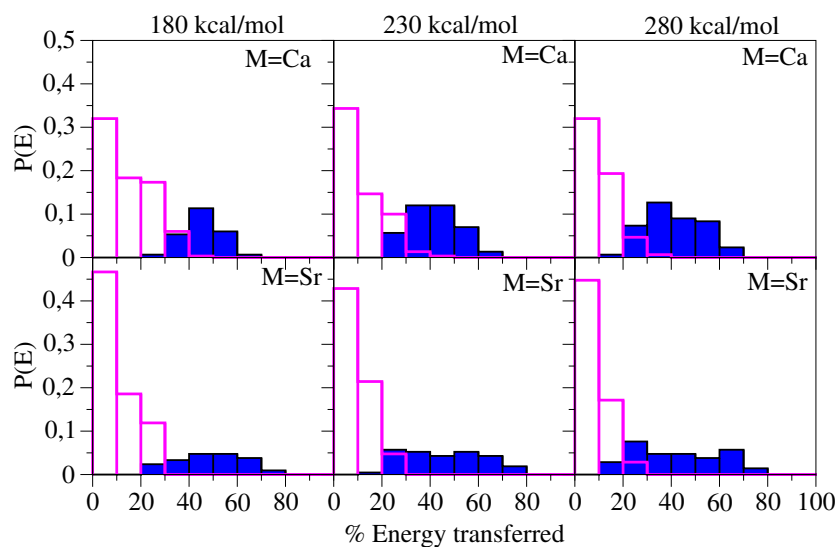


Figure 73: Probability of transferring a given % of the collision energy to the $[M(\text{formamide})]^{2+}$ ion for the non-reactive trajectories (white) and the reactive ones (blue), at the three collision energies considered (180, 230, and 280 kcal mol⁻¹ from left to right). G96LYP/6-31G(d) is used for the two molecular ions.

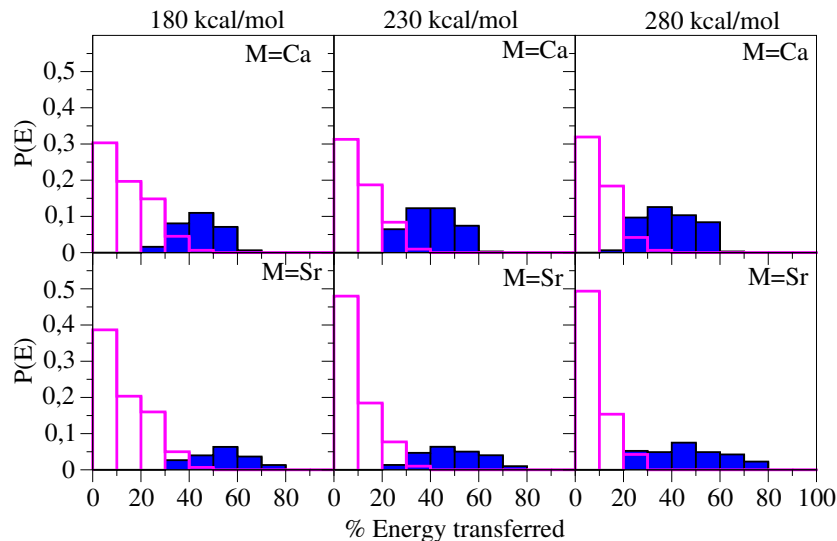


Figure 74: Probability of transferring a given % of the collision energy to the $[M(\text{formamide})]^{2+}$ ion for the non-reactive trajectories (white) and the reactive ones (blue), at the three collision energies considered (180, 230, and 280 kcal mol⁻¹ from left to right). The trajectories were calculated using BLYP/6-31G(d) for M = Ca and G96LYP/6-31+G(d,p) for M = Sr.

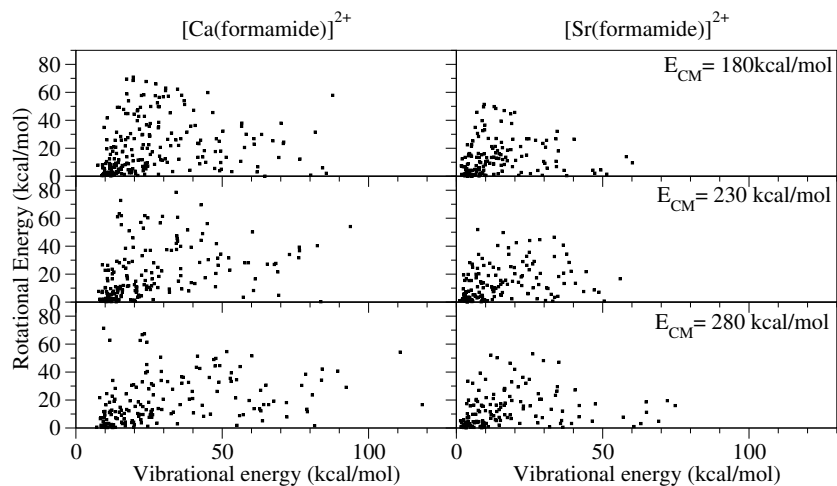


Figure 75: Scattering plot of vibrational versus rotational energy distributions obtained from nonreactive $[\text{M}(\text{formamide})]^{2+}$ trajectories for the three collision energies considered. The level of theory used for both metals is: G96LYP/6-31G(d).

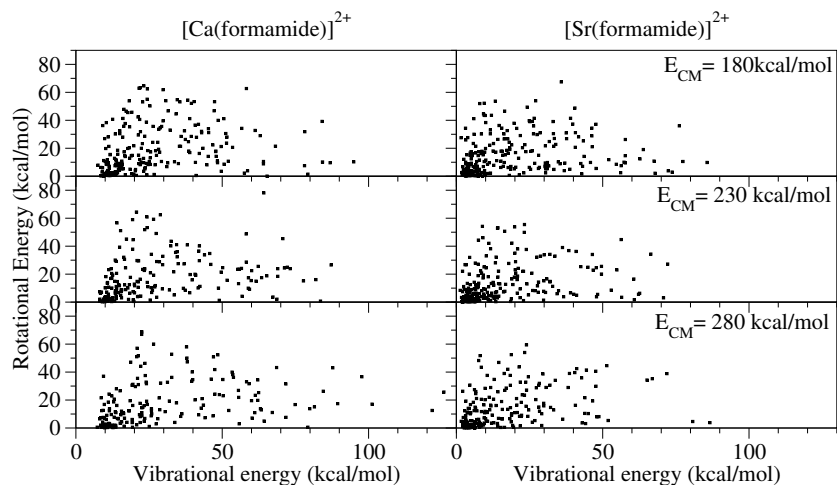


Figure 76: Scattering plot of vibrational versus rotational energy distributions obtained from nonreactive $[\text{M}(\text{formamide})]^{2+}$ trajectories for the three collision energies considered. The trajectories were calculated using BLYP/6-31G(d) for $\text{M} = \text{Ca}$ and G96LYP/6-31+G(d,p) for $\text{M} = \text{Sr}$.

Fig. 75 unambiguously show that vibrational excitation is independent from the rotational excitation. Similar results are obtained using BLYP/6-31G(d), $M = \text{Ca}$, and G96LYP/6-31+G(d,p), $M = \text{Sr}$, as shown in Fig. 76.

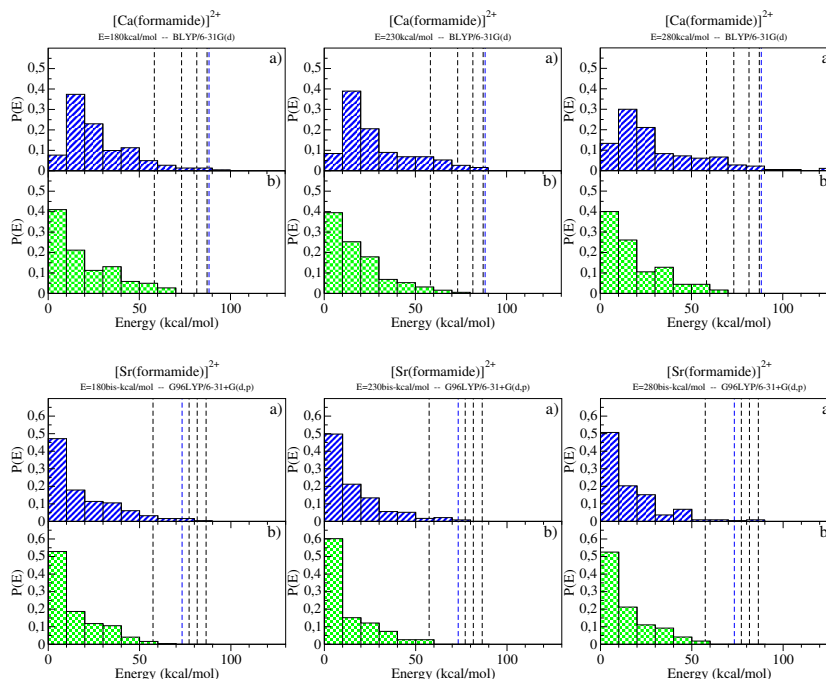


Figure 77: Vibrational (a panels) and rotational (b panels) energy distribution for the non-reactive trajectories at the three collision energies: 180, 230 and 280 kcal mol⁻¹ from left to right. The top panels correspond to $M = \text{Ca}$ while the bottom ones are for $M = \text{Sr}$. The dashed vertical lines mark the energy for the different TS that can be reached from min1 structure. The values for $M = \text{Ca}$ are compute using the BLYP/6-31G(d) approach while the values for $M = \text{Sr}$ are computed at the G96LYP/6-31+G(d,p) level of theory.

Rotational effects

In the collision between the molecular ion and Ar, the translational energy is converted into vibrational and rotational energy on the ion. The rotational effect can have an important effect on the rate constants when the moments of inertia of the reactant and TS are significantly different. Therefore, we evaluated the role of the external rotational energy in the rate constants which may be changed. These are k_{01} , k_{1G} , k_{110} , k_{101} , and k_{15} for both metals. In addition to these rate constant, k_{15} must be considered when $M = \text{Sr}$. The curves for $k(E, J)$ computed at high-level (B3LYP/cc-pWCVTZ, Ca and G96LYP/6-311+G(3df,2p), Sr) and with our low-level approach G96LYP/6-

31G(d), are shown in Figs. 78 and 79. As explained in the Methodology section, K quantum number can be treated as an active rotor (solid lines) with different values for the angular momentum J ; or as an adiabatic rotor (dashed lines), where all the rotational energy is placed on the x, y -axes (blue diamonds, **case1**); equally distributed among the three axes (green crosses, **case2**); or in the z -axis (brown circles, **case3**).

No important effects of the external rotational energy are observed when the quantum number K is treated as an active rotor. However, when K is treated adiabatically we observe a decrease in the reaction speed with the exception of k_{1G} that at high energy experiments slightly increases. This effect is more pronounced the higher the energy placed on the z -axis of the molecule, especially for $\text{int10} \rightarrow \text{min1}$ and $\text{int5} \rightarrow \text{min1}$ reactions (Fig. 78 and 79). Coherently, if all the energy is placed on the z -axis for these reactions, they start at much higher internal energies and the values of k_{101} and k_{51} decrease several orders of magnitude.

The effect of considering the external rotation when computing $k(E, J)$ for formamide neutral loss reaction (k_{01}) is more complex, because the effects on the reaction speed depend on how the rotational energy is distributed within the molecule. It must be recalled that this reaction corresponds to the Ca–O bond cleavage until its eventual dissociation. When all the rotational energy is placed on the z -axis (case 3) this cleavage is not favored and consequently the reaction rate decreases (brown circles, dashed line). Conversely, if all the energy is placed on the x, y -plane (case 1), the rate constant increases slightly and the kinetics speed up (blue diamonds, dashed line).

The general conclusion is that the effect of external rotation, when it is relevant, is generally to slow down the kinetics of the system.

Appendix 2

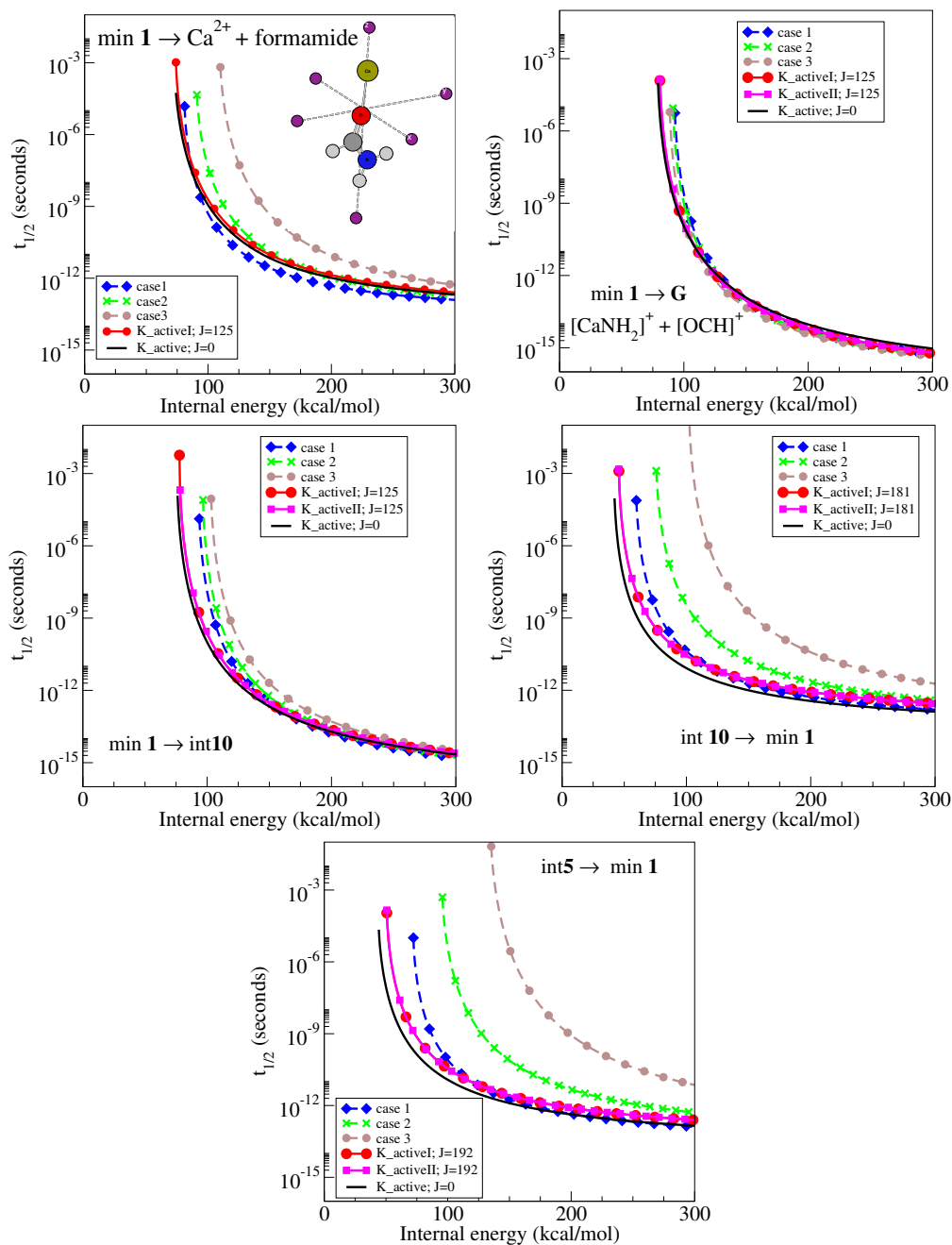


Figure 78: RRKM rate constants for $M = \text{Ca}$ taking into account rotational energy in different ways (see text). The $k(E, J)$ showed are computed at the B3LYP/cc-pWCVTZ level of theory.

Appendix 2

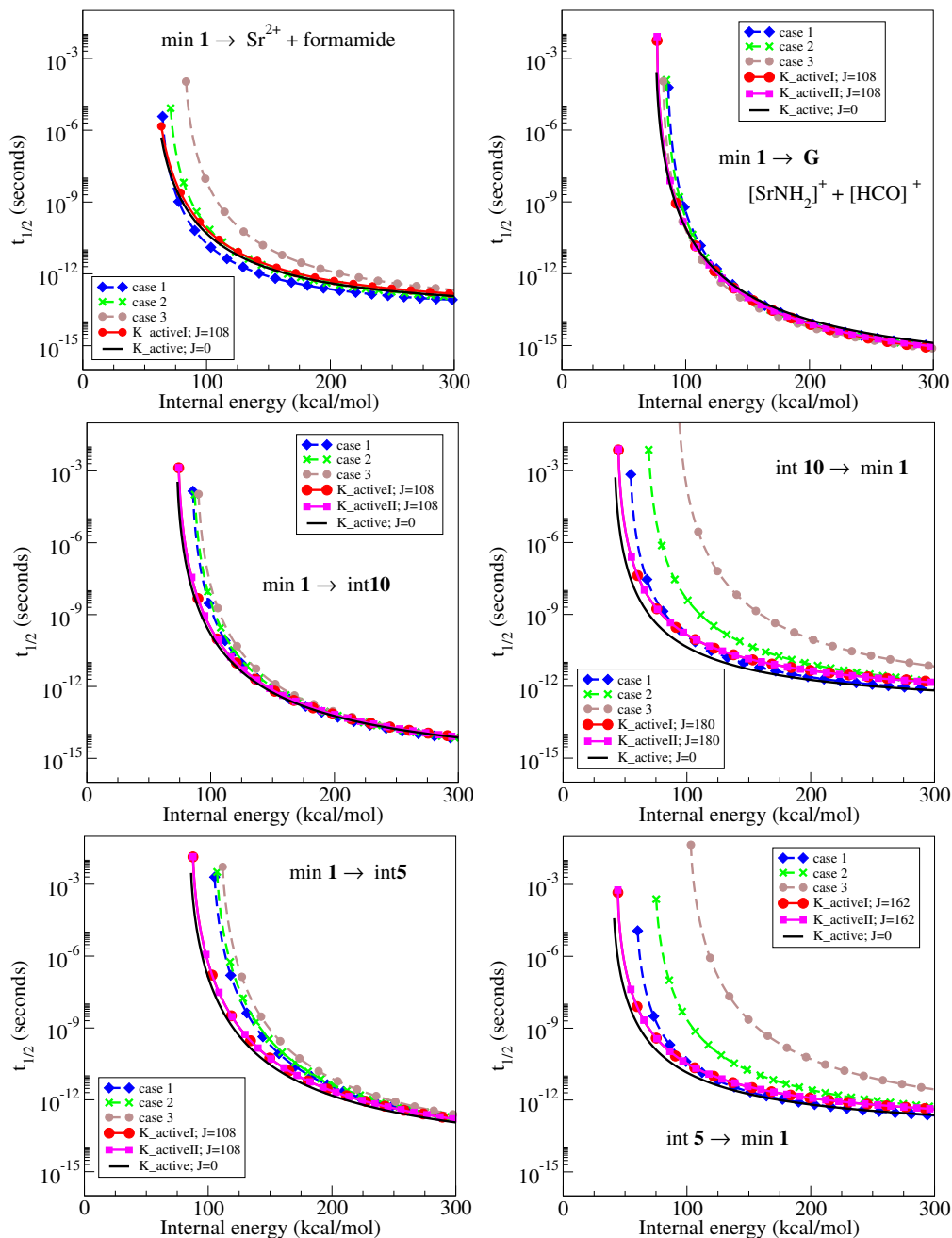


Figure 79: RRKM rate constants for $M = \text{Sr}$ taking into account rotational energy in different ways (see text). The $k(E, J)$ showed are computed at the G96LYP/6-311+G(3df,2p) level of theory.

Appendix 3

Articles resulting from this PhD thesis.



Contents lists available at SciVerse ScienceDirect

Computational and Theoretical Chemistry

journal homepage: www.elsevier.com/locate/comptc

The importance of deformation on the strength of beryllium bonds

Ana Martín-Sómer, Al Mokhtar Lamsabhi, Otilia Mó, Manuel Yáñez*

Departamento de Química, Facultad de Ciencias, Módulo 13, Universidad Autónoma de Madrid, Campus de Excelencia UAM-CSIC, Cantoblanco, 28049 Madrid, Spain

ARTICLE INFO

Article history:

Received 25 April 2012

Accepted 10 June 2012

Available online 26 June 2012

Keywords:

Beryllium bonds

Non-covalent interactions

G4 calculations

Deformation

Frontier orbital theory

ABSTRACT

High-level G4 ab initio calculations have been carried out to investigate the binding in $\text{NH}_3 \cdot \text{BeH}_{2-n}\text{X}_n$ ($\text{X} = \text{F}, \text{Cl}, \text{Br}; n \leq 2$) complexes. The results obtained show that these dimers are stabilized by quite strong beryllium bonds, which are accompanied by a dramatic distortion of the $\text{BeH}_{2-n}\text{X}_n$ Lewis acids, which depart noticeably from linearity whereas the $\text{Be}-\text{H}$ and $\text{Be}-\text{X}$ bonds become significantly longer. This deformation plays a crucial role as far as the relative stability trends are concerned since it amounts to about a 30% of the total interaction energy. More importantly, this deformation significantly enhances the electron acceptor capacity of the Lewis acid, which follows completely different trends from those expected for the undistorted systems. Consistently, a frontier orbital theory is able to explain the trends observed in the interaction energies, provided that it is carried out on the distorted systems rather than on the systems in their equilibrium conformation.

© 2012 Elsevier B.V. All rights reserved.

1. Introduction

Many weak interactions in chemistry, even if they are usually considered non-covalent interactions [1], involve a non-zero charge transfer between the systems which interact, in such a way that one of them behaves as a Lewis base, the electron donor, and the other as the Lewis acid, the electron acceptor. This is typically the case in $\text{X}-\text{H} \cdots \text{Y}$ conventional hydrogen bonds (HBs) [2], in which there is a certain charge transfer from the lone pairs of the HB acceptor into the σ_{XH}^* antibonding orbital of the HB donor. The population of the σ_{XH}^* antibonding orbital actually results in the lengthening of the $\text{X}-\text{H}$ bond and in the red-shifting of the $\text{X}-\text{H}$ stretching frequency, which is one of the signatures of these non-covalent interactions [3]. We have recently shown [4] that the interaction of BeX_2 derivatives with different bases, B, exhibits many similarities with conventional hydrogen bonds. Actually the $\text{B} \cdots \text{BeX}_2$ interaction involves also a charge transfer from the lone-pair of the base towards the p empty orbital of Be as well as into the σ_{BeX}^* antibonding orbital, leading to a linkage between both moieties which we named beryllium bonds [4]. The first of these charge transfers triggers a significant deformation of the BeX_2 moiety which in the $\text{B} \cdot \text{BeX}_2$ complex departs significantly from linearity. The second charge transfer process indicated above results in a clear lengthening of the $\text{Be}-\text{X}$ bonds, and in a concomitant red-shifting of the antisymmetric $\text{X}-\text{Be}-\text{X}$ stretching frequency, whereas the symmetric one appears blue-shifted [4]. Also recently, we have shown, in a study on the relative stability of $\text{X} \cdot \text{BH}_{3-n}\text{F}_n$ and $\text{X} \cdot \text{BH}_{3-n}\text{Cl}_n$ with a large variety of bases [5], that the trends

observed in their relative stabilities was a challenge for the different models proposed in the literature to describe these complexes [6–8]. In fact, the only model which was found to reproduce the stability trends, in both families of complexes, was the frontier orbital theory [9,10], but using in the analysis the frontier orbitals of the distorted monomers [5]. The main conclusion then was that when the interaction between a Lewis base and a Lewis acid is such that it produces a significant structural distortion in one of the interacting systems or in both of them, not only the distortion energy is a fundamental ingredient to explain the relative stabilities of the complexes formed, but also the significant perturbation that the distortion induces in the electron acceptor and/or electron donor properties of the interacting subunits [5].

The aim of the present paper is to investigate whether a similar situation is observed when dealing with beryllium bonds, i.e., with complexes formed when a typical Lewis base, like ammonia, interacts with Be derivatives in which the H atoms in the parent compound BeH_2 are replaced by one or two halogen substituents. We have considered as substituents in this study fluorine, chlorine and bromine.

2. Computational details

Since the energetic effects of the deformation may be crucial when determining the relative stabilities of the complexes between NH_3 and $\text{BeH}_{2-n}\text{X}_n$ ($\text{X} = \text{F}, \text{Cl}, \text{Br}; n \leq 2$), their total energies, as well as those of the independent monomers were obtained at the G4 level of theory [11], which usually provides very accurate values for thermodynamic magnitudes. We have considered it of interest to explore also the performance of the B3LYP density functional theory (DFT) approach for the description of these subtle ef-

* Corresponding author.

E-mail address: manuel.yanez@uam.es (M. Yáñez).

fects, mainly to have an assessment of a method that may be needed when beryllium bonds involve very large systems, for which the Gn theories [12] can become prohibitively expensive. Actually previous assessments in the literature have shown that this method, which combines Becke's three parameter (B3) exchange functional [13] with the Lee–Yang–Parr (LYP) non-local correlation functional [14] is particularly well suited to provide accurate optimized geometries, which are often superior to those obtained by means of correlated ab initio methods such as MP2 [15–19]. For these optimizations we have employed a rather extended 6-311+G(3df,2p) basis set, which will ensure the adequate description of polarization effects and of regions of space significantly apart from the nuclei. All these calculations have been carried out with the Gaussian09 suite of programs [20].

The strength of the bonding between both subunits can be quantitatively measured by the dissociation energy, D_e , defined as the difference between the energy of the complex and the energy of the two isolated subunits in their equilibrium conformation. However, since the formation of the complex induces a noticeably large distortion of the Lewis acid, as it has been shown previously in the literature [5] and we will discuss later, the value of D_e actually underestimates the strength of the bond, because of the large relaxation energy of the two monomers on going from the structure in the complex to their respective equilibrium conformations. A more realistic measure of the strength of the new bond is given by the interaction energy, E_{int} , defined as the difference between the energy of the complex and the energy of both monomers when they have the same structure as in the complex.

The charge transfer from the ammonia molecule to the $\text{BeH}_{2-n}\text{X}_n$ ($X = \text{F}, \text{Cl}, \text{Br}$) moiety will be quantified by means of the second order perturbation NBO analysis [2], which permits to evaluate the interaction energies between the occupied MOs of the Lewis base and the empty MOs of the Lewis acid. Within this formalism it is also possible to calculate the electron population of the initially empty orbitals of the latter, when it forms part of the complex. Also, a good index of the strength of the beryllium bond formed would be the Wiberg bond index which can be evaluated in the framework of this approach [2]. A complementary view of the bonding in the complexes under scrutiny can be achieved through the use of the atoms in molecules (AIM) theory [21], which is based in a topological analysis of the electron density. For this purpose we have obtained the molecular graphs for the isolated monomers and the complexes they form. The molecular graph is the ensemble of maxima (nuclei), saddle points (bond critical points, BCPs) of the electron density, and the bond paths which connect the former through the corresponding BCP. The values of the electron density and the energy density at these BCPs is a good index of the strength and the nature of the interaction. A negative value of the energy density is an indication of covalency in the interaction [22]. Also

useful is the description that can be obtained within the framework of the electron localization function (ELF) theory [23], which permits the partition of the molecular space in basins associated with regions occupied by electron pairs [24]. These basins are usually classified in mono-synaptic or di(poly)-synaptic, when they involve electron shells of a single atom or of two (several) ones. The population of these basins also provides interesting clues regarding the strength of the bonding between two atoms. The NBO, AIM and ELF calculations have been carried out with the NBO-5G [25], Aim-All [26] and the TopMod [27] packages, respectively.

3. Results and discussion

3.1. Structure and bonding

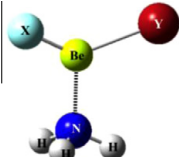
The structures of the complexes between ammonia and the $\text{BeH}_{2-n}\text{X}_n$ ($X = \text{F}, \text{Cl}, \text{Br}$) derivatives are summarized in Table 1, together with those of the different monomers.

As previously reported in the literature the first conspicuous fact is that the formation of the complex leads to a dramatic distortion of the $\text{BeH}_{2-n}\text{X}_n$ moiety, which deviates significantly from linearity, whereas the bonds lengthen in some cases as much as 0.1 Å. It is interesting to note that the XBeY angle is in all cases in the range 134–139°. Also in all cases the Be–N distance is much shorter than the sum of the corresponding van der Waals radii, and only slightly longer than in typical Be–N covalent bonds (~ 1.6 Å).

This is consistent with the molecular graph of these complexes (see Fig. 1) which show the existence of a BCP between Be and N with electron densities of the same order of magnitude as those associated to conventional covalent bonds involving Be atoms. Also, in all cases the energy density is negative, indicating a non-negligible covalent character in the bond formed between Be and N. Note for instance, that the electron density at the Be–N linkage in the $\text{NH}_3:\text{BeCl}_2$ complex is only slightly smaller than that found in the Be–Cl BCP. Also coherently, the Wiberg bond orders (~ 0.35) are sizably large for a very polar bond. Also, the ELF (see Fig. 2) shows the existence of a disynaptic basin between Be and N with a reasonably high electron population which indicates a significant covalent character for this interaction.

It is worth noting that the significant distortion of the $\text{BeH}_{2-n}\text{X}_n$ subunits is clearly seen in the molecular graphs of Fig. 1, which show that besides the bending of these subunits in the complex, there is a large decrease in the electron density at the Be–H and Be–X BCPs on going from the linear isolated molecule to the bent one in the complex. As a matter of fact, one would expect, a large charge donation from the lone pair of the ammonia molecule into the $2p$ empty orbital of Be and into the σ_{BeX}^* and σ_{BeH}^* antibonding orbitals of the $\text{BeH}_{2-n}\text{X}_n$ system. The population of the $2p$ will lead

Table 1
Optimized geometries for the $\text{NH}_3:\text{BeH}_{2-n}\text{X}_n$ ($X = \text{F}, \text{Cl}, \text{Br}$) and G4 calculated dissociation (D_e , kJ mol^{-1})^a and interaction energies (E_{int} , kJ mol^{-1})^a. Bond lengths^b in Å and bond angles in degrees.

	Complex	$R_{\text{N-Be}}$	$R_{\text{Be-X}}^c$	$R_{\text{Be-Y}}$	$\angle \text{XBeY}$	D_e	E_{int}
	$\text{NH}_3:\text{BeH}_2$	1.782	1.359 (1.325)	1.359 (1.325)	139.1	104 (96)	138 (133)
	$\text{NH}_3:\text{BeHF}$	1.783	1.359 (1.319)	1.422 (1.367)	137.2	101 (92)	139 (134)
	$\text{NH}_3:\text{BeF}_2$	1.777	1.435 (1.376)	1.435 (1.376)	138.5	122 (112)	178 (161)
	$\text{NH}_3:\text{BeHCl}$	1.754	1.349 (1.318)	1.884 (1.795)	135.3	115 (103)	161 (149)
	$\text{NH}_3:\text{BeCl}_2$	1.745	1.874 (1.796)	1.874 (1.796)	134.7	133 (116)	188 (170)
	$\text{NH}_3:\text{BeHBr}$	1.747	1.346 (1.318)	2.053 (1.952)	134.9	121 (94)	167 (154)
	$\text{NH}_3:\text{BeBr}_2$	1.737	2.038 (1.950)	2.038 (1.950)	134.3	139 (120)	193 (173)

^a The values within parenthesis were calculated at the B3LYP/6-311+G(3df,2p) level.

^b The values within parenthesis correspond to the bond lengths of the $\text{BeH}_{2-n}\text{X}_n$ isolated monomers in their equilibrium conformation.

^c X is always a H atom when $X \neq Y$.

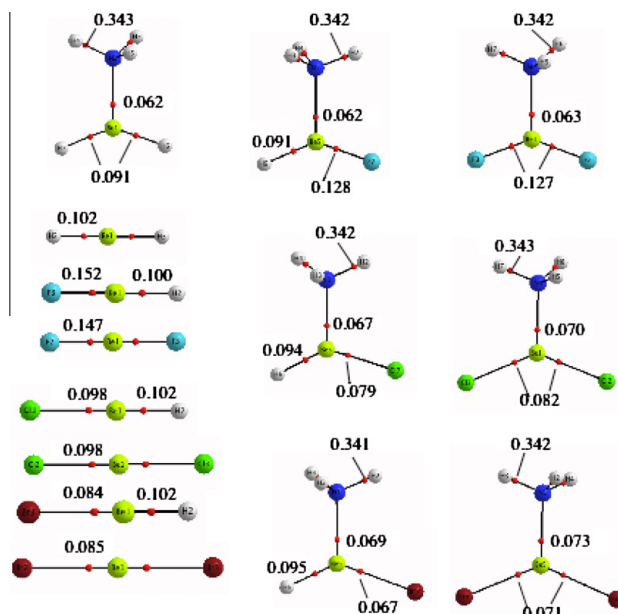


Fig. 1. Molecular graphs of the $\text{NH}_3:\text{BeH}_{2-n}\text{X}_n$ ($\text{X} = \text{F}, \text{Cl}, \text{Br}$) complexes and $\text{BeH}_{2-n}\text{X}_n$ ($\text{X} = \text{F}, \text{Cl}, \text{Br}$) isolated species. Red dots denote BCPs. Electron densities are in a.u. (For interpretation of the references to color in this figure legend, the reader is referred to the web version of this article.)

immediately to the bending of the $\text{BeH}_{2-n}\text{X}_n$ and the second charge transfer to the lengthening of the BeH and BeX bonds, and to a decrease in the electron density at the corresponding BCPs. Both effects are actually clear signatures of the formation of the beryllium bond. It is worth mentioning that in the particular cases investigated here, the charge donation from the ammonia molecule to the $\text{BeH}_{2-n}\text{X}_n$ moiety is so large, that the NBO analysis finds a very polar $\text{Be}-\text{N}$ covalent linkage, with a strong participation (90% or greater) of the hybrids centered at the N atom.

3.2. Interaction energy trends

The calculated dissociation and interaction energies have been summarized in Table 1. It can be observed that the B3LYP method slightly underbinds these complexes with respect to the G4 values. Nevertheless, the DFT approach correctly represents the trends along the series of the compounds considered since there is a very good linear correlation (see Fig. S1 of Supporting information) between the G4 and the B3LYP/6-311+G(3df,2p) calculated values with a correlation coefficient $r^2 = 0.999$.

The most interesting finding however is that the trends when the H atoms in BeH_2 are sequentially replaced by halogen atoms is not the same for all of them, and whereas for Cl and Br both D_e and E_{int} increase almost linearly, D_e goes through a minimum when only one H is substituted by F. This minimum practically disappears when looking at the interaction energies, since the E_{int} value for the complex involving the parent compound and the monosubstituted F derivative are practically equal (see Fig. 3 and Table 1).

In general, it has been normally assumed that when H is substituted by a more electronegative element, the intrinsic acidity of the system should increase [28]. However, it has been shown that this is not the case when the hydrogen atoms of BH_3 are successively replaced by F atoms [5]. Actually, although BF_3 is a stronger

Lewis acid than BH_3 , the monosubstituted and disubstituted derivatives, namely BH_2F and BHF_2 , are not. Our present results indicate that a similar behavior is observed when the sequential substitution is done on BeH_2 , since although BeF_2 behaves as a stronger Lewis acid than BeH_2 , BeHF does not. Why F is an exception with respect to the expected regular behavior? In principle a good measure of the ability of these systems to behave as Lewis acids should be given by the relative energy of their LUMO, in the sense that the lower in energy of the LUMO the higher the acidity of the system. However, an inspection of the variation of the LUMO's energy for $\text{BeH}_{2-n}\text{X}_n$ ($\text{X} = \text{F}, \text{Cl}, \text{Br}$) molecules as a function of the number of halogen substituents (see Fig. 4a) shows that independently of the nature of the halogen substituent, the energy of the LUMO reaches a maximum for $n = 1$. This would be qualitatively in agreement with the smaller D_e energy for the $\text{NH}_3:\text{BeHF}$ with respect to $\text{NH}_3:\text{BeH}_2$, but it will never explain the linear increase observed when $\text{X} = \text{Cl}, \text{Br}$. Even in the case of F substituent, one would expect a rather significant decrease in the dissociation energy, which is however very small.

This disagreement is not solved when the deformation energy of the interacting systems is included, because, as shown in Fig. 3, E_{int} exhibits the same behavior as a function of the number of halogen substituents as D_e does. However, as pointed out by Alkorta et al. [5], the distortion of the interacting molecules does not have only a significant energetic effect, which accounts for the significant difference between D_e and E_{int} values (see Table 1), but also changes significantly the intrinsic properties of the systems, in particular those related with their electron donor and/or electron acceptor capacity. In fact the bending of the $\text{BeH}_{2-n}\text{X}_n$ subunit implies an automatic mixture of the empty 2p orbital of Be with its 2s orbital, which in the linear system cannot occur because these two orbitals belong to different irreducible representations. The mixture of the 2s orbital with the 2p one should result in a stabilization of the LUMO, but the most significant result is that its energy varies

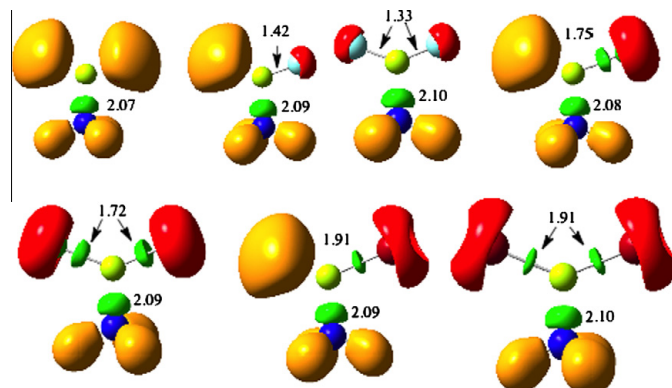


Fig. 2. ELF for the $\text{NH}_3:\text{BeH}_2-n\text{X}_n$ ($\text{X} = \text{F}, \text{Cl}, \text{Br}$) complexes. Green lobes denote disynaptic basins involving two heavy atoms. Orange lobes are disynaptic basins in which H is one of the atoms involved. Red and blue lobes correspond to lone-pairs or core monosynaptic basins. The populations shown are e^- . (For interpretation of the references to color in this figure legend, the reader is referred to the web version of this article.)

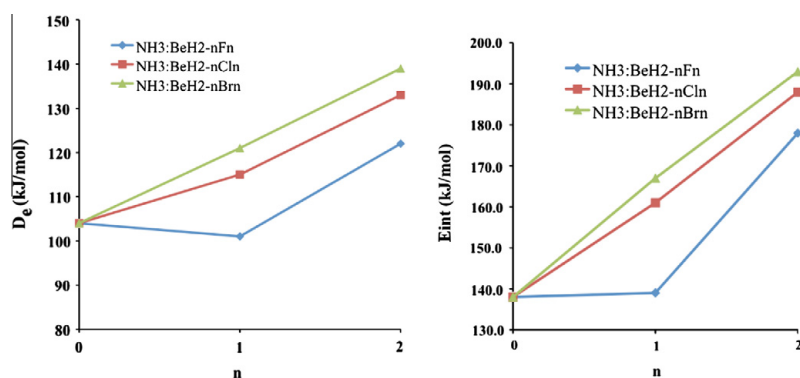


Fig. 3. Variation of the dissociation energy (D_e) and the interaction energy (E_{int}) for the BeH_2-nX_n ($\text{X} = \text{F}, \text{Cl}, \text{Br}$) complexes as a function of the number, n , of halogen substituents.

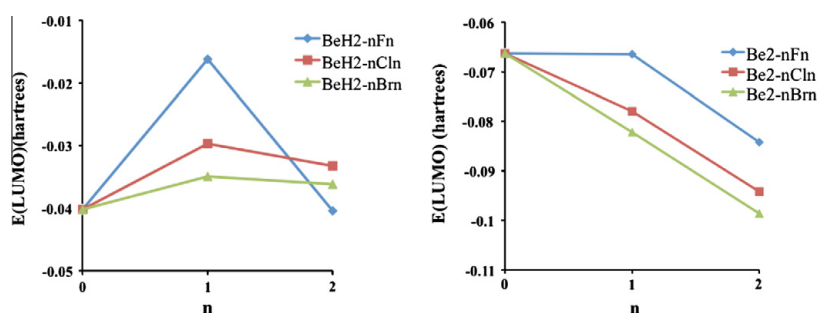


Fig. 4. Variation of the energy of the LUMO for the BeH_2-nX_n ($\text{X} = \text{F}, \text{Cl}, \text{Br}$) complexes as a function of the number, n , of halogen substituents. (left) Molecules in their equilibrium conformation; (right) molecules with the structure they have in the corresponding $\text{NH}_3:\text{BeH}_2-n\text{X}_n$ complex.

as a function of the number of halogen substituents in a quite different way as it does when the system is in its equilibrium conformation, as illustrated in Fig. 4b. The energy of the LUMO for the distorted BeH_2 and BeHF molecules is practically the same, what is now in nice agreement with the fact that both $\text{NH}_3:\text{BeH}_2$ and $\text{NH}_3:\text{BeHF}$ complexes have almost identical interaction energy

(see Table 1). Also, consistently with the linear increase of the interaction energies for the complexes containing Cl and Br, the LUMO of the distorted molecules decreases also linearly. It is worth noting that these energy values also permit to explain why BeBr_2 is the strongest Lewis acid, followed by BeCl_2 and BeF_2 , whereas a similar trend is observed for BeHBr , BeHCl and BeHF .

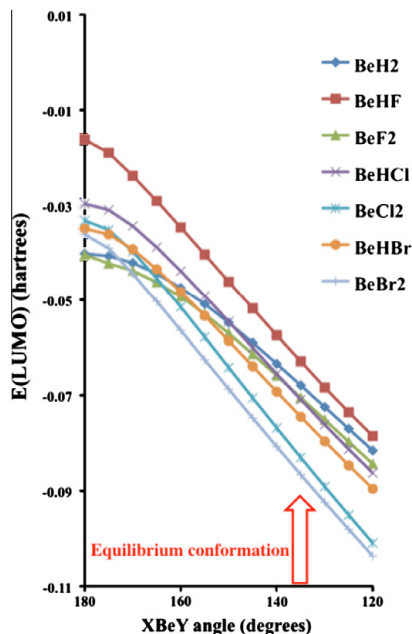


Fig. 5. Variation of the energy of the LUMO for the $\text{BeH}_{2-n}\text{X}_n$ ($\text{X} = \text{F}, \text{Cl}, \text{Br}$) complexes as a function of the XBeY angle. The arrow indicates the value of this angle when the molecule forms part of the corresponding $\text{NH}_3:\text{BeH}_{2-n}\text{X}_n$ complex.

Still it is necessary to explain, why the energy of the LUMO for the distorted BeHCl and BeHBr is larger than that of the distorted BeH_2 , whereas for BeHF , is almost equal. This can be easily understood if one examines the variation of the LUMO's energy as a function of the XBeY angle, and one remembers that the equilibrium conformation in all the complexes is reached for values of this angle around 135° (see Fig. 5).

It can be observed that the energy of the LUMO decreases faster for systems containing two halogen substituents than for those which contain only one or none. Hence, although for the linear molecules the LUMO of the parent compound is lower in energy than the LUMO of all the other derivatives, the order becomes reversed for the distorted systems. As shown in Fig. 5, the faster variation of the LUMO's energy of the halogen substituted derivatives leads to curves with a much higher slope than that corresponding to BeH_2 . The obvious consequence is that a crossing between the former and the latter takes place, which for systems like BeCl_2 or BeBr_2 occurs already at quite large angles (larger than 160°). However, although as already mentioned, the slope of the curve for BeHF is greater than that of BeH_2 , the energy gap between the LUMOs of the two undistorted linear molecules is so big that the crossing between both curves occurs for values of the XBeY angle much smaller than 120° , and therefore beyond the value of the bond angle corresponding to the equilibrium conformation. Consequently, when the equilibrium conformation is reached ($\sim 135^\circ$) the LUMO of all the derivatives is already below in energy than that of the parent compound, with the only exception of BeHF .

4. Concluding remarks

From our survey we can conclude that the $\text{BeH}_{2-n}\text{X}_n$ ($\text{X} = \text{F}, \text{Cl}, \text{Br}$) derivatives yield quite strong beryllium bonds when interact-

ing with ammonia. These strong interactions are accompanied by a dramatic distortion of these Lewis acids, which depart noticeably from linearity whereas the $\text{Be}-\text{H}$ and $\text{Be}-\text{X}$ bonds become significantly longer in the corresponding $\text{NH}_3:\text{BeH}_{2-n}\text{X}_n$ complexes than in the isolated systems in their equilibrium conformation. More importantly, the deformation undergone by the Lewis acid in the complex plays a crucial role as far as the relative stability trends are concerned. On the one hand, about 30% or more of the interaction energy comes from the deformation energy of the monomers. On the other hand, the deformation significantly enhances the electron acceptor capacity of the Lewis acid, which follows completely different trends from those expected for the undistorted systems. In this respect, a frontier orbital theory is able to explain the trends observed in the interaction energies, provided that it is carried out on the distorted systems rather than on the systems in their equilibrium conformation.

Acknowledgments

This work has been partially supported by the DGI Projects No. CTQ2009-13129-C02-01, CTQ2009-07197-E, by the Project MADRISOLAR2, Ref.: S2009PPQ/1533 of the Comunidad Autónoma de Madrid, by Consolider on Molecular Nanoscience CSC2007-00010, and by the COST Action CM0702. A generous allocation of computing time at the CCC of the UAM is also acknowledged. A.M.S. acknowledges a FPI grant from the Ministry of Science and Innovation of Spain.

Appendix A. Supplementary material

Supplementary data associated with this article can be found, in the online version, at <http://dx.doi.org/10.1016/j.comptc.2012.06.009>.

References

- [1] P. Hobza, R. Zahradník, K. Müller-Dethlefs, The world of non-covalent interactions, Collect. Czech. Chem. Commun. 71 (2006) 443–531.
- [2] A.E. Reed, L.A. Curtiss, F. Weinhold, Intermolecular interactions from a natural bond orbital, donor-acceptor viewpoint, Chem. Rev. 88 (1988) 899–926.
- [3] H. Kleeberg, D. Klein, W.A.P. Luck, Quantitative infrared spectroscopic investigations of hydrogen-bond cooperativity, J. Phys. Chem. 91 (1987) 3200–3203.
- [4] M. Yáñez, P. Sanz, O. Mó, I. Alkorta, J. Elguero, Beryllium bonds, do they exist?, J. Chem. Theor. Comput. 5 (2009) 2763–2771.
- [5] I. Alkorta, J. Elguero, J.E. Del Bene, O. Mó, M. Yáñez, New insights into factors influencing B–N bonding in $\text{X}:\text{BH}_{3-n}\text{F}_n$ and $\text{X}:\text{BH}_{3-n}\text{Cl}_n$ for $\text{X} = \text{N}_2, \text{HCN}, \text{LiCN}, \text{H}_2\text{CNH}, \text{NF}_3, \text{NH}_3$ and $n = 0-3$: the importance of deformation, Chem. Eur. J. 16 (2010) 11897–11905.
- [6] T. Brinck, J.S. Murray, P. Politzer, A computational analysis of the bonding in boron-trifluoride and boron-trichloride and their complexes with ammonia, Inorg. Chem. 32 (1993) 2622–2625.
- [7] B.D. Rowsell, F.J. Gillespie, G.L. Heard, Ligand close-packing and the Lewis acidity of BF_3 and BCl_3 , Inorg. Chem. 38 (1999) 4659–4662.
- [8] F. Bessac, G. Frenking, Why is BCl_3 a stronger Lewis acid with respect to strong bases than BF_3 ?, Inorg. Chem. 42 (2003) 7990–7994.
- [9] K. Fukui, T. Yonezawa, H. Shingu, A molecular orbital theory of reactivity in aromatic hydrocarbon, J. Chem. Phys. (1952) 722.
- [10] I. Fleming, Frontier Orbitals and Organic Chemical Reactions, Wiley, London, 1978.
- [11] L.A. Curtiss, P.C. Redfern, K. Raghavachari, Gaussian-4 theory, J. Chem. Phys. 126 (2007) 12.
- [12] L.A. Curtiss, P.C. Redfern, K. Raghavachari, Gn theory, Wiley Interdiscip. Rev. Comput. Mol. Sci. 1 (2011) 810–825.
- [13] A.D. Becke, Density-functional thermochemistry. III. The role of exact exchange, J. Chem. Phys. 98 (1993) 5648–5652.
- [14] C. Lee, W. Yang, R.G. Parr, Development of the Colle-Salvetti correlation-energy formula into a functional of the electron density, Phys. Rev. B 37 (1988) 785–789.
- [15] K. Kim, K.D. Jordan, Comparison of density-functional and MP2 calculations on the water monomer and dimer, J. Phys. Chem. 98 (1994) 10089–10094.
- [16] C.W. Bauschlicher Jr., A comparison of the accuracy of different functionals, Chem. Phys. Lett. 246 (1995) 40–44.

- [17] A.L. Llamas-Saiz, C. Foces-Foces, O. Mó, M. Yáñez, E. Elguero, J. Elguero, The geometry of pyrazole: a test for ab initio calculations, *J. Comput. Chem.* 16 (1995) 263–272.
- [18] A.M. Mebel, K. Morokuma, M.C. Lin, Modification of the Gaussian-2 theoretical-model – the use of coupled-cluster energies, density-functional geometries, and frequencies, *J. Chem. Phys.* 103 (1995) 7414–7421.
- [19] J.A. Montgomery Jr., M.J. Frisch, J. Ochterski, G.A. Petersson, A complete basis set model chemistry. VI. Use of density functional geometries and frequencies, *J. Chem. Phys.* 110 (1999) 2822–2827.
- [20] M.J. Frisch, G.W. Trucks, H.B. Schlegel, G.E. Scuseria, M.A. Robb, J.R. Cheeseman, G. Scalmani, V. Barone, B. Mennucci, G.A. Petersson, H. Nakatsuji, M. Caricato, X. Li, H.P. Hratchian, A.F. Izmaylov, J. Bloino, G. Zheng, J.L. Sonnenberg, M. Hada, M. Ehara, K. Toyota, R. Fukuda, J. Hasegawa, M. Ishida, T. Nakajima, Y. Honda, O. Kitao, H. Nakai, T. Vreven, J. Montgomery, J.E. Peralta, F. Ogliaro, M. Bearpark, J.J. Heyd, E. Brothers, K.N. Kudin, V.N. Staroverov, R. Kobayashi, J. Normand, K. Raghavachari, A. Rendell, J.C. Burant, S.S. Iyengar, J. Tomasi, M. Cossi, N. Rega, J.M. Millam, M. Klene, J.E. Knox, J.B. Cross, V. Bakken, C. Adamo, J. Jaramillo, R. Gomperts, R.E. Stratmann, O. Yazyev, A.J. Austin, R. Cammi, C. Pomelli, J.W. Ochterski, R.L. Martin, K. Morokuma, V.G. Zakrzewski, G.A. Voth, P. Salvador, J.J. Dannenberg, S. Dapprich, A.D. Daniels, O. Farkas, J.B. Foresman, J.V. Ortiz, J. Cioslowski, D.J. Fox, Gaussian09, Revision A.02, Gaussian Inc., Wallingford CT, 2009.
- [21] R.F.W. Bader, *Atoms in Molecules. A Quantum Theory*, Clarendon Press, Oxford, 1990.
- [22] D. Cremer, E. Kraka, Chemical bonding without binding electron densities – is differential density analysis sufficient for bonding description?, *Angew. Chem.* 96 (1984) 612–614.
- [23] A.D. Becke, K.E. Edgecombe, A simple measure of electron localization in atomic and molecular systems, *J. Chem. Phys.* 92 (1990) 5397–5403.
- [24] A. Savin, R. Nesper, S. Wengert, T.F. Fäster, ELF: the electron localization function, *Angew. Chem. Int. Ed. Engl.* 36 (1997) 1808–1832.
- [25] E.D. Glendening, J. Badenhoop, A.E. Reed, J.E. Carpenter, J.A. Bohmann, J.A. Morales, F. Weinhold, NBO 5G Program, 2001.
- [26] T.A. Keith, AIMAll (Version 11.12.19), in: T.G. Software (Ed.), Overland Park KS, USA, 2011.
- [27] S. Noury, X. Krokidis, F. Fuster, B. Silvi, Computational tools for the electron localization function topological analysis, *Comput. Chem.* 23 (1999) 597–604.
- [28] J.A. Plumley, J.D. Evanseck, Periodic trends and index of boron Lewis acidity, *J. Phys. Chem. A* 113 (2009) 5985–5992.

Are Boryl Radicals from Amine–Boranes and Phosphine–Boranes the Most Stable Radicals?

Ana Martín-Sómer, Otilia Mó, and Manuel Yáñez^{*[a]}

The relative stability of the radicals that can be produced from amine–boranes and phosphine–boranes is investigated at the G3-RAD level of theory. Aminyl ($[\text{RNH}]^{\cdot}\text{BH}_3$) and phosphinyl ($[\text{RPH}]^{\cdot}\text{BH}_3$) radicals are systematically more stable than the boryl analogues, $[\text{RNH}_2]^{\cdot}\text{BH}_2^{\cdot}$ and $[\text{RPH}_2]^{\cdot}\text{BH}_2^{\cdot}$. Despite similar stability trends for $[\text{RNH}]^{\cdot}\text{BH}_3$ and $[\text{RPH}]^{\cdot}\text{BH}_3$ radicals with respect to boryl radicals, there are significant dissimilarities between amine– and phosphine–boranes. The homolytic bond

dissociation energy of the N–H bond decreases upon association of the amines with BH_3 , whereas that of the P–H bond for phosphines increases. The stabilization of the free amine is much smaller than that of the corresponding aminyl radical, whereas for phosphines this is the other way around. The homolytic bond dissociation energy of the B–H bond of borane decreases upon complexation with both amines and phosphines.

1. Introduction

The association of amines and phosphines with borane not only leads to the formation of very stable complexes, the amine–boranes and phosphine–boranes, but also strongly modifies the properties of both the free phosphine (or amine) and the free borane. For instance, whereas phosphines are very volatile and pyrophoric, phosphine–boranes are much less volatile and not at all pyrophoric.^[1] More importantly, in the gas phase, free amines and phosphines are typical N and P bases, whereas amine–boranes and phosphine–boranes are very strong N and P acids, respectively.^[2] For instance, the association of aniline with borane leads to a typical nitrogen base (aniline) in an aniline–borane complex that behaves as an N acid stronger than phosphoric acid, which is an oxyacid.^[2b] Recently, it has also been shown that a tricoordinated amine–boron derivative acts as a Lewis base, rather than as a Lewis acid.^[3]

Interest in these complexes has been revived in recent years because of their very rich chemistry,^[4] their potential application in molecular hydrogen storage,^[5] and because they can be used as hydrogen-atom-releasing systems in radical reactions.^[6] Some of them have been used as new photoinitiating species,^[6d,g,i] although this application is frequently hindered by the high B–H dissociation energy,^[6k] and in enantioselective radical processes.^[7] They are also very nucleophilic^[8] and have been used as polarity-reversal catalysts,^[6c,e,9] and some of them present interesting photochemical properties.^[10]

In most experimental applications, however, only boryl radicals are obtained because the complexes normally used in the corresponding radical reactions involve tertiary amines or phosphines,^[6a–c,e–l,11] and therefore, no hydrogen atoms at

these sites are available for removal to produce the corresponding N- or P-centered radicals. The same situation arises when dealing with N-heteroaryl boranes.^[6l,k] However, in principle, if the amine– or phosphine–borane involves primary or secondary amines or phosphines, they can yield aminyl or phosphinyl radicals by hydrogen abstraction on the amine (or phosphine) function or boryl radicals, if hydrogen abstraction takes place from the borane.^[6l] More importantly, as it is the case with their intrinsic acidity,^[2] the ability to release hydrogen atoms increases in the complex compared with that of the isolated subunits.^[5a,6f] It has also recently been shown that amine–boranes involving secondary amines, $\text{R}_2\text{NH}:\text{BH}_3$, may undergo catalytic dehydrocoupling either producing $[\text{R}_2\text{N}=\text{BH}_2]_2$ cyclic dimers or, if R is a bulky substituent, $\text{R}_2\text{N}=\text{BH}_2$ monomeric species.^[12] These results indicate that both the amino and borane centers behave as active radical centers. It is not clear, however, which of the two processes is intrinsically the most favorable; in other words, is the formation of the boryl radical the most favorable process? This is the question we have tried to answer herein by investigating the stability of boryl radicals obtained from a series of amine– and phosphine–boranes, involving primary and secondary amines and phosphines with respect to the radicals obtained when the H atom is lost from the amino or phosphine group.

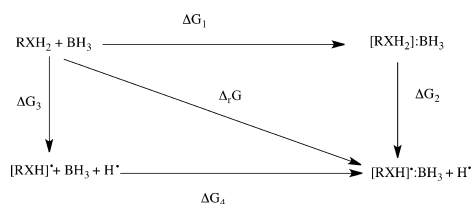
Computational Details

An accurate theoretical description of radicals is not a trivial matter. The relative stability of BH_2^{\cdot} , as defined from the homolytic bond dissociation energy of BH_3 , varies significantly with the theoretical model used in the calculation and the theoretical values differ significantly from the available experimental ones.^[6l] In this context, it should be mentioned that some accurate bond dissociation energies for $\text{H}_{3-n}\text{BX}_n$ ($\text{X} = \text{F}, \text{Cl}, \text{Br}, \text{I}, \text{NH}_2, \text{OH}$, and SH) have been reported.^[13]

[a] A. Martín-Sómer, O. Mó, M. Yáñez
Departamento de Química, Facultad de Ciencias
Módulo 13, Universidad Autónoma de Madrid
Campus de Excelencia UAM-CSIC, Cantoblanco
28049 Madrid (Spain)

For our study, we used the G3-RAD method,^[14] which is a composite approach, similar to G3 theory, which has been specifically designed to provide reliable thermochemistry for radicals. In this composite method, the correlation contributions from diffuse and high-angular momentum components in the basis set were additive and were evaluated at the MP4/6-31+G(d) and MP4/6-31G(2df,p) level of theory, respectively, and added to the energy of the radical obtained from a CCSD(T)/6-31G(d) calculation. A further contribution from enlarging the number of polarization functions was obtained at the MP2/G3Large level. The total final energy was obtained after adding an empirical high-level correction (HLC) term that depended on the number of α and β valence electrons and the zero-point energy (ZPE) correction. For these G3-RAD calculations, we used B3LYP/6-31+G(d,p) optimized geometries. The thermal corrections to calculate free energies were also obtained at this latter level of theory. Because the G3-RAD method can become too computationally demanding, the final free energies were also obtained in single-point B3LYP/6-311++G(3df,2p) calculations, by using the B3LYP/6-31+G(d,p)-optimized geometries and thermal corrections to assess the reliability of this cheaper theoretical model.

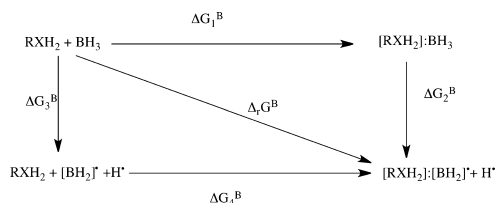
The effects of the association with BH_3 on the relative stability of the radicals $[\text{RXH}]^\bullet\text{:BH}_3$ ($\text{X}=\text{N}, \text{P}$) produced from the corresponding amine- and phosphine-boranes could be analyzed in terms of the thermodynamic cycle shown in Scheme 1.



Scheme 1. Thermodynamic cycle relating the stabilization of free amines or phosphines ($\text{X}=\text{N}, \text{P}$) and their aminyl and phosphinyl radicals by association with BH_3 .

In Scheme 1, ΔG_1 and ΔG_4 measure the stabilization of the amine (phosphine) and of the corresponding $[\text{RXH}]^\bullet$ ($\text{X}=\text{N}, \text{P}$) radical by association with BH_3 , respectively, whereas ΔG_3 and ΔG_2 measure the homolytic $\text{X}-\text{H}$ bond dissociation energy for the free amine (phosphine) and for the amine (phosphine) in the complex with BH_3 , respectively.

Similarly, the effects on the stability of the $[\text{BH}_2]^\bullet$ boryl radical by its association with amines or phosphines could be analyzed by means of the thermodynamic cycle shown in Scheme 2, in which



Scheme 2. Thermodynamic cycle relating the stabilization of BH_3 and its $[\text{BH}_2]^\bullet$ boryl radical by association with amines and phosphines ($\text{X}=\text{N}, \text{P}$).

ΔG_1^B and ΔG_4^B measure the stabilization of BH_3 and the $[\text{BH}_2]^\bullet$ radical by their interaction with an amine (phosphine), and ΔG_3^B and ΔG_2^B measure the homolytic $\text{B}-\text{H}$ bond dissociation energy for the free BH_3 molecule and for the same molecule within the complex with the amine (phosphine).

For the sake of consistency, the free energies of the amine- and phosphine-boranes $\text{RXH}_2\text{:BH}_3$ ($\text{X}=\text{N}, \text{P}$) and of the free amines and phosphines needed to calculate the free energy changes in Schemes 1 and 2 were calculated at the G3B3 level of theory.

2. Results and Discussion

In our survey, we considered primary amine- and primary phosphine-boranes $\text{RXH}_2\text{:BH}_3$ ($\text{X}=\text{N}, \text{P}$), in which the substituent R could be a saturated alkyl group, namely, methyl, *c*-propyl, and isopropyl; an unsaturated one, namely, vinyl and ethynyl; or an aromatic one, phenyl, *p*- NH_2 -phenyl, *p*- NO_2 -phenyl, and benzyl. To see if some significant differences on the relative stability of the radicals produced were observed when changing from primary to secondary amine- or phosphine-boranes, we also included dimethyl, diethynyl, and diphenyl derivatives in our set as representative cases of saturated, unsaturated, and aromatic substituents. For the last two cases, and for the sake of economy, the calculations were performed only at the DFT level. The optimized geometries of the free amines (phosphines), amine- and phosphine-borane complexes, and all the radicals they produce by the homolytic dissociation of the $\text{X}-\text{H}$ ($\text{X}=\text{N}, \text{P}$) and the $\text{B}-\text{H}$ bonds as well as their total free energies are available from the authors upon request. In Table 1, we have summarized the relative free energies of the $\text{RXH}_2\text{:}[\text{BH}_2]^\bullet$ ($\text{X}=\text{N}, \text{P}$) boryl radicals with respect to the corresponding aminyl and phosphinyl $[\text{RXH}]^\bullet\text{:BH}_3$ radicals, so that positive values indicate that the latter are more stable than the former.

It is apparent that, regardless of the level of theory used, the boryl radicals are systematically less stable than the radicals in which the H atom departs from the NH_2 or PH_2 groups. The

Table 1. Relative free energies [kJ mol^{-1}] of $\text{RXH}_2\text{:}[\text{BH}_2]^\bullet$ ($\text{X}=\text{N}, \text{P}$) boryl radicals with respect to the corresponding $[\text{RXH}]^\bullet\text{:BH}_3$ ($\text{X}=\text{N}, \text{P}$) counterparts.

R	Amine-boranes		Phosphine-boranes	
	G3-RAD	B3LYP	G3-RAD	B3LYP
primary derivatives				
methyl (1)	38.7	67.7	13.2	18.1
<i>c</i> -propyl (2)	54.0	83.4	15.3	21.4
isopropyl (3)	34.6	60.7	10.6	14.7
vinyl (4)	89.6	118.0	28.4	36.1
ethynyl (5)	93.7	132.7	31.1	39.9
phenyl (6)	81.9	108.4	27.1	33.8
<i>p</i> - NH_2 -phenyl (7)	99.7	125.7	31.1	40.6
<i>p</i> - NO_2 -phenyl (8)	30.4	56.3	−3.8	−5.8
benzyl (9)	42.8	70.1	11.4	14.2
secondary derivatives				
dimethyl (10)	72.3	85.3	10.4	17.1
diethynyl (11)	–	185.9	–	56.3
diphenyl (12)	–	119.4	–	31.2

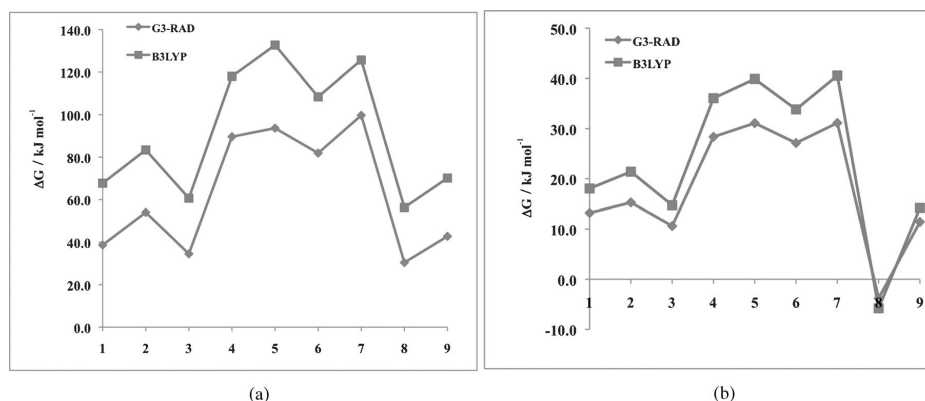


Figure 1. Variation of the free energy gap of the boryl radicals $\text{RXH}_2\cdot\text{BH}_2$ ($\text{X} = \text{N, P}$) with respect to a) the corresponding aminyl $[\text{RNH}]\cdot\text{BH}_3$ radicals, and b) the corresponding phosphinyl $[\text{RPH}]\cdot\text{BH}_3$ radicals. Positive values of ΔG indicate that boryl radicals are less stable than aminyl or phosphinyl ones.

only exception to this general behavior is that of the phosphine in which the substituent is *p*- NO_2 -phenyl (**8**), which is discussed in detail later. It can also be observed that the B3LYP method overestimates the free energy gaps between boryl and aminyl or phosphinyl radicals (see Figure 1); this overestimation is larger when dealing with amine–boranes (note the different scale). Nevertheless, the stability trends are very well reproduced by the B3LYP method, as shown in Figure 1.

It is also worth noting that the relative stability of the radicals does not change significantly with the characteristics of the alkyl substituents because it is similar for methyl (**1**) and isopropyl (**3**) substituents. However, the gap becomes larger for the *c*-propyl (**2**) derivative, in which, due to ring strain, the hybridization of the C atom attached to the N or P atom is different from that of substituents **1** and **3**. The sensitivity of the relative stability to the hybridization of the C atom directly bonded to the amino or phosphine group is also evident when looking at the sizable increase in the energy gap between boryl and N- or P-centered radicals when the substituent is unsaturated [vinyl (**4**), ethynyl (**5**)] or aromatic [phenyl (**6**)]. Notably, the calculated energy gap for the benzyl (**9**) substituent is consistently similar to that of the alkyl substituents **1** and **3**, which indicates that the presence of an aromatic ring in the benzyl group has no influence on this gap and that only the hybridization of the C atom attached to the basic site matters. It is also interesting to observe that the inclusion of an electron-releasing amino group in the *para* position of the aromatic ring, upon going from the phenyl substituent (**6**) to the *p*- NH_2 -phenyl one (**7**) increases the energy gap. If the substituent group at the *para* position is electron withdrawing, as in the *p*-nitrophenyl (**8**), the gap decreases dramatically. As a conse-

quence, the phosphine is the only case in which the boryl radical is predicted to be slightly more stable than the phosphinyl one (see Table 1). It is worth noting, however, that the decrease in the energy gap is much larger for the amine–borane (51.5 kJ mol^{-1}) than for the analogous phosphine–borane (30.9 kJ mol^{-1}). This dissimilarity between stability of the *p*- NO_2 -phenylamine and *p*- NO_2 -phenylphosphine radicals has its origin in the structural peculiarities of the $[\text{p-NO}_2\text{-phenyl-NH}_2\cdot\text{BH}_2]$ radical with respect to the $[\text{p-NO}_2\text{-phenyl-PH}_2\cdot\text{BH}_2]$ one. As shown in Figure 2, in the former, a three-membered

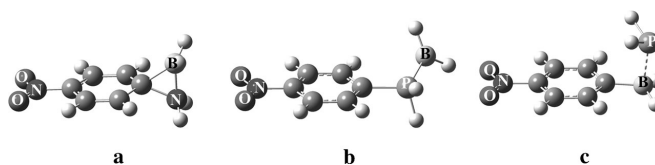


Figure 2. Local minima of the $[\text{p-NO}_2\text{-phenyl-NH}_2\cdot\text{BH}_2]$ (a), $[\text{p-NO}_2\text{-phenyl-PH}_2\cdot\text{BH}_2]$ (b and c) radicals. Structure c is obtained by starting from a cyclic arrangement similar to that in form a.

ring is formed through the bonding of the BH_2 group to the substituted aromatic carbon (structure a), whereas this cyclization is not observed for the phosphine analogue (structure b). The main consequence is that, whereas $[\text{p-NO}_2\text{-phenyl-PH}_2\cdot\text{BH}_2]$ is a boryl radical, with a spin density at the boron atom of 0.75, $[\text{p-NO}_2\text{-phenyl-NH}_2\cdot\text{BH}_2]$ is not. The bond between the B and the C atoms of the aromatic ring favors a spin-density redistribution and the spin density appears to be mainly localized at the two carbon atoms at the *ortho* position with respect to the nitro group, whereas that at the boron atom is rather small (0.2). We have tried to find an a-type cyclic structure for the $[\text{p-NO}_2\text{-phenyl-PH}_2\cdot\text{BH}_2]$ radical, similar to the one found for $[\text{p-NO}_2\text{-phenyl-NH}_2\cdot\text{BH}_2]$, but the three-membered ring is never formed because it collapses into a new structure (Figure 2c), in which a deep rearrangement

takes place. Indeed, the initial bond between the P atom and the aromatic ring is replaced by a C–B bond, whereas the PH_2 group has a weak interaction with the BH_2 one. Furthermore, the spin density is mainly located on the PH_2 group, so the complex can be viewed as an interaction between a $p\text{-NO}_2\text{-phenyl-BH}_2$ molecule and a PH_2^\bullet radical. The $[p\text{-NH}_2\text{-phenyl-NH}_2\text{:BH}_2]^\bullet$ and $[\text{phenyl-NH}_2\text{:BH}_2]^\bullet$ a-type structures, in which the NH_2 and the BH_2 groups form a three-membered ring with one carbon of the aromatic ring, were also found to be local minima, but higher in energy than those of conventional b-type structures.

The enhanced stability of aminyl and phosphinyl radicals with respect to the boryl counterparts is also observed for the secondary amine- and phosphine-boranes (10–12), although, in general, the gap is even larger, in particular, if the substituent is unsaturated or aromatic (see Table 1).

2.1. Effects of Borane on the Stability of Aminyl and Phosphinyl Radicals

If the relative stability trends for amine-boranes and phosphine-boranes are compared (see Figure 3), the first conspicuous fact is that the energy gap between the aminyl and boryl radicals is at least twice that between the phosphinyl and boryl radicals.

These significant quantitative differences can be rationalized by means of the thermodynamic cycle shown in Scheme 1. The free energies associated with the processes defined in this cycle for both amine- and phosphine-boranes are shown in Table 2.

As it could be easily anticipated, the values for ΔG_2 and ΔG_3 are positive and larger for amines and amine-boranes than those for the phosphine analogues; this shows that the homolytic dissociation of the N–H bonds demands more energy than that of the P–H bonds. There is however a significant difference. As illustrated in Figure 4, whereas the association of amines with BH_3 leads to a decrease in the homolytic bond dissociation energy of the N–H bond ($\Delta G_2 < \Delta G_3$), for the phosphines it is the other way around and the homolytic bond

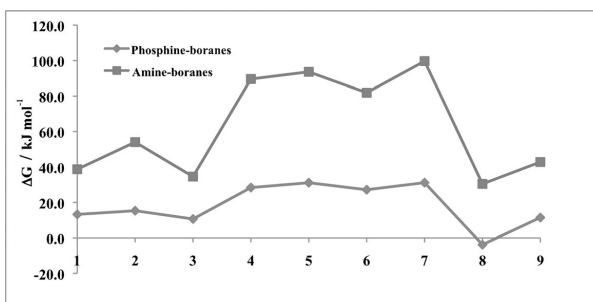


Figure 3. Variation in the free energy gap between boryl radicals, $\text{RXH}_2\cdot[\text{BH}_2]^\bullet$ ($\text{X} = \text{N}, \text{P}$), and the corresponding aminyl, $[\text{RNH}]^\bullet\text{:BH}_3$, and phosphinyl, $[\text{RPH}]^\bullet\text{:BH}_3$, radicals.

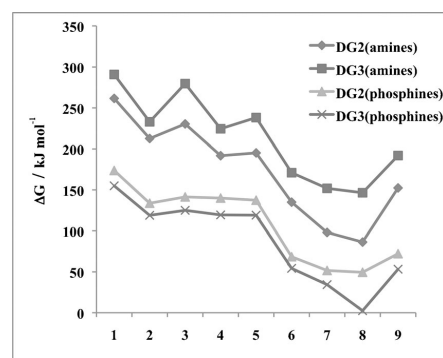


Figure 4. Values of ΔG_2 and ΔG_3 from the thermodynamic cycle shown in Scheme 1 for the series of primary amines and phosphines investigated herein; for the former $\Delta G_2 < \Delta G_3$, whereas for the latter $\Delta G_2 > \Delta G_3$.

dissociation energy of the P–H bond increases upon complexation with BH_3 ($\Delta G_2 > \Delta G_3$).

Very importantly, for both series of compounds, complexation with BH_3 stabilizes both the free amine (or free phosphine; $\Delta G_1 < 0$) and the corresponding radical ($\Delta G_4 < 0$). The stabilization of this radical through association with BH_3 is in agreement with the findings of Braida et al.,^[15] who showed

Table 2. Free energies [kJ mol^{-1}] corresponding to the processes involved in the thermodynamic cycle shown in Scheme 1 for primary amines, RNH_2 , and phosphines, RPH_2 .

R	ΔG_1		ΔG_2		ΔG_3		ΔG_4	
	RNH_2	RPH_2	RNH_2	RPH_2	RNH_2	RPH_2	RNH_2	RPH_2
1	−96.8	−77.6	261.6	173.7	290.9	155.0	−126.0	−59.0
2	−91.1	−72.2	212.6	133.7	233.0	118.9	−111.5	−57.3
3	−90.2	−77.0	230.4	141.4	279.7	125.0	−139.5	−60.6
4	−81.0	−71.3	191.8	140.0	224.5	119.4	−113.7	−50.7
5	−38.0	−55.0	195.2	137.4	238.2	119.1	−81.0	−36.7
6	−69.1	−68.0	135.0	68.5	171.0	54.3	−105.1	−53.7
7	−75.3	−75.8	98.1	51.7	151.9	34.4	−129.1	−58.6
8	−55.6	−65.5	86.4	49.5	146.5	2.5	−115.7	−18.5
9	−90.6	−77.3	152.4	72.2	192.0	53.3	−130.2	−58.3

that strong adducts could be formed between $\cdot\text{AR}_3$ ($\text{A}=\text{C}, \text{Si}, \text{Ge}$) radicals and boranes BX_3 .

Again there is a subtle difference between amines and phosphines. The stabilization of the free systems upon association with borane (ΔG_1) is similar for both amines and phosphines (see Figure 5). In general, this stabilization is slightly greater for amines, but not always. However, the stabilization of the aminyl radicals upon BH_3 attachment (ΔG_4) is twice as large (in absolute value) as that of the phosphinyl radicals. The most important consequence is that for amines the radical becomes much more stabilized than the free amine ($|\Delta G_4| > |\Delta G_1|$), whereas for phosphines it is the other way around ($|\Delta G_4| < |\Delta G_1|$). It is worth mentioning that there is also an interesting difference in the B–N and B–P distances. For the amines, hydrogen abstraction from the amino group to form the corresponding aminyl radical leads to a shortening of the B–N bond (ca. 0.17 Å), whereas the opposite is found for phosphines, for which a similar process leads to a slight lengthening of the P–B linkage (ca. 0.02 Å).

2.2. Effects of Amines and Phosphines on the Stability of Boryl Radicals

The picture of the factors affecting the relative stability of boryl radicals with respect to aminyl and phosphinyl radicals can only be complete by analyzing the effect of amines and phosphines on the formation of boryl radicals. The energetics involved in these processes can be understood by means of the thermodynamic cycle outlined in Scheme 2. The values of the free energies involved are summarized in Table 3. Notably, the value of ΔG_1^B is the same as that of ΔG_1 in the cycle outlined in Scheme 1, since it corresponds to stabilization of the free amine or phosphine by association with BH_3 . It is also evident that ΔG_3^B is independent of the nature of the amine or phosphine because it corresponds to the formation of the boryl radical $\text{BH}_2\cdot$ from BH_3 .

The first conspicuous fact gained from the values in Table 3 is that the homolytic bond dissociation energy of the B–H bond of borane decreases upon complexation with amines and phosphines ($\Delta G_3^B < \Delta G_3^B$); this decrease is significantly greater for the phosphines. A similar effect with other Lewis bases was reported previously in the literature.^[16] It should be

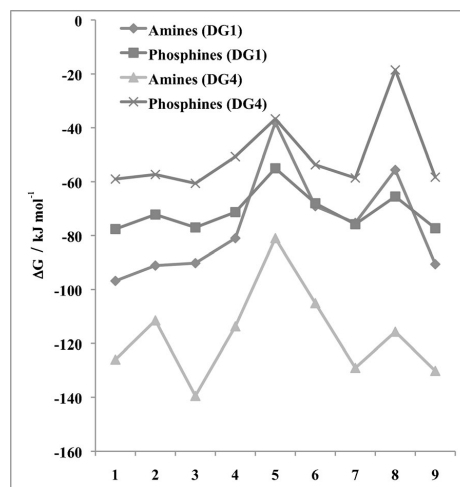


Figure 5. Values of ΔG_1 and ΔG_4 from the thermodynamic cycle shown in Scheme 1 for the series of primary amines and phosphines investigated herein; for the former $|\Delta G_4| > |\Delta G_1|$, whereas for the latter $|\Delta G_4| < |\Delta G_1|$.

noted that the formation of boryl radicals from aminoboranes is accompanied by a slight shortening of the B–N bond (ca. 0.04 Å). The same effect, but much larger, is observed for phosphine–boranes, for which shortening of the B–P bond is about 0.08 Å. Hence, very importantly, the boryl $\text{BH}_2\cdot$ radical becomes more stabilized than BH_3 by association with amines and phosphines, as reflected by the larger absolute value of ΔG_4^B with respect to that of ΔG_1^B ; this stabilization effect is larger for phosphines than that for amines. The fact that the relative stability of aminyl with respect to boryl radicals is much larger than that between phosphinyl and boryl radicals is the result of two concomitant factors: 1) aminyl radicals are more stabilized upon association with BH_3 than the parent free amines, whereas for phosphines it is the other way around; and 2) phosphines stabilize the boryl radical more than amines.

The dissimilarities between amines and phosphines are also mirrored in the free energy of the overall formation reactions ($\Delta_r G$ and $\Delta_r G^B$ in Schemes 1 and 2, respectively) of the aminyl, phosphinyl, and boryl radicals (see Table 4). These processes are endergonic, with the exception of the formation of $[\text{RPH}]\cdot\text{BH}_3$ phosphinyl radicals if substituent R is a *p*- NH_2Ph - (7), *p*- NO_2Ph - (8), or benzyl (9) group, but they are more endergonic for amines than those for phosphines; this reflects the lower homolytic dissociation energy of the P–H bond with respect to that of the N–H bond.

Consistently with our previous discussion, the formation of the

Table 3. Free energies [kJ mol^{-1}] corresponding to the processes^[a] involved in the thermodynamic cycle shown in Scheme 2.

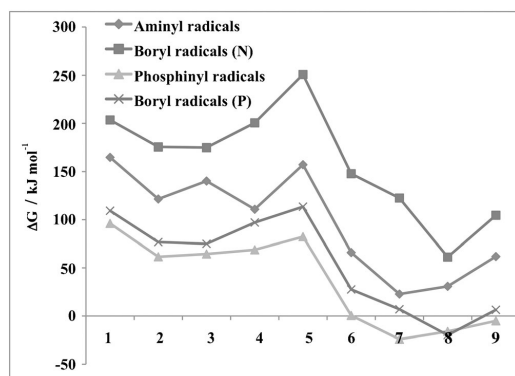
R	ΔG_1^B		ΔG_2^B		ΔG_4^B	
	RNH_2	RPH_2	RNH_2	RPH_2	RNH_2	RPH_2
1	−96.8	−77.6	300.3	186.9	−144.0	−238.2
2	−91.1	−72.2	266.6	149.0	−172.0	−270.7
3	−90.2	−77.0	265.0	152.0	−172.7	−272.5
4	−81.0	−71.3	281.5	168.4	−147.0	−250.4
5	−38.0	−55.0	288.8	168.5	−96.7	−234.0
6	−69.1	−68.0	216.9	95.6	−199.7	−319.8
7	−75.3	−75.8	197.8	82.8	−225.0	−340.5
8	−55.6	−65.5	116.8	45.7	−286.3	−367.3
9	−90.6	−77.3	195.2	83.7	−242.8	−341.1

[a] $\Delta G_3^B = 347.5 \text{ kJ mol}^{-1}$ corresponds to the process $\text{BH}_3 \rightarrow \text{BH}_2\cdot + \text{H}\cdot$.

Table 4. Free energies, $\Delta_r G$ and $\Delta_r G^\circ$ [kJ mol⁻¹], corresponding to the formation of aminyl ([RNH]·:BH₃), phosphinyl ([RPH]·:BH₃), boryl(N) ([RNH₂]:BH₂·), and boryl(P) ([RPH₂]:BH₂·) radicals (see Schemes 1 and 2).

R	$\Delta_r G$		$\Delta_r G^\circ$	
	[RNH]·:BH ₃	[RPH]·:BH ₃	[RNH ₂]:BH ₂ ·	[RPH ₂]:BH ₂ ·
1	164.8	96.1	203.5	109.3
2	121.5	61.5	175.5	76.8
3	140.2	64.4	174.8	75.0
4	110.8	68.7	200.5	97.1
5	157.2	82.4	250.8	113.5
6	65.9	0.5	147.8	27.6
7	22.8	-24.1	122.5	7.0
8	30.8	-16.0	61.2	-19.8
9	61.8	-5.0	104.7	6.4

boryl [RXH₂]:BH₂· (X=N, P) radicals is more endergonic than the formation of the analogous N- and P-centered radicals. Significantly, due to the lower stabilization of the phosphinyl radicals upon BH₃ association and to the very large stabilization of the BH₂· boryl radical when associated with a phosphine, the gap between the free energies for the formation of the [RPH]·:BH₃ and [RPH₂]:BH₂· radicals is much smaller than that found for the formation of [RNH]·:BH₃ and [RNH₂]:BH₂· radicals, as illustrated in Figure 6.

**Figure 6.** Values of $\Delta_r G$ and $\Delta_r G^\circ$ for the formation of aminyl ([RNH]·:BH₃), phosphinyl ([RPH]·:BH₃), boryl (N) ([RNH₂]:BH₂·), and boryl (P) ([RPH₂]:BH₂·) radicals.

3. Conclusions

From our theoretical survey, we concluded that aminyl ([RNH]·:BH₃) and phosphinyl ([RPH]·:BH₃) radicals produced from amine- and phosphine-boranes were systematically more stable than the boryl analogues [RNH₂]:BH₂· and [RPH₂]:BH₂·. This enhanced stability was particularly large if the substituents attached to the NH₂ or PH₂ groups were unsaturated or aromatic. The larger stability of the N- and P-centered radicals with respect to B-centered ones was also observed for different kinds of secondary amines and phosphines. This similar qualitative behavior of amines and phosphines hide, how-

ever, some significant quantitative dissimilarities between both families of compounds. The association of the amines with BH₃ led to a decrease in the homolytic bond dissociation energy of the N–H bond ($\Delta G_2 < \Delta G_3$). In contrast, for the phosphines, the homolytic bond dissociation energy of the P–H bond increased upon complexation with BH₃ ($\Delta G_2 > \Delta G_3$). Also, although for both series of compounds the complexation with BH₃ stabilized both the free amine (or the free phosphine) and the corresponding aminyl (or phosphinyl) radical, the stabilization of the free amine was much smaller than that undergone by the corresponding aminyl radical, whereas for phosphines it was the other way around.

The homolytic bond dissociation energy of the B–H bond of borane decreased upon complexation with both amines and phosphines ($\Delta G_2^\circ < \Delta G_3^\circ$). Hence, the boryl BH₂· radical became more stabilized than BH₃ by association with amines and phosphines, although this effect was larger for phosphines.

The formation of [RNH]·:BH₃, [RPH]·:BH₃, [RNH₂]:BH₂·, and [RPH₂]:BH₂· radicals was an endergonic process, with the exception of the [RPH]·:BH₃ [R = *p*-NH₂Ph- (7), *p*-NO₂Ph- (8), Ph-CH₂- (9)] phosphinyl radicals. In all cases, the formation of boryl radicals was more endergonic than the formation of the aminyl and phosphinyl counterparts. However, the free energy gap between boryl and aminyl was much larger than that between boryl and phosphinyl radicals.

Acknowledgements

This work has been partially supported by the DGI (project no. CTQ2012-35513-C02-01), by the COST Action CM1204, by the Project MADRISOLAR2 (ref.: S2009PPQ/1533) of the Comunidad Autónoma de Madrid. A.M.S. acknowledges a FPI contract from the Ministerio de Economía y Competitividad of Spain. Computing time at Centro de Computación Científica of the Universidad Autónoma de Madrid is also acknowledged.

Keywords: ab initio calculations • amines • boranes • phosphines • radicals

- [1] A. C. Gaumont, B. Carboni, *Sci. Synth.* **2004**, 6, 485–512.
- [2] a) M. Hurtado, M. Yáñez, R. Herrero, A. Guerrero, J. Z. Dávalos, J.-L. M. Abboud, K. B. J. C. Guillemin, *Chem. Eur. J.* **2009**, 15, 4622–4629; b) A. Martín-Sómer, A. Lamsabhi, M. Yáñez, J. Z. Dávalos, J. Gonzalez, R. Ramos, J. C. Guillemin, *Chem. Eur. J.* **2012**, 18, 15699–15705.
- [3] R. Kinjo, B. Donnadieu, M. A. Celik, G. Frenking, G. Bertrand, *Science* **2011**, 333, 610–613.
- [4] A. Staubitz, A. P. M. Robertson, M. E. Sloan, I. Manners, *Chem. Rev.* **2010**, 110, 4023–4078.
- [5] a) M. H. Matus, M. T. Nguyen, D. A. Dixon, *J. Phys. Chem. A* **2007**, 111, 1726–1736; b) T. B. Marder, *Angew. Chem. Int. Ed.* **2007**, 46, 8116–8118; *Angew. Chem.* **2007**, 119, 8262–8264; c) U. Eberle, M. Felderhoff, F. Schueth, *Angew. Chem. Int. Ed.* **2009**, 48, 6608–6630; *Angew. Chem.* **2009**, 121, 6732–6757; d) J.-L. M. Abboud, B. Nemeth, J.-C. Guillemin, P. Burk, A. Adamson, E. R. Nerut, *Chem. Eur. J.* **2012**, 18, 3981–3991.
- [6] a) J. A. Baban, B. P. Roberts, *J. Chem. Soc. Chem. Commun.* **1983**, 1224–1226; b) J. A. Baban, V. P. J. Marti, B. P. Roberts, *J. Chem. Soc. Perkin Trans. 2* **1985**, 1723–1733; c) J. A. Baban, B. P. Roberts, *J. Chem. Soc. Perkin Trans. 2* **1988**, 1195–1200; d) M. Lucarini, G. F. Pedulli, L. Valgimigli, *J. Org. Chem.* **1996**, 61, 4309–4313; e) B. P. Roberts, *Chem. Soc. Rev.*

- 1999, 28, 25–35; f) W. Tantawy, H. Zipse, *Eur. J. Org. Chem.* **2007**, 5817–5820; g) J. Lalevee, M. A. Tehfe, X. Allonas, J. P. Fouassier, *Macromolecules* **2008**, 41, 9057–9062; h) J. Lalevee, N. Blanchard, A.-C. Chany, M.-A. Tehfe, X. Allonas, J.-P. Fouassier, *J. Phys. Org. Chem.* **2009**, 22, 986–993; i) J. C. Walton, *Angew. Chem. Int. Ed.* **2009**, 48, 1726–1728; *Angew. Chem.* **2009**, 121, 1754–1756; j) S.-H. Ueng, A. Solov'yev, X. Yuan, S. J. Geib, L. Fensterbank, E. Lacote, M. Malacria, M. Newcomb, J. C. Walton, D. P. Curran, *J. Am. Chem. Soc.* **2009**, 131, 11256–11262; k) J. Lalevee, N. Blanchard, M.-A. Tehfe, A.-C. Chany, J.-P. Fouassier, *Chem. Eur. J.* **2010**, 16, 12920–12927; l) J. Hioe, A. Karton, J. M. L. Martin, H. Zipse, *Chem. Eur. J.* **2010**, 16, 6861–6865.
- [7] a) M. P. Sibi, S. Manyem, J. Zimmerman, *Chem. Rev.* **2003**, 103, 3263–3295; b) P. L. H. Mok, B. P. Roberts, *J. Chem. Soc. Chem. Commun.* **1991**, 150–152.
- [8] B. Sheeller, K. U. Ingold, *J. Chem. Soc. Perkin Trans. 2* **2001**, 480–486.
- [9] a) H. S. Dang, B. P. Roberts, *Tetrahedron Lett.* **1992**, 33, 4621–4624; b) H. S. Dang, B. P. Roberts, *Tetrahedron Lett.* **1992**, 33, 6169–6172; c) H. S. Dang, B. P. Roberts, *J. Chem. Soc. Perkin Trans. 1* **1993**, 891–898.
- [10] a) N. Kano, A. Furuta, T. Kambe, J. Yoshino, Y. Shibata, T. Kawashima, N. Mizorogi, S. Nagase, *Eur. J. Inorg. Chem.* **2012**, 1584–1587; b) S. Telitel, A.-L. Vallet, S. Schweizer, B. Delpech, N. Blanchard, F. Morlet-Savary, B. Graff, D. P. Curran, M. Robert, E. Lacote, J. Lalevee, *J. Am. Chem. Soc.* **2013**, 135, 16938–16947.
- [11] B. P. Roberts, A. J. Steel, *J. Chem. Soc. Perkin Trans. 2* **1994**, 2411–2422.
- [12] C. A. Jaska, K. Temple, A. J. Lough, I. Manners, *J. Am. Chem. Soc.* **2003**, 125, 9424–9434.
- [13] D. J. Grant, D. A. Dixon, *J. Phys. Chem. A* **2009**, 113, 777–787.
- [14] a) D. J. Henry, C. J. Parkinson, L. Radom, *J. Phys. Chem. A* **2002**, 106, 7927–7936; b) D. J. Henry, M. B. Sullivan, L. Radom, *J. Chem. Phys.* **2003**, 118, 4849–4860.
- [15] B. Braidă, E. Derat, P. Chaquin, *ChemPhysChem* **2013**, 14, 2759–2763.
- [16] P. R. Rablen, *J. Am. Chem. Soc.* **1997**, 119, 8350–8360.

Received: February 20, 2014
Published online on May 28, 2014

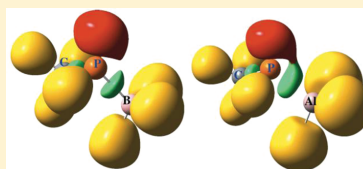
Unexpected Acidity Enhancement Triggered by AlH_3 Association to Phosphines

Ana Martín-Sómer, Al Mokhtar Lamsabhi, Otilia Mó, and Manuel Yáñez*

Departamento de Química, Facultad de Ciencias, Módulo 13, Universidad Autónoma de Madrid, Campus de Excelencia UAM-CSIC, Cantoblanco, 28049-Madrid, Spain

Supporting Information

ABSTRACT: The complexes formed by the interaction between a series of phosphines R-PH_2 ($\text{R} = \text{H}, \text{CH}_3, \text{c-C}_3\text{H}_5, \text{C}_6\text{H}_5$) and AlH_3 have been investigated through the use of high-level G4 ab initio calculations. These very stable complexes behave as much stronger acids than the isolated phosphines. This dramatic acidity enhancement, which can be as high as 174 kJ mol^{-1} , results from a much greater stabilization of the anionic deprotonated species with respect to the neutral one, upon AlH_3 association. This effect depends quantitatively on the nature of the substituent R and is smaller for $\text{R} = \text{C}_6\text{H}_5$ because of the conjugation of the P lone pair with the aromatic system. More unexpectedly, however, the phosphine–alane complexes, $\text{RPH}_2\text{:AlH}_3$, are more acidic than the corresponding phosphine–borane $\text{RPH}_2\text{:BH}_3$ analogues. This unexpected result is due to the enhanced stability of the anionic deprotonated species for complexes involving AlH_3 , because the delocalization of the newly created P lone pair with the P–Al bonding density is more favorable when the Lewis acid is aluminum trihydride than when it is borane.



INTRODUCTION

Although noncovalent interactions play a significant role in nature,^{1–4} and they are present in most of the known molecular assemblies, there is not a clear-cut definition of them.⁵ Typically, most of these interactions, such as hydrogen bonds,^{6–13} halogen bonds,^{14–17} beryllium bonds,¹⁸ metal ion–molecule complexes,^{19–31} van der Waals complexes,^{32–36} etc., involve closed-shell species. This would permit a first distinction between noncovalent interactions and typical covalent bonds which usually involve the interaction between open-shell systems. Nevertheless, in most of the aforementioned examples of noncovalent interactions, some charge transfer between the two interacting moieties takes place. These partial charge transfers go from the lone pair of one of the interacting subunits, which behave as a Lewis base (in a hydrogen-bond complex the proton acceptor), toward empty orbitals of the other interacting subunit, acting as a Lewis acid (in a hydrogen-bond complex, the proton donor). These charge donations can be very strong in those cases in which the electron acceptor has low-lying empty orbitals and therefore behaves as a strong Lewis acid. This is typically the case of borane, in which the B atom has empty low-lying 2p orbitals, which easily accept electrons from the lone pair of a Lewis base, leading to a strong interaction usually known as a dative bond, which is nevertheless distinguished in the IUPAC's definition from a conventional covalent bond.³⁷ It is important to emphasize that strictly speaking, however, the difference between the interaction between a Lewis base and BH_3 and the interaction between a hydrogen-bond (HB) donor and an HB acceptor is only quantitative, in the sense that the charge transfer in the first case is much larger than in the second.

Actually, in very strong hydrogen bonds,^{38–44} the charge donation from the HB acceptor to the HB donor is already rather significant. This charge transfer obviously implies a certain redistribution of the electron density of both interacting subunits, which in the case of an $\text{X-H}\cdots\text{Y}$ HB complex is reflected in the lengthening of the X–H bond of the proton donor. When dealing with BH_3 complexes, the interaction usually leads to a significant distortion of BH_3 , which in the complex is not planar any more, but also in significant changes in the properties of the Lewis base.⁴⁵ For instance, when BH_3 interacts with phosphines to yield phosphine–boranes, both the physical and the chemical properties of the phosphine change.⁴⁶ Whereas the isolated phosphines have low stability and are pyrophoric, phosphine–boranes are rather stable solid compounds.⁴⁶ Also, whereas isolated phosphines are weak acids in the gas phase, phosphine–boranes exhibit an intrinsic acidity, which in terms of the acidity constant, is 17 orders of magnitude greater than that of the isolated phosphine, due to a much larger stabilization of the deprotonated than of the neutral phosphine upon complexation with BH_3 .⁴⁶ Similar acidity enhancements were also reported for complexes involving Lewis bases other than phosphines⁴⁷ and BF_3 as Lewis acid.⁴⁸

The aim of this study is to investigate, through the use of high-level ab initio and density functional approaches, what would be the effect of replacing BH_3 by AlH_3 . In order to analyze this question we have selected, as suitable model

Received: May 1, 2012

Revised: May 24, 2012

Published: May 25, 2012

Table 1. G4-Calculated Acidity ($\Delta_{\text{acid}}G^0$, kJ mol⁻¹) and Acidity Enhancement ($\Delta\Delta_{\text{acid}}G^0$, kJ mol⁻¹) for R-PH₂ Phosphines and the Corresponding R-PH₂:AlH₃ Phosphine-Alanes and R-PH₂:BH₃ Phosphine-Boranes

R	$\Delta_{\text{acid}}G^0$			$\Delta\Delta_{\text{acid}}G^0$	
	RPH ₂	RPH ₂ :AlH ₃	RPH ₂ :BH ₃	RPH ₂ :AlH ₃	RPH ₂ :BH ₃
H	1507.8 (1509.7 ± 2.1) ^a	1325.5	1378.1 ^b	182.3	129.7 ^b
CH ₃	1533.6 (1530.0 ± 2.5) ^c	1359.3	1375.0 ± 2.5 ^d	174.3	158.6 ^e
<i>c</i> -C ₃ H ₅	1512.7 (1510.0 ± 3.0) ^c	1352.1	1408.9 ± 2.8 ^d	160.6	104.8 ^e
C ₆ H ₅	1457.6 (1457.3 ± 0.8) ^c	1324.6	1375.0 ± 2.5 ^d	133.0	82.6 ^e

^aExperimental value taken from ref 66. ^bThis work. G4-calculated value. ^cExperimental values taken from ref 46. ^dExperimental values corresponding to the phosphine-boranes analogues were taken from ref 46. These values show that the acidity enhancement is greater for the alane than for the borane derivatives. ^eValues taken from ref 46.

systems, three different R-PH₂ phosphines, where the R substituent represents three very different situations: an alkyl group (methyl), a saturated nonaromatic ring (*c*-C₃H₅), and an aromatic ring (phenyl), and for which both the intrinsic acidity of the isolated phosphines and that of the corresponding phosphine-boranes are known. To the aforementioned three phosphines we have added PH₃ as a good reference system and because PH₃AlH₃ may serve as a hydrogen storage system,⁴⁹ as is the case for other AlH₃ complexes with nitrogen bases.⁵⁰ It is worth mentioning that phosphine-alanes have also an interesting chemistry⁵¹ and can act as catalysts in many chemical processes.⁵²

■ COMPUTATIONAL DETAILS

To calculate the intrinsic acidity of the systems under investigation with reliable accuracy we have used the G4 composite ab initio theory.⁵³ This composite technique, based on B3LYP-optimized geometries, improves the performance of lower *Gn* formalisms, yielding final total energies effectively at the CCSD(T,full)/G3LargeXP + HF limit level, and provides very accurate estimates for a great variety of reaction enthalpies.⁵³ However, this theory is very time-consuming when trying to investigate larger systems to those considered in this work, so we have also decided to carry out an assessment of a cheaper theoretical model based on the use of the B3LYP density functional theory (DFT) approach.^{54,55} This model has been shown to perform very well as far as the calculation of the intrinsic acidities of phosphine-boranes is concerned,⁴⁶ but its reliability when using heavier Lewis acids has not been investigated. In this model the geometries and the corresponding harmonic vibrational frequencies are obtained by using a 6-31+G(d,p) basis set, whereas the final energies are obtained by means of single-point calculations using a more extended 6-311+G(3df,2p) basis set expansion. Since aluminum is much larger than B we have explored also the performance of a functional including dispersion interactions, namely, B97D⁵⁶ as well as the M06 functional.⁵⁷ In both cases the basis sets used for geometry optimizations and to get the final energies were the same used for the B3LYP calculations. The calculated values obtained with these theoretical models are compared with those calculated at the G4 level of theory in Table S1 of the Supporting Information. It can be seen that, although the DFT models perform very well for the isolated phosphines, with differences below 4 kJ mol⁻¹, the performance is a little poorer for the phosphine-alanes, but still the correlation between the G4 and the B3LYP values is very good (see Figure S1 of the Supporting Information) indicating that the relative acidity trends are very well reproduced at the latter level.

The charge donation from the phosphorus lone pairs into the AlH₃ empty orbitals, which constitutes the main ingredient in

the bonding between phosphines and aluminum trihydride, will be analyzed in terms of the values of the orbital interaction energies obtained through a second-order perturbation approach in the framework of the natural bond orbital (NBO) method.⁸ Using this same approach the population of the initially empty orbitals in the AlH₃ moiety will be also an interesting measurement of the strength of the interaction. This information will be complemented with the one obtained through two alternative partition techniques, namely, the atoms in molecules (AIM)⁵⁸ and the electron localization function (ELF) theories.^{59,60} By means of the former we will be able to build up the molecular graph of each of the complexes formed as the ensemble of bond critical points (BCPs) and bond paths. The electron density associated to the P-Al BCP should be a good quantitative measurement of the strength of the linkage, but at the same time, the densities associated to the remaining bonds of the system will provide useful information on the electron density redistribution undergone by two interacting subunits upon complexation.^{61,62} A similar but complementary information can be obtained by means of the ELF theory which permits the partition of the molecular space in regions associated with the probability of finding electron pairs, usually named monosynaptic and di- (or poly) synaptic basins, depending on the number of atomic valence shells participating in it. The electron population of the disynaptic basins located between two atoms of the system provides reliable information of the strength of the linkage between them. All the NBO calculations have been carried out with the NBO5G package,⁶³ whereas the AIM and ELF ones have been carried out with the AIMALL⁶⁴ and the TopMod⁶⁵ series of programs, respectively.

■ RESULTS AND DISCUSSION

The optimized geometries of the isolated phosphines and their phosphorus deprotonated anions, together with those of the complexes they formed with AlH₃, are given in Table S2 of the Supporting Information. The G4 and B3LYP/6-311+G(3df,2p) final energies are summarized in Table S3 of the Supporting Information. The calculated intrinsic acidities, measured as the Gibbs free energy associated with the reaction



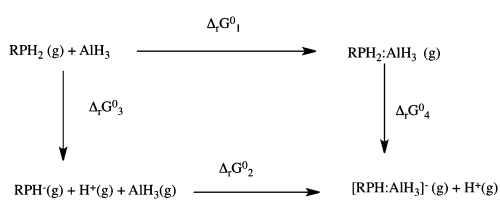
are presented in Table 1.

As also found for phosphine-boranes,⁴⁶ the phosphine-alanes behave as phosphorus acids in the gas phase. For example, for the CH₃PH₂:AlH₃ adduct, the C-H deprotonation and the Al-H deprotonation processes are 138 and 201 kJ mol⁻¹, respectively, less favorable than the P-H deprotonation.

The first conspicuous fact is the significant increase of the acidity of the phosphine when the aluminum trihydride molecule is attached to the phosphorus atom. Interestingly,

this enhancement is larger than the one reported for the corresponding phosphine–borane complexes.⁴⁶ Similar to what was found for phosphine–boranes, this acidity enhancement points out to a different stabilization of the neutral and the deprotonated species, which are related with the corresponding intrinsic acidities through the thermodynamic cycle shown in Scheme 1.

Scheme 1



In this scheme, $\Delta_r G^0_3$ and $\Delta_r G^0_4$ define the intrinsic acidity of the isolated phosphine and that of the phosphine:AlH₃ complex, respectively, assuming, as is the case, that in both cases the proton is lost from the PH₂ group. These free energies have been called generically $\Delta_{\text{acid}} G^0$ in Table 1. Hence, $\Delta_r G^0_1$ and $\Delta_r G^0_2$ measure the stabilization of the neutral phosphine and that of its deprotonated species, respectively, upon complexation with AlH₃. Accordingly, the aforementioned acidity enhancement just indicates that $\Delta_r G^0_2$ clearly dominates over $\Delta_r G^0_1$. In other words, that the stabilization of the anionic species is significantly higher than the stabilization undergone by the neutral phosphine, as is indeed the case as shown in Table 2.

Table 2. Stabilization Free Energies of Neutral ($\Delta_r G^0_1$) and Deprotonated ($\Delta_r G^0_2$) Phosphines, RPH₂, upon AlH₃ and BH₃ Complexation^{a,b}

R	$\Delta_r G^0_1$		$\Delta_r G^0_2$	
	RPH ₂ :AlH ₃	RPH ₂ :BH ₃	RPH ₂ :AlH ₃	RPH ₂ :BH ₃
H	−23.2	−51	−205.5	−180
CH ₃	−43.3	−56	−217.6	−176
<i>c</i> -C ₃ H ₅	−42.6	−56	−203.2	−163
C ₆ H ₅	−37.1	−50	−170.1	−129

^aValues for the complexation with BH₃ taken from ref 46, except for R = H which corresponds to the G4 calculations of this work. ^bAll values are in kJ mol^{−1}.

Quite unexpected, however, the acidity enhancement predicted for the phosphine–alanes is significantly larger, as clearly shown in Table 1, than that measured for the phosphine–boranes. On the other hand this acidity enhancement depends on the nature of the substituent and is significantly larger for R = CH₃ or *c*-propyl than for R = Ph.

These results open the following questions: why is the interaction of AlH₃ larger for the deprotonated than for the neutral species, why does this effect depend significantly on the nature of the R substituent, and why is the effect on the intrinsic acidities larger than that observed upon complexation with BH₃?

It is apparent from the electron densities at the P–Al BCPs (see Figure 1) that these bonds are much stronger in the anionic than in the neutral systems, which seems to indicate

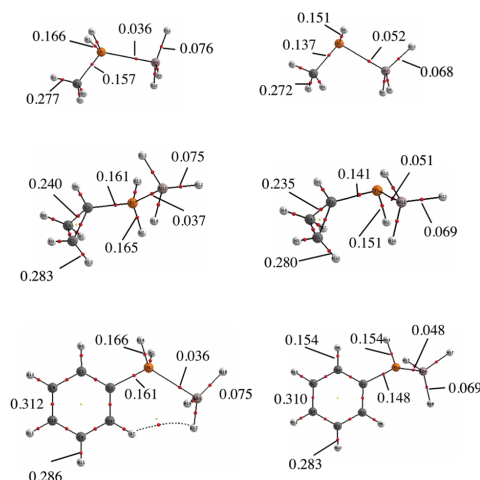


Figure 1. Molecular graphs of phosphine–alanes and their P deprotonated species. Red dots denote the BCPs. Electron densities are in au.

that the deprotonated anionic form is a better electron donor than the corresponding neutral phosphine. This is not surprising since the formation of the anion triggers a significant increase of the orbital energies, and in particular in the energy of the highest occupied molecular orbital (HOMO).

This change on going from the neutral to the deprotonated species is nicely reflected in the NBO characteristics of the P–Al bond (see Table 3). In the anion, the contribution of the Al

Table 3. Characteristics of the P–Al Bonds in Terms of the Percentage of Hybrid Orbitals Participating in Each MO and P–Al Wiberg Bond Index for Phosphine–Alanes and Their Deprotonated Forms^a

system	P–Al bond	Wiberg bond index
CH ₃ PH ₂ :AlH ₃	85% P (37% s + 62% p) + 15% Al (12% s + 86% p)	0.489
[CH ₃ PH] [−] :AlH ₃	76% P (23% s + 77% p) + 24% Al (22% s + 78% p)	0.728
<i>c</i> -propyl-PH ₂ :AlH ₃	85% P (36% s + 64% p) + 15% Al (13% s + 87% p)	0.493
[<i>c</i> -propyl-PH] [−] :AlH ₃	76% P (22% s + 78% p) + 24% Al (22% s + 78% p)	0.726
PhPH ₂ :AlH ₃	P (LP) → Al (3p) 426 kJ mol ^{−1}	0.488
[PhPH] [−] :AlH ₃	77% P (17% s + 83% p) + 23% Al (22% s + 78% p)	0.675

^aFor PhPH₂:AlH₃ the NBO method does not localize any P–Al bond. Instead a strong charge donation from the P lone pair into the 3p empty orbital of Al is found. The corresponding interaction energy is included.

hybrids to the bond increase from about 15% to 24%, with a similar increase in the contribution of the 3s orbital with respect to the 3p orbital in the corresponding hybrid. Not surprisingly then, the Wiberg bond index⁶⁷ for the P–Al linkage is about 45% larger for the anion than for the neutral species (see Table 3).

It is important to note that, as shown in Table 2, $\Delta_r G^0_1$ is not very sensitive to the nature of the substituent, which means that most of acidity enhancement is associated to the effects on the values of $\Delta_r G^0_2$. Hence, to understand why the acidity enhancement depends on the nature of the R substituent we will concentrate our attention on the deprotonated species. The clue to understand why the smallest effect is observed for R = Ph is to notice that phenylphosphine is the stronger acid of the three phosphines considered. This is the result of the significant stabilization of the anion through the conjugation of the P lone pair, created in the deprotonation process, with the aromatic system. The complexation of the anion with AlH_3 necessarily competes with this delocalization, since a significant amount of the lone-pair charge is transferred to the alane molecule, and less is available for the conjugation with the aromatic ring. This is mirrored in a significant decrease (about 120 kJ mol^{-1}) in the second-order interaction energies between the P lone pair and the aromatic system, on going from PhPH to $\text{PhPH}:\text{AlH}_3$.

The greater acidity enhancement effect observed for alane with respect to borane complexes is in principle unexpected if one takes into account that BH_3 should behave as a better Lewis acid than AlH_3 . In fact, the dissociation energies of the complexes of AlH_3 with PF_3 , PCl_3 , PMe_3 , and $\text{P}(\text{CN})_3$ were reported to be smaller than for the analogous complexes in which AlH_3 is replaced by BH_3 .⁶⁸ Indeed, this is also observed when looking at the stabilization of the neutral phosphines ($\Delta_r G^0_1$) under investigation here (see Table 2). Why, however, is the stabilization of the anion greater when it donates to AlH_3 than when it does so to BH_3 (see Table 2)? The explanation is nicely visualized in the corresponding ELF plots (see Figure 2).

In this figure we compare the ELF of $\text{CH}_3\text{PH}_2:\text{XH}_3$ and its phosphorus deprotonated species with those of $\text{CH}_3\text{PH}_2:\text{AlH}_3$ and its phosphorus deprotonated species. It is apparent that the differences are very tiny when comparing the corresponding neutral complexes. However, likely due to the larger size of the Al orbitals, there is a clear delocalization of the lone pair created

on the P atom upon its deprotonation and the disynaptic P–Al basin, which is not observed in the case of the phosphine–borane. This electron delocalization results in an increase electron flux to the bonding region, which is reflected in an increase of the electron population of the P–Al disynaptic basin, which would explain the enhanced stability of the $[\text{CH}_3\text{P}(\text{H})\text{AlH}_3]^-$ with respect to that of the $[\text{CH}_3\text{P}(\text{H})\text{BH}_3]^-$ counterpart and, therefore, the larger acidity of the phosphine–alane. The same delocalization is observed for the other derivatives as illustrated in the Figure S2 of the Supporting Information.

CONCLUSIONS

The association of phosphines RPH_2 (R = CH_3 , *c*- C_3H_5 , C_6H_5) with aluminum trihydride yields to very stable complexes which behave as much stronger acids than the isolated phosphines. This dramatic acidity enhancement, which can be as high as 174 kJ mol^{-1} , is due to the fact that the interaction of the deprotonated phosphine with AlH_3 is much stronger than that calculated for the neutral system. Actually, the deprotonation significantly increases the electron donor capacity of the phosphine moiety, whose HOMO becomes much higher in energy than that of the neutral compound. This effect depends quantitatively on the nature of the substituent R and is smaller for R = C_6H_5 because of the conjugation of the P lone pair with the aromatic system that cannot occur when R is an alkyl substituent. More unexpectedly, however, the phosphine–alane complexes, $\text{RPH}_2:\text{AlH}_3$, are more acidic than the corresponding phosphine–borane analogues, $\text{RPH}_2:\text{BH}_3$. This unexpected result is due to the enhanced stability of the anionic deprotonated species for complexes involving AlH_3 , because a delocalization of the newly created P lone pair with the P–Al disynaptic basin is more favorable when the Lewis acid is aluminum trihydride than when it is borane.

ASSOCIATED CONTENT

Supporting Information

Calculated acidities of phosphines and phosphine–alanes obtained at the G4 level and by using the B3LYP, M06, and B97D functionals; linear correlations between G4- and DFT-calculated acidities for phosphines and phosphine–alanes; B3LYP/6-31+G(d,p)-optimized geometries; G4 and B3LYP/6-311+G(3df,2p) total free energies for phosphines and phosphine–alanes; ELF plots for the RPH_2 (R = CH_3 , *c*- C_3H_5 , C_6H_5) phosphines and their complexes with AlH_3 . This material is available free of charge via the Internet at <http://pubs.acs.org>.

AUTHOR INFORMATION

Notes

The authors declare no competing financial interest.

ACKNOWLEDGMENTS

This work has been partially supported by the DGI projects nos. CTQ2009-13129-C02-01 and CTQ2009-07197-E, by the project MADRISOLAR2, ref.: S2009PPQ/1533 of the Comunidad Autónoma de Madrid, by Consolider on Molecular Nanoscience CSC2007-00010, and by the COST Action CM0702. A generous allocation of computing time at the CCC of the UAM is also acknowledged. A.M.-S. acknowledges an FPI Grant from the Ministry of Science and Innovation of Spain.

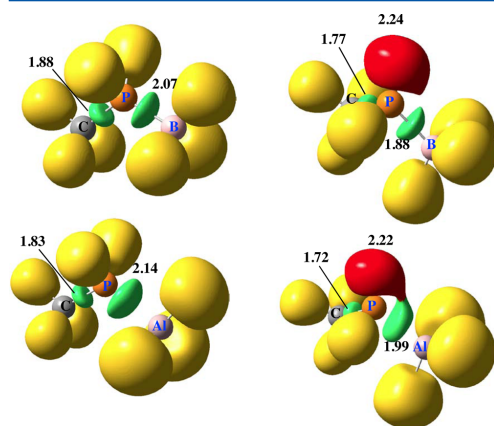


Figure 2. ELF (= 0.85) for the $\text{CH}_3\text{PH}_2:\text{XH}_3$ (X = B, Al) complexes and their corresponding phosphorus deprotonated species, $[\text{CH}_2\text{PH}]:\text{XH}_3$ (X = B, Al). Green lobes denote disynaptic basins involving two heavy atoms. Yellow lobes are disynaptic basins in which H is one of the atoms involved. Red lobes correspond to lone pairs. The populations shown are in e^- .

REFERENCES

- (1) Hobza, P.; Zahradnik, R.; Müller-Dethlefs, K. *Collect. Czech. Chem. Commun.* **2006**, *71*, 443–531.
- (2) Hobza, P.; Müller-Dethlefs, K. *Non-covalent Interactions: Theory and Experiment*; RSC: London, 2009.
- (3) Whittell, G. R.; Hager, M. D.; Schubert, U. S.; Mannes, I. *Nat. Mater.* **2011**, *10*, 176–188.
- (4) Yakhmi, J. V. *J. Mater. Educ.* **2011**, *33*, 149–160.
- (5) Espinosa, E.; Alkorta, I.; Elguero, J.; Molins, E. *J. Chem. Phys.* **2002**, *117*, 5529–5542.
- (6) Pimentel, G. C.; McClelland, A. L. *The Hydrogen Bond*; W.H. Freeman and Co.: San Francisco, CA, 1960.
- (7) Kollman, P. A.; Allen, L. C. *Chem. Rev.* **1972**, *72*, 283ff.
- (8) Reed, A. E.; Curtiss, L. A.; Weinhold, F. *Chem. Rev.* **1988**, *88*, 899–926.
- (9) Curtiss, L. A.; Blander, M. *Chem. Rev.* **1988**, *88*, 827–841.
- (10) Alkorta, I.; Rozas, I.; Elguero, J. *Chem. Soc. Rev.* **1998**, *27*, 163–170.
- (11) Meot-Ner, M. *Chem. Rev.* **2005**, *105*, 213–284.
- (12) *Hydrogen Bonding. New Insights*; Grabowski, S. J., Ed.; Springer: Heidelberg Germany, 2006.
- (13) Grabowski, S. J. *Chem. Rev.* **2011**, *111*, 2597–2625.
- (14) Cooke, S. A.; Cotti, G.; Evans, C. M.; Holloway, J. H.; Kisiel, Z.; Legon, A. C.; Thumwood, J. M. *A. Chem.—Eur. J.* **2001**, *7*, 2295–2305.
- (15) Karpfen, A. *Theor. Chem. Acc.* **2003**, *110*, 1–9.
- (16) Pennington, W. T.; Hanks, T. W.; Arman, H. D. In *Halogen Bonding: Fundamentals and Applications*; Metrangola, P.; Resnati, G., Eds.; Springer-Verlag: Berlin, Germany, 2008; Vol. 126, pp 65–104.
- (17) Alkorta, I.; Blanco, F.; Elguero, J. *Struct. Chem.* **2009**, *20*, 63–71.
- (18) Yáñez, M.; Sanz, P.; Mó, O.; Alkorta, I.; Elguero, J. *J. Chem. Theory Comput.* **2009**, *5*, 2763–2771.
- (19) Blades, A. T.; Jayaweera, P.; Ikononou, M. G.; Kebarle, P. *Int. J. Mass Spectrom. Ion Processes* **1990**, *102*, 251–267.
- (20) Alcamí, M.; Mó, O.; Yáñez, M.; Anvia, F.; Taft, R. W. *J. Phys. Chem.* **1990**, *94*, 4796–4804.
- (21) Cerda, B. A.; Wesdemiotis, C. *J. Am. Chem. Soc.* **1996**, *118*, 11884–11892.
- (22) Burda, J. V.; Sponer, J.; Hobza, P. *J. Phys. Chem.* **1996**, *100*, 7250–7255.
- (23) Leon, E.; Amekraz, B.; Tortajada, J.; Morizur, J.-P.; González, A. I.; Mó, O.; Yáñez, M. *J. Phys. Chem. A* **1997**, *101*, 2489–2495.
- (24) Burda, J. V.; Sponer, J.; Leszczynski, J.; Hobza, P. *J. Phys. Chem. B* **1997**, *101*, 9670–9677.
- (25) Luna, A.; Amekraz, B.; Tortajada, J.; Morizur, J. P.; Alcamí, M.; Mó, O.; Yáñez, M. *J. Am. Chem. Soc.* **1998**, *120*, 5411–5426.
- (26) Peschke, M.; Blades, A. T.; Kebarle, P. *J. Am. Chem. Soc.* **2000**, *122*, 10440–10449.
- (27) Mó, O.; Yáñez, M.; Gal, J.-F.; Maria, P.-C.; Decouzon, M. *Chem.—Eur. J.* **2003**, *9*, 4330–4338.
- (28) Corral, I.; Mó, O.; Yáñez, M. *J. Phys. Chem. A* **2003**, *107*, 1370–1376.
- (29) Corral, I.; Mó, O.; Yáñez, M.; Salpin, J.-Y.; Tortajada, J.; Radom, L. *J. Phys. Chem. A* **2004**, *108*, 10080–10088.
- (30) Corral, I.; Mó, O.; Yáñez, M. *Int. J. Quantum Chem.* **2006**, *106*, 659–663.
- (31) Corral, I.; Trujillo, C.; Salpin, J. Y.; Yáñez, M. In *Challenges and Advances in Computational Chemistry and Physics. Vol. 12 Kinetics and Dynamics: From Nano- to Bio-Scale*; Paneth, P., Dybala-Defratyka, A., Eds.; Springer: London, 2010; Vol. 12.
- (32) Blaney, B. L.; Ewing, G. E. *Annu. Rev. Phys. Chem.* **1976**, *27*, 553–584.
- (33) Hutson, H. M. *Annu. Rev. Phys. Chem.* **1990**, *41*, 123–154.
- (34) Jeziorski, B.; Moszynski, R.; Szalewicz, K. *Chem. Rev.* **1994**, *94*, 1887–1930.
- (35) Chalasinski, G.; Szczesniak, M. M. *Chem. Rev.* **1994**, *94*, 1723–1765.
- (36) Muller-Dethlefs, K.; Hobza, P. *Chem. Rev.* **2000**, *100*, 143–167.
- (37) <http://goldbook.iupac.org/index.html> (accessed May 20, 2012, IUPAC Goldbook).
- (38) Seidl, E. T.; Schaefer, H. F. *J. Am. Chem. Soc.* **1989**, *111*, 1569–1574.
- (39) González, L.; Mó, O.; Yáñez, M.; Elguero, J. *J. Chem. Phys.* **1998**, *109*, 2685–2693.
- (40) González, L.; Mó, O.; Yáñez, M.; Elguero, J. *ChemPhysChem* **2001**, *7*, 465–467.
- (41) Asfin, R. E.; Denisov, G. S.; Tokhadze, K. G. *J. Mol. Struct.* **2002**, *608*, 161–168.
- (42) Gilli, P.; Bertolasi, V.; Pretto, L.; Ferretti, V.; Gilli, G. *J. Am. Chem. Soc.* **2004**, *126*, 3845–3855.
- (43) Pakiari, A. H.; Eskandari, K. *J. Mol. Struct.: THEOCHEM* **2006**, *759*, 51–60.
- (44) Choudhury, R. R.; Roussel, P.; Capet, F.; Chitra, R. *J. Mol. Struct.* **2009**, *938*, 229–237.
- (45) Alkorta, I.; Elguero, J.; Del Bene, J. E.; Mó, O.; Yáñez, M. *Chem.—Eur. J.* **2010**, *16*, 11897–11905.
- (46) Hurtado, M.; Yáñez, M.; Herrero, R.; Guerrero, A.; Dávalos, J. Z.; Abboud, J.-L. M.; Khater, B.; Guillemin, J. C. *Chem.—Eur. J.* **2009**, *15*, 4622–4629.
- (47) Ren, J. H.; Workman, D. B.; Squires, R. R. *J. Am. Chem. Soc.* **1998**, *120*, 10511–10522.
- (48) Ren, J. H.; Cramer, C. J.; Squires, R. R. *J. Am. Chem. Soc.* **1999**, *121*, 2633–2634.
- (49) Grant, D. J.; Dixon, D. A. *J. Phys. Chem. A* **2005**, *109*, 10138–10147.
- (50) Nguyen, V. S.; Swinnen, S.; Matus, M. H.; Minh, T. N.; Dixon, D. A. *Phys. Chem. Chem. Phys.* **2009**, *11*, 6339–6344.
- (51) Elms, F. M.; Gardiner, M. G.; Koutsantonis, G. A.; Raston, C. L.; Atwood, J. L.; Robinson, K. D. *J. Organomet. Chem.* **1993**, *449*, 45–52.
- (52) Bouhadir, G.; Amgoune, A.; Bourissou, D. *Adv. Organomet. Chem.* **2010**, *58*, 1–107.
- (53) Curtiss, L. A.; Redfern, P. C.; Raghavachari, K. *J. Chem. Phys.* **2007**, *126*, 12.
- (54) Becke, A. D. *J. Chem. Phys.* **1993**, *98*, 1372–1377.
- (55) Lee, C.; Yang, W.; Parr, R. G. *Phys. Rev. B* **1988**, *37*, 785–789.
- (56) Grimme, S. *J. Comput. Chem.* **2006**, *27*, 1787–1799.
- (57) Zhao, Y.; Truhlar, D. G. *J. Phys. Chem.* **2006**, *110*, 5121–5129.
- (58) Bader, R. F. W. *Atoms in Molecules. A Quantum Theory*; Clarendon Press: Oxford, U.K., 1990.
- (59) Becke, A. D.; Edgecombe, K. E. *J. Chem. Phys.* **1990**, *92*, 5397–5403.
- (60) Silvi, B.; Savin, A. *Nature* **1994**, *371*, 683–686.
- (61) Alcamí, M.; Mó, O.; Yáñez, M.; Abboud, J. L. M.; Elguero, J. *Chem. Phys. Lett.* **1990**, *172*, 471–477.
- (62) Corral, I.; Mó, O.; Yáñez, M. *Encyclopedia of Computational Chemistry*. <http://www.mrw.interscience.wiley.com/eccarticles/cn0062/frame.html> (accessed June 21, 2004).
- (63) Glendening, E. D.; Badenhop, J. K.; Reed, A. E.; Carpenter, J. E.; Bohmann, J. A.; Morales, J. A.; Weinhold, F. NBO 5.0; University of Wisconsin: Madison, WI, 2001.
- (64) Keith, T. A., Ed.; AIMALL (Version 12.05.09). T. G. Gristmill Software: Overland Park, KS, 2011.
- (65) Noury, S.; Krokidis, X.; Fuster, F.; Silvi, B. *Comput. Chem.* **1999**, *23*, 597–604.
- (66) Ervin, K. M.; Lineberger, W. C. *J. Chem. Phys.* **2005**, *122*, 194303.
- (67) Wiberg, K. B. *Tetrahedron* **1968**, *24*, 1083–1088.
- (68) Loschen, C.; Voigt, K.; Frunzke, J.; Diefenbach, A.; Diefenbach, M.; Frenking, G. *Z. Anorg. Allg. Chem.* **2002**, *628*, 1294–1304.

Can an Amine Be a Stronger Acid than a Carboxylic Acid? The Surprisingly High Acidity of Amine–Borane Complexes

Ana Martín-Sómer,^[a] Al Mokhtar Lamsabhi,^[a] Manuel Yáñez,^{*,[a]} Juan Z. Dávalos,^{*,[b]} Javier González,^[b] Rocío Ramos,^[b] and Jean-Claude Guillemin^{*,[c]}

Abstract: The gas-phase acidity of a series of amine–borane complexes has been investigated through the use of electrospray mass spectrometry (ESI-MS), with the application of the extended Cooks kinetic method, and high-level G4 ab initio calculations. The most significant finding is that typical nitrogen bases, such as aniline, react with BH₃ to give amine–borane complexes, which, in the gas phase, have acidities as high as those of either phosphoric, oxalic, or salicylic acid; their acidity is higher than many carboxylic acids, such as formic, acetic, and propanoic acid. Indeed the complexation of different amines with BH₃

leads to a substantial increase (from 167 to 195 kJ mol^{−1}) in the intrinsic acidity of the system; in terms of ionization constants, this increase implies an increase as large as fifteen orders of magnitude. Interestingly, this increase in acidity is almost twice as large as that observed for the corresponding phosphine–borane analogues. The agreement between the experimental and the G4-based calculated values is

Keywords: ab initio calculations • acidity • amine–borane complexes • electrospray mass spectrometry • extended Cooks kinetic method

excellent. The analysis of the electron-density rearrangements of the amine and the borane moieties indicates that the dative bond is significantly stronger in the *N*-deprotonated anion than in the corresponding neutral amine–borane complex, because the deprotonated amine is a much better electron donor than the neutral amine. On the top of that, the newly created lone pair on the nitrogen atom in the deprotonated species, conjugates with the BN bonding pair. The dispersion of the extra electron density into the BH₃ group also contributes to the increased stability of the deprotonated species.

Introduction

There are many interactions in chemistry, from van der Waals complexes to dative bonds, including hydrogen bonds,^[1–3] halogen bonds,^[4–7] and beryllium bonds,^[8,9] which involve closed-shell systems. One of the common characteristics of these interactions, with the only exception being the van der Waals complexes, is that there is a charge transfer, to either a large or a small extent, between the interacting

subunits. In the case of the X–H...Y hydrogen bonds (HBs), this charge transfer involves the transfer of electron density from the lone pairs of the HB acceptor, Y, into the σ_{XH}^* antibonding orbital of the HB donor, and it is responsible for the elongation of the X–H bond and the red shifting of the X–H stretching band. For beryllium compounds, B:BeX₂, electron density is transferred from the lone pairs of the Lewis base, B, into both the empty 2p orbital of the Be atom and the σ_{BeX}^* antibonding orbital.^[8] The consequences of these charge transfers are the bending of the BeX₂ moiety and the significant elongation of the Be–X bonds. Hence, one important common feature of these interactions between closed-shell systems is that the deformation of the interacting subunits usually triggers significant, even dramatic, changes in their chemical properties. This change in chemical properties has been found in the case of many complexes involving BH₃ and some of its derivatives, for which these interactions are particularly strong.^[10–15] The important point we want to emphasize here is that the deformation plays a crucial role when these complexes are formed, so that the strength of the interaction actually can only be correctly rationalized by taking into account the effects that the deformation has on the donor and the acceptor properties of the interacting systems.^[16,17] Only when these effects are accounted for is it then possible to explain, for instance, why BH₂F and BHF₂ are weaker Lewis acids than BH₃, whereas boron trifluoride is a stronger acid than borane.^[16]

[a] A. Martín-Sómer, Dr. A. M. Lamsabhi, Prof. M. Yáñez
Departamento de Química, Facultad de Ciencias, Módulo13,
Universidad Autónoma de Madrid. Cantoblanco,
28049-Madrid (Spain)
Fax: (+34) 91-497-5238
E-mail: manuel.yanez@uam.es

[b] Dr. J. Z. Dávalos, J. González, R. Ramos
Instituto de Química Física Rocasolano, CSIC. C/Serrano,
119.28006 Madrid (Spain)
Fax: (+34) 91-564-2431
E-mail: jdavalos@iqfr.csic.es

[c] Dr. J.-C. Guillemin
Institut des Sciences Chimiques de Rennes,
UMR 6226 CNRS-ENSCR
Avenue du Général Leclerc, CS 50837, 35708 Rennes (France)
Fax: (+33) 223-23-81-08
E-mail: jean-claude.guillemin@ensc-rennes.fr

Supporting information for this article is available on the WWW under <http://dx.doi.org/10.1002/chem.201202192>.

The charge redistribution, which occurs upon the formation of the aforementioned dative bonds, results in changes in the chemical properties of the interacting systems, changes that affect, in particular, their intrinsic reactivity. A paradigmatic example is the change that phosphines undergo when they form the corresponding phosphine–borane complexes. Whereas the free phosphines are usually pyrophoric, phosphine–borane complexes are not at all pyrophoric and are much less volatile; but what is more important is that they are much stronger acids in the gas phase.^[11,14]

Amine–borane complexes have received lately a lot of attention as potential devices for hydrogen storage^[18,19] and because they exhibit diverse types of reactivity. They are useful borane sources in many reactions that are carried out in either aqueous or alcoholic solvents. They can also be converted into aminoboranes through dehydrogenation processes,^[20–23] which involve, in some cases, frustrated Lewis pairs^[24] and can be used for the quantitative analysis of amines.^[25] Aliphatic and heterocyclic amine–borane complexes exhibit potent cytotoxic activity in vitro and in vivo against murine and human tumor models, because these compounds were shown to inhibit DNA synthesis.^[26] They may also act as alternative reducing agents,^[27–29] in particular for reductive alkylation of proteins.^[30] They can play important roles in heterogeneous catalysis and in nanoscience.^[31,32] Very recently, it has been shown that the gas-phase protonation of amine–borane complexes leads in all cases to the formation of dihydrogen.^[19] Our aim was to show that intrinsic acidity is an important characteristic of amine–borane complexes. Herein, we show, using a combined experimental and theoretical study, that typical conventional bases such as aniline become acidic—with acidities as high as phosphoric acid—when they form complexes with borane, whereas the acidity of other nitrogen bases, such as dimethylamine, aziridine, and cyclopropylamine, becomes as high as that of formic, acetic, and propionic acids.

Experimental Section

Materials: Ammonia borane and dimethylamine borane were purchased from Aldrich and used without further purification. The syntheses of methylamine borane,^[33] aziridine borane,^[34] allylamine borane,^[19,35] propargylamine borane,^[19] cyclopropylamine borane,^[36] trifluoroethylamine borane,^[19] and aniline borane^[37] have already been reported in the literature.

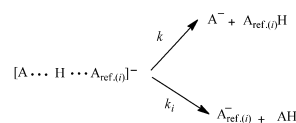
Determination of gas-phase acidities (ΔG_{acid}^0), deprotonation enthalpies (ΔH_{acid}^0), and deprotonation entropies (ΔS_{acid}^0): The gas-phase acidity of a protic acid (AH), $\Delta G_{\text{acid}}^0(\text{AH})$, is defined as the Gibbs free-energy change for reaction 1. The corresponding enthalpy and entropy changes are referred to as gas-phase deprotonation enthalpy (ΔH_{acid}^0) and deprotonation entropy (ΔS_{acid}^0), respectively.



Extended Cooks kinetic method (EKM): The acidity, deprotonation enthalpy, and deprotonation entropy of amine–borane complexes have been experimentally determined by means of the “extended kinetic method” (EKM)^[38–46] using a triple-quadrupole mass spectrometer

(Varian MS-320) with an electrospray source (ESI).

EKM is an improved version of the simple Cooks kinetic method^[47–50] which takes into account entropic effects on the competitive dissociations of a mass-selected proton-bound heterodimer anion, $[\text{A} \cdots \text{H} \cdots \text{A}_{\text{ref}(i)}]^-$ generated in the gas phase, where AH is the amine–borane complex under investigation and $\text{A}_{\text{ref}(i)}\text{H}$ is a set of conjugate bases of reference acids with known gas-phase acidity values. The heterodimers $[\text{A} \cdots \text{H} \cdots \text{A}_{\text{ref}(i)}]^-$ are accelerated and undergo collision-induced dissociation (CID) in a collision cell of the spectrometer. The CID process may give rise to two deprotonated species, A^- and $\text{A}_{\text{ref}(i)}^-$, via the two competitive dissociation channels with rate constants k and k_i , respectively (see Scheme 1).



Scheme 1. Collision-induced dissociations of $[\text{A} \cdots \text{H} \cdots \text{A}_{\text{ref}(i)}]^-$.

If the concentration of the secondary fragment anions is negligible, the starting point of the kinetic method is to assume that the ratio of measured peak intensities $[\text{A}^-]/[\text{A}_{\text{ref}(i)}^-]$ is equal to the ratio of rate constants k/k_i . Then, assuming no-reverse activation energy, the acidities of AH and $\text{A}_{\text{ref}(i)}\text{H}$ are related by a linear equation (2), which statistical procedure has been developed by Armentrout,^[40] and it can be expressed as:

$$\ln\left(\frac{k}{k_i}\right) = \ln\left[\frac{[\text{A}^-]}{[\text{A}_{\text{ref}(i)}^-]}\right] \quad (2)$$

$$= \frac{\Delta H_{\text{ref}(i)}^0 - \Delta H_{\text{ref}(i)}^{\text{av}}}{RT_{\text{eff}}} - \left[\frac{\Delta H_{\text{acid}}^0 - \Delta H_{\text{ref}(i)}^{\text{av}}}{RT_{\text{eff}}} - \frac{\Delta(\Delta S^0)}{R} \right]$$

where, $\Delta H_{\text{ref}(i)}^{\text{av}}$ is the average deprotonation enthalpy of the reference acids $[\text{A}_{\text{ref}(i)}\text{H}]$, T_{eff} is an “effective temperature”^[51,52] related to the excitation energy of the dissociating $[\text{A} \cdots \text{H} \cdots \text{A}_{\text{ref}(i)}]^-$ heterodimers. The entropic term $\Delta(\Delta S^0)$ can be expressed as the difference in the deprotonation entropies of the two acids^[53,54] $\Delta(\Delta S^0) \approx \Delta S_{\text{acid}}^0 - \Delta S_{\text{ref}(i)}^0$ or, assuming that the last term is equal to average deprotonation entropy, as $\Delta(\Delta S^0) \approx \Delta S_{\text{acid}}^0 - \Delta S_{\text{ref}(i)}^{\text{av}}$. Thus, for a series of experiments using several reference acids, under different collision energies, the set of plots of $\ln(k/k_i)$ versus $(\Delta H_{\text{ref}(i)}^0 - \Delta H_{\text{ref}(i)}^{\text{av}})$ follows a linear relationship characterized by a slope equal to $1/RT_{\text{eff}}$ and a y intercept including terms expressed between brackets in Equation (2). Inasmuch as these parameters are not independent, a further plot of them (intercepts versus slopes) yields a second straight line with a slope given by the deprotonation enthalpy difference $(\Delta H_{\text{ref}(i)}^0 - \Delta H_{\text{ref}(i)}^{\text{av}})$ and an intercept given by $\Delta(\Delta S^0)/R$. Finally, the gas-phase acidity, ΔG_{acid}^0 , of AH is derived from equation, $\Delta G_{\text{acid}}^0 = \Delta H_{\text{acid}}^0 - T(\Delta S_{\text{acid}}^0)$.

Stock solutions (ca. $10^{-3} \text{ mol L}^{-1}$, in methanol) of the amine–borane complex, AH, and reference acid, $\text{A}_{\text{ref}(i)}\text{H}$, were mixed in appropriate volume ratios (ca. 1:1), and further diluted also with methanol to achieve a final concentration of approximately $10^{-4} \text{ mol L}^{-1}$ for both, the amine–borane complex and the reference acid (sample solution). All the sample solutions were directly infused into the ESI source at flow rate of $10 \mu\text{L min}^{-1}$.

The ESI conditions were optimized to obtain the maximum intensity of the heterodimer $[\text{A} \cdots \text{H} \cdots \text{A}_{\text{ref}(i)}]^-$. Thus, the ESI needle voltage was varied between -2.5 and -5.0 kV , the capillary voltage was kept within the range, -20 to -70 V . Compressed air was used as the nebulizing gas while nitrogen was used as the desolvation gas; the drying gas temperature was set between 100 and 250°C . CID-MS-MS spectra were obtained after selection of the heterodimer $[\text{A} \cdots \text{H} \cdots \text{A}_{\text{ref}(i)}]^-$ by the first quadrupole (Q1) and activated by collision in the second quadrupole (Q2) using

argon at a nominal pressure of 0.2 mTorr to maintain single collision conditions. The dissociation products were mass analyzed by scanning the third quadrupole (Q3). The CID experiments were performed using 6 to 13 different collision energies, corresponding to the center-of-mass energies (E_{CM}) from 0.75 to 3.0 eV. E_{CM} was calculated using the expression, $E_{\text{CM}} = \left(\frac{m}{m+M}\right)E_{\text{lab}}$, where E_{lab} is the collision energy in the laboratory frame, m is the mass of argon and M is the mass of proton-bound heterodimer anion $[\text{A} \cdot \text{H} \cdot \text{A}_{\text{ref}(i)}]^-$.

Eighteen compounds with known gas-phase acidities, ΔG^0_{acid} , ranging from 1343.5 to 1463.1 kJ mol⁻¹ were chosen as the reference acids, $\text{A}_{\text{ref}(i)}\text{H}$ ($i=1-18$). The details of the experimental data obtained using the EKM method for each amine–borane complex under investigation are described in the Supporting Information (Tables S1–S22, Figures S1–S36).

Computational details: The rationalization of increased acidity of amine–borane complexes with respect to the free amines requires a reliable analysis of the electronic changes undergone by the amine when it interacts with BH_3 . The first requirement to be sure that the model will be reliable is to have good agreement between the measured and the calculated acidities, because this will be indirect evidence that the structures used in the calculations, for both the neutral and the deprotonated systems, are the same as those being probed experimentally. For this reason we used a high-level ab initio approach, that is, the one based on G4 theory, which has been shown to provide very accurate values for the enthalpies of various reactions.^[55] Considering that these high-level approaches may be prohibitively expensive when investigating very large systems, we have considered it of interest to explore the performance of a model, based on the use of the B3LYP density functional theory approach,^[56,57] which has been shown to perform very well for the calculation of the intrinsic acidities of phosphine–borane complexes.^[14] For this model, the geometries were optimized using a 6-31+G(d,p) expansion and the final energies were obtained in single-point calculations using the aforementioned optimized geometries and a 6-311++G(3df,2p) basis set. All these calculations have been carried out with the Gaussian09 suite of programs.^[58]

Because one of the main parts in the bonding between amines and borane is the dative bond formed upon the transfer of electron density from the lone pair of the nitrogen atom of the amine to the empty 2p orbital of BH_3 , the NBO approach, as implemented using the NBO-5G suite of programs,^[60] is particularly well suited to describe these interactions, and allows also the calculation of the Wiberg bond order.^[59] A complementary description of the bonding in amine–borane complexes can be obtained by means of the atoms in molecules (AIM)^[61] and the electron localization function (ELF) theories.^[64,65] The AIM and ELF calculations were carried out by using the AimAll^[63] and the TopMod^[66] packages, respectively.

Results and Discussion

To determine experimentally the gas-phase acidity of amine–borane complexes, AH , applying the EKM method [Eq. (2)], we selected four reference acids $\text{A}_{\text{ref}(i)}\text{H}$ for each amine–borane complex, based on the stability of the anions for the proton-bound heterodimer $[\text{A} \cdot \text{H} \cdot \text{A}_{\text{ref}(i)}]^-$ and the CID product ions (A^- and $\text{A}_{\text{ref}(i)}^-$). As an example, we present in Figure 1 two thermo-kinetic graphs for benzylamine borane. The first graph (Figure 1a) is a set of the plots of $\ln([A^-]/[A_{\text{ref}(i)}^-])$ versus $(\Delta H^0_{\text{ref,acid}(i)} - \Delta H^{\text{av}}_{\text{ref,acids}})$, where $\Delta H^{\text{av}}_{\text{ref,acids}}$ ((1462.2 ± 8.9) kJ mol⁻¹) is the average of deprotonation enthalpies of the reference acids, $\Delta H^0_{\text{ref,acid}(i)}$ ($i=10, 11, 13$, and 14) (see the Supporting Information). The data were fitted by a set of ten regression lines, each one corresponding to experiments done with collision energies, E_{CM} ,

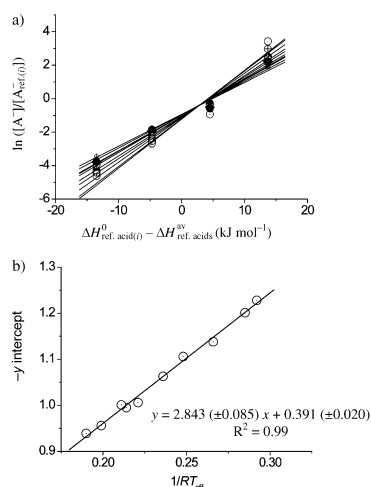


Figure 1. EKM plots for $\text{AH}=\text{benzylamine borane}$: a) plots of $\ln([A^-]/[A_{\text{ref}(i)}^-])$ versus $(\Delta H^0_{\text{ref,acid}(i)} - \Delta H^{\text{av}}_{\text{ref,acids}})$ from the CID of heterodimer $[\text{A} \cdot \text{H} \cdot \text{A}_{\text{ref}(i)}]^-$ (formed with four reference acids $i=10, 11, 13$, and 14) at ten collision energies E_{CM} (0.75–3.0 eV, intervals of 0.25 eV). b) Plot of y intercept points, $[(\Delta H^0_{\text{acid}} - \Delta H^{\text{av}}_{\text{ref,acids}})/RT_{\text{eff}} - \Delta(\Delta S^0)/R]$, versus slopes $1/RT_{\text{eff}}$.

in the range 0.75–3.0 eV (intervals of 0.25 eV). The second thermo-kinetic plot (Figure 1b) was generated by plotting the y intercept values (related to the expression within the square brackets in Equation (2)) versus the slopes, $1/RT_{\text{eff}}$, which were extracted from the first graph. The gas-phase thermochemical quantities of benzylamine borane were derived from the slope and the negative y intercept values of the linear fit of the second plot: $\Delta H^0_{\text{acid}} = (1465.0 \pm 8.9)$ kJ mol⁻¹, $\Delta S^0_{\text{acid}} = (95.1 \pm 8.4)$ J mol⁻¹ K⁻¹ and $\Delta G^0_{\text{acid}} = (1436.7 \pm 8.9)$ kJ mol⁻¹.

The calculated and measured gas-phase acidities of the amine–borane complexes under investigation are summarized in Table 1.

For the sake of completeness, this table also includes the gas-phase acidities of the free amines. Only for some of the amines considered here are the experimental gas-phase acidities known. Unfortunately, the EKM method used in this work is not well suited to measure the acidity of very weak acids, such as the amines. Nevertheless, it is worth noting that for those cases in which the experimental acidity is known, the agreement with our G4-based calculated values is excellent, and therefore our estimates for the unknown gas-phase acidities should be accurate. This agreement between experimental and calculated values is also excellent for the gas-phase acidities of amine–borane complexes. The agreement is slightly worse when the B3LYP values are used, values that are, in general, slightly lower than the experimental values. Nevertheless, there is a reasonably good linear correlation between the B3LYP/6-311+G(3df,2p) gas-phase acidities and the G4-based calculated values (see

Table 1. Experimental and G4-based calculated gas-phase acidities, ΔG^0_{acid} [kJ mol⁻¹], for several amines and the corresponding amine–borane complexes; $\Delta\Delta G^0_{\text{acid}}$ [kJ mol⁻¹] is the increase in acidity on going from the free amine to the amine–borane complex.

Amine	Free amine		Amine–borane complex		$\Delta\Delta G^0_{\text{acid}}$ [kJ mol ⁻¹] calcd
	ΔG^0_{acid} [kJ mol ⁻¹] exptl ^[a]	calcd	ΔG^0_{acid} [kJ mol ⁻¹] exptl	calcd ^[b]	
ammonia	1656.8 ± 1.6	1657.2	–	1462.1 (1456.7)	195.1
methylamine	1651 ± 11.0	1656.1	1461.0 ± 9.2	1462.4 (1455.2)	193.7
dimethylamine	1623 ± 8.8	1621.8	1457.9 ± 9.2	1453.7 (1444.4)	168.1
allylamine	–	1616.5	1443.7 ± 8.8	1444.2 (1437.4)	172.3
cyclopropylamine	–	1618.3	1440.5 ± 9.2	1447.3 (1442.1)	171.0
benzylamine	–	1588.9	1436.7 ± 8.9	1438.1 (1435.5)	150.8
aziridine	–	1603.3	1443.4 ± 8.9	1435.5 (1432.2)	167.8
propargylamine	–	1608.8	1435.1 ± 8.9	1431.1 (1425.4)	177.7
trifluoroethylamine	–	1579.4	1405.0 ± 9.4	1400.5 (1393.5)	178.9
aniline	1502 ± 8.4	1506.7	1365.7 ± 9.4	1360.3 (1353.6)	146.4

[a] Values taken from Ref. [67]. [b] Values within parentheses were obtained at the B3LYP/6-311 + G(3df,2p)//B3LYP/6-31 + G(d,p) level.

the Supporting Information, Figure S37), and therefore in the case where the gas-phase acidities of larger amine–borane complexes needs to be estimated, this theoretical model can be used as a good alternative to G4 theory, which may be prohibitively expensive.

The calculated values given in Table 1 correspond to processes in which the proton is lost from the amino group of the amine–borane complex. The anion so produced is in all cases, except for PhCH₂NH₂·BH₃ and CF₃CH₂NH₂·BH₃, the most stable one. For both PhCH₂NH₂·BH₃ and CF₃CH₂NH₂·BH₃, the most stable anions (see the Supporting Information, Figure S38) correspond to structures in which the proton is lost from borane moiety. The increased stability of these two structures, which can be viewed as the interaction between a NH₂BH₂ group and either the C₆H₅CH₂⁻ or the CF₃CH₂⁻ anions, respectively, just reflects the high stability of both the neutral NH₂BH₂ group and the accompanying anions. Accordingly, these boron-deprotonated structures are predicted to be 22 and 15 kJ mol⁻¹ more stable than the corresponding amine-deprotonated species, respectively. Nevertheless, the good agreement between the calculated and experimental values in Table 1 for these two amine–borane complexes seems to indicate that under the experimental conditions only the amine-deprotonated species is formed. To explain this apparent dichotomy we investigated in detail and compared BH₃ and NH₂ deprotonation by using PhCH₂NH₂·BH₃, as a suitable example. As illustrated in Figure 2, the most stable anion (structure **C**) is the result of the dissociation of the borane-deprotonated species **B**, which involves a barrier (transition state, **TSBC**) of 100 kJ mol⁻¹. However, direct deprotonation of the BH₃ group of PhCH₂NH₂·BH₃ to yield less favorable (by 300 kJ mol⁻¹) than the direct deprotonation of the amino group to yield anion **A**; this was found to be the case for all other amine–borane complexes investigated herein. It is also worth noting that the transfer of a proton from the BH₃ group in anion **A** to the N atom, is accompa-

nied by cleavage of the C–N bond. The consequence is that the transition state associated with this proton transfer, namely **TSAC**, directly connects anions **A** and **C**, through a barrier of 228 kJ mol⁻¹. Hence, in spite of its increased stability, form **C** can only be reached through a very energetically demanding processes, from either structures **A** or **B**.

In addition, an examination of the molecular electrostatic potential of both benzylamine and CF₃CH₂NH₂ shows that for both molecules the positive potential areas (blue) are those close to the amino group (Figure 3). This means that the association of the molecule with the reference anion takes place at the amino group and never at the BH₃ group; the interaction of the latter with the attacking anion would be highly repulsive because of the hydride character of the BH₃ hydrogen atoms. These data are consistent with the much less favorable deprotonation of the BH₃ group. Hence, under

normal experimental conditions, the deprotonation of the amino group will be always favored and, as indicated above,

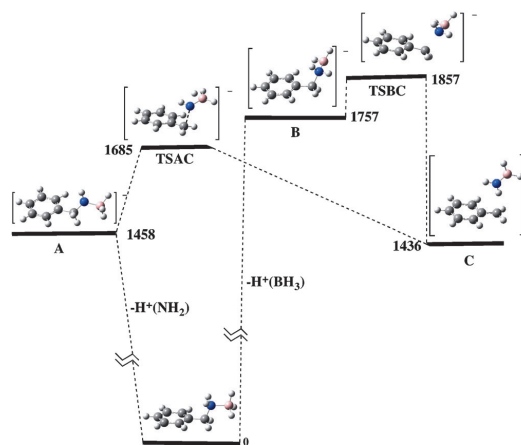


Figure 2. Energy profile of the NH₂ and BH₃ deprotonation processes of benzylamine·BH₃. All values are in kJ mol⁻¹.

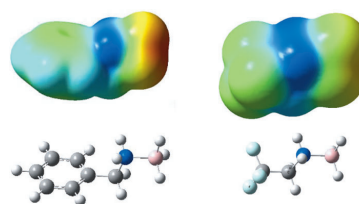
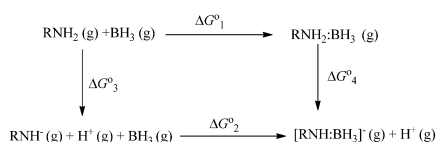


Figure 3. Molecular electrostatic potential of PhCH₂NH₂·BH₃ (left) and CF₃CH₂NH₂·BH₃ (right). Blue areas correspond to positive values of the potential, whereas red areas correspond to negative values of the potential.

its conversion into the more stable structure **C** would not take place because the transformation would involve a very high activation barrier.

Notably, there is a large increase in acidity on going from the free amine to the corresponding amine–borane complex (Table 1). Furthermore, these increases in acidity depend on the nature of the group attached to the nitrogen atom. It can be observed, for instance, that whereas the deprotonation of ammonia and methylamine borane leads to similar levels of stabilization, the deprotonation of dimethylamine borane leads to about 25 kJ mol^{−1} less stabilization. Also, smaller increases in acidity are observed for aniline and benzylamine. The origin of the increased acidity can be understood by means of the thermodynamic cycle presented in Scheme 2. In this scheme, the values of ΔG_1^0 and ΔG_2^0 rep-



Scheme 2. Thermodynamic cycle involving amines, deprotonated amines, and the corresponding borane complexes.

resent the stabilization upon borane-complex formation of the free amine and its conjugate base, respectively. Accordingly, ΔG_3^0 and ΔG_4^0 are the gas-phase acidities of the free amine and the corresponding amine–borane complex, respectively. Hence, this implies that if the absolute value of ΔG_4^0 is greater than that of ΔG_3^0 by a certain amount, then the absolute value of ΔG_2^0 would be greater than that of ΔG_1^0 by the same amount. Therefore, the stabilization of the deprotonated species by association to BH₃ is larger than that of the corresponding neutral free amine, as corroborated by the G4-based calculated values (see Table 2), which shows that the stabilization of the deprotonated species is 216 kJ mol^{−1} on average whereas for the neutral species this stabilization is only 88 kJ mol^{−1} on average.

The data in Table 2 can be easily rationalized by taking into account that deprotonated amines are much better elec-

tron donors than their neutral counterparts. The loss of a proton leads to a significant increase in the energy of the HOMO of the system and a parallel increase of its electron-donor capacity. This is also reflected in the characteristics of the bond formed between the nitrogen atom and the boron atom (see the Supporting Information, Table S23). The donation of lone pair of the nitrogen atom into the empty 2p orbital of the boron atom, leads to a strongly polar chemical bond in which the contribution (82%) of the nitrogen-based hybrid orbitals to the bond is dominant. For the deprotonated species, the contribution of the boron-based hybrid orbitals to the bond is significantly higher (from 18% to 24%), whereas a concomitant increase of the s character of the hybrid orbitals participating in the bond is also observed. Consequently, the bond between the boron atom and the nitrogen atom of the deprotonated amine is stronger and this is reflected in both the value of the Wiberg bond index and the value of the electron density, ρ_b , at the corresponding bond critical point (see the Supporting Information, Table S23).

The ELF plots (Figure 4) are consistent with the previous analysis and they show how the lone pair that is created upon the deprotonation of the amino groups connects (par-

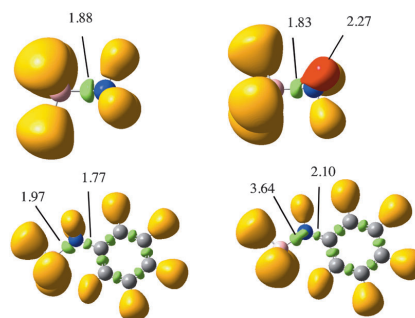


Figure 4. ELF (0.80) for the NH₃–BH₃ and C₆H₅NH₂–BH₃ complexes and their corresponding nitrogen-deprotonated species. Green lobes denote disynaptic basins involving two heavy atoms. Orange lobes are disynaptic basins in which H is one of the atoms involved. Red lobes correspond to lone pairs. The populations shown are e[−].

Table 2. Stabilization free energy of neutral (ΔG_1^0) and deprotonated (ΔG_2^0) amines upon BH₃ association.

Amine	ΔG_1^0	ΔG_2^0
ammonia	−77.9	−273.1
methylamine	−96.3	−290.1
dimethylamine	−107.8	−276.0
allylamine	−95.0	−209.1
cyclopropylamine	−71.2	−251.3
benzylamine	−112.4	−263.2
aziridine	−97.7	−265.5
propargylamine	−90.2	−267.9
trifluoroethylamine	−78.5	−257.3
aniline	−57.7	−209.1

tially delocalizes) with the disynaptic B–N basin. This effect becomes more apparent in the case of aniline, where the new nitrogen lone pair and the B–N disynaptic basin appear as a unique basin of population 3.64 electrons.

The reason why the increase in acidity is much smaller for aniline than for other amines in the series is related to the aromatic character of the system. As shown in Table 2, the free aniline is a poorer electron donor than the other amines as reflected in the lower ΔG_1^0 value, because the lone pair on the nitrogen atom conjugates with the aromatic system. This is consistent with the fact that NBO analysis (see the Supporting Information, Table S23) does not locate

a B–N bond (with the default indexes of the NBO 5.0 program) but instead locates a dative bond between the lone pair of the nitrogen atom and the empty p orbital on the boron atom. The conjugation of one of the lone pairs with the aromatic system is increased in the case of the deprotonated amine, thus leading to a shortening by 0.13 Å of the C–N bond, as well as a significant increase of both the electron density at the corresponding bond critical point (see the Supporting Information, Table S23) and the electron population of the C–N disynaptic basin (Figure 4). Still, the N–B bond is 0.09 Å shorter in the deprotonated amine because it is a better donor toward the boron atom than the neutral amine, through the second lone-pair. However, the donor capacity of the second lone pair is smaller because the aforementioned conjugation necessarily decreases the intrinsic basicity of the amino group.

The origin of the differences between methylamine and dimethylamine is more subtle. As shown in Table 2 the value of ΔG^0_1 is larger for dimethylamine than methylamine as expected from the increase in the number of methyl substituents. However, the ΔG^0_2 values show the reverse order. The fact that the anion of dimethylamine apparently behaves as a weaker electron donor than the anion of methylamine is an unexpected result. This result likely reflects the higher ability of the $(\text{CH}_3)_2\text{N}^-$ with respect to CH_3HN^- to disperse the excess negative charge, thus leading to the former having a higher relative stability. These differences are not observed, however, for the corresponding $[(\text{CH}_3)_2\text{N}\cdot\text{BH}_3]^-$ and $[\text{CH}_3\text{HN}\cdot\text{BH}_3]^-$ complexes where the negative charge is dispersed among the nitrogen atom and the BH_3 moiety. The participation of the BH_3 moiety in the dispersion of the negative charge of the deprotonated form of the amine–borane complex is one of the factors that contributes to the increase in acidity of these compounds.^[11]

Notably, the increase in acidity that occurs upon coordination of the amines to BH_3 is very large; aniline borane has practically the same gas-phase acidity as phosphoric acid $((1351 \pm 21) \text{ kJ mol}^{-1})$ ^[67] and most of the amine–borane complexes studied herein have gas-phase acidities similar to typical carboxylic acids, such as formic, ethanoic, and propionic acid.^[67]

The increase in acidity measured and calculated herein for amine–borane complexes is significantly larger than that measured and calculated for the phosphine–borane analogues.^[11] For instance, whereas the increase in acidity observed for phenylphosphine and methylphosphine upon BH_3 association is 82 and 118 kJ mol^{-1} , respectively, the increase in acidities for the amine–borane analogues are almost twice these values, being 146 and 194 kJ mol^{-1} , respectively. This observation points to the interaction between the empty p orbital of the boron atom and the lone pair of the nitrogen atom being stronger than that involving the lone pair of a phosphorus atom; this difference is presumably due to the large difference in the size of the orbitals participating in the interaction in the latter case.

Conclusion

From our combined experimental and theoretical survey we conclude that the complexation of different amines with BH_3 leads to new compounds (amine–borane complexes), which exhibit a much larger (from 146 to 195 kJ mol^{-1}) gas-phase acidity. In terms of ionization constants this increment would be about 15 (or more) orders of magnitude. The unexpected consequence is that typical nitrogen bases such as aniline, lead to amine–borane complexes, which, in the gas-phase, are as strong an acid as either phosphoric, oxalic, or salicylic acid, and stronger than many carboxylic acids, such as formic, acetic, and propanoic acid. This increase in acidity is almost twice as large as that observed for the corresponding phosphine–borane analogues. The agreement between the experimental and the G4-based calculated values is excellent. The analysis of the electron density rearrangements of the amine and the borane moieties indicates that the dative bond is significantly stronger in the complex formed from the deprotonated amine than in the corresponding neutral amine–borane complex, because the deprotonated amine is a much better electron donor than the neutral amine. Furthermore, the newly created lone pair on the nitrogen atom of the deprotonated amine, conjugates with the B–N bonding pair, thus stabilizing the anion. The contribution of BH_3 to the dispersion of the excess electron density of the anion is another factor contributing to the increased stability of the anions and therefore to the increased acidity of the amine–borane complexes with respect to the isolated amines.

Acknowledgements

This work was partially supported by the DGI (Projects No. CTQ2009-13129-C01, CTQ2009-07197-E), by the Project MADRISOLAR2, Ref.: S2009PPQ/1533 of the Comunidad Autónoma de Madrid, by Consolider on Molecular Nanoscience CSC2007-00010, and by the COST Action CM0702. We also gratefully acknowledge the support of Spanish MICINN Projects: CTQ 2009-13652 and “Acciones Integradas 2009” (Ref. FR2009-0068): -PHC PICASSO 22973TL. A generous allocation of computing time at the CCC of the UAM is also acknowledged. Helpful discussions with Prof. O. Mó are greatly acknowledged.

- [1] G. C. Pimentel, A. L. McClelland, *The Hydrogen Bond*, W. H. Freeman and Co., San Francisco, **1960**.
- [2] P. A. Kollman, L. C. Allen, *Chem. Rev.* **1972**, 72, 283–303.
- [3] S. J. Grabowski, *Hydrogen Bonding: New Insights*, Springer, Heidelberg, **2006**.
- [4] P. Metrangola, G. Resnati, *Chem. Eur. J.* **2001**, 7, 2511–2519.
- [5] P. Politzer, P. Lane, M. C. Concha, Y. G. Ma, J. S. Murray, *J. Mol. Model.* **2007**, 13, 305–311.
- [6] M. Palusiak, S. J. Grabowski, *Struct. Chem.* **2008**, 19, 5–11.
- [7] P. Politzer, J. S. Murray, T. Clark, *Phys. Chem. Chem. Phys.* **2010**, 12, 7748–7757.
- [8] M. Yáñez, P. Sanz, O. Mó, I. Alkorta, J. Elguero, *J. Chem. Theory Comput.* **2009**, 5, 2763–2771.
- [9] Q. Z. Li, X. F. Liu, R. Li, J. B. Cheng, W. Z. Li, *Spectrochim. Acta Part A* **2012**, 90, 135–140.
- [10] T. Brinck, J. S. Murray, P. Politzer, *Inorg. Chem.* **1993**, 32, 2622–2625.

- [11] J. H. Ren, D. B. Workman, R. R. Squires, *J. Am. Chem. Soc.* **1998**, *120*, 10511–10522.
- [12] S. Fau, G. Frenking, *Mol. Phys.* **1999**, *96*, 519–527.
- [13] F. Bessac, G. Frenking, *Inorg. Chem.* **2003**, *42*, 7990–7994.
- [14] M. Hurtado, M. Yáñez, R. Herrero, A. Guerrero, J. Z. Dávalos, J.-L. M. Abboud, B. Khater, J. C. Guillemin, *Chem. Eur. J.* **2009**, *15*, 4622–4629.
- [15] B. Németh, B. Khater, T. Veszpremi, J. C. Guillemin, *Dalton Trans.* **2009**, 3526–3535.
- [16] I. Alkorta, J. Elguero, J. E. Del Bene, O. Mó, M. Yáñez, *Chem. Eur. J.* **2010**, *16*, 11897–11905.
- [17] A. Martín-Sómer, A. M. Lamsabhi, O. Mó, M. Yáñez, *Comput. Theor. Chem.* **2012**, DOI:10.1016/j.comptc.201206009.
- [18] K. Müller, K. Stark, B. Müller, W. Arlt, *Energy Fuels* **2012**, *26*, 3691–3696.
- [19] J. L. Abboud, B. Németh, J. C. Guillemin, P. Burk, A. Adamson, E. R. Nerut, *Chem. Eur. J.* **2012**, *18*, 3981–3991.
- [20] C. A. Jaska, K. Temple, A. J. Lough, I. Manners, *Chem. Commun.* **2001**, 962–963.
- [21] B. L. Dietrich, K. I. Goldberg, D. M. Heinekey, T. Autrey, J. C. Linehan, *Inorg. Chem.* **2008**, *47*, 8583–8585.
- [22] T. M. Douglas, A. B. Chaplin, A. S. Weller, *J. Am. Chem. Soc.* **2008**, *130*, 14432–14433.
- [23] L. J. Sewell, A. B. Chaplin, A. S. Weller, *Dalton Trans.* **2011**, *40*, 7499–7501.
- [24] A. J. M. Miller, J. E. Bercaw, *Chem. Commun.* **2010**, *46*, 1709–1711.
- [25] R. E. Lyle, E. W. Southwic, *Anal. Chem.* **1968**, *40*, 2201–2202.
- [26] B. S. Burnham, *Curr. Med. Chem.* **2005**, *12*, 1995–2010.
- [27] R. O. Hutchins, K. Learn, B. Nazer, D. Pytlewski, A. Pelter, *Org. Prep. Proced. Int.* **1984**, *16*, 335.
- [28] A. E. Leontjev, L. L. Vasiljeva, K. K. Pivnitsky, *Russ. Chem. Bull.* **2004**, *53*, 703–708.
- [29] M. A. Funke, H. Mayr, *Chem. Eur. J.* **1997**, *3*, 1214–1222.
- [30] J. C. Cabacungan, A. I. Ahmed, R. E. Feeney, *Anal. Biochem.* **1982**, *124*, 272–278.
- [31] M. Lelental, *J. Catal.* **1974**, *32*, 429–433.
- [32] S. B. Kalidindi, U. Sanyal, B. R. Jagirdar, *ChemSusChem* **2011**, *4*, 317–324.
- [33] R. E. McCoy, S. H. Bauer, *J. Am. Chem. Soc.* **1956**, *78*, 2061–2065.
- [34] B. P. Robinson, K. A. H. Adams, *Tetrahedron Lett.* **1968**, *9*, 6169–6171.
- [35] F. M. Tayler, GB 909390 19621031 Patent, CAS 58:40084.
- [36] K. M. Johnson, J. N. Kirwan, B. P. Roberts, *J. Chem. Soc. Perkin Trans. 2* **1990**, 1125–1132.
- [37] C. J. Foret, M. A. Chiusano, J. D. O'Brien, R. D. Martin, *J. Inorg. Nucl. Chem.* **1980**, *42*, 165–169.
- [38] X. H. Cheng, Z. C. Wu, C. Fenselau, *J. Am. Chem. Soc.* **1993**, *115*, 4844–4848.
- [39] B. A. Cerda, C. Wesdemiotis, *J. Am. Chem. Soc.* **1996**, *118*, 11884–11892.
- [40] P. B. Armentrout, *J. Am. Soc. Mass Spectrom.* **2000**, *11*, 371–379.
- [41] X. B. Zheng, R. G. Cooks, *J. Phys. Chem. A* **2002**, *106*, 9939–9946.
- [42] K. M. Ervin, *J. Am. Soc. Mass Spectrom.* **2002**, *13*, 435–452.
- [43] L. Drahos, K. Vekey, *J. Mass Spectrom.* **2003**, *38*, 1025–1042.
- [44] K. M. Ervin, P. B. Armentrout, *J. Mass Spectrom.* **2004**, *39*, 1004–1015.
- [45] L. Drahos, C. Peltz, K. Vekey, *J. Mass Spectrom.* **2004**, *39*, 1016–1024.
- [46] G. Bouchoux, *Mass Spectrom. Rev.* **2007**, *26*, 775–835.
- [47] R. G. Cooks, T. L. Kruger, *J. Am. Chem. Soc.* **1977**, *99*, 1279–1281.
- [48] R. G. Cooks, J. S. Patrick, T. Kotiaho, S. A. McLuckey, *Mass Spectrom. Rev.* **1994**, *13*, 287–339.
- [49] R. G. Cooks, P. S. H. Wong, *Acc. Chem. Res.* **1998**, *31*, 379–386.
- [50] R. G. Cooks, J. T. Koskinen, P. D. Thomas, *J. Mass Spectrom.* **1999**, *34*, 85–92.
- [51] K. M. Ervin, *Int. J. Mass Spectrom.* **2000**, *195*, 271–284.
- [52] L. Drahos, K. Vekey, *J. Mass Spectrom.* **1999**, *34*, 79–84.
- [53] J. H. Ren, J. P. Tan, R. T. Harper, *J. Phys. Chem. A* **2009**, *113*, 10903–10912.
- [54] S. Mukherjee, J. H. Ren, *J. Am. Soc. Mass Spectrom.* **2010**, *21*, 1720–1729.
- [55] L. A. Curtiss, P. C. Redfern, K. Raghavachari, *J. Chem. Phys.* **2007**, *126*, 084108.
- [56] A. D. Becke, *J. Chem. Phys.* **1993**, *98*, 1372–1377.
- [57] C. Lee, W. Yang, R. G. Parr, *Phys. Rev. B* **1988**, *37*, 785–789.
- [58] M. J. Frisch, G. W. Trucks, H. B. Schlegel, G. E. Scuseria, M. A. Robb, J. R. Cheeseman, G. Scalmani, V. Barone, B. Mennucci, G. A. Petersson, H. Nakatsuji, M. Caricato, X. Li, H. P. Hratchian, A. F. Izmaylov, J. Bloino, G. Zheng, J. L. Sonnenberg, M. Hada, M. Ehara, K. Toyota, R. Fukuda, J. Hasegawa, M. Ishida, T. Nakajima, Y. Honda, O. Kitao, H. Nakai, T. Vreven, J. A. Montgomery Jr., J. E. Peralta, F. Ogliaro, M. Bearpark, J. J. Heyd, E. Brothers, K. N. Kudin, V. N. Staroverov, R. Kobayashi, J. Normand, K. Raghavachari, A. Rendell, J. C. Burant, S. S. Iyengar, J. Tomasi, M. Cossi, N. Rega, J. M. Millam, M. Klene, J. E. Knox, J. B. Cross, V. Bakken, C. Adamo, J. Jaramillo, R. Gomperts, R. E. Stratmann, O. Yazyev, A. J. Austin, R. Cammi, C. Pomelli, J. W. Ochterski, R. L. Martin, K. Morokuma, V. G. Zakrzewski, G. A. Voth, P. Salvador, J. J. Dannenberg, S. Dapprich, A. D. Daniels, O. Farkas, J. B. Foresman, J. V. Ortiz, J. Cioslowski and D. J. Fox, Gaussian09, Revision A.02, Gaussian, Inc., Wallingford CT, **2009**.
- [59] K. B. Wiberg, *Tetrahedron* **1968**, *24*, 1083–1088.
- [60] E. D. Glendening, J. Badenhoop, K. A. E. Reed, J. E. Carpenter, J. A. Bohmann, J. A. Morales, F. Weinhold, *NBO 5G Program*, Theoretical Chemistry Institute, University of Wisconsin, Madison, WI, **2001**.
- [61] R. F. W. Bader, *Atoms in Molecules. A Quantum Theory*, Clarendon Press, Oxford **1990**.
- [62] D. Cremer, E. Kraka, *Angew. Chem.* **1984**, *96*, 612–614; *Angew. Chem. Int. Ed. Engl.* **1984**, *23*, 627–628.
- [63] AIMAll (Version 11.12.19), ed. T. A. Keith, TK Gristmill Software, Overland Park KS, USA, **2011**.
- [64] A. D. Becke, K. E. Edgecombe, *J. Chem. Phys.* **1990**, *92*, 5397–5403.
- [65] B. Silvi, A. Savin, *Nature* **1994**, *371*, 683–686.
- [66] S. Noury, X. Krokidis, F. Fuster, B. Silvi, *Comput. Chem. Eng.* **1999**, *23*, 597–604.
- [67] NIST Chemistry Webbook. Standard Reference Database Number 69. Eds P. J. Linstrom and W. G. Mallard, Release June 2005, National Institute of Standards and Technology, Gaithersburg MD, 20899 (<http://webbook.nist.gov>). **2012**.

Received: June 20, 2012

Published online: October 11, 2012

A RRKM study and a DFT assessment on gas-phase fragmentation of formamide- M^{2+} ($M = \text{Ca}, \text{Sr}$)[†]

Cite this: *Phys. Chem. Chem. Phys.*, 2014, 16, 14813

Ana Martín-Sómer,^{ab} Marie-Pierre Gaigeot,^{bcd} Manuel Yáñez^{*a} and Riccardo Spezia^{*bc}

A kinetic study of the unimolecular reactivity of formamide- M^{2+} ($M = \text{Ca}, \text{Sr}$) systems was carried out by means of RRKM statistical theory using high-level DFT. The results predict M^{2+} , $[\text{M}(\text{NH}_2)]^+$ and $[\text{HCO}]^+$ as the main products, together with an intermediate that could eventually evolve to produce $[\text{M}(\text{NH}_3)]^{2+}$ and CO, for high values of internal energy. In this framework, we also evaluated the influence of the external rotational energy on the reaction rate constants. In order to find a method to perform reliable electronic structure calculations for formamide- M^{2+} ($M = \text{Ca}, \text{Sr}$) at a relatively low computational cost, an assessment of different methods was performed. In the first assessment twenty-one functionals, belonging to different DFT categories, and an MP2 wave function method using a small basis set were evaluated. CCSD(T)/cc-pWCVTZ single point calculations were used as reference. A second assessment has been performed on geometries and energies. We found BLYP/6-31G(d) and G96LYP/6-31+G(d,p) as the best performing methods, for formamide- Ca^{2+} and formamide- Sr^{2+} , respectively. Furthermore, a detailed assessment was done on RRKM reactivity and G96LYP/6-31G(d) provided results in agreement with higher level calculations. The combination of geometrical, energetics and kinetics (RRKM) criteria to evaluate DFT functionals is rather unusual and provides an original assessment procedure. Overall, we suggest using G96LYP as the best performing functional with a small basis set for both systems.

Received 23rd April 2014,
Accepted 28th May 2014

DOI: 10.1039/c4cp01756k

www.rsc.org/pccp

1. Introduction

Doubly charged molecular ions, formed by association of a neutral base with a doubly charged metal ion, are of great importance in chemical and biochemical processes, both in solution and in the gas phase.¹ Indeed, they are fundamental in gas-phase ion chemistry and in mass spectrometry in spite of their short lifetime.^{2–4} They also play important roles in photochemical processes,^{5,6} as well as in astrochemistry and the chemistry of the atmospheres.^{7–10} It has also been postulated that they may have played some role in the origin of life,^{11–15} since doubly charged metal ions may have induced the precipitation of nucleic acid molecules. Nevertheless, these multiply charged ions were, for a long time, oddities in the gas phase due to the difficulties in generating and stabilizing them. The so-called

intrinsic reactivity is of great importance since the absence of interactions with a solvent can result in very different reactivity patterns; in many cases it allows for a better understanding of chemical bonding. With the advent of electrospray ionization techniques in 1990,¹⁶ generation of doubly-charged ions in the gas-phase from aqueous solutions became feasible and therefore the interest in gas-phase reactions between di-cations and neutral molecules has grown significantly. Many theoretical studies have been performed to understand the structures and relative stabilities of such ion-molecule complexes, providing detailed information on the nature of their interactions and binding energies.^{17–22} However, information about their unimolecular reactivity is much scarcer and fragmentary. One of the main reasons is that doubly- or multiply-charged species are rare in the gas-phase because many of these species are either thermochemically or kinetically unstable.¹ This is indeed the case when they are the result of the association of a doubly (or multiply) charged transition metal ion (M^{2+}) with an organic base (B). The system undergoes a spontaneous deprotonation of the base leading to the monocation $[\text{M}(\text{B}-\text{H})]^+$, the species experimentally observed.^{23–26} However, this is not the case with alkaline-earth dications such as Ca^{2+} and Sr^{2+} , since $[\text{CaB}]^{2+}$ and $[\text{SrB}]^{2+}$ are stable and detectable in the gas phase.²⁷ This opened the possibility of studying for the first time the unimolecular reactivity of complexes formed by these metal dications with

^a Departamento de Química, Facultad de Ciencias, Módulo 13. Universidad Autónoma de Madrid, Campus de Excelencia UAM-CSIC, Cantoblanco, E-28049 Madrid, Spain. E-mail: manuel.yanez@uam.es

^b Université d'Evry Val d'Essonne, UMR 8587 LAMBE, Boulevard F. Mitterrand, 91025 Evry Cedex, France. E-mail: riccardo.spezia@univ-evry.fr

^c CNRS, Laboratoire Analyse et Modélisation pour la Biologie et l'Environnement, UMR 8587, France

^d IUF: Institut Universitaire de France, 103 Blvd St Michel, 75000 Paris, France

[†] Electronic supplementary information (ESI) available. See DOI: 10.1039/c4cp01756k

different neutral bases such as urea, glycine, thiourea, selenourea, uracil and its thio derivatives.^{28–34} All these studies show that there is a competition between Coulomb explosions and neutral loss fragmentation.

Recently, Eizaguirre *et al.* studied the interactions and dissociation patterns of formamide–Ca²⁺ and formamide–Sr²⁺ complexes.^{35,36} The study combined collision induced dissociation (CID) experiments and high-level DFT calculations to analyze the topology of the potential energy surface (PES). The reactivity is similar for both cationic metals with some minor differences; a mechanism leading to the different fragments was proposed based on the computed PESs. Although it is possible to extract some conclusions about the reactivity from the topology of the PES, this constitutes only a first rough approach, and there are still open questions. For instance, why the most abundant product in the experiments (M²⁺) corresponds to the more endothermic process on the PES? Or why the [M(NH₂)]⁺ + [HCO]⁺ Coulomb explosion product appears only for M = Ca? Since often the products that are thermodynamically favoured are not kinetically favoured (and *vice versa*) we decided to carry out a kinetic study to shed light on these points.

In CID experiments the molecular ion is made to collide with a rare gas at low collision energies, in such a way that part of the kinetic energy is transferred to the molecular ion as vibrational and rotational internal energy. From the theoretical point of view, one way to rationalize the fragments observed experimentally is to apply RRKM statistical kinetic theory,^{37,38} providing the kinetics of the unimolecular reactions undergone by the doubly charged ion after the collisional excitation. Such calculations require a reliable description of the potential energy surface as well as reliable predictions of molecular properties, and this can be attained through the use of *ab initio* methods. CID experiments are now routinely applied to small and large molecules such as peptides and proteins,^{39–41} and combining CID with RRKM in these latter cases requires electronic representations computationally less expensive than *ab initio* methods. A similar situation occurs when coupling RRKM and direct dynamics simulations of the fragmentation.^{42–46} This calls for resorting to less computationally demanding theoretical approaches, such as density functional theory (DFT).⁴⁷ To be sure about the reliability of the results obtained *via* DFT it is, however, necessary to carry out an assessment in order to choose the most appropriate functional.

Thus, one of the aims of this paper is to test a variety of DFT methods as well as the MP2 wave function method against benchmark CCSD(T) results for the two aforementioned systems, using a small basis set (6-31G(d)). This would allow us to validate the accuracy of non-expensive methods that might be used for computationally expensive treatments such as dynamics simulations or bigger systems like oligopeptides. The geometries and energies will be obtained with 21 different DFT approaches. These methods will also be assessed from the kinetic point of view, a rather unusual approach providing an original way to assess DFT functionals also on kinetics rather than simply on energetics and/or frequencies. As the main aim of this study we will perform a kinetic study on the unimolecular reactivity of

formamide–M²⁺ (M = Ca, Sr), thus complementing the previous investigations based only on the topology of the PESs.^{35,36}

2. Computational details

2.1. Quantum chemistry

Geometry optimization and frequency calculations were performed using density functional theory (DFT) and Møller–Plesset perturbation theory at second order (MP2). In the first assessment we tested functionals from four different categories of DFT methods.

(i) GGA functionals that depend explicitly on the gradient of the electron density as well as the density itself: BLYP,^{48,49} G96LYP,^{49,50} and PBE⁵¹ (PBE exchange with PBE correlation, also called PBEPBE).

(ii) Hybrid GGA functionals that depend on Hartree–Fock (HF) exchange as well as the electron density and its gradient: PBE0 (also called PBE1PBE, which adds 25% of HF exchange to the PBE functional), B3LYP,^{49,52} B3P86,^{52,53} B3PW91,^{52,54} B97-2,⁵⁵ BH&H (0.5E_X^{HF} + 0.5E_X^{LSDA} + E_C^{LYP}), BH&HLYP (0.5E_X^{HF} + 0.5E_X^{LSDA} + 0.5ΔE_X^{Becke88} + E_C^{LYP}), mPW1PW91,^{54,56} O3LYP,^{49,57,58} and X3LYP.^{49,59}

(iii) Meta-GGA functionals that depend on the electron density, its gradient, and the kinetic energy density: M06L,⁶⁰ TPSS,⁶¹ and VSXC.⁶²

(iv) Hybrid meta-GGA functionals that depend on HF exchange, the electron density and its gradient, and the kinetic energy density: M05,⁶³ M05-2X,⁶⁴ M06,⁶⁵ M06-2X,⁶⁵ and BMK.⁶⁶

CCSD(T) single-point calculations on DFT optimized geometries were used as benchmark values in this first assessment. Formamide–Ca²⁺ geometries and frequencies were computed at the B3LYP/cc-pWCVTZ level of theory while formamide–Sr²⁺ geometries and frequencies were obtained using the G96LYP functional together with the 6-31+G(d,p) basis set expansion for C, N, O and H and an improved LANL2DZ basis set for the Sr²⁺ cation.³⁵ Using these geometries, CCSD(T) single point calculations were performed using the cc-pWCVTZ basis set for formamide–Ca²⁺ and the 6-311+G(3df,2p) basis set with an extended LANL2DZ for the Sr²⁺ cations³⁵ in the formamide–Sr²⁺ system. In all the cases ZPVE corrections were obtained at the same level used for geometry optimization and scaled by the corresponding empirical factor proposed by Merrick *et al.*⁶⁷

Keeping in mind that we are looking for a low computationally demanding method, we have selected for both DFT and MP2 calculations a 6-31G(d) basis set for C, N, O, Ca and H atoms and a LANL2DZ with an ECP basis set for Sr²⁺ cations. This basis set expansion, although small, provides both reliable geometries and fundamental frequencies (necessary to compute RRKM unimolecular rate constants).⁶⁷ From now on, we will refer to this model as the *low-level* approach. Out of these twenty-one functionals we selected three (the two best and B3LYP) to evaluate the effect of adding diffuse functions and higher-angular momentum components in the basis set evaluating its performance using the 6-31+G(d,p) basis set (keeping LANL2DZ for Sr atoms).

These three functionals plus the MP2 *ab initio* method together with 6-31G(d) were used in the second step to assess

the whole potential energy surface (PES). In this case, and due to the lack of specific experimental information, we will use results previously obtained by Eizaguirre *et al.*^{35,36} as a reliable reference for the assessment of DFT. These results were in turn compared with high-level *ab initio* calculations. For the sake of simplicity, when speaking of these benchmark values, we will allude them as the *high-level* approaches. These optimized structures were taken as the starting structures to be re-optimized with each of the low-level methods; then we computed harmonic vibrational frequencies and final energies. The harmonic frequencies were also used to estimate the zero point vibrational energy (ZPVE) corrections, which were systematically scaled by the corresponding empirical factor proposed by Merrick *et al.*⁶⁷ However, the reported interaction energies were not corrected with the basis set superposition error (BSSE). There are two main reasons for doing so: the energies used as reference were not corrected with BSSE; also if the RRKM results are coupled with direct dynamics simulations this latter approach will not take into account BSSE either. All the calculations in this study have been carried out using the Gaussian09 suite of programs.⁶⁸

We have studied different structures from the previously described PESs of formamide–Ca²⁺ and formamide–Sr²⁺ systems.^{35,36} These surfaces can also be found in Fig. S1 and S2 of the ESI,[†] together with the structure of the corresponding stationary points. Correspondingly, in what follows, *min1* will refer to the global minimum of the PES; *intX*, where *X* is a number according to the nomenclature used in ref. 36, will name the different intermediates on the PES and *TS_X_Y* the transition state connecting the *X* and *Y* local minima, *k_{XY}* (*t_{XY}* when considering half-life times) denoting the RRKM rate constants. To denote the exit channels we will use letters A, B, C and so on.

2.2. RRKM rate constants

Fig. 1 shows the kinetic schemes associated with the PES for formamide–M²⁺ (M = Ca, Sr) unimolecular reactions. The rate constants, *k*, for each individual reaction are also indicated in the kinetic scheme. For the exit channels there is no backward reaction because in CID experiments there is no equilibrium between fragments and parent ions.

Tight-TS. For the unimolecular reactions where TS location is assumed to be fixed at a saddle point (tight-TS), we have used RRKM statistical theory in order to compute quantum harmonic microcanonical rate constants, *k(E)*, that ignoring rotations reads³⁷

$$k(E) = \frac{\sigma N^\#(E - E_0)}{h \rho(E)} \quad (1)$$

where σ is the reaction degeneracy, E_0 is the activation energy, $N^\#(E - E_0)$ is the TS sum of states and $\rho(E)$ is the reactant density of states. The latter two quantities are only for active degrees of freedom. Thus, we compute *k(E)* by using properties of minima and saddle points on the PES, which is only possible for unimolecular reactions involving all of the intermediates. When using *k(E)* we refer to *k(E, J)* with *J* = 0. When considering the influence of the rotational energy in the microcanonical rate constants we will use *k(E, J)* in order to stress the fact that we are varying *J* and *K* rotational quantum number values

(we will later provide details on how *J* and *K* can be considered in RRKM theory).

Loose-TS. For channels with no reverse activation energy (loose-TS) the TS is more difficult to define because there is no saddle point along the reaction path. The TS is located on the basis of the minimum sum of states and varies with the internal energy.

To compute the RRKM rate constants for the loose-TS we adopted the microcanonical variational transition state theory (μ VTST) in its vibrator formulation.^{69,70} First we perform a scan along the reaction coordinate. Then, at each point of the scan we do an optimization, freezing this internal coordinate and the energy is computed. The Hessian matrices describing the modes orthogonal to the reaction path are evaluated according to the standard procedure of Hu and Hase,⁷⁰ and the sum of states are calculated for the corresponding optimized structure. We repeat this procedure for each internal energy considered and the structure corresponding to the minimum sum of states is assigned as the TS. An example of a loose-TS is the formamide neutral loss reaction. In this example, the reaction coordinate corresponds to the Ca–O distance and thus we used this as the scanned coordinate. In Fig. 2 we can observe how the location of the TS (minimum sum of states) with respect to the reaction coordinate changes with the internal energy of the reactant molecule, getting closer to the reactants as the internal energy increases.

External rotations. RRKM theory treats modes either as active, which exchange energy freely, or adiabatically, which remain in the same quantum number during the unimolecular decomposition. Normally, the modes treated as active are all the normal modes. If the external rotational degrees of freedom are to be taken into account there are different ways of doing so in the framework of RRKM theory.⁷¹ In this study we have considered an *almost symmetric top*, where $I_x \approx I_y$, for which rotational energy is given by the following approximation:⁷²

$$E_{\text{rot}}(J, K) = \left(\frac{1}{I_x} + \frac{1}{I_y} \right) \frac{[J(J+1) - K^2] \hbar^2}{4} + \frac{K^2 \hbar^2}{2I_z} \quad (2)$$

that can be written as

$$E_{\text{rot}}(J, K) = B[J(J+1) + (A - B)K^2] \quad (3)$$

where $A = \hbar^2/2I_z$, $B = \left(\frac{1}{I_x} + \frac{1}{I_y} \right) \frac{\hbar^2}{4}$, $J = 0, 1, 2, \dots$ and $K = 0, \pm 1, \pm 2, \dots, \pm J$. The symmetry axis is the z-axis and the other two moments of inertia are $I_x \approx I_y$. The quantum number *J* is a constant of motion and therefore is always adiabatic, *i.e.* there is no exchange. On the other hand, the quantum number *K* can be treated as an active rotor – it allows energy exchange between vibrational and rotational modes—or as an adiabatic rotor.

If we assume that *K* is conserved, and thus treated as adiabatic, the RRKM unimolecular rate constant for energy *E* and specific values of *J* and *K* is³⁷

$$k(E, J, K) = \frac{\sigma N^\# [E - E_0 - E_{\text{rot}}^\#(J, K)]}{h \rho [E - E_{\text{rot}}(J, K)]} \quad (4)$$

where $E_{\text{rot}}^\#$ is the rotational energy for the transition state and E_{rot} is the same for the minimum energy structure

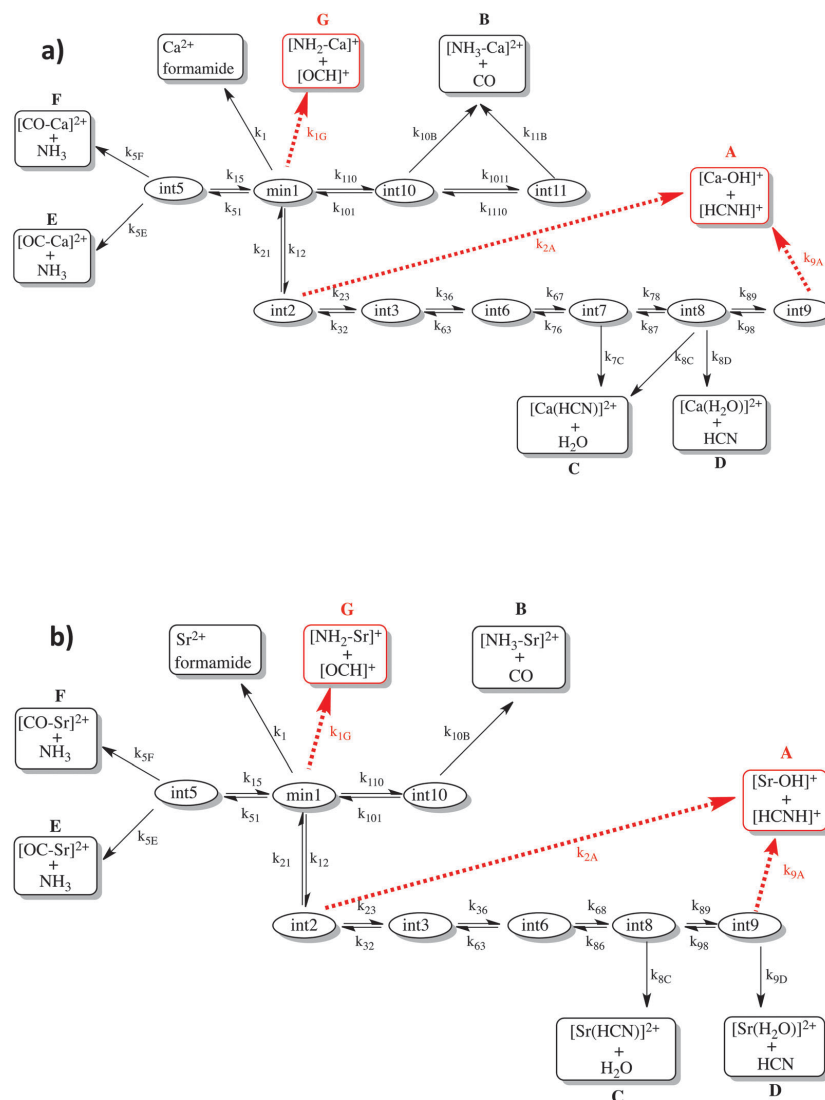


Fig. 1 Mechanistic model for the kinetic study employed in the present work. Panel (a) formamide-Ca²⁺ and panel (b) formamide-Sr²⁺. Solid black lines denote neutral loss reactions while the red dashed lines correspond to Coulomb explosions.

(both obtained by eqn (2)). With this assumption (J and K being adiabatic) we consider three particular cases for partitioning the rotational energy within the molecular axes. In case 1, all the rotational energy is placed on the xy -plane, and corresponds to $K = 0$, and

$$J = \frac{\left(-1 + \sqrt{1 + 4\frac{E_{\text{rot}}}{B}}\right)}{2}; \quad \bar{B} = \left(\frac{1}{I_x} + \frac{1}{I_y}\right)\frac{\hbar^2}{4} \quad (5)$$

where E_{rot} is the rotational energy of the ion after collision. In case 2 the rotational energy is equally distributed among the three axes, so $E_{x,y} = 2/3E_{\text{rot}}$ and $E_z = 1/3E_{\text{rot}}$. Finally, in case 3 all the rotational energy is placed along the z -axis such that

$$K = \sqrt{\frac{1}{3} \frac{E_{\text{rot}}}{A - B}} \quad (6)$$

The $k(E, J)$ microcanonical rate constant with K active can be determined by two different approaches. One approach for

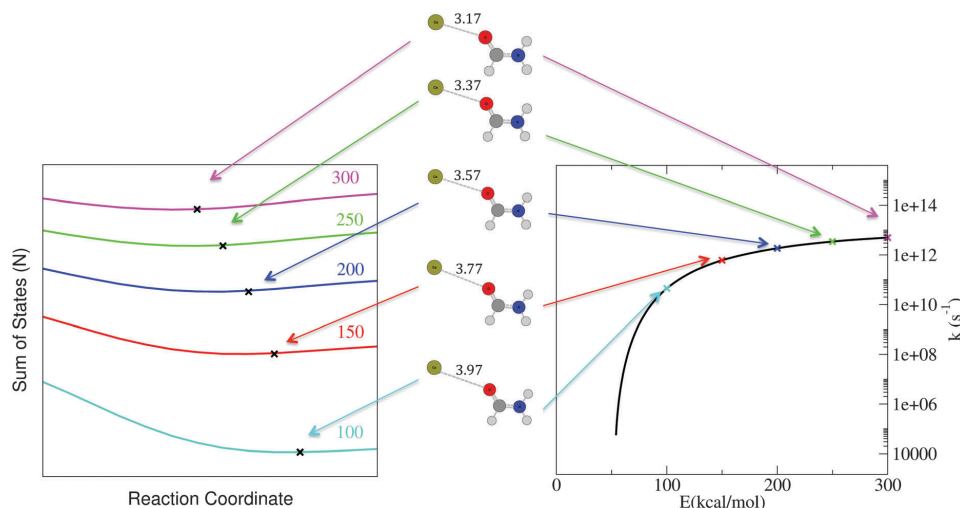


Fig. 2 On the left side the sum of states vs. the reaction coordinate for formamide-Ca²⁺ at different internal energies (all in kcal mol⁻¹). The crosses mark the minimum of the sum of states for each energy. On the right side the microcanonical rate constant k is represented vs. the internal energy. The crosses mark the $k(E)$ values corresponding to the minimum sum of states for specific internal energies. In the middle the formamide-Ca²⁺ geometries are represented for each of the points with the values (in Å) for Ca-O distance.

treating the K -dependent term as an active degree of freedom is to calculate the density of states for the reactant and the sum of states for the TS by summing over contributions from all possible values of K to give⁷¹

$$k(E, J) = \frac{\sigma \sum_{K=J}^{K=J} N^{\#} [E - E_0 - E_{\text{rot}}^{\#}(J, K)]}{h \sum_{K=J}^{K=J} \rho [E - E_{\text{rot}}(J, K)]} \quad (7)$$

In the second approach, the unimolecular rate constant, $k(E, J)$, for total energy E and angular momentum J is written as⁷¹

$$k(E, J) = \frac{\sigma N^{\#} [E - E_{\text{rot}}^{\#}(J) - E_0]}{h \rho [E - E_{\text{rot}}]} \quad (8)$$

where $N^{\#}$ and ρ are now written as convolutions between the densities and the sum of states for the internal degrees of freedom and the active external rotation, respectively

$$N^{\#}(E^{\#}) = \int_0^{E^{\#}} N_{\text{vib}}^{\#}(E) \rho_{\text{rot}}(E^{\#} - E) dE \quad (9)$$

$$\rho(E_v) = \int_0^{E_v} \rho_{\text{vib}}(E) \rho_{\text{rot}}(E_v - E) dE \quad (10)$$

$E^{\#}$ is the active energy of the TS and E_v is the active energy of the energized reactant; the total energy is $E = E_v + E_{\text{rot}}(J) = E^{\#} + E_{\text{rot}}^{\#}(J) + E_0$ with $E_{\text{rot}}(J)$ and $E_{\text{rot}}^{\#}(J)$ being the adiabatic rotational energies of the reactant and the TS respectively.

For all the calculations, the sum and density of states were computed using a semiclassical state counting.^{73–75} We used

the quantum RRKM model which assumes that ZPE flows freely within the molecule.^{76,77} All the calculations were performed using the RRKM code given by Zhu and Hase.⁷⁸

3. Benchmarking methods

3.1. Preliminary assessment

A wide window of functionals combined with a small basis set were evaluated in a preliminary assessment (“low-cost” method). However, caution must be taken when selecting a DFT method to use for a specific problem or a specific system because often a DFT method that correctly predicts certain properties, such as geometries or binding energies, will prove to be much less accurate for the computation of other properties, such as barrier heights or conformational energy differences. On the other hand, those energies are the energetic properties governing the different reactive pathways. Therefore, the crucial point is whether this “low-cost” approach performs well enough when treating di-cationic systems. Hence, in this assessment, we considered energetics corresponding to the principal reaction mechanisms: M-O²⁺ dissociation energy to obtain formamide + M²⁺, as a representative example of neutral loss, and the barrier height for the fragmentation of the global minimum (min1) into [M(NH₂)]⁺ + [HCO]⁺, as an example of Coulomb explosion. The goal is to find the method that performs better for both processes (metal-ligand bond energy and barrier height). For this assessment we will use CCSD(T) single-point calculations on DFT optimized geometries as reference. We evaluated 21 functionals using the 6-31G(d) basis set plus three functionals (BLYP, G96LYP and B3LYP) using the 6-31+G(d,p) basis set.

In all cases the Sr basis set is LANL2DZ. The results are shown in Table 1.

Table 1 M–O²⁺ dissociation energy (NL) and Coulomb explosion ([M(NH₂)⁺ + [HCO]⁺) energy barrier (CE) computed with different DFT functionals, all with the 6-31G(d) basis set but when explicitly written. The third column shows the energy difference between M–O²⁺ dissociation energy and Coulomb explosion energy barrier (gap). The fourth column is the same energy difference without taking into account the ZPVE correction (gap*). The first row corresponds to the benchmark method. All values are in kcal mol^{−1}

	NL	CE	Gap	Gap*
M = Ca				
CCSD(T)/cc-pWCVTZ	90.76	77.45	13.31	10.10
BLYP	88.02	81.51	6.51	2.95
BLYP/6-31+G(d,p)	82.74	78.77	3.97	0.38
G96LYP	84.30	82.22	2.09	−1.57
VSXC	86.42	85.34	1.08	−2.60
G96LYP/6-31+G(d,p)	80.19	79.71	0.48	−3.10
PBEPBE ^a	87.50	88.10	−0.60	−4.23
MP2	86.24	87.62	−1.38	−4.46
O3LYP	85.21	88.66	−3.45	−6.70
X3LYP ^a	89.74	93.42	−3.69	−6.94
B3LYP	88.86	92.58	−3.72	−6.94
B3LYP/6-31+G(d,p)	84.58	88.80	−4.22	−7.51
TPSS	87.14	92.32	−5.18	−8.55
M06-2X ^a	89.22	95.53	−6.30	−9.05
M05	87.22	93.90	−6.68	−9.67
M05-2X	90.04	99.18	−9.13	−11.86
M06 ^a	86.21	95.39	−9.17	−12.27
BH&HLYP	90.18	99.68	−9.50	−12.57
B972	85.60	95.23	−9.63	−12.85
B3PW91	86.23	96.05	−9.81	−13.11
M06L ^a	82.73	92.99	−10.26	−13.91
MPW1PW91	87.42	98.17	−10.75	−13.95
PBE1PBE ^a	87.87	98.74	−10.86	−14.17
B3P86	87.27	98.24	−10.97	−14.30
BMK	86.59	99.49	−12.90	−15.95
BH&H	95.56	110.00	−14.44	−17.32
M = Sr				
CCSD(T)/6-311+G(3df,2p)	78.97	86.95	−7.98	−11.60
G96LYP/6-31+G(d,p)	73.28	81.57	−8.30	−11.91
BLYP/6-31+G(d,p)	63.82	85.49	−21.67	−25.79
BLYP	63.92	87.52	−23.61	−27.86
VSXC	65.98	91.38	−25.39	−29.18
G96LYP	60.68	87.97	−27.29	−31.31
PBEPBE ^a	64.55	94.35	−29.80	−33.85
B3LYP/6-31+G(d,p)	66.58	98.09	−31.50	−35.26
O3LYP	64.07	97.17	−33.11	−37.29
TPSS	66.32	100.40	−34.07	−38.24
M06L ^a	65.12	99.54	−34.42	−38.66
B3LYP	66.17	101.90	−35.72	−39.68
X3LYP ^a	66.93	103.13	−36.20	−40.15
M06-2X ^a	69.08	105.52	−36.44	−38.99
M05	66.02	104.81	−38.80	−42.11
B972	65.56	104.85	−39.29	−43.20
M06 ^a	65.59	105.38	−39.79	−43.14
MP2	63.01	102.86	−39.85	−43.34
B3PW91	65.19	105.31	−40.12	−44.11
BH&HLYP	69.58	110.35	−40.77	−43.69
B3P86	66.21	107.48	−41.27	−45.26
MPW1PW91	66.75	108.35	−41.60	−45.38
PBE1PBE ^a	66.98	109.07	−42.09	−45.96
M05-2X	69.15	112.44	−43.29	−46.48
BMK	65.91	111.91	−46.00	−48.68
BH&H	73.02	119.79	−46.77	−49.75

^a ZPVE was not corrected by the scale factor because it was not available.

From the values in Table 1 we observe that for M = Ca only five methods give the correct qualitative result showing that as predicted by the reference CCSD(T) calculations the neutral loss is higher in energy than the activation barrier for the Coulomb explosion (positive values). In the case of Sr containing systems all the functionals reproduce CCSD(T) results qualitatively (same sign). The best performing method depends on the metal: when M = Ca the best performing model is BLYP/6-31G(d) while when M = Sr the best one is G96LYP/6-31+G(d,p); it gives almost the same value as the reference. This latter result is in agreement with previous assessments,⁷⁹ and this level is the one used in geometry optimization for the Sr containing system. Therefore, we have selected these methods for a subsequent assessment evaluating the whole PES, comparing geometries and relative energies (*vide infra*). It should be noted that in general all the functionals investigated perform well for the description of the NL dissociation energy, so the differences in correctly reproducing the gap mainly arise from the significant differences in the estimation of the Coulomb explosion barrier. Indeed, the functionals like BLYP that do not include Hartree–Fock exchange perform better than the hybrid ones. Actually it can be observed that the agreement with the CCSD(T)-reference value decreases as the amount of Hartree–Fock exchange increases, being worse for BH&HLYP than for B3LYP. In general, the inclusion of Hartree–Fock exchange introduces a partial self-interaction correction, but at the same time it removes the non-dynamic correlation effects described by the GGA functionals.^{80,81} This actually may explain the good performance of methods like BLYP for the particular case of the CE barrier, where static correlation must be important taking into account that, at the barrier, the wavefunction must be the mixture of covalent and ionic components. However, the good performance could be due to cancellation of errors affecting both estimated energies. Since one of our objectives is to compare the formamide–Ca²⁺ and formamide–Sr²⁺ reactions, it is advisable to use the same theoretical model to reproduce both PESs. Hence, for this purpose we have chosen the G96LYP/6-31G(d) approach, which is among the best performing for both systems. For the sake of completeness, we will also test the heavily used B3LYP functional and the MP2 *ab initio* method using in all cases a 6-31G(d) basis set. In this assessment we have used as a reference the potential energy surface obtained by Eizaguirre *et al.* for formamide–Ca²⁺ and formamide–Sr²⁺.^{35,36}

3.2. Geometry assessment

A comparison of the geometries obtained with the aforementioned four methods with those reported previously^{35,36} shows rather small differences for both metals (Ca and Sr). This is very well reflected by the small errors affecting the rotational constants *A*, *B*, and *C* (see Fig. 3), which are sensitive criteria when comparing different geometries. All the values are given in Tables S1 and S2 in the ESI†

The results show that globally there are no significant differences in the geometries optimized with the low-level approaches, although for some structures the magnitude of the relative error is slightly large. We will briefly comment on

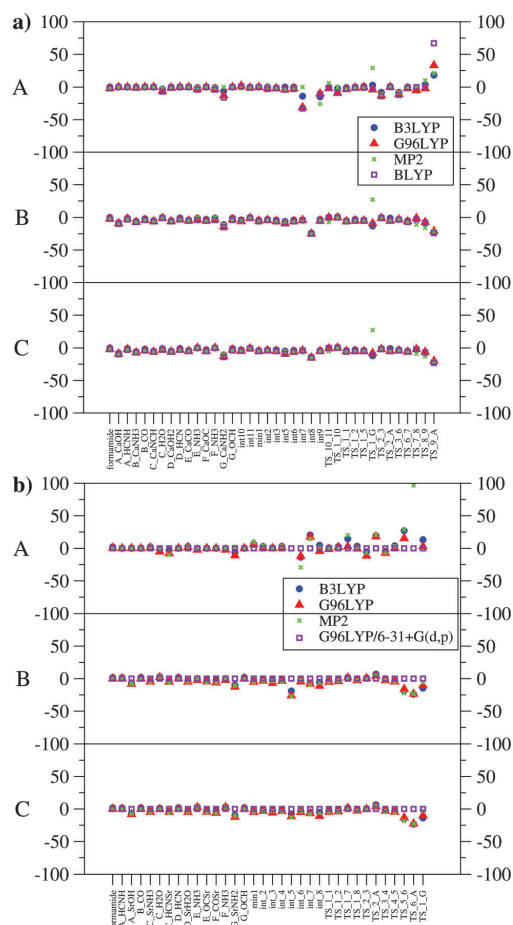


Fig. 3 Relative error (%) deviations for rotational constants of (a) formamide- Ca^{2+} computed at B3LYP/6-31G(d) (blue circles), G96LYP/6-31G(d) (red triangles), MP2/6-31G(d) (green crosses), and BLYP/6-31G(d) (purple squares) and (b) formamide- Sr^{2+} computed at B3LYP/6-31G(d) (blue circles), G96LYP/6-31G(d) (red triangles), MP2/6-31G(d) (green crosses) and G96LYP/6-31+G(d,p) (purple squares).

the structures with the most significant deviations, namely *int8* and *TS_1_G*. Tables with all relative error values are given in the ESI.†

The structure with the highest errors is *int8* for both metals. These errors in the three rotational constants arise from differences in the oxygen-metal-nitrogen angle, which are about 180° with the trial methods and 120° in the reference structure (see Fig. 4a). As expected, the rotational constant *A* is the most sensitive to these structural changes. The *TS_1_G* structure is well described with the three DFT functionals while MP2 overestimates the three rotational constants by about 30% for $\text{M} = \text{Ca}$ and the rotational constant *A* (268% relative error)

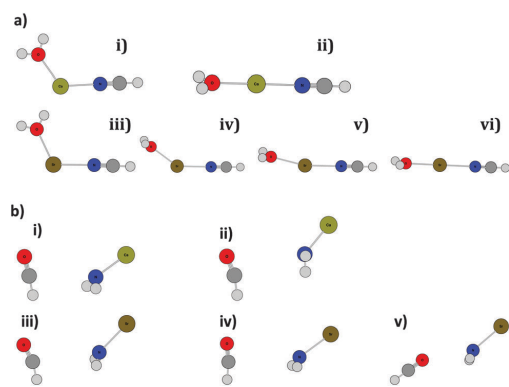


Fig. 4 (a) *Int8* structure for $\text{M} = \text{Ca}$ optimized with (i) B3LYP/cc-pWCVTZ, (ii) BLYP/6-31G(d) and for $\text{M} = \text{Sr}$ optimized with (iii) G96LYP/6-31+G(d,p), (iv) B3LYP/6-31G(d), (v) G96LYP/6-31G(d) and (vi) MP2/6-31G(d), (b) *TS_1_G* structure for $\text{M} = \text{Ca}$ optimized with (i) B3LYP/cc-pWCVTZ, (ii) BLYP/6-31G(d) and for $\text{M} = \text{Sr}$ optimized with (iii) G96LYP/6-31+G(d,p), (iv) B3LYP/6-31G(d) and (v) MP2/6-31G(d).

for $\text{M} = \text{Sr}$. These discrepancies are mainly due to differences in the relative orientation of the two departing fragments (Fig. 4b). Another structure with remarkably relative errors is *TS_9_A*, in particular when $\text{M} = \text{Sr}$, again due to the different relative orientations of the departing fragments.

In summary, the only structures that show more significant errors with respect to the reference arise from the different orientation of subunits that are weakly bound. The optimized geometries for all the stationary points are available in the ESI.†

3.3. Energy assessment

Let us focus now on the performance of the low-level approaches when dealing with energies. Relative energies were evaluated for each method by subtracting from the energy of the corresponding structure (the sum of the energy of the fragments for the exit channels), the energy of the global minimum, *min1*; including the corresponding ZPVE corrections. The absolute error and relative error values for all the structures are given in Tables S3 and S4 in the ESI.† Fig. 5 shows the relative errors for $\text{M} = \text{Ca}$ and $\text{M} = \text{Sr}$, respectively. In general the agreement is quite good and the trends are the same for the four methods.

The root-mean-square error or deviation (RMSD) of the values obtained with the low-level approach from the values computed at high-level, is reported in Table 2. The normalized RMSD ($\text{NRMSD} = \text{RMSD}/(b_{\text{max}} - b_{\text{min}})$ where *b* stands for reference values) is also reported because it is useful to compare how the performance of each method varies when the cationic metal changes from Ca^{2+} to Sr^{2+} .

It can be seen that for $\text{M} = \text{Ca}$ all methods perform almost equally well, whereas for $\text{M} = \text{Sr}$, G96LYP/6-31+G(d,p) seems to be the best option since it shows the lowest RMSD. Let us recall that G96LYP/6-31+G(d,p) is the method used in the geometry optimization of the benchmark values for $\text{M} = \text{Sr}$. These results

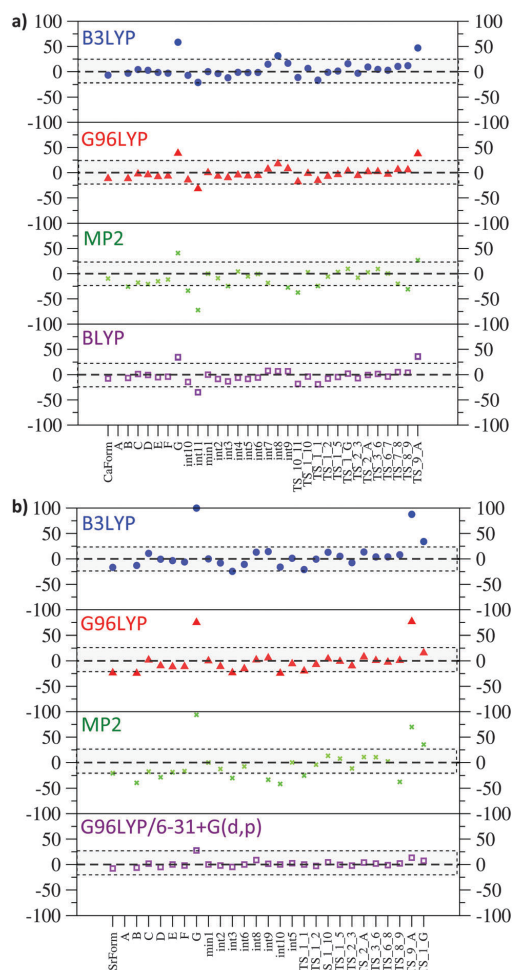


Fig. 5 Relative errors in (a) formamide- Ca^{2+} relative energies computed with B3LYP/6-31G(d) (blue circles), G96LYP/6-31G(d) (red triangles), MP2/6-31G(d) (green crosses), and BLYP/6-31G(d) (purple squares) and (b) formamide- Sr^{2+} relative energies with B3LYP/6-31G(d) (blue circles), G96LYP/6-31G(d) (red triangles), MP2/6-31G(d) (green crosses), and G96LYP/6-31+G(d,p) (purple squares).

are in agreement with those obtained in the first assessment discussed above. The next best performance is obtained using

G96LYP/6-31G(d) for both systems. In general, there is a better agreement between low-level and high-level methods when the cation is Ca^{2+} .

It is worth noting that whereas the first assessment on formamide- Ca^{2+} (see Table 1) shows a better performance for MP2/6-31G(d) than for B3LYP/6-31G(d), this is not the case when comparing the whole PES, where B3LYP has a slightly better performance than MP2.

3.4. Kinetic assessment

A further step in our assessment needs to include the kinetic behaviour. To this end, we computed the RRKM rate constants, $k(E)$, corresponding to the different reactions shown in Fig. 1, with the same four methods used before for geometry and energy assessment. This will imply an indirect assessment of three properties: energy barriers, geometries, and harmonic frequencies, needed to compute RRKM rate constants.

From now on we will use half-life times, $t_{1/2}$, instead of rate constants, k . This quantity is proportional to the reaction rate constant $t_{1/2}(E) = -(\ln 0.5)/k(E)$ and gives us an idea of how fast a reaction occurs. In order to compare the performance of the different methods, the curves for $t_{1/2}$ vs. E were shifted in the x-axis at a quantity equal to the activation barrier energy, E_{act} . Thus E stands for the internal energy available to react, i.e. internal energy over the activation barrier. The average of the relative errors is plotted in Fig. 6.

It should be noted that $t_{1/2}$ is a very sensitive quantity, especially at small E , just over the energy barrier, so not surprisingly the relative errors are large in this region. As the energy increases the errors decrease and the curves tend to converge to a given value. In general, trends are similar for both metals. The MP2 method is clearly the most unfavourable with very high relative errors. B3LYP and G96LYP perform much better than MP2, but still the relative errors are significant. At small energies G96LYP is better than B3LYP but as the energy increases the order changes, with B3LYP becoming slightly more preferable. The best performance is observed for BLYP when $M = \text{Ca}$, and G96LYP/6-31+G(d,p) for $M = \text{Sr}$.

4. Kinetic behaviour (RRKM)

Now we have computed the rate constants, which take into account dynamical effects that are not present in the topological analysis of the PES, we can evaluate the kinetics of the system by comparing the rate constants for the different reactions that the system may undergo (see Fig. 1). Due to the complex

Table 2 Root mean-square-deviation (RMSD) in kcal mol^{-1} and normalized RMSD (NRMSD)

	Formamide- Ca^{2+}				Formamide- Sr^{2+}			
	B3LYP ^a	G96LYP ^a	MP2 ^a	BLYP ^a	B3LYP ^a	G96LYP ^a	MP2 ^a	G96LYP ^b
RMSD	7.5	6.4	8.6	6.0	14.5	12.5	14.7	3.2
NRMSD	8%	6%	9%	6%	16%	13%	16%	3%

^a 6-31G(d). ^b 6-31+G(d,p).

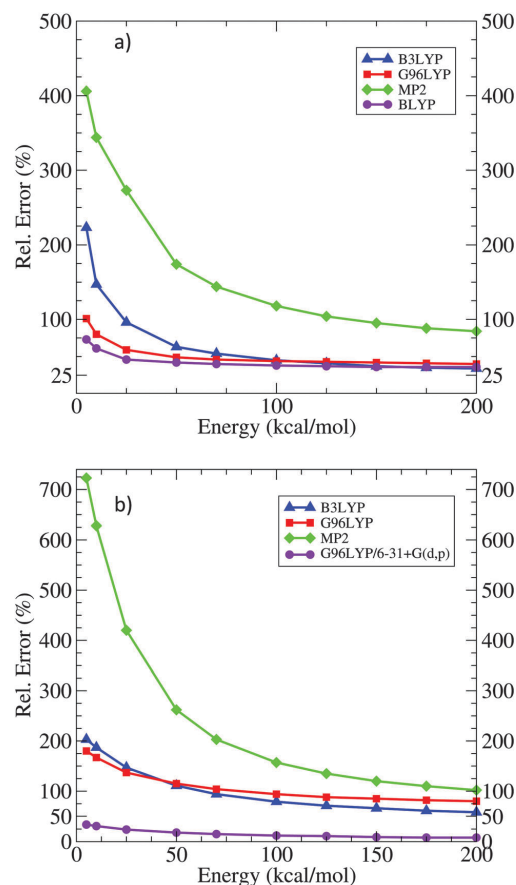


Fig. 6 Average of the relative errors at $E = 5, 10, 25, 50, 70, 100, 125, 150, 175$ and $200 \text{ kcal mol}^{-1}$ with four trial methods. (a) Formamide–Ca²⁺ and (b) formamide–Sr²⁺.

kinetics of formamide–M²⁺ species, characterized by a large number of intermediates, as a first approach, we will consider only the reactivity of the global minimum, min1. In Fig. 7, $t_{1/2}(E)$ is plotted as a function of the energy for all the reactions with origins in the global minimum, min1, namely the loss of formamide (t_{01}), the Coulomb explosion yielding $[\text{M}(\text{NH}_2)]^+$ and $[\text{HCO}]^+$ (t_{1G}) and three isomerization reactions to the intermediates 2, 5 and 10 (t_{12} , t_{15} , and t_{110}) with their corresponding backward reactions (t_{21} , t_{51} , and t_{101}). Internal energies up to $300 \text{ kcal mol}^{-1}$ were considered. This is an upper limit for the low collision energy regime of the CID experiments, since the energy transferred in the collision process is rarely a high percentage of the relative collision energy. This time, the x-axis corresponds to the total internal energy of the molecule. In order to go on with the evaluation of the different low-level methods we will compare the high-level results with one low-level method. For the sake of consistency we have used G96LYP/6-31G(d), since

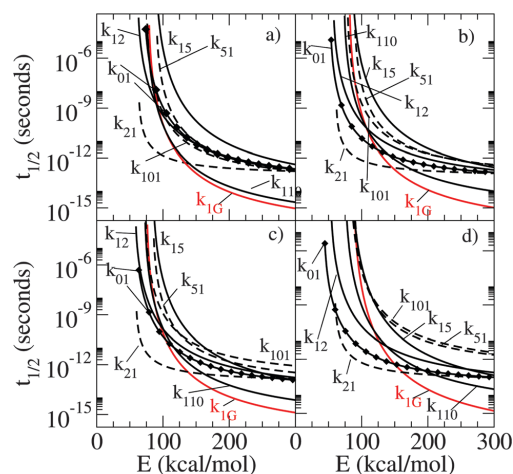


Fig. 7 Half-life reaction time ($t_{1/2}$) as a function of internal energy for the corresponding RRKM rate constants describing the reaction pathways starting from min1. The top panels are for the formamide–Ca²⁺ system at (a) B3LYP/cc-pwCVTZ and (b) G96LYP/6-31G(d). The bottom panels show formamide–Sr²⁺ using (c) G96LYP/6-311+G(3df,2p) and (d) G96LYP/6-31+G(d). Solid lines correspond to forward reactions while dashed lines stand for the backward reactions.

it is the best performing method when considering both systems. We will see that even with the high relative errors obtained, the kinetics of the system is qualitatively well described at this level.

Let us first comment on the kinetic picture obtained by high-level calculations. At low energies the reactivity is under a picosecond time scale. As the energy increases, the reaction speed increases in such a way that at the highest energies all the reactions occur in picoseconds or less. The trends are quite similar with the two metals. In the whole range, the backward isomerization reactions are faster than the forward ones, with the only exception of the min1 \rightarrow int10 isomerization process that, in the whole range of energies is faster than the corresponding backward reaction. Hence, with only this exception, the intermediates will convert back to min1. At low internal energies the loss of formamide, t_{01} , and the Coulomb explosion leading to the G exit channel, t_{1G} , are equally fast when $M = \text{Ca}$, while for $M = \text{Sr}$ the former exit channel is opened at lower internal energies and is faster than t_{1G} . As the energy increases, different reactions speed up, in particular t_{1G} and t_{110} , which become the two fastest reactions at high energies ($> 30 \text{ kcal mol}^{-1}$ for Ca and $100 \text{ kcal mol}^{-1}$ for Sr). Therefore, the products we will expect to observe at low energies are (i) M²⁺ from formamide neutral loss (t_{01}), in a greater proportion for $M = \text{Sr}$ than for $M = \text{Ca}$, (ii) the product G, $[\text{M}(\text{NH}_2)]^+$ and $[\text{HCO}]^+$, by a Coulomb explosion (t_{1G}), and (iii) at high energies also int10 (t_{110}), which could eventually evolve to product B (CO neutral loss).

Comparing now with the kinetic picture obtained at the G96LYP/6-31G(d) level of theory we do not observe significant differences. The main discrepancy is in the formamide neutral loss channel whose rate constant is overestimated, with the

consequence that this reaction is faster in relation to the others (that remain unchanged) and the energy range (where this reaction is the fastest) is now larger. Also we noted that, in the case of formamide- Sr^{2+} , t_{51} is underestimated with respect to the high-level value, so the $\text{min1} \rightarrow \text{int5}$ reaction becomes faster than the backward reaction at around $100 \text{ kcal mol}^{-1}$. Still this reaction is slower than t_{1G} , t_{01} , and t_{110} so it does not imply a remarkable change in the qualitative kinetic picture. Thus we would expect the same products for both doubly charged metal ions M^{2+} , $[\text{M}(\text{NH}_2)]^+$ and $[\text{HCO}]^+$ together with int10 at high energies.

These results are in agreement with the experiments concerning the M^{2+} peak, which appears as the most intense one in the MS/MS spectra.^{35,36} Also the mass corresponding to $[\text{M}(\text{NH}_3)]^{2+}$ species (CO neutral loss) is observed for both di-cationic systems, although in the case of Sr the origin can also be attributed to $[\text{Sr}(\text{H}_2\text{O})]^{2+}$. On the other hand, the $[\text{M}(\text{NH}_2)]^+/\text{[HCO]}^+$ product is observed only for $\text{M} = \text{Ca}$.

4.1. Rotational effects

During collision, the translational energy is transferred to the vibrational and rotational modes of the molecular ion. When the moments of inertia for the reactant are significantly different from those of the TS, the rotational energy can have an important influence on the reaction rate constant (see, for example, the work of Spezia *et al.*⁸²). We evaluated the role of the external rotation energy in the rate constants which may be changed, namely, k_{01} , k_{1G} , k_{110} , k_{101} , k_{51} , together with k_{15} in the case of $\text{M} = \text{Sr}$, both at high-level and at our low-level approach, G96LYP/6-31G(d). The corresponding curves of $k(E, J)$ can be found in Fig. S3 of the ESI†. Again the trends are the same for the two metals. As aforesaid, the K quantum number can be treated as active or adiabatically. No important effects of the external rotational energy are observed when the quantum number K is treated as an active rotor. However, when K is treated adiabatically we observe a decrease in the reaction speed with the exception of k_{1G} that at high energy experiments slightly increases. This effect is more pronounced the higher the energy placed on the z-axis of the molecule, especially for $\text{int10} \rightarrow \text{min1}$ and $\text{int5} \rightarrow \text{min1}$ reactions (see Fig. 8b). Coherently, if all the energy is placed on the z-axis for these reactions, they start at much higher internal energies and the values of k_{101} and k_{51} decrease several orders of magnitude.

The effect of considering the external rotation when computing $k(E, J)$ for formamide neutral loss reaction (k_{01}) is more complex (Fig. 8a), because the effects on the reaction speed depend on how the rotational energy is distributed within the molecule. It must be recalled that this reaction corresponds to the Ca-O bond cleavage until its eventual dissociation. When all the rotational energy is placed on the z-axis (case 3) this cleavage is not favoured and consequently the reaction rate decreases (brown circles, dashed line). Conversely, if all the energy is placed on the x,y-plane (case 1), the rate constant increases slightly and the kinetics speed up (blue diamonds, dashed line).

We would like to remark that the kinetic analysis shows M^{2+} as one of the main products in agreement with the experimental spectra and in contrast to the static picture provide

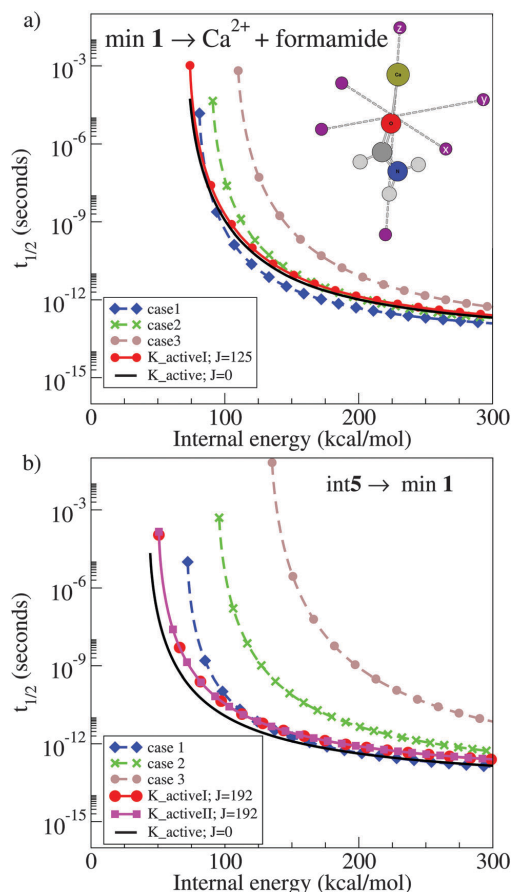


Fig. 8 $k(E)$ computed at B3LYP/cc-pWCVTZ for (a) $\text{min1} \rightarrow \text{Ca}^{2+} + \text{formamide}$ neutral loss and (b) $\text{int5} \rightarrow \text{min1}$ reactions, taking into account the rotational energy. The quantum number K can be treated as an active rotor (solid lines) with different values for the angular momentum J ; or as an adiabatic rotor (dashed lines), where all the rotational energy is placed on the x,y-axes (blue diamonds, dashed line) or in the z-axis (brown circles, dashed line). The figure also shows the B3LYP/cc-pWCVTZ optimized structure for min1 along with its principal axes of inertia.

by the topological analysis of the PES. On the other hand, $[\text{Sr}(\text{NH}_2)]^+$ and $[\text{HCO}]^+$ products are not detected in the CID experiment³⁵ and RRKM rate constants predict these species to be one of the main products. However, $[\text{Sr}(\text{NH}_2)]^+$ has been detected in similar experiments with the urea- Sr^{2+} system.²⁷ Further investigations are needed in order to clarify this point. It should also be taken into account that RRKM is a statistical theory that can only describe reactive mechanisms in which the energy flows through the ion's vibrational modes because it assumes that dissociation takes place after complete intramolecular vibrational energy redistribution (IVR). However, it

has been shown, both experimentally and computationally, that there are other (non-RRKM) mechanisms in CID processes in which the collision locally activates one (or few) vibrational mode of the ion, and the fragmentation occurs before complete IVR can take place.^{43–46,83–88} This overall situation is a dynamical picture that cannot be described by means of statistical theories and makes it necessary to resort to other techniques such as chemical dynamics simulations, which will be the aim of future work.

5. Conclusions

Among all the approaches considered, we found that G96LYP/6-31G(d) is the best compromise to reproduce PES and kinetics obtained from higher level calculations, for both formamide-Ca²⁺ (B3LYP/cc-pWCVTZ) and formamide-Sr²⁺ (G96LYP/6-311 + G(d,p)). Thus, it can be used to compare the reactivity of both systems.

Concerning the kinetics of the unimolecular reactivity of these doubly charged cations, we observed similar trends with the two metals, expecting as the main products M²⁺ from formamide neutral loss, the product G, [M(NH₂)]⁺ and [HCO]⁺, from a Coulomb explosion, and at high energies also int10, which could eventually evolve to product B (CO neutral loss). Note that experiments were not able to assign the *m/z* 52.46 peak that can correspond to either [SrNH₃]²⁺ or [⁸⁷Sr(H₂O)]²⁺: our calculations suggest that it is originated by CO neutral loss (and thus it corresponds to [SrNH₃]²⁺). The effect of external rotation, when it is relevant, is generally to slow down the kinetics of the system. Using G96LYP/6-31G(d) the kinetics is qualitatively well described, when compared to higher level calculations.

The statistical approach used in this work (RRKM) allowed us to describe part of the kinetics of the system, but there are still open questions, such as why the [Sr(NH₂)⁺]/[HCO]⁺ product does not appear in the experimental MS/MS spectra. Thus, it would be necessary to resort to other non-statistical techniques, such as chemical dynamics simulations, to completely account for the dynamical picture behind the CID process of the doubly charged cations considered in this study. Our research is currently going in that direction.

Acknowledgements

We acknowledge Álvaro Cimas for fruitful discussions and Elizabeth A. Kish for careful reading of the manuscript. This work was partially supported by the DGI Project No. CTQ2012-35513-C02-01, the COST Action CM1204, and the Project MADRISOLAR2, Ref.: S2009PPQ/1533 of the Comunidad Autónoma de Madrid. AMS acknowledges a FPI contract from the Ministerio de Economía y Competitividad of Spain. Computing time at Centro de Computación Científica of the Universidad Autónoma de Madrid is also acknowledged. This work was granted access to the HPC resources under the allocation 2013082123 made by GENCI (Grand Equipement National de Calcul Intensif).

References

- 1 D. Schöder and H. Schwarz, *J. Phys. Chem. A*, 1999, **103**, 7385–7394.
- 2 D. N. Heller, J. Yergey and R. J. Cotter, *Anal. Chem.*, 1983, **55**, 1310–1313.
- 3 J. M. Miller, K. Balasanmugam, J. Nye, G. B. Deacon and N. C. Thomas, *Inorg. Chem.*, 1987, **26**, 560–562.
- 4 A. R. Katritzky, P. A. Shipkova, R. D. Burton, S. M. Allin, C. H. Watson and J. R. Eyler, *J. Mass Spectrom.*, 1995, **30**, 1581–1587.
- 5 L. M. Roth and B. S. Freiser, *Mass Spectrom. Rev.*, 1991, **10**, 303–328.
- 6 S. D. Price, *J. Chem. Soc., Faraday Trans.*, 1997, **93**, 2451–2460.
- 7 E. L. Breig, M. R. Torr, D. G. Torr, W. B. Hanson, J. H. Hoffman, J. C. G. Walker and A. O. Nier, *J. Geophys. Res.*, 1977, **82**, 1008–1012.
- 8 G. A. Victor and E. R. Constantinides, *Geophys. Res. Lett.*, 1979, **6**, 519–522.
- 9 C. Simon, K. Lilensten, O. Dutuit, R. Thissen, O. Witasse, C. Alcaraz and H. Soldi-Lose, *Ann. Geophys.*, 2005, **23**, 781–797.
- 10 R. Thissen, O. Witasse, O. Dutuit, C. S. Wedlund, G. Gronoffe and J. Lilenstena, *Phys. Chem. Chem. Phys.*, 2011, **13**, 18264–18287.
- 11 R. R. Julian and J. L. Beauchamp, *Int. J. Mass Spectrom.*, 2003, **277**, 147–159.
- 12 G. O. Arrhenius, *Helv. Chim. Acta*, 2003, **86**, 1569–1586.
- 13 R. Lathe, *Icarus*, 2003, **168**, 18–22.
- 14 M. Franchi, J. P. Ferris and E. Gallori, *Origins Life Evol. Biospheres*, 2003, **33**, 1–16.
- 15 H. J. Morowitz, V. Srinivasan and E. Smith, *Biol. Bull.*, 2010, **219**, 1–6.
- 16 J. B. Fenn, *Angew. Chem., Int. Ed.*, 2003, **42**, 3871–3894.
- 17 E. Magnusson, *J. Phys. Chem. A*, 1994, **98**, 12558–12569.
- 18 S. Petrie, *J. Phys. Chem. A*, 2002, **106**, 7034–7041.
- 19 G. N. Merril, S. P. Webb and D. B. Bivin, *J. Phys. Chem. A*, 2003, **107**, 386–396.
- 20 R. Spezia, G. Tournois, T. Cartailier, J. Tortajada and Y. Jeanvoine, *J. Phys. Chem. A*, 2006, **110**, 9727–9735.
- 21 M. Belcastro, T. Marino, N. Russo and M. Toscano, *J. Mass Spectrom.*, 2005, **40**, 300–306.
- 22 I. S. Saminathan, J. Zhao, K. W. M. Siu and A. C. Hopkinson, *Phys. Chem. Chem. Phys.*, 2011, **13**, 18307–18314.
- 23 S. Guillaumont, J. Tortajada, J.-Y. Salpin and A. M. Lamsabhi, *Int. J. Mass Spectrom.*, 2005, **243**, 279–293.
- 24 N. G. Tsierkezos, D. Schröder and H. Schwarz, *Int. J. Mass Spectrom.*, 2004, **235**, 33–42.
- 25 A. M. Lamsabhi, M. Alcamí, O. Mó, M. Yáñez, J. Tortajada and J.-Y. Salpin, *ChemPhysChem*, 2007, **8**, 181–187.
- 26 W. Buchmann, R. Spezia, G. Tournois, T. Cartailier and J. Tortajada, *J. Mass Spectrom.*, 2007, **42**, 517–526.
- 27 A. Eizaguirre, O. Mó, M. Yáñez, J. Tortajada and J.-Y. Salpin, *J. Phys. Chem. B*, 2013, **117**, 2088–2095.
- 28 I. Corral, O. Mó, M. Yáñez, J.-Y. Salpin, J. Tortajada and L. Radom, *J. Phys. Chem. A*, 2004, **108**, 10080–10088.

- 29 I. Corral, O. Mó, M. Yáñez, J.-Y. Salpin, J. Tortajada, D. Moran and L. Radom, *Chem. – Eur. J.*, 2006, **12**, 6787–6796.
- 30 C. Trujillo, O. Mó, M. Yáñez, J.-Y. Salpin and J. Tortajada, *ChemPhysChem*, 2007, **8**, 1330–1337.
- 31 C. Trujillo, O. Mó, M. Yáñez, J. Tortajada and J.-Y. Salpin, *J. Phys. Chem. B*, 2008, **112**, 5479–5486.
- 32 C. Trujillo, A. M. Lamsabhi, O. Mó, M. Yáñez and J.-Y. Salpin, *Org. Biomol. Chem.*, 2008, **6**, 3695–3702.
- 33 Á. Cimas, J. A. Gámez, O. Mó, M. Yáñez and J.-Y. Salpin, *Chem. Phys. Lett.*, 2008, **456**, 156–161.
- 34 I. Corral, C. Trujillo, J.-Y. Salpin and M. Yáñez, *Challenges and Advances in Computational Chemistry and Physics*, Springer, 2010.
- 35 A. Eizaguirre, O. Mó, M. Yáñez and J.-Y. Salpin, *Phys. Chem. Chem. Phys.*, 2011, **13**, 18409–18417.
- 36 A. Eizaguirre, O. Mó, M. Yáñez, J.-Y. Salpin and J. Tortajada, *Org. Biomol. Chem.*, 2012, **10**, 7552–7561.
- 37 T. Baer and W. L. Hase, *Unimolecular Reaction Dynamics. Theory and experiments*, New York, 1996.
- 38 K. K. Murray, R. K. Boyd, M. N. Eberlin, G. J. Langley, L. Li and Y. Naito, *Pure Appl. Chem.*, 2013, **85**, 1515–1609.
- 39 J. Laskin and J. H. Futrell, *Mass Spectrom. Rev.*, 2003, **22**, 158–181.
- 40 B. Paizs and S. Suhai, *Mass Spectrom. Rev.*, 2005, **24**, 508–548.
- 41 A. G. Harrison, *Mass Spectrom. Rev.*, 2009, **28**, 640–654.
- 42 O. Meroueh and W. L. Hase, *Int. J. Mass Spectrom.*, 2000, **201**, 233–244.
- 43 Y.-J. Chen, P. T. Fenn, K.-C. Lau, C. Y. Ng, C.-K. Law and W.-K. Li, *J. Phys. Chem. A*, 2002, **106**, 9729–9736.
- 44 S. O. Meroueh, Y. Wang and W. L. Hase, *J. Phys. Chem. A*, 2002, **106**, 9983–9992.
- 45 E. Martínez-Núñez, A. Fernández-Ramos, S. A. Vázquez, J. M. C. Marqués, M. Xue and W. L. Hase, *J. Chem. Phys.*, 2005, **123**, 154311.
- 46 R. Spezia, Á. Cimas, M.-P. Gaigeot, J.-Y. Salpin, K. Song and W. L. Hase, *Phys. Chem. Chem. Phys.*, 2012, **14**, 11724–11736.
- 47 W. Kohn, *Rev. Mod. Phys.*, 1999, **71**, 1253–1266.
- 48 A. D. Becke, *Phys. Rev. A: At., Mol., Opt. Phys.*, 1988, **38**, 3098–3100.
- 49 C. Lee, W. Yang and R. G. Parr, *Phys. Rev. B: Condens. Matter Mater. Phys.*, 1988, **37**, 785–789.
- 50 P. M. W. Gill, *Mol. Phys.*, 1996, **89**, 433–445.
- 51 J. P. Perdew, K. Burke and M. Ernzerhof, *Phys. Rev. Lett.*, 1996, **77**, 3865–3868.
- 52 A. D. Becke, *J. Chem. Phys.*, 1993, **98**, 1372–1377.
- 53 J. P. Perdew, *Phys. Rev. B: Condens. Matter Mater. Phys.*, 1986, **33**, 8822–8824.
- 54 J. P. Perdew, *Electronic Structure of Solids '91*, Berlin, Germany, 1991.
- 55 P. J. Wilson, T. J. Bradley and D. J. Tozer, *J. Chem. Phys.*, 2001, **115**, 9233–9242.
- 56 C. Adamo and V. Barone, *J. Chem. Phys.*, 1998, **108**, 664–675.
- 57 N. C. Handy and A. J. Cohen, *Mol. Phys.*, 2001, **99**, 403–412.
- 58 W.-M. Hoes, A. J. Cohen and N. C. Handy, *Chem. Phys. Lett.*, 2001, **341**, 319–328.
- 59 X. Xu and W. A. Goddard, *Proc. Natl. Acad. Sci. U. S. A.*, 2004, **101**, 2673–2677.
- 60 Y. Zhao and D. G. Truhlar, *J. Chem. Phys.*, 2006, **125**, 194101.
- 61 J. Tao, J. P. Perdew, V. N. Staroverov and G. E. Scuseria, *Phys. Rev. Lett.*, 2003, **91**, 146401.
- 62 T. Van Voorhis and G. E. Scuseria, *J. Chem. Phys.*, 1998, **109**, 400–410.
- 63 Y. Zhao, N. E. Schultz and D. G. Truhlar, *J. Chem. Phys.*, 2005, **123**, 161103.
- 64 Y. Zhao, N. E. Schultz and D. G. Truhlar, *J. Chem. Theory Comput.*, 2006, **2**, 364–382.
- 65 Y. Zhao and D. Truhlar, *Theor. Chem. Acc.*, 2008, **120**, 215–241.
- 66 A. D. Boese and J. M. L. Martin, *J. Chem. Phys.*, 2004, **121**, 3405–3416.
- 67 J. P. Merrick, D. Moran and L. Radom, *J. Phys. Chem. A*, 2007, **111**, 11683–11700.
- 68 M. J. Frisch, G. W. Trucks, H. B. Schlegel, G. E. Scuseria, M. A. Robb, J. R. Cheeseman, G. Scalmani, V. Barone, B. Mennucci, G. A. Petersson, H. Nakatsuji, M. Caricato, X. Li, H. P. Hratchian, A. F. Izmaylov, J. Bloino, G. Zheng, J. L. Sonnenberg, M. Hada, M. Ehara, K. Toyota, R. Fukuda, J. Hasegawa, M. Ishida, T. Nakajima, Y. Honda, O. Kitao, H. Nakai, T. Vreven, J. J. A. Montgomery, J. E. Peralta, F. Ogliaro, M. Bearpark, J. J. Heyd, E. Brothers, K. N. Kudin, V. N. Staroverov, T. Keith, R. Kobayashi, J. Normand, K. Raghavachari, A. Rendell, J. C. Burant, S. S. Iyengar, J. Tomasi, M. Cossi, N. Rega, J. M. Millam, J. E. K. M. Klene, J. B. Cross, V. Bakken, C. Adamo, J. Jaramillo, R. Gomperts, R. E. Stratmann, O. Yazyev, A. J. Austin, R. Cammi, C. Pomelli, J. W. Ochterski, R. L. Martin, K. Morokuma, V. G. Zakrzewski, G. A. Voth, P. Salvador, J. J. Dannenberg, S. Dapprich, A. D. Daniels, O. Farkas, J. B. Foresman, J. V. Ortiz, J. Cioslowski and D. J. Fox, Gaussian, Inc., Wallingford CT, 2010.
- 69 B. C. Garret and D. G. Truhlar, *J. Chem. Phys.*, 1979, **70**, 1593–1598.
- 70 X. Hu and W. L. Hase, *J. Chem. Phys.*, 1991, **95**, 8073–8082.
- 71 L. Zhu and W. L. Hase, *Chem. Phys. Lett.*, 1990, **175**, 117–124.
- 72 C. H. Townes and A. L. Schadow, *Microwave Spectrometry*, McGraw-Hill, New York, 1955.
- 73 D. C. Tardy, B. S. Rabinovitch and G. Z. Whitten, *J. Chem. Phys.*, 1968, **48**, 1427–1429.
- 74 G. Z. Whitten and B. S. Rabinovitch, *J. Chem. Phys.*, 1964, **41**, 1883.
- 75 G. Z. Whitten and B. S. Rabinovitch, *J. Chem. Phys.*, 1963, **38**, 2466–2473.
- 76 G. Vayner, S. V. Addepalli, K. Song and W. L. Hase, *J. Chem. Phys.*, 2006, **125**, 014317.
- 77 U. Lourderaj, K. Park and W. L. Hase, *Int. Rev. Phys. Chem.*, 2008, **27**, 361–403.
- 78 L. Zhu and W. L. Hase, *QCPE Bull.*, 1994, **14**, 664.

- 79 A. Eizaguirre, M. Yáñez, J. Tortajada and J.-Y. Salpin, *Chem. Phys. Lett.*, 2008, **464**, 240–244.
- 80 N. E. Schultz, Y. Zhao and D. G. Truhlar, *J. Phys. Chem. A*, 2005, **109**, 11127–11143.
- 81 J. N. Harvey, *Annu. Rep. Prog. Chem., Sect. C*, 2006, **102**, 203–226.
- 82 Y. Jeanvoine, M.-P. Gaigeot, W. L. Hase, K. Song and R. Spezia, *Int. J. Mass Spectrom.*, 2011, **308**, 289–298.
- 83 P. T. Fenn, Y.-J. Chen, S. Stimson and C. Y. Ng, *J. Phys. Chem. A*, 1997, **101**, 6513–6522.
- 84 E. Martínez-Núñez, S. A. Vázquez and J. M. C. Marqués, *J. Chem. Phys.*, 2004, **121**, 2571–2577.
- 85 E. Martínez-Núñez, S. A. Vázquez, F. J. Aoiz and J. F. Castillo, *J. Phys. Chem. A*, 2006, **110**, 1225–1231.
- 86 J. Liu, K. Song, W. L. Hase and S. L. Anderson, *J. Chem. Phys.*, 2003, **119**, 3040–3050.
- 87 U. Lourderaj and W. L. Hase, *J. Phys. Chem. A*, 2009, **113**, 2236–2253.
- 88 R. Spezia, J.-Y. Salpin, M.-P. Gaigeot, W. L. Hase and K. Song, *J. Phys. Chem. A*, 2009, **113**, 13853–13862.

Some Interesting Signatures of Non-Covalent Interactions*

Ana Martín-Sómer,^a M. Merced Montero-Campillo,^a Otilia Mó,^a Manuel Yáñez,^a
Ibón Alkorta,^b and José Elguero^b

^a*Departamento de Química, Facultad de Ciencias, Módulo 13. Universidad Autónoma de Madrid, Campus de Excelencia UAM-CSIC. Cantoblanco, E-28049 Madrid, Spain.*

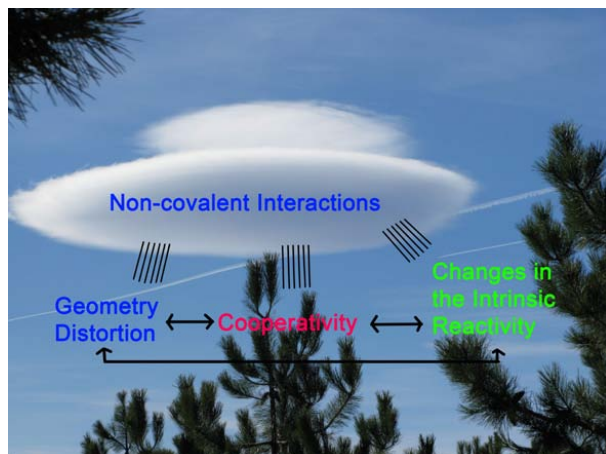
^b*Instituto de Química Médica, CSIC, Juan de la Cierva, 3, E-28006 Madrid, Spain*

Abstract. Non-covalent interactions involving closed-shell systems exhibit some common features, among which we have selected four that can be considered signatures of linkages as hydrogen bonds, halogen bonds, but which are particularly strong for beryllium bonds. These four signatures, namely geometrical distortion, cooperativity, changes in the intrinsic reactivity and changes in the magnetic properties of the interacting subunits arise essentially from the perturbations undergone by their electron densities through polarization or charge transfer effects. Structural changes due to hybridization changes of the active center lead to interaction energies that can only be adequately accounted for, if the effects of the distortion on the intrinsic reactivity of the system, and not only its deformation energy, are taken into consideration. Cooperativity and anti-cooperativity can be easily understood in terms of acid-base Lewis concepts, but when the interaction involves Lewis bases which contain hydrogen atoms and the charge transfer towards the Lewis acid is significant, the former can become a strong Brønsted acid, whose acidity may be tuned by adequately choosing the Lewis acid. Magnetic properties such as chemical shifts and coupling constants also reflect the perturbations of the electron density and accordingly cooperative effects. Self-assembling of ditopic systems in which an active Lewis base center and an active Lewis acid center are at the terminal positions may lead to n-mers stabilized by strong cooperative effects. These four signatures are common to any interaction involving two closed-shell systems, one acting as Lewis acid and the other as Lewis base, and the only difference between the nature of the interactions is quantitative.

Keywords: Non-covalent interactions; beryllium bonds; cooperativity; metallocycles; deformation; acidity enhancement; self-assembling

***This paper is dedicated to Mirjana Eckert-Masić, a great scientist and a better friend**

Table of Contents



1. Introduction

Chemical bonding is at the very heart of chemistry and is probably one of its most fundamental concepts. However, there is not a clear-cut definition of what a chemical bond is and this is particularly so when we refer to “non-covalent interactions”. It is of common use to denote under this general name all weak interactions, typically between closed-shell systems with no electron sharing between the interacting subunits. There is however a great variety of non-covalent interactions attending both to their energy and to their nature, and some of them are almost as strong as conventional covalent linkages. Non-covalent interactions have received a great deal of attention already at the end of the XIX century after the seminal work of J. D. Van der Waals,¹ followed later on by the contributions of P. Debye on polarization effects,² F. London on dispersion forces,^{3,4} and J. E. Lennard-Jones on the development of a still used potential.⁵

The continued interest on non-covalent interactions along the whole XX century and the beginning of the XXI is not at all surprising taking into account that they are responsible for the organization of practically all molecular assemblies, either natural like DNA, or artificial like the so-called metal-organic-frameworks (MOFs), or “soft matter”, term commonly employed to describe materials that are held together by non-covalent interactions involving energies of the order of the thermal energy, kT . Among the different non-covalent interactions, the so called hydrogen bonds are the most studied since the publication of Linus Pauling's book on chemical bonding,⁶ in which he credited T. S. Moore and T. F. Winmill as the first ones mentioning this kind of linkages in their study of amines in aqueous solution.⁷ The discovering of hydrogen bonds was followed by a significant number of other closed-shell interactions as dihydrogen bonds,⁸ halogen bonds,⁹ beryllium bonds,¹⁰ pnictogen bonds,¹¹ and others, some of which were characterized for the first time in the present century.

In most of these non-covalent interactions, probably with the only exception of van der Waals clusters, electrostatic and polarization interactions are important contributors to their stability. In some cases polarization effects are so strong that actually a net charge transfer between the interacting sub-units takes place.¹² This is the case in beryllium bonds, where a Lewis base interacts with a beryllium derivative acting

as Lewis acid, and where a significant charge transfer from the Lewis base towards the empty p orbitals of Be, as well as into the σ_{BeX}^* antibonding orbitals of the BeX_2 compound takes place.¹⁰ A similar process, although in general much weaker, can be also identified in conventional $\text{X-H}\cdots\text{Y}$ hydrogen bonds, which usually involves a small charge transfer from the lone pairs of the HB acceptor Y, into the σ_{XH}^* antibonding orbitals of the HB donor.¹³ These charge density fluctuations associated with the formation of these, usually weak, linkages are behind the cooperative or non-pairwise effects. It is well known for instance, that the HBs in water trimer are stronger than the HB that holds together the water dimer, due to the fact that the presence of more than one of these weak interactions within the same system, results in a reinforcement (or weakening) of each of the individual interactions, what is known as cooperativity (or anti-cooperativity). But this is not the only effect of the charge density redistribution undergone by the monomers which participate in the interaction. One of the signatures of these linkers is the deformation undergone by the Lewis acid and/or the Lewis base. This feature has been recognized long time ago, and it is well established that the energy used in the deformation of the interacting monomers is a fundamental component to get physically meaningful interaction energies.¹⁴ Nevertheless, recently it was proved that a fundamental ingredient to account for the relative stabilities of the complexes formed through these interactions is the change produced in the intrinsic reactivity of the monomers, as a consequence of the aforementioned deformations.^{15,16} Depending on the magnitude of the charge transfer from the Lewis base to the Lewis acid, the intrinsic reactivity of both moieties can dramatically change.

The aim of this feature article is to offer a general perspective on these basic and common characteristics of closed-shell interactions, namely the role of the deformation, the cooperative effects, and the effects on the intrinsic reactivity of the interacting subunits, paying also attention to these phenomena when associated with the presence of recently described beryllium bonds.

2. Methodology

In some manner the theoretical treatment of most non-covalent interactions is a challenge because it is necessary to reproduce very small interaction energies generally as the difference between two big numbers, the energy of the complex and the sum of the energies of the two interacting subunits. This can be critical when dealing with van der Waals complexes, where the larger component of the interaction energy comes from dispersion, which is a second order correction which cannot be described neither at the HF or at the DFT level; but even in other cases in which the interaction includes a good amount of electrostatic, polarization or even covalent effects, the accurate description of the corresponding closed-shell interaction is not trivial. Correlation effects are very important and the basis set has to be flexible enough to well describe the small electron density within the region of the interaction, so in general the inclusion of diffuse components becomes mandatory. In the cases to be described along this paper, different theoretical schemes have been employed, but even when the results were obtained through the use of DFT approaches, the methods were previously assessed using *ab initio* CCSD(T) calculations as a reference.

The bonding was usually analyzed by means of the Quantum Theory of Atoms in Molecules (QTAIM)¹⁷ or the electron localization function (ELF) theory.^{18,19} The first one is based on a topological analysis of the electron density, which permits to build up the so called molecular graphs as the ensemble of the critical points of the electron density: maxima associated with the position of the nuclei, first order saddle points

usually called bond critical points (BCPs), second order saddle points or ring critical points (RCPs) or minima which correspond to cage critical points (CCP). The zero flux lines containing a BCP and connecting the different maxima complete the molecular graph. In general there is a clear correlation between the density at the BCPs and the strength of the linkage.

An alternative view can be obtained through the use of ELF, which permits to divide the physical space in basins associated with the probability of locating an electron pair. These basins may be monosynaptic, if they depend on the orbitals centered on a single atom, core or electron-pairs, or disynaptic when the basin includes the participation of orbitals from two bonded atoms, so the basin is occupied by a bonding pair. The populations of these basins also permit to have useful information of the bonding and its strength.

3. The role of the deformation

3.1. Strong deformation of the Lewis acid

Several characteristics of the complexes involving borane and some of its derivatives, in particular those in which the hydrogen atoms have been substituted by halogens, have received a great deal of attention; but in this section we will focus our interest on questions related with the deformation of borane and borane derivatives when attached to a Lewis base. It has been known for a long time that these derivatives depart significantly from planarity when they form complexes with typical bases.¹⁴ It is also known that the amount of energy to be paid strongly depends on the nature of the atoms attached to B, so it is significantly larger for BF_3 than for BH_3 .^{20,21} The main consequence is that the conventional dissociation energies, defined as the energy difference between the complex and that of the isolated Lewis base and Lewis acid in their equilibrium conformation, is not a good measure of the strength of the interaction because this dissociation energy is the smaller, the greater the deformation of the interacting subunits.¹⁵ This actually explains why the dissociation energy of BH_3 complexes is greater than that of BF_3 complexes, even though BF_3 should be a stronger acid than BH_3 .

It is important to emphasize however, that the inclusion of the deformation energy does not always solve the possible inconsistencies. A paradigmatic example is that of the complexes between ammonia and BF_3 and BCl_3 , where the dissociation energy of the complex into $\text{NH}_3 + \text{BX}_3$ ($\text{X} = \text{F}, \text{Cl}$) is larger for the BCl_3 complex than for the BF_3 .²² Why BCl_3 behaves apparently as a stronger Lewis acid than BF_3 is not a trivial question, that certainly cannot be explained in terms of the deformation energies, because the deformation energies of BF_3 and BCl_3 are practically identical. The origin of the larger acidity of BCl_3 can be traced using the frontier orbital energy, which shows that the LUMO of BCl_3 lies lower in energy than that of BF_3 , and therefore one should expect the former to be a better electron acceptor, and as a consequence a better Lewis acid than the latter.²²

However, even this model may be incomplete if the effect of the deformations on the properties of the interacting units is not taken into account. Naively, one would expect the Lewis acidity to increase by successive substitution by F atoms as $\text{BH}_3 < \text{BH}_2\text{F} < \text{BHF}_2 < \text{BF}_3$. Indeed, the energy of the LUMO decreases practically linearly with the increase in the number of fluorine substituents as shown in Figure 1a. However, high-level ab initio calculations¹⁵ show the variation of the dissociation

energy of $\text{NH}_3:\text{BH}_{3-n}\text{F}_n$ complexes into $\text{NH}_3 + \text{BH}_{3-n}\text{F}_n$ is far from being linear, since, as shown in Figure 1b, BH_2F , BHF_2 and BF_3 are found to be weaker Lewis acids than borane, so that the curve presents a minimum for BHF_2 .

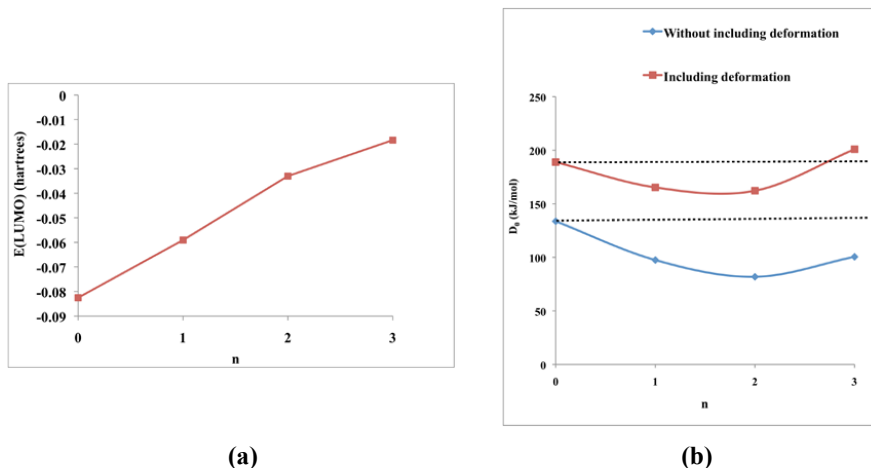


Figure 1. (a) Variation of the energy of the LUMO of the $\text{BH}_{3-n}\text{F}_n$ compounds, in their equilibrium conformation, as a function of the number (n) of fluorine substituents (b) Variation of the dissociation energy of the $\text{NH}_3:\text{BH}_{3-n}\text{F}_n$ clusters as a function of the number (n) of fluorine substituents, including and without including the energy term associated with the deformation of the Lewis acid and the Lewis base. The latter is almost negligible as compared with the former.

The apparently anomaly is only partially solved when the energy contributions of the deformation are included in the model, and BF_3 is found to be, as expected, a stronger Lewis acid than BH_3 . Quite surprisingly however, BH_2F and BHF_2 are still predicted to be weaker Lewis acids than the unsubstituted parent compound! The origin of this unexpected behavior is closely related to the deformation, although not only to the energy involved in such a deformation, that is included in the red curve of Figure 1, but also to its effects on the electron acceptor properties of the Lewis acid. Indeed, the $\text{BH}_{3-n}\text{F}_n$ compounds are planar in their equilibrium conformation, so their LUMO is a pure $2p$ orbital centered on the boron atom. However, when the system becomes pyramidal in the complex, the symmetry changes and the $2p$ orbital can now mix with the $2s$ orbital, so that the LUMO orbital of the distorted $\text{BH}_{3-n}\text{F}_n$ compound is a sp hybrid, whose energy depends on how large the s participation is (See Figure 2a). The main consequence is that the energy of the LUMO varies with the number of the F substituents as shown in Figure 2b.

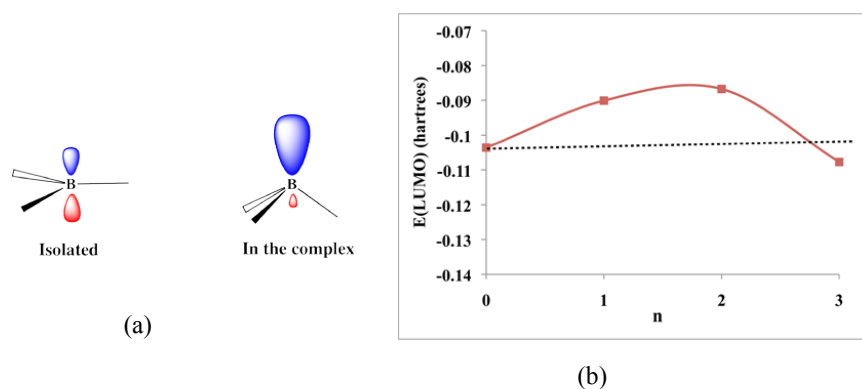


Figure 2. a) Schematic representation of the LUMO for $\text{BH}_{3-n}\text{F}_n$ compounds in their equilibrium (isolated) conformation and in the distorted conformation they adopt in $\text{NH}_3:\text{BH}_{3-n}\text{F}_n$ complexes. b) Variation of the energy of the LUMO as a function of the number of fluorine substituents for $\text{BH}_{3-n}\text{F}_n$ compounds in the distorted geometry they adopt in $\text{NH}_3:\text{BH}_{3-n}\text{F}_n$ complexes.

Hence, in contrast with what would be expected, the energy of the LUMO does not increase linearly with the number of electronegative substituents attached to the boron atom, and rather the energy goes through a maximum at BHF_2 . Not surprisingly then, the interaction energy between this compound and ammonia, as illustrated in Fig. 1 is the lowest of the four derivatives, followed by BH_2F . Also consistently with the calculated interaction energies including the deformation contributions, BF_3 should be a stronger Lewis acid than BH_3 , since its LUMO is the lowest one of the whole series.

This situation is not only found in boron complexes, but is also reproduced when dealing with beryllium bonds.²³ Again surprisingly in the $\text{NH}_3:\text{BeH}_{2-n}\text{F}_n$ complexes the interaction energy does not increase steadily with the number of fluorine substituents (See Figure 3a) because the value calculated for the $\text{NH}_3:\text{BeHF}$ complex is smaller than the one calculated for the unsubstituted parent compound. If the LUMO of the three Lewis acids, namely BeH_2 , BeHF and BeF_2 in their equilibrium conformations is taken as a measure of their intrinsic capacity as electron acceptors (See Figure 3b) one should conclude that the Lewis acidity of BeH_2 and BeF_2 should be practically equal, whereas that of BeHF should be much smaller than the other two, what is in clear contrast with the calculated dissociation energies. Both variations are reconciled however if we consider the variation of the LUMO of the distorted Lewis acids, rather than that at equilibrium. As shown in Figure 3b, for the beryllium derivatives with the geometry they have in the complexes with ammonia, BeHF is predicted to exhibit an acidity similar to the unsubstituted parent compound, whereas BeF_2 should be a much stronger electron acceptor.²³

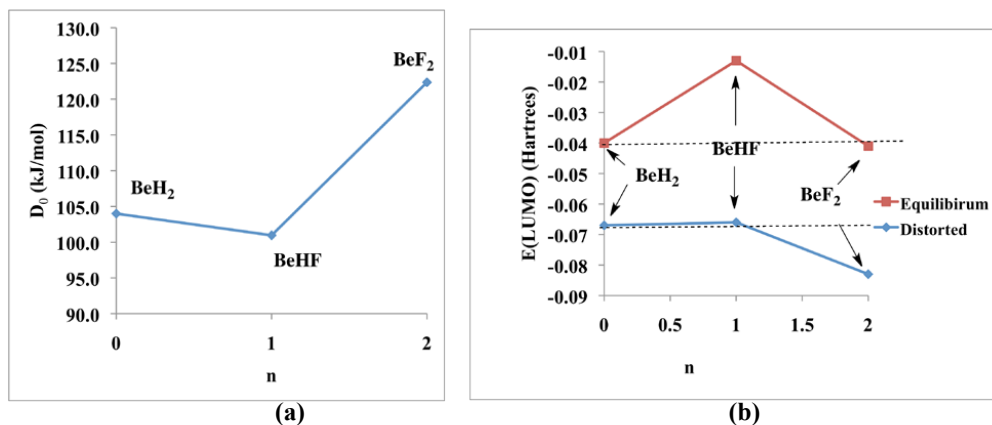


Figure 3. a) Variation of the dissociation energy of the $\text{NH}_3:\text{BeH}_{2-n}\text{F}_n$ clusters as a function of the number (n) of fluorine substituents. b) Variation of the energy of the LUMO for the three Lewis acids at their equilibrium conformation and at the distorted conformation they have in the $\text{NH}_3:\text{BeH}_{2-n}\text{F}_n$ complexes.

3.2. Strong deformation of the Lewis base

In the examples described in the previous section, although both the Lewis acid and the Lewis base undergo a certain deformation, these effects were more evident in the former. However, this is not always so and in other systems is the deformation of the Lewis base, as we shall illustrate in this section, the one that dominates.

In 2011, Stephens, Tew, Mikhailov, Walker and Legon described, for the first time, the structure in the gas-phase of the transition-metal olefin complex $\text{C}_2\text{H}_4 \cdots \text{Ag}-\text{Cl}$.²⁴ The compound was synthesized in a pulsed-jet-Fourier-transform microwave (MW) spectrometer as represented in Figure 4.

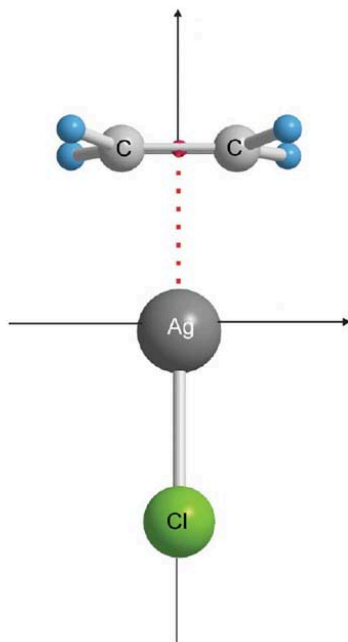
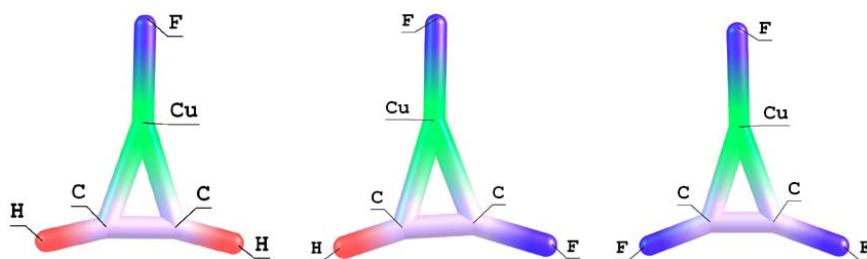


Figure 4. Experimental MW structure of complex $\text{C}_2\text{H}_4\cdots\text{Ag}-\text{Cl}$.

The authors reported unpublished results indicating that the complex $\text{C}_2\text{H}_4\cdots\text{Cu}-\text{Cl}$ is very similar. By combining experimental results and $\text{fc-CCSD(T)/cc-pVQZ}$ theoretical calculations, they reached the following conclusions: the C–C bond of ethylene (ethene) lengthens on formation of the complex and simultaneously the ethylene molecule undergoes a small angular distortion. The distortion is such that the four H atoms move in a direction away from Ag but remain coplanar. The two C atoms are no longer contained in this plane, however.

Shortly after, we studied¹⁶ the copper complex and, using the facility of theoretical methods [MP2 and CCSD(T) computational levels] to explore large zones around a problem, we extend the study of ethylene to acetylene (ethyne) and to their fluoro derivatives (Figure 5) by analogy with the results reported in section 3.1.



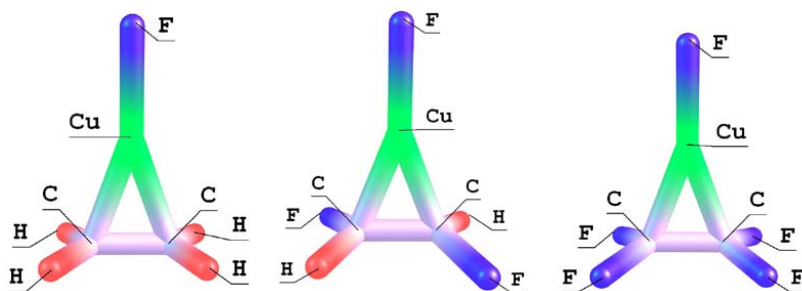


Figure 5. Complexes between CuF and acetylene, fluoroacetylenes, ethylene and fluoroethylene derivatives.

Several conclusions were obtained, such as the metallocyclic nature of these three-membered C-C-Cu rings, with interaction energies between CuF and CC double and triple bonds close to those of conventional covalent ones.¹⁶ Though, for the purpose of this review, we will focus on the effect of fluorine substitution on the strength of the interaction of CuF with the organic part, because this is related to the important question of the deformation of the base.

The increase of the interaction energies with the number of fluorine substituents is only observed in the acetylene series. An analysis of the bonding in both series of complexes indicates a similar nature, that fits very well the Dewar-Chatt-Duncanson model, and therefore, the reason for this unexpected behavior could only be associated once more with the effects triggered by the distortion of the system, quantitatively different for acetylene than for ethylene derivatives and much larger for the F-substituted derivatives than for the unsubstituted parent compounds.

There are two alternative ways of partitioning the dissociation energy (D_e) into interaction and deformation energies, the classical one, in which the deformation energy, E_{def} , is the energy needed to distort both monomers from their equilibrium conformation to the one they have in the complex or an alternative one in which D_e is partitioned into the energy needed to deform the complex, E_{defC} , plus the interaction energy between both undistorted monomers, E_{intD} . E_{intD} is then calculated maintaining fixed the structure of the monomers in their equilibrium conformation, whereas only the distance between the CuF molecule and the unsaturated compound and their relative orientation were allowed to change (See Figure 6).

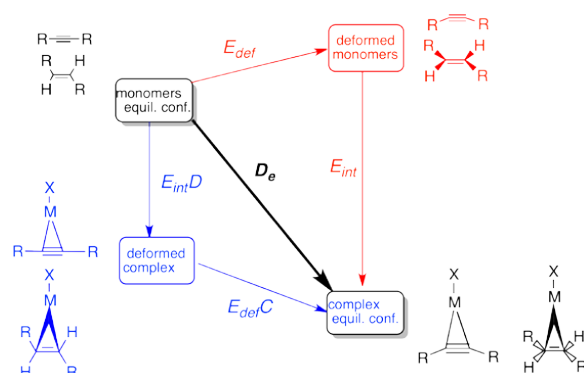


Figure 6. Thermodynamic cycle relating D_e with the deformation energy of the interacting monomers, E_{def} , and the deformation energy of the complex, E_{defC} . E_{int} is the interaction energy.

The surprising finding as illustrated in Figure 7 is that whereas the $E_{int}D$, in which the distortion of the monomers are not allowed, follows the same trend for both families of complexes upon F substitution (red arrows), this is not the case for E_{int} which increases for the ethylene series (blue arrow) but decreases for the acetylene one (green arrow).

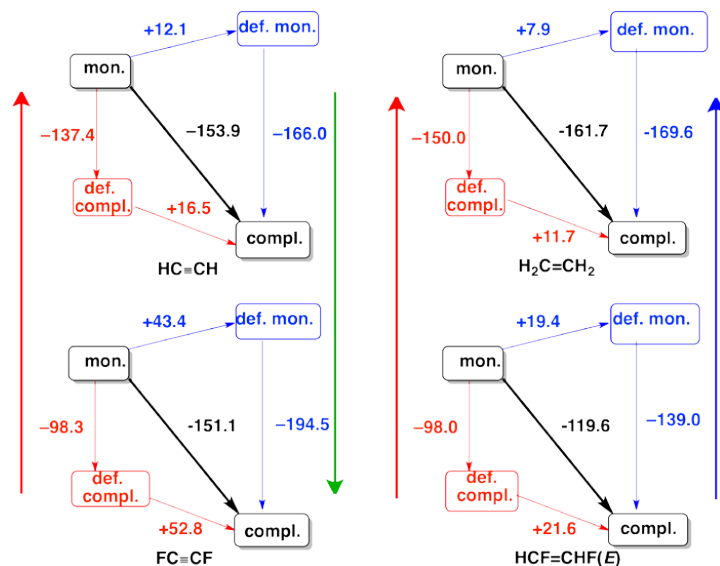


Figure 7. Thermodynamic cycles showing the values of D_e , E_{int} , $E_{int}D$, E_{def} and E_{defC} for the complexes formed by the interaction of acetylene, ethylene and its fluoro disubstituted derivatives with CuF.

A perusal of the values in Figure 7 clearly shows that this opposite behavior has its origin on the much larger deformation energy of the complex involving $\text{FC}\equiv\text{CF}$ ($+52.8\text{ kJ}\cdot\text{mol}^{-1}$) than of the complex involving $\text{HFC}=\text{CHF}$ ($21.6\text{ kJ}\cdot\text{mol}^{-1}$). The origin of this significant difference can be understood by looking at the variation of the interaction energy as a function of the deformation, as measured by the angle α defined in Figure 8.

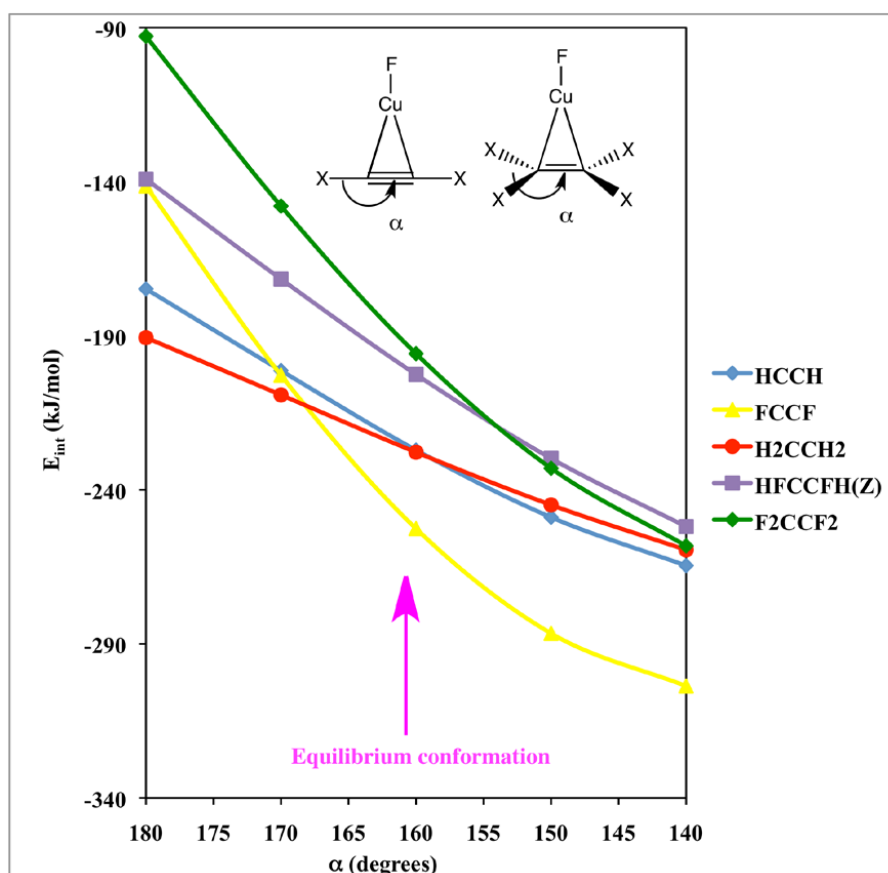


Figure 8. Variation of the interaction energy between CuF and ethylenic and acetylenic derivatives as a function of the deformation of the unsaturated organic compound.

It can be observed that the two parent compounds exhibit a rather similar behavior upon deformation (curves red and blue) since the curves have rather similar slopes. However, the F disubstitution leads to a more significant decrease of the interaction energy with the deformation for the FCCF (yellow curve) than for the HFCCFH compound (purple curve). Very importantly, at the equilibrium conformation the

potential energy curve for the FCCF complex has already crossed (around 170°) the one corresponding to the unsubstituted HCCH parent compound, whereas this crossing did not take place yet for the HFCCFH complex, explaining why for the acetylenic series the interaction energy of the difluoro derivative is greater, in absolute value, than that of the parent compound, whereas this is not the case for the difluoro ethylenic derivative. Still, we need to understand why the slope of the yellow curve is much larger than that of the purple one, which is a direct consequence of the presence of H atoms in the latter. The deformation of the Lewis base results in a hybridization change of the C atoms and therefore in a change in their electronegativity. This electronegativity change results unavoidably in an electron density redistribution of the system, whose energetic cost is largely mitigated by the presence of hydrogen atoms, which very easily adapt to these changes. Similar effects on the stabilization of strained systems and on carbocations and carbanions have been reported before in the literature. This reasoning seems to be apparently inconsistent with the fact that the fully substituted F_2CCF_2 derivative leads to stabilization energies which are still smaller, in absolute value, than those of the unsubstituted parent compound, even though no hydrogen atoms are present. However, Figure 8 shows that, consistently with our previous arguments, the slope of the curve for the F_2CCF_2 complex (green curve) is very similar to that of the FCCF complex (yellow curve). The difference arises from the fact that the gap between the interaction energies of H_2CCH_2 and F_2CCF_2 undistorted complexes ($\alpha = 180^\circ$) is huge ($\approx 100 \text{ kJ mol}^{-1}$), so even though the slope of the green curve (F_2CCF_2) is much larger than that of the red curve (H_2CCH_2) the crossing between both happens at angles much smaller ($< 140^\circ$) than the equilibrium conformation angle ($\approx 160^\circ$).

In summary, although in both series of complexes the bonding partner is essentially the same, the significant differences in the variation of the interaction energies with the deformation of the Lewis base, explain why the trends of the interaction energies are opposite for both series of complexes.

4. Cooperative effects

4.1. Cooperativity between beryllium bonds and hydrogen bonds

As mentioned in the introduction one of the signatures of non-covalent interactions is cooperativity, a phenomenon that has been very well characterized in hydrogen bonds, but that may also be present when other non-covalent interactions are involved, such as beryllium bonds, which as indicated in previous sections, involve a significant charge transfer from the Lewis base to the beryllium compound, which is one of the ingredients necessary to observe non-pair wise effects. The cooperativity between beryllium bonds and hydrogen bonds results evident when considering the interactions between imidazole dimers or water clusters and BeX_2 derivatives.²⁵ Imidazole dimers were characterized both experimentally and theoretically almost two decades ago.²⁶ Indeed both monomers are held together by a rather strong intermolecular hydrogen bond, but imidazole also forms strong beryllium bonds with BeX_2 derivatives, as beryllium dihydride (see Figure 9). The important finding however is that when both non-covalent interactions are present in the same system, i.e., when the molecular assembly that forms the beryllium bond is the imidazole dimer, rather than the monomer, both the intermolecular hydrogen bond and the beryllium bond become reinforced.²⁵

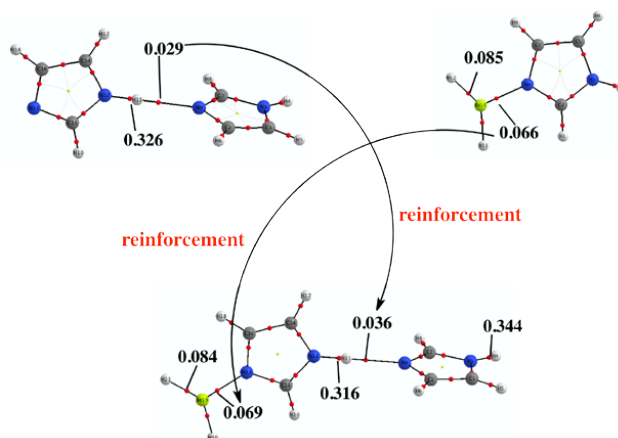


Figure 9. Molecular graphs of imidazole dimer, imidazole-BeH₂ complex and (imidazole)₂BeH₂ complex, showing the reinforcement of both the intermolecular hydrogen bond and the beryllium bond in the latter. Red dots denote BCPs. Electron densities are in a.u.

This is nicely illustrated by the changes in the electron densities at the corresponding BCPs, which in the case of the intermolecular hydrogen bond increases from 0.029 to 0.036 a.u., and for the beryllium bond increases from 0.066 to 0.069 a.u. The first reinforcement can be understood by using the acid-base model proposed to explain the cooperativity in HBs.²⁷ Indeed, in the formation of the beryllium bond, the imidazole subunit acting as a proton donor behaves simultaneously as electron donor towards BeH₂. This significant charge transfer renders this subunit electron deficient and accordingly its N-H group becomes a better proton donor reinforcing the intermolecular hydrogen bond, which becomes 0.10 Å shorter. Note that not only the electron density at the HB BCP increases, but that at the N-H group acting as proton donor decreases from 0.326 to 0.316 a.u., and consistently the N-H bond length increases 0.01 Å. Concomitantly, the fact that the imidazole molecule which forms the beryllium bond with the beryllium dihydride is a better proton donor results in an increase of its intrinsic basicity, i.e., in its ability to behave as electron donor reinforcing the beryllium bond, which also becomes 0.013 Å shorter.

The interaction of beryllium hydride with water clusters puts in evidence the appearance of cooperative and anti-cooperative effects.²⁸ This is very well illustrated when comparing the complexes formed when the water dimer (**WD**) interacts with BeH₂, with those involving water trimers (**WT**). The local minima for both kinds of clusters are shown in Figure 10, the global minimum being structures [**WD:BeH₂**]**a** and [**WT:BeH₂**]**a**, respectively.

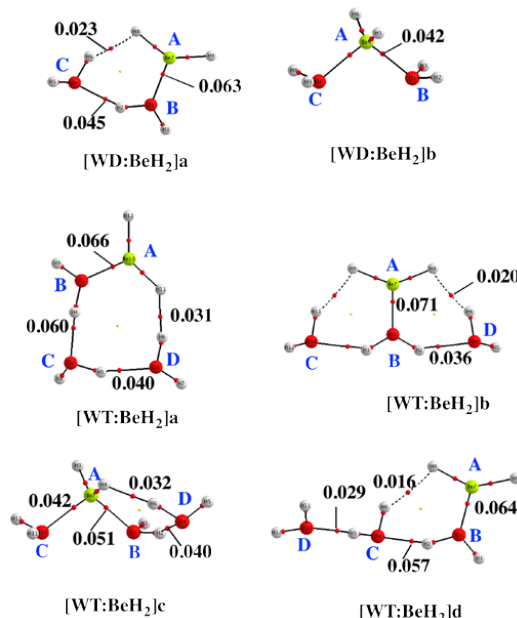


Figure 10. Molecular graphs of the clusters formed between water dimer (**WD**) and trimers (**WT**) and BeH_2 . Red dots denote BCPs. Electron densities are in a.u.

One of the most unexpected results is that the complex in which Be appears tetracoordinated, namely structure **[WT: BeH_2]c** is not the most stable one, even though Be is very often called the *tetrahedral proton*, reflecting its propensity to tetracoordinate.²⁹⁻³¹ This structure can be seen as the result of the solvation of the Be tetracoordinated complex **[WD(BeH_2)]b**. A comparison of the molecular graph of **[WT: BeH_2]c** with that of **[WD(BeH_2)]b** shows that the **AB** beryllium bond becomes clearly reinforced, whereas the other **AC** beryllium bond remains unperturbed. Also, the **BD** HB between both water molecules is stronger than in the water dimer (BCP electron density 0.025 a.u.). However, these bond reinforcements are not enough to compensate the effects that stabilize the global minimum **[WT: BeH_2]a**. Indeed, when the molecular graph of the complex **[WT(BeH_2)]a** is compared with that of **[WD(BeH_2)]a**, one may observe that besides the new, rather strong, HB formed between **C** and **D**, the electron density at the **AB** beryllium bond, at the **BC** HB and at the **DA** dihydrogen bond (**CA** in the dimer) clearly increases. The formation of **[WT(BeH_2)]b** leads to both cooperative and anti-cooperative effects. The electron density at the **AB** beryllium bond increases on going from **[WD(BeH_2)]a** to **[WT(BeH_2)]b** but the electron density at the **CB** and **BD** HBs and at the **AC** and **AD** dihydrogen bonds decreases. The enhancement in the stability of the beryllium bond reflects the increase in the electron donor capacity of the water molecule **B** interacting with BeH_2 because it is acting as a double proton donor, but for the same reason, the HBs between this water molecule and the other two become weaker.²⁸

Cooperativity is also sizable when the intramolecular hydrogen bonds are involved in the interaction with beryllium bonds. A paradigmatic example is provided by malonaldehyde.²⁵

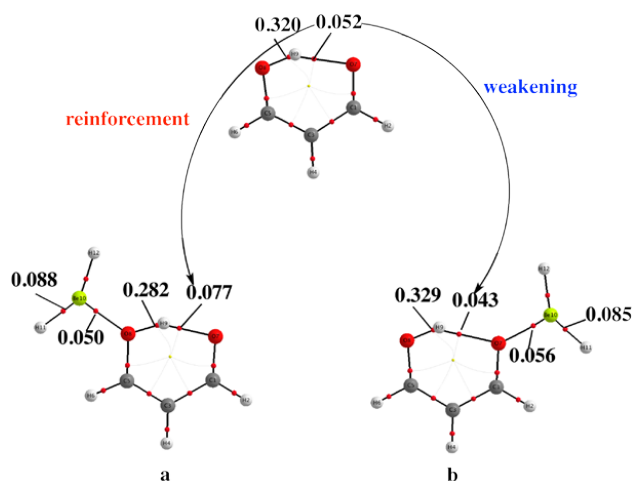


Figure 11. Molecular graphs of the malonaldehyde and its complexes when BeH_2 is attached to its O-H group (a) or to its carbonyl group (b). Red dots denote BCPs. Electron densities are in a.u.

Figure 11 shows the significant changes undergone by the intramolecular hydrogen bond when malonaldehyde interacts with BeH_2 , and these changes depend on the site to which the beryllium dihydride molecule is attached. The association to the OH group leads to a dramatic increase of its intrinsic acidity which results in a concomitant reinforcement of the intramolecular HB that shrinks 0.157 \AA , whereas the OH bond length increases 0.034 \AA . Consistently the electron density at the HB and at the OH BCPs increases and decreases by 0.025 and 0.038 a.u. , respectively. Conversely, the attachment of BeH_2 to the carbonyl group of malonaldehyde results in a dramatic decrease of its intrinsic basicity leading to a much weaker intramolecular HB, whose length increases 0.074 \AA , whereas the OH bond shrinks 0.010 \AA . Again, consistently, the electron densities at the corresponding BCPs decrease and increase by 0.009 a.u. , respectively.²⁵

4.2. Effects of the cooperativity on the self-assembling of ditopic systems

The significant Lewis acidity of beryllium derivatives permits to design interesting ditopic systems, *i.e.* molecular systems that have two separated binding regions, by introducing a $-\text{BeR}$ group as the terminal substituent in a good Lewis base. Such compounds would be good candidates to form chains of complexes attached via

beryllium bonds. The first systems of this kind explored by our groups were the (iminomethyl)beryllium hydride and (iminomethyl)beryllium fluoride [$\text{HC}(\text{BeX})=\text{NH}$, $\text{X} = \text{H}, \text{F}$] (see Scheme 1).³² In this overview we will focus our attention exclusively on the latter.



Scheme 1. (Iminomethyl)beryllium hydride and (iminomethyl)beryllium fluoride ditopic systems.

As it could be anticipated in the light of the discussions of previous sections, the interaction between two monomers of (iminomethyl)beryllium fluoride (IMBF) lead to the formation of a rather strong beryllium bond in which the imino nitrogen of one of the monomers behaves as a Lewis base by donating charge to the Be atom of the other monomer acting as a Lewis acid. The strength of this $\text{N} \cdots \text{Be}$ linkage is mirrored in the short N-Be distance (1.75 Å), which is only slightly longer than the van der Waals radius of the N atom. However, what is of importance is the strong cooperativity observed when the trimer is formed. Indeed, the two $\text{N} \cdots \text{Be}$ bonds are now stronger and accordingly, the N-Be distance shrinks 0.03 Å, the electron density at the $\text{N} \cdots \text{Be}$ BCP increases by 0.005 a.u. and the interaction energy per monomer goes from $-119.0 \text{ kJ mol}^{-1}$ in the dimer to $-137.0 \text{ kJ mol}^{-1}$ in the trimer.³² Similar cooperative effects, as we shall discuss later, enter into play also in the stabilization of larger n-mers. It is important to mention that for the tetramer and for longer n-mers a cyclic self-assembling arrangement is also possible. In Figure 12 the two possible conformations for the decamer, linear and cyclic, are shown. Systematically the cyclic structure is found to be more stable than the linear one, because the former has one more beryllium bond than the latter.³² For the particular case of the decamer this energy gap amounts to 35.5 kJ mol^{-1} . This gap is smaller in terms of free energies because the cyclic structure is entropically disfavored. However, the extra beryllium bond which stabilizes the cyclic structures more than compensate the entropic stability loss, and also in terms of free energies the cyclic structures are more stable than the linear ones.

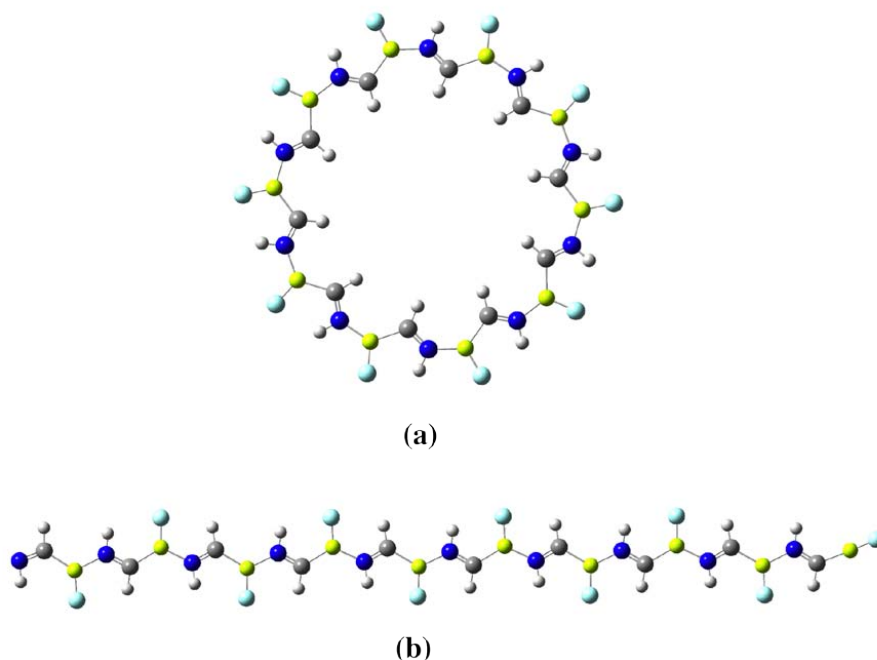


Figure 12. The two possible conformations, cyclic (a) and linear (b) of the decamer of IMBF.

Cooperative effects for the different n -mers are nicely reflected in the length of the beryllium bond formed. As mentioned before the Be-N distance decreases significantly on going from the dimer to the trimer; but on moving to longer n -mers, it is observed (see Figure 13a) that the shortening strongly depends on the relative position of the monomers involved in the beryllium bond, so that systematically the shortest Be-N distances are those between the monomers at the center of the chain and they increase steadily when moving to the ends of the chain. Also importantly, as clearly shown in Figure 13, the overall shortening of the central Be-N linkages is the larger the longer the chain, so the shortest Be-N distance (1.672 Å) is found for the central units of the decamer. Consistently, the variation of the electron densities at the corresponding BCPs is the opposite, and the central units exhibit the beryllium bonds with the larger values of the electron density (See Figure 13b). It is also worth noting that cooperative effects have also a significant and opposite influence on the C-Be bond lengths. Indeed, the significant amount of charge received by the Be-F group leads to a significant electron density redistribution. Part of this charge populates the initially empty p orbital of Be and accordingly its hybridization changes. This is reflected in a loss of linearity and in a weakening of the Be-C bond, whose length increases as shown in Figure 13c. Coherently with our previous discussion, this figure shows that the lengthening of the Be-C bond also depends of the relative position of the IMBF units within the n -mer, due to the enhancement of cooperativity when moving towards its center.³²

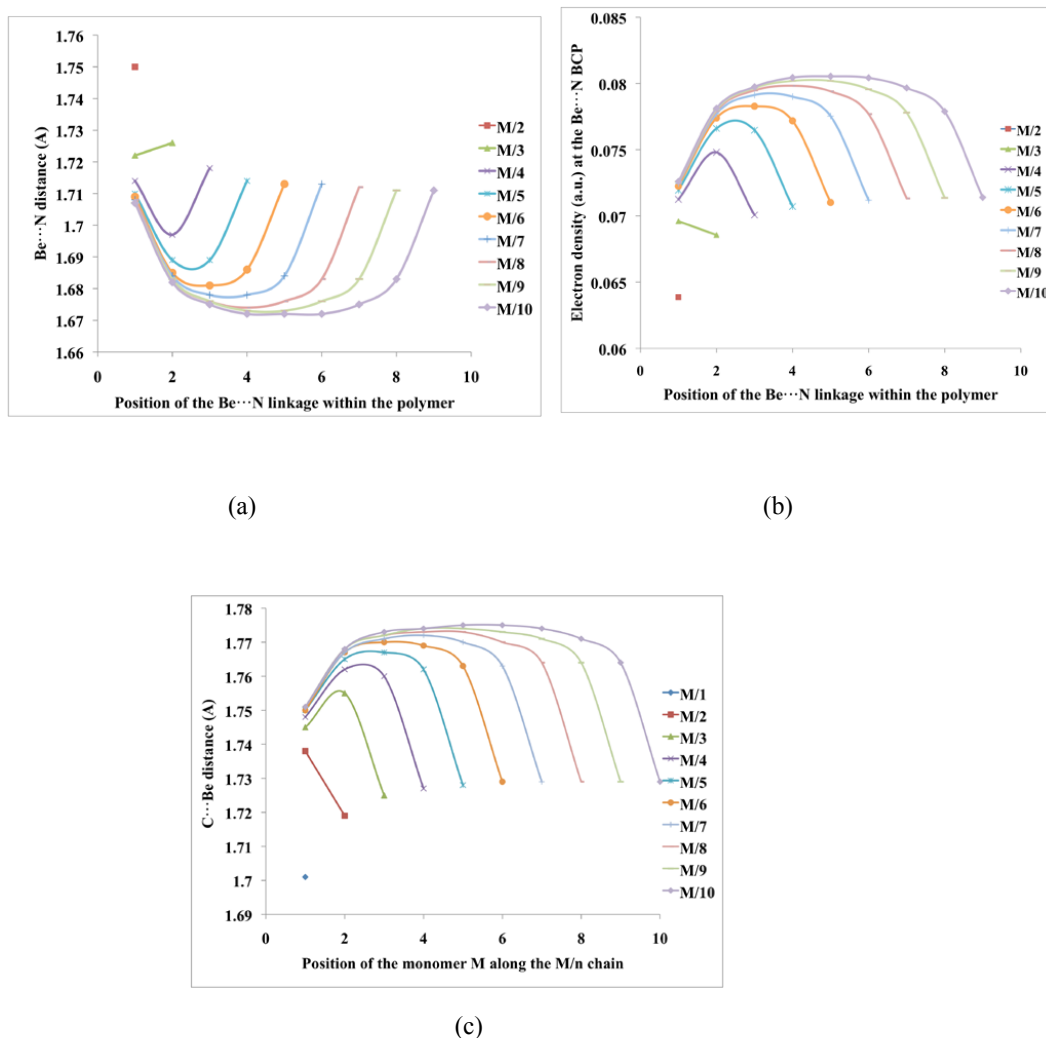


Figure 13. Evolution of: (a) the Be...N distances (b) the electron densities at the Be...N BCPS (c) the Be-C bond length in linear n-mers (M/1-M/10) of IMBF

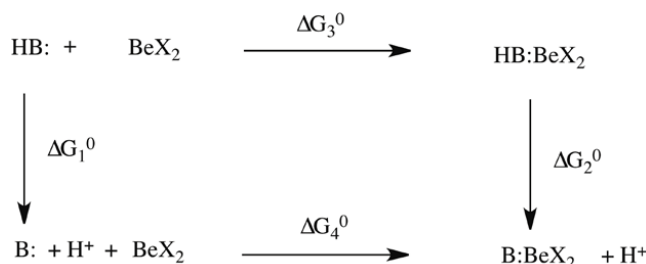
Finally, it has been shown that not only the structural parameters, and the electrons densities clearly reflect the significant cooperative effects along the series of n-mers discussed above, but also their NMR magnetic properties. Indeed the ^{13}C chemical shifts show exactly the same behavior as the Be...N distances shown in Figure 13a. In other words, the chemical shifts also depend on the size of the n-mer and on the position of the atom along the chain. In fact, the ^{13}C chemical shifts are more negative for the carbon atoms close to the center of the chain than for the atoms close to its ends.

Also, a similar size effect as the one discussed above for the interatomic distances is observed for the chemical shifts.³²

It should also be mentioned that the formation of the $\text{N}\cdots\text{Be}$ beryllium bonds has a dramatic effect on the ^{15}N chemical shifts. Whereas the ^{15}N chemical shifts for the N of the terminal monomers and therefore not participating in any beryllium bond are between -183 and -146 ppm, the values for the nitrogen atoms participating in the beryllium bonds are much smaller in absolute value, between -60 and -15 ppm.³²

5. Effects on the intrinsic properties of the interacting monomers

The dissociation of an acid in its conjugate base and a proton is one of the most important reactions in chemistry; acidity is maybe the most relevant physicochemical property of a molecular system from a biological point of view. The ability of a given compound to lose a proton is related to its relative stability with respect to its conjugated base; therefore, the creation of new non-covalent interactions in a molecular system, as those we describe in this paper, plays a crucial role on modifying acidity properties when compared to non interacting units. Several examples of this kind were studied in detail by our group in recent years.³³⁻³⁷



Scheme 2. Thermodynamic cycle associated with the acidity enhancement of a general HB Brønsted acid upon complexation with BeX_2 compounds.

As a general rule, it has been observed that when a given compound forms a beryllium bond, the conjugated base becomes a much better electron donor than the acid from which it comes as compared with the same acid-base pair in absence of beryllium bonds, resulting in an acidity enhancement triggered by the beryllium bond. This acidity enhancement is the consequence of the significant amount of charge transferred from the Lewis base towards the available empty orbitals of the beryllium compound, accompanied, as explained in previous sections, by the corresponding deformation mainly of the BeX_2 subunit. Scheme 2 summarizes the thermodynamics underlying these processes, paying attention to changes on Gibbs free energy. ΔG_1^0 corresponds to the dissociation process of the free acid, whereas ΔG_2^0 is the dissociation process of the same acid in presence of beryllium bonds. ΔG_3^0 and ΔG_4^0 are the free energies associated to the complexation process of the free acid and its conjugate base with the beryllium compound, respectively. Since ΔG_4^0 is usually twice as large as ΔG_3^0 , then ΔG_1^0 has to be considerably larger than ΔG_2^0 . This is equivalent to saying that HB-BeX_2 is more acidic than its related free acid.

Let's see some particular examples of this acidity enhancement triggered by the formation of a beryllium bond in the system. Table 1 contains ΔH_1^0 and ΔH_2^0 values (related to ΔG_1^0 and ΔG_2^0 in the general cycle described above) for some representative compounds upon association with beryllium dihydride. Typical bases in the gas phase like water, imidazole, pyrazole or aniline become more acidic than phosphoric acid, and an unsaturated hydrocarbon as ethylene is as acidic as formic acid upon complexation.³⁷ This effect is even more dramatic when BeH_2 is replaced by BeCl_2 , and for instance aniline reaches an acidity value of $1316.4 \text{ kJ}\cdot\text{mol}^{-1}$, almost as acidic as chloric acid.³⁷

Table 1. Proton dissociation enthalpies for some selected bases and their complexes with BeH_2 at G4 level of theory. The third column shows the acidity enhancement.

Base	$\Delta H_1^0 (\text{kJ}\cdot\text{mol}^{-1})$	$\Delta H_2^0 (\text{kJ}\cdot\text{mol}^{-1})$	$\Delta H_1^0 - \Delta H_2^0 (\text{kJ}\cdot\text{mol}^{-1})$
H_2O	1629.9	1360.0	269.9
NH_3	1688.8	1435.0	253.8
$\text{H}_2\text{C}=\text{CH}_2$	1710.0	1441.5	268.5
imidazole $\text{C}_3\text{H}_3\text{N}_2$	1463.2	1351.8	111.4
pyrazole $\text{C}_3\text{H}_3\text{N}_2$	1483.4	1374.8	108.6
aniline $\text{C}_6\text{H}_5\text{NH}_2$	1537.8	1358.9	178.9

Sometimes, more than one non-covalent interaction is involved in the acidity enhancement phenomenon, as it is the case for squaric acid $\text{C}_4\text{O}_4\text{H}_2$ and its derivatives.³⁸ Left part of Figure 14 shows the molecular graphs of isolated squaric acid and its complex with BeF_2 , in which two non covalent interactions are present: a beryllium bond ($\text{O}\cdots\text{Be}$) plus a hydrogen bond ($\text{OH}\cdots\text{F}$). In this case, ΔG_1^0 and ΔG_2^0 values are 1291.0 and $1183.0 \text{ kJ}\cdot\text{mol}^{-1}$, respectively, whereas ΔG_3^0 and ΔG_4^0 values are -92.2 and $-200.2 \text{ kJ}\cdot\text{mol}^{-1}$ at G4 level of theory.³⁸ A much larger gaining on stability of the conjugated squaric anion on complexing BeF_2 is related with an acidity enhancement of more than $100 \text{ kJ}\cdot\text{mol}^{-1}$ in complexed squaric acid. This effect is nicely reflected on the electron density values at the BCP in O-H bond: from 0.361 a.u. (free acid) to 0.310 a.u. (complex). Although more acidic than squaric acid, the acidity enhancement is not so remarkable in the sulfur derivative $\text{C}_4\text{S}_4\text{H}_2$, ($71.9 \text{ kJ}\cdot\text{mol}^{-1}$) in which changes on BCPs density values are smaller from the free acid to the complex (0.212 a.u. to 0.207 a.u.). Beryllium and hydrogen bonds are stronger in the squaric acid case than in its sulfur derivative.³⁸

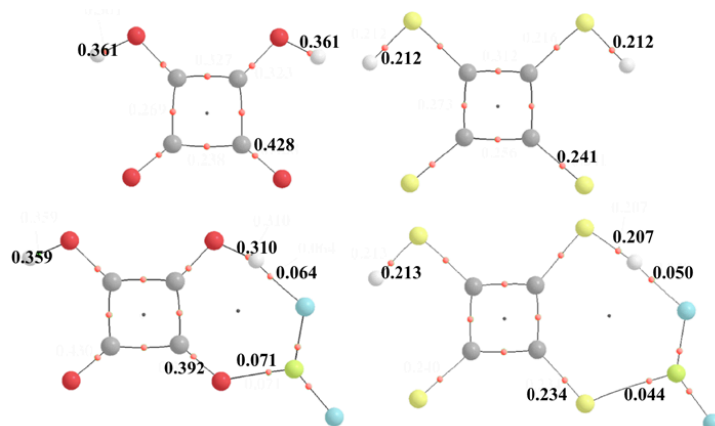


Figure 14. Molecular graphs of free squaric acid $C_4O_4H_2$ and its sulfur derivative $C_4S_4H_2$, along with their corresponding BeF_2 complexes. Red dots denote BCPs. Electron densities are in a.u.

Other Lewis acids different from beryllium, as boron or aluminum, can also induce significant acidity enhancements. Similar closed-shell interactions as those described for beryllium compounds are found in boranes BX_3 and alanes AlX_3 , compounds that suffer a significant distortion when forming dative bonds with Lewis basis as it was previously shown on preceding sections. Therefore, the intrinsic acidity of phosphine is notably different from that of phosphine-boranes (seventeen orders of magnitude greater in terms of the corresponding equilibrium constant), but the most relevant finding is that these theoretical predictions are fully ratified by the experimental evidence. In fact, high-level *ab initio* calculations predict that phenylphosphine-borane complex should be $76 \text{ kJ}\cdot\text{mol}^{-1}$ more acidic than the isolated phosphine, in excellent agreement with the experimental FT-ICR measurements that yield for this acidity gap $82.6 \pm 3.3 \text{ kJ}\cdot\text{mol}^{-1}$.³³ This acidity enhancement is even larger when the phosphine is replaced by the corresponding amine, and the acidity gap between aniline-borane and the free aniline is $136 \text{ kJ}\cdot\text{mol}^{-1}$.³⁵

It is worth noting that the acidity enhancement is also larger for phosphine-alanes³⁴ than for the corresponding phosphine-borane analogues, an unexpected result since boranes should be, in principle, better Lewis acids than alanes. Once again, the reason behind this phenomenon is the greater stabilization of the deprotonated phosphine which is significantly larger in complexes with alanes than in complexes with boranes. On passing from neutral to deprotonated phosphine, a new lone electron pair from P atom is available in both kind of complexes. However, this lone electron pair is much more delocalized in the alane complex than in the borane complex, as revealed by the ELF analysis shown in Figure 15. In the P-Al bonding region the disynaptic basin is richer in electrons than the analogue P-B region, resulting in a larger stability of the deprotonated alane complex that is related with the unexpected acidity enhancement of phosphine-alane complexes.³⁴

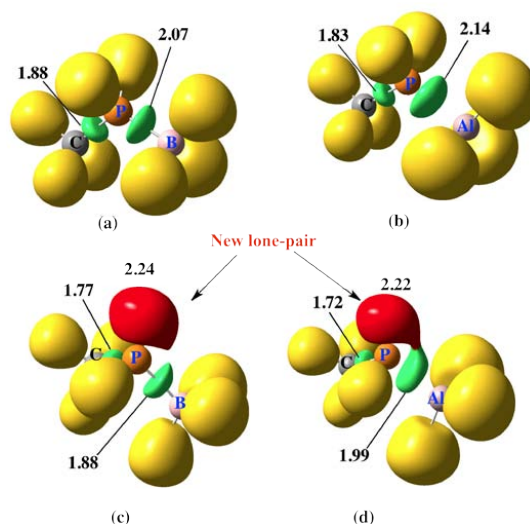
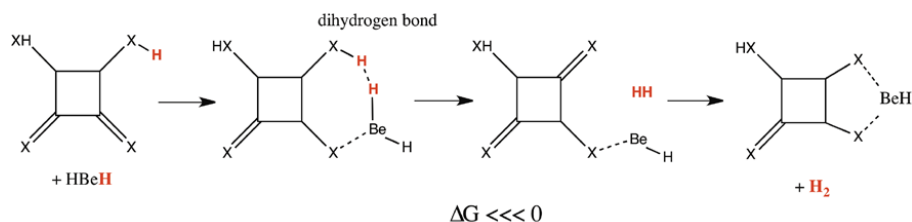


Figure 15. ELF ($= 0.85$) for the $\text{CH}_3\text{PH}_2:\text{XH}_3$ complexes : (a) $\text{X} = \text{B}$; (b) $\text{X} = \text{Al}$ and their corresponding P deprotonated species ((c) and (d)). Green lobes denote disynaptic basins involving two heavy atoms. Yellow lobes are disynaptic basins in which H is one of the atoms involved. Red lobes correspond to lone pairs. The populations shown are e^- .

6. Spontaneous loss of H_2

The formation of beryllium bonds may produce an acidity enhancement that finally can result in a spontaneous proton-transfer processes.^{39,40} In the particular case of squaric acid and its derivatives,⁴¹ a remarkable increase in acidity is observed upon complexation with beryllium difluoride, as a consequence of the electron density redistribution in the system caused by the beryllium bond formation as previously described.



Scheme 3. Spontaneous hydrogen loss process on squaric acid and squaric acid derivatives ($\text{X} = \text{O}, \text{S}, \text{Se}$).

As a last piece in this chain of physicochemical transformations, when beryllium difluoride is replaced by beryllium dihydride this redistribution of charge leads to a spontaneous loss of a hydrogen molecule. For BeH_2 the stable conformation shown in Scheme 3 in which a beryllium bond and a dihydrogen bond coexist in the complex is no longer stable, and the dihydrogen bonded complex presents a rather small energy barrier in terms of electronic energy to produce H_2 , that vanishes in terms of Gibbs free energy. This exergonic process is illustrated on Scheme 3, resulting in a new neutral $\text{C}_4\text{X}_4\text{H}^*\text{BeH}$ complex plus a hydrogen molecule. At G4 level of theory, the total Gibbs free energy released in the reaction $\text{C}_4\text{O}_4\text{H}_2 + \text{BeH}_2 \rightarrow \text{C}_4\text{O}_4\text{H}^*\text{BeH} + \text{H}_2$ is $-195.7 \text{ kJ}\cdot\text{mol}^{-1}$, as a result of the spontaneous proton transfer from the squaric moiety, induced by the beryllium bond.⁴¹ This finding might be relevant as beryllium hydride has been considered a high hydrogen storage capacity material.

7. Bonding perturbation and coupling constants: the case of halogen bonds

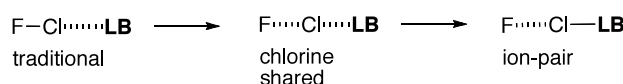
The subject of halogen bonding is very active,⁴²⁻⁴⁴ and cannot be covered, even briefly, in a review like the present one. For this reason and because this is an original approach of our research, we will summarize the part concerning indirect spin-spin coupling constants (SSCC) in halogen-bonded complexes. The molecule we have almost always used is chlorine fluoride (FCl) because it has a large dipole interacting with the Lewis base (**LB**) by the chlorine end. All the geometry calculations were done at the MP2/aug'-cc-pVTZ level and the SSCC ones, using the equation-of-motion (EOM) with the coupled-cluster-singles-and-doubles (CCSD) methods. That SSCC is a very interesting probe of the bond between two atoms A and B is known from McConnell's time (1956) when he related $^nJ_{AB}$ to the bond-order between atoms A and B.⁴⁵ This is particularly relevant for non-covalent interactions, like SSCC through hydrogen bonds.⁴⁶

We studied several kinds of complexes (Scheme 4) depending on the **LB** being a ^{15}N , a ^{13}C , a ^{31}P or a ^{17}O atom derivative. Three couplings were calculated and discussed: $^1J_{\text{YCl}}$ (usually, $^1J_{\text{FCl}}$), $^{1X}J_{\text{CILB}}$ and $^{2X}J_{\text{YLB}}$ (usually $^{2X}J_{\text{FLB}}$). The superscript X stands for halogen by analogy with the H superscript for hydrogen in HBs.

Y-ClLB	
F-Cl.....NR NR = NCH, NH ₃ , ... F-Cl.....NCX ----- F-Cl.....N(sp, sp ² , sp ³)	F-Cl.....CNX
F-Cl.....PCX ----- Y-ClPH ₂ F	X.....HBO.....Z NCH.....HBO.....ClF FH.....HBO.....ClF FCl.....HBO.....ClF

Scheme 4. Halogen-bonded complexes.

Our first paper concerned F-Cl...N systems with a large variety of nitrogen derivatives and the relation of the different SSCC with the F-Cl and the F...N distances.⁴⁷ When the Cl...N distance decreases the structures change from traditional XBs, to chlorine-shared XB, to finally ion-pairs (see scheme 5). Along the chlorine-transfer coordinate in F-Cl...NH₃, ¹J_{FCl} decreases but remains positive, ²XJ_{FN} continuously increases in absolute value, and ¹XJ_{CIN} initially increases in absolute value and then decreases but remains negative. Its value in the ion-pair complex does not approach the value of ¹J_{CIN} for isolated H₃NCI⁺. The problem of chlorine-shared vs. ion-pair halogen bond has been extended to sp, sp² and sp³ N atom derivatives.⁴⁸



Scheme 5. Kinds of halogen bonds as a function of the Cl...LB distance. LB stands for Lewis Base.

Similar conclusions were reached with F-Cl...CNX systems where XBs and HBs were compared reaching the conclusion that they behave similarly.⁴⁹ A representation of ²XJ_{FC} vs. R(F-Cl) is given in Figure 16.

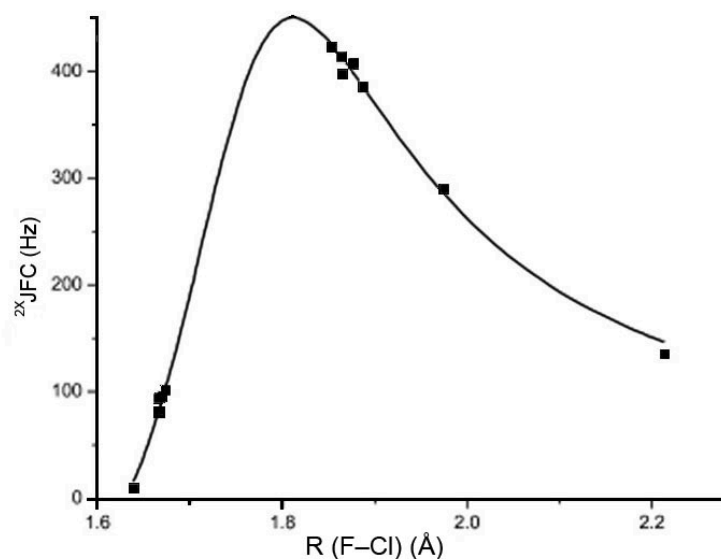


Figure 16. ²XJ_{FC} vs. R(F-Cl) for complexes FCl:CNX.

We move from N to P to explore the pnictogen group 15, replacing nitriles by ylidenephosphines.⁵⁰ We found two minima that we name configuration I and configuration II (with the π cloud of the triple bond) (see Scheme 6).



Scheme 6. Configurations I and II for halogen bonds involving ylidenephosphines.

We have represented in Figure 17 the surprising result that both kind of complexes belong to the same curve when $^1J_{\text{FCl}}$ is plotted against $R(\text{F}-\text{Cl})$.

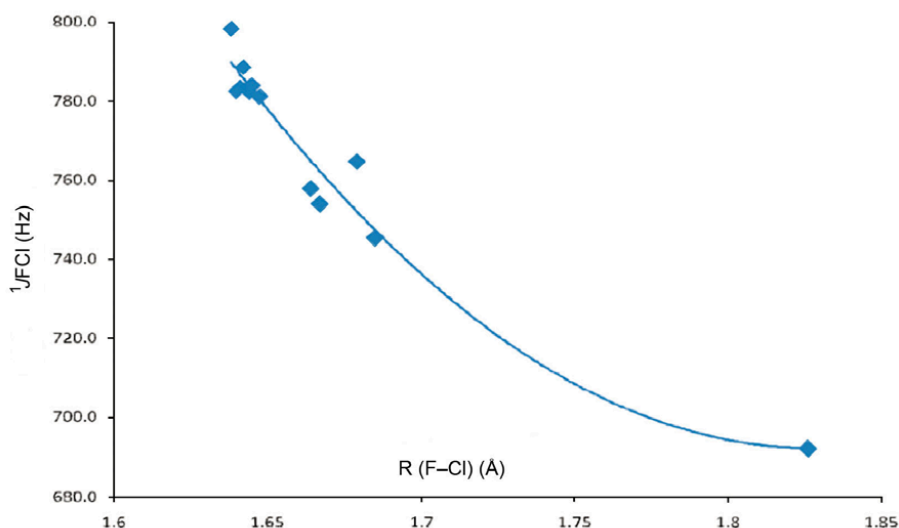
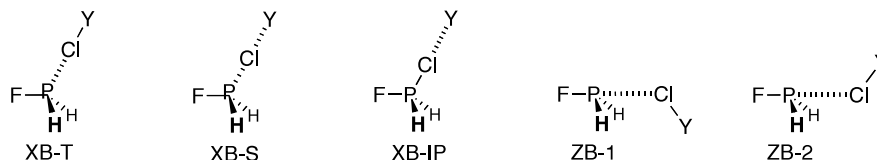


Figure 17. $^1J_{\text{FCl}}$ vs. the F-Cl distances for complexes with configuration I and II.

$^1J_{\text{FCl}}$ coupling constants decrease to a greater extent for configuration II complexes compared to configuration I, a reflection of the longer F-Cl distances in II. Despite shorter F-P and Cl-P distances in configuration II, $^{2X}J_{\text{FP}}$ and $^{1X}J_{\text{ClP}}$ values are significantly reduced compared with those for configuration I. The nature of the F-P coupling is dramatically different in configurations I and II, as evidenced by the relative importance of PSO, FC, and SD components.⁵⁰

A more recent work uses a different type of molecules to study Cl...P systems: Y-Cl...PH₂F.⁵¹ The types of halogen bonds, traditional (XB-T), chlorine-shared (XB-S) and ion-pair (XB-IP) were found as well as two kind of pnictogen-bonds (ZB-1 and ZB-2) (see Scheme 7):



Scheme 7. Types of halogen and pnictogen bonds found for the interactions between FPH₂ and FCl.

The $^{1X}J_{\text{PCl}}$ vs. the P-Cl distance for complexes with halogen bonds was adjusted using a Morse curve (Figure 18). At long distances, $^{1X}J_{\text{PCl}}$ values for complexes with traditional halogen bonds increase as the P-Cl distance decreases. As this distance decreases further, the curvature changes as the halogen bond changes from traditional to chlorine-shared, and $^{1X}J_{\text{PCl}}$ attains its maximum values for chlorine-shared halogen bonds. A further decrease in the P-Cl distance leads to a decrease in $^{1X}J_{\text{PCl}}$ and eventually to a change of sign as the halogen bond changes from chlorine-shared to ion-pair.

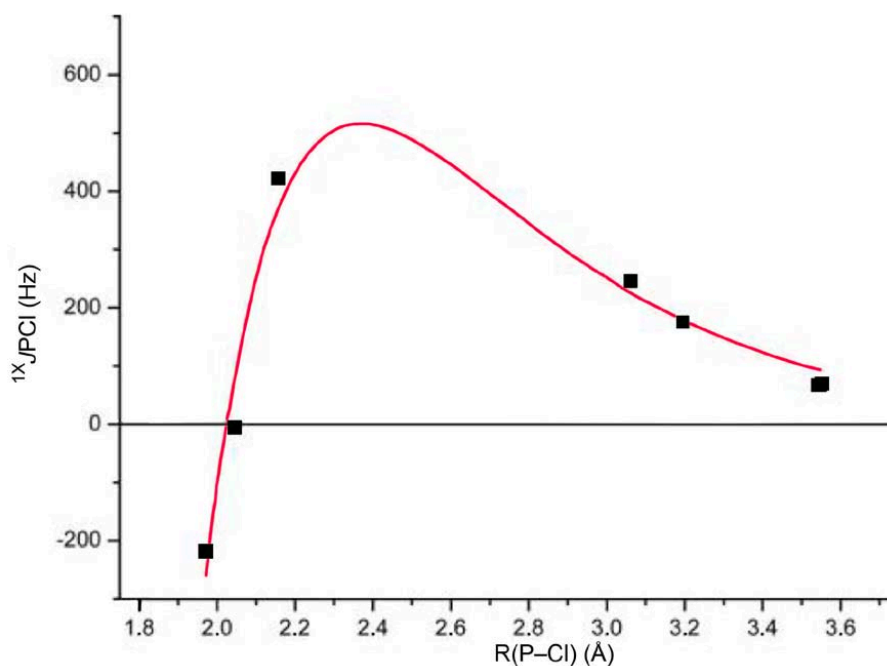


Figure 18. Coupling constant $^{1X}J_{\text{PCl}}$ versus the P-Cl distance for complexes with halogen bonds.

Our last contributions are related to ternary systems where the central part is the ambident HBO (oxoboron) molecule.^{52,53} This compound is a better proton acceptor and a weaker proton donor than HCN and we have used it to explore non-additive effects with different X and Z molecules (Scheme 4), the most relevant for the present purpose is the complex where X = Z = FCl (Figure 19).

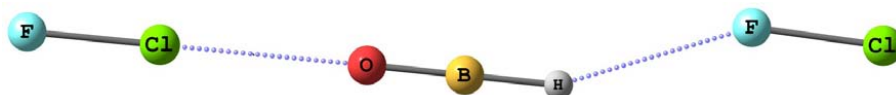


Figure 19. A representation of the Cl–F···HBO···Cl–F complex.

Different SSCC as well as the total binding energies were calculated and analyzed for 46 ternary complexes. The cooperativity effects of the ternary complexes have been evaluated. In all cases, the intermolecular distances obtained in the ternary complexes were smaller than the ones in the corresponding binary complexes. In what respect to the energy, synergism were observed with respect to the sum of the interaction energy of the two former binary complexes. The larger cooperativity energies were obtained in the complexes where LiH were involved both as Lewis acid and Lewis base. The non-pairwise binding energy in the ternary complexes was found to correlate with both the binding energies of the X:HBO and HBO:Z binary complexes.

8. Concluding remarks

The survey presented along this paper shows four distinctiveness of non-covalent interactions, which arise essentially from the perturbations undergone by the electron densities of the interacting subunits, triggered by polarization or charge transfer effects. These changes in the electron density distribution are reflected in structural distortions of both interacting subunits, although often they are more significant for one of the species. The geometrical changes do not only imply a certain energetic cost, but they also change the intrinsic properties of the distorted systems, mainly when the changes in the structure are due to changes in the hybridization pattern of some of the active centers involved. In these cases, the calculated interaction energies can only be adequately accounted for if the effects of the distortion on the intrinsic reactivity of the system, and not only their deformation energy, are taken into consideration. The second effect of the electron density redistribution is cooperativity and/or anti-cooperativity, which can be easily understood in terms of acid-base Lewis concepts, because the system that acts as a Lewis base feels its Lewis acidity enhanced, and vice-versa the one that acts as Lewis acid behaves as a better Lewis base. When the interaction involves Lewis bases which contain hydrogen atoms and the charge transfer towards the Lewis acid is significant, the Lewis base can become a strong Brønsted acid. Indeed, typical bases, such as aniline, become Brønsted acids stronger than phosphoric acid in the gas phase, upon association with BH₃ or with BeX₂ derivatives. Therefore this third effect arising from the electron density perturbation may permit to adequately modulate and tune the intrinsic properties of either subunits. A fourth effect is clearly seen when analyzing the magnetic properties of the interacting systems, whose chemical shifts and coupling constants reflect the aforementioned perturbations of the electron density and

accordingly the cooperative effects, if they are present. A paradigmatic example is provided by the n-mers formed when ditopic systems, in which an active Lewis base center and an active Lewis acid center are at the terminal positions of a molecular compound. These systems may self-assemble very easily due to the stabilizing cooperative effects.

These four signatures are particularly strong when beryllium bonds are formed, because beryllium derivatives are extremely good electron acceptors and therefore very strong Lewis acids. However, they are common to any interaction involving two closed-shell systems, one acting as Lewis acid and the other as Lewis base, and the only difference between the nature of the interactions is quantitative.

Acknowledgements. This work has been partially supported by the Ministerio de Economía y Competitividad (Project No. CTQ2012-35513-C02), the Project MADRISOLAR2, Ref.: S2009PPQ/1533 of the Comunidad Autónoma de Madrid, by Consolider on Molecular Nanoscience CSC2007-00010, and by the CMST COST Action CM1204. AMS acknowledges a FPI contract from the Ministerio de Economía y Competitividad of Spain. A generous allocation of computing time at the CTI (CSIC) and at the CCC of the UAM is also acknowledged.

REFERENCES

- 1 J.D. Van der Waals *On the Continuity of the Gaseous and Liquid States*; PhD Thesis, Edited by J. S. Rowlinson. Dover Phoenix Ed.: New York, 2004.
- 2 *The Collected Papers of P. J. W. Debye*; Interscience: New York, 1954.
- 3 W. Heitler and F. London, *Z. Phys.* **44** (1927) 455. English translation in H. Hettema, *Quantum Chemistry, Classic Scientific Papers*, World Scientific, Singapore (2000).
- 4 R. Eisenschitz and F. London, *Z. Phys.* **60** (1930) 491. English translation in H. Hettema, *Quantum Chemistry, Classic Scientific Papers*, World Scientific, Singapore (2000).
- 5 J.E. Lennard-Jones, *Proc. R. Soc. Lond. A* **106** (1924) 463-477.
- 6 L. Pauling *The Nature of the Chemical Bond*; Cornell University Press: Ithaca, New York, 1939.
- 7 T.S. Moore and T.F. Winmill, *J. Chem. Soc. Trans.* **101** (1912) 1635-1676.
- 8 R. Custelcean and J.E. Jackson, *J. Am. Chem. Soc.* **120** (1998) 12935-12941.
- 9 P. Metrangolo and G. Resnati, *Chem.-Eur. J.* **7** (2001) 2511-2519.
- 10 M. Yáñez, P. Sanz, O. Mó, I. Alkorta and J. Elguero, *J. Chem Theor. Comput.* **5** (2009) 2763-2771.
- 11 S. Zahn, R. Frank, E. Hey-Hawkins and B. Kirchner, *Chemistry-a European Journal* **17** (2011) 6034-6038.
- 12 O. Mó, M. Yáñez, L. González and J. Elguero, *ChemPhysChem* **2** (2001) 465-467.

- 13 A.E. Reed, L.A. Curtiss and F. Weinhold, *Chem. Rev.* **88** (1988) 899-926.
- 14 B. Swanson, D.F. Shriver and J.A. Ibers, *Inorg. Chem.* **8** (1969) 2182-&.
- 15 I. Alkorta, J. Elguero, J.E. Del Bene, O. Mó and M. Yáñez, *Chem.-Eur. J.* **16** (2010) 11897-11905.
- 16 G. Sánchez-Sanz, I. Alkorta, J. Elguero, M. Yáñez and O. Mó, *Phys. Chem. Chem. Phys.* **14** (2012) 11468-11477.
- 17 R.F.W. Bader *Atoms in Molecules. A Quantum Theory*; Clarendon Press: Oxford, 1990.
- 18 A.D. Becke and K.E. Edgecombe, *J. Chem. Phys.* **92** (1990) 5397-5403.
- 19 A. Savin, R. Nesper, S. Wengert and T.F. Fäsler, *Angew. Chem. Int. Ed. Engl.* **36** (1997) 1808-1832.
- 20 T. Brinck, J.S. Murray and P. Politzer, *Inorg. Chem.* **32** (1993) 2622-2625.
- 21 B.D. Rowsell, F.J. Gillespie and G.L. Heard, *Inorg. Chem.* **38** (1999) 4659-4662.
- 22 F. Bessac and G. Frenking, *Inorg. Chem.* **42** (2003) 7990-7994.
- 23 A. Martín-Sómer, A. Lamsabhi, O. Mó and M. Yáñez, *Comput. Theor. Chem.* **998** (2012) 74-79.
- 24 S.L. Stephens, D.P. Tew, V.A. Mikhailov, N.R. Walker and A.C. Legon, *J. Chem. Phys.* **135** (2011) 10.
- 25 O. Mó, M. Yáñez, I. Alkorta and J. Elguero, *J. Chem. Theory Comput.* **8** (2012) 2293-2300.
- 26 R.A. Jockusch and E.R. Williams, *J. Phys. Chem. A* **102** (1998) 4543-4550.
- 27 O. Mó, M. Yáñez and J. Elguero, *J. Chem. Phys.* **97** (1992) 6628-6638.
- 28 L. Albrecht, R.J. Boyd, O. Mó and M. Yáñez, *Phys. Chem. Chem. Phys.* **14** (2012) 14540-14547.
- 29 T.M. McCleskey, D.S. Ehler, T.S. Keizer, D.N. Asthagiri, L.R. Pratt, R. Michalczyk and B.L. Scott, *Angew. Chem.-Int. Edit.* **46** (2007) 2669-2671.
- 30 B.L. Scott, T.M. McCleskey, A. Chaudhary, E. Hong-Geller and S. Gnanakaran, *Chem. Commun.* **25** (2008) 2837-2847.
- 31 S. Gnanakaran, B. Scott, T.M. McCleskey and A.E. Garcia, *J. Phys. Chem. B* **112** (2008) 2958-2963.
- 32 I. Alkorta, J. Elguero, M. Yáñez and O. Mó, *Phys. Chem. Chem. Phys.* **16** (2014) 4305-4312.
- 33 M. Hurtado, M. Yáñez, R. Herrero, A. Guerrero, J.Z. Dávalos, J.-L.M. Abboud, B. Khater and J.C. Guillemin, *Chem.-Eur. J.* **15** (2009) 4622-4629.
- 34 A. Martín-Sómer, A. Lamsabhi, O. Mó and M. Yáñez, *J. Phys. Chem. A* **116** (2012) 6950-6954.
- 35 A. Martín-Sómer, A. Lamsabhi, M. Yáñez, J.Z. Dávalos, J. Gonzalez, R. Ramos and J.C. Guillemin, *Chem.-Eur. J.* **18** (2012) 15699-15705.
- 36 O. Mó, M. Yáñez, I. Alkorta and J. Elguero, *J. Mol. Model.* **19** (2013) 4139-4145.
- 37 M. Yáñez, O. Mó, I. Alkorta and J. Elguero, *Chem. Eur. J* **35** (2013) 11637-11643.
- 38 M.M. Montero-Campillo, A.M. Lamsabhi, O. Mó and M. Yáñez, *J. Mol. Model.* **19** (2013) 2759-2766.

- 39 M. Yáñez, O. Mó, I. Alkorta and J. Elguero, *Chem. Phys. Lett.* **590** (2013) 22-26.
- 40 O. Mó, M. Yáñez, I. Alkorta and J. Elguero, *Mol. Phys.* **112** (2014) 592-600.
- 41 M.M. Montero-Campillo, M. Yáñez, A.M. Lamsabhi and O. Mó, *Chem. Eur. J.* DOI: **10.1002/chem.201304259** (2014).
- 42 J.G. Hill and X. Hu, *Chem.-Eur. J.* **19** (2013) 3620–3628.
- 43 M.R. Scholfield, C.M. Vander Zanden, M. Carter and P.S. Ho, *Protein Sci.* **22** (2013) 139–152.
- 44 M.P. Johansson and M. Swart, *Phys. Chem. Chem. Phys.* **15** (2013) 11543–11553.
- 45 *Calculation of NMR and EPR Parameters*; M. Kaupp, M. Bühl, V. G. Malkin, Eds.; Wiley-VCH: Weinheim, 2004.
- 46 J.E. Del Bene In *Calculation of NMR and EPR Parameters*; M. Kaupp, M. Bühl and V.G. Malkin, Eds.; Wiley-VCH: Weinheim, 2004.
- 47 J.E. Del Bene, I. Alkorta and J. Elguero, *J. Phys. Chem. A* **112** (2008) 7925–7929.
- 48 J.E. Del Bene, I. Alkorta and J. Elguero, *Chem. Phys. Lett.* **508** (2011) 6-9.
- 49 J.E. Del Bene, I. Alkorta and J. Elguero, *J. Phys. Chem. A* **114** (2010) 12958–12962.
- 50 I. Alkorta, G. Sánchez-Sanz, J. Elguero and J.E. Del Bene, *J. Phys. Chem. A* **116** (2012) 2300-2308.
- 51 J.E. Del Bene, I. Alkorta and J. Elguero, *J. Phys. Chem. A* **118** (2014) 2360-2366.
- 52 J.E. Del Bene, I. Alkorta and J. Elguero, *Chem. Phys. Lett.* **538** (2012) 5-9.
- 53 J.E. Del Bene, I. Alkorta, G. Sánchez-Sanz and J. Elguero, *Z. Phys. Chem.* **227** (2013) 821–838.



Author: Ana Martín Sómer
Supervisors: Manuel Yáñez
Riccardo Spezia